Assessment of Large Eddy Simulation in the Conjugate Heat Transfer context for engine operability : application to Hydrogen enrichment and Spinning Combustion Technology

Pasquale Walter Agostinelli

THÈSE

En vue de l'obtention du

DOCTORAT DE L'UNIVERSITÉ DE TOULOUSE

Délivré par :

Institut National Polytechnique de Toulouse (Toulouse INP)

Discipline ou spécialité :

Energétique et Transferts

Présentée et soutenue par :

M. PASQUALE WALTER AGOSTINELLI

le jeudi 7 avril 2022

Titre :

Assessment of Large Eddy Simulation in the Conjugate Heat Transfer context for engine operability: application to Hydrogen enrichment and Spinning Combustion Technology

---

Ecole doctorale :

Mécanique, Energétique, Génie civil, Procédés (MEGeP)

Unité de recherche :

Centre Européen de Recherche et Formation Avancées en Calcul Scientifique (CERFACS)

Directeur(s) de Thèse :

M. LAURENT GICQUEL

M. GABRIEL STAFFELBACH

Rapporteurs :

M. ANTONIO ANDREINI, UNIVERSITA DEGLI STUDI DI FIRENZE

M. RONAN VICQUELIN, CENTRALESUPELEC GIF SUR YVETTE

Membre(s) du jury :

MME FRANÇOISE BAILLOT, UNIVERSITE DE ROUEN, Président

M. DAVIDE LAERA, CERFACS, Invité(e)

M. ISAAC BOXX, DLR Stuttgart, Membre

M. JAMES R. DAWSON, NORWEGIAN UNI OF SCE AND TECHN TRONDHEIM, Membre

M. LAURENT GICQUEL, CERFACS, Membre

M. STÉPHANE RICHARD, GROUPE SAFRAN, Invité(e)

Abstract

As society evolves towards a green economy to face climate change, the combustion community is expected to develop new technologies and design low emission combustors for the aviation and energy sectors. In that respect, hydrogen is today a promising technical solution since it offers no direct CO_2 production and even when it is mixed with classical fossil fuels it helps the stabilization of leaner and greener flames. However, the development of H_2 combustion chamber is a technological challenge raising multiple questions in terms of reliability, efficiency and safety, especially for airplanes. When it comes to helicopter engines, there exists no specific pollutant emission regulation as of now and, due to their low power, helicopters are ideal testbed for new technologies. More specifically and to illustrate this ideal development context, Safran Helicopter Engines (SHE) has recently developed the Spinning Combustion Technology (SCT) gaining in engine operability and lean blow-out (LBO) capabilities.

Due to its large potential in predicting complex reactive flows, Large Eddy Simulation (LES) has proven useful to support this design challenge, whether it is oriented toward a change in fuel (H_2) or a change in combustor geometry (SCT). However, since engine operability is a very fine phenomenon given its multi-physics nature, large efforts and attention should be paid on the proper modeling of the different physics coexisting in these systems. In this work, a full assessment of high-fidelity LES models is proposed and organized in three parts.

First, main modeling challenges are addressed. As H_2-enrichment and real engine conditions yield reduced flame thickness and more stringent requirements in terms of domain discretization, a Static Mesh Refinement (SMR) approach is derived and validated on different configurations. In parallel and since real flow prediction will depend on the applied thermal boundaries, Conjugate Heat Transfer (CHT) simulations are proposed and validated on a partially premixed swirled flame, the right dynamics being correctly predicted only with a correct estimation of the heat transfer at the walls. Finally, the effect of variable transport properties, typical of H_2 mixture flows, on a swirled premixed flame is analyzed, confirming that a proper description of the chemistry and transport properties are needed when dealing with not-conventional fuel mixtures.

Second, the effects of H_2-enrichment and elevated pressure (up to 5 bar) are investigated for a swirled CH_4 flame. Both drastic changes on the flame shape and its dynamics are observed, eventually triggering thermoacoustic oscillations.

Third, the flame stabilization and the LBO dynamics in the SCT are specifically studied. CHT-LES is able to retrieve the experimentally observed dynamics when decreasing the equivalence ratio and provides better results than typical adiabatic simulations. To finish, LES is used as an industrial tool to design a new burner closer to real SCT engines.

By addressing these challenges, this work demonstrates the assessment of LES, in a CHT context, for predicting engine operability when dealing with innovative technologies and therefore highlights the central role of High Power Computing (HPC) and high-fidelity LES in the transition towards a decarbonized future.

Preface

This manuscript was submitted to the Institut National Polytechnique de Toulouse (INP) for partial fulfillment of the requirements for the PhD degree. This work was carried out at the Centre Européen de Recherche et de Formation Avancée en Calcul Scientifique (CERFACS) and at Safran Helicopter Engines (SHE), from September 2018 to November 2021. The performed work has been supervised by the thesis director Dr. Laurent Gicquel (CERFACS) and co-supervised by Prof. Thierry Poinsot (IMFT), Dr. Davide Laera (CERFACS) and Dr. Stéphane Richard (SHE). During the research activity, important cooperation was settled with research labs running experiments: Prof. James Dawson and PhD candidate Yi Hao Kwah at the Norwegian University of Science and Technology (NTNU) as well as Dr. Isaac Boxx and Dr. Ianko Chterev at the German Space Agency (DLR). During this activity, the PhD candidate was Co-Principal Investigator for the PRACE REVOLUTION Project (35M CPUh) and, with the H2OPE team, was awarded the 1^{st} place Atos – Joseph Fourier Prize 2021, an international prize rewarding scientific excellence in Advanced Computing & Artificial Intelligence, with a focus on Decarbonation. A list of the scientific articles resulting from this research activity is hereafter provided.

1. **Agostinelli, P. W.**, Laera, D., Boxx I., Gicquel, L., & Poinsot, T. (2021). Impact of wall heat transfer in Large Eddy Simulation of flame dynamics in a swirled combustion chamber. *Combustion and Flame, 234, 111728.*
2. **Agostinelli, P. W.**, Rochette, B., Laera, D., Dombard, J., Cuenot, B., & Gicquel, L. (2021). Static mesh adaptation for reliable large eddy simulation of turbulent reacting flows. *Physics of Fluids, 33(3), 035141.*
3. **Agostinelli, P. W.**, Kwah, Y. H., Richard, S., Exilard, G., Dawson, J. R., Gicquel, L., & Poinsot, T. (2020). Numerical and Experimental Flame Stabilization Analysis in the New Spinning Combustion Technology Framework. In *Proceedings of the ASME Turbo Expo 2020: Turbomachinery Technical Conference and Exposition, GT2020-15035.*
4. Laera, D., **Agostinelli, P. W.**, Selle, L., Cazères, Q., Oztarlik, G., Schuller, T., Gicquel, L., & Poinsot, T. (2020). Stabilization mechanisms of CH4 premixed swirled flame enriched with a non-premixed hydrogen injection. *Proceedings of the Combustion Institute. 38(4), 6355-6363.*
5. **Agostinelli, P. W.**, Laera, D., Boxx I., Gicquel, L., & Poinsot, T. (2021). On the impact of H2-enrichment on flame structure and combustion dynamics of a lean partially-premixed turbulent swirling flame. *Combustion and Flame, 241, 112120.*
6. **Agostinelli, P. W.**, Laera, D., Boxx I., Gicquel, L., & Poinsot, T. (2021). Large Eddy Simulations of mean pressure and H2 addition effects on the stabilization and dynamics of a partially-premixed swirled-stabilized flame. *Combustion and Flame - submitted.*
7. **Agostinelli, P. W.**, Kwah, Y. H., Richard, S., Exilard, G., Dawson, J. R., Gicquel, L., & Poinsot, T. (2021). On the Lean Blow-Out dynamics in the Spinning Combustion Technology. *Combustion and Flame – submitted.*
8. Kwah, Y. H., **Agostinelli, P. W.**, Richard, S., Exilard, G., Pascaud, S., Gicquel, L., & Dawson, J. R. (2022). Ignition Dynamics of a Laboratory-Scale Spinning Combustor. *Journal of Engineering for Gas Turbines and Power - accepted. Presented at ASME Turbo Expo 2022.*

Acknowledgements

First of all, I would like to express my sincere gratitude to Prof. Antonio Andreini and Prof. Ronan Vicquelin for reviewing this thesis manuscript and providing valuable feedback on its technical content.

Je tiens à remercier mes directeurs de thèse Dr. Laurent Gicquel et Prof. Thierry Poinsot pour le soutien continu de mon étude et de mes recherches, pour leur patience et leurs immenses connaissances. Leurs conseils m'ont aidé tout au long de la recherche et de la rédaction de cette thèse.

Les mots seuls ne peuvent exprimer ma gratitude envers mon encadrant industriel, Dr. Stéphane Richard, sans sa motivation et ses encouragements je n'aurais pas terminé ce travail. Ses commentaires perspicaces et ses questions difficiles m'ont incité à élargir mes recherches sous divers angles. De même, Dr. Gorka Exilard m'a beaucoup aidé au début de ma thèse et je veux le remercier pour son soutien.

Un ringraziamento molto speciale va al Dr. Davide Laera, con cui gran parte del lavoro in questa tesi é stato portato avanti. Senza dubbio, il suo supporto e le innumerevoli discussioni e sfide che abbiamo affrontato in questi anni sono stati di fondamentale importanza per la mia attività di ricerca.

Je tiens également à remercier les seniors du CERFACS Dr. Gabriel Staffelbach, Dr. Florent Duchaine et Dr. Jerome Dombard pour leurs conseils techniques trés utiles liés au HPC et aux codes.

Mon séjour au CERFACS n'aurait pas été si agréable sans l'aide de Chantal Nasri, Michelle Campassens, Marie Labadens, Lydia Otero et Séverine Toulouse. Elles m'ont aidé dans toutes les démarches administratives avec beaucoup de gentillesse, de disponibilité, et toujours avec le sourire. Un grand merci aussi à la meilleure équipe du CERFACS, l'equipe CSG: Isabelle d'Ast, Gérard Déjean, Fabrice Fleury et Fred Blain. Ils ont toujours été disponibles et leur réponses rapides et précises m'ont beaucoup aidé lors des difficultés techniques.

Contents

Chapter 1

Introduction

Contents

This chapter introduces the performed work, presenting the industrial and research context in which it has been carried out. The relevance of combustion is depicted together with the linked burning environmental issues. The latter indeed push for a revolution in the combustion science and new technologies are being developed or becoming of interest not only for research purposes but also for industrial applications. On one side, hydrogen, also in combination with classical fuels, is seen as a possible solution to reduce the carbon footprint of the energy and aeronautical sectors. On the other side, Spinning Combustion Technology is being developed as an industrial operative solution to increase the operability of real helicopter engines. In this context, the role of numerical simulations in the research analysis as well as in the industrial design phase of these new technologies is presented while the objectives and organization of the thesis are detailed.

1.1 Combustion: the past or the future?

Combustion is a chemical reaction that involves the oxidation of a fuel by an oxydant with the release of heat and electromagnetic radiation: it is usually accompanied by the presence of a flame and high-temperature gases produced by the chemical reactions. The use of the combustion process has been shaping the history of human kind: from 1.5 million of years ago, when the control of fire by the first men was a turning point in human cultural evolution, up to the industrial revolution in the 18^{th} century, when for the first time coal was used as fuel to produce energy and mechanical power through steam engines.

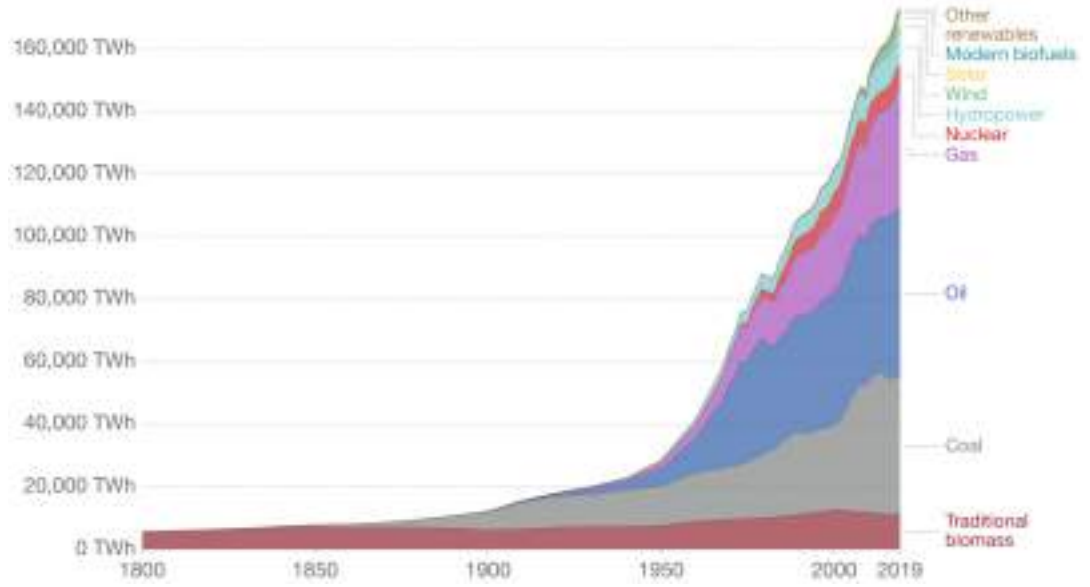

Figure 1.1: Global primary energy consumption by source since the industrial revolution [1, 2].

Since the industrial revolution, the global energy system has drastically changed together with the evolution of technology and society, especially in the last century after the second world war during the economic boom. This transformation is evidenced in Fig. 1.1, presenting the global energy consumption from 1800 onwards. The latter is based on historical estimates using the substitution method accounting from fuel inefficiency from Smil [2] and from data published in the BP's Statistical Review of World Energy [1]. Clearly, the global energy demand has grown exponentially in the past two centuries. At the same time, a significant change in the sources of energy can be observed: while before 1950, coal and traditional biomass were the principal sources, afterward, oil and gas started to supply the increase of energy demand. Only recently, renewable energy sources

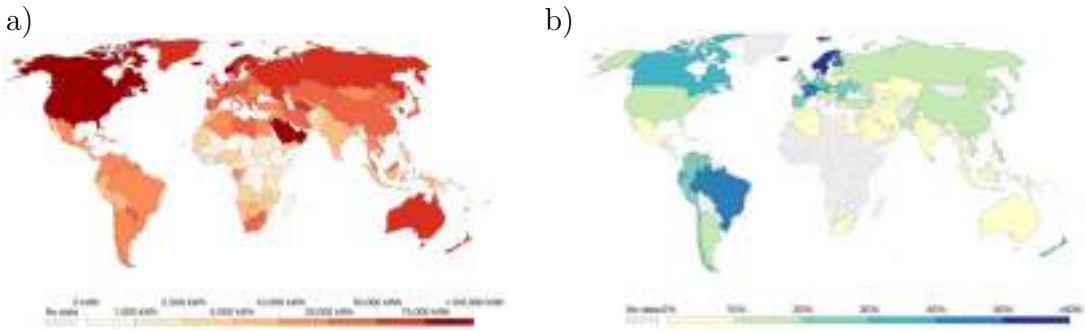

Figure 1.2: Global map presenting (a) the energy use per person and (b) the share of primary energy from low-carbon sources across countries in 2019 [1, 2].

have increased their relevance in the global scenario, with nuclear and hydropower sources being the first to be developed.

However, the increase in global energy demand is not geographically distributed in a homogenous way. Figure 1.2(a) presents a global map showing the per-capita energy use in 2019 [1, 2]. The per-capita map is more useful than the total countries consumption since the latter shows differences across countries that reflect the differences in population size more than differences in people customs. As expected, the most developed and rich countries are the largest energy consumers reaching up to 100 MW, including for example United States, Canada and rich nations in the Middle East: the average person in these countries has a need of energy that is 100 times the one of the average person living in the poorest countries. This vast difference in global consumption reveals that the habits and customs of the most developed countries have been responsible for most of the global energy demand increase in the last century.

Despite being the largest energy consumer, the most developed countries have recently put their attention on burning environmental issues such as global warming, climate change and pollution. As a consequence, significant development of low-carbon energy sources has been facilitated and encouraged. Figure 1.2(b) presents the 2019 data about the share of primary energy from low-carbon sources defined as the sum of nuclear and renewable sources: the latter comprise solar, wind, hydropower, geothermal, wave as well as tidal and bioenergy while traditional biofuels are not included. The most low-carbon sources users are Iceland, with up to 79% originating from hydropower and geothermal energy, Sweden and Norway (up to 69% and 66% respectively), followed by France (49%) with a large amount of nuclear energy. Developed countries such as United Kingdom and Germany use up to 20% of low-carbon sources while Italy and United States stop at around 16% [3]. On the contrary, developing countries and emerging economies,

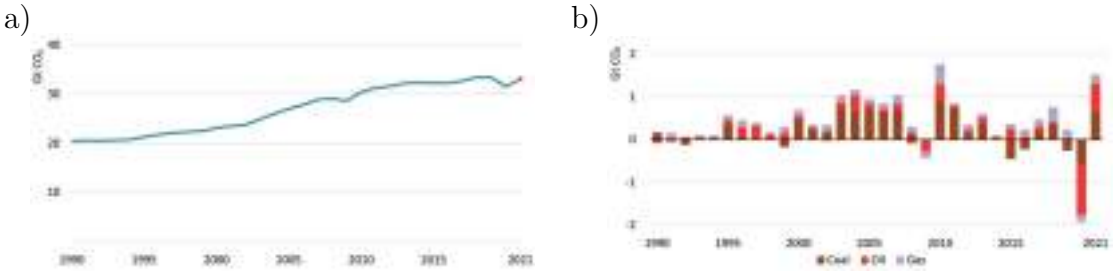

Figure 1.3: Global (a) energy-related CO_2 emissions and (b) change in CO_2 emissions by fuel in the period 1990-2021 [4].

such as India and South Africa produce lower amount of eco-friendly energy, facing at the same time social and economic issues arising with the evolution of society.

Even if large efforts have been devoted to reduce the carbon footprint in the last years, the global situation does not leave space to positive hope. Figure 1.3(a) presents the global energy-related CO_2 emissions in the period 1990-2021 as published in the last Global Energy Review 2021 by the International Energy Agency that aims at assessing the effects of economic recoveries on global energy demand and CO_2 emissions [4]. Clearly, CO_2 emissions have been continuously increasing in the last years, despite the larger use of low-carbon energy sources, reaching a peak of 31.5 Gt in 2019 with an average concentration of 412.5 parts per million in 2020, a value 50% larger than when the industrial revolution began. Two small declines are visible in 2009 and 2020 as a consequence of the global financial crisis and of the Covid-19 pandemic respectively. Despite that, global CO_2 emissions are forecast to rebound and continue to increase overwhelming the 2019 peak by 2022.

Figure 1.3(b) helps visualize the trend of change in CO_2 emissions by fuel in the same period. Clearly the strong increase of CO_2 emissions in the early 2000's was mainly due to coal combustion that however has been reduced in the last years. At the same time, the negative trend in 2020 was mainly due to the global lower demand of oil due to the pandemic. Briefly, CO_2 emissions due to combustion of coal, oil and gas are projected to continue increasing in the next years while the current low-carbon energy sources development is not sufficient to supply the increase in global energy demand.

Therefore, to achieve the ambitious goal of net zero carbon emissions by 2050 and to limit the rise in global temperatures to 1.5 °C, the gap between rhetoric and actions must be cleared. The International Energy Agency recently proposed a roadmap for the Global Energy Sector [5] in which it illustrates the fundamental steps needed to reach net zero carbon. Figure 1.4 presents the key milestones in

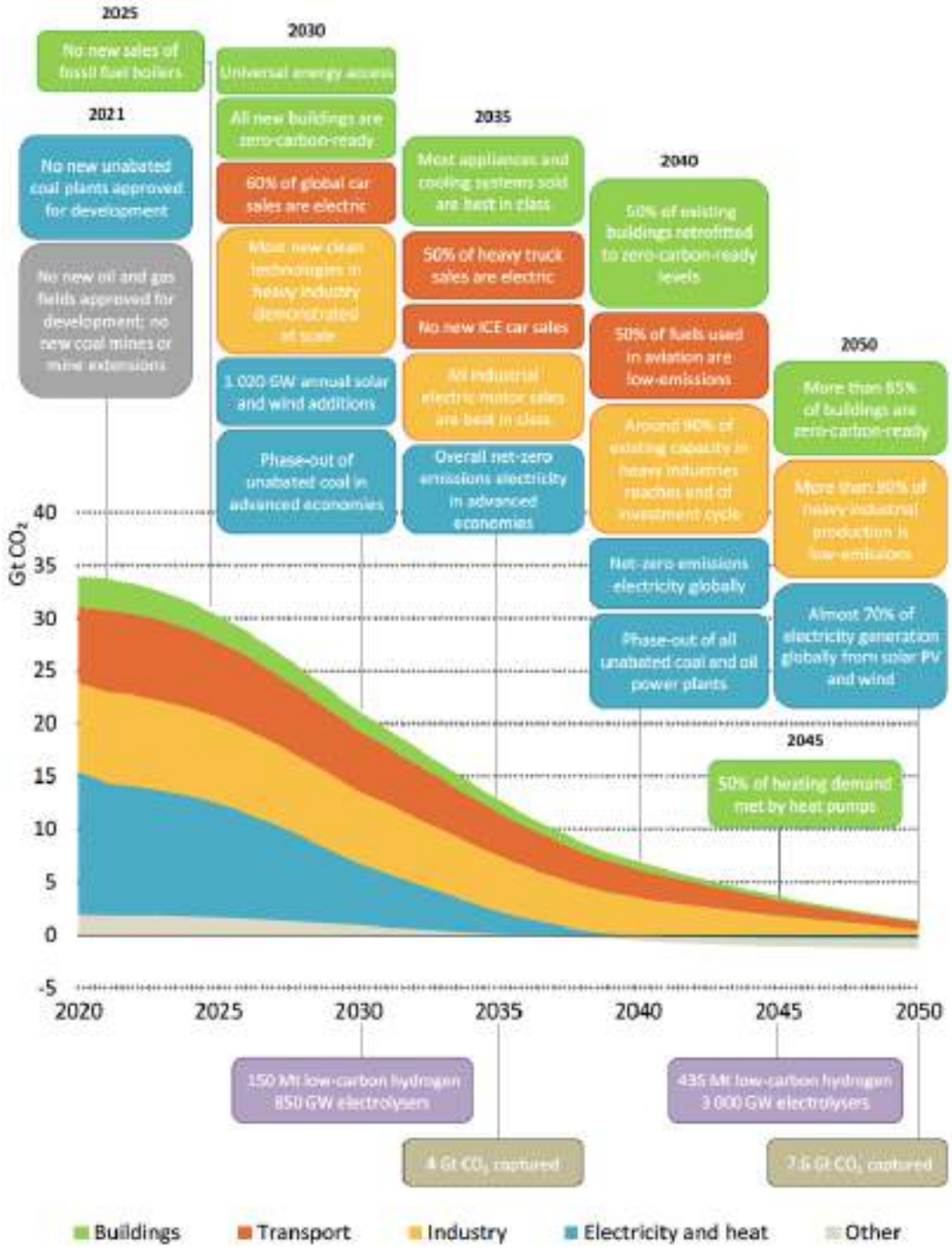

Figure 1.4: Key milestones in the pathway to net zero carbon emissions by 2050 as suggested by the International Energy Agency in his Roadmap for the Global Energy Sector [4].

this ambitious pathway together with the projected Gt of CO_2 emissions for the different sectors: buildings, transport, industry, electricity and heat. In this plan, starting from now, no new coal/oil/gas plants should be approved for electricity production and around 1000 GW produced by solar and wind should be added

annually. In this way, the overall net-zero emissions electricity would be achieved in advanced economies in 2035, while by 2050 almost 70% of electricity generation would be supplied by solar and wind sources. For industry, that accounts for almost 10 Gt of CO_2 emissions nowadays, most new clean technologies in heavy production should have been demonstrated at scale by 2030: in this way, by 2050, more than 90% of heavy industrial production would be low-emissions. For buildings, no new fossil fuel boilers should be sold starting in 2025. Likewise most appliances and cooling systems sold by 2035 should be best in their class. Last but not least, the transport sector that is responsible for around 8 Gt of CO_2 emissions, should be rapidly shaped by a large amount of electric cars and heavy trucks while making enormous progresses in the aviation sector for which the 50% of fuels used should be low-emissions by 2040.

To conclude, the pathway toward net zero carbon emissions should involve all the energy sectors and requires large technology development and international co-operation among different countries. In this context, while global consumption of classical carbon fuels such as oil, coal and gas is supposed to be strongly reduced in the next years, combustion of low-emission fuels would become a key strategy to reduce carbon emissions, especially in the transport and industry sectors. Therefore, combustion science, which has been shaping the history of human kind in the past centuries, is now expected to drastically evolve in order to give a green future to the next generations: would we be able to accept and overcome this challenge?

1.2 Decarbonize Aviation: Hydrogen for net zero carbon emissions

In the pathway toward net zero carbon emissions proposed by the International Energy Agency, one of the key sector that should be drastically affected is the transport that accounts for 8.5 Gt of CO_2 emissions in 2019, before the Covid-19 pandemic. While electric cars are already on the market starting changing the road transport sector, decarbonization of aviation still remains a major challenge because of the need to rapidly develop new fuels and propulsion technologies that usually have a time to market of decades. In 2019, the European Commission published its Green Deal with the objective of net zero carbon emissions across all sectors by 2050, including aviation. This specific objective and timing clearly puts much more pressure than the target proposed by the Air Transport Action Group (ATAG) that aimed at a 50 % reduction of CO_2 emissions by 2050 with respect to the 2005 levels.

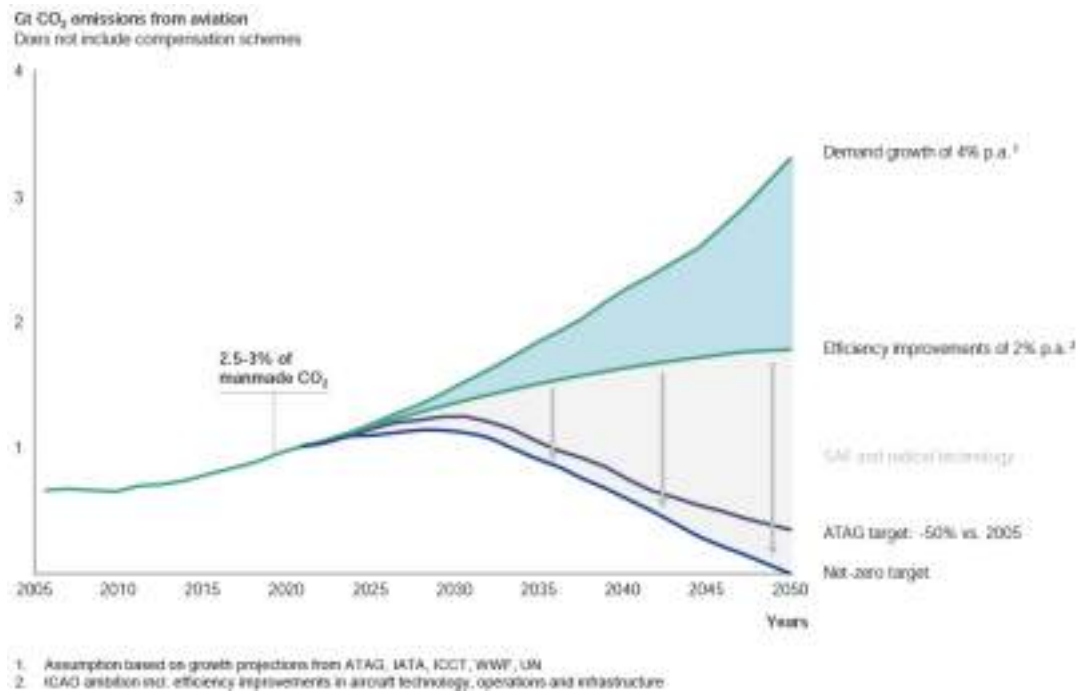

Figure 1.5: Projection of CO_2 emissions from the aviation sector as forecasted by McKinsey & Company in 2020 [6].

Figure 1.5 presents the projection of CO_2 emissions from the aviation sector as forecasted by McKinsey & Company in 2020 in their fact-based study of hydrogen technology, economics, and climate impact by 2050 that was sponsored by more than 20 industrial partners [6]. Nowadays, aviation accounts for 3% of global CO_2 emissions. But pollution is not only about CO_2: aeronautical engines also emit NO_x, water vapor and soot. While CO_2 remains for 50-100 years at high altitudes, NO_x stays only for some weeks but enhance ozone and results to be as dangerous as CO_2 emissions. On the other side, water vapor is also a strong greenhouse gas: its effects are weaker with respect to CO_2 but, in combination with soot, it causes also the formation of contrails and cirrus. Even if it is difficult to compute the total effect of classical fuels aeronautical engines, it is possible to estimate the impact on the climate in equivalent CO_2 emissions based on the concept of Global Warming Potential (GWP). This leads to a new estimation of the aviation impact on climate change, accounting for up to 7% of the global CO_2 equivalent emissions, making its revolution a key strategy in the pathway toward decarbonization. Indeed, if no action is pursued toward this direction, aviation will account for more than 3 Gt of CO_2 emissions by 2050 considering a demand growth of 4% (but not the pandemic due to Covid-19). Even if the efficiency improvements due to research and developments of current engines are taken into account, a final projection of 2 Gt of CO_2 is reached, that is twice the

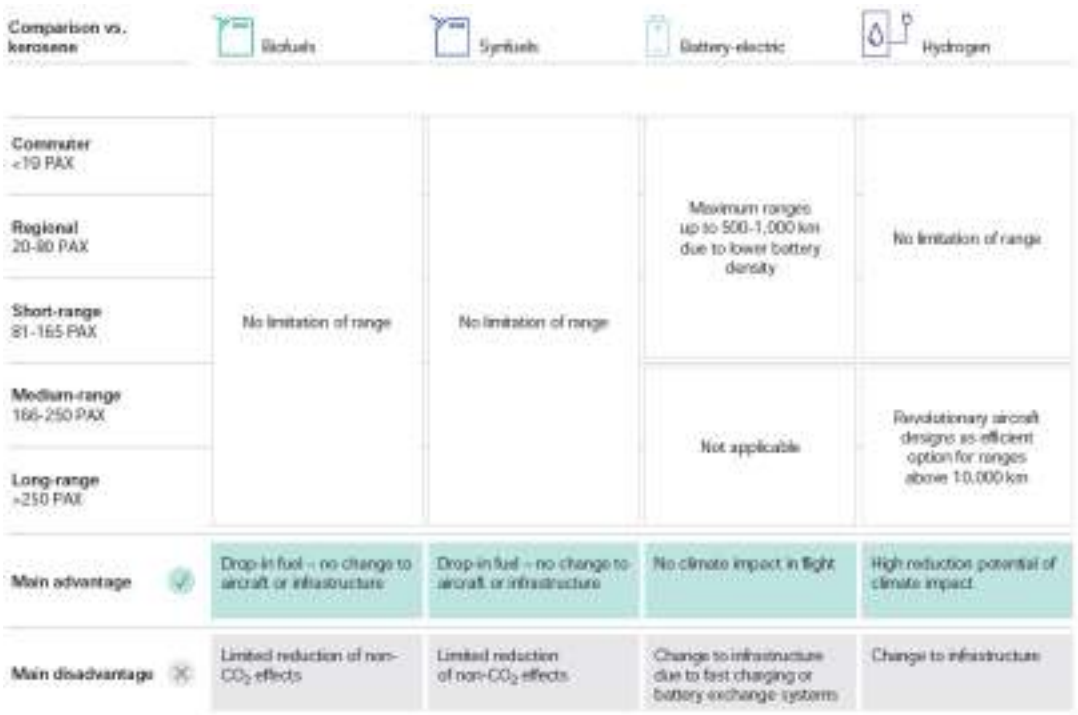

Figure 1.6: Comparison of new technologies and sustainable aviation fuels [6].

current levels and an extremely high level with respect to the ATAG target or to the zero net carbon emissions EU target.

Different fuels and technologies have been analyzed, as depicted in Fig. 1.6. First sustainable aviation fuels (SAF) are considered. Biofuels (e.g. HEFA) are produced from biomass, waste or crops/algae: these are the furthest developed environmental-friendly fuels but have the main disadvantage of not strongly reducing the CO_2 emissions. The other alternative considered by the study is Synfuel (i.e. synthetized fuel): electricity is used to first produce hydrogen and to capture carbon, then combining the two into a kerosene-like fuel (power-to-liquid). The main advantage of such an alternative is that it suits current aircraft and fuel infrastructure while the principal drawback is the limited reduction of non-CO_2 effects. On the other side, hydrogen can be combusted as a fuel in an engine or reacted in a fuel-cell powering electric motors, drastically reducing the impact of aviation on climate. However, also in this case, a strong revolution of the infrastructure is required and should be sustained by large efforts in research and development. Note that green hydrogen is considered as the starting point of both the last two fuels, namely it is supposed to be produced via electrolyze from renewable energy[1]. At the same time, also battery-electric and hybrid-electric

[1]Note that in 2020 more than the 90% of hydrogen produced in Europe was "gray", that is produced by fossil fuels. Therefore large efforts should be devoted to increase the amount of

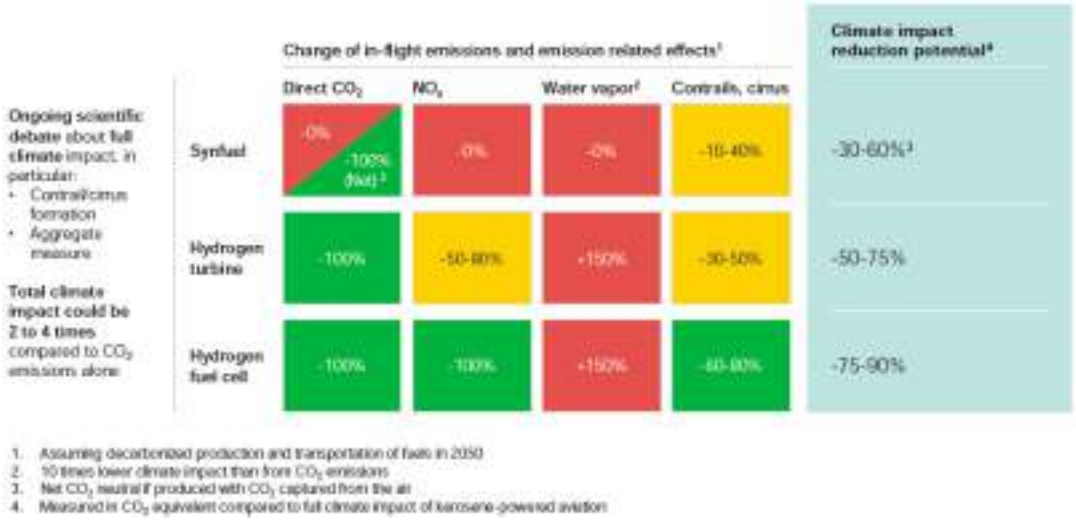

Figure 1.7: Comparison of climate impact from H_2 propulsion and synfuel [6].

aircraft have been considered: even if battery technology has greatly improved in the last decades, the main issue remains the low energy density (i.e. low power/kg ratio) with respect to hydrocarbon fuels, making the battery-electric option to be feasible only in the short-range segment.

Figure 1.7 presents the comparison of climate impact from H_2 propulsion (fuel cells and turbines) and synfuel in order to asses the change of in-flight emissions for those new technologies. When it comes to synfuel, the in-flight CO_2 emissions is about the same amount of kerosene in the exhaust gas but depending on how you count it results in a 0% decrease if carbon is captured from an industrial process or -100% less CO_2 if carbon is captured from direct air capture. On the contrary, NO_x emissions and water vapor are expected to remain largely unchanged but, since synfuel comes with fewer aromatics, soot is less likely to be produced therefore less contrails are formed. H_2 combustion instead does not release CO_2 in flight. Moreover, it is likely that H_2 will be burnt in leaner conditions because it has a wider flammability limits and hence will have a lower adiabatic flame temperature with a higher reaction rate and a faster mixing rate as well as a lower residence resulting in a lower production of NO_x if compared to kerosene or synfuels. On the contrary, H_2 produces 2.5 times more water vapor compared to kerosene for the same energy content. The same happens for hydrogen fuel cell, except that there is no emission of NO_x in the reaction of H_2 and water vapor is assumed cooler which results in less contrails and cirrus formation at high altitude. Therefore, aircraft using fuel cell systems are the best option to reduce climate impact, immediately followed by H_2 turbines.

green hydrogen produced.

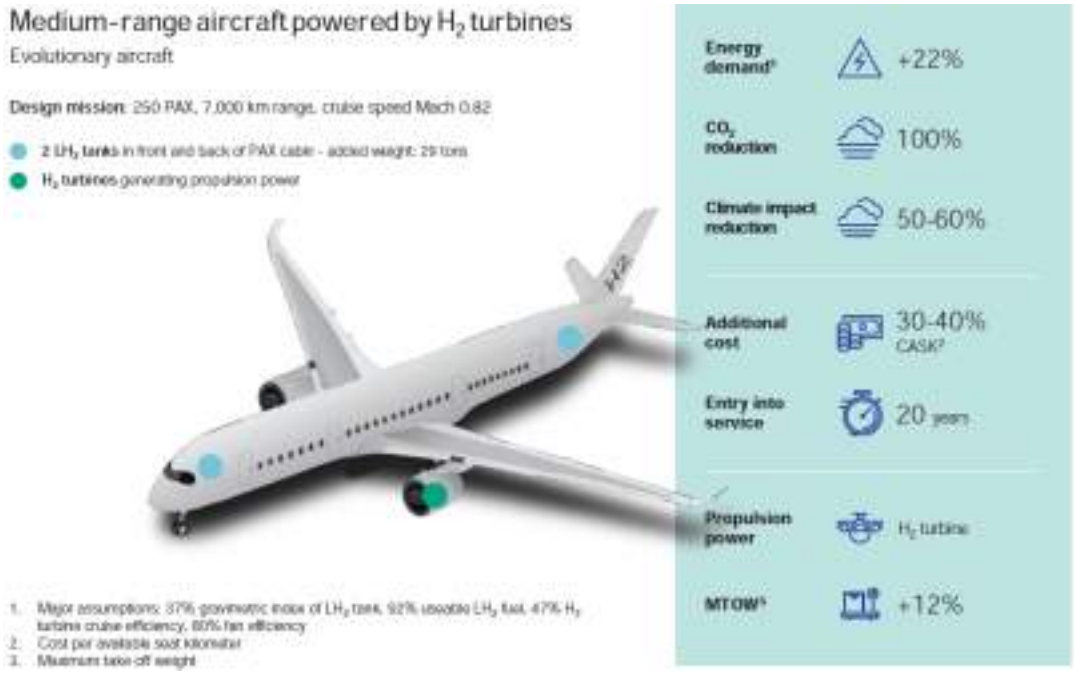

Figure 1.8: Projected feasibility and cost of a medium-range aircraft powered by H_2 turbines by McKinsey & Company in 2020 [6].

As a consequence, hydrogen fuel cells have been considered as the best option for commuter and regional aircrafts up to the 1000 km range. However, for medium ranges and high cruise speeds, the new heavier propulsions based on fuel cells could not be feasible since they increase the aircraft's energy and power requirements with their correlated cooling requirements. Therefore, H_2 turbines have been considered as the best option for this range, as shown in Fig. 1.8. In this design, fuselage would be extended by about 10 m to integrate the two liquid H_2 tanks behind and in front of the passenger cabin: main issues would be to carry the weight of the hydrogen tanks over the long flight distance and safety issues around reliable in-flight LH_2 distribution from tank to engines. For these reasons, the long-range segment would be more reasonably propelled by synfuels instead of H_2 turbines.

Finally, the research and innovation roadmap for decarbonizing aviation is shown in Fig. 1.9. The process involves the development of technology fundamentals, the scaling-up of these technologies to mid-range aircraft and finally the development of first prototypes of new aircraft concepts. Before developing full aircraft systems and infrastructures, research should be carried out on different aircraft components. First, effort should be put for developing lightweight and safe LH_2 tanks. Second, fuel cells should be improved in terms of system scaling (i.e. increase power density, optimize cooling and weight) and in terms of reliability of the components (i.e. extended lifetime). Finally, H_2 turbines should

Figure 1.9: Research and Innovation roadmap for decarbonizing aviation [6].

be developed, especially in terms of new design for H_2 combustion chambers, cryogenic compressors, control systems to regulate fuel flow to reduce NO_x and cooling system. To conclude, this study showed the enormous potential of hydrogen propulsion to reduce aviation's climate impact, whether it is used in fuel cells or H_2 turbines directly[1].

In the above pathway, the development of H_2 combustion chamber is a major technological challenge: hydrogen is an extremely light molecule, presents large diffusivity and when it burns shows high adiabatic flame temperature and a flame speed which is up to ten times larger than classical hydrocarbons, potentially enhancing the risks of premature failure of system components or explosions which raise multiple questions in terms of reliability, efficiency and safety. Despite that issue, when it is mixed with classical fossil fuels, hydrogen is expected to help the stabilization of leaner and greener flames thanks to the larger flammability limits and higher reactivity. Therefore, it has also the potential to improve the current operating limits of lean combustors that have been already developed in the past decades to reduce pollution and improve efficiency [7, 8]: these lean combustors indeed usually present operability issues, such as thermoacoustic instabilities

[1]It is interesting to mention here that hydrogen could be also a relevant solution for storing energy from renewables: it can be produced via electrolysis when energy supply is larger than the demand, and it can be burnt in H_2 turbines to get back electricity when energy demand is higher than production.

a) b)

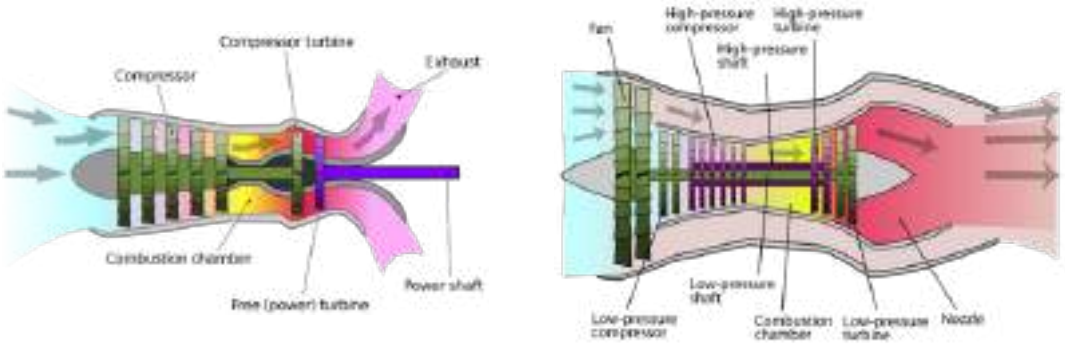

Figure 1.10: Schematic diagram showing the operation of (a) a turboshaft engine used in most helicopters and (b) a turbofan engine for commercial aircraft applications.

[9, 10, 11, 12, 13], lean blow-off [14, 15] and extinctions [16, 17]. For these reasons, large efforts are being devoted to the analysis of hydrogen combustion also in combination with classical hydrocarbon fuels and different international research projects have been funded by the European Union (such as ENABLEH2, CLEANSKY, MAGISTER, ANNULIGHT) to understand more about lean combustor operability and hydrogen injection effect, with the hope to achieve the ambitious but incumbent net zero carbon target.

1.3 Helicopter Engines' Operability: the Spinning Combustion Technology

When it comes to helicopter engines, due to the reduced number of flying helicopters and their missions' duration compared to aircrafts, there exists no specific pollutant emission regulation. However helicopters are on the first line along the pathway for zero net carbon emissions in aviation: thanks to their low power needs and small size compared to most fixed wing aircraft, helicopters are the ideal testbed and prototypes for new technologies, and lessons learned can be successively extended to larger applications. Different solutions are being tested and developed nowadays: from reducing the pollutant emissions of classical thermal engines to hybrid-electric helicopters.

Most medium-high power helicopters rely on turboshaft engines, Fig. 1.10(a), that are conceptually similar to turbofan (turbojet) engines implemented on most commercial (military) aircraft, Fig. 1.10(b). The only main difference is the presence of a free turbine that powers the helicopter blades through the shaft and the gearbox. In the turboshaft, first, a multistage compressor slows down the air and increases its pressure up to 15 times the atmospheric pressure. Second, the combustion chamber is designed to inject the right amount of fuel and to

a) b)

Figure 1.11: Airbus H160 equipped with the SCT Arrano engine developed by Safran Helicopter Engines and presenting 15% of reduced fuel consumption.

promote an efficient combustion process. Then, the hot gases expand through a first turbine that drives in this way the compressor and finally through a power (free) turbine that extracts part of the flow energy and powers the shaft. A first gearbox in the turboshaft allows for reduction of the free turbine speed (around 30'000 rpm) to approximately 5000 rpm. An additional gearbox then connects the shaft to the helicopter blades for further reducing the rotational speed (to some hundreds rpm) that otherwise would induce aerodynamic problems at the blade tips (e.g. shocks). The operation of a turbojet engine is equivalent except that there is no power turbine to drive the shaft and the flow is left to expand in a convergent nozzle to increase its kinetic energy and push the plane forward thanks to the law of action and reaction. In most commercial aircraft, a more complex version of the turbojet is used, namely the turbofan. In this case, Fig. 1.10(b), part of the incoming air is deviated and slightly compressed through a fan, driven by a low pressure turbine, and is not used for providing hot gases. The remaining part of the air passes instead through the core that is a turbojet engine. The fan has been introduced some decades ago to reduce the fuel consumption for the same thrust and hence the cost and the pollutant emissions of aircrafts. The bypass ratio (BPR) of a turbofan engine (i.e. the ratio between the mass flow rate passing through the fan to the one entering the core) is usually higher for commercial aircrafts and lower (up to 0, i.e. turbojet) for military applications, for which a tradeoff between fuel consumption and requirements of combats has to be chosen.

Despite the use of a fan, the shaft or different number of turbines and compressors, the core of all the aeronautical engines remains the combustion chamber that is conceptually equal for all the configurations. Therefore, research and development on helicopter engines can be easily extended to larger aeronautical engines, especially for what regards the combustion process.

a) b)

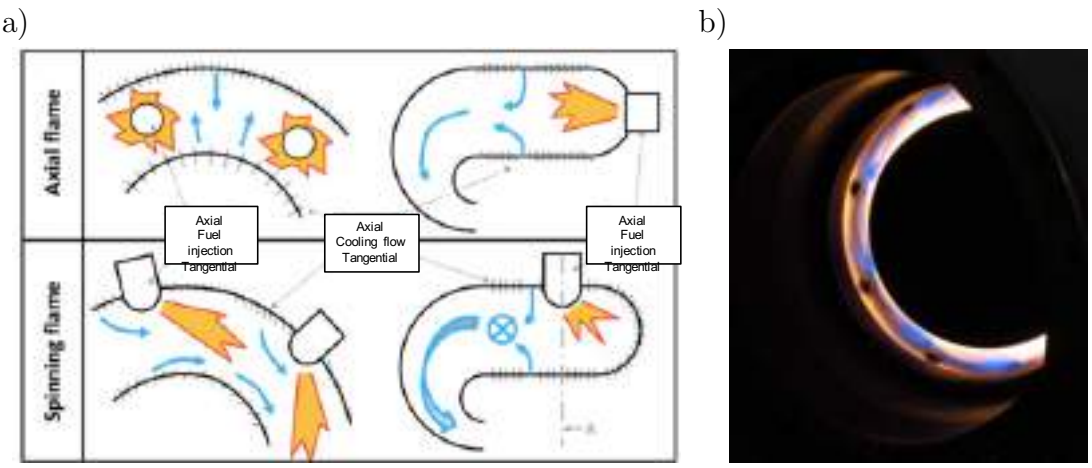

Figure 1.12: (a) Comparison between conventional axial combustion and spinning flame combustion concepts and (b) example of Lean Blow Off test at Safran Helicopter Engines facility [18].

In this context, Airbus has recently certified its new H160, Fig. 1.11(b), which is the cleaner and quieter helicopter of its class, initiating the pathway for a reduced carbon footprint in helicopter operations and achieving a 15% reduction in fuel consumption. The core of this new helicopter is the Arrano engine produced by Safran Helicopter Engines, Fig. 1.11(a), that is equipped with the recently developed and patented Spinning Combustion Technology (SCT) [18]. From an operational and construction point of view, SCT uses a lower number of injectors, with savings in cost and weight larger than 40%. It also leads to savings in maintenance costs because the injectors are placed on the external crankcase of the engine: time of maintenance and respective ground time are therefore reduced.

Figure 1.12(a) presents a comparison between a conventional axial combustion and the spinning flame combustion concepts. The innovation point of this technology is to introduce a strong azimuthal flow in the annular chamber that enhances flame-flame interactions so as to improve ignition and lean blow-off (LBO) capabilities, Fig. 1.12(b), while also improving stability over a wide range of operating conditions. Note that although swirling flows are typical nowadays in the combustion community for single injectors and have been extensively studied in the literature [19, 20], "global" swirling flow is much less frequent when it comes to aeronautical applications (e.g. Short Helical Combustor [21], CHAIRLIFT combustor [22]) and clear needs of understanding appears since the physical phenomena involved are multiple and complex combining fluid mechanics, acoustics, combustion, heat transfer and nonlinear system dynamics. In this regard, several open questions need to be answered: where does the enhanced thermoacoustic stability comes from in SCT? How are LBO capabilities improved? Are we able to correctly analyze and predict flame-wall interactions in these combustors and

their effect on operability? How can we extend the operability of a lean combustor? How can we use this know-how to improve classical lean combustors? Note also that, current state of the art for helicopter engines involves the use of rich burners instead of lean combustors technologies because of the stringent certification requirements in terms of ignition and lean-blow off capabilities, leading to a limited impact on pollutant emissions, in particular soots. Since SCT has shown improved capabilities in these terms, Safran Helicopter Engines has the ambition in the future to propose SCT for leaner combustors in order to find a tradeoff between lean blow off capabilities and emissions. SCT has been defined as the future of aeronautical engines and a key step toward net zero carbon emissions: being able to fully master this technology now means that associated industrial design projects will gain significant maturity and years of progress prior to market.

1.4 Role of numerical simulations

Despite the climate change emergency, the development of low-emission gas turbine combustors still remains a major design challenge for propulsion and land-based power generation applications. Indeed, multiple numerical and experimental studies have been carried out, showing that lean combustors typically present various and undesirable flame dynamics issues, such as thermoacoustic oscillations [11, 23, 24, 25] or lean blow-off (LBO) [14, 15, 26] that strongly affect engines' operability. If one tries to understand more about the flame dynamics in engines, he/she will find huge practical problems since there is limited access to measurements during engine operation. This makes the industrial design phase and the academic analysis processes even more difficult.

To support this design challenge, different experimental test benches have been built and operated in the past decades in order to analyze the combustion process and understand more about these issues. On these test benches indeed, different diagnostics are available to acquire data about reacting flows such as OH-Planar Laser Induced Fluorescence, OH* chemiluminescence, Particle Image Velocimetry or pressure recordings [27, 28, 29]. Coupled with such advanced diagnostics, experiments have been fundamental in the past decades to design lean combustors and understand the fundamental of the classical flame dynamics issues. However, despite the increasing number of available diagnostics, usually experimental data do not completely reveal the entire flow field variables in the whole combustor and analysis of geometry effect can be long and expensive due to the need of building new mechanical part each time. Therefore, together with experiments, Computational Fluid Dynamics (CFD) has been used to better

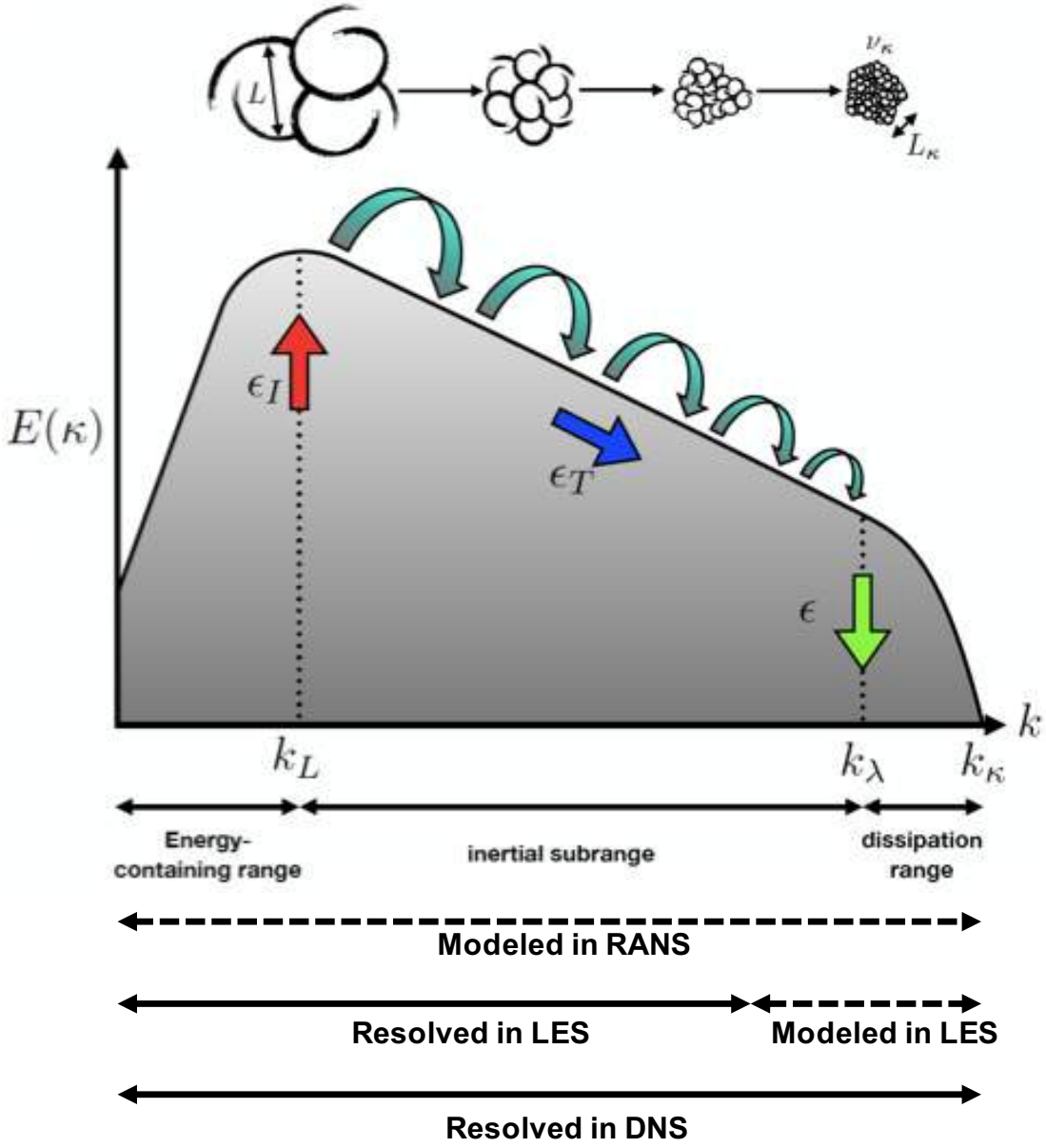

Figure 1.13: Turbulent kinetic energy spectrum showing the resolved and modeled scales for RANS, LES and DNS.

understand fluid mechanics since the 60s, when the simultaneous development of numerical methods to discretize the Navier-Stokes equations and the improvement of computational performances had place.

The Navier-Stokes equations are indeed a set of partial differential equation, formulated by Claude Navier and George Stokes in the XIX century, that describe the motion of a viscous fluid. Three different strategies are possible to approach these equations in CFD methods, Fig. 1.13, based on the way the flow scales of turbulent are resolved or modeled: Reynold's Averaged Navier-Stokes Equations (RANS), Large Eddy Simulation (LES) and Direct Numerical Simulation

(DNS) [30, 31, 32].

In RANS, the Navier-Stokes equations are averaged in time, leading to steady non-linear equations that describe the mean flow properties. As a consequence, no information about the unsteady turbulent evolution of the flow can be predicted. On top of that, due to the well-known closure problem in turbulence modeling caused by the presence of non-linear terms arising when time averaging the equations, additional models should be introduced to account for the turbulent kinetic energy cascade that involves the transfer of energy from large scales of motion to the small scales. Figure 1.13 presents the turbulent kinetic energy spectrum as a function of the characteristic length of the eddies: in RANS all the scales of turbulence are modeled, from the largest ones up to the dissipation range. In this context, also Unsteady formulation of the RANS equations (URANS) has been proposed, providing good prediction of the transient flow evolution in time when subject to time-dependent boundary conditions or transient phenomena. However, also in this formulation, the turbulent energy cascade is modeled from the inertial subrange to the dissipation one.

On the contrary, DNS solves the full Navier-Stokes equations and is able to resolve all the scales of turbulence without the need of modeling them. The main issue regarding this approach is the cost that makes it unfeasible for analyzing complex flow or for industrial applications. Indeed, to resolve all the turbulence scales, the spatial discretization of the computational domain should be as refined as the Kolmogorov scale. The latter being proportional to the integral length scale of the flow scale following $Re^{9/4}$ (i.e. Reynolds number), it is evident that the requirements in terms of spatial discretization become rapidly impractical as the Reynolds number increases. This is typically the case of industrial applications, for which unfeasible High Performance Computing (HPC) resources would be needed for carrying out DNS. For this reason, DNS are typically used nowadays for academic flow problems at low Reynolds number to get more insights about flow turbulence.

LES is placed in the middle of the two above mentioned approaches. In LES, the Navier-Stokes equations are spatially filtered, leading to additional non-linear terms like in RANS. As opposed to RANS however, these terms refer only to the small flow scales linked to turbulence dissipation and, according to the Kolmogorov theory, they result to be statistically similar for all the type of flows and hence can be more easily modeled through sub-stresses grid (SGS) models. On the contrary, large turbulent scales that strongly depend on the flow problem taken into consideration are correctly resolved by LES without any model. In this way, LES is able to predict the unsteady evolution and the main turbulent

activity of the flow, while modeling only the turbulent dissipation happening at the smallest scales.

In the present work, LES are preferred over the cheaper options like RANS or the unaffordable DNS since it gives a better accuracy over URANS while keeping a modest computational cost compared to DNS. Indeed, the LES approach has been mainly used in the combustion community for the analysis of practical flow configurations because of its ability to accurately predict the interactions between turbulent flow, spray and flame for stabilized flames [19, 33] or even pollutant emissions [34, 35, 36, 37]. However, since the engine operability is a very fine phenomenon given its multi-physics nature, large efforts and attention should be paid on the proper modeling of the different physics coexisting in these systems. Therefore, LES can be a strategic key to help design innovative lean combustors but the assessment of its accuracy and results is a mandatory first step.

1.5 Objectives and organization of the thesis

From the presented social, academic and industrial context, it clearly appears that the development of new low-carbon combustion technologies is a climate emergency today and the LES approach can be useful to support this design challenge, whether it is oriented toward a change in fuel (e.g. hydrogen) or a change in combustor geometry (e.g. SCT). In this regard, a full assessment of the high-fidelity LES approach and the proposed models is here proposed and organized following three main key questions:

- Which developments and methods are needed for LES to support the design challenge of low-carbon combustion technologies?
- Is it possible to analyze the effect of Hydrogen enrichment on classical hydrocarbon flame dynamics?
- Can we study the Spinning Combustion Technology to get more insights on the improved operability capabilities?

To completely address these key questions, this thesis is structured in three main parts, according to the following organization:

1. **Methods for reliable LES of novel combustion technologies**: The objective here is to individuate and overcome the main modeling challenges that high-fidelity LES can encounter when simulating new low-carbon combustion technologies. First, Chapter 2 describes the governing Navier-Stokes equations and the numerical models used in LES. Then, a brief

presentation of the main numerical challenges encountered is given, namely the required tradeoff between discretization accuracy and simulations cost, the modeling of heat transfer at the walls, and the development of accurate chemical mechanisms and variable transport properties. Flame stabilization location indeed cannot be predicted in new combustor technologies a priori, generally leading to not-optimized hand-made meshes. On top of that, hydrogen-enriched flames are characterized by reduced flame thickness, leading to more stringent requirements in terms of domain discretization. This issues are addressed in Chapter 3 where static mesh adaptation criteria for reliable LES of reactive flows are derived: certain Quantity of Interests (QOIs) are selected in order to flag the domain regions where important physics happens and where refinement is of interest. The developed Static Mesh Refinement (SMR) strategy allows therefore to increase the LES accuracy while keeping a reasonable simulation cost. To validate this approach, the method is applied first to the VOLVO academic test bench and then to the real engines-like PRECCINSTA test bench. Note that the accuracy of LES also strongly depends on the boundary conditions used and, in particular, the thermal boundary conditions that account for heat transfer at the walls which can strongly affect the prediction of flame stabilization and dynamics. This issue is addressed through Conjugate Heat Transfer (CHT) simulations: the LES solver is coupled with a heat conduction solver that computes the temperature fields in the solid parts of the combustors. Indeed, changing the combustor geometry or introducing hydrogen enrichment (which has higher adiabatic flame temperature) can modify the temperature fields at the combustor walls, leading to high temperature spots and hence reducing the life-time of combustor components due to increased thermal stress. The methodology used for CHT simulations is described and validated on the PRECCINSTA test bench flame in Chapter 4. In particular, it is shown how the PRECCINSTA test bench is very sensible to how thermal boundary conditions are treated: the right flame dynamics could be correctly predicted by LES only when the CHT approach is implemented, leading to a correct estimation of the heat transfer at the walls. Finally, a proper description of the chemical mechanism and the transport properties is required when dealing with not-conventional fuel mixtures especially if H_2 is present. The used mechanism is introduced in Chapter 5, together with the issue of variable transport properties present when a light-molecule like hydrogen is mixed with classical hydrocarbon heavier molecules. In this case, the effect of variable transport properties

on the flame stabilization is analyzed for the IMFT MIRADAS configuration, confirming that a proper description of the chemistry and transport properties is needed to provide LES results in good agreement with experimental data.

2. **Hydrogen enrichment**: The objective of this second part of the thesis is to physically investigate the effect of hydrogen enrichment on methane flame stabilization and dynamics by use of LES. First, in Chapter 6, the effect of hydrogen enrichment on the methane flame is analyzed both in terms of flame stabilization, temperature fields at the combustor walls and flame dynamics. In particular, a 50% in volume of hydrogen enrichment is seen to be sufficient to drastically change the flame shape and to induce strong thermoacoustic bi-modal oscillations that are correctly captured by LES in the CHT context. Second, the effect of elevated pressure on a hydrogen enriched flame is analyzed in Chapter 7. The HIPOT test bench indeed can reach a pressure up to 5 bar, a condition much closer to real aeronautical engines that operates at higher pressure with respect to the atmospheric one. In this way, it is possible to get more insights about how hydrogen enrichment modify the flame dynamics when more realistic operating conditions are selected.

3. **Spinning Combustion Technology**: The objective of this third part of the thesis is to get more insights on the recently developed Spinning Combustion Technology and how it can provide improved operability capabilities. To this scope, the annular test bench operated at the Norwegian University of Science and Technology (NTNU) has been modified in order to introduce a strong azimuthal flow component like-wise SCT real combustors. The flame stabilization in this test bench is analyzed through LES and compared with experiments in Chapter 8. Chapter 9 focuses on the flame dynamics and presents a numerical and experimental study of the Lean Blow-Out capabilities in this test bench. The LES simulations performed in the CHT context allow to analyze not only the impact of the flame dynamics on the temperature of the combustor parts but are also useful to investigate the geometry effect on the LBO limits. Afterwards, a more applied and industrial study is presented in Chapter 10: LES are used as an industrial design tool to propose a new modification of the NTNU test bench to have a closer correspondence with the real helicopter engines. This new test bench is showed to be fully operational and to comply with various industrial criteria used to design real combustors at Safran Helicopter

Engines, confirming the maturity of this modeling strategy to analyze and design novel aeronautical engines.

By addressing these challenges, the author demonstrates the assessment of LES, in a CHT context, for predicting engine operability when dealing with innovative low-carbon technologies, from different fuel composition (such as H_2 enrichment) to new combustor geometry (such as the SCT) and therefore highlights the central role of HPC and high-fidelity LES in the transition towards a decarbonized future.

1.6 Acknowledgments

This work has received funding under the Horizon 2020 European Union program from the Marie Skłodowska-Curie Innovative Training Networks Grant Agreement No 766264 (MAGISTER) granted to Safran Helicopter Engines, and the Grant Agreement 952181 (COEC - Center of Excellence in Combustion) granted to CERFACS. HPC resources from GENCI and from the PRACE Projects 2020225434 (FANTASTIC-H2) and 2020225436 (REVOLUTION) are also acknowledged (60M CPUh).

Part I

Methodologies for reliable LES of novel combustion systems

Chapter 2

Large Eddy Simulation: modeling and challenges

Contents

This chapter aims at giving an overview of the Large Eddy Simulation approach. First, the governing Navier-Stokes equations in the LES formulation and the physical assumptions made are briefly recalled. Then, the AVBP LES solver is presented together with the available boundary conditions and the combustion model. Finally, the main challenges regarding high-fidelity LES simulations of reacting flows, especially when dealing with new combustion technologies, are discussed.

2.1 Overview of the LES approach

The Naver-Stokes equations are briefly recalled in this section together with the principal physical assumptions made.

2.1.1 Naver-Stokes equations

The compressible Navier-Stokes equations [38] describing the motion of a viscous fluid read:

$$\frac{\partial \rho}{\partial t} + \frac{\partial (\rho v_j)}{\partial x_j} = 0 \tag{2.1}$$

$$\frac{\partial (\rho v_i)}{\partial t} + \frac{\partial (\rho v_i v_j)}{\partial x_j} = -\frac{\partial p}{\partial x_i} + \frac{\partial \tau_{ji}}{\partial x_j} + \rho \sum_{k=1}^{N} Y_k f_{k,i} \qquad i,j = 1..N_{dim} \tag{2.2}$$

$$\frac{\partial (\rho E)}{\partial t} + \frac{\partial (\rho E v_j)}{\partial x_j} = \frac{\partial q_i}{\partial x_i} + \frac{\partial (\sigma_{ji} v_i)}{\partial x_j} + \rho \sum_{k=1}^{N} Y_k f_{k,i} (v_i + V_{k,i}) + \dot{\omega}_T + \dot{Q}_R + \dot{Q}_{ext} \tag{2.3}$$

In addition, when dealing with multispecies mixtures, the set of transport equations that describe the evolution of each species mass fractions Y_k have to be considered:

$$\frac{\partial (\rho Y_k)}{\partial t} + \frac{\partial (\rho Y_k v_j)}{\partial x_j} = -\frac{\partial (\rho Y_k V_{k,j})}{\partial x_j} + \dot{\omega_k} \qquad k = 1..N_s \tag{2.4}$$

Here, x_j refers to the j^{th} spatial coordinate axis, following Einstein's summation convention, and t stands for time. N_{dim} is the physical spatial dimension of the problem while N_s is the number of species considered in the gas mixture. p, ρ, E and T are the pressure, density, total sensible energy and temperature respectively. v_i and $V_{k,i}$ denote the instantaneous fluid velocity and the diffusion velocities of species k in the i^{th} direction. λ is the heat conduction coefficient, $\dot{\omega_T}$ the heat release rate due to chemical reactions while τ_{ji} the second-order, symmetric viscous stress tensor. $f_{k,i}$ refers to the volume force acting in the i^{th} direction on species k. $\dot{Q_R}$ and $\dot{Q_{ext}}$ indicate the heat production and loss due to radiation and external sources respectively.

The diffusion velocities $\overrightarrow{V_k}$ for the species k can be computed starting from the following equations [39],

$$X_k \overrightarrow{V}_k = -\sum_{j=1}^{N} D_{kj} \overrightarrow{d}_j - D_k^T (\nabla T / T) \tag{2.5}$$

where $\overrightarrow{d}_j$ can be computed as

$$\overrightarrow{d}_j = \nabla X_j + (X_j - Y_j) \frac{\nabla p}{p} + \frac{\rho}{p} \sum_{k=1}^{N_s} Y_j Y_k \left(\overrightarrow{f}_k - \overrightarrow{f}_j \right) \tag{2.6}$$

X_k denotes the mole fraction of species k while D_{kj} is the multicomponent diffusion coefficient describing the diffusion of species k in a mixture of species j (and viceversa, the matrix D being symmetric). The diffusion velocities are

influenced by three contributions visible on the right hand side of Eq. 2.6, namely gradients of species concentration, pressure gradients and volume forces. Species diffusion due to the Soret effect (i.e. due to thermal gradients) is taken into account by the last term in Eq. 2.5, where D_k^T is the thermal diffusion coefficient.

2.1.2 Physical assumptions

The above NS equations can be simplified by enforcing some physical assumptions as hereafter briefly recalled.

1. *Newtonian fluid.* Fluids are assumed to follow the Stokes's constitutive law of independence of viscosity from position. In this way, there is a direct proportionality between the viscous stress tensor τ and the velocity gradient ∇u and the constant of proportionality is the flow dynamic viscosity μ. Hence, considering that when the strain rates are zero the deformation law must reduce to the hydrostatic pressure condition, the viscous stress tensor component $\tau_{i,j}$ can thus be computed as

$$\tau_{i,j} = \left[\left(\mu' - \frac{2}{3}\mu \right) \frac{\partial u_k}{\partial x_k} \delta_{ij} + \mu \left(\frac{\partial u_i}{\partial x_j} + \frac{\partial u_j}{\partial x_i} \right) \right]. \tag{2.7}$$

   The coefficient μ' is related to bulk fluid expansion but it is rarely encountered in practice [40], so

$$\tau_{i,j} = \left[\left(-\frac{2}{3}\mu \right) \frac{\partial u_k}{\partial x_k} \delta_{ij} + \mu \left(\frac{\partial u_i}{\partial x_j} + \frac{\partial u_j}{\partial x_i} \right) \right]. \tag{2.8}$$

   Viscosity is a function of temperature and pressure. For a given pressure, a widely used approximation resulted from a kinetic theory by Sutherland [41] can be used:

$$\mu = \mu_{ref} \left(\frac{T}{T_{ref}} \right)^{3/2} \frac{T_{ref} + S}{T + S}, \tag{2.9}$$

   where μ_{ref} is the dynamic viscosity at the temperature T_{ref} and S is a coefficient characteristic of the mixture.

2. *Perfect gas.* Mixtures are considered to be ideal gases for which molecules are not subject to interparticle interactions. This assumption relies on the fact that the considered mixtures are analyzed at low density conditions since pressure is sufficiently low (maximum 5 bar in the present study) and

temperature is far from the critical point [40]. Therefore, the fluid follows the ideal gas equation of state

$$p = \rho RT, \tag{2.10}$$

where R is the gas constant of the considered mixture.

In addition, the specific heats at constant volume C_v and constant pressure C_p of the mixture can be computed as

$$C_p = \sum_{k=1}^{N} C_{pk} Y_k, \tag{2.11}$$

$$C_v = \sum_{k=1}^{N} C_{vk} Y_k, \tag{2.12}$$

and are assumed to be functions of temperature only. Therefore internal energy and enthalpy can be computed as

$$E = \int_{T_{ref}}^{T_{fin}} C_v(T) dT - RT_{ref}, \tag{2.13}$$

$$H = \int_{T_{ref}}^{T_{fin}} C_p(T) dT, \tag{2.14}$$

where T_{ref} and T_{fin} are the reference and the final evaluation temperature respectively.

3. *Arrhenius model.* The mean free times of reacting molecules are assumed to be small if compared to the chemical time scales. This assumption allows to compute the Maxwellian production rates from kinetic theory as follows

$$\dot{\omega}_k = \sum_{j=1}^{M} \dot{\omega}_{kj} = W_k \sum_{j=1}^{M} \nu_{kj} \mathrm{Q}_j, \tag{2.15}$$

where $\dot{\omega}_{kj}$ is the rate of production of species k in reaction j. W_k is the molecular weight of species k and Q_j corresponds to the rate of the j^{th} reaction. The stoichiometric coefficient of species k in the j^{th} reaction is denoted by ν_{kj}.

The forward K_{fj} and the reverse reaction rate K_{rj} coefficients can be defined as

$$K_{fj} = A_{fj} T^{\beta_j} \exp\left(-\frac{E_j}{RT}\right) = A_{fj} T^{\beta_j} \exp\left(-\frac{T_{aj}}{T}\right), \tag{2.16}$$

where $[X_k]$ is the molar concentration of species k.

In this way, the rate of reaction is computed as

$$\mathcal{Q}_j = K_{fj} \prod_{k=1}^{N} [X_k]^{\nu'_{kj}} - K_{rj} \prod_{k=1}^{N} [X_k]^{\nu''_{kj}} . \tag{2.17}$$

4. *Zero body forces and external heat sources.* Body forces and external heat sources are not considered in the present study.

5. *Simplified transport properties.* The Schmidt (Sc), the Prandtl (Pr) and the Lewis (Le) numbers describe the transport properties of a species in a mixture and define the ratio between thermal D_{th}, mass D_k and momentum D_ν diffusivities. In particular:

$$Sc_k = \frac{\nu}{D_{km}} = \frac{D_\nu}{D_k}, \tag{2.18}$$

$$Pr = \frac{\mu C_p}{\lambda} = \frac{D_\nu}{D_{th}}, \tag{2.19}$$

$$Le_k = \frac{\lambda}{\rho C_p D_k} = \frac{D_{th}}{D_k} = \frac{Sc_k}{Pr} \tag{2.20}$$

Sc and Le are generally assumed to be constant for each species in the flow domain, leading to a constant Pr number for the mixture. This assumption is reasonable in many classical flames, such as a premixed CH_4-Air flame, where the variation in Le is usually negligible [38]. This allows also for a notable reduction of cost of the simulation since there is no need to compute the diffusion coefficient matrix $D_{j,k}$[42] for each domain point. In addition, for the CH_4-Air flames, Soret and Dufour effects on the flame speed or structure can be generally neglected [43]. On the contrary, when hydrogen is considered also in combination with hydrocarbon fuels, more attention should be paid at the transport property modeling since large variations of Pr number and significant Soret/Dufour effects can be observed (see Chapter 5). Note that, when considering the simplified transport property assumption with zero body forces, one obtains an approximation that does not ensure mass conservation as proposed by Hirschfelder and Curtiss [44]:

$$X_k \overrightarrow{V}_k = -D_{km} \nabla X_k. \tag{2.21}$$

To enforce mass conservation, a correction velocity V_j^c is considered, hence modifying the species transport equation:

$$\frac{(\partial \rho Y_k)}{\partial t} + \frac{\partial (\rho Y_k (v_j + V_j^c))}{\partial x_j} = \frac{\partial}{\partial x_j} \left(\rho D_{km} \frac{W_k}{W} \frac{\partial X_j}{\partial x_j} \right) + \dot{\omega}_k. \tag{2.22}$$

2.1.3 LES governing equations

In LES, the full compressible Navier-Stokes equations described in Section 2.1.1 are spatially filtered using a Favre procedure [31, 32, 38]. This operation leads on one side to the presence of filtered primitive flow quantities that are resolved by the grid and that correspond to the large flow turbulent scales. On the other side, quantities that correspond to the smallest flow turbulent scales cannot be resolved and should be appropriately modeled. The governing equations in the LES formulation read:

$$\frac{\partial \bar{\rho}}{\partial t} + \frac{\partial \left(\bar{\rho}\widetilde{v_j}\right)}{\partial x_j} = 0 \tag{2.23}$$

$$\frac{\partial(\bar{\rho}\widetilde{v_i})}{\partial t} + \frac{\partial}{\partial x_j}\left(\bar{\rho}\widetilde{v_i}\widetilde{u_j}\right) = -\frac{\partial \bar{p}}{\partial x_i} + \frac{\partial \overline{\tau_{ji}}}{\partial x_j} + \frac{\partial \overline{\tau_{ji}^t}}{\partial x_j} + \bar{\rho} g_i \tag{2.24}$$

$$\frac{\partial(\bar{\rho}\widetilde{E})}{\partial t} + \frac{\partial}{\partial x_j}\left(\bar{\rho}\widetilde{E}\widetilde{v_j}\right) = -\frac{\partial \overline{q_j}}{\partial x_j} - \frac{\partial \overline{q_j^t}}{\partial x_j} + \frac{\partial(\overline{\sigma_{ji} v_i})}{\partial x_j} + \bar{\rho}\sum_{d=1}^{N_{dim}}(g_d \widetilde{v_d}) + \overline{\dot{\omega}_T} + \overline{\dot{Q}_r} \tag{2.25}$$

$$\frac{\partial(\bar{\rho}\widetilde{Y_k})}{\partial t} + \frac{\partial}{\partial x_j}\left(\bar{\rho}\widetilde{Y_k}\widetilde{u_j}\right) = -\frac{\partial \overline{J_{j,k}}}{\partial x_j} - \frac{\partial \overline{J_{j,k}^t}}{\partial x_j} + \overline{\dot{\omega}_k} \tag{2.26}$$

where $\widetilde{(.)}$ and $\overline{(.)}$ refer to Favre and Reynolds averaged quantities respectively.

2.1.4 Numerical assumptions and models

Some additional assumptions are required to formulate LES models that account for unresolved quantities.

1. *No turbulent correlation terms*: The turbulent correlation terms present in the viscous, heat diffusion and species diffusion terms are neglected. This is assumption is justified in the high Reynold's number limit [38] and is made in most LES codes.

2. *Boussinesq approximation*: To develop turbulence models, the Boussinesq approximation is generally used. It relies on the hypothesis that turbulent flux follows similar functions and forms as molecular diffusion as well as it abides by the assumption of local equilibrium and scale separation. Though some experimental observation reported the limited validity of this assumption [45], it is widely used in most LES.

3. *No unresolved quantity contribution to chemistry*: Chemical source terms depend only on the instantaneous filtered species mole fractions, temperature and pressure. Therefore, the heat release due to combustion $\overline{\dot{\omega}_T}$ can be expressed as function of the resolved, instantaneous, species production rates (for a detailed discussion of the combustion model used see section 2.2.3).

These assumptions allow simplifying the governing equations and obtain models for unresolved quantities:

- **Filtered viscous flux.** The filtered heat flux can be approximated as

$$\overline{q_i} = -\overline{\lambda \frac{\partial T}{\partial x_i}} + \sum_{k=1}^{N} \overline{J_{i,k} h_{s,k}}, \tag{2.27}$$

$$\approx -\bar{\lambda} \frac{\partial \widetilde{T}}{\partial x_i} + \sum_{k=1}^{N} \overline{J_{i,k}} \widetilde{h}_{s,k}, \tag{2.28}$$

  where $h_{s,k}$ is the sensible enthalpy of species k. The filtered species diffusive flux reads

$$\overline{J_{i,k}} = -\overline{\rho \left(D_k \frac{W_k}{W} \frac{\partial X_k}{\partial x_i} - Y_k V_i^c \right)}, \tag{2.29}$$

$$\approx -\bar{\rho} \left(\bar{D}_k \frac{W_k}{W} \frac{\partial \widetilde{X}_k}{\partial x_i} - \widetilde{Y}_k \tilde{V}_i^c \right). \tag{2.30}$$

  The laminar viscous stress tensor can be computed as

$$\begin{aligned} \overline{\tau_{ij}} &= \overline{2\mu \left(S_{ij} - \frac{1}{3} \delta_{ij} S_{ll} \right)}, \\ &\approx 2\bar{\mu} \left(\widetilde{S}_{ij} - \frac{1}{3} \delta_{ij} \widetilde{S}_{ll} \right). \end{aligned} \tag{2.31}$$

  Note that S_{ij} denotes the symmetric part of the second order velocity gradient tensor.

- **Sub grid scale (SGS) turbulent flux and source terms.** The SGS stress tensor $\overline{\tau_{ji}^t}$ reads,

$$\overline{\tau_{ij}}^t = -\bar{\rho} \left(\widetilde{u_i u_j} - \tilde{u}_i \tilde{u}_j \right). \tag{2.32}$$

  This term can be modeled following the Boussinesq assumption as,

$$\overline{\tau_{ij}}^t = 2\bar{\rho} \nu_t \left(\widetilde{S}_{ij} - \frac{1}{3} \delta_{ij} \widetilde{S}_{ll} \right). \tag{2.33}$$

Different models can be used for evaluating the turbulent viscosity coefficient ν_t: in the present study, the Sigma model [46] is used.

The SGS heat flux is given by

$$\overline{q_i}^t = \bar{\rho}\left(\widetilde{u_i E} - \tilde{u}_i \tilde{E}\right), \tag{2.34}$$

and is can be computed as

$$\overline{q_i}^t = -\lambda_t \frac{\partial \widetilde{T}}{\partial x_i} + \sum_{k=1}^{N} \overline{J_{i,k}}^t \widetilde{h}_{s,k}, \tag{2.35}$$

where

$$\lambda_t = \frac{\mu_t \overline{C_p}}{Pr^t}. \tag{2.36}$$

While the turbulent viscosity μ_t can be estimated from the SGS model (in this case the Sigma model), the determination of the turbulent Prandtl number Pr^t is generally left to the user. The SGS species diffusion is given by,

$$\overrightarrow{J_{i,k}}^t = \bar{\rho}\left(\widetilde{u_i Y_k} - \widetilde{u}_i \tilde{Y}_k\right). \tag{2.37}$$

It can be approximated as

$$\overline{J_{i,k}}^t = -\bar{\rho}\left(D_k^t \frac{W_k}{W}\frac{\partial \tilde{X}_k}{\partial x_i} - \widetilde{Y}_k \widetilde{V}_i^{c,t}\right). \tag{2.38}$$

At the same time, D_k^t denotes the turbulent species diffusion coefficient that can be computed from the turbulent Schmidt number Sc_k^t (specified by the user) as

$$D_k^t = \frac{\nu_t}{Sc_k^t}. \tag{2.39}$$

- **Filtered source terms.**

  As already mentioned, turbulent source terms are considered to depend on the instantaneous filtered quantities only. Therefore, the reaction rates can be calculated as

$$\overline{\mathcal{Q}_|} = K_{fj} \prod_{k=1}^{N} \left[\widetilde{X_k}\right]^{\nu'_{kj}} - \widetilde{K_{rj}} \prod_{k=1}^{N} \left[\widetilde{X_k}\right]^{\nu''_{kj}}, \tag{2.40}$$

while the species production rates read,

$$\widetilde{\dot{\omega}_k} = \sum_{j=1}^{M} \widetilde{\dot{\omega}_{kj}} = W_k \sum_{j=1}^{M} \nu_{kj} \overline{\Omega_j}. \tag{2.41}$$

At the same time, heat release rate due to combustion $\overline{\dot{\omega}_T}$ can be computed as

$$\widetilde{\dot{\omega}_T} = \sum_{k=1}^{N} \Delta h^0_{f,k} \widetilde{\dot{\omega}_k}, \tag{2.42}$$

where $h^0_{f,k}$ is the enthalpy of formation of species k at temperature T_0.

2.2 The AVBP LES solver

AVBP is a high-fidelity LES solver co-developed by CERFACS (cerfacs.fr/avbp) and has been used in this work to carry out the numerical simulations. AVBP is widely used for research purposes throughout Europe and the world (CIEMAT, Spain; Technische Universität München, Germany; EM2C, France; CORIA, France; Stanford University, USA; Sherbrooke University, Canada; von Karman Institute, Belgium). The code is also used for various industrial applications, for aeronautical (Safran Group) and energy production (Siemens, Ansaldo, Alstom) gas turbines as well as piston engines (Renault, PSA Peugeot Citroen) and furnaces (Total, John Zink, Schlumberger). All developments and methods devised during this work will be kept within the context of development of AVBP and thereby benefit all the research entities using the code. AVBP solves the three-dimensional Navier-Stokes equations for compressible two-phase and reactive flows on multi-element unstructured grids. It relies on an explicit resolution of the equations using the LES approach where the large structures are resolved and small scales are modelled as recalled in section 2.1.3. The LES SGS models available in AVBP are the Dynamic Smagorinsky, WALE, and the SIGMA models [46]. In order to handle arbitrary grids, the data structure of AVBP employs a cell-vertex finite-volume formalism. In addition, LES of turbulent flows and acoustics requires low-dissipation schemes. The numerical method is therefore based on a Finite-Element low-dissipation and the numerical integration of AVBP is based on a centred scheme and uses a Taylor-Galerkin weighted residual central distribution scheme, called TTGC, which is third-order in time and space [47, 48]. Turbulent premixed combustion can be described by the well-known TFLES model [49]. The possibility to correctly reproduce acoustics and its coupling with the turbulent combustion is the main reason that has driven the choice of selection of AVBP

for the present study with respect to other valid alternatives as YALES2 [50] and OpenFOAM [51]. The pure acoustic analysis has been be performed with the Helmholtz solver AVSP developed at CERFACS. With respect to valid alternative as COMSOL Multiphysic [52], AVSP [53] has been selected to compute thermoacoustic modes for its integration with the LES solver AVBP. For the same reason, AVTP [54, 55] has been chosen to compute heat conduction in the solid. In the following, first the development, validation and HPC performance of the code are briefly discussed. Second, the available boundary conditions and the combustion model are recalled.

2.2.1 Development, validation and HPC performance

The AVBP solver follows the continuous development strategy with 2 main releases every year. The important development of the physical models done at CERFACS is completed by academical studies carried out at the EM2C lab of Ecole Central Paris (ECP) and at the Institut de Mécanique des Fluides de Toulouse (IMFT). All major developments are documented and incorporated in the final releases by senior researchers and tracked using a git repository. All new releases are verified by a Quality Program Form (QPF) to account for any possible modification in the behaviour of the solver. During the QPF, the new release of the solver is validated on test cases for which DNS or analytical solutions are available and results are also compared against previous versions of the solver. The QPFs include a wide variety of tests such as 1D Euler Lagrange flame to validate the evaporation and spray combustion models, turbulent channels to validate sub-grid scale models or propagation of 1D acoustic waves to test the gain and phase of the numerical schemes.

Recently, a series of numerical simulations have been performed by the author to further validate the AVBP solver with particular focus on the numerical schemes dissipation and dispersion properties (hence, without a LES model). These simulations were carried out for the Mini-Symposium on Verification and Validation of Combustion DNS during the Seventeenth International Conference on Numerical Combustion held in Aachen in May 2019. This mini-symposium aimed at comparing and benchmarking different DNS codes, models, and methods available in the combustion community. For this purpose, the Taylor-Green Vortex (TGV) setting [56] has been selected as a benchmark, both for nonreactive and reactive flows for a total of four different setups. Initial velocity, temperature, and composition fields were prescribed together with the domain dimensions, the

suggested mesh resolution, the chemical scheme and the transport property modeling (e.g. variable Prandtl number but constant Lewis) [57, 58].

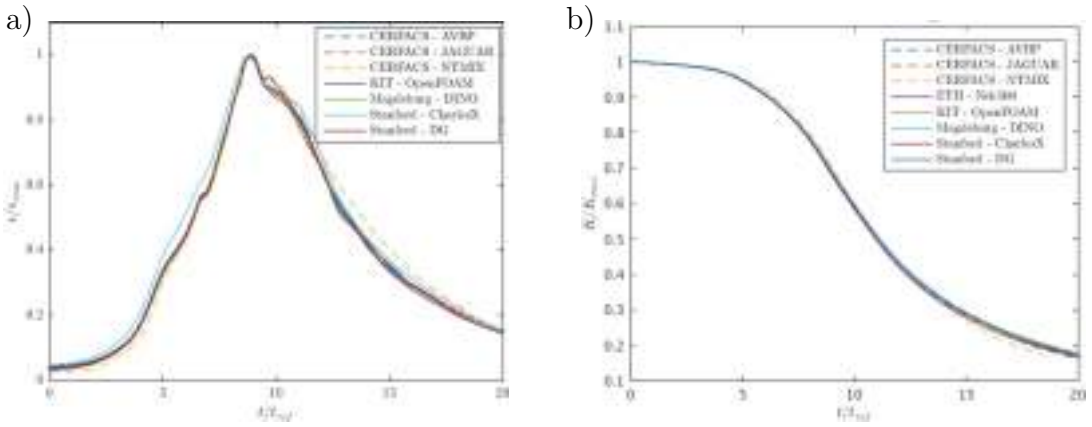

Figure 2.1: Mini-Symposium on Verification and Validation of Combustion DNS codes in the Taylor-Green vortex benchmark. (a) Kinetic energy evolution in time and (b) corresponding kinetic energy dissipation rate.

The AVBP solver has showed perfect agreement with the reference results from the DINO code [58] and with most of the codes used in the combustion community. For example, Fig. 2.1 presents the results for the 3D cold flow case. The kinetic energy evolution in time in the domain is well captured by AVBP together with the corresponding kinetic energy dissipation rate.

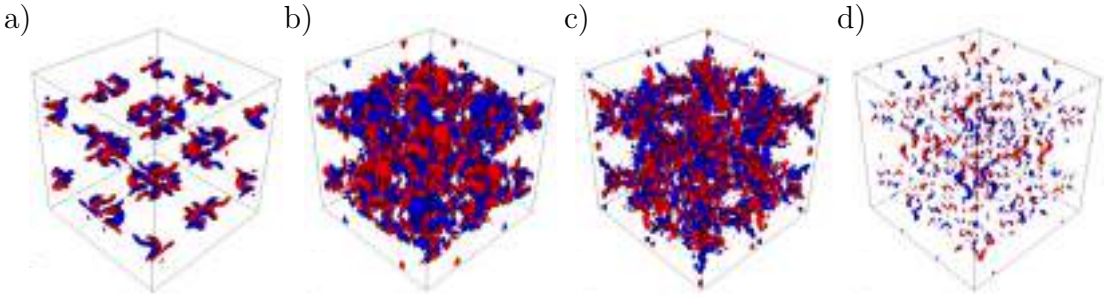

Figure 2.2: Time evolution of isosurfaces of z-vorticity for the 3D cold flow TGV benchmark predicted by AVBP. (a) Vortex roll-up at t/τ_{ref} = 5.46. (b) Coherent structure breakdown at t/τ_{ref} = 8.0. (c) Onset of turbulence t/τ_{ref} = 12.11. (d) Decay at t/τ_{ref} = 18.55.

AVBP is able to capture the correct time evolution of initial vortices: the time evolution of isosurfaces of z-vorticity at different times is illustrated in Fig. 2.2. After $t/\tau_{ref} = 5.46$ the vortices start to roll-up and a breakdown of the coherent structures occurs at $t/\tau_{ref} = 8.0$. Then, the onset of turbulence is visible at $t/\tau_{ref} = 12.11$ before the decay of turbulent activity due to dissipation at t/τ_{ref}

= 18.55. Results validate the AVBP code and further confirm the good behavior of the numerical scheme used in terms of dissipation and dispersion properties.

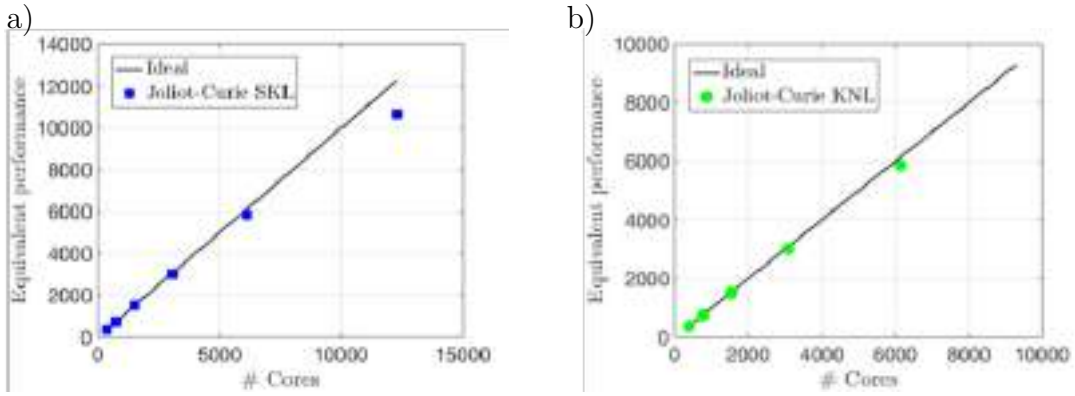

Figure 2.3: Strong scalability of the AVBP code in the (a) SKL and the (b) KNL partitions of the Joliot-Curie machine operated by GENCI.

In addition to the extensive validation, an important advantage of the AVBP code is its strong scalability which allows for carrying out the simulations on a large number of CPU cores without affecting the performances. Indeed, the AVBP code has been tested and optimized for a variety of computers and architectures, with results demonstrating an excellent scalability of the code for several PRACE supercomputers and architectures up to 65k cores. Recently, the strong scalability (Fig. 2.3) of the code has also been tested in the (a) SKL and the (b) KNL partitions of the Joliot-Curie machine operated by GENCI. Tests have been performed using a 150M cells mesh, representative of the largest mesh used in this work (see Chapter 7). In both cases, results demonstrate a good scaling up to 10000 cores, confirming the excellent HPC performance of the AVBP code.

2.2.2 Boundary conditions

The boundary conditions used in the present work are briefly summarized hereafter together with their numerical implementation in the LES solver.

- *Mass flow inlets.* From experimental data, the air and fuel mass flow rates are known together with the fresh gas temperature. Therefore mass flow inlet boundary conditions can be imposed by specifying the mass flow rates $\dot{m}_{fuel}$, $\dot{m}_{air}$ and the temperature. At the same time, to account for acoustics at the boundaries, Navier-Stokes Characteristic Based boundary Conditions (NSCBC) are used [30] and a reflection coefficient has to be imposed to match the acoustic impedance.

- *No slip adiabatic walls.* No-slip condition on the walls imposes a zero velocity at the walls. In case where heat transfer is expected not to be relevant for certain surfaces, adiabaticity is imposed by enforcing a zero temperature gradient normal to the walls.

- *No slip walls with heat transfer.* When heat transfer is expected to be relevant, heat losses can be introduced as thermal boundary conditions through the definition of a heat resistance and a reference temperature [59]. At the same time, this boundary condition can be used to couple the LES code to the AVTP heat conduction code [54, 55] (see Chapter 4 for the detailed discussion of this methodology).

- *Outflow.* Outflow conditions can be imposed based on the NSCBC theory [30]. In this case, the outlet pressure is specified together with the reflection coefficient for the acoustic impedance. Note that for thermoacoustic studies, the atmosphere is taken into account in the present work to capture the experimental impedance at the outlet.

- *Periodicity.* When dealing with single-sector of annular burners, periodicity is imposed at the section surface limits. This allows for a drastic reduction of the simulations' cost compared to full annular predictions especially whenever these are not expected to be crucial for achieving a good simulation accuracy.

2.2.3 Combustion model

In LES of reactive industrial flows the flame is usually too thin to be resolved on the numerical mesh without asking for non-feasible HPC resources. To solve this issue, AVBP relies on the Thickened Flame LES (TFLES) model in which flames are artificially thickened in order to be resolved on the numerical mesh, without modifying their flame speeds [49, 60, 61, 62, 63, 64]. The thickening process is done by multiplying the diffusion terms and dividing the reaction rates by a local thickening factor F. Since a thickened flame is less sensitive to turbulence, an efficiency function is introduced to compensate for the corresponding reduction of the flame surface [49, 61]. Multiple expressions can be found in the literature for an efficiency function Ξ_Δ which corresponds to the SGS flame/turbulence interaction model: Ξ_Δ is expressed as the ratio between the total flame front wrinkling, and its resolved part. The transport equations for the filtered species mass fractions $\widetilde{Y}_k$ and the conservation equation for the filtered total energy $\widetilde{E}$ can be written as,

$$\frac{\partial \bar{\rho}\tilde{Y}_k}{\partial t} + \frac{\partial}{\partial x_j}\left(\bar{\rho}\tilde{u}_j\tilde{Y}_k\right) = \frac{\partial}{\partial x_j}\left[\left(\Xi_\Delta F\frac{\mu}{S_{c,k}} + (1-S)\frac{\mu_t}{S^t_{c,k}}\right)\frac{W_k\partial\tilde{X}_k}{W\partial x_j} - \bar{\rho}\tilde{Y}_k\left(\tilde{V}^c_j + \tilde{V}^{c,t}_j\right)\right] + \frac{\Xi_\Delta}{F}\dot{\omega}_k\left(\widetilde{Y}_k, \widetilde{T}\right), \tag{2.43}$$

$$\frac{\partial \bar{\rho}\tilde{E}}{\partial t} + \frac{\partial}{\partial x_j}\left(\bar{\rho}\tilde{u}_j\widetilde{E}\right) = -\frac{\partial}{\partial x_j}\left[\widetilde{u}_i\bar{P}\delta_{ij} - \tilde{u}_i\bar{\tau}_{ij}\right] + \frac{\partial}{\partial x_j}\left[C_p\left(\Xi_\Delta F\frac{\mu}{P_r} + (1-S)\frac{\mu_t}{P^t_r}\right)\frac{\partial\widetilde{T}}{\partial x_j}\right] + \frac{\partial}{\partial x_j}\left[\sum_{k=1}^{N}\left(\left[\Xi_\Delta F\frac{\mu}{S_{c,k}} + (1-S)\frac{\mu_t}{S^t_{c,k}}\right]\frac{W_k\partial\tilde{X}_k}{W\partial x_j} - \bar{\rho}\tilde{Y}_k\left(\widetilde{V}^c_j + \tilde{V}^{c,t}_j\right)\right)\tilde{h}_{s,k}\right] + \frac{\Xi_\Delta\dot{\omega}_T\left(\tilde{Y}_k, \widetilde{T}\right)}{F}, \tag{2.44}$$

where ρ is the density, u the velocity vector, X_k and W_k the mole fraction and atomic weight of species k, Sc_k and Sc^t_k the Schmidt and turbulent Schmidt numbers, P the pressure field, C_p the mass heat capacity at constant pressure, $\tilde{h}_{s,k}$ the sensible enthalpy of species k, $\tilde{\tau}$ the filtered viscous stress tensor, Pr and Pr^t the Prandtl and turbulent Prandtl numbers, and $\dot{\omega}_T$ the heat release rate. The following relation for the correction diffusion velocities is used:

$$\widetilde{V}^c_i + \widetilde{V}^{c,t}_i = \sum_{k=1}^{N}\left(\Xi_\Delta F\frac{\mu}{\bar{\rho}S_{c,k}} + (1-S)\frac{\mu_t}{\bar{\rho}S^t_{c,k}}\right)\frac{W_k\partial\tilde{X}_k}{W\partial x_j}. \tag{2.45}$$

Note that the local thickening factor F is applied only in the vicinity of the flame front thanks to a sensor S which detects the presence of a reaction zone based on the fuel breakdown reaction. The value of the thickening factor F is chosen in order to have n_F points in the flame thickness. The suitable n_F value can be identified based on one-dimensional premixed flame computations. Generally 5 points are required to correctly solve for the flame in global reduced chemistry, while when using ARC chemistry with heavier fuels (e.g. heptane, dodecane) with lower diffusivities a n_F of 8-10 is required [47]. Hence, if Δ_x is the characteristic mesh size and δ_T is the thermal flame thickness, the thickening factor can be locally evaluated as

$$F(\overrightarrow{x}, t) = \frac{n_F\Delta_x(\overrightarrow{x})}{\delta_T(\phi, T)}. \tag{2.46}$$

Note that the local applied thickening factor F varies both in space $\overrightarrow{x}$ and time t since the characteristic mesh size Δ_x is usually not uniform and varies in space and the thermal flame thickness δ_T depends mainly on the equivalence ratio ϕ and on the temperature T of the fresh gases which can vary as well both in space and time.

2.3 Modeling challenges

The performed research activities aim to cope with a wide range of questions raised when dealing with novel combustion systems from both a physical understanding and a numerical modeling point of view. Indeed, to extend the LES approach to more complex bi-fuel configurations when enriching combustion with hydrogen, also operated at elevated pressure, and when simulating novel spinning combustion devices, multiple challenges need to be addressed:

- *Multi-physics.* The first challenge is linked to the multi-physics nature of the phenomena present in these burners which involves combustion and acoustics. Therefore, a compressible reactive solver with high-order low-dissipative and low-dispersive numerical schemes has to be used to analyse the thermoacoustic response of the flame. This choice strongly impacts the cost of the simulations since a time step of the order of 10^{-8} - 10^{-9} s is required for the temporal accuracy and stability of the needed numerical schemes to abide to the Courant-Friedrichs-Lewy (CFL) requirement which rules in compressible solvers.

- *Chemical kinetics and transport properties.* A new chemical kinetic scheme has to be derived for describing bi-fuel flames. In addition, the particular diffusion properties of hydrogen raises questions about the transport properties modeling. Moreover, for the analyses of SCT combustors, classical globally reduced 2-step chemistry is not necessarily suitable since, despite being computationally cheap, it does not provide accurate prediction of the flame response to strain and extinction which are two fundamental points in the analysis of engine operability (e.g. LBO capabilities) [47]. These are however fundamental processes of spinning combustion devices and are also important in flame-wall interactions. As a consequence, for the present work, the use of more expensive but accurate Analytically Reduced Chemistry (ARC) [65] has been devised.

- *Thermal load impact.* Even though the impact of the thermal boundary conditions on the flame stabilization and dynamics is well known in the literature, LES simulations are often performed with simple boundary conditions at the walls where temperature is either imposed or adiabaticity is assumed. When dealing with hydrogen, the thermal load on the combustor components will be more intense since hydrogen flames tend to stabilize closer to combustor walls. For SCT combustors, the thermal boundary state can also play a major role in defining the flame quenching or stabilization process close to the walls. To consider these effects and provide accurate thermal boundary conditions, Conjugate Heat Transfer (CHT) simulations have been performed by coupling the LES solver with the AVTP heat conduction solver [54, 55, 66]. Note that compared to the computationally expensive fluid solver, the additional computational cost due to the solid solver is not significant, justifying its use in this case. However, the total computational cost will again increase due to the additional simulation time needed to reach thermal equilibrium in the solid domain which can double the effective cost of the initial simulation.

- *Wall-flame interactions.* For this specific physics which is clearly at play in spinning combustors as experimentally observed in real engines, the classical thickened-flame model is known to produce questionable results. Higher mesh resolution is hence needed in order to resolve the flame interaction with the walls, increasing the overall number of cells for such computation and hence its cost.

- *Acoustics and combustion dynamics:* H_2-enrichment modifies the combustion dynamics and can trigger dangerous thermoacoustic oscillations [67, 68, 69]. High-fidelity simulations of H_2-enriched flames experiencing thermoacoustic oscillations are however marginally investigated in the literature even though they can reveal physical insights not otherwise observable with experiments only. To fill this gap of knowledge, high-fidelity LES are used in the present work to get more insights on the physical mechanisms driving these instabilities. To this scope, low-dissipation numerical scheme and a proper representation of the acoustic properties at the boundaries must be used to guarantee the correct representation and propagation of the resonant acoustic mode for the analysis of the thermoacoustic flame behaviour.

- *Pressure effects.* Real engines operate at elevated pressure but most of the academic experiments are conducted at atmospheric pressure because of the

less expensive and complex setup required. Currently, the HIPOT PRECCINSTA test bench is the only test rig capable of operating at elevated pressure, with different hydrogen content and equipped with high quality experimental diagnostics useful to validate the simulations and analyze the pressure effect on the flame dynamics [67]. On the numerical side however, this means that much thinner flame fronts are expected: more refined mesh and HPC resources are needed to allow for flame resolution.

- *HPC optimization*: As opposed to DNS where all scales are resolved, LES are susceptible to uncertainty due to the inherent modeling of the small scales, hence underlining the importance of the mesh resolution. In a mesh-converged wall-resolved LES, the numerical dissipation generated by the numerical schemes would be with orders of magnitude smaller than the one provided by the SGS model. However, this, in combination with all the above-mentioned challenges, implies the generation of massive meshes that are impractical to run. Therefore, in order to improve the mesh without considerably increasing the cost of the simulation, local refinement is needed. As a matter of fact, the use of a proper mesh adaptation strategy can effectively produce the desired local mesh refinement to match the velocity field and flame structure measured experimentally. However, Static Mesh Refinement (SMR) of reactive LES are quasi inexistent in the community, the critical point being to define a Quantity of Interest that flags the regions where important physics happens and where mesh refinement is needed to increase the overall LES accuracy. In this context, a novel mesh adaptation strategy for high-fidelity LES of reactive turbulent flows has been proposed to optimize the HPC resources.

Among these challenges, three developments have been found to be the keystone for achieving good LES prediction of novel combustion systems and are addressed in the following Chapters. First, in Chapter 3, a novel Static Mesh Refinement strategy for reliable LES of reactive flows is proposed and validated on the VOLVO and the PRECCINSTA test benches [70]. Second, the CHT approach and the effect of wall heat transfer modeling on the PRECCINSTA flame dynamics are presented in Chapter 4 [59]. Finally, Chapter 5 presents the challenge of dealing with bi-fuel flames from a chemical kinetics and transport properties modeling point of view together with a successful application to the MIRADAS flame [71].

Chapter 3

Static mesh refinement for turbulent reacting flows

Contents

The design challenge of reliable lean combustors needed to decrease pollutant emissions has clearly progressed with the common use of experiments as well as Large Eddy Simulation (LES). However, the accuracy of such numerical predictions depends very often on the user's experience to choose the most appropriate flow modeling and, more importantly, the proper spatial discretization for a given computational domain. The present Chapter focuses on the last issue and proposes a static mesh refinement strategy based on flow physical quantities. To do so, a combination of sensors based on the dissipation and production of kinetic energy coupled to the flame-position probability is proposed to detect the regions of interest where flow physics happens and grid adaptation is recommended for good LES predictions. Thanks to such measures a local mesh resolution can be achieved in these zones improving the LES overall accuracy while, eventually, coarsening everywhere else in the domain to reduce the computational cost. The proposed mesh refinement strategy is detailed and validated on two reacting-flow problems: a fully premixed bluff-body stabilized flame, i.e. the VOLVO test case, and a partially premixed swirled flame, i.e. the PRECCINSTA burner, which is closer to industrial configurations. For both cases, comparisons of the results

with experimental data underline the fact that the predictions of the flame stabilization, and hence the computed velocity and temperature fields, are strongly influenced by the mesh quality and significant improvement can be obtained by applying the proposed strategy. Note that these results have been published in *Physics of Fluids* [70].

3.1 State of the art

Few decades ago, Large Eddy Simulation (LES) had demonstrated its capability in predicting complex flows at Reynolds numbers that could not be reached by Direct Numerical Simulation (DNS), opening the opportunity of improving the understanding of turbulence in simple geometries [32]. Nowadays, thanks to the progress in computer technology and the significant advances in flow modeling (e.g. SGS models [72, 73], near-wall models), LES has become a reference method also for simulating flow physics in complex geometries, including swirling reacting flows in combustors [74, 75, 76, 77]. In the aeronautical sector, together with experiments, because of its ability to accurately predict the interactions between turbulence, acoustic, spray and flame, the LES approach has been widely used [19, 33] to study unsteady combustion thermoacoustic instabilities [23, 24], lean blow-off [14, 15], extinctions [16, 78] or even to address pollutant emissions [35, 36].

However, the accuracy of these predictions often relies on the user's experience in choosing the most appropriate flow modeling along with the proper spatial discretization for a given computational domain. Sensitivity of the solution to the mesh is in fact a well-known issue in Computational Fluid Dynamics (CFD) both for non-reactive [79, 80, 81] and reactive flows [75, 82]. In the context of Reynolds Averaged Navier-Stokes (RANS) prediction independence of the mesh is often requested and homogenous mesh refinement is commonly applied but it is also found to be computationally expensive and, therefore, not often practical [83].

To circumvent such a challenge, Adaptive Mesh Refinement (AMR) methods have been developed in an attempt to locally adapt a mesh. Two different philosophies are at the basis of AMR: Static Mesh Refinement (SMR) and Dynamic Mesh Refinement (DMR). SMR is more suitable for quasi-steady problems. It relies on computed flow statistics (e.g. mean field, RMS etc.) from which it is possible to identify flow regions where refinement is of interest. In these zones, h-refinement methods are usually applied subdividing the cells of a given mesh isotropically or anisotropically [84, 85] until an optimised grid is obtained. On the contrary, DMR is more appropriate for unsteady cases where flow statistics have no specific physical meaning because the flow is in full transition: i.e. it evolves

drastically in space and time (e.g. in explosion, ignition). This second strategy relies on an 'on-the-fly' evaluation of the important flow regions so that the spatial discretization of the computational domain changes as the computation proceeds. The optimized mesh can be obtained using p-refinement so that the order of discretization is locally increased avoiding changes in mesh topology. An alternative is to use a r-refinement in which cells of a given mesh are redistributed within the computational domain, clustering them in the zones of interest [86]. All of these different AMR methods have been developed and successfully applied to RANS for both non reactive flows [87, 88] or reactive cases [89]. Solution-based methods have been proposed to adapt a given mesh with the objective of minimizing an interpolation error, for example by taking the hessian matrix of a certain quantity [84]. Adjoint-based techniques have also been used in some cases to estimate errors sensitivity [90] and perform mesh adaptation [91, 92]. Both solution-based and adjoint-based methods have been successfully applied to external flows [93] as well as to turbo-machinery applications [94, 95, 96], like a high pressure turbine cascade [97]. Combination of the two methods have also been proposed for turbo-machinery applications [98] while focus on adjoint quantities such as total pressure ratio, total temperature ratio and adiabatic efficiency has been recently pointed out [99]. Finally dedicated methodologies to adapt a mesh focusing on shock waves-boundary layer interactions also exist [100]. Applications to LES are clearly more difficult and rare mainly due to the only recent maturity of such an unsteady turbulence modeling approach [101].

For non-reactive turbulent flows, AMR for LES has been assessed on structured meshes making use for example of the multi-scale decomposition theory [102]. Following RANS, anisotropic mesh adaptation using an Hessian-based error indicator considering small scale energy has also been recently proposed with the idea of identifying the optimal spatial resolution by minimizing the solution sensitivity [103]. The main limitation of these applications is linked to the use of structured mesh which can hardly manage complex geometries, leaving the method to be applicable only to turbulent channel flows or to flows on backward-facing steps and only recently to swirling flows [104]. The simulation of complex geometries indeed require unstructured grids. In this context, a double criterion ensuring both correct discretization of the mean field and a sufficient LES quality to ensure enough explicit prediction of the turbulent scale motions [45] has recently been proposed for iso-thermal flows in a complex meso-combustor [105]. Swirling flow have also been investigated [106]. In this case, the adopted AMR strategy consisted in defining regions where a mesh refinement was to be applied

making use of a sensor based on the dissipation rate of kinetic energy, achieving an improvement on the prediction of the pressure losses through the swirlers.

For reactive flows, a grid sensitivity analysis has been recently obtained in the DNS framework for a turbulent hydrogen jet flame using a structured grid [107]. However, and to the author's knowledge, AMR of reactive LES is quasi inexistent even though literature does not lack of works where the impact of the mesh on the accuracy of the numerical predictions is addressed. For example, the VOLVO academic test-bench [108, 109, 110], in which a fully premixed flame is stabilized behind a bluff-body, has been shown to be strongly sensitive to numerics [111], chemical mechanisms [47], thermal radiation [112] and also mesh refinement level [113], making this configuration very well suited for a first application of LES AMR methods. A first application going in this direction was proposed by Drennan *et. al* [114] with a structured grid. Following the experience with Hessian-based AMR methods in RANS, cells were added in regions of large flow shear and temperature gradients in an attempt to obtain a grid independent LES prediction. Complementarily, systematic analysis of the solution mesh sensitivity for turbulent reactive flows has been recently performed on the partially premixed swirled flame in the well-known PRECCINSTA test bench [27]. Bénard *et al.* [115] compared solutions obtained on different unstructured meshes with increasing homogeneous refinement levels, evidencing how the flame stabilisation and lift-off is impacted by the mesh quality. This last work however did not propose an AMR strategy to efficiently refine the mesh in the required regions.

From the previous literature review it is evident that solution mesh sensitivity of LES is a well-known issue, especially for turbulent reacting flows in complex geometries. A direct consequence is that grid generation may become very time-consuming, particularly if high-quality meshes are needed to minimize numerical errors. Industrially, there is clearly a need of limiting this time-consuming process. Likewise approaching a automated-mesh-generation strategy in which results do not depend on the user's experience (which is more likely to fail if dealing with new lean combustor geometries, e.g. Spinning Combustion Technology [77]) can only be the result of a well-established AMR strategy. From the academic point of view, focus should lie on the accuracy of LES and solution mesh sensitivity which may hide flow modeling issues. However, there is clearly a lack of AMR strategies for LES of turbulent reactive flows in complex geometries [101].

This Chapter aims at filling this gap of knowledge by proposing a SMR methodology so as to allow to refine a mesh and increase the accuracy of LES prediction while reducing the solution sensitivity to the grid. The method is based on three physical quantities (or Quantity of Interest, QOI [106]) computed

from mean flow data, namely the dissipation rate of resolved kinetic energy, the production rate of the resolved turbulent kinetic energy and the probability to find the flame in a certain region. Once these fields are evaluated, it is possible to define the Region of Interest (ROI) where important flow physics happens and where higher mesh refinement level is required. To do so, QOIs are obtained and time-averaged during the computation (i.e. according to the SMR approach). They are provided to the MMG3D library [116] that refines the mesh in the ROI thanks to a h-refinement method[1]. A new computation is then carried out on the refined mesh and QOI are again averaged to re-apply the refinement procedure if needed, following the idea of iterative refinement proposed by Daviller *et al.* [106]. This strategy is applied and validated on the two previously mentioned configurations: the VOLVO and PRECCINSTA test-rigs.

The Chapter is organized as follows. Criteria and strategy for the mesh refinement are detailed in section 3.2. Results on the VOLVO test case are discussed in section 3.3 followed by the PRECCINSTA flame in section 3.4.

3.2 Criteria for mesh refinement

The proposed mesh adaptation strategy relies on a Static Mesh Refinement (SMR) procedure which aims at generalizing the original contribution proposed by Daviller *et al.* [106] to complex turbulent reacting flows. The idea behind this procedure is that the criteria at the basis of the mesh refinement should represent the important physics of the problem [117]. This can be done by selecting certain Quantity of Interests (QOIs) which flag the flow regions where physics happens and potentially require mesh refinement. Once a proper QOI is selected, the SMR procedure is applied (Fig. 3.1). Note that the approach is iterative: (1) LES prediction is produced on an arbitrary initial mesh to compute average fields for a given QOI. (2) Starting from the QOI field, a metric field is computed containing the information on the desired local mesh refinement (or coarsening). (3) LES is performed on the new mesh, resulting in a novel evaluation of the QOIs. Such steps can then be repeated until the LES accuracy is deemed satisfactory.

The use of a SMR method in place of a DMR one gives the possibility to look at the quasi-steady flow statistics and that can also provide information not only about the physics happening, for example by looking at the rms values which describe the dynamics of the system, but also about the mesh quality as

[1]Note that, when it comes to computational cost, one advantage of SMR with respect to DMR is the less complex handling of parallel computing strategies. DMR necessarily requires a check of load balancing among CPUs according to new mesh size and element distribution across partitions which may affect the calculation speed. This is not the case for SMR.

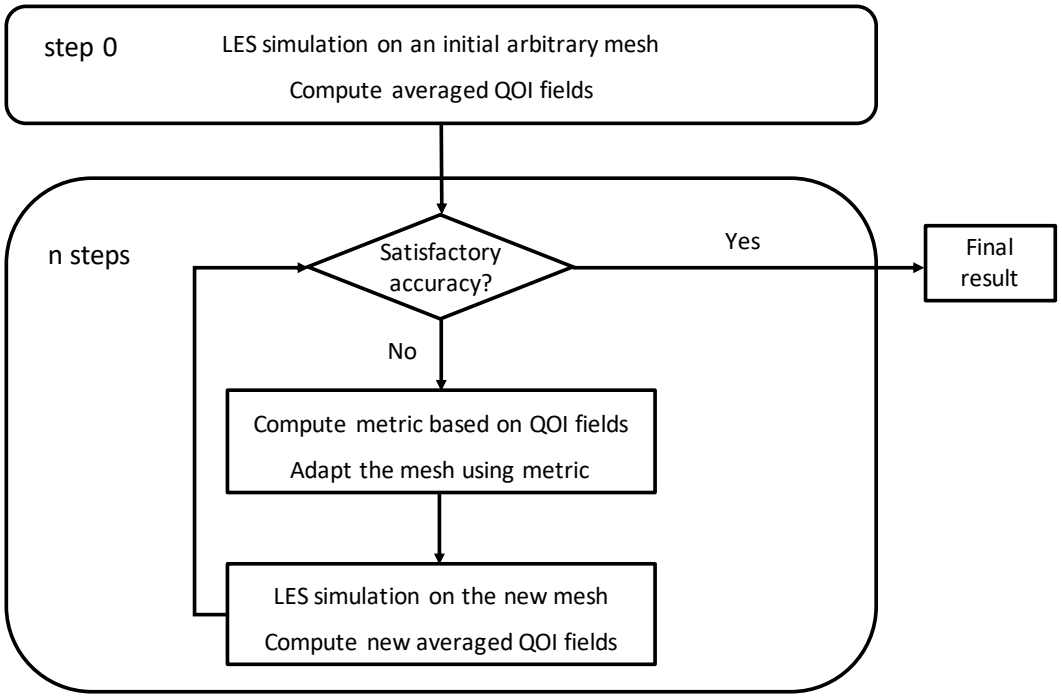

Figure 3.1: Generalized scheme of Static Mesh Refinement procedure.

well as indicate if further refinement is required, for example by looking at SGS model output. To tackle turbulent reactive flows and define proper QOI's, the retained strategy divides the complexity of the problem into two distinct parts: the aerodynamics and the flame. The justification of this choice is twofold. First, from a practical point of view, what typically happens in reactive computations is that preliminary validations are conducted on corresponding non-reactive cases, so that aerodynamics should be first correctly captured. Second, from a physical point of view, it is evident that if aerodynamics is not well predicted, the flame cannot be correctly predicted since flame stabilization and dynamics are primarily driven by aerodynamics.

3.2.1 Aerodynamics criteria

To point out the physical mechanisms that generate pressure losses in swirlers, Daviller *et al.* [106] proposed to look at the conservation equation for kinetic energy $E_c = 1/2\rho u_i u_i$ which for constant-density flows [118] reads:

$$\underbrace{\frac{\partial E_c}{\partial t}}_{1} + \underbrace{\frac{\partial}{\partial x_j}\left(u_j P_t\right)}_{2} = \underbrace{\frac{\partial\left(\tau_{ij} u_i\right)}{\partial x_j}}_{3} - \underbrace{\tau_{ij}\frac{\partial u_i}{\partial x_j}}_{4}. \tag{3.1}$$

In Eq. (3.1) terms (1), (2), (3) and (4) correspond to the temporal variation of the kinetic energy, the mechanical energy flux (i.e. advection of total pressure

P_t), the viscous diffusion and the viscous dissipation respectively. The viscous dissipation term (4) Φ controls the losses of total pressure P_t and hence the swirler pressure losses:

$$\Phi = \tau_{ij}\frac{\partial u_i}{\partial x_j} = \frac{\mu}{2}\left(\frac{\partial u_i}{\partial x_j} + \frac{\partial u_j}{\partial x_i}\right)^2. \tag{3.2}$$

Φ plays also an important role in turbulence theory since it corresponds to the fluid friction irreversibilities and controls the dissipation rate of the small scales [119]. Indeed, if considering a steady flow subject to no external force, it is possible to integrate Eq. (3.1) over the computational domain to express the pressure losses directly as a function of the integral of the volumetric dissipation rate:

$$Q_v \Delta P_t = \int_{flow\ \ domain} \Phi \ \ dV \tag{3.3}$$

where the first term represents the product of the volume flow rate Q_v and the pressure loss between inlet and outlet sections ΔP_t. From Eq. (3.3) it is evident that to correctly predict the pressure loss across a swirler, LES should properly capture the dissipation rate. Φ could then be used to construct the first QOI. However, while the equations above are exact for DNS, LES only solves for filtered velocity $\tilde{u}_i$ as recalled in Chapter 2 [30, 31]. This results in two contributions when evaluating the total resolved kinetic energy transport equation namely the laminar viscosity μ and the turbulent viscosity μ_t which takes into account the SGS model. Following these considerations, Daviller *et al.* proposed the definition of the metric *LIKE* constructed starting from the adimentionalized time-average dissipation rate QOI field ($\Phi^\star$):

$$\overline{\tilde{\Phi}} = \overline{(\mu+\mu_t)\left(\frac{\partial \tilde{u}_i}{\partial x_j} + \frac{\partial \tilde{u}_j}{\partial x_i}\right)^2}, \tag{3.4}$$

$$\Phi^\star = \left[1 - \left(\frac{\overline{\tilde{\Phi}} - \overline{\tilde{\Phi}}_{\min}}{\overline{\tilde{\Phi}}_{\max} - \overline{\tilde{\Phi}}_{\min}}\right)\right]^\alpha, \ \Phi^\star \in [0:1], \tag{3.5}$$

$$\text{LIKE} = \Phi^\star(1-\epsilon) + \epsilon. \tag{3.6}$$

In Eq. (3.5) α is a smoothing parameter while ϵ in Eq. (3.6) allows limiting the new cell volume (Δ) which is reduced up to $\epsilon\Delta$ if $\bar{\Phi} = \bar{\Phi}_{\max}$. This is fundamental to avoid drastically reducing the time-step in explicit compressible LES codes subject to CFL condition. Note also that this formulation does not take into account dilatation dissipation due to compressibility effects [120] but it can be considered as a first order approximation for compressible flows.

While the LIKE criterion has been showed to be well suited to improve flow pressure loss predictions (more details in Ref. [106]), in order to completely characterise a turbulent flow in LES including the turbulent activity, the adequate unsteady velocity field should also be properly captured. Recalling the Reynolds decomposition to differentiate mean velocity $\overline{u_i}$ from its fluctuation u_i', performing the Favre and time averaged of Eq. (3.1), it is possible to obtain a balance equation for the mean specific kinetic energy $K = \frac{1}{2}(\overline{u_i})^2$ and the turbulent specific kinetic energy $k = \frac{1}{2}\overline{(u_i')^2}$ for constant-density flows reads:

$$\underbrace{\frac{DK}{Dt}}_{1} = \underbrace{\overline{u_i'u_j'}\frac{\partial \overline{u_i}}{\partial x_j}}_{2} - \underbrace{\nu\frac{\partial \overline{u_i}}{\partial x_j}\frac{\partial \overline{u_i}}{\partial x_j}}_{3} + \underbrace{\frac{\partial}{\partial x_l}\left[\nu\frac{\partial K}{\partial x_l} - \frac{\overline{p}}{\rho}\overline{u_l} - \overline{u_i}\overline{u_i'u_l'}\right]}_{4}, \tag{3.7}$$

$$\underbrace{\frac{Dk}{Dt}}_{1} = \underbrace{-\overline{u_i'u_j'}\frac{\partial \overline{u_i}}{\partial x_j}}_{2} - \underbrace{\nu\overline{\frac{\partial u_i'}{\partial x_j}\frac{\partial u_i'}{\partial x_j}}}_{3} + \underbrace{\frac{\partial}{\partial x_l}\left[-\overline{\frac{p'u_l'}{\rho}} + 2\nu\overline{u_i's_{il}'} - \frac{1}{2}\overline{u_i'u_i'u_l'}\right]}_{4}. \tag{3.8}$$

The terms (1) in Eqs. (3.7), (3.8) correspond to the temporal variation of mean specific kinetic energy K and turbulent specific kinetic energy k, respectively. Terms (4) relate to the flux of mechanical energy. These terms disappear in the integral formulation over the fluid domain if the flow is subject to no power of external viscous forces. Terms (3) are the dissipation of the mean kinetic energy (Φ_m) and of the turbulent kinetic energy (Φ_t), respectively, their sum being Φ. Note that the contribution of Φ_m and Φ_t to the temporal evolution of mean and turbulent kinetic energies is always negative meaning that they drain energy from the fluid and they dissipate the mechanical energy into heat. With the exception of the sign, terms (2) in Eqs. (3.7), (3.8) are equal and refer to the production of turbulent kinetic energy (P_k). The P_k contribution can be either positive or negative, meaning that it represents a transfer of energy from the mean kinetic energy to the turbulent one and vice-versa. Adding Eqs. (3.7), (3.8) the conservation equation for the total specific kinetic energy averaged in time is obtained $\overline{K_c} = \frac{1}{2}\overline{(u_i)^2} = \frac{1}{2}(\overline{u_i})^2 + \frac{1}{2}\overline{(u_i')^2} = K + k$. In such a case, terms (2) cancel each other and the dissipation of total kinetic energy (formulated in Eq. (3.4) for LES) used in the previously defined LIKE criterion (Eq. (3.6)) is retrieved. These considerations highlight a possible limitation on the use of LIKE to capture the full dynamics of a turbulent flow, i.e., while the evolution of the total kinetic energy is well captured by LIKE, the same cannot be said for its distribution between mean and turbulent kinetic energy. The dynamics of the flow is therefore not guarantied unless the absolute level of Φ is known which is not the case in LES due to modelling.

To address this issue, it is interesting to look at the three different fields Φ_m, Φ_t and P_k in the filtered LES formulation. These can then be used as QOI to identify the flow regions where the variation of turbulent and mean kinetic energy is maximum. Note that density is taken into account to be coherent with Eq. (3.4).

$$\overline{\tilde{\Phi}_m} = \overline{(\mu + \mu_t)} \frac{\partial \overline{\tilde{u}_i}}{\partial x_j} \frac{\partial \overline{\tilde{u}_i}}{\partial x_j}, \tag{3.9}$$

$$\overline{\tilde{P}_k} = -\overline{\rho} \overline{\tilde{u}_i' \tilde{u}_j'} \frac{\partial \overline{\tilde{u}_i}}{\partial x_j}, \tag{3.10}$$

$$\overline{\tilde{\Phi}_t} = \overline{(\mu + \mu_t) \frac{\partial \tilde{u}_i'}{\partial x_j} \frac{\partial \tilde{u}_i'}{\partial x_j}}. \tag{3.11}$$

A constructed field $\Phi_{m,t,p}$ is hereby proposed as a combination of these three QOI:

$$\Phi_{m,t,p} = \underbrace{\beta \frac{\overline{\tilde{\Phi}_m} - \left(\overline{\tilde{\Phi}_m}\right)_{min}}{\left(\overline{\tilde{\Phi}_m}\right)_{max} - \left(\overline{\tilde{\Phi}_m}\right)_{min}}}_{1} + \underbrace{\gamma \frac{\mid \overline{\tilde{P}_k} \mid + \overline{\tilde{\Phi}_t} - \left(\mid \overline{\tilde{P}_k} \mid + \overline{\tilde{\Phi}_t}\right)_{min}}{\left(\mid \overline{\tilde{P}_k} \mid + \overline{\tilde{\Phi}_t}\right)_{max} - \left(\mid \overline{\tilde{P}_k} \mid + \overline{\tilde{\Phi}_t}\right)_{min}}}_{2}. \tag{3.12}$$

Term (1) in Eq. (3.12) corresponds to the non-dimensional dissipation rate of mean kinetic energy $\overline{\tilde{\Phi}_m}$, while the term (2) is the non-dimensional sum of the absolute production $\mid \overline{\tilde{P}_k} \mid$ and the dissipation rate of turbulent kinetic energy $\overline{\tilde{\Phi}_t}$. While the first term looks for regions where variations of mean kinetic energy are more important, the second one underlines regions where variations in turbulent kinetic energy are large. To balance the two contributions, the coefficients β and γ are here introduced. To choose their values, after the first refinement iteration in which they can be equal to 1, it is possible to look at the convergence rate of the mean (β) and the turbulent (γ) kinetic energies in the flow field with respect to the previous refinement iteration. Once the field $\Phi_{m,t,p}$ is defined, it is possible to limit its variation in $[\epsilon : 1]$ following the same procedure as in Eqs. (3.5), (3.6).

Note that, in the limits of the following applications (see section 3.3 and section 3.4), $\mid \overline{\tilde{P}_k} \mid$ and $\overline{\tilde{\Phi}_t}$ happen with very similar intensity in the same regions of the domain, meaning that when energy is driven from the mean flow to the turbulent activity ($\overline{\tilde{P}_k}$) it is also like to be dissipated ($\overline{\tilde{\Phi}_t}$). Therefore, the general procedure can be further simplified by canceling out the $\overline{\tilde{P}_k}$ term from eq. 3.12, since $\overline{\tilde{P}_k}$ and $\overline{\tilde{\Phi}_t}$ give similar information in terms of QOI. The metric ends up in being a balance between $\overline{\tilde{\Phi}_m}$ and $\overline{\tilde{\Phi}_t}$ thanks to the the parameters β and γ. The same role is played by α in eq 3.5: when increasing α one increases the importance

given to smaller dissipation values (i.e. typically $\overline{\tilde{\Phi}_t}$) with respect to large values (i.e. typically $\overline{\tilde{\Phi}_m}$) and it is equivalent to increase γ with respect to β. Therefore it is useful to look at the different fields in order to correctly control the metric construction, giving for example a physical meaning and a proper value to α in the LIKE criterion or fixing the β and γ in the generalized procedure.

3.2.2 Flame criterion

Flames are usually too thin to be fully-resolved in numerical simulations. A combustion model is thus usually used to overcome this limitation. While multiple models could be found in the literature (see Ref. [121] for an exhaustive review) this work will deal with the Thickened Flame model (TFLES) in which flames are artificially thickened to be resolved on the mesh, without modifying their flame speeds [49, 60, 61, 62, 63, 64] (see Chapter 2 for more details). The thickening process is done by multiplying diffusion terms and dividing reaction rates by a local thickening factor F. In case of a turbulent flame, since a thickened reactive layer is less sensitive to turbulence, an efficiency function Ξ_Δ is introduced to compensate for the corresponding reduction of flame surface [49, 61].

The value of the thickening factor F is chosen in order to guarantee n_F points (usually between 5-8 depending on the complexity of the chemical description [47]) in the flame thermal thickness (δ_T) and can be locally evaluated as:

$$F(\overrightarrow{x}, t) = \frac{n_F \Delta_x(\overrightarrow{x})}{\delta_T(\phi, T)}, \tag{3.13}$$

where $\Delta_x$is the characteristic mesh size. Note that the local applied thickening factor F varies both in space $\overrightarrow{x}$ and time t since Δ_x is usually not uniform and varies in space and the thermal flame thickness δ_T depends mainly on the equivalence ratio ϕ and on the temperature T of the fresh gases which can vary as well both in space and time.

Following these definitions, to build a proper flame refinement criterion two data are needed: the time-averaged flame position and the local mesh size. The first can be easily computed using a flame sensor S. This sensor is equal to unity in the region where the flame is present and is zero elsewhere. It is straightforward to understand that the time-averaged field $\overline{S}$ represents the local probability of finding a flame. Note that it is possible to define a threshold value ($\overline{S}_{limit}$) to flag the domain regions where the probability to find the flame is at least $\overline{S}_{limit}$. For example, the iso-contour at $\overline{S}_{limit} = 0.1$ splits the domain in two region: one where $\overline{S}_{limit} > 0.1$ and the probability to find the flame is more then 10%

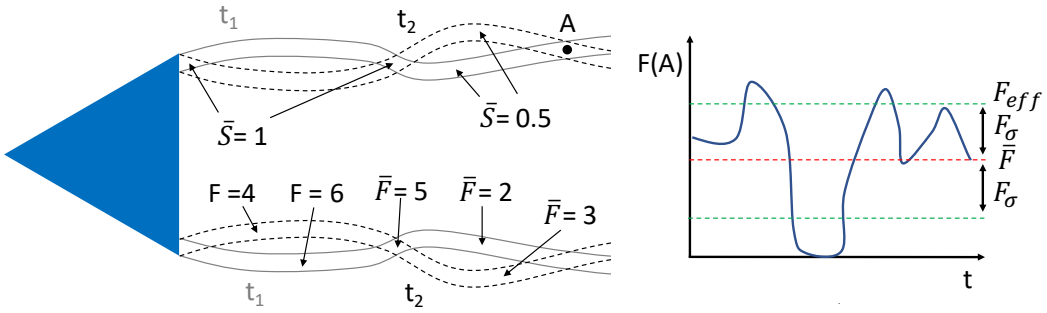

Figure 3.2: Example of $\overline{S}$ and $\overline{F}$ fields. Flame has different position in the two instants t_1 and t_2 and different instantaneous F. It is evident how $\overline{S}$ corresponds to the probability to locally find the flame and $\overline{F}$ under-estimate the local thickening required.

and should be taken into consideration for mesh refinement, the other where $\overline{S}_{limit} < 0.1$ and the probability to find the flame is less then 10% and one can decide to avoid refining in this region.

In the regions detected by this sensor, a target flame resolution F_{target} can then be defined. By comparing this value with the time-averaged thickening $\overline{F}$, according to Eq. (3.13), the information on the characteristic mesh size is retrieved. However, $\overline{F}$ may locally underestimate the thickening needed for the calculation. This is explained hereafter with the help of the schematic shown in Fig.3.2: (1) combustion being an unsteady process, the flame may not always be locally present in a specific region. (2) Local variations of equivalence ratio (e.g. in partially premixed flames) may furthermore induce variations in flame thickness and hence in instantaneous locally applied F. To take into account these local variation of F, an effective thickening field F_{eff} can be reconstructed from the time-averaged field $\overline{F}$ and its standard deviation F_σ: $F_{eff} = \overline{F} + F_\sigma$. [1]

Once the field F_{eff} is computed and a suitable F_{target} chosen, it is possible to build the Flame Effective Thickening (FET) metric as follows:

$$FET = \begin{cases} \frac{F_{target}}{F_{eff}} & \text{if } \overline{S} \geq S_{limit} \text{ and } F_{target} \leq F_{eff} \\ 1 & \text{elsewhere,} \end{cases} \tag{3.14}$$

where S_{limit} is a threshold value on the flame sensor. The refined mesh is then obtained by multiplying each cell characteristic size Δ_x by the FET metric achieving the desired resolution (i.e. desired thickening F) in the region where the probability to find the flame is higher or equal to S_{limit}. Using the FET metric, it is also straightforward to compute an *a priori* (i.e. before refinement)

[1] It is worth notice that if F can be described by a Gaussian distribution, F_{eff} statistically does not underestimate the local maximum thickening F for the 84.15% of the time, which is considered to be a reasonable condition.

estimation of the required number of cells of the refined mesh ($N_{refined}$) as a function of F_{target} and S_{limit}:

$$N_{refined} = \sum_{i}^{N_{coarse}} \left(\frac{\Delta_{x \text{ refined}}}{\Delta_{x \text{ coarse}}} \right)^3_i = \sum_{i}^{N_{coarse}} \left(\frac{1}{FET} \right)^3_i . \tag{3.15}$$

Note also that this approach can be easily extended to cover other sub-grid combustion models. In fact, the flame sensor S, and hence the flame probability $\overline{S}$, can always be defined independently from the sub-grid combustion model used. For example, starting from the heat release rate field $\dot{q}$ one can choose to set $S = 1$ in the region where $\dot{q}$ is larger than a certain threshold value. Equivalently an iso-C (i.e. progress variable) or iso-Z (i.e. mixture fraction) values can be introduced in place of $\overline{S}$ (any combustion marker would work). In this way the reactive ROI can be defined following the same procedure. The only difference stays in the refinement level which cannot be chosen on the base of the thickening factor F for other specific turbulent combustion models. However, it is straightforward to select the refinement level in order to have the desired mesh size with respect to the characteristic length of the problem, for example the thermal flame thickness δ_T.

The refined mesh is obtained by multiplying each cell characteristic size Δ_x by the FET metric. As a results, the metric leads to a mesh with the desired resolution (i.e. desired thickening F) in the region where the probability to find the flame is higher or equal to S_{limit}. The statistical approach here proposed allows to have a resolution higher then the desired one for most of the time (i.e. 84.15% in the Gaussian distribution scenario) and avoids asking for too high resolution which is effectively needed just for small part of the time. Indeed, if one takes directly the F_{max} (instead of F_{eff}) value into consideration, the real resolution of the refined mesh will be always higher than the desired one, leading to a heavy mesh and high computational cost. For this reason and for the good behaviour confirmed in the applications, F_{eff} is considered to be a reasonable reference to build the FET metric. From an industrial point of view, the choice of this criterion is very promising since the user can either ask for a certain resolution in the flame region (i.e. defining F_{target}) either asks for the maximum possible resolution with a certain mesh cells number. For example, it is straightforward to compute *a priori* (i.e. before refinement) the resulting number of cells of the refined mesh ($N_{refined}$) as a function of F_{target}:

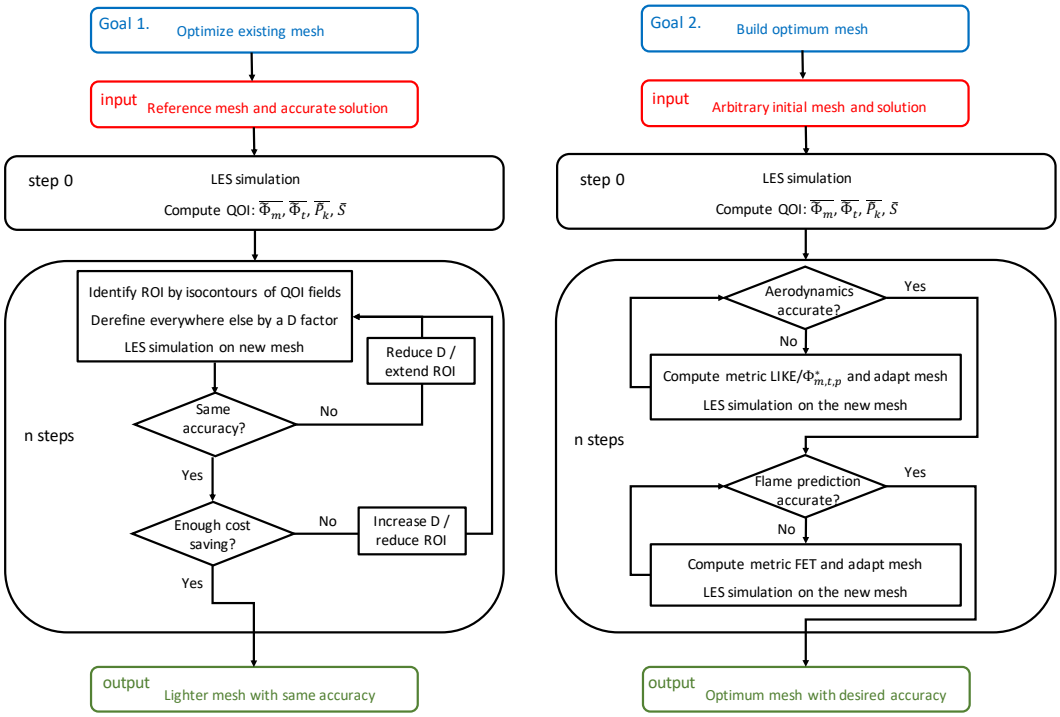

Figure 3.3: Scheme of the two mesh adaptation procedures: optimization of existing reference mesh and building of optimal mesh from initial arbitrary one.

3.2.3 Refinement procedure

The two previously defined QOI's for aerodynamics and flame are now combined following the two procedures schematized in Fig. 3.3 to either build an optimal mesh or optimize an existing one (to avoid waste of computational resources). The optimization of an existing reference mesh which already has satisfactory accuracy with respect to experimental data is based on the observation that hand-made meshes usually overestimate the needed number of cells in regions where no relevant physics happens. For example, when dealing with reactive flows, common practice is to refine in the region where flame is expected to be according to user's experience and, to be sure that the flame is well-resolved, this generally brings to an over-estimation of the ROI. The procedure to optimize an existing mesh is straightforward: first LES is computed on the reference mesh to evaluate the QOI's $\overline{\tilde{\Phi}_m}$, $\overline{\tilde{\Phi}_t}$, $\overline{\tilde{P}_k}$ and $\overline{S}$. Then it is possible to identify the ROI by defining limits on the QOI: for example $\overline{\tilde{\Phi}_{mlimit}} = 0.01 * \overline{\tilde{\Phi}_{mmax}}$, $\overline{\tilde{\Phi}_{tlimit}} = 0.01 * \overline{\tilde{\Phi}_{tmax}}$ and $\overline{\tilde{P}_{klimit}} = 0.01 * \overline{\tilde{P}_{kmax}}$ to identify the ROI where most of mean kinetic energy dissipation and production or dissipation of turbulent kinetic energy happen while a $\overline{S}_{limit} = 0.01$ defines the ROI where there is a large probability to find the flame.

The ROI can be defined as the union of these regions, as follows,

$$\begin{aligned} ROI = &\left(\overline{\tilde{\Phi}_m} \geq \overline{\tilde{\Phi}}_{mlimit}\right) \cup \left(\overline{\tilde{\Phi}_t} \geq \overline{\tilde{\Phi}}_{tlimit}\right) \\ &\cup \left(\mid \overline{\tilde{P}_k} \mid \geq \mid \overline{\tilde{P}_k} \mid_{limit}\right) \cup \left(\overline{S} \geq \overline{S}_{limit}\right). \end{aligned} \tag{3.16}$$

A uniform metric D (larger than 1) can be then defined in the rest of the domain to derefine the mesh. LES is performed on the new mesh reiterating the described procedure if needed.

The building of an optimal mesh starting from an arbitrary initial mesh follows the initial step of computing the QOI's. At this point, due to the possible additional difficulty of a totally wrong initial solution, a check on the accuracy of the aerodynamics prediction is needed. If accuracy is not satisfactory, based on an analysis of the fields $\overline{\tilde{\Phi}_m}$, $\overline{\tilde{\Phi}_t}$, $\overline{\tilde{P}_k}$ it is possible to decide to use the LIKE metric with proper α parameter or $\Phi^*_{m,t,p}$ metric if $\overline{\tilde{\Phi}_t}$, $\overline{\tilde{P}_k}$ happen in different regions of the domain. The refinement step brings to a new mesh on which LES can be computed and accuracy of the aerodynamic field checked until it becomes satisfactory. At this point, if the flame prediction is not accurate, the FET metric can be evaluated and used to refine the mesh in the flame region. The iterative refinement procedure finally leads to an optimum mesh with the desired solution accuracy. In the following both proposed strategies are first applied and validated on the academic VOLVO test case (section 3.3). The methodology is then applied to the PRECCINSTA rig (section 3.4) showing that the method can be successfully applied to more complex configurations.

3.3 A fully premixed bluff-body stabilized flame: the VOLVO test case

Well-known as a benchmark for turbulent reacting simulations [111, 122, 123], the VOLVO combustor [108, 109, 110] consists in a 3D propane-air turbulent premixed flame burning in a straight rectangular cross-section channel (0.12 m $\times$ 0.24 m). A bluff-body flame-holder is used to stabilize the flame. Fresh gas conditions are $T = 288\ K$ and $P = 101325\ Pa$. The computational domain shown in Fig. 3.4 has the exact longitudinal and transverse dimensions as the original burner. LES are performed using the AVBP solver developed by CERFACS [124]. It solves the fully compressible Navier-Stokes multispecies equations on unstructured grids (Chapter 2). The flow is integrated using the fully compressible explicit Lax-Wendroff (LW) convection scheme [125] (second order in

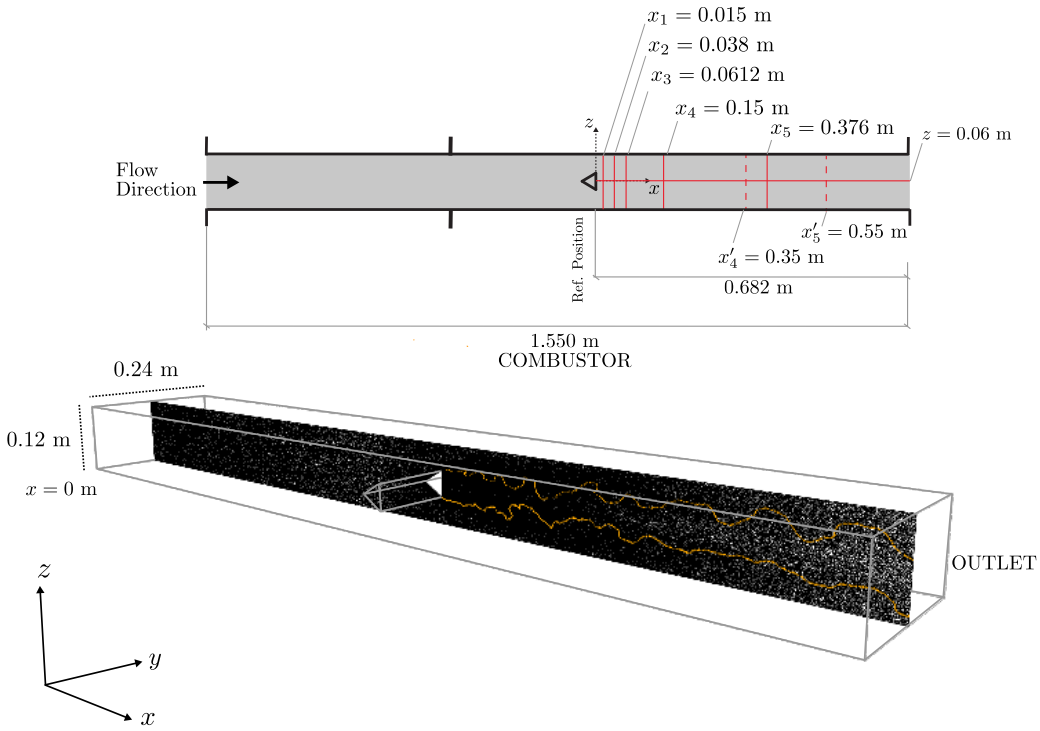

Figure 3.4: Overview of the computational domain. The flame is represented through an iso-contour of progress variable $c = 0.5$ (orange line). Measurements were made on seven longitudinal ($x_1, x_2, x_3, x_4, x'_4, x'_5$ and x_5) and one (z) transverse locations.

time and space). Inlet and outlet boundary conditions are treated with Navier-Stokes Characteristic Boundary Conditions (NSCBC) [30]. These two boundary conditions are modeled as non-reflecting sections to avoid exciting a particular acoustic mode. At the inlet, gaseous propane is premixed with air at an equivalence ratio equal to 0.65 and injected at an inlet bulk velocity $U_0 = 17.3\ m/s$. Turbulence is injected at the inlet using the method of Guezennec *et al.* [126] to recover the turbulence intensity measurements [108]. As the wall temperature is not provided in the experiments [108], the walls are modeled as adiabatic no-slip walls. The TFLES model with the Charlette model [61] and a coefficient $\beta_{Ch} = 0.5$ is used.

3.3.1 Results and discussion

Validation of the proposed methodology is hereafter detailed for the optimization of an existing mesh (section 3.3.1.1) and afterward to look for an optimal mesh (section 3.3.1.2).

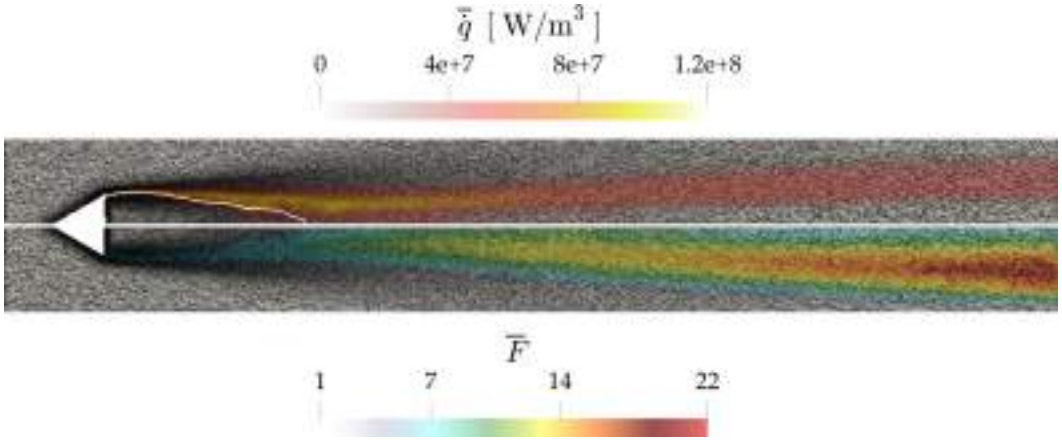

Figure 3.5: Overview of the reference mesh (68M) used by Rochette *et al.*[47]. The flame is represented through an averaged field of heat release rate $\overline{\dot{q}}$. The averaged thickening factor field $\overline{F}$ is also shown. The white iso-contour delimits the recirculation zone ($U_x = 0\ m/s$).

3.3.1.1 Optimizing an existing mesh

The previously proposed strategy (Fig. 3.3) is at first assessed. To do so, the previous calculations of this flame using the same solver performed by Rochette *et al.* [47] is used as a reference. Figure 3.5 reports the averaged field of heat release rate $\overline{\dot{q}}$ and the thickening factor $\overline{F}$ fields predicted by Rochette *et al.* [47] superimposed on the computational grid. With this grid the flame is anchored to the flame-holder between the recirculation zone and the high sheared fresh gas region. It is wrinkled by the eddies generated by the bluff-body and burns until the end of the combustion chamber. The grid consists of 68 million tetrahedral elements for which the mesh has been manually refined in shear and combustion regions achieving a $\Delta_x = 500\ \mu m$ just downstream of the flame-holder. This results in a near wall region of the flame holder dimensionless wall distances of $y^+ = 25$, versus $y^+ = 80$ near the combustor walls. It is possible to notice that the mesh exhibits clusters of cells where no important physics occurs. Following the strategy, the ROI are identified using the previously described QOIs.

Regions of large mean and turbulent kinetic energy dissipation rate are respectively identified by $\overline{\tilde{\Phi}}$ (Eq. (3.4)) and $\overline{\tilde{\Phi}_m}$ (Eq. (3.9)) as presented in Fig. 3.6. The $\overline{\tilde{\Phi}}$ field activates in shear regions just downstream of the flame-holder as well as at the boundary of the recirculation zone and in the boundary-layer nearby the walls. The $\overline{\tilde{\Phi}_m}$ field well detects the dissipation of mean kinetic energy that happens in the wall boundary-layers and in the shear region downstream of the bluff-body. The magnitude of these two fields is comparable, confirming that most of the kinetic energy dissipation acts on the mean form in the shear-region downstream the bluff-body. The gray and the white iso-contours correspond to

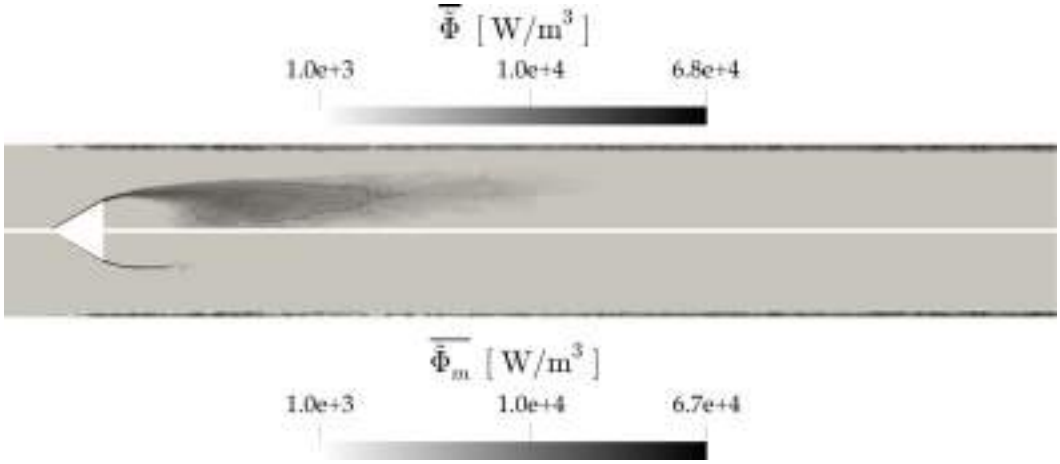

Figure 3.6: QOI fields of $\overline{\tilde{\Phi}}$ and $\overline{\tilde{\Phi}_m}$ for case 68M. The grey and the white iso-contour delimit the ROI where most of the kinetic energy dissipation happen with the values of $\overline{\tilde{\Phi}} = 0.01\ \overline{\tilde{\Phi}}_{max}$ and $\overline{\tilde{\Phi}_m} = 0.01\ \overline{\tilde{\Phi}}_{mmax}$ respectively. Note that log scale is used.

$\overline{\tilde{\Phi}} = 0.01\ \overline{\tilde{\Phi}}_{max}$ and $\overline{\tilde{\Phi}_m} = 0.01\ \overline{\tilde{\Phi}}_{mmax}$ and identify the ROI where most of the dissipation happens.

The QOI fields of $\overline{\tilde{P}_k}$ (Eq. 3.10) and $\overline{\tilde{\Phi}_t}$ (Eq. 3.11) are compared in Fig. 3.7. The gray and the white iso-contours correspond to $\mid \overline{\tilde{P}_k} \mid = 0.01 \mid \overline{\tilde{P}_k} \mid_{max}$ and $\overline{\tilde{\Phi}_t} = 0.01\ \overline{\tilde{\Phi}}_{tmax}$ and identify the regions where large production and dissipation rates of turbulent kinetic energy happen, respectively. Production is negative in the region upstream the bluff-body's corner where the flow axially accelerates and turbulent kinetic energy is converted into mean kinetic energy, reducing the turbulence activity in the flame region. In the downstream shear-layer production is positive, indicating that turbulence and eddies are produced by the bluff-body. In the latter, $\overline{\tilde{\Phi}_t}$ is also activated and its intensity reduces moving downstream as turbulence is no more produced and dissipated. Analysis of the QOI magnitudes suggest that $\overline{\tilde{\Phi}_t}$ is much lower than $\overline{\tilde{P}_k}$ and $\overline{\tilde{\Phi}_m}$. Therefore, when it is added to $\overline{\tilde{\Phi}_m}$, the resulting $\overline{\tilde{\Phi}}$ field is very similar to the $\overline{\tilde{\Phi}_m}$. This explains why, when an α value of 1 in the LIKE criterion is imposed, the mesh is refined just in the region where $\overline{\tilde{\Phi}_m}$ is present. On the contrary, if a large α value is used, more effort is concentrated to smaller $\overline{\tilde{\Phi}}$ values which correspond to regions where $\overline{\tilde{\Phi}_t}$ is present. Note also that regions of large positive $\overline{\tilde{P}_k}$ and large $\overline{\tilde{\Phi}_t}$ largely correspond (i.e. shear-layer downstream the bluff-body and middle region) since when turbulence is produced its dissipation also increases. On one side, the analysis of these fields suggest that, for the present case, taking into consideration a $\overline{\tilde{\Phi}} = 0.01\ \overline{\tilde{\Phi}}_{max}$ defines a sufficiently large ROI that includes regions where large dissipation of mean and turbulent kinetic energy happen ($\overline{\tilde{\Phi}_m}$ and $\overline{\tilde{\Phi}_t}$). On the other side, while

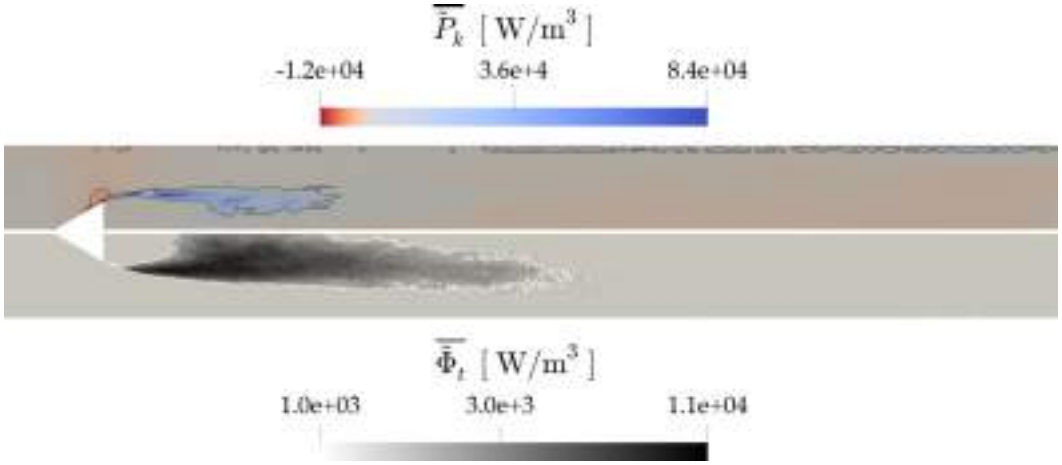

Figure 3.7: QOI fields of $\overline{\tilde{P}_k}$ and $\overline{\tilde{\Phi}_t}$ for case 68M. The gray and the white iso-contours correspond to $\mid \overline{\tilde{P}_k} \mid = 0.01 \mid \overline{\tilde{P}_k} \mid_{max}$ and $\overline{\tilde{\Phi}_t} = 0.01$ $\overline{\tilde{\Phi}}_{tmax}$ and identify the regions where large production and dissipation rates of turbulent kinetic energy happen respectively. Note that log scale is used only for $\overline{\tilde{\Phi}_t}$ field.

the region where $\overline{\tilde{P}_k}$ is negative is well captured by the $\overline{\tilde{\Phi}} = 0.01\ \overline{\tilde{\Phi}}_{max}$ iso-contour, in the region where production is negative no dissipation happens and it must be taken into account by defining a ROI delimited by the $\mid \overline{\tilde{P}_k} \mid = 0.01 \mid \overline{\tilde{P}_k} \mid_{max}$ for example. In the present case the union of the regions delimited by $\overline{\tilde{\Phi}}$ and $\mid \overline{\tilde{P}_k} \mid$ are able to identify a ROI where most of the aerodynamics activity happens.

For the reactive part, the time-averaged flame sensor $\overline{S}$ is shown in Fig 3.8. The bluff-body region exhibits a $\overline{S}$ equal to unity suggesting an attached flame. Moving downstream, $\overline{S}$ is more spread indicating oscillations of the reactive layer due to interaction with the eddies generated by the bluff-body. A value of $\overline{S} = 0.5$ is sufficient in this case to flag the ROI (i.e., where the probability to find the flame is higher than 50%). Finally, the bottom part of Fig. 3.8 shows the number of QOI's which are locally activated simultaneously. The zone where no QOI is active will be coarsened (by an iso-factor D of 2), whereas the remaining mesh will be untouched. Observing the entire ROI, the only zone where all three QOIs are activated locates in the shear-layer region after the bluff body where large aerodynamics activity and flame are both present. Otherwise only one QOI seems at once underlining the importance of using all three quantities of interests to capture all the physics of the problem.

The resulting optimised mesh shown in Fig. 3.9 consists of 45M cells, i.e., 33% lighter with respect to the reference one [1]. As expected the mesh is finer in the

[1]Note that for all meshes generated in this work, the minimum cell sized is kept the same as the reference mesh in order to obtain a computational cost directly proportional to the number of elements (without modifying the time-step due to CFL condition).

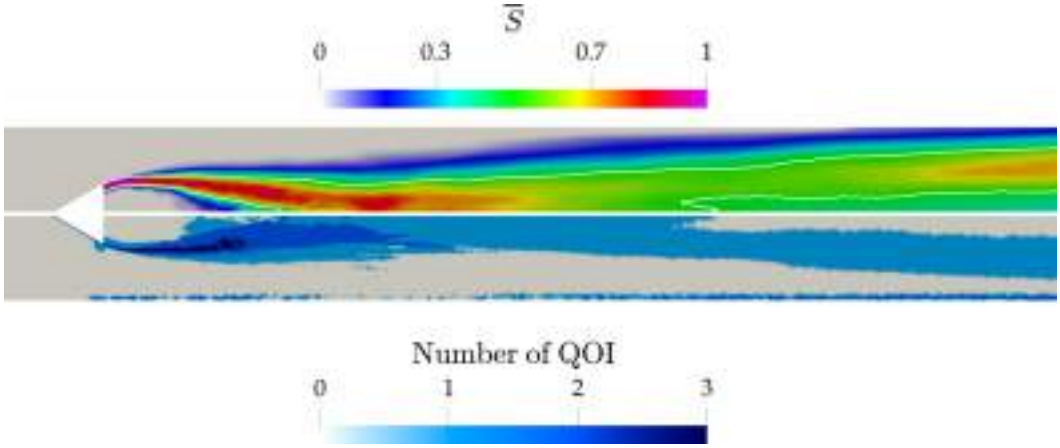

Figure 3.8: QOI field of $\overline{S}$ for case 68M and number of matching criteria delimiting a ROI. The white iso-contour correspond to $\overline{S} = 0.5$

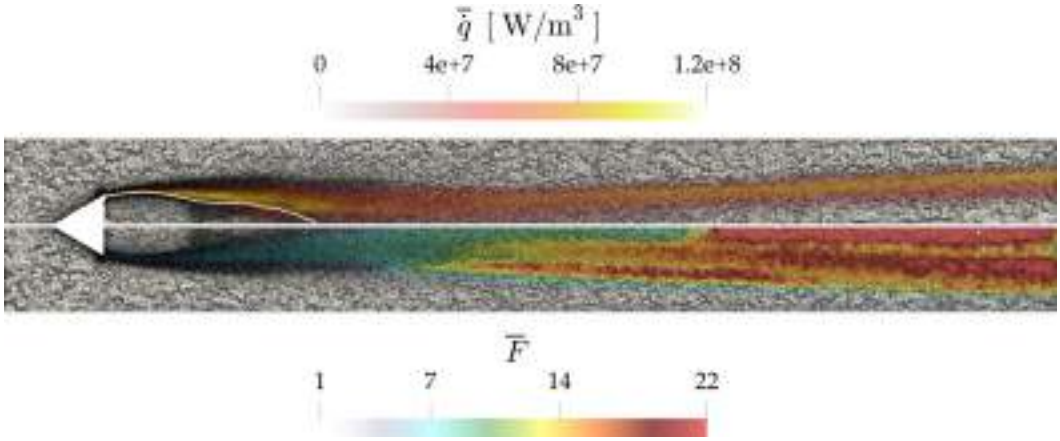

Figure 3.9: Overview of the 45M optimized mesh obtained by coarsening regions where no important physics occurs. The flame is represented through an averaged field of heat release rate $\overline{\dot{q}}$. Time-averaged thickening factor field $\overline{F}$ is also shown. The white iso-contour delimits the recirculation zone ($U_x = 0\ m/s$).

shear and flame regions and coarser in fresh and burnt gas zones.

The time-averaged heat release rate $\overline{\dot{q}}$ and thickening factor field $\overline{F}$ for the optimized mesh case (45M) can be compared to the reference mesh of Fig. 3.5. The heat release rate fields are very similar, while looking at $\overline{F}$, it is possible to observe an increase of the thickening factor along the axial direction with respect to the reference mesh. This behaviour is linked to the increasing cell sizes. Such maximum thickening values are not pathological for the simulation, but obviously the bigger are the cell sizes, the lower the accuracy of the LES in predicting flame-turbulence interaction.

A second possible exercise could be to further refine this 45M elements mesh up to the same cost as the one of the reference mesh (i.e., $\simeq$ 68M), to verify if

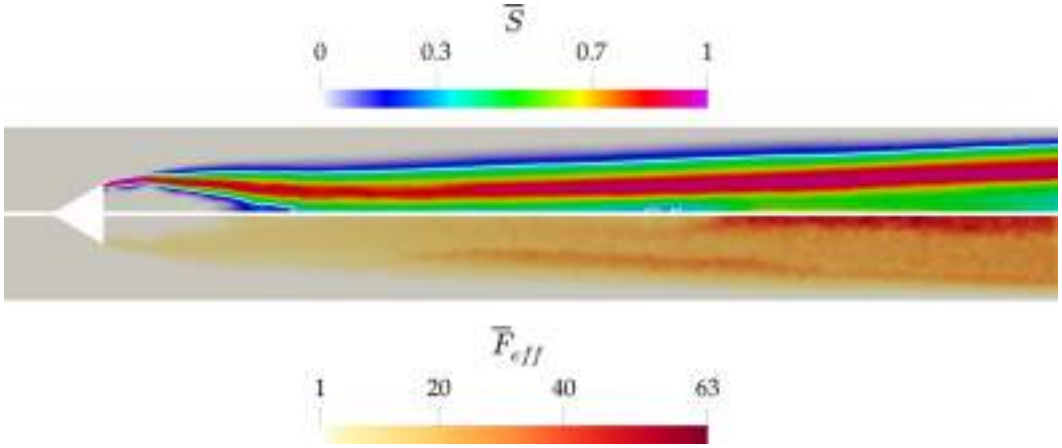

Figure 3.10: QOI fields of flame probability $\overline{S}$ and the effective thickening $\overline{F_{eff}}$ for case 45M. The white iso-contour correspond to $\overline{S} = 0.3$

better results can be obtained. Since the aerodynamic field is now well-captured, the FET criterion is hereby used. The flame probability $\overline{S}$ and the effective thickening field $\overline{F}_{eff}$ for the optimized 45M mesh are presented in Fig. 3.10. The ROI where the probability to find the flame is higher than 30% can then be easily flagged by the line where $\overline{S}$=0.3 (white iso-contour), top part of Fig. 3.10. The field $\overline{F}_{eff}$ can then be used to build the FET metric as explained in section 3.2.2. However, in the present application, the idea is to improve the reference mesh without overcoming a fixed computational cost. To do so, F_{target} is fixed following Eq. (3.15) in order to have very similar number of cells as in the reference mesh. In that case, the *a priori* evaluation of cells number leads to $F_{target} \approx 40$ and to a refined mesh with 67M of cells which is comparable to the reference mesh. The resulting mesh (67M) in shown in Fig. 3.11. It has the same cost as the reference mesh but with a better resolution in the ROI. As expected the mesh is finer at the end of the burner in combustion regions.

The time-averaged heat release rate $\overline{\dot{q}}$ and thickening factor field $\overline{F}$ for the refined mesh case (67M) are superimposed to the grid in Fig. 3.11. The averaged flame and the recirculation zone (white iso-contour) downstream the bluff-body are very similar to the 45M and 68M cases. However, it is evident that $\overline{F}$ is much more homogeneous, especially in the region far downstream as expected and the instantaneous applied thickening F is statistically always lower than F_{target}.

A comparison of the three aerodynamic predicted fields and the experiments is finally presented to further validate the refinement procedure in Fig. 3.12. The axial profiles of the mean axial velocity component are reported in Fig. 3.12(a). It is evident how the reference mesh and the optimized 45M mesh give very similar results, confirming that the ROI where important physics happen are well

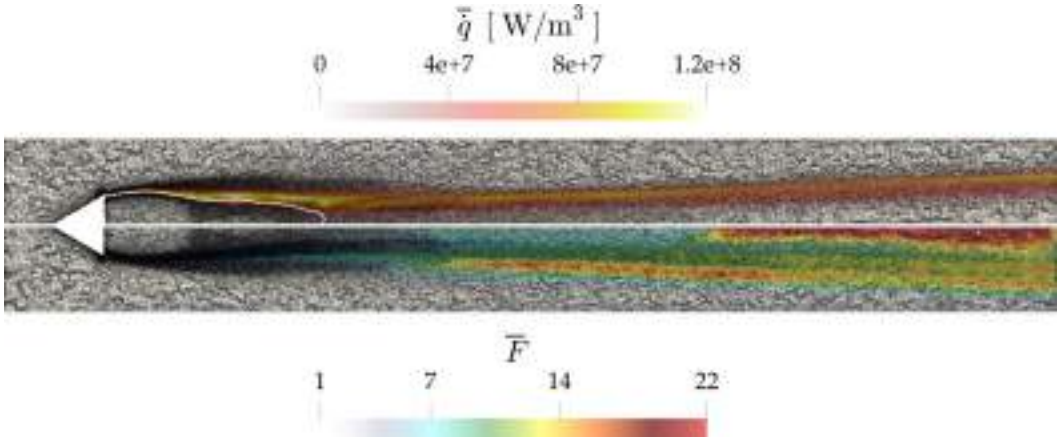

Figure 3.11: Overview of the 67M optimized mesh obtained by refining in high thickening regions using the FET criterion. The flame is represented through a time-averaged field of heat release rate $\overline{\dot{q}}$. The time-averaged thickening factor field $\overline{F}$ is also shown. The white isocontour delimits the recirculation zone ($U_x = 0\ m/s$).

identified by the proposed procedure. The 67M mesh instead shows improved results in the prediction of the recirculation zone and also in the acceleration of the burnt gases, which is a direct result of the increased resolution in the last part of the combustion chamber. The mean normalized axial velocity component is well captured in all cases, as showed by the transverse profiles at different measurement planes in Fig. 3.12(b), confirming that the optimized 45M mesh does not worsen the LES prediction of the reference mesh. Same conclusions can be deduced by looking at transverse profiles of normalized RMS of the axial and transverse velocity fluctuations from x_1 to x_5 shown in Fig. 3.12(c-d), respectively. The optimized 45M mesh gives the same solution accuracy as the reference case and the refined mesh (67M) shows closer results to the experimental data, for example in the prediction of low turbulence activity (low U_{rms} values) far from the axis.

From this analysis, it is evident that the selected QOI's are able to flag important flow regions that determine the LES accuracy, both in terms of aerodynamics and reaction zone. Following the optmization procedure, it is possible to speed up the calculation while having the same accuracy of the reference mesh. Another step of refinement can then improve results accuracy without overwhelming the cost of the reference mesh. A comparison of these results with the $arc - ttgc$ solution [47] shows that it is possible to reach the same accuracy with a 2step chemistry and the Lax Wendroff scheme (which are must cheaper) when using an optimized mesh that follows a mesh refinement procedure based on physical QOI, like the one proposed.

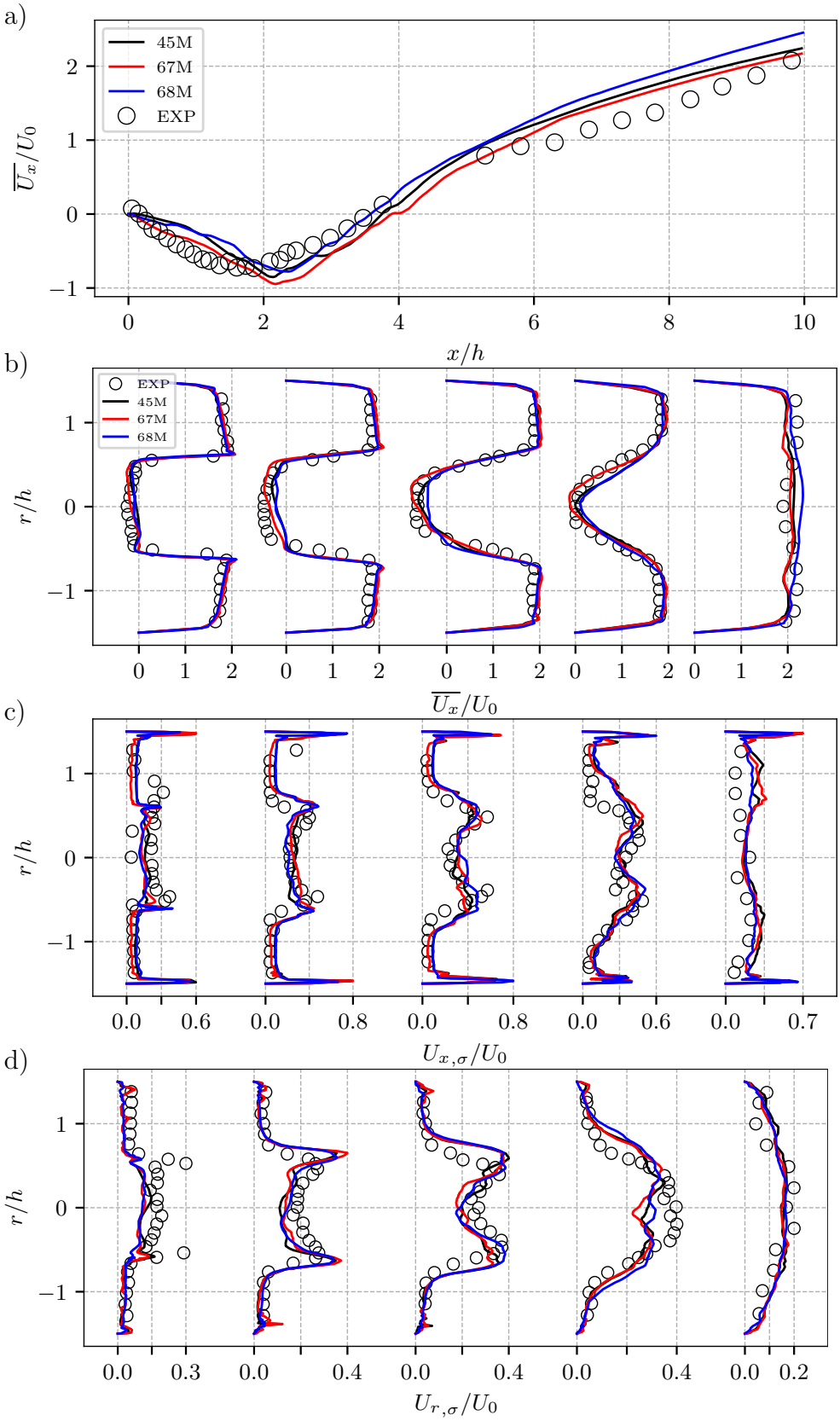

Figure 3.12: Comparison between experimental velocity profiles and LES for the 45M, 67M and 68M (reference) cases. (a) Mean axial velocity evolution along the central axis. (b) Transverse profiles at measurement planes x_1- x_5 of the mean normalized axial velocity, (c) the normalized RMS axial velocity component and (d) the normalized RMS transverse velocity component.

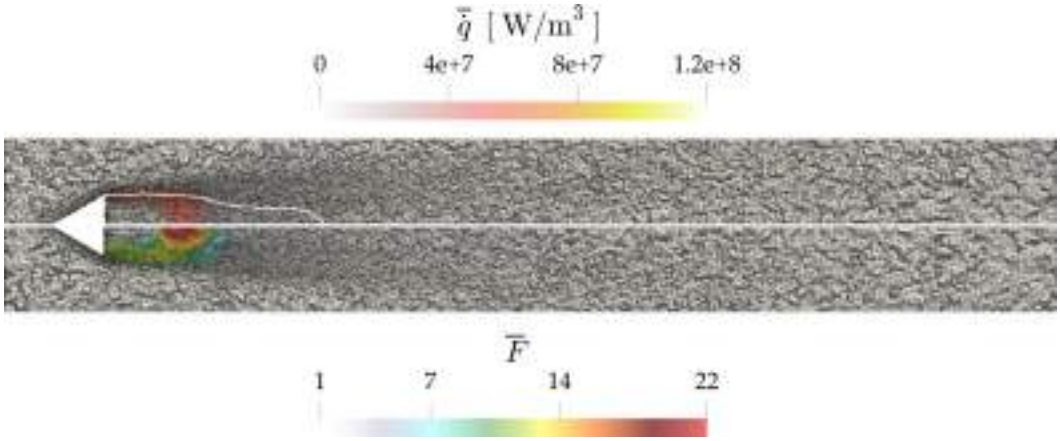

Figure 3.13: Overview of the initial 10M coarse mesh obtained by coarsening by a factor of two everywhere in the domain the reference mesh. The flame is represented through an averaged field of heat release rate $\overline{\dot{q}}$. Thickening factor field $\overline{F}$ is also shown. The white iso-contour delimits the recirculation zone ($U_x = 0\ m/s$).

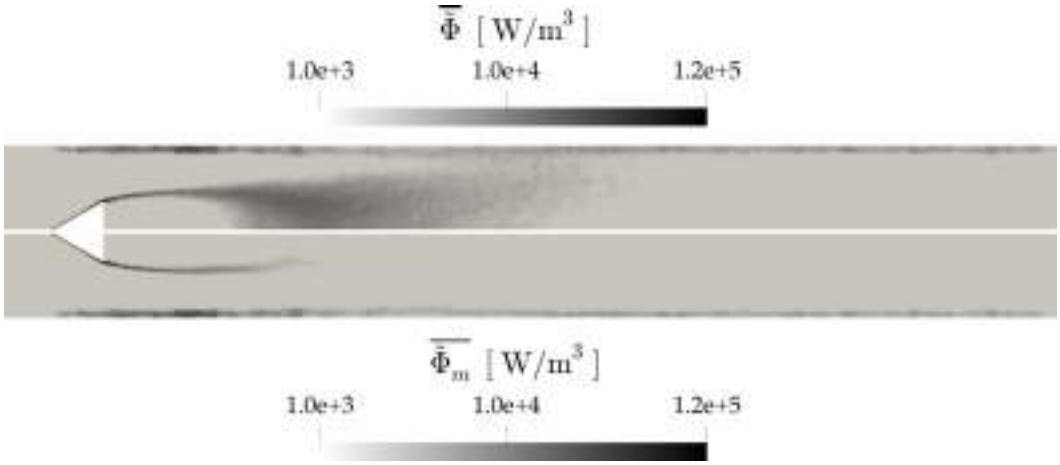

Figure 3.14: QOI fields of $\overline{\tilde{\Phi}}$ and $\overline{\tilde{\Phi}_m}$ for case 10M. Note that log scale is used.

3.3.1.2 Building an optimum mesh

The second refinement strategy proposed in Fig. 3.3 is now discussed. It consists in building an optimum mesh from an arbitrarily (coarse) one which in this case is the 10M mesh shown in Fig. 3.13 together with the predicted time-averaged heat release rate $\overline{\dot{q}}$ and thickening field$\overline{F}$. Due to a poor mesh resolution, the flame shape is totally wrong compared to the reference case: the flame is short and burns inside of the wake of the flame-holder and the recirculation zone (white iso-contour) is too long. The objective is thus to converge to a correct solution starting from a wrong one through the mesh refinement strategy.

Following the mesh refinement procedure, all QOI's are computed on the

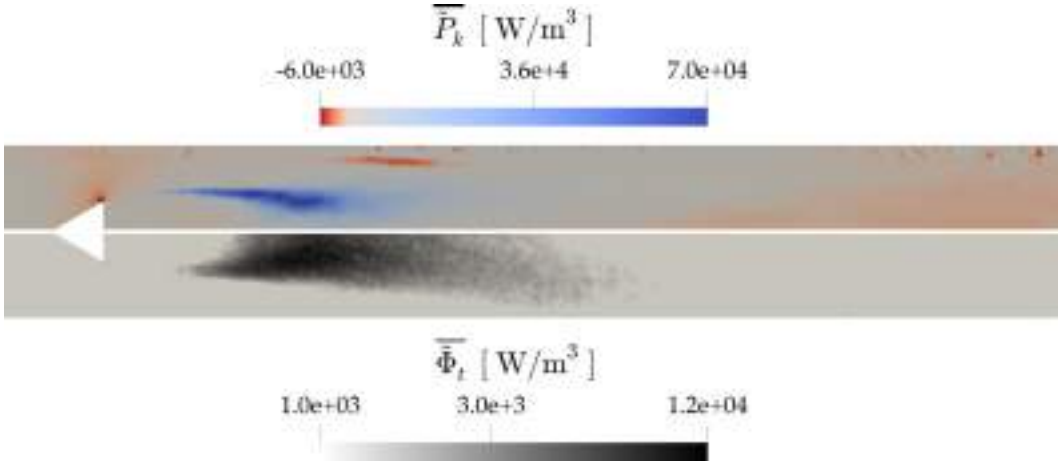

Figure 3.15: QOI fields of $\overline{\tilde{P}_k}$ and $\overline{\tilde{\Phi}_t}$ for case 10M. Note that log scale is used only for $\overline{\tilde{\Phi}_t}$ field.

coarse mesh. Total dissipation rate of kinetic energy $\overline{\tilde{\Phi}}$ and its mean part $\overline{\tilde{\Phi}_m}$ are presented in Fig. 3.14. The field structure already observed on the reference mesh (Fig. 3.6) is recovered also on the coarse mesh with the only difference being the magnitude of dissipation which is (as expected) higher with the coarse mesh. As a result, dissipation of mean kinetic energy happens mainly at the wall boundary-layer and in the shear-layer of the bluff-body.

Dissipation rate of turbulent kinetic energy $\overline{\tilde{\Phi}_t}$ is presented in Fig. 3.15 together with the production rate $\overline{\tilde{P}_k}$. As on the reference mesh, $\overline{\tilde{\Phi}_t}$ is large in the wake of the bluff-body and $\overline{\tilde{P}_k}$ exhibits a negative (red) region at the flame-holder corner (where turbulent kinetic energy is transferred to the mean field) and a positive (blue) region in the shear-layer (where mean kinetic energy is transferred to turbulence).

From the aerodynamics QOI fields, the LIKE criterion (Eq. (3.6)) is at first used to build a refinement metric. As a results from the comparison between the different QOI's, a value of α of 1 is selected, together with a ϵ of 0.5 to avoid refining too much in small regions. The resulting mesh of 17M did not provide satisfactory accuracy in the aerodynamic field prediction (results not shown) and the same procedure is applied again resulting in the 29M mesh shown in Fig. 3.16. A correct prediction of the flame shape which now extends once again until the end of the combustion chamber is achieved as it is possible to observe from the averaged heat release rate $\overline{\dot{q}}$ and thickening factor field $\overline{F}$. This indicates that the refinement of the shear-layer achieved with the aerodynamic QOI's increases the accuracy of the prediction of the velocity gradients in these regions allowing the presence of the flame as in the experiments. Nevertheless, the maximum thickening factor obtained with this 29M mesh is still too high if

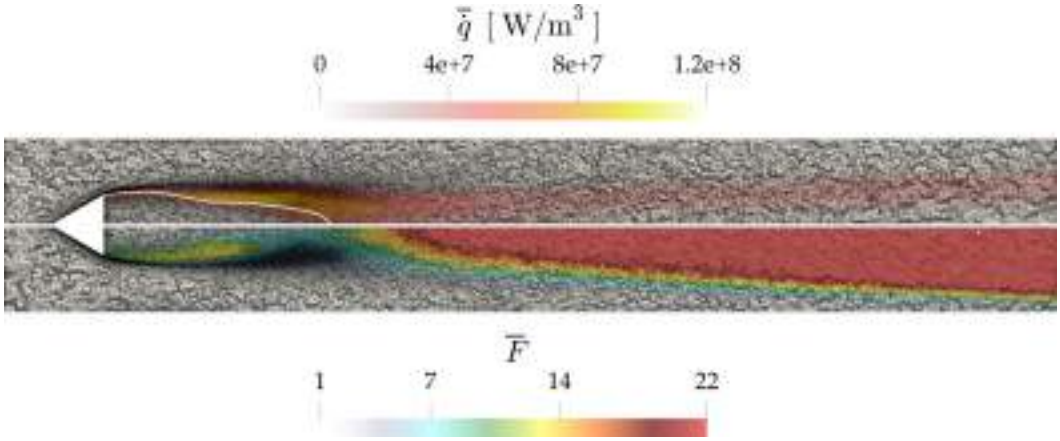

Figure 3.16: Overview of the 29M mesh obtained after the aerodynamics second refinement step using LIKE criterion. Time-averaged heat release rate $\overline{\dot{q}}$ and thickening factor field $\overline{F}$ are superimposed to the grid. The white iso-contour delimits the recirculation zone ($U_x = 0\ m/s$).

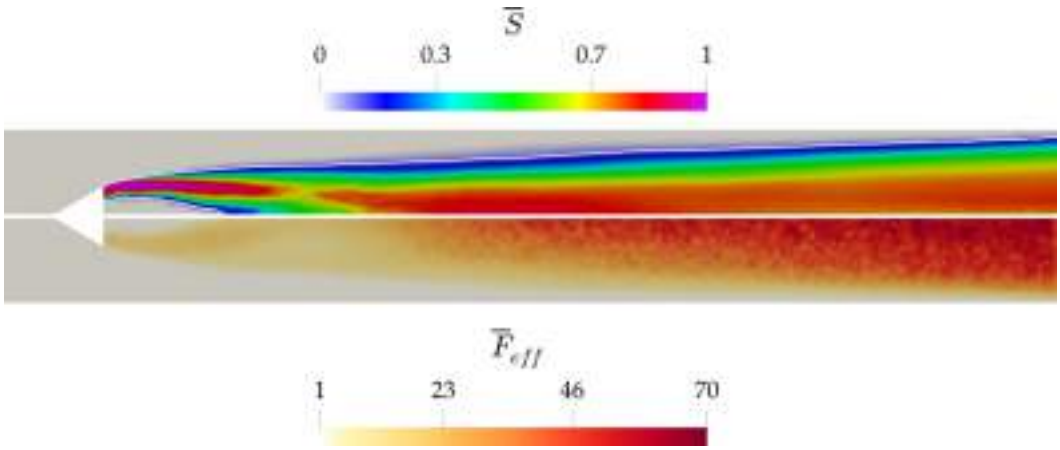

Figure 3.17: QOI fields of flame probability $\overline{S}$ and the effective thickening $\overline{F_{eff}}$ for case 29M. The white iso-contour correspond to $\overline{S} = 0.1$.

compared to the reference case especially at the end of the burner. This may cause an incorrect estimation of the flame-turbulence interaction especially if the characteristic length of turbulence across the computational domain is changing due to turbulence production/dissipation [47].

As before, to improve the resolution in the flame region, the FET flame criterion is used. QOI fields of flame probability $\overline{S}$ and the effective thickening $\overline{F_{eff}}$ are showed in Fig. 3.17 and used to build the FET criterion.

The *a priori* estimation of the number of cells (Eq. (3.15)) is then used to chose $\overline{F}_{target}$ and $\overline{S}_{limit}$. The obtained curves are showed in Fig. 3.18. With the objective to achieve the same cost as the previously discussed optimized 45M mesh, a $\overline{F}_{target}$ of 15 and a $\overline{S}_{limit}$of 0.1 are selected. Note that for low values of $\overline{S}_{limit}$ the cells number do not change significantly because the region where $\overline{F}_{eff}$

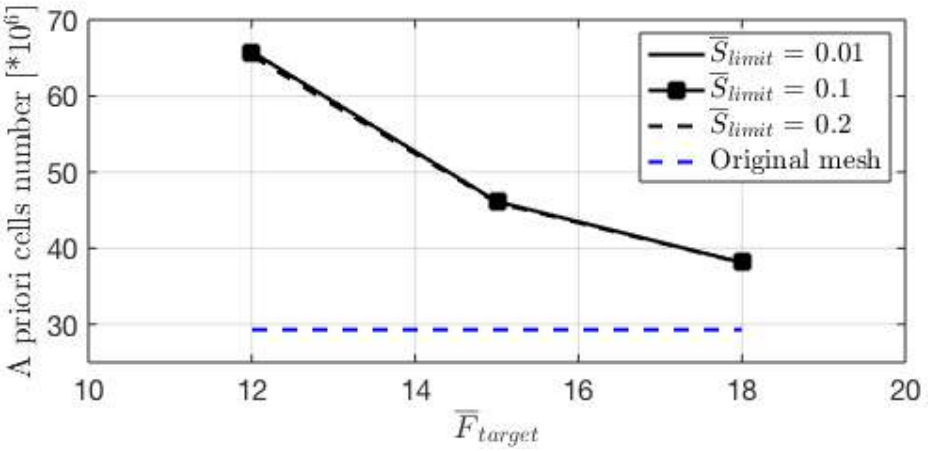

Figure 3.18: A priori computation of the refined mesh cells number for case 29M ad a function of $\overline{F}_{target}$ and the $\overline{S}_{limit}$.

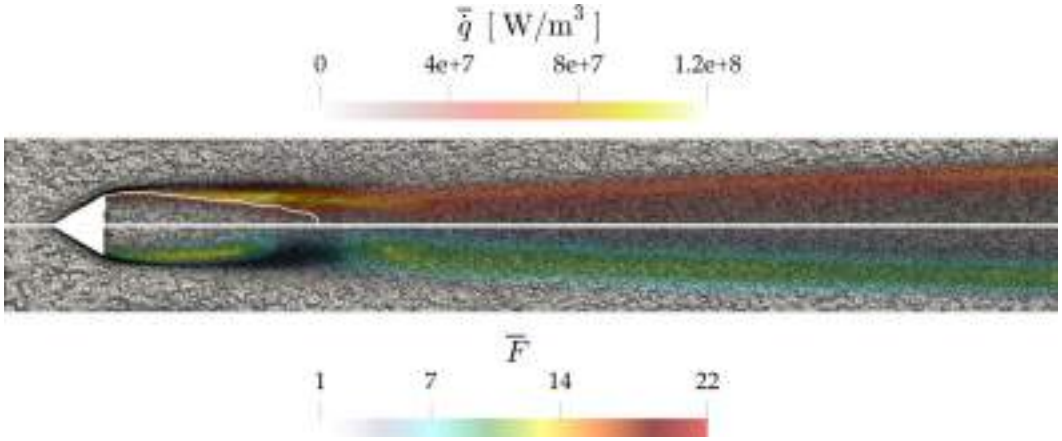

Figure 3.19: Overview of the 46M mesh obtained after the combustion refinement step mesh by using the FET criteria ($\overline{F}_{target} = 15$, $\overline{S}_{limit} = 0.1$). Averaged heat release rate $\overline{\dot{q}}$ and thickening factor field $\overline{F}$ are superimposed to the grid. The white iso-contour delimits the recirculation zone ($U_x = 0\ m/s$).

is large (i.e. where refinement is of interest) corresponds to a region where $\overline{S}$ is large (see Fig. 3.17) and it is always identified if $\overline{S}_{limit}$ is sufficiently small.

The resulting 46M mesh is shown in Fig. 3.19, together with the averaged heat release rate $\overline{\dot{q}}$ and thickening factor field $\overline{F}$. Comparison with the 29M mesh (Fig. 3.16) shows a large improvement in the resolution of the flame in the last part of the domain, visible as a much more homogeneous and small thickening factor $\overline{F}$.

The improvement of the LES accuracy thanks to the refinement procedure is clearly visible if comparing the data against the LES using the 10M (coarse), 29M (only aerodynamic refinement), 46M (optimum mesh) and 68M (reference) meshes in Fig 3.20 and Fig 3.21. Axial profiles of the mean axial velocity compo-

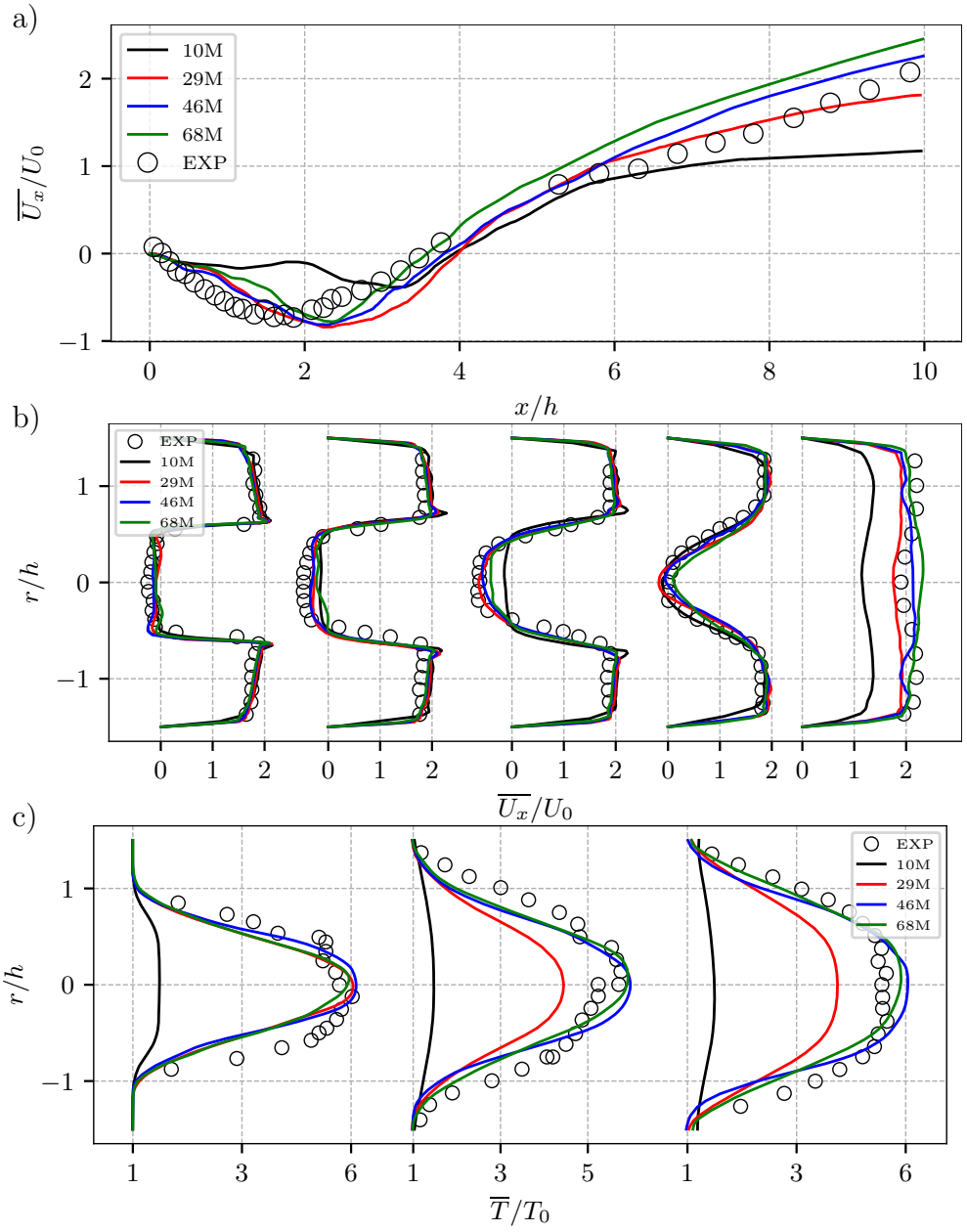

Figure 3.20: Comparison between experimental data and LES for the 10M, 29M, 46M and 68M (reference) cases. (a) Mean axial velocity evolution along the central axis. Transverse profiles at measurement planes x_1- x_5 of the (b) mean normalized axial velocity. Transverse profiles of (c) normalized mean temperature at measurement planes x_4, x_4' and x_5'.

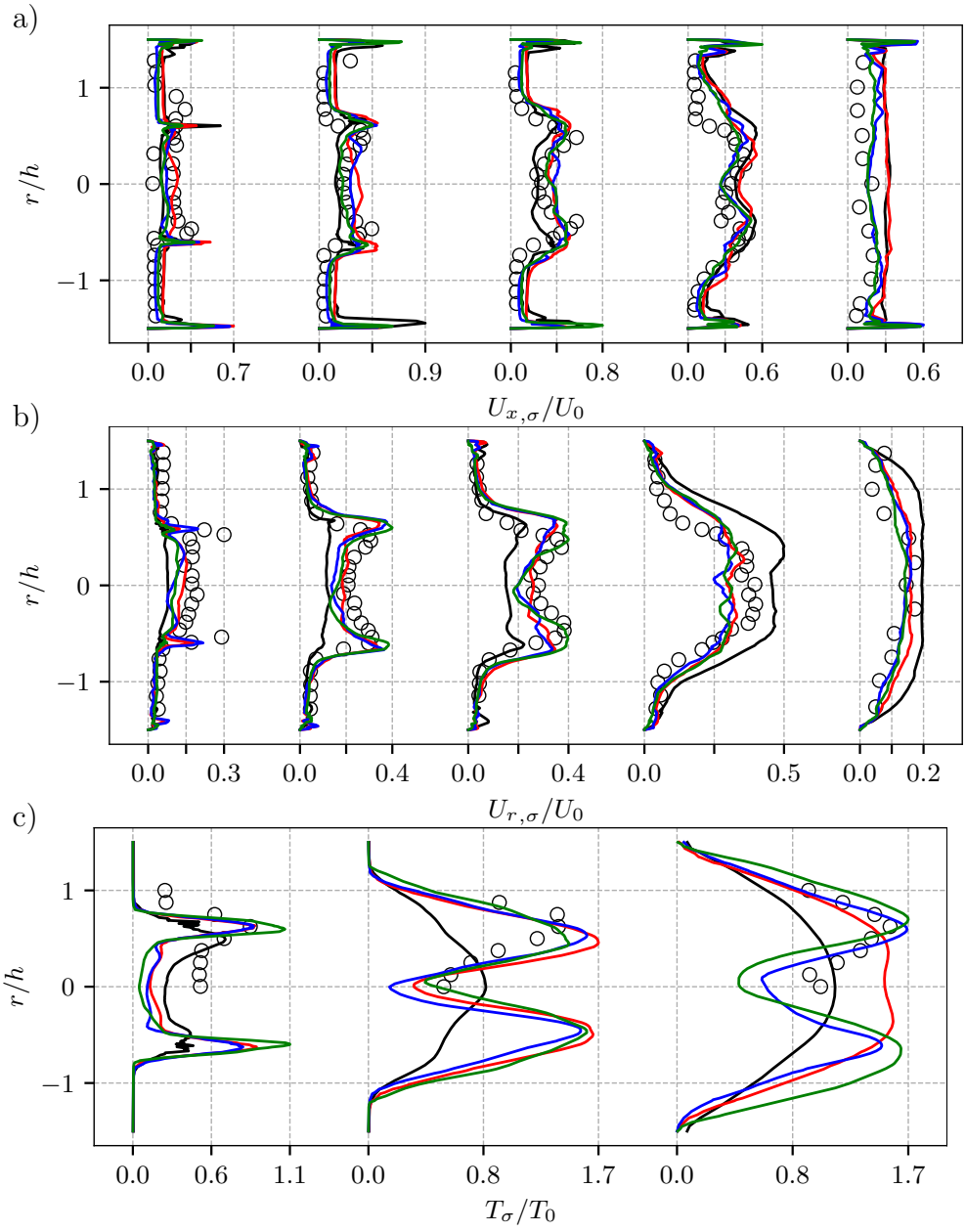

Figure 3.21: Comparison between experimental data and LES for the 10M, 29M, 46M and 68M (reference) cases. Transverse profiles at measurement planes x_1- x_5 of the (a) normalized RMS of axial velocity component and (b) the normalized RMS of transverse velocity component. (c) Transverse profiles of normalized RMS temperature at measurement planes x_2, x_4 and x_5.

nent are presented in Fig 3.20(a). The accuracy of the axial velocity prediction increases with the refinement steps. Starting from an incorrect solution where the recirculation zone length is over-predicted and the burnt gas acceleration is under-predicted (cf. case 10M), the method is able to recover both the correct mean aerodynamic and reactive fields and provides as accurate results as the reference case with a much lighter mesh. The mesh refinement quality is valid for the entire extension of the computational domain and not only at the center line of the burner as observed in Fig 3.20(b) where the transverse profiles of the mean normalized axial velocity are reported. Another key feature concerns the turbulent behaviour of the flow. Obviously, the 10M mesh is not able to accurately predict the turbulence activity. Figure 3.21(a-b) reports the transverse profiles of normalized RMS of the axial and transverse velocity from x_1 to x_5 respectively. The refinement process is able to recover the turbulent activity of the flow as well as for the mean aerodynamic field. Also note that the refinement quality is homogeneous since the axial and transverse turbulent fluctuations are evenly accurate. In addition to the velocity results, the averaged transverse temperature profiles presented in Fig. 3.20(c) confirm the good prediction of the mean reactive flow. Note that the correct profiles are only recovered at the ultimate refinement step, i.e using the flame criterion, while the aerodynamic refinement shows good accuracy just downstream the bluff-body. Finally, Fig. 3.21(c) shows the normalized RMS transverse temperature profiles. The flame/turbulence interaction is also well predicted with the optimum mesh, i.e., the one where the FET criterion is used. Therefore, the proposed mesh refinement procedure has been successfully applied and validated on the academic VOLVO test case. Following this methodology, it is possible to flag and refine in the ROI where important physics happen and to converge toward the correct flow prediction even if starting from an arbitrary wrong solution. The proposed procedure based on physical QOI is able in fact to increase the LES accuracy of turbulent reactive flows prediction while increasing their efficiency by keeping low the simulation cost with respect to a classical hand-made mesh.

3.4 A partially premixed swirled flame: the PRECCINSTA test bench

The proposed mesh refinement strategy is here applied to the gas turbine model combustor PRECCINSTA, a well-known gas turbine model combustor derived from an industrial design by Safran Helicopter Engines and operated by DLR [27].

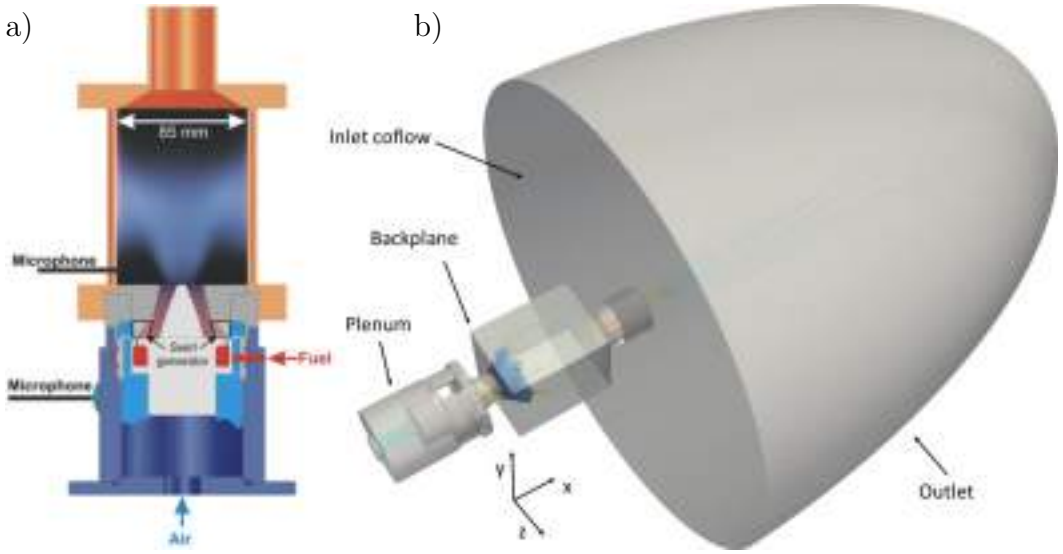

Figure 3.22: Schematic of the experimental test bench: injector with combustion chamber and photo of the flame (a) [27]. Computational domain used in LES (b). Note that in LES the atmosphere is taken into account and the inlet fuel geometry is simplified to the 12 small tubes without the fuel plenum.

A schematic of the experimental test bench is shown in Fig. 3.22(a) [27], presenting the injector with the combustion chamber together with an image of the flame. Dry air is fed at ambient temperature trough the plenum and a swirl motion is imposed before the combustion chamber thanks to 12 radial swirler vanes. The test bench is a partially (i.e. technically) premixed case, since the fuel gas (CH_4) is injected into the air stream through small holes within the radial swirler. The high momentum ensures good mixing before entering the combustion chamber even if local equivalence ratio variations have been reported in the literature [27]. The combustion chamber has a 85 mm large squared section and it is delimited by large quartz windows of thickness 1.5 mm which allow for optical access for diagnostics. Finally the hot gases exit through a cone-shaped exhaust pipe.

This configuration has been widely described and studied both experimentally [27, 127, 128, 129] and also numerically [74, 75, 115, 130, 131, 132, 133, 134, 135, 136, 137]. Most of the studies refer to the two regimes experimentally observed by Meier *et al.* [27]: for a global equivalence ratio of $\phi = 0.7$ (thermal power $P_{th} = 25$ kW) an unstable flame with a thermoacoustic limit cycle at 290 Hz is detected while, for a global equivalence ratio of $\phi = 0.83$ ($P_{th} = 30$kW) a quiet and stable flame is obtained. The thermoacoustic behavior of the flame has been numerically analyzed via compressible LES by Franzelli *et al.* [130] who also analyzed the impact of detailed chemistry on the LES accuracy [131]. A fully-

compressible LES-pdf approach, originally developed by Gao and O'Brien [138], comprising the Eulerian stochastic fields methods has been proposed by Friendrich *et al.* [132, 137] to detect the thermo-acoustic instability. A mesh refinement study has been only recently proposed by Bénard *et al.* [115]. The latter focuses on the stable case $\phi = 0.83$ and analyses via incompressible LES the effect on the flame structure of 4 homogeneously refined meshes ranging from 1.7 M cells (the coarsest mesh) to 110M and 877 M cells (the most refined ones), which leads to a F_{max} of 5.7 and 3.3, respectively. Following the choice of Bénard *et al.* [115] in this section the proposed mesh refinement strategy is applied to the stable flame, avoiding additional complexities due to thermoacoustic oscillations. Note that the method is perfectly suitable for applications to unstable flames if the defined QOI are time-averaged for longer times if compared to thermoacoustic oscillations.

The good quality and the extensive amount of experimental data available for the selected operating case in addition to its industrial-like design makes the PRECCINSTA test bench very suitable for the application of the proposed mesh refinement strategy. In particular, for what regards the aerodynamic field, measurements of the three velocity components were performed in one vertical plane along radial profiles at the heights h = 1.5, 2.5, 5, 15, 25 and 35 mm from the backplane using Laser Doppler velocimetry [27]. The uncertainty of the velocity measurements is typically 1.5–2% for the mean value and 2–2.5% for the RMS value. To check the accuracy of flame prediction, Laser Raman scattering experimental data [27] are available providing quantitative measurements of major species (CH_4, O_2, N_2, CO, CO_2, H_2O and H_2) and temperature in the vertical xy plane at different sections downstream the backplane (h = 6, 10, 15, 20, 30, 40, 60 and 80 mm). The systematic and statistical uncertainties are less than 4% and 2.5% respectively for temperature and less than 5% and 7% respectively for all species, except for CO and H_2 for which the statistical uncertainty is between 20% and 50%. In addition, PLIF of OH radicals was applied to visualize the flame structures together with line-of-sight integration of OH* chemiluminescence, which represents a qualitative indicator for the heat release rate for lean premixed flames.

LES are performed considering the computational domain shown in Fig. 3.22(b) and using the same numerical method as for the VOLVO test case (section3.3). Thermal boundary conditions are imposed by fixing a reference temperature T_{ref} and a suitable thermal resistance. At the bluff-body and at the backplane, thermal resistances are imposed based on experimental work by Yin *et al.* [129] that provided the surface temperature for operating conditions of thermal power P_{th}

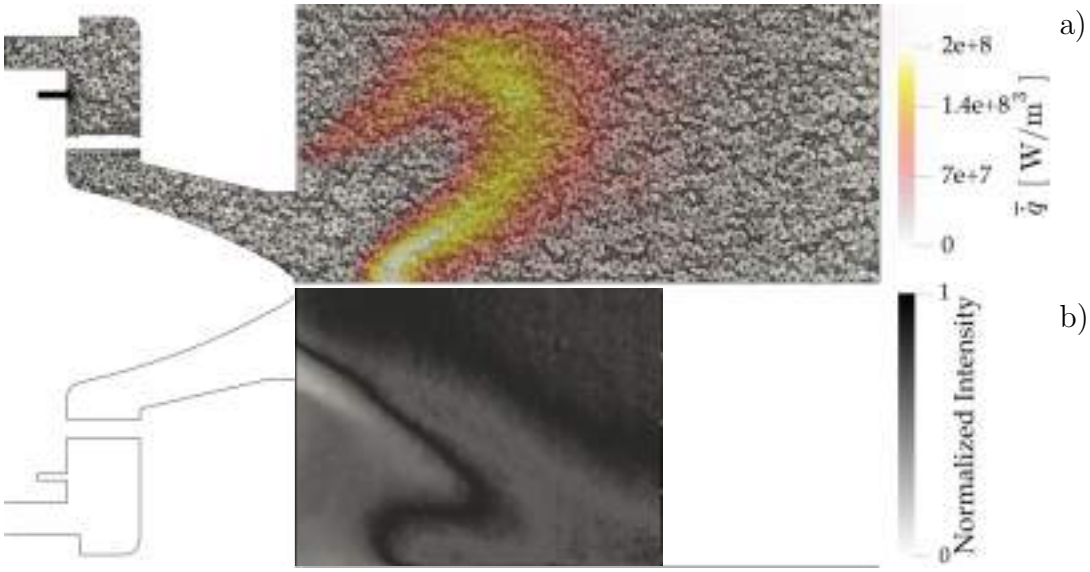

Figure 3.23: (a) Overview of the 3M coarse mesh. The characteristic mesh size Δx of 1.2 mm corresponds to the coarse mesh resolution proposed by Bénard et al [115]. The flame is represented through an averaged field of heat release rate $\bar{\dot{q}}$. (b) Experimental normalized time-averaged OH PLIF image [27].

= 20KW and equivalence ratio $\phi = 0.7$. The latter condition has been simulated in AVBP and the thermal resistances have been tuned to match the experimental thermal profiles (Chapter 4), assuming that the thermal resistance does not change while changing operating conditions (while surface temperature of course does). The same procedure has been applied for the chamber walls, based on the flow thermal profiles measured by Meier *et al.* [27]. The others walls are assumed to be adiabatic since no heat transfer is expected and no-slip conditions are imposed for all the walls. Since the current approach does not take into account the experimentally observed pre-heating of the flow in the plenum, a temperature of the flow of 320K is imposed at the inlet as generally proposed in the literature and also as T_{ref} for the walls thermal boundary conditions. The flame is modeled with the Thickened Flame model (TFLES), as in the VOLVO test case. In order to better take into account the local equivalence ratio variation due to the partially premixed case, the CH_4-Air chemistry is described by an ARC mechanism comprising 20 species, 166 reactions, and 9 quasi-steady state species derived from the GRI-Mech 3.0 and validated by Laera *et al.* [71].

3.4.1 Results and discussion

The starting mesh is shown in Fig. 3.23. It is composed by 2.8M of cells and it is homogeneously refined in the combustion chamber and in the swirler zone

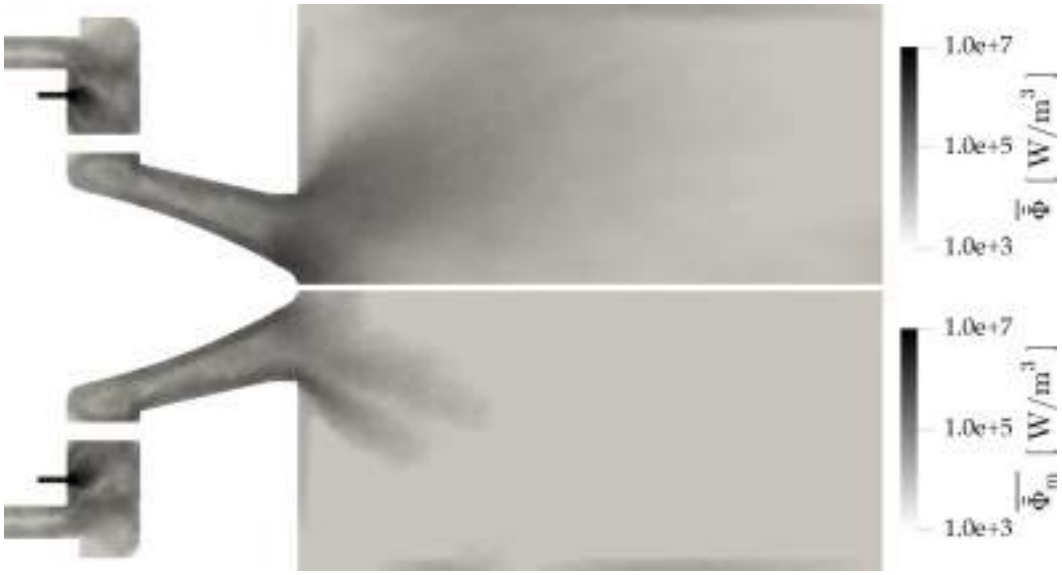

Figure 3.24: QOI fields of $\overline{\tilde{\Phi}}$ and $\overline{\tilde{\Phi}_m}$ for 3M coarse mesh. Note that log scale is used.

with a characteristic mesh size Δx of 1.2 mm which corresponds to the coarse mesh resolution proposed by Bénard *et al.* [115]. Note that the small tubes for technically premixed fuel injection are discretized with 8 cells in the diameter (i.e. 0.125 mm of characteristic size), corresponding to the smallest cells in the domain and to the largest CFL number. To avoid decreasing too much the timestep Δt of the compressible LES code, no mesh refinement is allowed in this region of the domain, assuming that a sufficient resolution for computing the jet penetration in the air flow is achieved with the current mesh size. The averaged heat release rate $\overline{\dot{q}}$ is superimposed to the mesh in Fig. 3.23(a). Due to a poor mesh resolution, the flame shape is totally wrong compared to the experimental time-averaged OH PLIF image (b): the flame has an M-shape, as opposed to the experimental data which show a clear V-shape, with the flame attached to the bluff-body and detached from the backplane. The wrong shape prediction is due to double effect induced by the low resolution. On one side the velocity field prediction is not accurate enough and, on the other side, the flame has an artificial thickness which is of the order of the bluff-body tip diameter: therefore the flame cannot stabilize close to the bluff-body tip since the two flames branches typical of a V-shape touch each other and merge in a M-flame. Temperature boundary condition does not impact the flame shape transition since increasing the T_{ref} of the bluff body does not lead to a V-shape flame.

As shown in the VOLVO test case, starting from this initial arbitrary mesh and solution, an optimum mesh with improved accuracy can be obtained by following the proposed mesh refinement strategy (section 3.3.1.2). First, aerodynamics

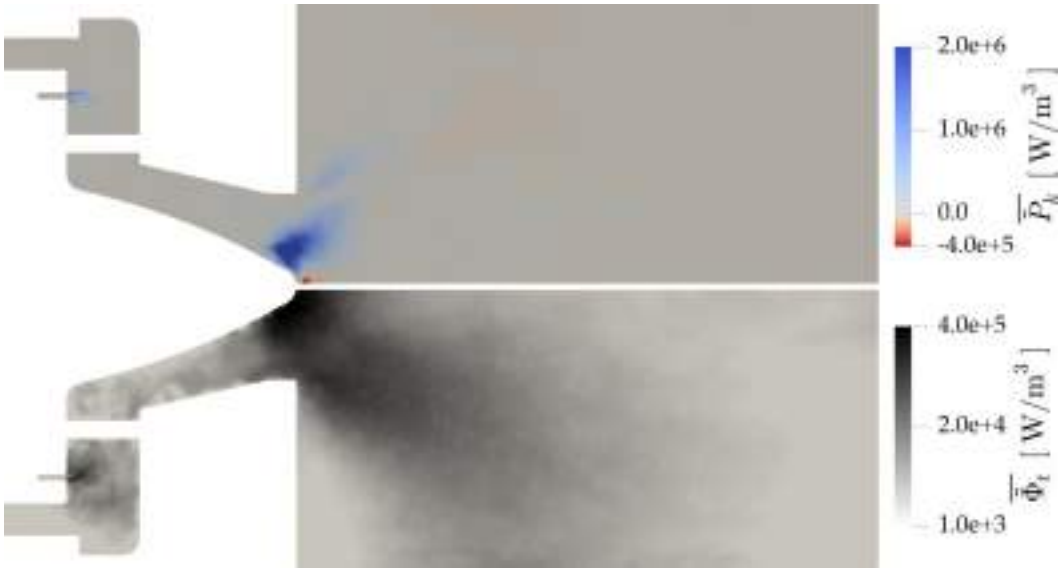

Figure 3.25: QOI fields of $\overline{\tilde{P}_k}$ and $\overline{\tilde{\Phi}_t}$ for 3M coarse mesh. Note that log scale is used only for $\overline{\tilde{\Phi}_t}$ field.

QOI are computed. Total dissipation rate of kinetic energy $\overline{\tilde{\Phi}}$ and its mean part $\overline{\tilde{\Phi}_m}$ are presented in Fig. 3.24. $\overline{\tilde{\Phi}_m}$ happens mainly in the small tubes and at the bluff body and swirler walls. Important dissipation is present also at the jet shear-layer. $\overline{\tilde{\Phi}}$ field is as expected very close in terms of magnitude and structure to its mean part, the only difference being the region at the bluff-body tip and in the jet core which correspond to region of dissipation of turbulent kinetic energy $\overline{\tilde{\Phi}_t}$. The latter is presented in Fig. 3.25 together with the production $\overline{\tilde{P}_k}$. $\overline{\tilde{\Phi}_t}$ is large in the wake of the bluff-body and $\overline{\tilde{P}_k}$ exhibits a negative (red) region at the bluff-body tip (where turbulent kinetic energy is transferred to the mean field) and a positive (blue) region in the shear-layer (where mean kinetic energy is transferred to turbulent one).

From the comparison between the different QOI's, a value of α of 5 is selected in order to flag regions of dissipation and production of turbulent kinetic energy which cannot be identified with a lower α parameter, due to the different order of magnitude of the different QOI's. Also in this case, a ϵ parameter of 0.5 is used to avoid over-refining in small regions.

Fig. 3.26 shows the mesh obtained after two refinement steps using aerodynamics $\overline{\tilde{\Phi}}$ field as QOI. An intermediate mesh of 5M is obtained after one iteration which, however, was not sufficient to guarantee a satisfactory accuracy in the aerodynamic field prediction. The achieved 10M mesh exhibits smaller cells and hence higher accuracy near the swirler and the bluff-body walls and also in the jet shear-layer and jet-core where most of the aerodynamics activity happens.

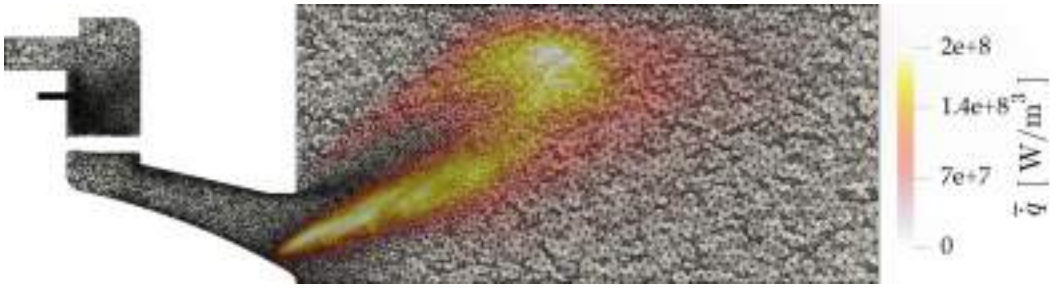

Figure 3.26: Overview of the 10M mesh. The flame is represented through an averaged field of heat release rate $\bar{\dot{q}}$.

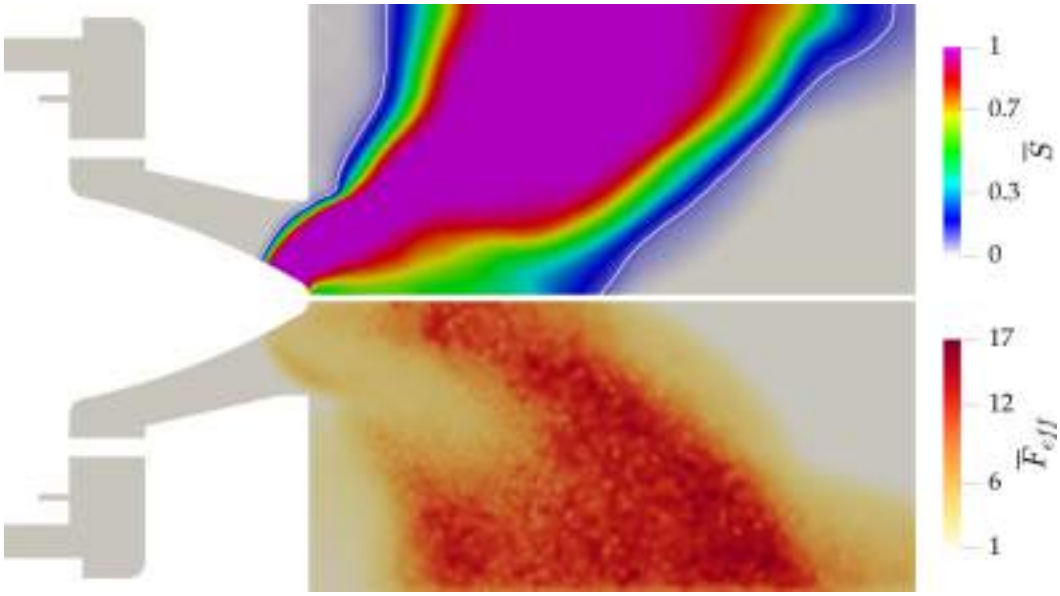

Figure 3.27: QOI fields of flame probability $\overline{S}$ and the effective thickening $\overline{F_{eff}}$ for case 10M. The white iso-contour corresponds to $\overline{S} = 0.1$.

The resulting averaged heat release rate $\bar{\dot{q}}$ corresponds to a correct V-shape flame, confirming that the refinement of the mesh in the shear-layer with the aerodynamic QOI is able to increase the accuracy of aerodynamics field prediction and to recover the correct flame shape. The LES prediction of the velocity field is in very good agreement with the experimental data (see Fig. 3.29 and Fig. 3.30). However, in order to improve the resolution in the flame region, the FET flame criterion is used to refine the 10M mesh in the reactive region. QOI fields of flame probability $\overline{S}$ and the effective thickening $\overline{F_{eff}}$ are shown in in Fig. 3.27 and used to build the FET criterion.

The white iso-contour corresponds to an $\overline{S}_{limit}$ of 0.1 that delimits the flame region where the FET criterion is applied. As there is no special target in terms of mesh cells number, the $\overline{F}_{target}$ is chosen in order to directly compare with the resolution of Bénard *et al.* [115]. The higher resolution achieved in their analysis bring to a $\overline{F}_{max}$ applied of 5.7 and 3.3 with 110M and 877 M cells respectively.

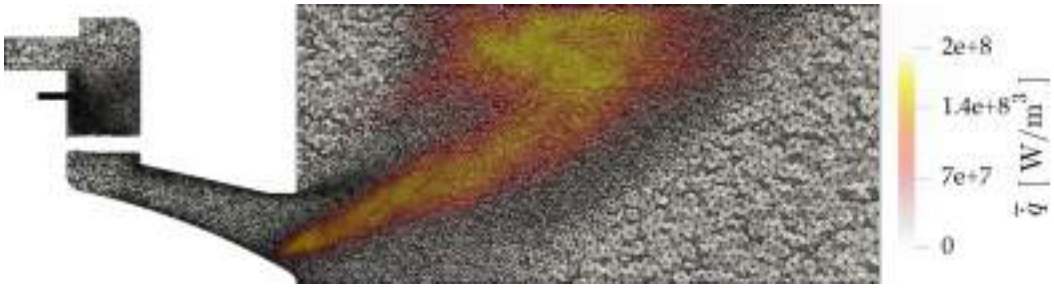

Figure 3.28: Overview of the 22M mesh. The flame is represented through an averaged field of heat release rate $\bar{q}$. The $\overline{F}_{target}$ of 5.7 assures same resolution in the flame region as in the 110 M cells mesh by Bénard et al [115].

By using the FET criterion with a $\overline{F}_{target}$ of 3.3 and 5.7 will bring to meshes of ≈22 M and ≈100 M cells respectively, following the a-priori calculation. For the present analysis, an $\overline{F}_{target}$ of 5.7 is selected in order to have the same resolution of the NAD3 mesh [115]. The resulting mesh is showed in Fig. 3.28 and is composed by 22M of cells, underlying how it is possible to efficiently build high resolution meshes by using a mesh refinement strategy based on physical QOI.

The final mesh shows very good agreement with the experimental data, both in terms of velocity field and flame prediction. In particular, profiles of velocity components at different measurement planes for the 3M, 5M, 10M and 22M meshes are showed in Fig. 3.29 and Fig. 3.30. Mean axial velocity Fig. 3.29(a) is wrongly predicted only by the coarse case (3M), which predicts a shorter recirculation zone. Some differences between LES and experiments remain visible at h = 15 and 25 mm downstream the backplane, suggesting that the opening angle is slightly under-predicted, and can be explained by taking into consideration the uncertainty of the experimental data. The corresponding RMS instead in Fig. 3.30(a) are over-estimated also by the 5M case, while the 10M and the 22M case are in good agreement with the experimental data. For what regards the mean radial velocity Fig. 3.29(b) and tangential velocity Fig. 3.29(c) again the coarsest mesh is the only one that does not provide very accurate results, indicating the first step of aerodynamic mesh refinement (i.e. 5M mesh) is able to improve the mean aerodynamic flow prediction. On the contrary, by looking at the radial velocity Fig. 3.30(b) and tangential velocity RMS Fig. 3.30(c), it is evident that the 5M case over-estimates the turbulent activity and that a second refinement step (i.e. 10M mesh) is mandatory to recover the experimental behavior.

The accuracy of flame prediction can be inferred from Fig. 3.31 and Fig. 3.32 where the profiles of temperature and selected species at different measurement

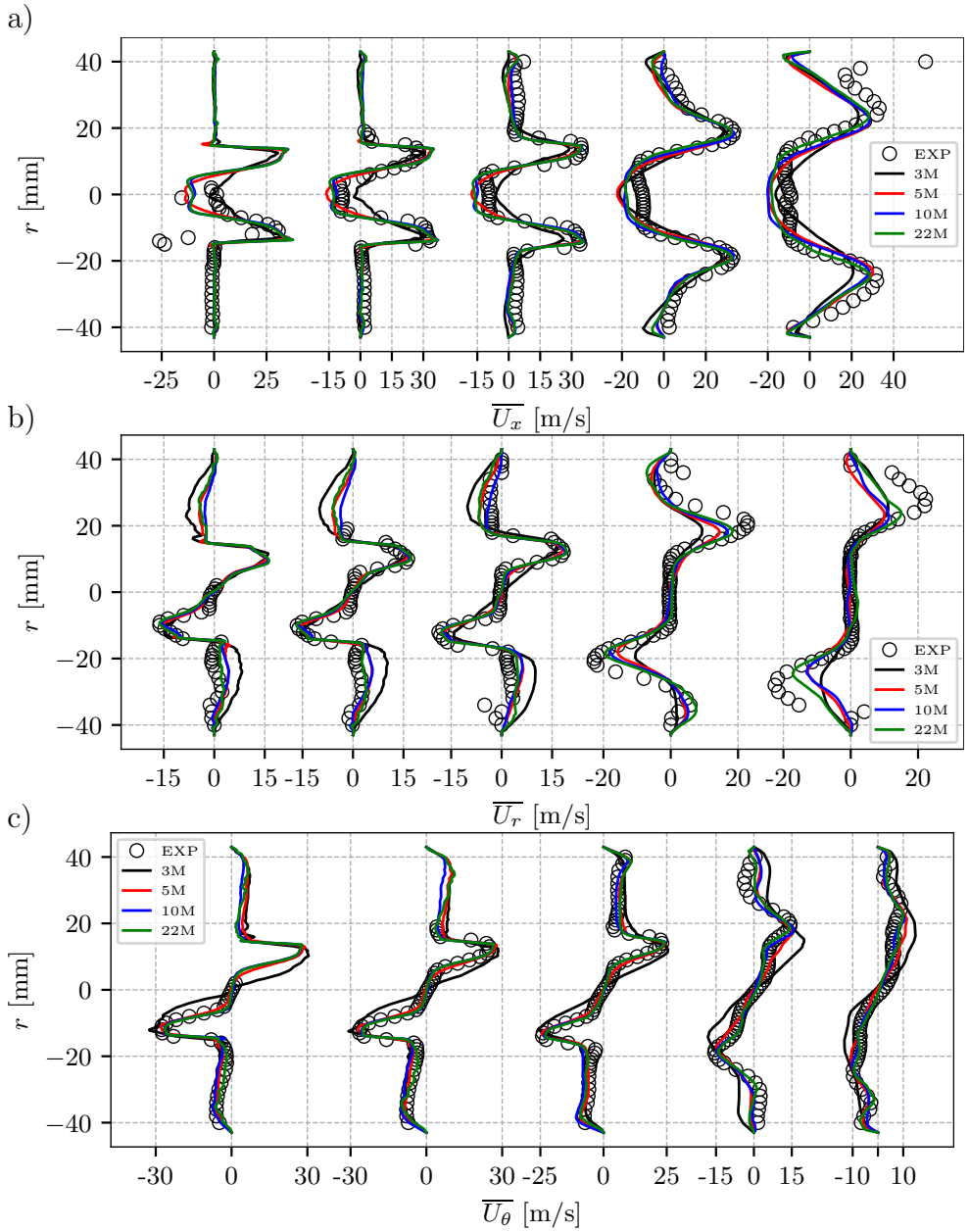

Figure 3.29: Profiles of mean velocity components at measurement planes at h = 1.5, 2.5, 5, 15, 25 mm downstream the backplane for the 3M, 5M, 10M and 22M cases. (a) Axial, (b) radial and (c) tangential velocity.

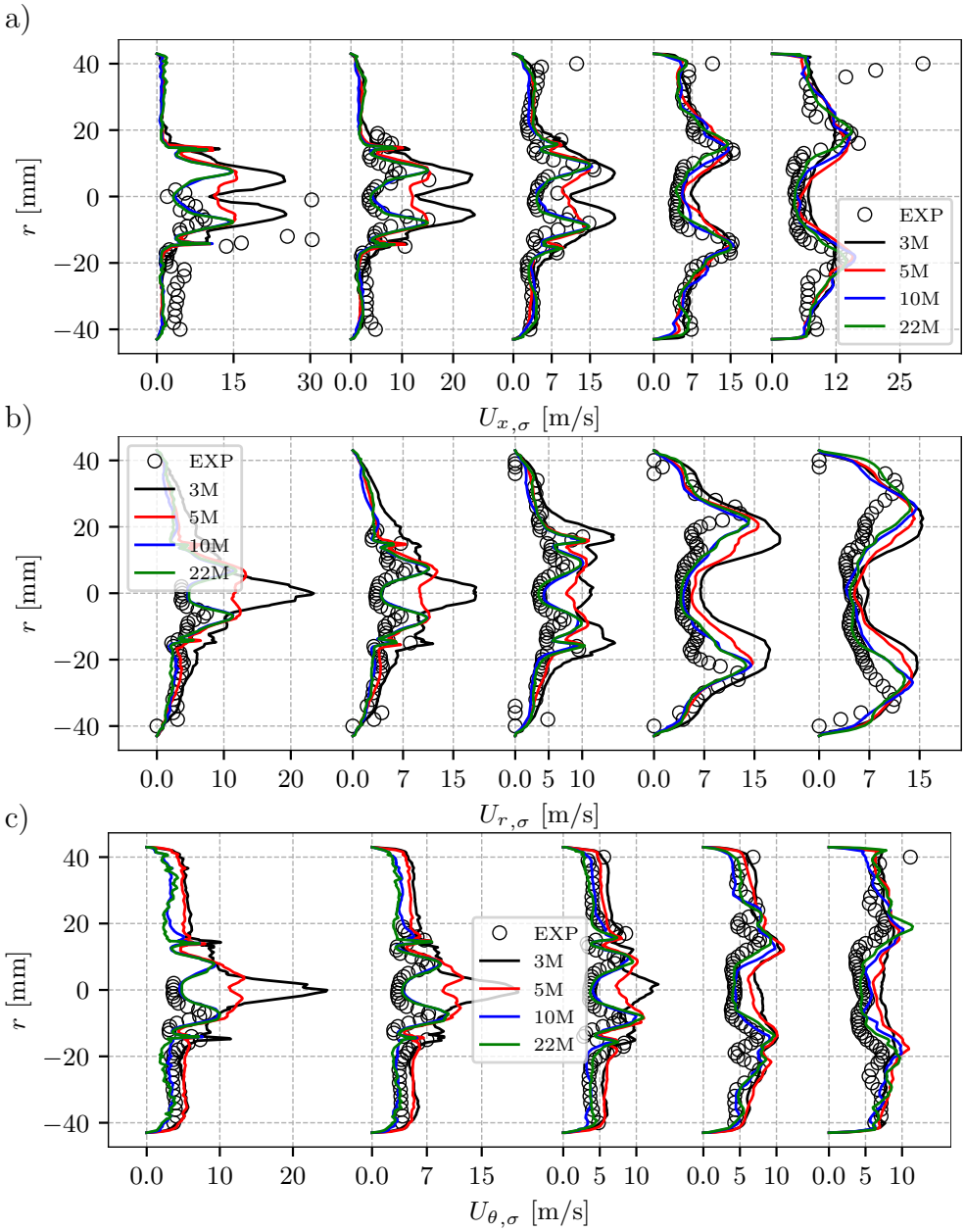

Figure 3.30: Profiles of RMS velocity components at measurement planes at h = 1.5, 2.5, 5, 15, 25 mm downstream the backplane for the 3M, 5M, 10M and 22M cases. (a) Axial, (b) radial and (c) tangential velocity.

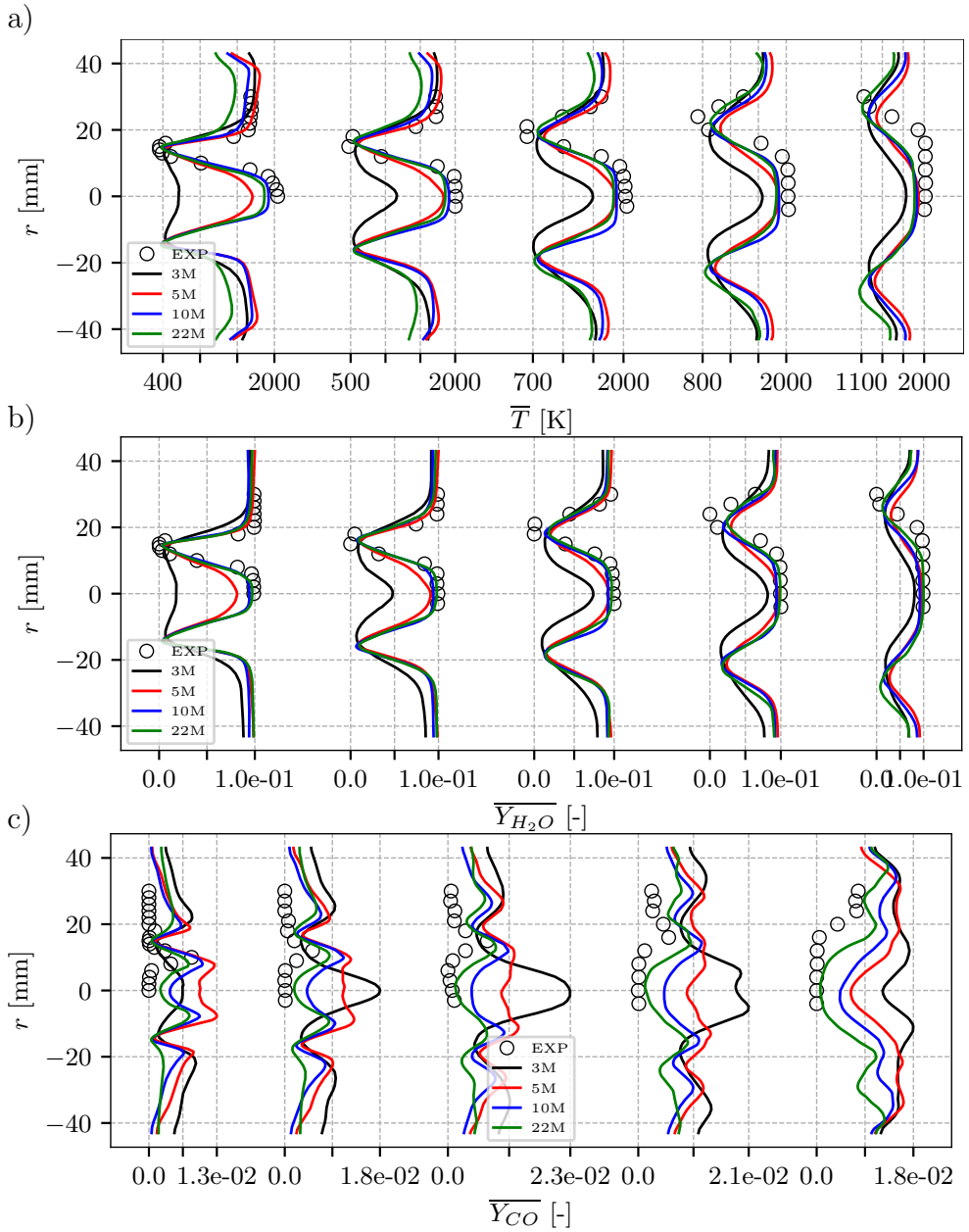

Figure 3.31: Profiles of mean temperature and selected species at measurement planes at h = 6, 10, 15, 20 and 30 mm downstream the backplane for the 3M, 5M, 10M and 22M cases. (a) Temperature, (b) H_2O mass fraction, (c) CO mass fraction.

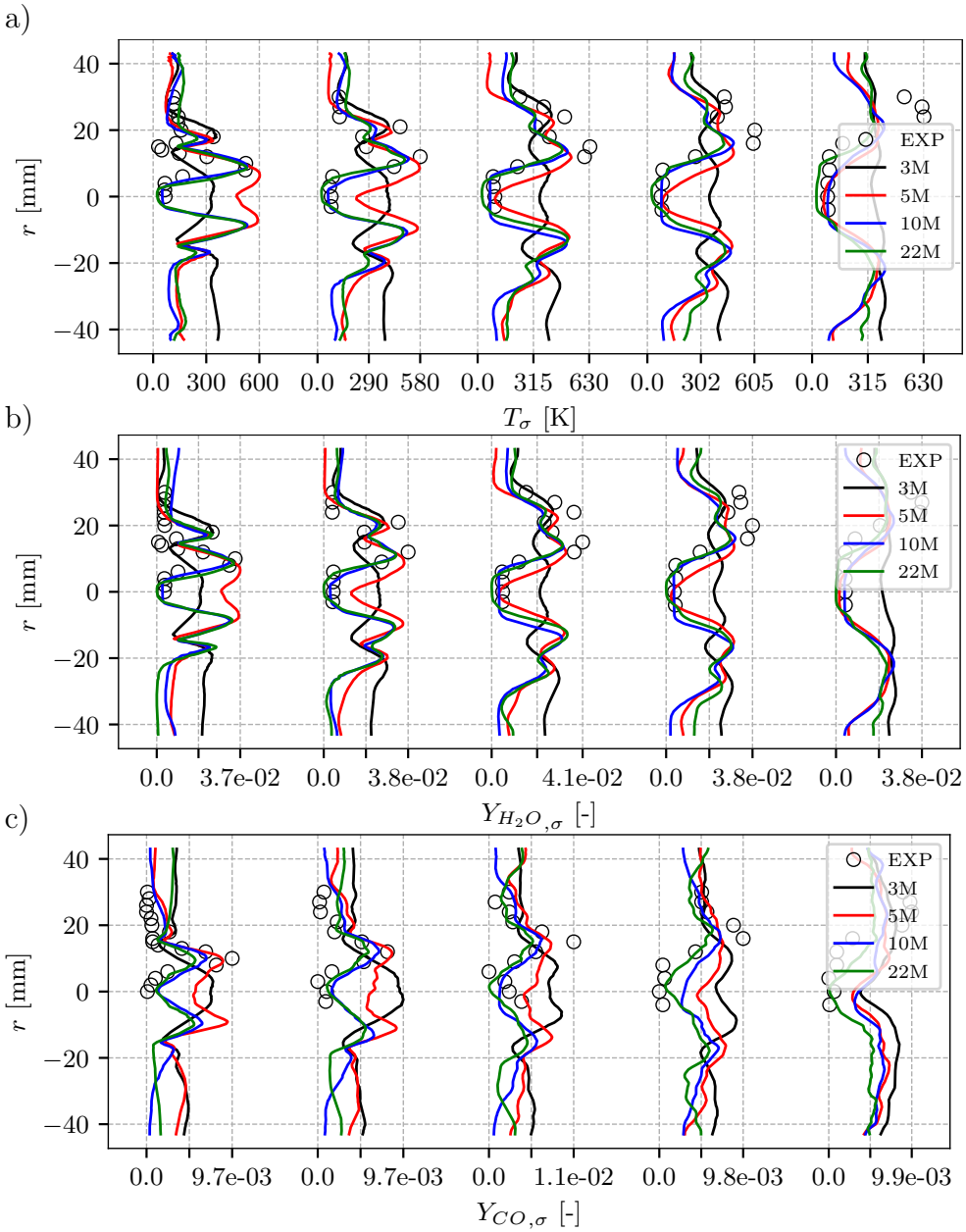

Figure 3.32: Profiles of RMS temperature and selected species at measurement planes at h = 6, 10, 15, 20 and 30 mm downstream the backplane for the 3M, 5M, 10M and 22M cases. (a) Temperature, (b) H_2O mass fraction, (c) CO mass fraction.

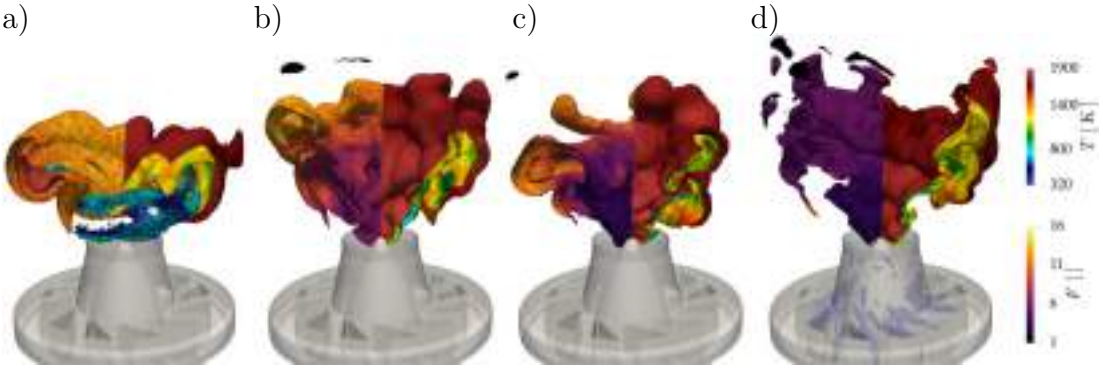

Figure 3.33: Iso-surfaces of $\dot{q} = 10\%\ \dot{q}_{max}$ colored by thickening field F (on the left) and temperature field T (on the right) for the 3M (a), 5M (b), 10M (c) and 22M (d) meshes. For the 3M case, an iso-surface of pressure at 101 kPa (colored by temperature field) evidences the Processing Vortex Core (PVC) present when the flame has an M-shape. For the 22M case, instantaneous iso-surface of CH_4 mass fraction equal to 0.08 colored by temperature field.

planes are shown for the 3M, 5M, 10M and 22M meshes. Mean temperature profiles Fig. 3.31(a) show good accuracy of the 10M and 22M meshes with experimental data, only marginal agreement of the 5M case and wrong prediction of the 3M case since the predicted flame shape is wrong. Some differences between LES and experiments remain visible also in this case at h = 15 and 25 mm downstream the backplane and can be explained by taking into consideration the uncertainty of the experimental data and the tuning procedure of the imposed thermal boundary conditions at the chamber walls. The RMS Fig. 3.32(a) are perfectly recovered by the refined meshes, confirming that two steps of aerodynamic refinement are needed for good prediction of aerodynamic activity. Selected species are H_2O and CO (but the same trend apply to the others). Mean Fig. 3.31(b) and RMS Fig. 3.32(b) of H_2O mass fraction show good agreement of the refined meshes (10M and 22M). Mean Fig. 3.31(c) and RMS Fig. 3.32(c) of CO mass fraction instead show that the 10M mesh is not able to correctly predict the minimum of mean value and activity along the axis while the 22M mesh is able to correctly recover the experimental data. This shows that when considering weak species (note the magnitude of mass fraction) the mesh resolution in the flame can play an important role for the LES accuracy prediction.

Finally, in Fig. 3.33 the instantaneous flames computed on the 3M (a), 5M (b), 10M (c) and 22M (d) meshes are presented. The flames are identified by iso-surfaces of $\dot{q} = 10\%\ \dot{q}_{max}$ colored by the instantaneous thickening field F (on the left) and the temperature field T (on the right). The difference of predicted flame-shape and length for the different mesh resolution is evident. The coarse

3M mesh (a) predicts an M-shape flame that does not touch the bluff-body tip and that is very close to the chamber backplane. The applied thickening is in the order of 16, bringing to an artificial flame thickness which is comparable to the bluff-body tip. As a consequence, the flame is detached and a large-scale hydrodynamics structure (the Precessing Vortex Core) can be detected by an iso-surface of low pressure [19, 139]. The PVC spiral structure is often detected in the PRECCINSTA burner when the flame has an M-shape while when a V-shape is present no PVC is detected [140, 141]. In experiments, depending on the operating conditions (i.e. thermal power P_{th} and equivalence ratio ϕ) the flame can either assume an attached V-shape with no PVC, a detached M-shape with PVC or a bi-stable behavior alternating intermittently between V- and M-shape. In the current operating conditions, the flame has a V-shape: it is therefore interesting to notice that the predicted M-shape is due to the poor mesh resolution and that the PVC is fictitious. The correct flame shape is recovered just after the first step of aerodynamic refinement with the 5M mesh (Fig. 3.33(b)), with the suppression of the PVC. The applied thickening factor is now halved in the region where mesh refinement has been applied, bringing to a lower artificial flame thickness. As the mesh refinement procedure goes on, the new 10M mesh Fig. 3.33(c) exhibits lower applied thickening and more accurate flame-turbulence interaction and turbulent activity prediction. The final step of the 22M mesh (Fig. 3.33(d)) shows that the instantaneous thickening is lower than the F_{target} = 5.7 except for the small portion of the flame near the backplane where the flame goes only for less than the 10% of the time (i.e. S_{limit} = 0.1). Finally, the resulting mesh exhibits a much more homogeneous applied thickening, and hence resolution in the flame, confirming that the method takes into account possible local variation in equivalence ratio due to the technical injection (see the instantaneous iso-surface of CH_4 mass fraction in (Fig. 3.33(d)). Note that an effect of the mesh resolution on the flame lift-off is visible. In particular, as observed in literature [115], an increase of the mesh resolution brings to an increase of the flame lift-off from the backplane, due to the improved prediction of flame response to stretch when an improved-resolution mesh is used.

3.5 Conclusions

In this Chapter, a new static mesh refinement strategy based on physical Quantities of Interest (QOI) has been proposed in LES of turbulent reactive flows. To define the regions of interest (ROI) where relevant flow physics happens, different QOI's have been defined for the aerodynamic field and for the flame. Analysis of

the balance equation for the mean and the turbulent kinetic energies have shown that the dissipation rate of the mean and the turbulent kinetic energy together with the production of turbulent kinetic energy have to be taken into account to correctly capture the flow activity. In addition, from the reactive flow point of view, a criterion based on the flame-position probability and on the effective applied thickening has been defined to obtain the desired mesh resolution in the flame region. At first, this mesh refinement strategy has been successfully applied and validated on the VOLVO test case: an academic fully premixed bluff-body stabilized flame. The method was able to correctly define the ROI where important physics happen: it was possible to locally refine the mesh in this region to improve the LES prediction accuracy or, alternatively, to fix the mesh size in this region and coarsen everywhere else in the domain to reduce the mesh size and hence the computation cost while keeping the same LES accuracy of a reference mesh. By comparing the results with the experimental data, it was evident that the prediction of the flame stabilization, and hence the computed velocity and temperature fields, are strongly influenced by the mesh quality that can be significantly improved by applying the proposed mesh refinement strategy. On the starting mesh, the flame was short and burnt inside the wake of the flame-holder and a long recirculation zone was predicted. The final mesh instead predicted a long flame which burned for the whole combustion chamber downstream the bluff-body, as in the experiments. Second, the method has been applied to a partially premixed swirler flame which is closer to the real industrial configurations, the PRECCINSTA test bench. Also in this case, it was possible to obtain a predicted V-shape flame in very good agreement with the experimental data starting from a wrong predicted M-shape flame. The key point of the proposed method relies in its versatility: in both the test cases the strategy was able to lead to a correct solution in very good agreement with the experiments starting from a totally wrong initial solution. Therefore, the proposed mesh refinement strategy is found to be able to identify the relevant physics of turbulent reacting flows that are essential for the overall LES accuracy.

Chapter 4

Conjugate Heat Transfer: impact of wall heat transfer on a swirled flame dynamics

Contents

The objective of this Chapter is to present the Conjugate Heat Transfer approach and to analyze the effect of wall heat transfer on the PRECCINSTA swirled flame dynamics. As a matter of facts, in LES, although rarely addressed systematically, it is known that thermal boundary conditions control the heat transfer between the flow and the combustor walls and that they play a major role in the accuracy of numerical simulations. This Chapter therefore presents a study on the impact of thermal wall boundary conditions for the PRECCINSTA test bench, operated by the German Space Agency (DLR). Two approaches are tested: Heat Resistances Tuning (HRT), where a local resistance is tuned using experimental temperature data, and full Conjugate Heat Transfer (CHT), where the chamber wall-temperature is solved and coupled to the flow computation. Results reveal that the HRT method captures the mean flame correctly but the predicted flame becomes unstable and responds to a thermoacoustic oscillation which is not observed experimentally. On the contrary, using CHT, the flame is correctly predicted and stable as in the experiments. Finally, to understand the differences between the HRT and the CHT simulations, Dynamic Mode Decomposition (DMD) analysis is performed showing that the correct response of the

flame branches to the pressure oscillations is recovered only in the CHT simulations for which thermoacoustically stable operations are retrieved. Note that these results have been published in *Combustion and Flame* [59].

4.1 Introduction

Despite the vaste use of Large Eddy Simulation (LES) to investigate flow physics in complex geometries such as swirling reacting flows often present in gas-turbine combustors [74, 75, 76, 77], such simulations are often performed with simple boundary conditions on walls, where temperature is either imposed or adiabaticity is assumed, although these thermal boundary conditions control the heat transfer between the flow and the combustor walls [66]. The chemical reactions inside the combustion chamber are furthermore strongly dependent on the temperature field so that wall boundary conditions can affect the flame shape [142], its stabilization [143] to the point where it can even extinguish the flame (e.g. when it interacts with walls [144, 145]). Thermoacoustic instabilities are also highly impacted by temperature boundary conditions: a change in the temperature field modifies the laminar flame speed [146] and the local speed of sound, impacting the frequency of the acoustic resonant modes [147, 148] as well as the response of the flame to acoustic oscillations, usually described by the Flame Transfer Function (FTF) [149].

Multiple experimental and numerical studies have focused on the impact of heat transfer on flame stabilization and dynamics. A detailed experimental analysis of the influence of heat losses on the flame shape was proposed by Guiberti *et al.* [142], who underlined the important role played by the temperature boundary conditions in the flame stabilization. Mejia *et al.* [150] experimentally investigated the impact of the wall-temperature on a laminar flame stabilized on a slot burner. Thermoacoustically stable or unstable configurations have been recorded depending on the temperature of the burner at the flame anchoring point which altered the flame foot dynamics. Indeed, as suggested by Kedia *et al.* [151], flame-wall interaction can be crucial in closing the feedback loop between heat release rate and velocity oscillations. The importance of the temperature field near the flame anchoring region has also been underlined by Hong *et al.* [152], who investigated the dynamic instability characteristics of a turbulent premixed flame in a backward-facing step combustor and showed that the wall thermal conductivity influenced the flame speed near the flame holder, leading to a distinct dynamic behavior of the flame for each flame holder material. For example, replacing the stainless steel flame holder with one made of ceramics inhibited

the onset of combustion instability. Similarly, Cuquel *et al.* [153] investigated the effect of unsteady heat losses between the flame base and burner rim on the FTF. Improved expressions for the FTF of conical flames submitted to velocity disturbances were obtained by including a model for the motion of the flame base due to the unsteady heat losses. An important effect of heat transfer has been observed for turbulent flames too. Lohrmann *et al.* [154] investigated the influence of the preheat temperature on the FTF of a turbulent swirl-stabilized premixed flame. By increasing the preheat temperature, the delay of the flame response decreased due to an increase in the turbulent flame speed that shifted the main reaction zone to an upstream location. The influence of the transient combustor wall-temperature on the thermoacoustic oscillations of turbulent premixed flames has been investigated by Heydarlaki *et al.* [155]. They showed that the probability of occurrence of large amplitude oscillations was dependent on the initial wall-temperature, confirming the strong non-linearity of the problem.

Different studies have tackled the Conjugate Heat Transfer (CHT) problem with numerical simulations to handle the heat transfer at the walls. Berger *et al.* [156] performed direct numerical simulations (DNS) of a bluff-body stabilized flame both with fluid only predictions and in a Conjugate Heat Transfer (CHT) context. It turned out that the flame stabilization depended not only on the solid material but also on the initial solution, highlighting that the nonlinear CHT problem can exhibit multiple solutions. The strong effect of heat transfer in bluff-body stabilized flames has also been underlined recently by Fureby [112]. Taking ,gas thermal-radiation and wall Conjugate Heat Transfer into account, LES predictions were in better agreement with experimental data in terms of mean velocity, temperature and CO mass-fraction profiles. The heat loss effects on the stabilization of a lean swirl-stabilized flame close to blow-off conditions was analyzed by Massey *et al.* [157], showing that the lift-off height is influenced by the wall heat transfer modelling. DNS was used to perform a sensitivity analysis of transfer functions of laminar flames [146], proving that the inlet air temperature affects both gas velocity and flame speed whereas the combustor wall-temperature determines the lift-off distance of the flame and controls the FTF delay. The same concept was underlined by Kaess *et al.* [158], who investigated the effect of the thermal wall boundary condition on the FTF of a laminar premixed flame trough LES. Their results showed that the flame anchoring position and the FTF were significantly altered when changing the adiabatic boundary condition to an isothermal boundary condition. In an experimental and numerical work, Chatelier *et al.* [159] showed that one of the main issues that should be taken into account in numerical simulations to capture the thermoacoustic response of

a swirled flame is the enthalpy defect impact on the flame structure due to heat losses.

This brief literature review confirms that wall heat transfer effects modify flame stabilization and flame dynamics. Nevertheless, while in experiments this requires a careful attention to the combustor initial conditions to avoid wall-temperature effect and obtain reproducible data, in Computational Fluid Dynamics (CFD) a correct assessment of the wall modelling is required to achieve reliable numerical predictions. If available, measured temperatures can be used as boundary conditions for simulations. However, in most configurations wall-temperature data are difficult to determine and they can change for each operating condition. In many cases, they are just not available. As a consequence, most CFD simulations either neglect heat-transfer effects, considering the combustor walls as adiabatic (e.g., see Ref. [76]) or an arbitrary wall-temperature field is imposed [115, 160, 161]. Both approaches still can capture the correct thermoacoustic behaviour as demonstrated in bluff-body stabilized flames [162, 163], lean-premixed swirl flames [76, 161], annular combustion chamber [164] or even rocket combustors [165]. However, these simplistic wall conditions fail when the instability-driving mechanisms are impacted by the unsteady heat-transfer to the walls, and recent studies have underlined how Conjugate Heat Transfer (CHT) can improve the prediction of thermoacustic instabilities. Shahi *et al.* [166] performed numerical simulations of a centerbody stabilized flame both with adiabatic/isothermal boundary wall conditions and with CHT to conclude that the use of the latter led to significant accuracy improvements in the prediction of the characteristics of the combustion instability. For a swirled-flame combustor, Kraus *et al.* [66] discussed the potential of CHT simulations to improve LES accuracy for the prediction of combustion instabilities in terms of frequency and amplitude of the oscillations due to the strong preheating of the gases in the combustor plenum.

In general, it is possible to classify the approach toward heat-transfer in four categories of increasing complexity, based on the thermal boundary conditions imposed at the walls [66]:

1. Adiabatic walls: in most recent LES the walls are considered as adiabatic and heat transfer is neglected [76, 162, 163, 164].

2. Imposed wall-temperature: when experimental data includes wall temperatures, it is possible to fix the temperature directly through Dirichlet boundary conditions [167, 168].

3. Imposed local thermal resistance: the local heat flux Φ_q can be computed from a reference temperature T_{ref}, the temperature of the fluid at the wall T_f provided by the simulation and a suitable thermal resistance R which takes into account the conduction through the solid [24, 71] and the external convection and radiation [77]: $\Phi_q = (T_f - T_{ref})/R$.

4. Conjugate Heat Transfer (CHT): the LES solver can be coupled with a code that solves for heat conduction in the solid parts of the combustor: the wall heat conduction and the unsteady flow solvers run in parallel and exchange values of wall-temperatures and heat flux at the boundaries [112, 166, 169].

Among the different gas turbine model combustors, the PRECCINSTA test bench (already presented in Chapter 3) is one of the most well-known in the combustion community. To the author's knowledge an analysis of the heat transfer impact on the thermoacoustic behavior of this test rig has never been performed. The analysis of the thermoacoustic oscillation performed via compressible LES by Roux *et al.* [74] and Franzelli *et al.* [130] were conducted for adiabatic walls, achieving good prediction of the oscillation mode but marginal agreement for the frequency of oscillation. More studies have focused on the impact of detailed chemistry [131], sub-grid scale closure for premixed turbulent combustion [75] and combustion TFLES model with a dynamic wrinkling formulation [136]. The first study that introduced heat losses at the walls in the PRECCINSTA test rig was conducted by Bénard *et al.* [115] in the context of a mesh sensitivity analysis in the stable flame regime. To do so the authors imposed a numerically-tuned temperature profile at the combustor walls and backplane to match the experimental fluid temperature profiles [27], but the centerbody on which the flame stabilizes was kept adiabatic. A similar approach has been recently used also by Fredrich *et al.* [132, 137], who proposed to detect the thermoacoustic instability with a fully-compressible LES-pdf approach. To take into account the heat losses, they fixed the chamber walls at a guessed temperature of 1400 K and the backplane at 700K, following the experimental data of Yin *et al.* [129]. However, using the same experimental data for the centerbody, they claimed that prescribing a wall-temperature of 700 K caused the flame to consistently lift off and fully detach from the nozzle and therefore assumed an adiabatic condition. It is important to note that the experiments conducted by Yin *et al.* [129] refer to different operating conditions with respect to the one simulated by Fredrich *et al.* [132, 137], potentially explaining the lift-off of the flame. In all these studies, since a pre-heating of the gases before entering the combustion chamber was experimentally observed to reach values between 320 K and 380 K, although not precisely measured [27],

the temperature of the fresh gases has been set to 320 K instead of the ambient temperature. To conclude, the lack of a clear and systematic analysis of the heat losses in this test rig can be due to two main factors: (a) the lack of experimental data of wall-temperatures (some measurements at the backplane and centerbody tip have been recently performed by Yin *et al.* [129] but in operating conditions different from the ones of Meier *et al.* [27]) and (b) the satisfactory agreement of LES predictions with adiabatic boundary conditions.

This Chapter addresses this issue by performing a systematic study of the impact of heat transfer in the PRECCINSTA test bench. Note that a new test campaign was conducted at DLR where the test rig was operated in different operating conditions with respect to the data available in the literature [27, 129].

In the following, the experimental setup, the observed flame shape and thermoacoustic behavior are first presented together with the numerical setup and the AVBP LES solver, section 4.2. Results are discussed in section 4.3. First, the Heat Resistance Tuning (HRT) approach for the thermal boundary condition determination using experimental measurements is presented in section 4.3.1. Second, since with the HRT approach the predicted flame becomes unstable and responds to a thermoacoustic oscillation that is not observed experimentally, a Conjugate Heat Transfer (CHT) simulation is discussed in section 4.3.2 after having presented the heat conduction AVTP solver. Finally, the instability-driving mechanism is physically investigated to understand the differences between the HRT approach and the CHT predictions in section 4.3.3.

4.2 Experimental and numerical setup

A schematic of the PRECCINSTA experimental test bench [27] (see also Chapter 3) is presented in Fig. 4.1(a) showing the injector and the combustion chamber, together with the experimental normalized time-averaged Line-of-sight (LOS) OH* chemiluminescence image.

The test rig has been recently been operated at different operating conditions to analyze the effects on flame dynamics. In this work, an experimentally stable condition is computed for a global equivalence ratio of $\phi = 0.8$ ($\dot{m}_{air} = 4.29$ g/s and $\dot{m}_{CH_4} = 0.2$ g/s) and a thermal power of $P_{th} = 10$ kW at atmospheric conditions. Measurements of the three velocity components were performed in one vertical plane along the radial direction using Stereoscopic Particle Image Velocimetry (sPIV). Planar Laser-Induced Fluorescence (PLIF) measurements of OH radicals are used to visualize the flame structures together with line-of-sight

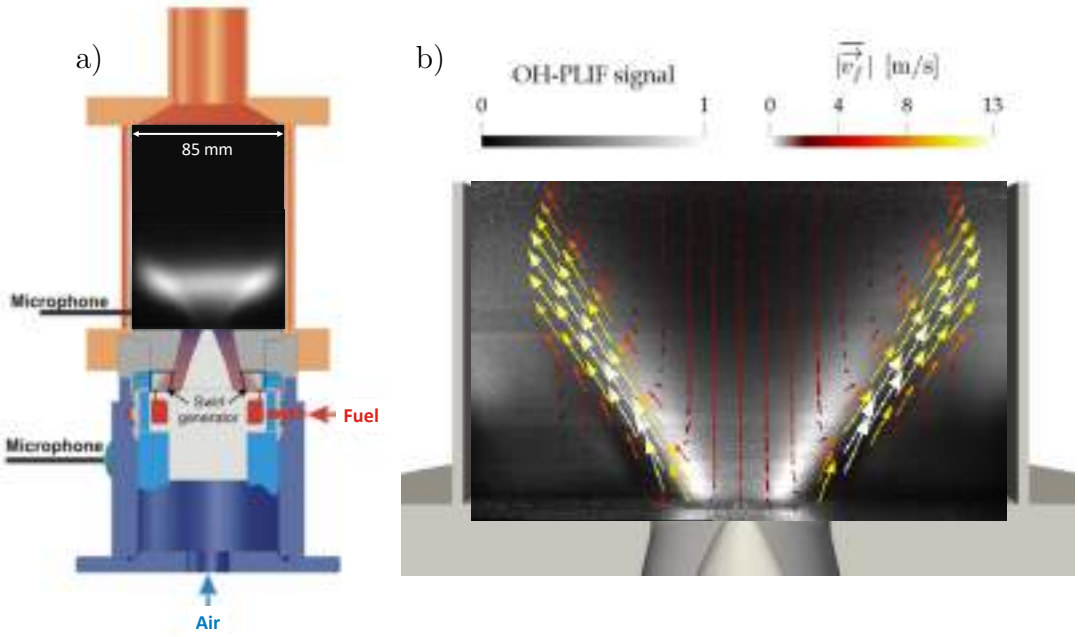

Figure 4.1: (a) Schematic of the experimental test bench: injector with combustion chamber and normalized time-averaged Line-Of-Sight (LOS) OH⋆ chemiluminescence indicating the flame; (b) Experimental normalized time-averaged OH-PLIF image. The arrows are tangential to the experimental time-averaged velocity field in the plane $\overrightarrow{\overrightarrow{v_{//}}}$, their length and color indicating the velocity magnitude.

integration of OH* chemiluminescence, which represents a qualitative indicator for the heat release rate for lean premixed flames [170].

The experimental normalized time-averaged OH-PLIF image on a vertical plane is presented in Fig. 4.1(b) together with the experimental time-averaged velocity field in the plane, $\overrightarrow{\overrightarrow{v_{//}}}$, indicated by the arrows which are tangential to the velocity vector and colored by its magnitude. A classical swirled flow structure of the velocity field can be observed. A strong Central Recirculation Zone (CRZ) downstream of the centerbody helps the flame stabilization by bringing back the hot burnt gases toward the flame root and weaker Outer Recirculation Zones (ORZs) are also present. Starting from the injector exit, the intense jet flow exiting from the swirler prevents flame anchoring: the flame is stabilized in the low-velocity region near the end of the CRZ close to the centerbody (note the metallic tip visible in the image) and it develops further downstream in a V-shape reaching the chamber walls at around 50 mm from the backplane where it quenches due to wall heat losses. A weaker signal is observed in the ORZs with respect to the primary zone close to the centerbody, indicating that the flame is not always present in these regions (as expected in a V-shape flame).

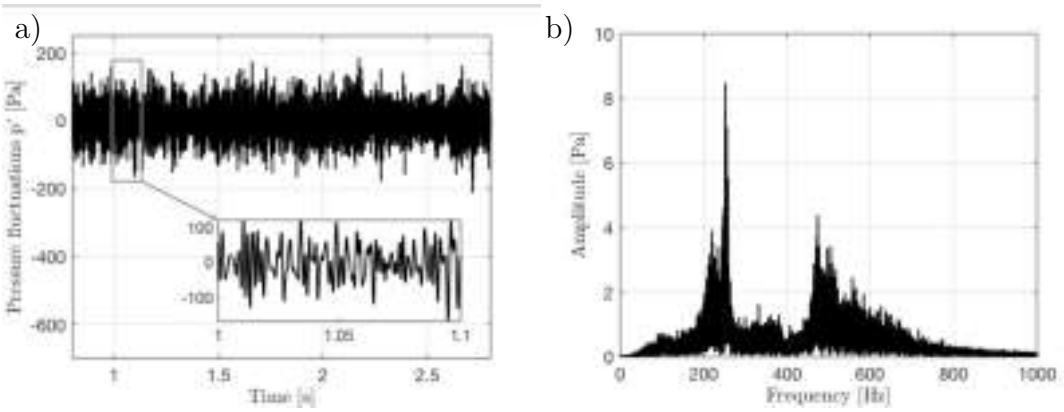

Figure 4.2: (a) Experimental pressure recorded at the combustion chamber backplane with a zoom on a part of the signal and (b) the signal spectrum obtained via Fast Fourier Transform (FFT).

Figure 4.2 reports (a) the pressure recorded experimentally at the combustion chamber backplane and (b) its spectrum computed using a Fast Fourier Transform (FFT) algorithm. Two weak modes appear at 260 Hz and 480 Hz: these frequencies match the first two acoustic modes of the system (see section. 4.3.3). The weak amplitude of the two pressure peaks (smaller than 10 Pa) indicates that no thermoacoustic activity takes place for these operating conditions.

The LES domain is shown in Fig. 4.3 with an overview of the unstructured grid: the outside atmosphere is taken into account to have the right impedance at the outlet of the combustion chamber and the inlet fuel geometry is simplified into 12 small tubes (colored in red) without the fuel plenum. In Fig. 4.3, an instantaneous isocontour of CH_4 is colored in blue to help visualize the technical fuel injection in the swirled flow. LES are performed using the AVBP code (Chapter 2). The SIGMA turbulent closure is used for the sub-grid stresses [46] and the TTGC scheme (third order in time and space) is used for the discretization of the convective terms [48]. Inlet and outlet boundary conditions are treated with the Navier-Stokes Characteristic Boundary Conditions (NSCBC) formalism [30] with a relaxation factor of $K_{air} = 50$ s^{-1} and $K_{fuel} = 5 \times 10^5$ s^{-1} imposed on the air and fuel inlets, respectively. All walls are treated as no-slip. Two of the four treatments listed in the introduction are compared. At first, a simplified HRT approach is proposed (see section 4.3.1). Results will be compared with predictions from a more reliable, but also more computationally demanding, fully coupled Conjugate Heat Transfer case (see section 4.3.2). Both cases are performed using the same computational grid of 20.3M tetrahedral elements which was optimized applying static mesh refinement criteria [70]. The final grid uses a mesh size in the flame zone just downstream of the centerbody

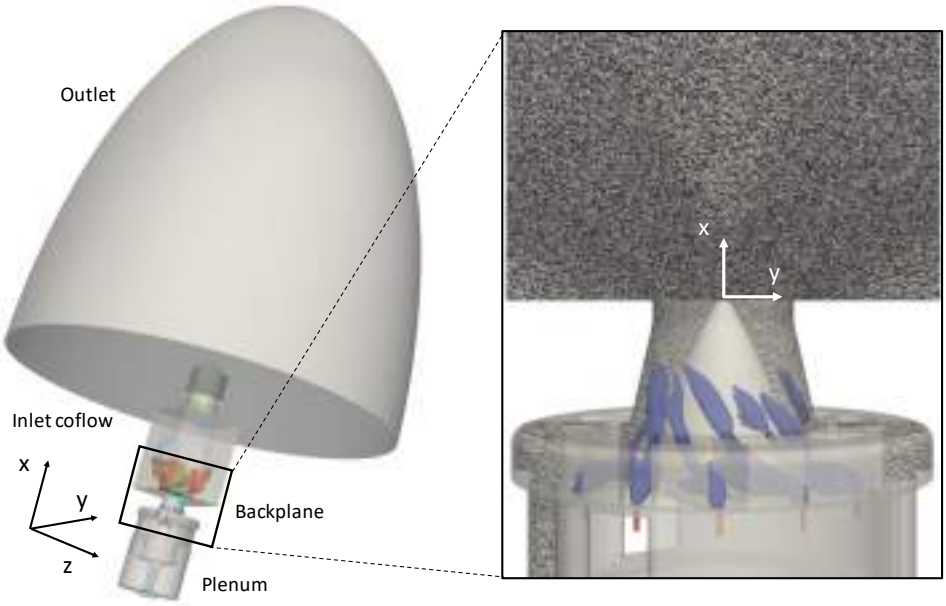

Figure 4.3: Computational domain used in LES with an overview of the mesh and the used coordinate system. Note that in LES the atmosphere is taken into account and the inlet fuel geometry is simplified to the 12 small tubes (colored in red) without the fuel plenum. The instantaneous isocontour of CH_4 (colored in blue) helps visualize the technical fuel injection in the swirled flow.

of $\Delta_x = 300\mu m$, assuring an almost unity y^+ value at the centerbody tip and $y^+ \sim 3$ at the chamber and backplane walls, hence allowing the use of a wall resolved LES approach. A proper mesh resolution at the walls is of fundamental importance to correctly estimate the thermal fluid boundary layer and hence the convective heat transfer at the walls. The dynamic formulation of the thickening flame model (DTFLES) [64] is used to resolve the flame. The model is coupled to the Charlette efficiency function [61] used with the standard coefficient $\beta_{Ch} = 0.5$ to retrieve flame-turbulence interaction. CH_4-Air chemistry is described through an Analytically Reduced Chemistry (ARC) mechanism consisting of 20 transported species, 166 reactions, and 9 quasi-steady state species, derived from the detailed GRI-Mech 3.0 scheme [171] and already validated for the PRECCINSTA flame [70]. More details about this scheme are provided in the supplementary materials of Ref. [71]. The thermal radiation from the hot gases is taken into account by the LES solver with the Optically Thin Assumption (OTA) [172] for the most radiating species CH_4, CO, CO_2, and H_2O[1]: gases are supposed to be optically thin and re-absorption is neglected while the Planck mean-absorption coefficients

[1]Note that the Optically Thin Assumption is a first approximation to take into account radiation from hot gases. More accurate models are considered out of the scope of the present work and could be indeed taken into account for future next steps.

are provided for each species as polynomial functions of temperature [173].

4.3 Results and discussion

LES results obtained with the HRT (section 4.3.1) and CHT approaches (section 4.3.2) are first compared, illustrating the impact of the wall boundary conditions for the current configuration. Then, the instability-driving mechanisms are investigated to understand the differences between the two approaches (section 4.3.3).

4.3.1 Heat Resistance Tuning (HRT) approach

The first approach consists of imposing a heat flux (Φ_q) at each point of the wall. The wall heat flux Φ_q is defined as $\Phi_q = (T_f - T_{ref})/R$ where T_{ref} is a reference temperature (usually the air temperature in the room or the external wall-temperature), T_f is the temperature of the fluid at the wall and R is a thermal resistance. While it is generally easy to set the reference temperature T_{ref}, defining a correct value for the resistance R is not straightforward and depends on the heat transfer at the combustion walls.

If the experimental temperature on the external side of the chamber walls ($T_{wall,ext}$) is available (see Fig. 4.4) and, therefore, chosen as T_{ref} in the calculation of Φ_q, the thermal resistance is fixed by the solid R_{cond} which takes into account heat conduction inside the chamber walls [24, 71]. In general, however, experimental data of wall-temperatures is not available (or incomplete). In these cases, a possible solution is to consider the ambient temperature as reference T_{ref} but doing so an additional thermal resistance should be added to R_{cond} to take into account the external heat losses due to natural (or forced) convection (R_{conv}). Expressions of this resistance can be found in the literature as correlations of the Nusselt number based on geometrical dimensions, Prandtl and Rayleigh (Reynolds) number for natural (forced) convection [174, 175][1].

In PRECCINSTA, experimental temperatures were measured by Yin *et al.* [129], who provided the surface temperature of the backplane and the centerbody tip for an operating condition with a thermal power $P_{th} = 20$KW and an equivalence ratio $\phi = 0.7$ (in the following referred to as case $P20_{CB}$ where the subscripts stands for *centerbody*) which is different from the operating condition selected

[1] In the same manner, a thermal resistance that accounts for radiation R_{rad} can be considered to act in parallel to the convection. Similarly to an electric circuit, an equivalent resistance can be defined as $R_{eq} = R_{cond} + \dfrac{1}{1/R_{conv} + 1/R_{rad}}$. See Appendix A for a more detailed discussion.

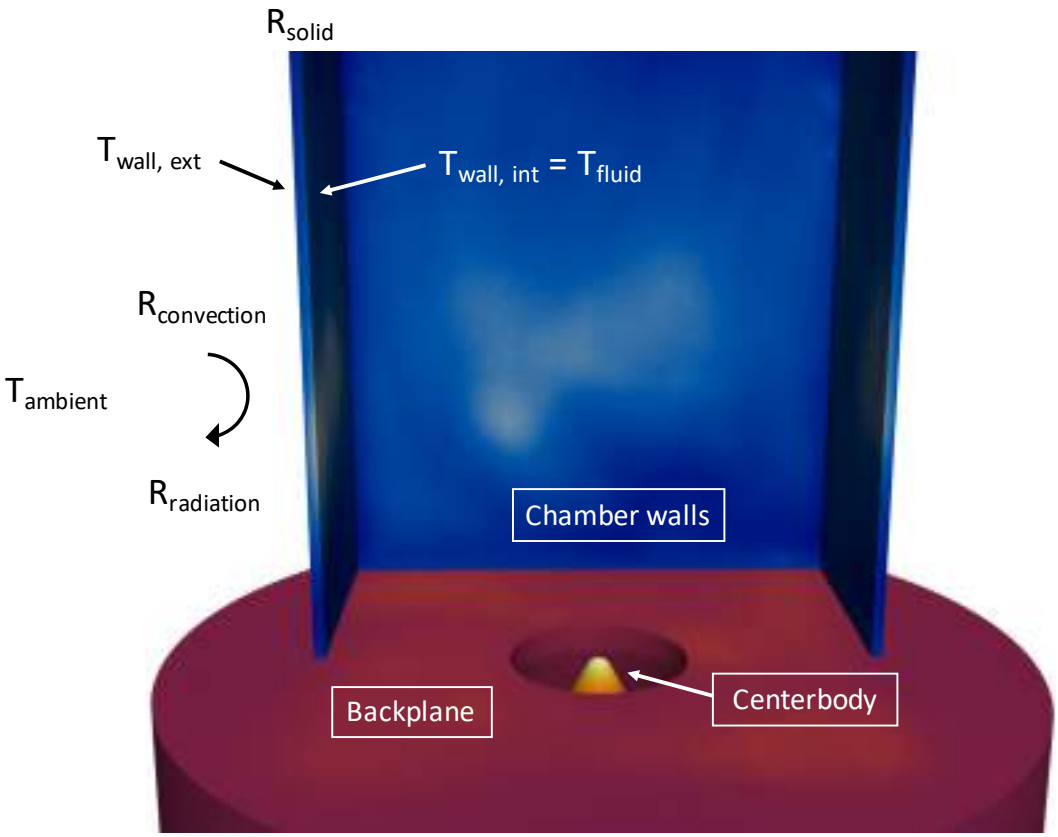

Figure 4.4: Schematic showing the different heat losses mechanisms at the combustor chamber walls and respective thermal resistances.

for the current study (in the following referred to as case $P10$). The other temperature measurements available refer to flow temperature profiles measured by Meier *et al.* [27] for operating conditions with a thermal power P_{th} = 30KW and equivalence ratio $\phi = 0.83$ (in the following referred to as case $P30_W$ where the subscripts stands for *walls*). The operating conditions and experimental data available are summarized in Table 4.1.

Case	P_{th}	ϕ	Exp. data	Ref.
$P20_{CB}$	20KW	0.7	$T_{backplane}$, $T_{centerbody}$	Yin *et al.* [129]
$P30_W$	30KW	0.83	T_f	Meier *et al.* [27]
$P10$	10kW	0.8	-	Present study

Table 4.1: Summary of the operating conditions considered in the HRT approach.

Even if this was done in previous publications, due to the thermal power differences, none of these measurements can be directly used for T_{ref} in the present study since wall surface temperatures cannot be considered independent of the global thermal load. On the contrary, thermal resistances are an intrinsic prop-

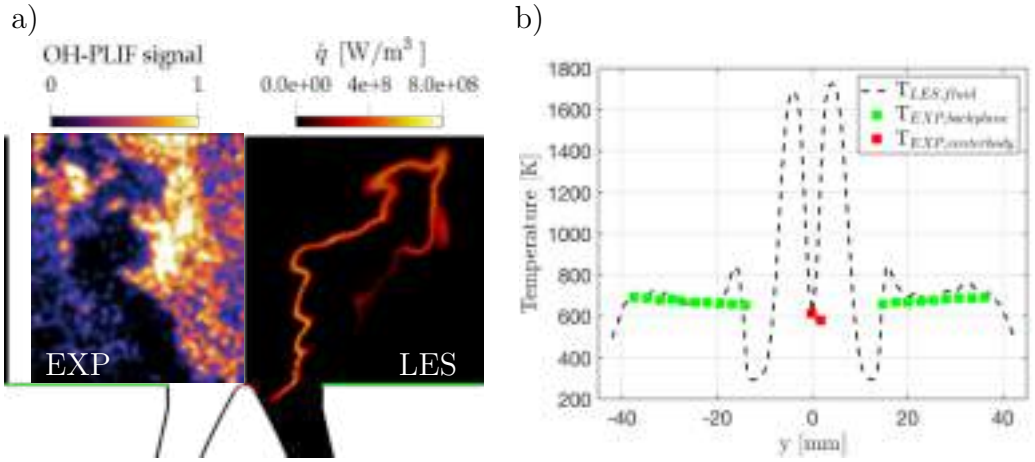

Figure 4.5: (a) Comparison of experimental instantaneous normalized OH-PLIF signal and instantaneous predicted heat release rate $\dot{q}$. Green and red lines indicate experimental data location at the backplane and centerbody tip respectively. (b) Comparison of experimental and LES profiles of mean temperature at the combustion chamber backplane and centerbody tip after tuning of the heat resistances. Condition $P20_{CB}$: $\mathbf{P}_{th}$ = 20KW and $\phi = 0.7$ [129].

erty of the system (determined by the rig geometry, wall material properties and, if present, cooling systems) and, as a first approximation, can be assumed not to change significantly while changing operating conditions[1]. The fact that measurements of wall-temperature at few regimes can be used to determine local wall heat resistances, valid for all regimes, is the basis of the Heat Resistance Tuning (HRT) approach used here: case $P20_{CB}$ is simulated first and the thermal resistances of the backplane and centerbody are tuned to match the surface temperature measurements. The same exercise is then re-proposed for case $P30_W$ retrieving the optimized resistance for the chamber walls. Before the iterative tuning procedure, the initial guess of the thermal resistances has been set for each surface as an equivalent resistance R_{eq} computed following the depicted methodology and making use of standard correlations. More information can be found in Appendix A. In both simulations, other walls are assumed to be adiabatic since no relevant heat transfer is expected. Note that to take into account the experimentally observed pre-heating of the flow in the plenum, the inlet temperature of the flow (and hence also T_{ref}) is imposed to 320K as proposed by Franzelli *et al.* [130].

The outcome of the HRT procedure for case $P20_{CB}$ is presented in Fig. 4.5. For this particular condition, the flame experimentally showed intermittent transitions between V- and M-shapes with an effect on the surface temperature of

[1]Of course thermal resistances are also dependent on the surface temperature since the latter affects the solid thermal conductivity, the radiation and the convection but these effects can be assumed to be negligible as a first approximation for small variations of surface temperature.

the backplane and centerbody. In our case, LES predicts a V-shape, as seen in Fig. 4.5(a) which compares the experimental instantaneous normalized OH-PLIF signal with the instantaneous predicted heat release rate $\dot{q}$. The LES flame is attached to the centerbody and detached from the backplane, with a weaker heat release rate in the ORZ, as in the experiments. The HRT procedure is performed using the measured surface temperature for the V-shape flame. The outcome of HRT is presented in Fig. 4.5(b) showing the comparison of experimental and predicted profiles of mean temperature at the backplane and at the centerbody tip. The final values of the thermal resistances $R_{backplane} = 4.3 \times 10^{-3}$ m^{2}K/W and $R_{centerbody} = 7.5 \times 10^{-3}$ m^{2}K/W allow LES to reproduce the measured thermal state at the walls. The temperature of the centerbody tip reaches 600 K and the backplane wall 650 K in LES while experimental measurements are 580 to 610 K and 630 to 670 K for the centerbody tip and chamber backplane, respectively. The simulation (Fig. 4.5(b)) predicts a locally higher temperature at $\pm$ 17 mm with respect to the experiments. This difference highlights a limitation of the HRT approach: in reality the solid conductivity (which is notably higher with respect to the fluid one) transfers more efficiently the heat from the hot spots to the colder regions thanks to transversal diffusion resulting in a more uniform temperature in the solid (i.e. typically the Biot number[1] is much lower than unity [66, 176]). However, this feature cannot be correctly reproduced by the HRT approach which assigns a single thermal resistance value for the whole surface[2].

Once thermal resistances for backplane and centerbody have been fixed, case $P30_W$ is simulated to tune the thermal resistance at the combustion chamber walls. Bénard *et al.* [115] conducted a similar tuning on the same case to find the temperature profile to be imposed at walls with a Dirichlet boundary condition. However, it is worth re-affirming that imposing a fixed temperature field is not appropriate in reactive LES for two reasons and that HRT is more powerful. First, temperature is an output of the simulation and its profile on the wall should depend on the evolution of the flow field and flame shape during the simulations. If a fixed temperature profile is rigidly imposed, the model will not be able to correctly capture temperature wall variations due to eventual interactions of the flame with the wall. Furthermore, since the wall surface temperature is case

[1] $Bi = hL/\lambda$ where h is the convective heat transfer coefficient, L the characteristic length and λ the thermal wall conductivity. In the current operating conditions, the convective heat transfer at the backplane is low due to low velocity (~ 2 m/s) in the ORZ, making the conduction heat transfer more efficient.

[2] Although imposing a spatial distribution of thermal resistances for each surface is possible, it is in practice difficult to validate due to the marginal amount of experimental data available and it is therefore out of the scope of the present work.

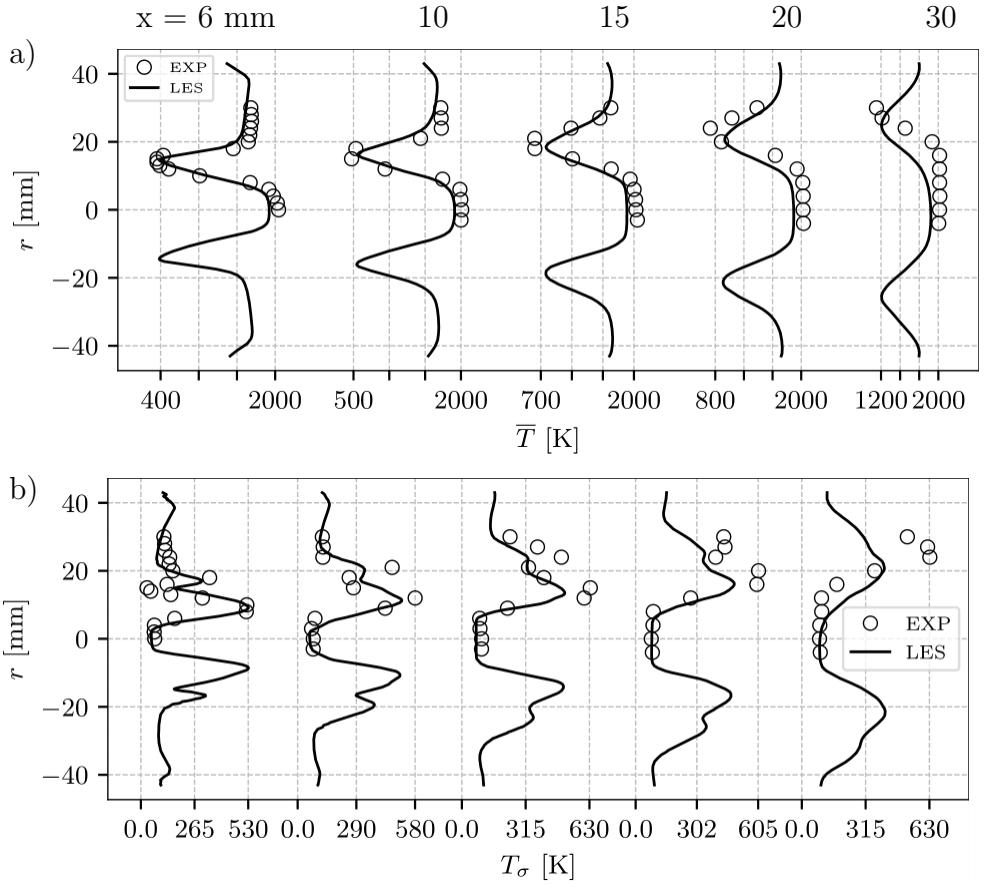

Figure 4.6: Comparison of experimental and predicted profiles of (a) mean and (b) RMS temperature at measurement planes at x = 6, 10, 15, 20 and 30 mm downstream of the combustion chamber backplane for tuning the thermal boundary conditions at the chamber walls. Condition $P30_W$: $\mathbf{P}_{th}$ = 30KW and $\phi = 0.83$. [27]

dependent, the procedure proposed by Bénard *et al.* [115] cannot be used for other operating conditions. The HRT strategy, relying on thermal resistances, is more general.

Results are presented in Fig. 4.6, which shows experimental and predicted profiles of (a) mean and (b) RMS temperature at different measurement planes downstream of the chamber backplane with the resulting value of $R_{walls} = 7{\times}10^{-2}$ m^2K/W. The LES temperature field is in good agreement with the experimental one. A small difference between LES and experiments is visible at the last profile (h = 30 mm) downstream of the backplane: the mean temperature field shows that the flame angle is slightly underestimated in this case and a lower temperature RMS peak is predicted. These differences can be explained by experimental uncertainties and by the fact that the tuning procedure does not rely in this case on a measured surface temperature (as in case $P20_{CB}$) but on the flow temperature, which adds further uncertainties.

The comparison between experimental time-averaged normalized OH-PLIF

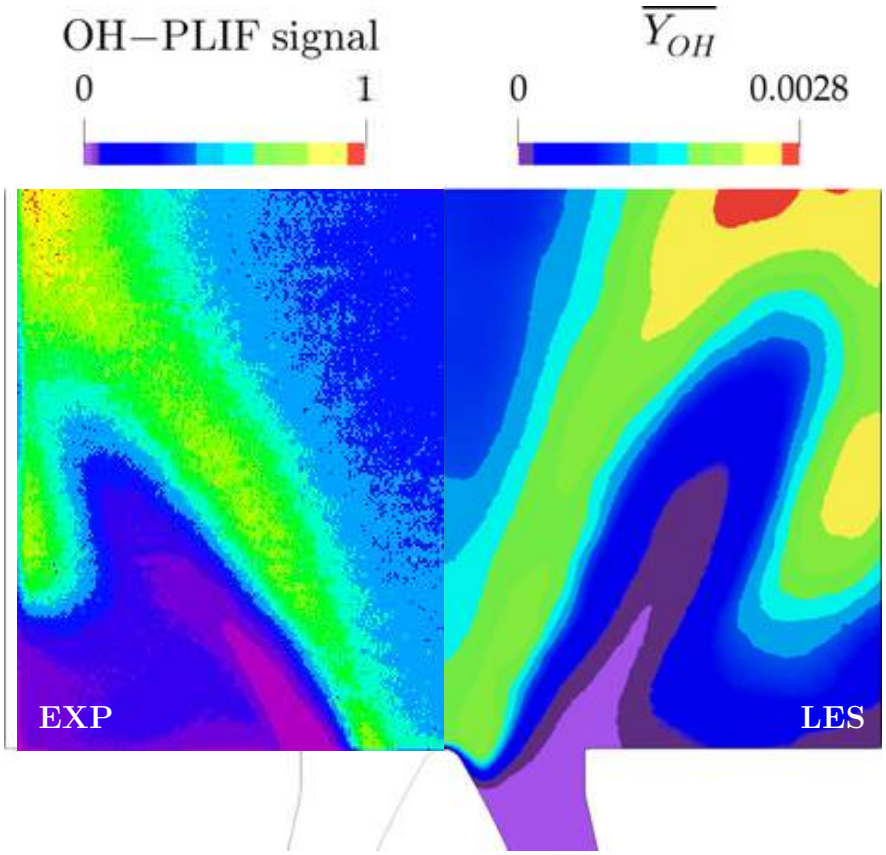

Figure 4.7: Comparison of experimental time-averaged normalized OH-PLIF signal and time and angle-averaged predicted OH mass fraction $\overline{Y_{OH}}$. Case $P30_W$: $\mathbf{P}_{th}$ = 30KW and $\phi = 0.83$ [27].

signal and time as well as angle-averaged LES predicted OH mass fraction $\overline{Y_{OH}}$ in case $P30_W$ is presented in Fig. 4.7. A correct V-shape flame is predicted by LES and global good agreement is achieved in terms of flame length and angle. The ORZs present weaker OH signal and the flame lift-off from chamber backplane is captured. The HRT also predicts a well-attached flame at the centerbody thanks to the correct heat resistance used for the centerbody walls (also tuned from case $P20_{CB}$). Generally speaking, this result confirms the relevance of the HRT approach for variable operating conditions: predicted wall-temperatures vary as the regime changes. The centerbody tip temperature reaches a value of around 900 K for case $P30_W$, notably higher than the one measured in condition $P20_{CB}$ of 600 K (which has a lower equivalence ratio $\phi = 0.7$ and a lower thermal power compared to case $P30_W$). This may explain why Fredrich *et al.* [132, 137] did not observe an attached flame at the centerbody by prescribing the same wall-temperature as in case $P20_{CB}$ of Yin *et al.* [129].

The HRT approach is then applied to case $P10$, which is the final objective of the present study. The mean LOS predicted heat release rate $\overline{\dot{q}}$ is compared

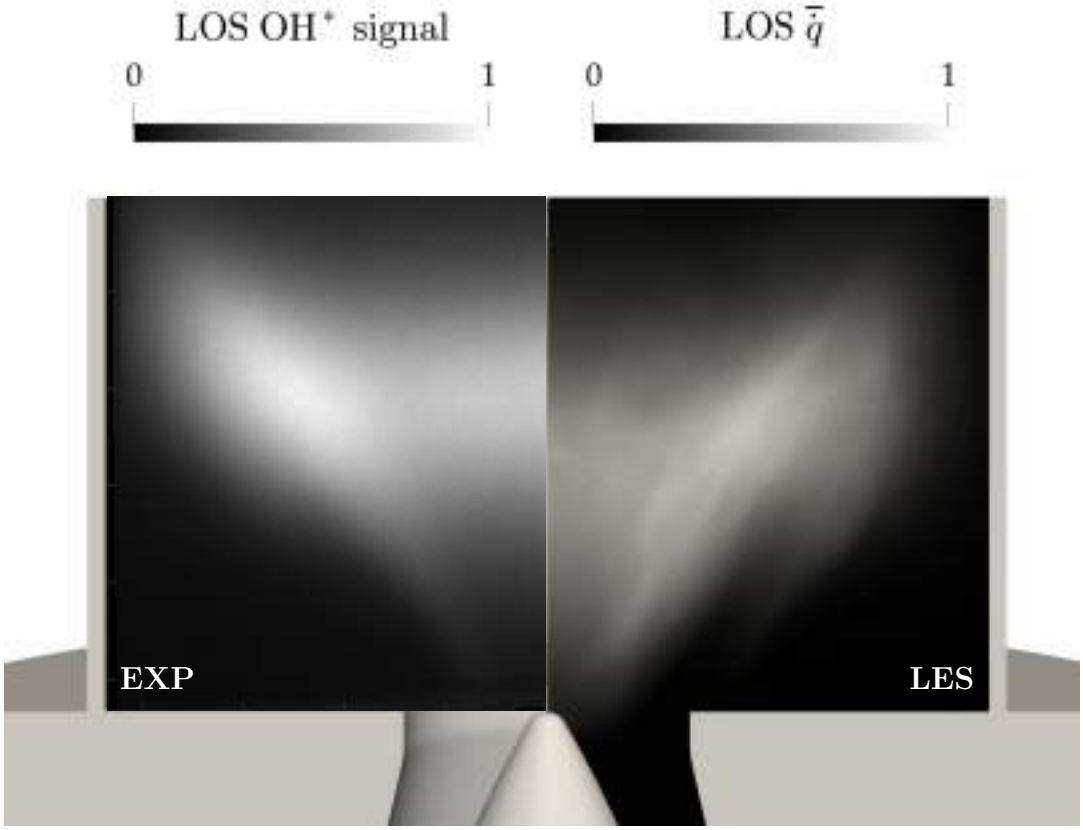

Figure 4.8: Validation of the LES simulations with HRT approach for case $P10$. Comparison of experimental normalized time-averaged LOS OH* chemiluminescence image with LOS of predicted heat release rate $\overline{\dot{q}}$.

with the experimental normalized time-averaged LOS OH* chemiluminescence in Fig. 4.8. LES captures the mean flame angle while the flame length is slightly underestimated. A global satisfactory agreement is achieved in terms of flame shape with the HRT approach, the only main difference being the region of heat release rate in the CRZ which is not observed in experiments.

Even though the mean flame is reasonably captured using the HRT method, the limits of this approach become visible when the flame dynamics are considered. Indeed, differences with the experiment can be noticed for heat release rate fluctuations and pressure oscillations predicted at the combustion chamber backplane shown in Fig. 4.9(a): unlike experimental recordings of Fig. 4.2, high amplitude pressure oscillations of $p'_{num} \simeq 800$ Pa (to be compared with experimental ones of $p'_{exp} \simeq 200$ Pa) are predicted by LES. Furthermore, the phase difference between the unsteady pressure (black line) and heat release rate (red line) oscillations is within the $\pi/2$ limit, satisfying the well-known Rayleigh criterion [177]. This hypothesis is further confirmed by the spectrum of the two signals shown in Fig. 4.9(b): differently from the experimental observations (Fig. 4.2(b)),

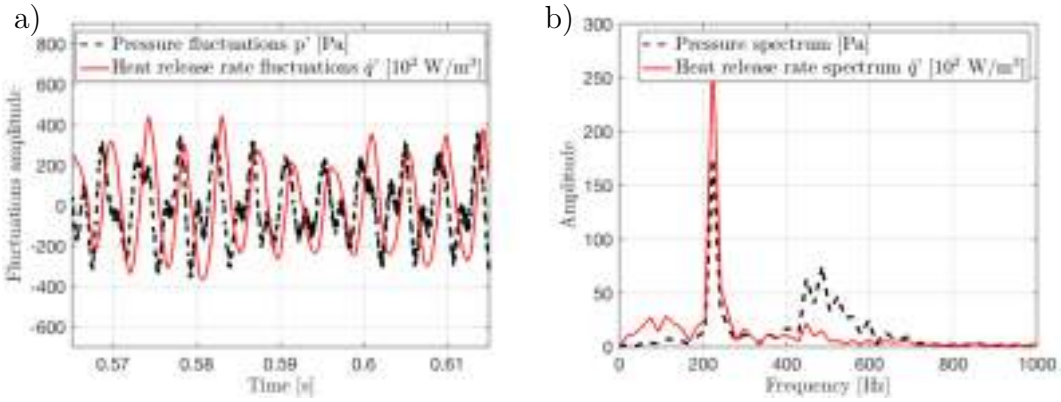

Figure 4.9: (a) Pressure and heat release rate fluctuations predicted at the combustion chamber backplane using the HRT approach. The phase difference between the unsteady pressure and heat release rate oscillations is less than $\pi/2$, satisfying the Rayleigh criterion. (b) Signals spectra via FFT, showing that heat release rate fluctuations correspond to a peak at 224 Hz, while pressure spectrum shows also a second peak at 480 Hz.

a strong peak almost one order of magnitude higher than in the experiments is observed in both heat release rate (red line) and pressure (black line) spectra at 224 Hz, indicating that the instability is fed by a flame/acoustics coupling. A second peak is also present in the pressure spectrum at 480 Hz.

To understand the dynamics of this numerically-predicted thermoacoustic oscillation, Fig. 4.10 shows the phase-locked instantaneous fields of axial velocity (left) and CH4 mass fraction (right) with the heat release rate fields $\dot{q}$ for four different phases of the heat release rate oscillating cycle at 224 Hz. Figures 4.10(a-c) correspond to the minimum ($\varphi = 0$) and maximum ($\varphi = \pi$) of the heat release rate in the cycle, respectively. The other two phases shown in Figs. 4.10(b-d) refer to instants at $\varphi = \pm\pi/2$ respectively. In all images, the black isocontours refer to temperature levels of 750 and 1500 K whereas the white isocontour refers to the CH_4 global mass fraction level corresponding to $\phi = 0.8$. When the heat release rate is minimum in Fig. 4.10(a) (that corresponds to a minimum in the plenum pressure), the axial velocity in the swirler is low, with a strong CRZ downstream of the centerbody. The CH_4 jets are injected in a low velocity air stream and are not significantly forced toward the centerbody walls. After $\varphi = \pi/2$ (Fig. 4.10(b)), the CRZ is still present in the chamber and the velocity in the swirler is still low: CH_4 accumulates in the swirler and pockets of higher ϕ are visible close to the centerbody. At the same time the flame gets longer because the equivalence ratio ϕ before the flame is now lower than the global value (i.e. the white isocontours are far from the flame front). At $\varphi = \pi$ (Fig. 4.10(c)), when

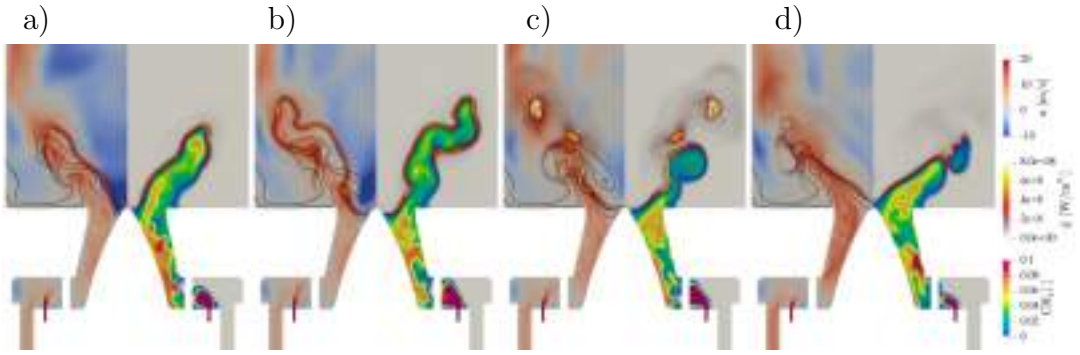

Figure 4.10: Phase-locked instantaneous fields of axial velocity (left) and CH_4 mass fraction (right) with superimposed the heat release rate field $\dot{q}$ for four different phases of the oscillating cycle. (a) and (c) correspond to the minimum and the maximum of heat release rate in the cycle, respectively. Black isocontour refer to temperature levels of 750 and 1500 K while white isocontour refer to the CH_4 global mass fraction level.

heat release rate and plenum pressure are maximum, the velocity in the swirler is high and starts to push the CH_4 jet downstream. At the same time the previous injected fuel-rich pocket has reached the flame front, which gets shorter and burns at the maximum of the heat release rate. Finally, at $\varphi = -\pi/2$ (Fig. 4.10(d)), the velocity in the swirler is at its maximum, causing the fuel jet to be strongly pushed toward the centerbody.

This thermoacoustic feedback loop resembles the one effectively present in the experiments conducted by Meier *et al.* [27] for $\phi = 0.7$ and $P_{th} = 25$ kW and is explained by the mechanism described by Franzelli *et al.* [130] using LES: the velocity field in the swirler follows the plenum pressure and oscillates, causing rich gas pockets to be periodically pushed into the chamber and producing fluctuations of the heat release rate. The fuel enters the swirl channel as a jet-in-crossflow and, depending on the momentum flux ratio, may impinge on the walls. This flapping of the fuel jet is less evident if compared to their LES but still noticeable. However, differently from the experiments of Meier *et al.* [27], this mechanism is not triggered experimentally for the studied case $P10$ and possible causes for its appearance are investigated hereafter.

One possible reason explaining why LES seems unstable is acoustic damping [178]. In the absence of additional passive damping such as Helmholtz resonators, the main contributor to damping is the losses of acoustic energy at the boundaries of the system [11, 179]. In LES, inlet and outlet boundary conditions are treated with the classical Navier-Stokes Characteristic Boundary Conditions (NSCBC) formalism [30]. According to the NSCBC theory [30, 180], the inlet and outlet reflection coefficients $\mathcal{R}$ are functions of the frequency and of the relaxation

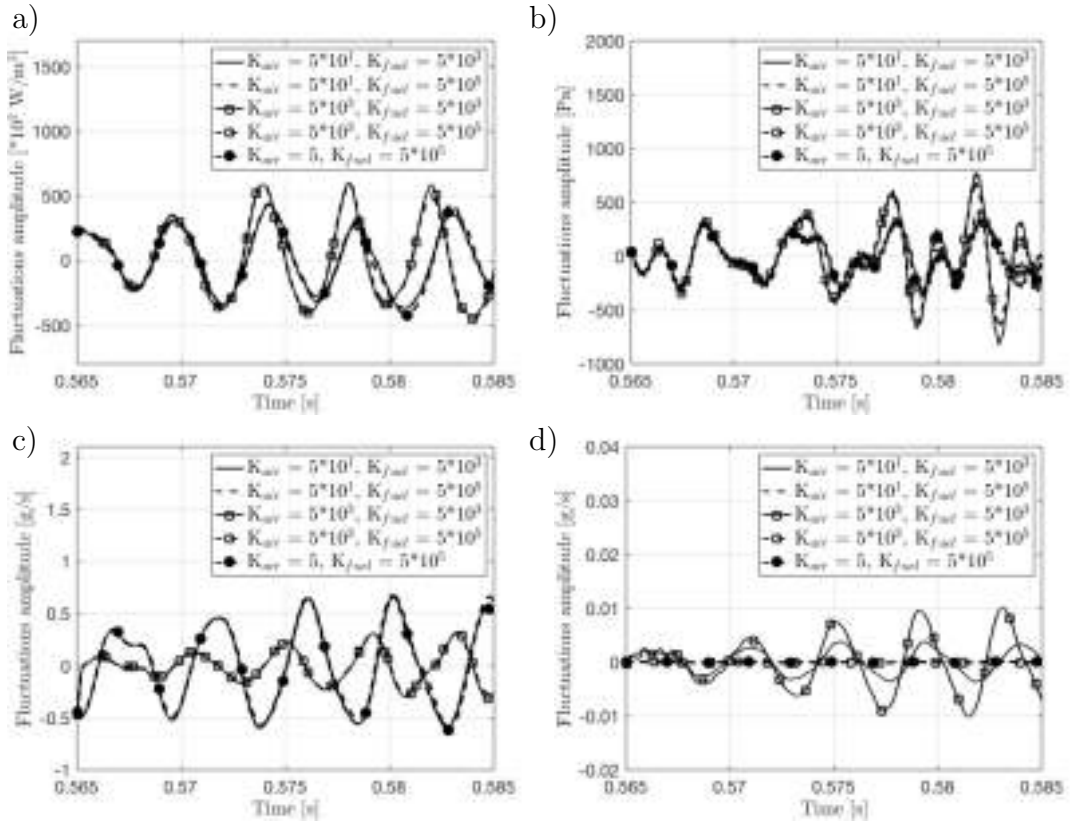

Figure 4.11: Effect of the acoustic impedance of the air and fuel lines. Predicted fluctuations of (a) heat release rate, (b) pressure signal at the combustion chamber backplane, (c) air mass flow rate and (d) fuel mass flow rate.

coefficient K used [181] to avoid that mean values drift away from their target values. At the outlet, including the atmosphere in the computational domain assures the correct representation of the acoustic impedance at the exit of the combustion chamber. A systematic analysis of the effect on the thermoacoustic oscillation amplitude of only the relaxation coefficients imposed at the air and fuel inlet lines was conducted. These K coefficients control the "stiffness" of the air and fuel lines which are unknown and may explain LES/EXP discrepancies. Figure 4.11 shows the fluctuations of (a) heat release rate, (b) pressure signal at the chamber backplane, (c) air mass flow rate and (d) fuel mass flow rate for different values of K. For a given value of $K_{air} = 50$ s^{-1} (soft air line), two different $K_{fuel} = 5 \times 10^3$ s^{-1} (soft fuel line) and $K_{fuel} = 5 \times 10^5$ s^{-1} (stiffer fuel line) are tested (continuous and dashed lines in Fig. 4.11). No difference can be detected between these two cases for heat release rate, pressure or air mass flow rate. On the contrary, a higher impact can be observed when K_{air} is increased to 5×10^3 s^{-1} making the air line stiffer keeping $K_{fuel} = 5 \times 10^3$ s^{-1} constant (continuous

line with rectangular marks in Fig. 4.11). The amplitude of (a) heat release rate and (b) pressure oscillations increase while the frequency slightly increases to 244 Hz. The oscillation of the air mass flow rate (c) is instead lower if compared to the cases at $K_{air} = 50$ s^{-1} since with a higher relaxation coefficient the boundary tends more rapidly to the mean target value ($u \rightarrow \bar{u}$) with an acoustic behaviour closer to a velocity node ($u' = 0$). In this configuration, fuel mass flow rate oscillations (Fig. 4.11(d)) slightly increase (0.01 g/s, i.e., 5% of the mean value) with a negligible impact on the instability amplitude. With a further reduction of K_{fuel} no significant change has been observed while a mean value drift occurred (not shown). As a final test, an almost anechoic condition is imposed at the inlet further reducing K_{air} to 5 s^{-1}: in this case, the amplitude and the frequency of oscillations for both heat release rate and pressure are unaffected by changes of K (dashed line with circular marks in Fig. 4.11).

These observations show that for case $P10$, the impedance of the fuel line (controlled by K_{fuel}) has no relevant impact on the predicted thermoacoustic oscillations[1]. This could be explained by the small fuel tube sections compared to the swirler dimensions that create acoustic reflections due to the cross section change [182]. A higher impact is observed when changing the air inlet line impedance (controlled by K_{air}). Nevertheless a stabilization of the observed thermoacoustic mode was never reached even when an almost anechoic boundary is imposed. An underestimation of the acoustic damping is therefore not responsible for the thermoacoustic oscillations observed in the simulations with the HRT approach. Even if HRT reproduces the mean flame shape reasonably, it fails to characterize its unsteady dynamics.

4.3.2 Conjugate Heat Transfer (CHT) approach

To remove uncertainties on the heat transfer between the fluid and the solid, CHT simulations are performed by coupling the LES solver with the AVTP code [54, 55] which solves for heat conduction in the walls of the chamber using the energy conservation equation,

$$\rho_s C_s \frac{\partial T(x_i, t)}{\partial t} = -\frac{\partial \Phi_{q,i}}{\partial x_i}, \tag{4.1}$$

[1]Franzelli *et al.* [130] predicted in the pulsating flame of Meier *et al.* [27] an oscillating frequency of 390 Hz which was higher than the experimental value of 290 Hz. This discrepancy was attributed to the acoustic impedance of the fuel line which was arbitrarily imposed in LES. The present analysis would suggest instead (for different operating conditions and hence pressure oscillations levels) that the impedance of the fuel line has no impact on the thermoacoustic instability and that the higher predicted frequency of oscillation was due to the adiabatic walls (i.e. higher sound speed) and to the K_{air} coefficient which has an impact on the frequency.

where ρ_s and C_s are the solid density and heat capacity respectively, T is the solid temperature and $\Phi_{q,i}$ is the conduction heat flux described by Fourier's law,

$$\Phi_{q,i} = -\lambda_s \frac{\partial T}{\partial x_i}, \tag{4.2}$$

and is controlled by the heat conductivity of the solid λ_s. AVTP takes into account local changes of λ_s and C_s due to the different materials of the rig (e.g. inconel, quartz, etc) and to the local temperature.

AVTP is coupled with the LES solver AVBP through a Parallel Coupling Strategy (PCS) in which both solvers run together and exchange information at each coupling iteration by using the CWIPI library [183]. In the AVBP/AVTP case, the LES solver uses the solid surface temperature T_s as boundary conditions at the walls computed by AVTP while the latter uses the heat flux Φ_q computed by AVBP. The time step at which the two codes advance are different: in AVBP, the time step δt is limited by the Courant-Friedrichs-Lewy (CFL) condition, which for a typical resolution of the fluid mesh brings to a time step δt_f of the order of 10^{-8} s. In AVTP, the time step is controlled by the Fourier number and leads to a time step δt_s of the order of 10^{-5} s. It is possible to synchronize the two solvers by changing the number of iterations that each of them performs in between two consecutive coupling iterations (i.e. at the information exchange time). Note also that the characteristic time of the flow τ_f (i.e. the flow-through time) is typically much smaller than the characteristic time of the heat transfer in the solid τ_s. The first can be computed as $\tau_f = \rho V/\dot{m}$ where ρ is the mean flow density, V is the volume of the combustion chamber and $\dot{m}$ is the mass flow rate and τ_f is typically of the order of milliseconds. The characteristic time of the heat transfer in the solid τ_s [176] can be computed as $\tau_s = V_s \rho_s C_s / hS$ where S is the surface area, V_s and ρ_s are the volume and the density of the solid and h is the heat transfer coefficient: hence τ_s is of the order of 1 - 10 s. The difference between τ_s and τ_f would lead to very long CPU time for the flow solver if the two solvers are synchronized in time. To speed up the convergence toward a solid steady state temperature, the two solvers can be de-syncronized in time by increasing the number of iterations performed by AVTP with respect to AVBP between two consecutive coupling iterations. This methodology is equivalent to decreasing the heat capacity of the solid and, hence, the characteristic time of the heat transfer in the solid τ_s. Once a steady state is reached (i.e. statistical convergence), the two solvers can be re-synchronized in time and the correct solid heat capacity recovered.

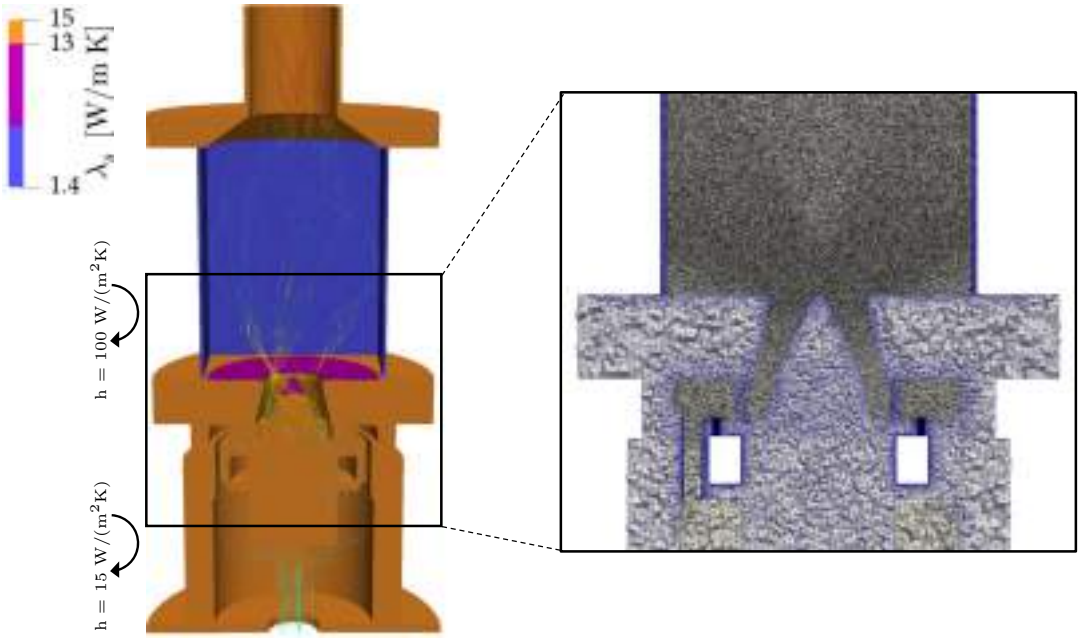

Figure 4.12: Computational domain used in CHT simulations with overview of the solid (blue) and fluid (black) meshes with thermal boundary conditions for the AVTP code. Assumed thermal conductivity λ_s for quartz (blue), inconel (purple) and stainless steel (orange) is also indicated.

The computational domain used in CHT AVBP-AVTP simulations is presented in Fig. 4.12 where the solid mesh is blue and the fluid black. The solid parts have been discretized using 16M tetrahedral cells and a resolution of at least 5 points through the chamber walls. A second-order Galerkin diffusion scheme is applied for spatial discretization and an implicit first-order Euler scheme is used for time integration. While the heat fluxes at the solid boundaries in contact with the fluid are determined from the LES solutions, thermal boundary conditions must be fixed for the solid surfaces that are not in contact with the fluid domain (e.g. external chamber walls, external plenum walls). To do so, the required heat exchange coefficients at the boundaries have been determined through correlations for natural convection on the external side of the chamber and plenum walls. Moreover, Fredrich *et al.* [132] showed that heat losses incurred through radiation can be important. Therefore, to take into account thermal radiation, it is possible to compute an equivalent heat transfer coefficient for the external chamber walls starting from the Stefan-Boltzmann law $\dot{q}_{rad} = \epsilon\sigma T^4$. This procedure yields higher heat transfer coefficients (i.e. h = 100 W/(m^{2}K) with a $\epsilon_{quartz} = 0.8$ for chamber walls and h = 15 W/(m^{2}K) for plenum walls) if compared to only convection [66] and are reported in Fig. 4.12. This approach neglects the internal wall radiation towards the hot gases, but can be considered as a first order

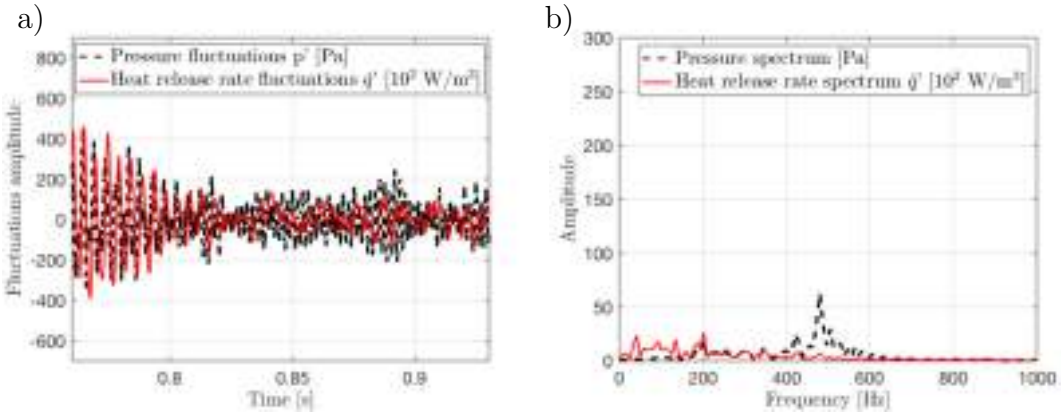

Figure 4.13: (a) Pressure and heat release rate fluctuations predicted at the combustion chamber backplane. From an unstable phase in which pressure and heat release rate oscillations were almost in phase, satisfying the Rayleigh criterion, a stable condition is recovered with CHT simulations. (b) Spectra of the stable part of the signals, showing that the heat release rate peak at 224 Hz is no more present.

approximation for taking into account radiation heat losses.

The time evolution of the heat release rate and pressure oscillations predicted at the combustion chamber backplane after the thermal convergence is presented in Fig. 4.13(a). From the unstable phase predicted with the simplified approach in which pressure and heat release rate oscillations were almost in phase satisfying the Rayleigh criterion, a stable condition is recovered when CHT simulations are started. The pressure fluctuations amplitude is of the order of 200 Pa and corresponds to the level observed experimentally (see Fig. 4.2). Moreover, heat release rate fluctuations seem no more correlated with pressure fluctuations. The spectra computed via Fast-Fourier Transform (FFT) of the stable part of the two signals (i.e., t $\geq$ 0.83 s) are presented in Fig. 4.13(b) and confirm this observation. No 224 Hz peak appears confirming that the experimentally observed stable condition is recovered. The pressure signal spectrum also shows only a weak 480 Hz peak that does not correlate with heat-release rate fluctuations.

The instantaneous field of solid temperature as computed by AVTP is shown in Fig. 4.14(a) together with an instantaneous iso-contour of predicted heat-release rate $\dot{q}$ at 10% of maximum value. The temperature of the chamber walls on the internal side reaches a maximum value of around 1350 K at 40 mm from the backplane where the flame is very close to the walls. The temperature goes down when proceeding toward the backplane where the flame is only sporadically present. The backplane has a temperature of around 600K, very similar to the one measured by Yin *et al.* [129] in case $P20_{CB}$. The Biot number being much

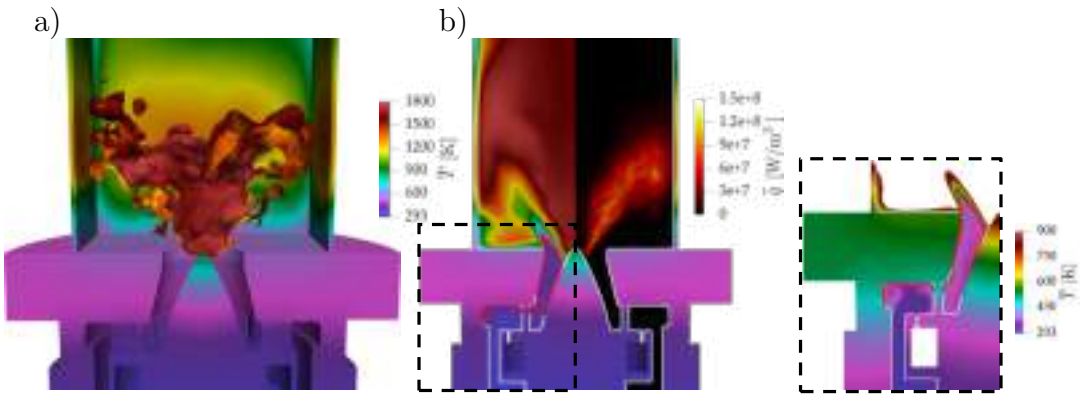

Figure 4.14: (a) Instantaneous field of solid temperature and iso-contour of heat-release rate $\dot{q}$ at 10% of maximum value; (b) cut-plane showing the time-averaged temperature $\overline{T}$ and heat release rate $\overline{\dot{q}}$ predicted by CHT simulations. The added red iso-contour line corresponds to a temperature of 450 K, showing the pre-heating of the fresh gases by the solid walls. A zoom showing the temperature field with a different colorbar helps visualize the pre-heating of the gases and the temperature gradient in the solid. The fluid domain is delimited by a white line to visualize the separation between solid and fluid parts.

lower than 1, the temperature at the backplane is more uniform than the one predicted, for example, with the HRT approach in case $P20_{CB}$ (see Fig. 4.5(a)). The predicted temperature at the centerbody tip instead is notably higher than the one measured in condition $P20_{CB}$ reaching a value of 800 K: even if the thermal power of case $P20_{CB}$ is higher with respect to case $P10$, the equivalence ratio ϕ is also higher in the latter case and yields a higher adiabatic flame temperature. The flame has a V-shape, with a flame-root well attached to the centerbody tip. Figure 4.14(b) shows the time-averaged temperature $\overline{T}$ and heat-release rate $\overline{\dot{q}}$ in a cut plane with a zoom showing the temperature gradient in the solid and the pre-heating of the gases. The fluid domain is delimited by a white line. The flow reaches 1800 K in the CRZ and downstream of the flame tip where burnt gases are present while the ORZs show lower temperature. The red iso-contour visible close to the centerbody corresponds to a temperature of 450 K and shows the pre-heating of the fresh gases due to the warmed-up solid which is visible also close to the fuel injection tubes. This is an important feature captured by the CHT simulations, since, as discussed, in previous studies a fresh gas temperature of 320 K has been usually considered, while in this case we observe a pre-heating temperature which is closer to 400 K (starting from a T_{inlet}=293K). Note that the temperature profile of the fresh gases is not homogeneous but reaches higher values close to the walls. The time-average of the predicted heat-release rate $\overline{\dot{q}}$ confirms the V-shape of the flame and shows that the chamber walls are notably hotter in the region where the flame tips reach the walls. No flame is predicted

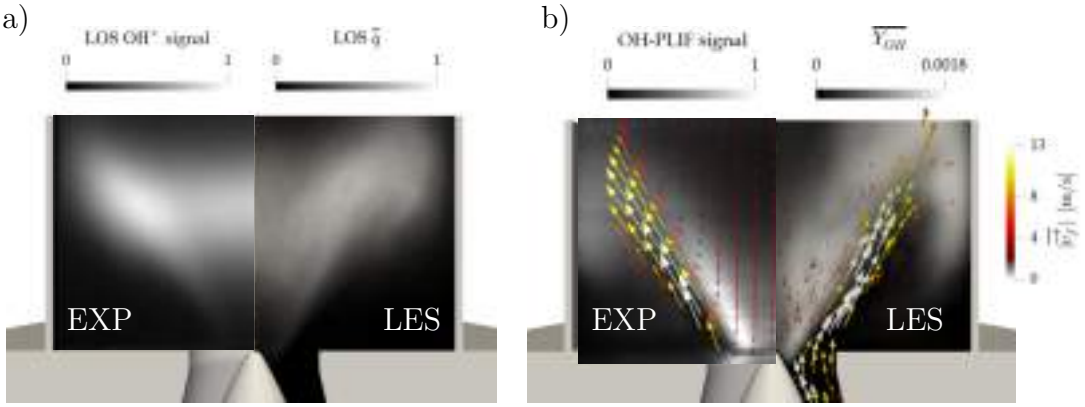

Figure 4.15: Validation of CHT simulations: (a) Comparison of experimental normalized time-averaged Line of Sight (LOS) OH* chemiluminescence image with LOS predicted heat release rate $\bar{\dot{q}}$; (b) Comparison of experimental normalized time-averaged OH-PLIF signal with predicted OH mass fraction $\overline{Y_{OH}}$. The arrows are tangential to the experimental and numerical time-averaged velocity field in the plane $\overline{\overrightarrow{v_{//}}}$. Their length and color indicate the velocity magnitude.

in the CRZ while in the ORZ weaker heat release rate can be noticed.

Finally, the CHT simulations are compared to experimental data in Fig. 4.15. Experimental normalized time-averaged LOS OH* chemiluminescence image (which is a qualitative indicator for the heat release rate for lean premixed flames) and LOS field of predicted heat release rate $\bar{\dot{q}}$ are shown in Fig. 4.15(a). The length and flame angle are retrieved by the CHT simulations and a better agreement is achieved with respect to the simplified approach (see Fig. 4.8). LES is also able to predict the high region of heat release rate in the top central part of the flame while low intensity is predicted in the CRZ, just downstream of the centerbody. The flame tip shape is correctly predicted together with the distance from the external chamber walls. Figure 4.15(b) presents the comparison of the experimental normalized time-averaged OH-PLIF signal with the predicted OH mass fraction $\overline{Y_{OH}}$. CHT simulations agree with the experimental data, both in terms of flame length and angle. The flame tip reaches a height of 50 mm from the backplane while low OH mass fraction intensity is predicted in the ORZ. As in experiments, LES predicts no OH mass fraction $\overline{Y_{OH}}$ in the high velocity region of the swirled flow. Experimental and numerical time-averaged velocity field in the plane $\overline{\overrightarrow{v_{//}}}$ are indicated by arrows that are tangential to the velocity vector and whose length and color indicate the velocity magnitude. Both in LES and experiments, a high velocity region (i.e. white arrows) is predicted at the exit of the swirler. A CRZ is also visible together with the ORZ where the velocity in the plane is very weak.

A more quantitative validation of the CHT simulations can be assessed by

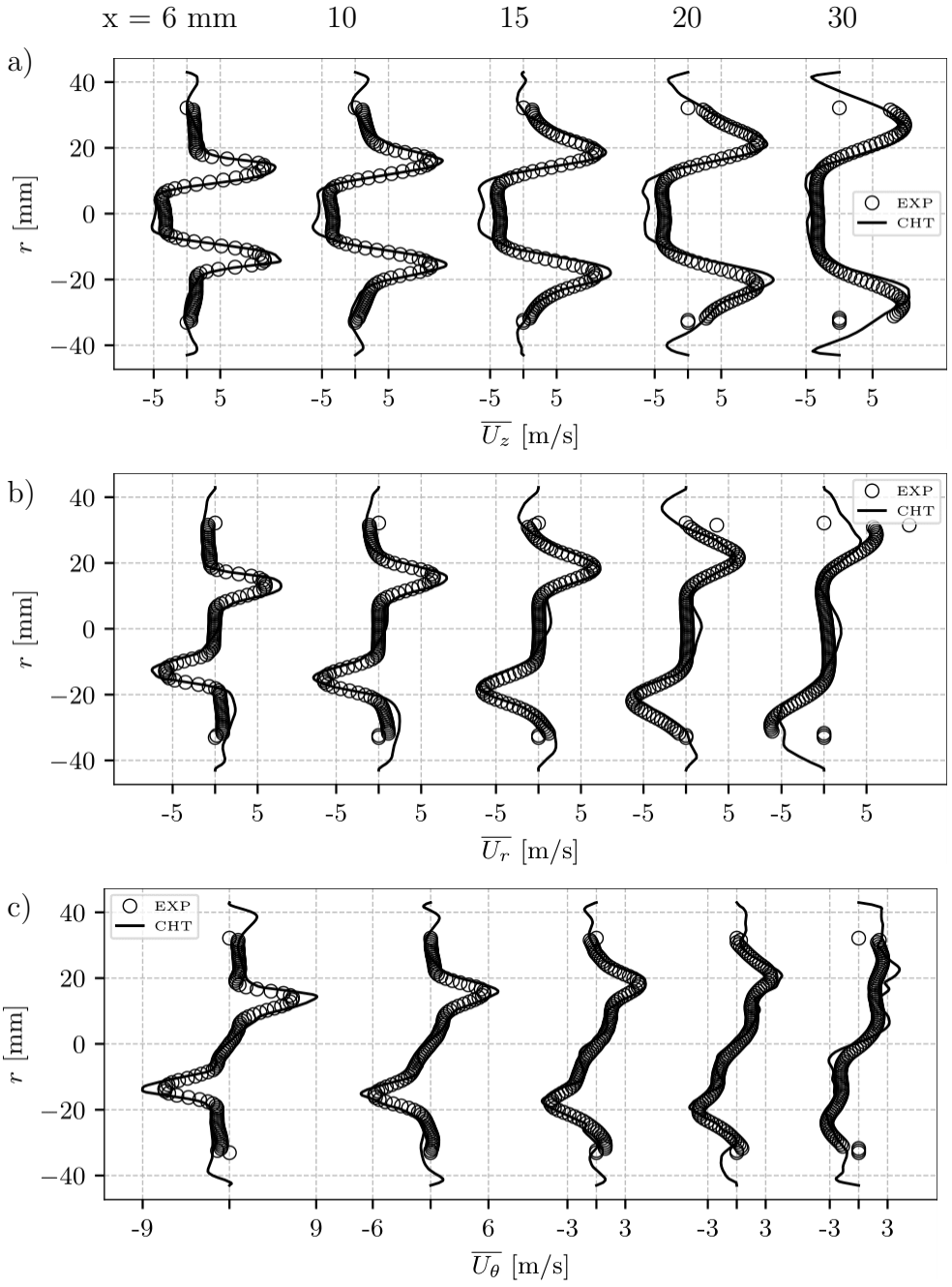

Figure 4.16: Profiles of Mean (a) axial velocity, (b) radial velocity and (c) tangential velocity at measurement planes at x = 6, 10, 15, 20 and 30 mm downstream of the combustion chamber backplane for the CHT simulations in comparison to experiments.

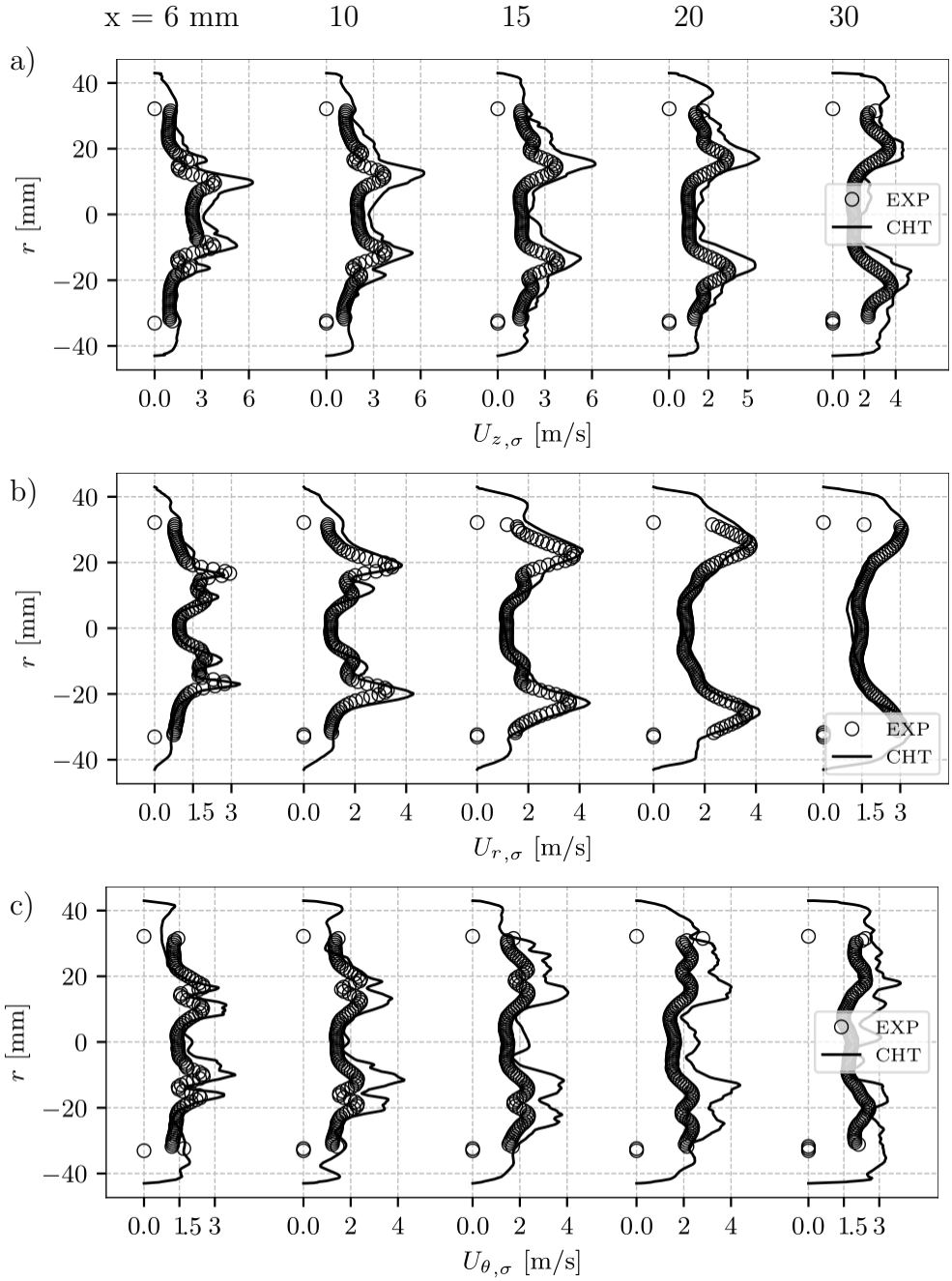

Figure 4.17: Profiles of RMS (a) axial velocity, (b) radial velocity and (c) tangential velocity at measurement planes at x = 6, 10, 15, 20 and 30 mm downstream of the combustion chamber backplane for the CHT simulations in comparison to experiments.

comparing the experimentally measured mean and rms profiles of velocity components at different measurement planes downstream of the backplane with the predicted profiles: LES captures the mean axial velocity component (Fig. 4.16(a)), both in terms of magnitude and opening of the swirled flow. The magnitude of the CRZ is slightly underestimated at h = 15 mm and 20 mm from the chamber backplane but a good match is retrieved at h = 30 mm. RMS oscillations are instead slightly over-estimated (Fig. 4.17(a)). This mismatch may be explained by uncertainties of the experimental values and the small absolute magnitude of the RMS. Mean and rms of both radial and tangential velocity are captured by LES as shown in Fig. 4.16(b-c) and Fig. 4.17(b-c), respectively. The poorer match for tangential velocity profiles may be due to PIV measurement uncertainties for which errors in the out-of-plane direction (in this case, the tangential) are typically higher than for the in-plane velocity components. [184].

4.3.3 Heat transfer impact on thermoacoustic driving mechanisms

The previous sections have shown that the correct stable thermoacoustic behavior of the flame was predicted only with CHT simulations and not with HRT. We analyze now the impact of heat transfer on the instability-driving mechanisms starting with acoustic modes structures.

Figure 4.18(a) shows the relative mean temperature difference between the CHT and the HRT simulations in the middle plane of the combustor with the white iso-contours indicating zero values. The combustion chamber has a slightly lower mean temperature in CHT while the ORZs present significantly lower temperature (dark blue zones). On the contrary, a strong pre-heating is observed in the swirler and close to the centerbody walls (red zones). At the same time, the flow in the plenum is slightly warmed while the flow at the air inlet is cooler since in CHT T_{inlet} is fixed at the ambient temperature (293K). This highlights the main differences between the HRT and the CHT approaches: the HRT method is not able to capture the detailed temperature variation at the walls since it also depends on the heat re-distribution due to conduction in the transverse direction [1]. Likewise, the unsteady heat transfer between the flow and the solid is a function of the relative flame position with respect to the walls which in turn is dependent on the non-homogeneous and unsteady preheating of the gases.[2]

[1]Note also that the HRT method is valid only when local 1D conduction can be assumed which is valid only in case of low thickness walls, which is not the case of the burner centerbody for example.

[2]Note that even in the unrealistic scenario in which a local tuning of R were possible, HRT would however miss the non-homogeneous preheating of the gases. More generally, the HRT

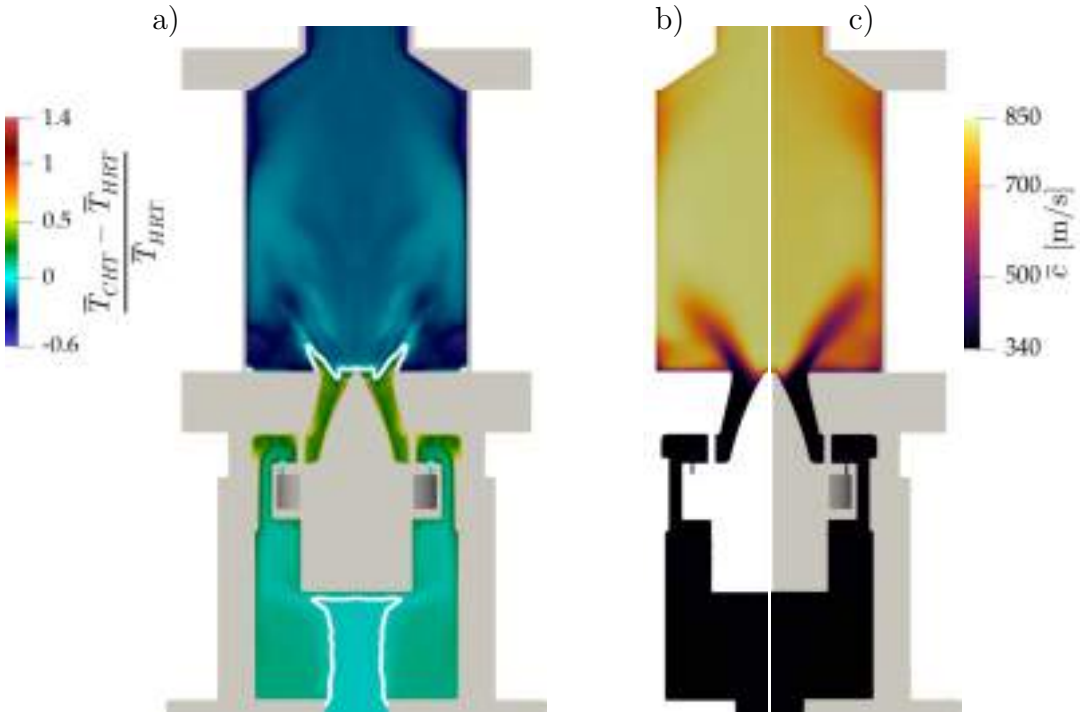

Figure 4.18: (a) Relative mean temperature difference between the CHT and the HRT approaches on the middle plane of the combustor with white iso-contours corresponding to zero values. Predicted time-averaged sound speed $\overline{c}$ field in (b) HRT-LES and (c) CHT-LES.

The corresponding time-averaged sound speed $\overline{c}$ are compared in Figs. 4.18(b-c): a globally lower sound speed value is achieved with CHT in the chamber with the most significant differences observed in the ORZs are probably due to the fact that the flame does not oscillate anymore and no heat release rate happens in these regions. Finally, another difference can be noted along the chamber walls: for HRT, the zones where the flame tips reach the wall are very hot, while for CHT, the temperature field, and hence the sound speed, close to the chamber walls are more homogeneous due to the heat conduction in the solid.

The two mean fields shown in Fig.4.18(b-c) are used to compute the first two acoustic modes of the system using the Helmholtz solver AVSP [53] giving comparable results in terms of both modes frequency and shapes. The first mode is predicted at a frequency of 257 Hz. Modulus and phase data (Fig. 4.19(a-b)) suggest that this 257 Hz mode is the 1/4 wave (or bulk) mode of the system: the amplitude of the pressure oscillation $\mid p' \mid$ is larger in the plenum (Fig. 4.19(a)) and the chamber as well as the plenum oscillate in phase (Fig. 4.19(b)). The

approach cannot reproduce all the situations in which the solid provides energy to the gases (e.g. bluff-body, plenum): since the reference temperature in HRT is fixed at 293 K it is always the gas that provides energy to the solid. Changing T_{ref} locally means introducing additional unknowns while also losing the possibility to apply tuned values of R for all different operating conditions.

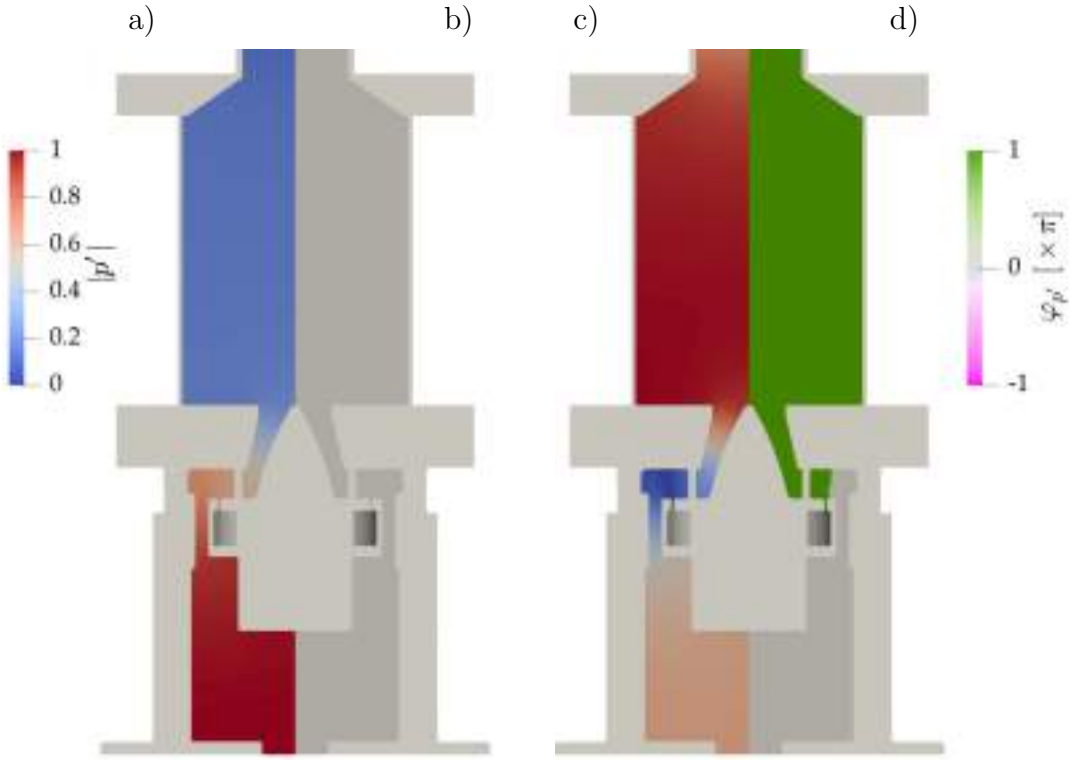

Figure 4.19: Acoustic modes computed with the Helmholtz solver. Both modelling approaches result in similar modes. (a) Amplitude and (b) phase of the first acoustic (plenum) mode at 257 Hz. (c) Amplitude and (d) phase of the second acoustic (chamber) mode at 480 Hz.

limit cycle frequency predicted by the HRT method is 224 Hz, close to the 1/4 wave mode frequency, suggesting that the flame with HRT boundary conditions couples with this first mode (see Fig. 4.9). The amplitude and phase of the second acoustic mode at 480 Hz are shown in Fig. 4.19(c) and Fig. 4.19(d), respectively. It corresponds to a 3/4 wave mode: a pressure antinode is found in the combustion chamber and the two volumes of the system (chamber and plenum) oscillate in phase opposition. Traces of this mode are also visible in the LES simulations (Fig. 4.9 and Fig. 4.13) matches this frequency. The flame does not couple with this mode during the limit cycle predicted by the HRT approach. Note also that the frequencies of the predicted acoustic modes match the two small peaks observable in the experimental pressure signal (Fig. 4.2). This analysis confirms that heat transfer does not change the system acoustics significantly.

The flame response was also investigated using Dynamic Mode Decomposition [185] (DMD) to reconstruct the oscillating modes of the system and extract the response of pressure, velocity components, heat release rate and equivalence ratio at the limit cycle frequency of 224 Hz [186]. The DMD input is 400 instantaneous 3D LES fields. Once the DMD mode has been computed at the frequency of interest, it is possible to investigate the coherent spatial

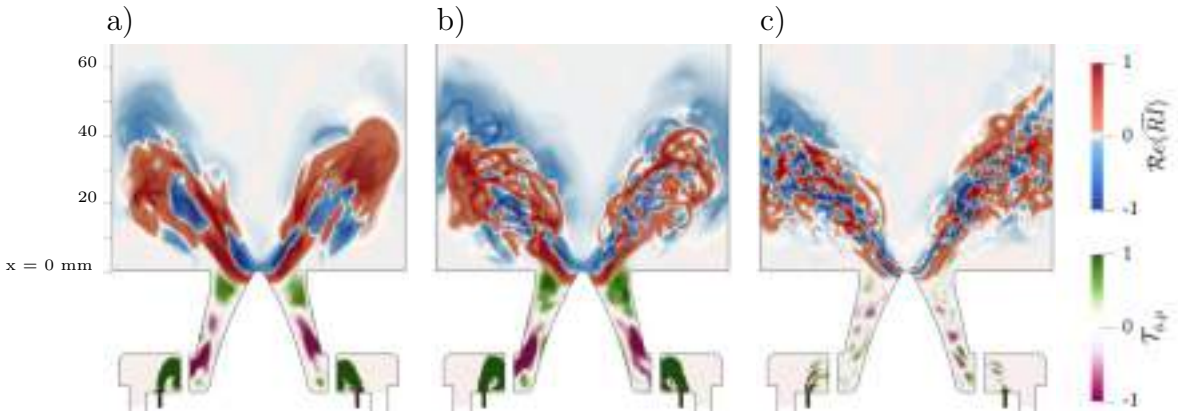

Figure 4.20: Cut-plane showing the Dynamic Mode Decomposition (DMD) at 224 Hz. Normalized real part of the Rayleigh index formulation in frequency domain $\mathcal{R}e(\widehat{RI})$ and normalized equivalence ratio - pressure fluctuations correlation index $\mathcal{T}_{\phi,p}$ for (a) the unstable flame predicted by LES with HRT approach, (b) the transient stabilization phase when switching to CHT and (c) the stable flame predicted by CHT.

features of each variable by comparing its phase with respect to a reference variable, in the present study pressure. If one selects the heat release rate as the variable of interest and computes the phase difference with respect to the pressure DMD mode, a three-dimensional Rayleigh index field is retrieved as $\mathcal{R}e(\widehat{RI}) = \mathcal{T}_{q,p} = |\hat{p}||\hat{q}|\cos(\varphi_q - \varphi_p)$ [187, 188]. An equivalence ratio - pressure fluctuations correlation index can be defined as $\mathcal{T}_{\phi,p} = |\hat{p}||\hat{\phi}|\cos(\varphi_\phi - \varphi_p)$ indicating whether fluctuations of equivalence ratio ϕ are contributing positively or negatively to pressure oscillations and hence to thermoacoustic instability.

The normalized real part of the Rayleigh index $\mathcal{R}e(\widehat{RI})$ and the normalized equivalence ratio - pressure fluctuations correlation index $\mathcal{T}_{\phi,p}$ for the unstable flame predicted by LES with the HRT approach are presented in Fig. 4.20(a). As expected, the Rayleigh index $\mathcal{R}e(\widehat{RI})$ presents large zones (colored in red) in which the flame oscillates in phase and drive pressure fluctuations. This mainly happens at the flame root near the centerbody and at the flame branches (10 mm $<$ x $<$ 40 mm). On the contrary, downstream of the centerbody, negative values (colored in blue) of Rayleigh index $\mathcal{R}e(\widehat{RI})$ are visible: when the flame detaches from the centerbody (Fig. 4.10(d)) it damps pressure oscillations. The flame tips (for x $>$ 40 mm) also show slight negative values of $\mathcal{R}e(\widehat{RI})$. The instability is supported by equivalence ratio fluctuations as underlined by the equivalence ratio - pressure fluctuations correlation index $\mathcal{T}_{\phi,p}$: regions just upstream of the flame root (near the centerbody) show a positive (colored in green) correlation index $\mathcal{T}_{\phi,p}$, indicating that the equivalence ratio fluctuations are in phase with the acoustic oscillations. These equivalence ratio oscillations are supported by the

flapping of the jet: since the first acoustic mode is a 1/4 wave mode (Fig. 4.19) where chamber and plenum oscillate in phase, it is straightforward to visualize the rich gas pocket periodically released in the combustion chamber corresponding to the green regions upstream the flame root at x = 0 mm. At the beginning, the correlation index $\mathcal{T}_{\phi,p}$ is green at the fuel tube exits: when pressure is increasing, the equivalence ratio is increasing in this region too (i.e. CH_4 is accumulated). Moving further downstream, when fuel pockets are convected to the middle of the centerbody, half a thermoacoustic cycle has passed and pressure is decreasing: therefore, these regions are flagged in purple (i.e. negative contributions) since when the pockets reach this zone locally increasing the equivalence ratio, pressure is decreasing. Finally, after one thermoacoustic cycle, the fuel pockets reach the flame-root and their contribution is again positive. This analysis confirms that rich gas pockets being periodically pushed into the chamber are feeding the thermoacoustic oscillation.

A different situation results from the DMD analysis when switching from the HRT to the CHT approach (i.e. for t < 0.8 s in Fig. 4.13(a)). The normalized real part of the Rayleigh index $\mathcal{R}e(\widehat{RI})$ and the normalized equivalence ratio - pressure fluctuations correlation index $\mathcal{T}_{\phi,p}$ computed during this transient phase are showed in Fig. 4.20(b). The flapping of the fuel jet is still present and the rich gas pocket periodically released in the combustion chamber can be identified by the green spots of $\mathcal{T}_{\phi,p}$. The $\mathcal{R}e(\widehat{RI})$ at the flame root resembles the one of the HRT unstable flame (Fig. 4.20(a)): the heat release rate fluctuations in this region are in phase with the pressure oscillations still present in this transition phase. Contrarily, the flame branches (10 mm < x < 40 mm) show lower positive values of $\mathcal{R}e(\widehat{RI})$ and a less coherent spatial distribution with respect to the unstable HRT flame (Fig. 4.20(a)). The flame tips (x > 40 mm) present marked zones of negative $\mathcal{R}e(\widehat{RI})$, indicating that these regions are contributing negatively to the thermoacoustic oscillations.

Finally, the normalized real part of the Rayleigh index $\mathcal{R}e(\widehat{RI})$ and the normalized equivalence ratio - pressure fluctuations correlation index $\mathcal{T}_{\phi,p}$ for the CHT stable flame are presented in Fig. 4.20(c). As expected in a thermoacoustically stable condition, the Rayleigh index $\mathcal{R}e(\widehat{RI})$ and the correlation index $\mathcal{T}_{\phi,p}$ fields do not show any coherent spatial distribution at the selected frequency.

The three Rayleigh index $\mathcal{R}e(\widehat{RI})$ maps shown in Fig. 4.20 can also be integrated over the combustor cross section S_c to obtain the one-dimensional mean

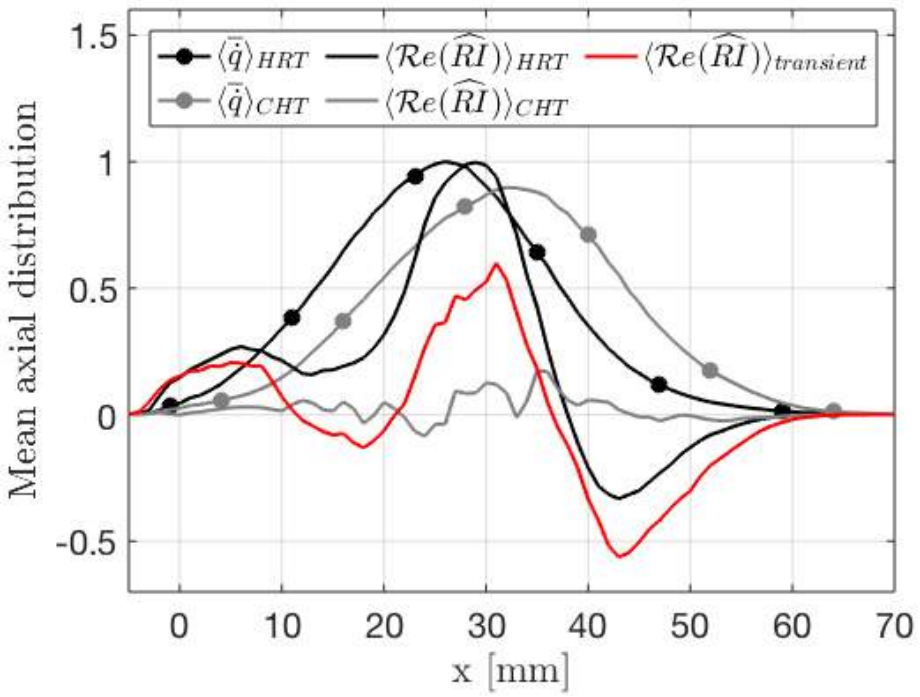

Figure 4.21: Mean axial distributions of normalized mean heat release rate $\langle\bar{\dot{q}}\rangle$ and DMD Rayleigh index $\langle\mathcal{R}e(\widehat{RI})\rangle$ for HRT (black) and CHT (gray) approaches. The Rayleigh index $\langle\mathcal{R}e(\widehat{RI})\rangle$ during the transient stabilization process (red) when switching to CHT is also showed.

axial distributions:

$$\langle\mathcal{R}e(\widehat{RI})\rangle(x) = \frac{1}{S_c}\iint_{S_c}\mathcal{R}e(\widehat{RI})(x,y,z)dydz. \tag{4.3}$$

A similar treatment is performed for the two mean heat release rate ($\langle\bar{\dot{q}}\rangle$) fields predicted with HRT (Fig. 4.8) and CHT (Fig. 4.15(a)).

The axial evolution of these quantities normalized with respect to their respective maximum value are plotted in Fig. 4.21. As already discussed, the flame with HRT is more compact with the peak of mean heat release rate at x = 27 mm (black line with circular mark). A more elongated distribution is instead observed with CHT (gray line with circular mark) where $\langle\bar{\dot{q}}\rangle$ peaks further downstream at x = 35 mm. The axial distributions of $\langle\mathcal{R}e(\widehat{RI})\rangle$ are consistent with Fig. 4.20. In the HRT case (black line) a significant positive contribution is present at the flame root (x < 10 mm) while the largest positive contribution is related to the central part of the flame branches (20 mm < x < 35 mm) just downstream of the maximum peak of $\langle\bar{\dot{q}}\rangle$. The flame tips (x > 40 mm) show instead a significant negative contribution that is not sufficient to stabilize the flame. The axial distribution of the Rayleigh index $\langle\mathcal{R}e(\widehat{RI})\rangle$ for CHT is almost zero as expected

for a thermoacoustically stable case (gray line). It is also interesting to plot the Rayleigh index $\langle \mathcal{R}e(\widehat{RI}) \rangle$ axial distribution during the transient stabilization process when switching to CHT (red line). While the $\langle \mathcal{R}e(\widehat{RI}) \rangle$ field at the flame root (x < 10 mm) is similar to the one of the HRT unstable flame (black curve), flame branches show a lower positive contribution (10 mm < x < 40 mm) and flame tips (x > 40 mm) show larger negative values: when switching to CHT simulations, the stabilization process starts at the flame branches and tips that are in contact with the combustion chamber walls. The instability-driving regions at the central part of the flame branches become less pronounced and the flame tips negative contributions to the thermoaoustic oscillation are enhanced, hence promoting the flame stabilization. The main difference in the heat transfer at the chamber walls between HRT and CHT is the rapid distribution of heat from hot regions where the flame reaches the walls: the latter can be predicted only by CHT simulations in which heat conduction through the solid is correctly taken into account.

4.4 Conclusions

In this Chapter, the impact of wall heat transfer treatments on the numerical prediction of the thermoacoustic behavior of the PRECCINSTA test bench was studied. First, a simplified approach (HRT) to specify thermal boundary condition based on the prescription of the thermal resistances tuned from experimental measurements is proposed. This approach provides satisfactory global agreement with experimental data in terms of mean flame shape but nonphysical unsteady dynamics: the LES flame exhibits a thermoacoustic oscillation which is not observed experimentally. This oscillation can not be suppressed by changing the acoustic impedance of the air or fuel inlets. However, going to full Conjugate Heat Transfer (CHT) simulations, the flame becomes stable, confirming the strong impact of heat transfer on the predictions of the present configuration.

No relevant difference between HRT and CHT cases is observed when comparing the sound speed fields or the system acoustic modes obtained with a Helmholtz solver: the acoustic properties of the system are captured correctly with both approaches. Dynamic Mode Decomposition (DMD) reveals that the instabilities of the HRT LES are coupled to a flapping motion of the fuel jets: the flame responds to these perturbations in phase with the acoustic pressure sustaining the thermoacoustic modes. On the contrary, for CHT simulations, the dynamics of the flame branches is slightly but sufficiently altered to modify the flame response, leading to the stabilization of the system.

To conclude, the correct prediction of wall heat transfer appears important to capture the experimental thermoacoustic behaviour of the PRECCINSTA combustor. More generally, this confirms that high fidelity can be achieved for combustion LES solvers only when precise boundary conditions are used not only for the inflow and outflow acoustic impedances but also for the wall thermal boundary conditions.

Chapter 5

Hydrogen flames: chemistry and transport property

Contents

This Chapter focuses on the chemistry and the problem of modeling transport property when dealing with hydrogen enriched flames. To this scope, LES of a lean turbulent CH_4/Air premixed flame enriched with a pilot hydrogen injection are performed. An Analytically Reduced Chemistry (ARC) mechanism is used to achieve a detailed description of CH_4/Air-H_2 chemistry. First, a validation of this kinetic scheme against the detailed GRI-3.0 mechanism is presented considering both simplified and complex transport properties. When hydrogen is added to the mixture, large variations of the mixture Prandtl and of the N_2 Schmidt numbers are observed depending on the local species concentration, features that are missed by simplified models. LES is then applied to study the structure and stabilization mechanisms of a hydrogen swirled enriched flame by using different transport modeling strategies. First, a lean (ϕ=0.8) fully premixed CH_4/Air case is considered and results are found to validate the LES approach. In agreement with experiments, a classical V-shape flame is stabilized in the low-velocity zone near the flame holder and created by the central recirculation zone (CRZ). Then, hydrogen enrichment is achieved injecting 2% of the CH_4 thermal power. Both premixed and diffusion flames are present in this case, impacting flame stabilization and angle. Indeed, at the flame root the main premixed flame is found to be stabilized on a diffusive flame kernel created by the injected hydrogen reacting

with the oxygen in excess of the premixed stream. Moreover, the H_2 consumed with the remaining oxygen in burnt gases leads to the formation of a second flame branch inside the CRZ which is responsible of an increase of the flame angle. Given the high concentration of hydrogen, an impact of the molecular transport models is observed in this case on the flame lift-off height highlighting the importance of using complex transport properties in any LES involving hydrogen combustion. Note that these results have been published in *Proceedings of the Combustion Institute* [71].

5.1 Literature review

The combination of hydrogen with standard carbon-based fuels is nowadays considered as one of the most promising technical solution for clean combustion [189]. Indeed, lean flame stabilisation is enhanced by the hydrogen high flame speeds [190] and its wide flammability range [191]. Furthermore, hydrogen offers no emissions of HC, CO or CO_2 [192].

For these reasons, multiple numerical and experimental studies have been carried out to study the impact of hydrogen addition on methane/air flames. Experiments and Direct Numerical Simulations (DNS) on laminar flame speeds [193, 194, 195, 196], lean and anomalous blow-off [197, 198], stabilization mechanisms and instabilities [199] have been performed for laminar flames. DNS of flame vortex interactions has been performed by Bougrine *et al.*, showing that hydrogen admixture enhances the flame wrinkling and consumption speed [200]. More realistic swirled configurations have been also investigated. Schefer *et al.* [201] experimentally studied the impact of hydrogen on flame stability and blowout maps for a lean premixed swirl-stabilized flame showing that the addition of a moderate amount of hydrogen to the methane/air mixture increased the peak OH concentration with a significant change in the flame structure which is shorter and more robust. A non-premixed unconfined configuration was investigated by Cozzi and Coghe [202]. Fuel mixtures containing a variable volumetric fraction of CH_4 and H_2 are injected in a swirling air flow. Again with hydrogen addiction a shorter and narrowed blue flame located closer to the burner head was observed. The impact of H_2 on emissions was also extensively studied. As an example, a decrease of NO_x level, if compared with a corresponding diffusion flame under same operating conditions, was observed for a fuel-lean confined swirl-stabilized methane-air flame by Kim *et al.* [203]. Recently, the impact of hydrogen enrichment on the shape of a confined swirled flames was experimentally investigated by Guiberti *et al.* [142] and Shanbhogue *et al.* [204]. In both studies, the probability of stabilizing

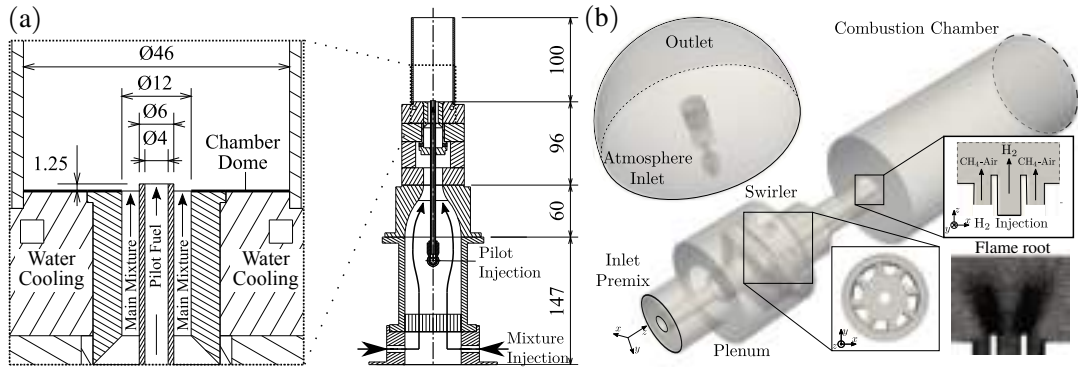

Figure 5.1: (a) Schematic of the MIRADAS experimental rig. (b) Numerical setup with details of the computational grid at the flame root.

a M-flame increases with the H_2 concentration in the combustible mixture. From a numerical point of view, the appeal of high-fidelity LES (e.g., see Ref. [205]) is increasing for these studies given their higher accurate prediction capabilities at a reasonable cost if compared to cheaper Unsteady Reynolds Averaged Simulations (URANS) and unaffordable DNS. Refs. [206, 207] reports some examples of studies on academic configurations and, very recently, the methodology was also extended to a full-scale gas turbine combustor [208]. In all these previous studies hydrogen is always considered fully premixed with the fuel mixture. Fewer are the investigations of direct H_2 injection in the combustion chamber. Indeed, in this case the pure H_2 flame will behave as a classical pilot flame typical of land-based gas turbines or aeroengines [189] opening new questions on the resulted flame structure and stabilization mechanisms.

The present Chapter aims to fill the observed gap of knowledge by performing experiments and high-fidelity LES of the impact of H_2 injection on flame structure and stabilization of a confined lean swirling flame. For this specific objective, simulations are performed coupling the LES solver AVBP with an Analytically Reduced Chemistry (ARC) scheme for CH_4/Air-H_2 chemistry. The impact of considering simplified or complex transport properties is also discussed. This is a topic well developed for classical single-fuel systems, but less investigated in case of bi-fuel configurations [209]. With respect to a classical lean CH_4/Air premixed swirled flame, simulations reveal that both premixed and diffusion flames are present when hydrogen is injected, impacting flame stabilization mechanisms and angle.

5.2 Experimental setup and Numerical model

The numerical simulations proposed in this work refer to the experimental activities performed in the MIRADAS combustor developed at IMFT laboratory, CNRS (Toulouse, France) [210]. Figure 5.1(a) reports a sketch of the combustor. A methane/air mixture is well premixed before entering the upstream longitudinal plenum. After being pushed through a radial swirler consisting of eight channels of section area radius of $r = 2.25$ mm oriented at 15° with respect to the swirl axis, the mixture enters the 100 mm long quartz flame tube through an annular gap of inner and outer diameters equal to 6 and 12 mm, respectively. Hydrogen is conveyed directly in the chamber through a 4 mm pilot line passing along the entire axis of the plenum. At the inlet of the combustion chamber, the two fuel lines are separated only by a thin annular lip of 1 mm (Fig. 5.1(a)). Two operating points are studied in this work. First, a perfectly premixed methane/air mixture with an equivalence ratio of $\phi = 0.8$ and thermal power of $P_{th} = 3.96$ kW is considered (case **REF**). Then, in case **PH2** flame is enriched through the pilot line injecting a mass flow of hydrogen corresponding to the 2% of the CH_4 thermal power of case **REF**. More details of the two operating conditions are summarized in Tab. 5.1. For **PH2**, the methane mass flow rate is slightly changed in order to keep constant the total thermal power. Note that this specific variation is so small that no significant change in the global equivalence ratio is achieved. For both cases, in the annular premix passage a well established turbulent flow reaches a Reynolds number of $Re_{pre,D_h} \simeq 7000$ using the equivalent hydraulic diameter $D_h = 6$ mm of the annular channel. The hydrogen flow is always laminar and $\mathrm{Re}_{\mathrm{H_2}} \simeq 25$.

Case	Main		Pilot	Global
	$\dot{m}_{Air}$ (g/s)	$\dot{m}_{\mathrm{CH_4}}$ (g/s)	$\dot{m}_{\mathrm{H_2}}$ (g/s)	ϕ
REF	1.693	7.912e-2	-	0.8
PH2	1.693	7.754e-2	6.597e-4	$\simeq 0.8$

Table 5.1: Different mass flow rates of air, methane and hydrogen and respective global equivalence ratios for the two operating conditions.

The domain used for the LES (Fig. 5.1(b)) has been discretized using an unstructured mesh which has been refined until a grid-independent solution is obtained. The final computational grid consists of approx. 23M tetrahedral elements. Note that to correctly capture the flame stabilization mechanisms, the grid is designed with a refinement of $\Delta x \simeq 80$ μm assuring approximately twelve points in the separation zone between the two fuel lines and in the finest region

positioned at the flame root (zoom box in Fig. 5.1(b)). Another refinement region with $\Delta x \simeq 300 - 350$ μm is located further downstream. Turbulent combustion is modeled using the classical dynamic TFLES model, which imposes a flame thickening everywhere a reactive zone is detected by a flame sensor [37]. Note that with this specific modeling formalism, once a target flame resolution is prescribed (i.e. 5 points in the flame front are specified for the present LES), the dynamic formulation of TFLES does not impose a constant level of thickening everywhere. Indeed, the model thickens the flame at the level that is required to reach the target resolution considering the local mesh size and laminar flame thickness (i.e. $\Delta_l \simeq 550$ μm in the present case). As a consequence, a thickening factor equals to unity is applied in the zones where the flame is already sufficiently resolved. This is typically what is happening in the proximity of the lip region of the present LES. Simulations are performed using AVBP with the classical numerical setup detailed in Chapter 2. Inlets and outlets are treated with the Navier-Stokes Characteristic Boundary Conditions [30] imposing the mass flow rates (Tab. 5.1), and ambient pressure, respectively. For both operating conditions, a measured temperature of $T_{bkpl} = 450$ K and $T_{lip} = 720$ K is fixed, respectively, at the chamber backplane and separator lip. Combustion chamber wall heat losses are taken into account imposing a temperature profile measured with a movable thermocouple from the external side of the flame tube and a thermal resistance of $R_{w,cc} = 9\text{e-}4$ m^{2}K/W computed assuming a conduction coefficient $\lambda = 2.17$ W/mK for the 2 mm thick quartz wall.

5.3 Chemistry and Transport properties

The CH_4/Air-H_2 chemistry is described by an ARC mechanism comprising 20 species, 166 reactions, and 9 quasi-steady state species derived from GRI-3.0 using ARCANE [211][1]. To validate the kinetic schemes, Cantera (`www.cantera.org`) calculations of a $1D$-counterflow diffusion flame of H_2 against equilibrium product from lean CH_4/Air combustion is presented in Fig. 5.2. The detailed GRI-3.0 scheme with multicomponent transport and Soret effect [212] is then compared to the reduced ARC mechanisms using both simplified and mixture average transport properties models. The latter model is the standard approach for complex transport. An alternative often present in LES codes is the simplified approach which consists in determining the viscosity from the Sutherland's law and deducing the mixture heat conductivity using a constant Prandtl number while each

[1] A complete description of the ARC mechanisms can be found in the Supplementary Material of Ref. [71]

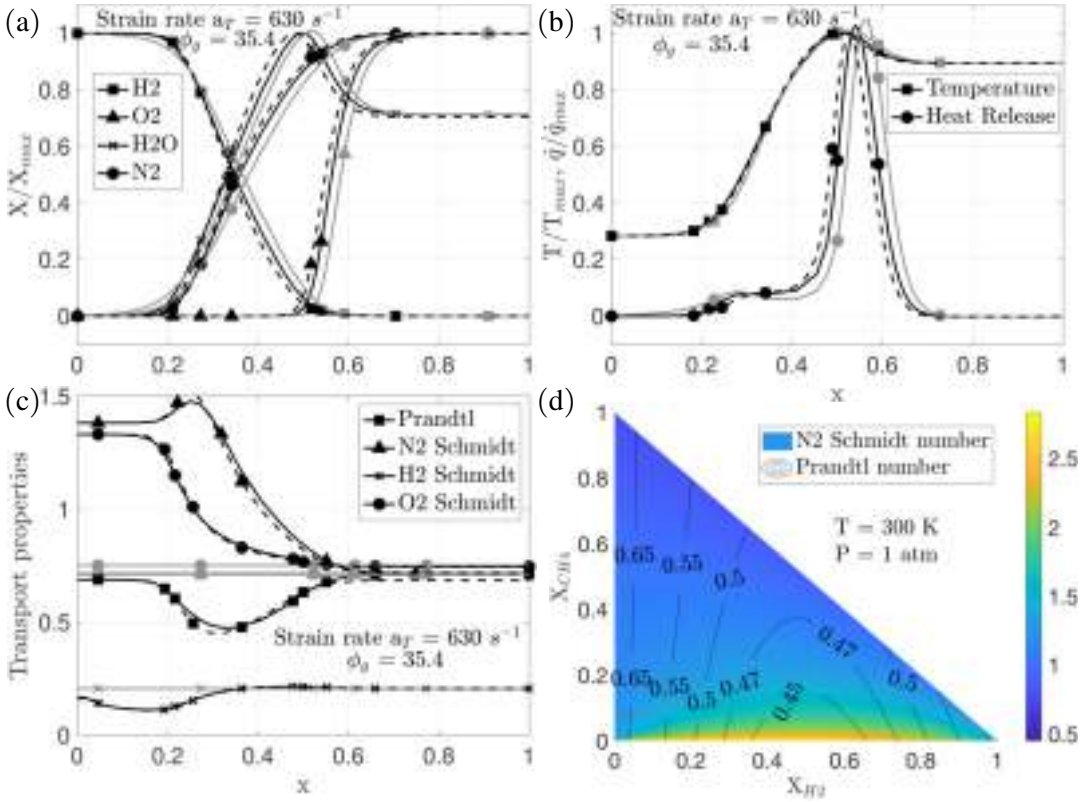

Figure 5.2: (a-b) Comparison between flame structures computed with Cantera using GRI-3.0 mechanism including multicomponent transport and Soret effect (dotted lines), the ARC scheme with a mixture transport model (dark line) and simplified transport model (light line), for a counterflow diffusion flame of H_2 against the equilibrium burnt gases from lean ($\phi = 0.8$) CH_4/Air premixed combustion. Normalized profiles of (a) mass fraction of selected species, (b) temperature and heat release rate. (c) Profiles of the transport properties. Computation inputs are: $p = 1$ bar, injection temperature of $T^i_{\mathbf{H_2}} = 570$ K and exhaust gas temperature $T^i_{\mathbf{g}} = 1800$ K. (d) Isolines of the Prandtl number and contour map of N_2 Schmidt number in ternary mixture of H_2, CH_4 and N_2 as a function of composition.

species diffusivity relies on a constant Schmidt number. Note that the diffusive flame addressed here is expected to be roughly representative of the H_2 combustion process of the final target configuration. The heat release profiles obtained with the three mechanisms present two reaction peaks, a primary peak in the rich side of the flame, very close to H_2 injection point and the second one, much larger, in the stoichiometric region of the flame. Normalized species, temperature and heat release profiles comparison show perfect agreement between GRI-3.0 scheme and the ARC scheme with complex transport while showing only satisfactory agreement with a simplified transport model, Fig. 5.2(a-b). Figure 5.2(c) shows the Prandtl (Pr) and Schmidt (Sc) numbers of selected species present in the

$1D$-counterflow diffusion flame confirming the variability present in this problem. Finally, the N_2 Sc and the mixture Prandtl number in a ternary mixture of N_2, H_2 and CH_4 are reported in Fig. 5.2(d). It is noted that the GRI-3.0 scheme and the ARC scheme with complex transport predict a Pr number dropping from 0.7 to 0.43 in the region just before the heat release peak, i.e., a region where H_2 and N_2 form a binary mixture of almost equal molar fraction. This leads to higher thermal conductivity and hence to a lower temperature peak in the flame if compared to constant transport property case. By looking at the isolines of the Prandtl number in Fig. 5.2(d), it can be noticed as Pr is a strong function of the H_2 molar fraction and assumes its minimum values when H_2 is present in a binary mixture with N_2[1] with almost equal molar fractions. Focusing on the Schmidt number, both the $1D$-counterflow diffusion flame of Fig. 5.2(c) and the ternary mixture of Fig. 5.2(d) show a variation of the N_2 Schmidt number from 2 when it diffuses in H_2 to only, 0.7 when it diffuses in other gases. Variations of the Schmidt numbers of other species, even if present, do not influence combustion since they are rapidly consumed (e.g. O_2, CH_4). Reduced diffusion of N_2 in H_2 due to the increase of Sc, will decrease the local H_2 molar fraction and the resulted flame will be shifted toward the H_2 side. Vice-versa, when simplified transport is used, N_2 will diffuse more in the H_2 side leading to a flame more shifted towards the oxidant side as shown in Fig. 5.2(b). Relaying on these results, variable Pr and N_2 Sc number functions of the molar fraction X_{CH_4}, X_{N_2} and X_{H_2} are implemented in AVBP and used for the following simulations. These allow to match the complex transport model perfectly for such flames. Complete expression of these functions are reported in Appendix B.

5.4 Results and discussion

Before discussing the reactive simulations, LES time averaged contours of axial U_x, radial U_r and tangential U_θ velocities in cold flow are shown in Fig. 5.3(a-c), respectively. The imposed swirl motion is not sufficient to achieve a complete vortex-breakdown: at the exit of the annular channel, a large radial component pushes the jet towards the chamber axis (Fig. 5.3(b)). As a consequence, the system features a central recirculation zone (CRZ) that is not completely developed as highlighted by the U_x=0 isoline (thick black line) in Fig. 5.3 (a). A good match

[1]It should be also noticed that similar results would have been achieved with a mixture of H_2 with other heavy components such as O_2. However, in the present configuration, oxygen is immediately burned so its concentration is extremely low in the zones where hydrogen is present. For this reason, N_2 is considered in Fig. 5.2(d).

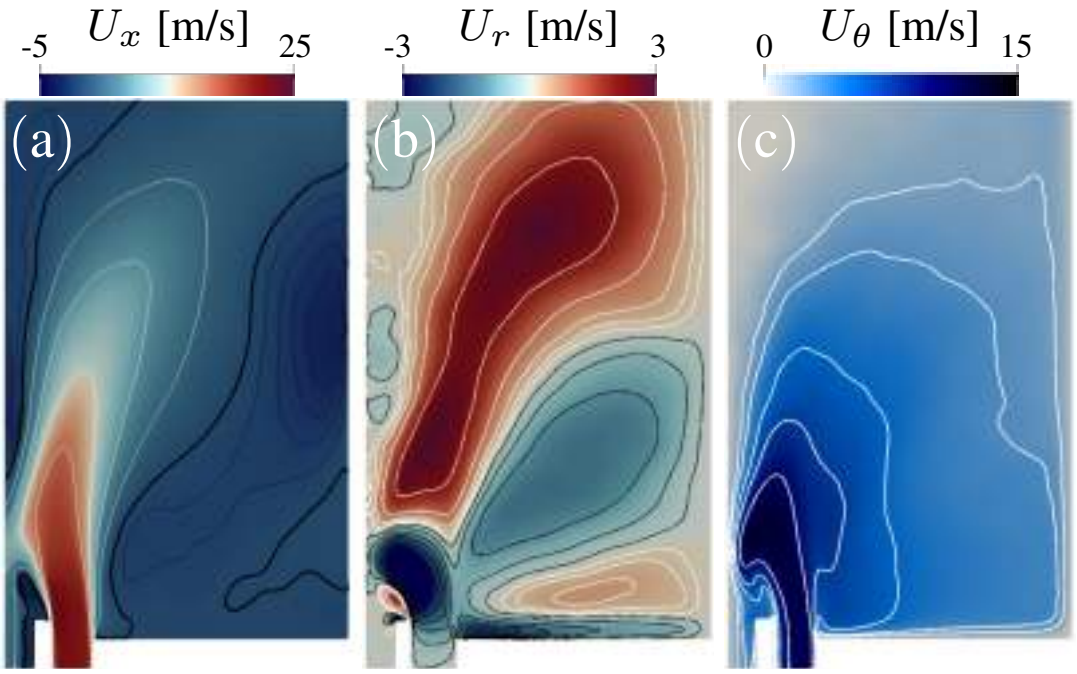

Figure 5.3: Time and angle average contours of axial U_x (a), radial U_r (b) and tangential U_θ (c) velocity components. Black lines indicate negative values, while positive velocities are in white. The thick black isoline in the axial velocity map is $U_x = 0$.

with experimental results is obtained for global quantities such as the swirl number computed at the entrance of the combustion chamber ($S_{LES} = 0.35$ against a geometrical value of $S_{th} = 0.3$) and injector head loss ($\Delta_{p,LES}$= 480 Pa against measured $\Delta_{p,exp}$= 550 Pa) confirming the accuracy of the proposed simulations.

5.4.1 REF case

First, the reactive case **REF**, i.e., with no injected hydrogen (Tab. 5.1), is discussed. Experimental flame shape obtained taking the line-of-sight (LOS) integration of the CH* chemiluminescence intensity signal (Fig. 5.4(a)) is compared with the LOS of the predicted heat release rate (Fig. 5.4(b)). Both maps are reported normalized with respect to their respective maximum value. The predicted global flame shape is in agreement with experiment. No flame is predicted in the corner recirculation zones (CRZ) proving the appropriateness of the assumed thermal boundary conditions. A good match is also found in terms of lift-off distance and flame angle, whereas LES slightly overestimates the flame total extension.The well-established V-shape of the flame is also clearly visible in Fig. 5.4(c) reporting time and angle average contours of heat release rate. Axial velocity contours are shown in Fig 5.4(d). Comparing with the corresponding

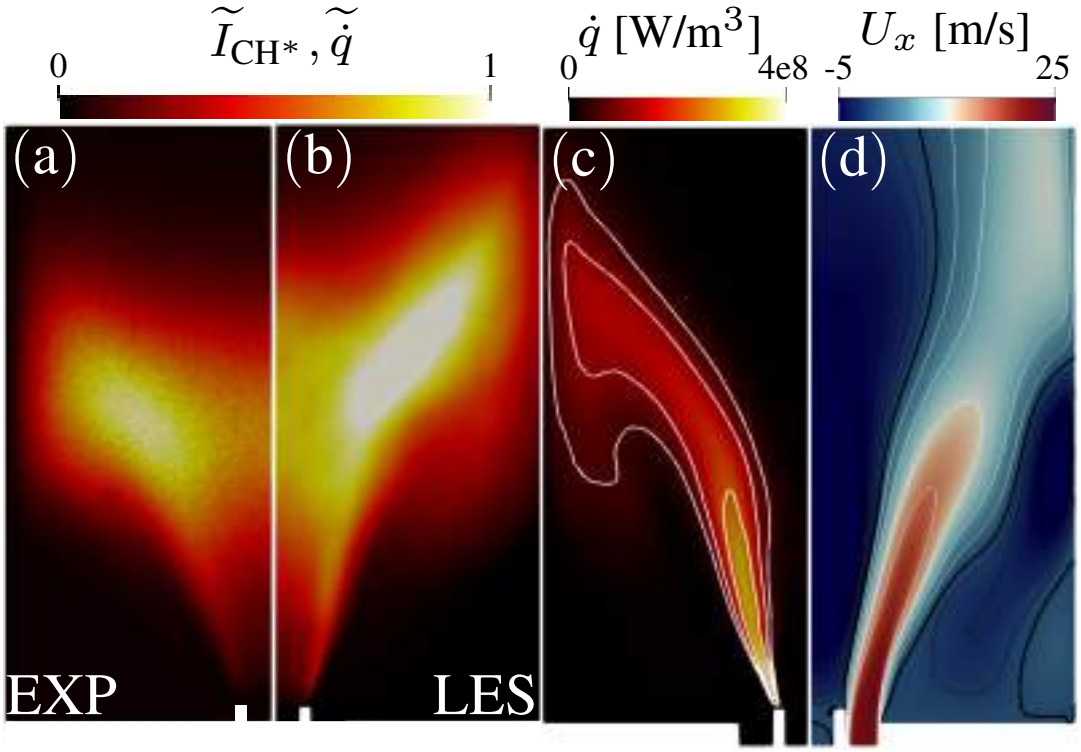

Figure 5.4: Comparison between the normalized line-of-sight (LOS) integration of measured CH* chemiluminescence intensity $\widetilde{I}_{CH^*}$ (a) and the normalized LOS integration of the heat release rate $\widetilde{\dot{q}}$ from LES (b). Time and angle average contours of heat release rate with $\dot{q} = 40, 100, 200$ MW/m^3 isolines (c). Time and angle average contours of axial velocity U_x (d). Black contours indicate negative values, while positive velocities are in white. Thick black line refers to $U_x = 0$.

map for the cold flow, Fig. 5.3(a), a proper vortex-breakdown with the formation of a complete and extended CRZ is achieved with combustion.

Zooming now at the flame root allows to discuss the flame stabilization mechanisms. An isoline at the 10% of the maximum of the mean heat release rate (red line) is plotted in Fig. 5.5 (a) over the axial velocity map. The swirled flame is stabilized inside the low velocity zone full of hot gases created by the CRZ on top of the separation lip. Plotting the same heat release rate level over the iso-contours of temperature in Fig. 5.5(b) underlines the fact that the flame stabilization happens along a temperature value of $\simeq$ 1300 K, which is close to the activation temperature of the reaction leading to the production of CH_3 from methane. Indeed, this specie is found to concentrate within the flame isoline, Fig. 5.5(c), proving that it is a good indicator of the position of the flame root.

Since no hydrogen is injected, very low X_{H_2} is obtained for this case (not shown), therefore the impact of the transport model is accordingly negligible.

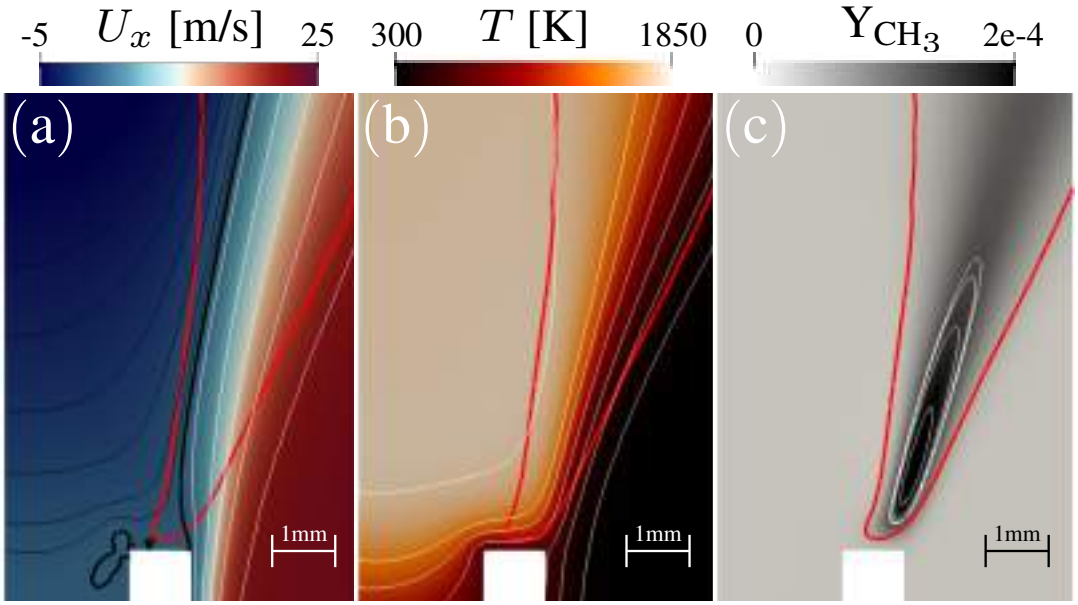

Figure 5.5: Zoom on the flame root. Isoline of heat release rate (red line) at $\dot{q}$ = 40 MW/m^3 (10% of heat release maximum value) plotted over the contours of axial velocity U_x m/s (a), temperature K (b), mass fraction of CH_3 (c). In the velocity map black curves indicate negative values, while positive velocities are in white. The thick black line is U_x = 0.

5.4.2 PH2 case

As soon as H_2 is injected from the pilot channel, the flame structure changes. Focusing on the measurements Fig. 5.6(a), comparing with the **REF** case, Fig. 5.4(a), a more intense zone is observed at the flame root and all along the outer side of the flame facing the CRZ. In agreement with the experiments, LES show high heat release rate in similar areas, Fig. 5.6(b). Nevertheless, some differences are observable. A mismatch of approx. 1 mm is indeed noted in the flame lift-off height. This may be due to the lip temperature which was measured in the experiments and imposed in the LES. Time and angle average contours of heat release rate reported in Fig. 5.6(c) give more insight on the flame structure. Again, if compared to case **REF**, higher mean values of heat release rate are obtained. The isoline of the 10% of the heat release rate maximum value (obtained for $\dot{q}$ = 200 MW/m^3) shows a flame shape similar to the **REF** case, Fig. 5.4(c). On the contrary, a flame branch in the CRZ is well detectable by the isoline at $\dot{q}$ = 40 MW/m^3, i.e, the same level used to indicate the flame in case **REF**. The central region is therefore hotter, with temperature that reaches 2000 K. A wider flame angle is then achieved, in line with experimental observations.

Looking at mass fractions of OH, HO_2 and CH_3 in the flame root region, high concentration of OH, Fig. 5.7(a), are found within the isoline at $\dot{q}$ = 40

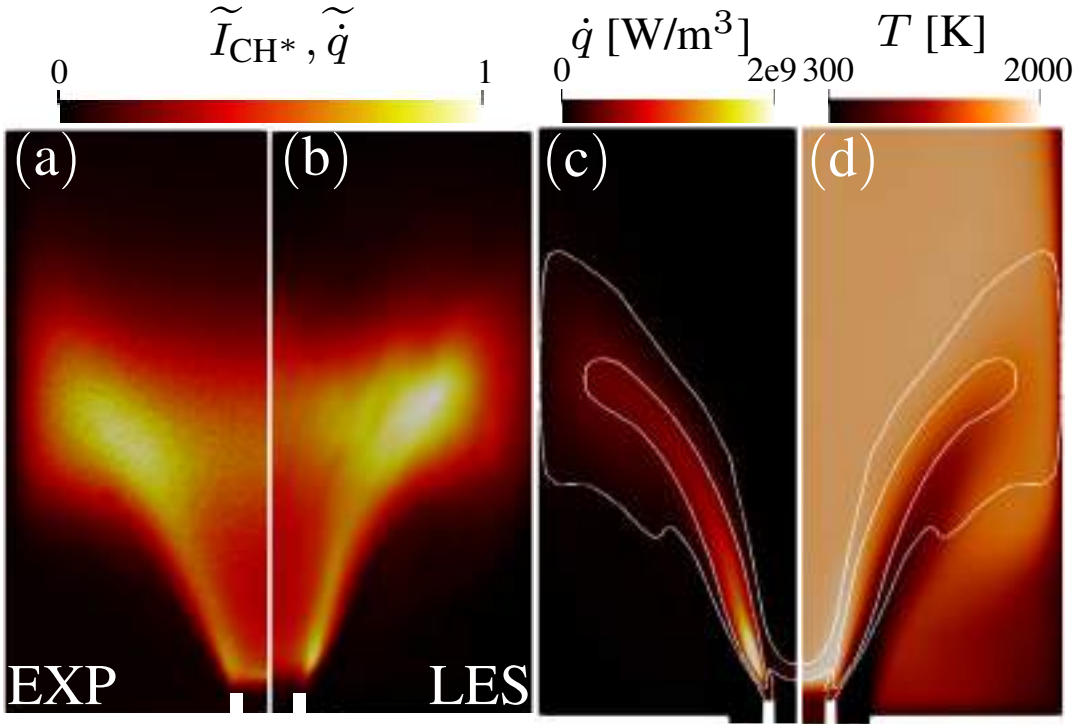

Figure 5.6: Comparison between the normalized line-of-sight integration of measured CH* chemiluminescence intensity $\widetilde{I}_{CH^*}$ (a) and the normalized LOS integration of the heat release rate $\widetilde{\dot{q}}$ from LES (b). Time and angle average contours of heat release rate (c) and temperature T (d) with isolines (white lines) of $\dot{q}$ = 40, 200 MW/m^3.

MW/m^3 suggesting that the injected H_2 is responsible for the heat release in this zone. Similarly, the presence of high concentration of HO_2 just above the splitter indicates that part of hydrogen is also immediately consumed in that region when a sufficient concentration of H_2 and O_2 is reached, Fig. 5.7(b). The high concentration of CH_3, Fig. 5.7(c), instead, indicates that the anchoring point of the CH_4 premixed flame is lifted off with respect to case **REF**. This specie is completely enclosed by the higher $\dot{q}$ = 200 MW/m^3 isoline confirming that, also for this case, CH_4 oxidation drives the mean heat release.

To better understand the interaction between hydrogen and the premix mixture, two Takeno flame indices (FI) [213] have been computed. To do so, variables are conditioned by the consumption rates of H_2 and CH_4, respectively, and then weighted by the magnitude of these variables to underline the regions in which heat release is more relevant:

$$FI_{\mathrm{Fuel}} = \dot{\omega}_{\mathrm{Fuel}} \frac{\nabla_{\mathrm{O_2}} \cdot \nabla_{Fuel}}{\nabla_{\mathrm{O_2}} \cdot \nabla_{\mathrm{Fuel}}} \bigg|_{\dot{\omega}_{\mathrm{Fuel}}<0} \tag{5.1}$$

Results in the flame root region are reported in Fig. 5.8. While the Takeno index of CH_4 is all positive, indicating that, as expected, it burns in premixed

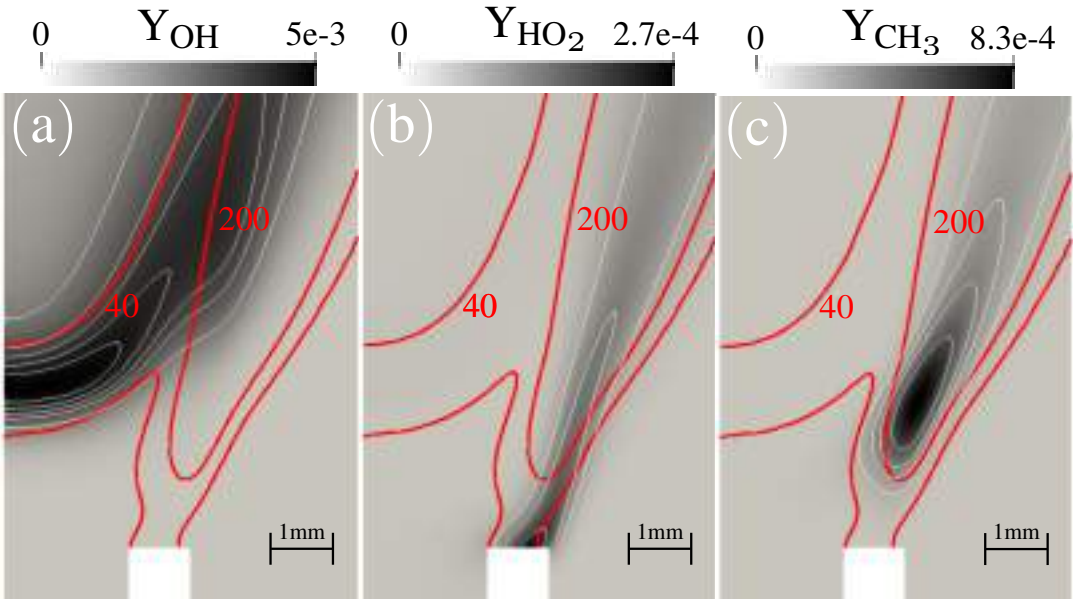

Figure 5.7: Time average mass fractions of OH, HO_2 and CH_3 at the flame root with isolines of heat release rate (red lines) at $\dot{q}$ = 40 and 200 MW/m^3.

mode, Fig. 5.8(a), the FI of H_2 detects that hydrogen is consumed in both premixed and diffusive regimes, Fig. 5.8(b). A large diffusive zone generated by the reaction of H_2 with residual O_2 in the burned gases is found in the CRZ, confirming the hydrogen nature of this second branch of the flame. At the flame root, a premixed region is predicted detached from the splitter and is believed to be generated by H_2 diffusion from the high concentration zone to the CH_4/Air stream. More interestingly, a second diffusive zone is predicted starting form the splitter wall until the premixed zone. This flame is obviously responsible of the HO_2 concentration previously discussed, Fig. 5.7(b), and has a direct role in the stabilization mechanisms of the flame. Indeed, plotting the two heat release isolines over the axial velocity field Fig. 5.8(c), it is possible to notice that differently from case **REF**, the hydrogen diffusive flame stabilizes in the low velocity region. This diffusive kernel appears to support the premixed CH_4 flame that is anchored more downstream in a higher positive velocity region. Observing now the temperature profile, black lines in Fig. 5.8(a-b), it is noted that hydrogen oxidation happens in a low temperature zone. The extension of the lower flammability limit temperature is a well-known property of H_2 that is characterized by reactions at very low activation energy (such as the one correlated to the HO_2 production) [214]. On the contrary, stabilization of the CH_4/Air flames happens at the same temperature value of the **REF** case. (T$\simeq$ 1300 K). This shows that the spatial position of the high heat release zone depends on the axial location

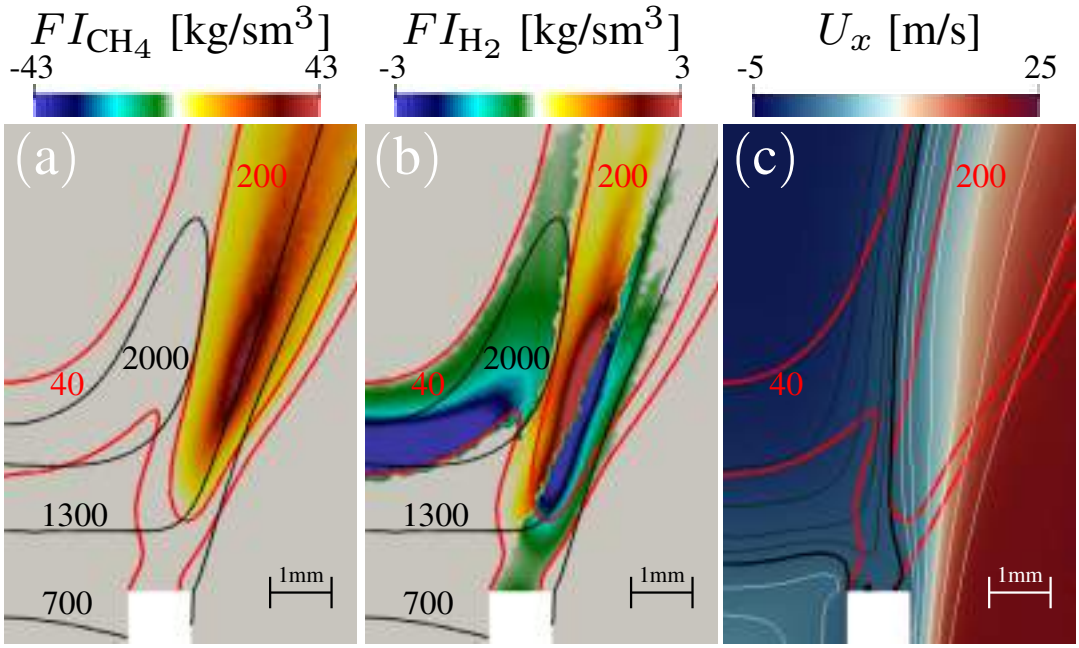

Figure 5.8: Zoom on the flame root. Computed dimensional Takeno index of CH_4 (a), dimensional Takeno index of H_2 (b) with isolines of temperature (black lines) at T= 700,1300 and 2000 K and heat release rate (red lines) at $\dot{q} = 40$ and 200 MW/m^3. (c) Contours of axial velocity U_x with isolines of heat release rate (red). Isolevels of negative velocity values are reported in black, while positive velocities are in white. The thick black line is $U_x = 0$.

of these isolines which is highly impacted by the Prandtl number of the mixture and the N_2 Schmidt number as discussed in section 5.3.

Indeed, focusing then on the transport properties, Fig. 5.9(a-b) shows, respectively, the Pr and the N_2 Sc contours variation in the region in which the H_2 (white lines) molar fraction is relevant. To highlight this result in Fig. 5.9(c), an instantaneous snapshot of H_2 mass concentration of the current simulation (right) is compared with an equivalent instant with simplified transport properties (left). In both images, isolines of the temperature field are also reported (black lines). With complex transport properties, Fig 5.9(c-right), it is noted that the concentration of H_2 moves upstream since N_2 diffuses less from the upper region (i.e. higher Schmidt number). Different diffusion of H_2, together with the higher thermal conductivity, i.e., lower Prandtl number, has a strong impact on the temperature field, making the hotter region following the movement of H_2 concentration downward. Simplified transport properties, Fig. 5.9(c-left), fails to correctly reproduce this mechanism, resulting in a less diffuse temperature field. As a consequence, the low-intense hydrogen reaction zone is more stretched and the CH_4 oxidation is pushed downstream resulting in a lifted flame.

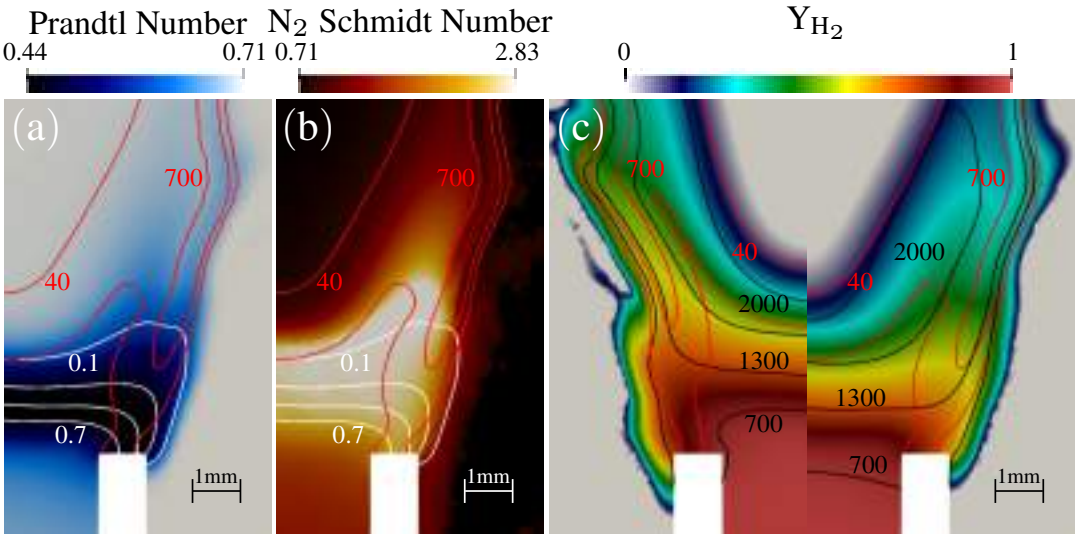

Figure 5.9: Zoom on the flame root. Instantaneous snapshot of Prandtl number (a) and N_2 Schmidt number (b) with isolines of heat release rate values (red lines) at $\dot{q}$ = 40 and 700 W/m^3 and H_2 molar fraction (white lines) at X_{H_2} = 0.1, 0.3, 0.5 and 0.7. (c) Comparison between simplified (left) and complex (right) transport properties computations on an instantaneous snapshot. Mass fraction of H_2 (log scale) is shown together with isolines of heat release rate (red lines) at $\dot{q}$ = 40 and 700 MW/m^3 and temperature (black lines) at T = 700, 1300 and 2000 K.

5.5 Conclusions

In this Chapter, the impact of non-premixed hydrogen addition on the flame shape and stabilization mechanisms of a swirled methane/air flame is proposed by a numerical analysis. In agreement with experiments, H_2 injection is found to have a marginal impact on the general flame shape, leading only to a more intense zone at the flame root and all along the outer side of the flame facing the CRZ. On the contrary, both premixed and diffusion flames were discovered by the LES when hydrogen is injected impacting the flame stabilization and its angle. Indeed, at the flame root the main premixed flame is found to be stabilized on a diffusive flame kernel created by the injected hydrogen reacting with the oxygen in excess of the lean premixed stream. Given the high concentration of H_2 in these regions, LES predictions are found to be influenced by the adopted transport models highlighting the importance of using complex transport properties in any LES involving hydrogen combustion.

Part II

Hydrogen enrichment: a partially premixed lean swirled flame

Chapter 6

Impact on flame structure and combustion dynamics

Contents

In this Chapter, Large Eddy Simulation (LES) are performed associated to Conjugate Heat Transfer (CHT) to analyze the impact of H_2-enrichment on the flame structure and combustion dynamics of a lean partially-premixed turbulent CH_4 swirling flame. Experimentally, the gas turbine model combustor is operated at atmospheric pressure with H_2 vol. fraction up to 50%. Numerically, to achieve a detailed description of the CH_4-H_2 / Air chemistry an Analytically Reduced Chemistry (ARC) mechanism is derived and validated for different H_2 enrichment levels. LES results are then compared and validated with experimental time-resolved stereo PIV, OH* chemiluminescence, OH-PLIF imaging and acoustic pressure measurements. When the pure CH_4 case is considered, and up to 20% of H_2 enrichment, no thermoacoustic oscillation is observed both experimentally and numerically. However the flame length reduces due to the corresponding increase in laminar flame speed and the heat release rate distribution becomes more compact when hydrogen is injected. At 50% of H_2, bi-modal thermoacoustic oscillations are observed experimentally and these are correctly predicted via LES. The flame responds to both the 1/4 wave mode of the plenum at low frequency and more significantly to a higher frequency mode of the combustion chamber. The differences between the pure CH_4 as well as low H_2-enriched stable cases and the 50% H_2-enriched unstable flame are analyzed to get more insights in to the instability driving mechanism. The coupling of LES with a heat transfer solver

in a Conjugate Heat Transfer (CHT) context reveals that H_2-enrichment leads to higher localized temperature at the centerbody tip, indicating the potential impact on the life-cycle of real combustors. Finally, Dynamic Mode Decomposition analysis performed on experimental OH-PLIF images and LES 3D fields allows to investigate the feeding mechanism of the thermoacoustic oscillations. Both the two modes oscillations are supported by variations in equivalence ratio linked to rich gas pockets periodically released into the chamber. In addition, the higher frequency chamber mode is also fed by vortices periodically detaching from the backplane and the centerbody walls causing a strong wrinkling of the flame front. Note that part of these results have been published in *Combustion and Flame* [25].

6.1 Introduction

Hydrogen is rapidly becoming one of the most relevant topic of discussion in the combustion community [215, 216, 217]. Due to their low carbon emissions [189, 218, 219], aeronautical and power generation industries are considering hydrogen and hydrogen-rich gases (e.g. syngas) as a solution to reduce their impact on the environment and to comply with the stringent European Union regulations on pollutants emissions. Another appealing strategy for achieving a rapid decarbonization is to implement H_2 in existing or modified gas turbines [210]. However, the different chemical properties of H_2 with respect to classical hydrocarbon fuels must be taken into account when considering this type of applications. The high reactivity of hydrogen and its wide flammability range [191] together with the high flame speed [190] can indeed contribute to enhancing the flame stabilization at lower equivalence ratio but at the same time increasing the risk of flashback [220, 221]. Moreover, the higher adiabatic flame temperature implies that the combustor walls are subjected to a larger localized thermal load and the acoustic modes of the combustion chamber can change due to the different sound speed field. The latter, together with the different flame stabilization, may change also the thermoacoustic behavior of a combustor [67, 68, 69]. Thermoacoustic instabilities are indeed one of the main design challenges when dealing with the development of lean combustors and low emission combustion technologies [11, 222]. In this context, research is needed to analyze the impact of hydrogen enrichment on the flame stabilization as well as its dynamics.

For laminar flames, multiple numerical and experimental studies have been carried out to analyze the impact of H_2-enrichment on CH4/air flames. Analyses

of laminar flames speeds [193, 194, 196], lean blow-off and extinction [197, 198], stabilization mechanisms and instabilities [199] have been performed.

Emissions variations due to H_2-enrichment have also been extensively studied. Ghoniem *et al.* [223] analyzed lean premixed combustion flames stabilized behind a backward-facing step and observed that hydrogen addition was capable to improve the flame stability while NO_x concentration was higher in the products as the overall burning temperature raised. However, hydrogen addition is able to extend the flammability limit, hence globally achieving lower NO_x. The same effect was observed by Kim *et al.* [203] for a lean confined swirl-stabilized methane-air flame: a decrease of NO_x level was present if compared to a corresponding diffusion flame under the same operating conditions.

The impact of hydrogen on flame shape and heat release rate distribution in more complex swirled-stabilized flames has been investigated [224, 225, 226, 227]. Schefer *et al.* [201] experimentally studied the H_2 impact on flame stability and blowout for a lean premixed swirl-stabilized flame showing that hydrogen addition to the methane/air mixture increased the peak OH concentration and led to a significant change in the flame structure that became shorter and more robust. A similar hydrogen addition effect was observed by Cozzi *et al.* [202] in a non-premixed unconfined configuration featuring a swirling flow: a shorter flame stabilized closer to the burner was obtained when hydrogen was enriching the flame. Flame stabilization has been analyzed recently by Guiberti *et al.* [142] and Shanbhogue *et al.* [204], showing that the probability of stabilizing the confined swirled M-flame is increasing with the H_2 concentration in the fuel mixture.

Many experimental studies have focused on the effect of hydrogen addition on flame dynamics and thermoacoustics instabilities. Schimek *et al.* [228] and Emadi *et al.* [229] showed that hydrogen can change the flame shape and subsequently alter the phase and amplitude of heat release oscillations in acoustically forced flames and therefore the corresponding Flame Transfer Function (FTF). Davis *et al.* [222] observed that hydrogen addition can modify also self-sustained oscillations by promoting the interaction between local heat release and vortices in the flow field due to the reduced flame size compared to the pure methane case allowing the vortices to travel downstream toward the flame front. Different studies have also analyzed that variation in hydrogen content can cause a shift in acoustic modes of combustors [230, 231, 232, 233] and believed to be linked, for partially premixed flames, to changes in laminar flame speed, sound speed field and convective time [222, 231, 234]. Despite the large number of studies devoted to the H_2-effect on self-sustained thermoacoustic oscillations, limited conclusive

explanations of the contradictory phenomena can be found in the literature. Allison *et al.* [231] for example observed that hydrogen addition resulted in a lower oscillation amplitude in a gas turbine combustor, while Zhang *et al.* [226] showed that, at various pressure conditions, hydrogen can trigger thermoacoustic instabilities at different operating conditions in line with the observations made by Shanbhogue *et al.* [204]. Recently, Zhang and Ratner [235] examined the effect of hydrogen addition on a lean premixed low swirl flame in a variable-length combustor. They confirmed that H_2-enrichment can trigger instabilities and shift the primary acoustic oscillation from low to relatively high-frequency when high hydrogen content is injected. More recently, a technically premixed natural gas turbine model combustor was operated at elevated pressure (up to 5 bar) with different hydrogen enrichment levels by Chterev and Boxx [67], presenting the impact on the flame shape, precessing vortex core (PVC) and thermoacoustic frequency and amplitude. H_2 enrichment increased in that case the phase delay between the pressure and heat release by decreasing the flame length while simultaneously increasing the sound speed in the combustor. Lately, Kang and Kim [236] demonstrated that lean-premixed and ultra-compact pure hydrogen flames can trigger high-frequency instabilities while the system was observed to remain completely stable in the low frequency range.

Fewer numerical works investigated the effect of H_2 enrichment on combustion dynamics. Nam and Yo [237] for example showed that adding hydrogen could inhibit a thermoacoustic instability. In fact, more efforts have been devoted numerically to the understanding of flame properties. Direct Numerical Simulations (DNS) have been performed to investigate the process of spontaneous ignition of hydrogen flames at laminar, turbulent, adiabatic and non-adiabatic conditions [238]. Examples of studies on academic configurations can be found in Refs. [206, 207]. Only very recently, has the methodology been extended to a full-scale gas turbine combustor [71, 208] thanks to the use of Large Eddy Simulation (LES) whose appeal for combustion applications [19, 23, 24, 77] has been recently increasing given its higher accurate prediction capabilities at a reasonable cost if compared to cheaper but less accurate Unsteady Reynolds Averaged Simulations (URANS) and the unaffordable DNS. Laera *et al.* [71] analyzed the case of a direct H_2 injection in the combustion chamber through a pilot lance typical of land-based gas turbines or aeroengines [189], opening new questions on the resulted flame structure, stabilization mechanisms and highlighting the importance of transport property modeling when dealing with hydrogen, a well-known issue for classical single-fuel systems [209].

The accuracy of such numerical predictions whenever applied to real configurations has been shown to be influenced by the exact reproduction of the thermal boundary conditions. It indeed controls the heat transfer between the flow and the combustor walls which affects the flame stabilization and dynamics [59, 66]. Despite these well-known effects, most numerical simulations either neglect heat-transfer effects imposing adiabaticity [76] or an arbitrary wall temperature field is imposed [115, 161]. This is due to the fact that experimental temperature data is usually not available and that many numerical studies reported satisfactory agreement with experiments even without considering heat-transfer in different configurations like bluff-body stabilized flames [162, 163], lean-premixed swirl flames [76, 161], annular combustion chamber [164] or even rocket combustors [165]. Nevertheless, recent studies have demonstrated that Conjugate Heat Transfer (CHT) simulations can improve the prediction of flame stabilization and thermoacustic instabilities [59, 66, 112, 166]. When hydrogen combustion is involved, the impact of the imposed thermal boundary conditions is expected to be even stronger, since H_2-enriched flames are shorter and tend to stabilize closer to the chamber walls due to the increased laminar flame speed which inevitably increase the thermal load on the combustor components.

Among the different test benches operated for investigation of thermoacoustic oscillations, the PRECCINSTA test rig (Chapters 3 and 4) has been recently operated with different H_2-enrichment levels to analyze its effect on the flame dynamics and the flame stabilization process. Datta *et al.* [239] showed that H_2 addition allows the flame to stabilize in the region near the centerbody when for the pure CH_4 case, the flame is lifted experiencing a PVC. Kushwaha *et al.* [240] proposed a schematic study to classify the different dynamical states present in the combustor: chaotic oscillations, intermittency and limit cycles have been observed for different levels of hydrogen enrichment and thermal powers.

In this context, despite the large potential of LES in the understanding of the H_2-enrichment impact on combustion dynamics, the limited number of recent numerical works devoted to this topic does not allow for obtaining concluding explanations of the hydrogen effect. This work aims therefore at filling this gap of knowledge by performing LES to analyze the impact of H_2-enrichment on the onset of self-sustained thermoacoustic oscillations in the lean partially-premixed turbulent swirling PRECCINSTA flame. Note that the test bench was operated in different operating conditions if compared to the data available in the literature [27, 129] allowing for different levels of H_2-enrichment reaching up to 50% in volume. In the present study, to take into account heat-transfer and analyze thermal load effects due to the different hydrogen contents, CHT simulations are

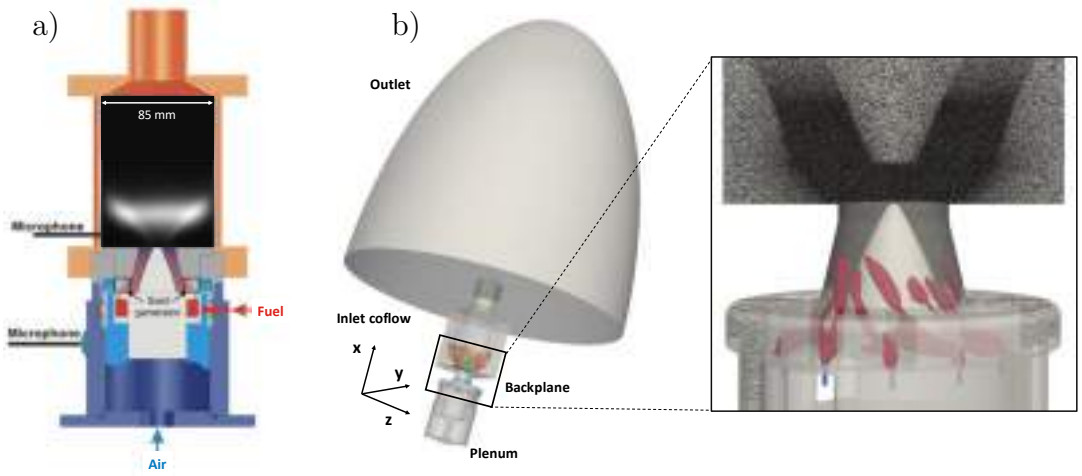

Figure 6.1: (a) Schematic of the experimental test bench: injector with combustion chamber and normalized time-averaged line-of-sight (LOS) OH* chemiluminescence for the pure CH_4 flame. (b) Computational domain used in LES with overview of the fluid mesh. Note that in LES the atmosphere is taken into account and the inlet fuel geometry is simplified to the 12 small tubes (colored in blue) without the fuel plenum. The instantaneous isocontour of CH_4 (colored in red) helps visualize the technical injection of the fuel in the swirled flow.

performed as discussed in Chapter 4. In the following, the experimental and the numerical setup are first presented in section 6.2 while a detailed description of the Analytically Reduced Chemistry (ARC) mechanism reduced for describing the CH_4-H_2/Air combustion is left to the Appendix C. Results are discussed in section 6.3. First, the experimental data and the numerical predictions of the 0% H_2 stable flame are briefly recalled in section 6.3.1 (see Chapter 4). The 20% H_2 flame is presented in section 6.3.2, showing the impact of hydrogen enrichment on the flame length and the thermal load on the combustor components. The impact of hydrogen addition is more evident in the 50% H_2 flame that becomes clearly unstable and experiences bi-modal thermoacoustic oscillations (section 6.3.3). Finally, computed acoustic modes and Dynamic Mode Decomposition analyses are used to get more insights on the instability driving mechanisms in an attempt to identify the triggering mechanism of the thermoacoustic oscillations when a sufficiently high hydrogen content is injected (section 6.3.4).

6.2 Operating conditions and numerical setup

The PRECCINSTA experimental test rig [27] is presented in Fig. 6.1 (a) illustrating the injector, the combustion chamber and the experimental normalized

time-averaged Line-of-sight (LOS) OH* chemiluminescence image for the reference pure CH_4 flame (presented in Chapter 4).

A new test campaign featuring different operating conditions compared to the data available in the literature was performed. To analyze the H_2-enrichment effect on the flame stabilization and flame dynamics, different hydrogen content reaching values up to 50% in volume have been injected as premixed with the CH_4 stream. In this work, first the experimentally stable condition with 0% H_2 (in the following referred to as case A) is considered for a global equivalence ratio of $\phi = 0.8$ and a thermal power of $P_{th} = 10$kW [59]. Second, 20% in fuel volume of H_2 is injected while keeping the thermal power P_{th} constant as well as a constant global equivalence ratio ϕ (case B). Finally, case C corresponding to a H_2 content of 50% in volume for a constant P_{th} and ϕ is analyzed. Note that this last case experienced significant thermoacoustic oscillations. All operating conditions considered are summarized in Table 6.1.

Case	H_2 [% fuel vol.]	$\dot{m}_{air}$ [g/s]	$\dot{m}_{CH_4}$ [g/s]	$\dot{m}_{H_2}$ [g/s]	ϕ	P_{th}
A	0%	4.29	0.2	-	0.8	10KW
B	20%	4.23	0.186	0.006	0.8	10KW
C	50%	4.12	0.154	0.019	0.8	10kW

Table 6.1: Summary of the operating conditions considered in the present work.

The test rig is equipped with different diagnostics. Using Stereoscopic Particle Image Velocimetry (sPIV), measurements of the three velocity components were performed in one vertical plane along the radial direction. Planar Laser-Induced Fluorescence (PLIF) measurements of OH radicals were also performed to visualize the flame structure together with line-of-sight integration of OH* chemiluminescence that provides a qualitative indicator of the local heat release rate for lean premixed flames [170]. Experimental data were acquired synchronously with acoustic pressure measurements in the combustion chamber and in the plenum to analyze the thermoacoustic oscillations.

Figure 6.1 (b) presents the computational domain used by LES with an overview of the unstructured mesh. The outside atmosphere is taken into account to impose the right impedance at the outlet of the combustion chamber and the inlet fuel geometry is simplified into 12 small tubes (colored in blue) without the fuel plenum: to help visualize the technical fuel injection in the swirled flow, an instantaneous isocontour of CH_4 is colored in red. LES are performed using the AVBP code with the classical numerical modeling (Chapter 2).

The LES computational grid consists of 76M tetrahedral cells that was refined in the flame region applying static mesh adaptation criteria [70]. The final mesh has a characteristic size in the flame zone just downstream of the centerbody tip of $\Delta_x = 200\ \mu m$ assuring a $y+$ value lower than unity at the centerbody tip and $y+ \sim 3$ at the chamber and backplane walls, hence allowing the use of a wall resolved LES approach and a reasonable estimation of the thermal boundary layer.

The CH_4-H_2/Air chemistry is described through an Analytically Reduced Chemistry (ARC) mechanism consisting of 18 transported species, 144 reactions, and 12 quasi-steady state species, derived from the detailed PoliMi scheme [241] using ARCANE [65]. The kinetic scheme has been validated through Cantera (www.cantera.org) calculations of a 1D-premixed and 1D-counterflow flames against experimental data and detailed schemes. A complete description of the ARC mechanism and its validation are reported in Appendix C[1].

H_2-enrichment reduces the flame thickness making it difficult to resolve the flame front on the computational grid while requiring reasonable HPC resources. To artificially thicken the flame and be able to resolve the flame front, the dynamic formulation of the thickening flame model (DTFLES) [64] is used. The thickening process is done by multiplying the diffusion terms and dividing the reaction rates by a local thickening factor F which depends on the local mesh size and the flame thickness. In turbulent cases, since a thickened reactive layer is less sensitive to turbulence, an efficiency function Ξ_Δ is introduced to compensate for the corresponding reduction of flame surface [61]. In this work, the DTFLES model is coupled to the Charlette efficiency function [62] used with the dynamic wrinkling formulation for the local on-the-fly estimation of the model parameter β_{Ch}[2]. The choice of the dynamic formulation with respect to the computationally less expensive non-dynamic approach (where β_{Ch} is usually fixed at

[1]Note that, for this Chapter and for Chapter 7, the transport properties modeling presented in Chapter 5 is not employed. As a matter of fact, in the PRECCINSTA cases, H_2 and CH_4 are well premixed, leading to small variation of Prandtl and Schmidt numbers as opposed to Chapter 5 where a pure hydrogen pilot injection is considered. Moreover, the flow is not laminar here and transport properties are set by turbulent Prandtl and Schmidt numbers. In addition, the flame in the PRECCINSTA burner is stabilized further downstream with respect to the mixing region, hence the small variation of transport properties is not expected to significantly impact the flame stabilization as opposed to the MIRADAS case.

[2]Note that the "relaxation" sensor is used to dynamically thicken the flame when dealing with ARC mechanism [242]. The latter identifies the highly reacting inner flame region by looking at the fuel source term intensity with respect to a reference value from one-dimensional premixed flame. A filtering-like operation is then used to broaden the sensor and enclose the region of relevant heat release rate and strong gradients across the flame front. Note also that, when it comes to the dynamic efficiency model, the progress variable, which is needed to evaluate β_{Ch}, is estimated in this work from the temperature field.

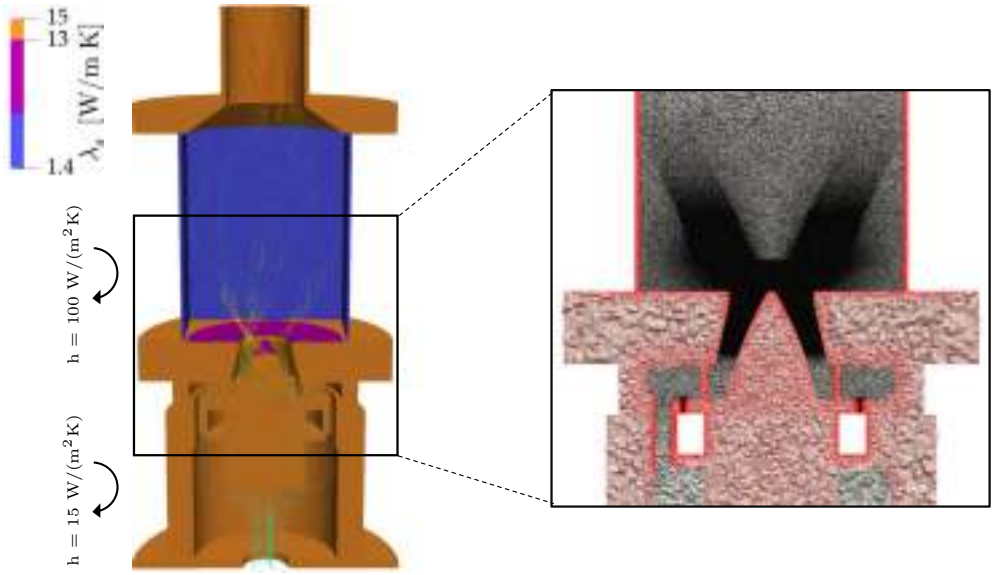

Figure 6.2: Computational domain used in CHT simulations with overview of the solid (red) and fluid (black) meshes with thermal boundary conditions for the AVTP heat-conduction solver. Assumed thermal conductivities λ_s for quartz (blue), inconel (purple) and stainless steel (orange) are also indicated.

0.5) is suggested from the work performed by Volpiani *et al.* [136]. They compared the two formulations in the PRECCINSTA test bench flames experienced by Meier *et al.* [27] and observed that while β_{Ch} was 0.5 for the stable flame, it was strongly oscillating around 0.8 for the pulsating flame, concluding that the self-excited mode of the pulsating flame was correctly predicted only with the dynamic formalism.

Inlet and outlet boundary conditions are treated with the Navier-Stokes Characteristic Boundary Conditions (NSCBC) [30] with a relaxation factor of $K_{air} = 50\,\mathrm{s}^{-1}$ and $K_{fuel} = 5 \times 10^5\,\mathrm{s}^{-1}$ imposed on the air and fuel inlets, respectively [59]. All walls are treated as no-slip. To take into account wall heat-transfer, CHT simulations are performed (Chapter 4).

The computational domain used in CHT simulations is shown in Fig. 6.2 where the solid mesh is indicated in red and the fluid in black. The solid parts have been discretized using 16M tetrahedral elements and a resolution of at least 5 points across the thin chamber walls. An implicit first-order Euler scheme is used for time integration and a second-order Galerkin diffusion scheme is applied for spatial discretization. While heat fluxes at the solid boundaries in contact with the fluid are determined from the LES flow, thermal boundary conditions must be indicated for the surfaces of the solid not in contact with the fluid domain (e.g. external chamber walls, external plenum walls). Following the methodology of

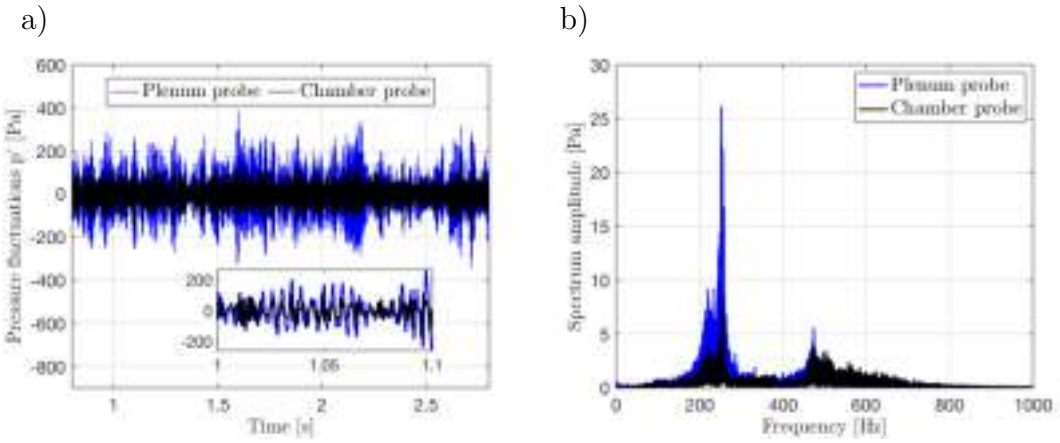

Figure 6.3: (a) Experimental pressure fluctuations recorded in the plenum (blue) and at the combustion chamber backplane (black) with a zoom on a part of the signal and (b) the signals spectra obtained via Fast Fourier Transform (FFT). Case *A*: 0% H_2 [59].

Chapter 4, the required heat exchange coefficients at these boundaries have been determined for the external side of the chamber and plenum walls (reported in Fig. 6.2). Finally, the thermal radiation from the hot gases is taken into account by the AVBP LES solver with the Optically Thin Assumption (OTA) [172] for the most radiating species CH_4, CO, CO_2, and H_2O: gases are supposed to be optically thin and re-absorption is neglected while the Planck mean-absorption coefficients are provided for each species as polynomial functions of temperature [173].

6.3 Results and discussion

Numerical and experimental results for case A (section 6.3.1), case B (section 6.3.2) and case C (section 6.3.3) are hereafter presented, illustrating the impact of the H_2-enrichment on the flame stabilization and the flame dynamics for the current configuration. Then, analysis of the instability mechanisms is performed to get more insights on the H_2-enriched flame (section 6.3.4).

6.3.1 Case *A*: pure CH_4 flame

CHT simulations of case A have been mostly presented in Chapter 4. In the following the main results are briefly recalled for the sake of comparison to the H_2-enriched cases.

Figure 6.3 presents (a) the experimental pressure fluctuations recorded in the plenum (blue) and at the combustion chamber backplane (black) along with (b) their power spectra computed using a Fast Fourier Transform (FFT) algorithm.

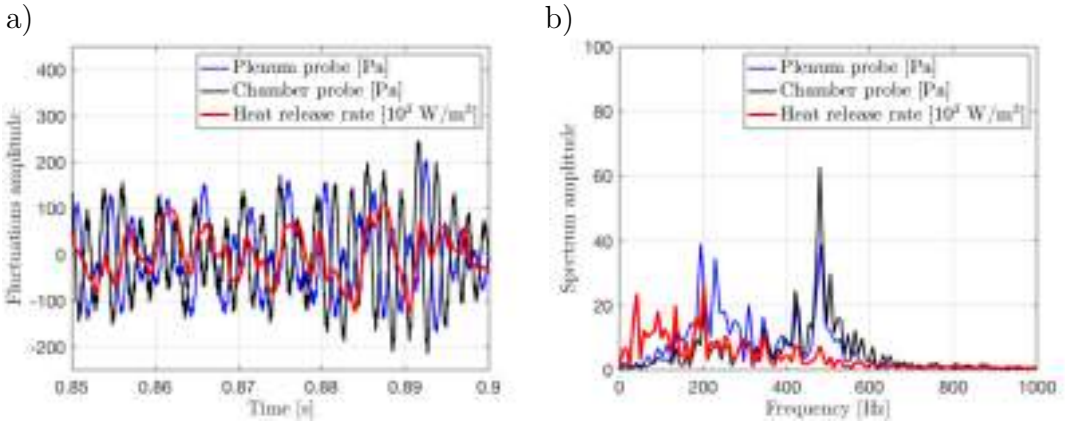

Figure 6.4: (a) LES predicted fluctuations of pressure in the plenum (blue) and at the combustion chamber backplane (black) and heat release rate (red). (b) Signals spectra obtained via Fast Fourier Transform (FFT). Case *A*: 0% H_2 [59].

As seen, the pressure signal has an amplitude of 400 Pa in the plenum, while the amplitude in the combustion chamber is close to 200 Pa. Two weak modes appear at 260 Hz and 480 Hz: the weak amplitude of the two peaks (smaller than 10 Pa in the chamber) indicates that no thermoacoustic activity takes place for this operating condition.

The time evolution of the heat release rate (red) and pressure oscillations predicted via LES in the plenum (blue) and at the combustion chamber backplane (black) are presented in Fig. 6.3 (a). The pressure fluctuation amplitude in the chamber and in the plenum is of the order of 200 Pa and corresponds to the level experimentally observed (Fig. 6.3). Heat release rate fluctuations are again seen not to be correlated with pressure fluctuations. The power spectra computed via Fast-Fourier Transform (FFT) are presented in Fig. 6.3 (b) and confirm this observation.

CHT simulations are compared to experimental data in Fig. 6.5. Experimental normalized time-averaged LOS OH* chemiluminescence image (which is a qualitative indicator for the heat release rate for lean premixed flames) and LOS field of the numerically predicted heat release rate $\overline{\dot{q}}$ are presented in Fig. 6.5 (a) and prove LES to retrieve the correct flame length and angle. High region of heat release rate is predicted in the top central part of the flame while low intensity is predicted in the Central Recirculation Zone (CRZ), just downstream of the centerbody. The flame tip shape and the distance from the external chamber walls are also retrieved. Comparison of the experimental normalized time-averaged OH-PLIF signal with the predicted OH mass fraction is shown in Fig. 6.5 (b). The flame has a V-shape, with a flame-root well attached to the centerbody tip.

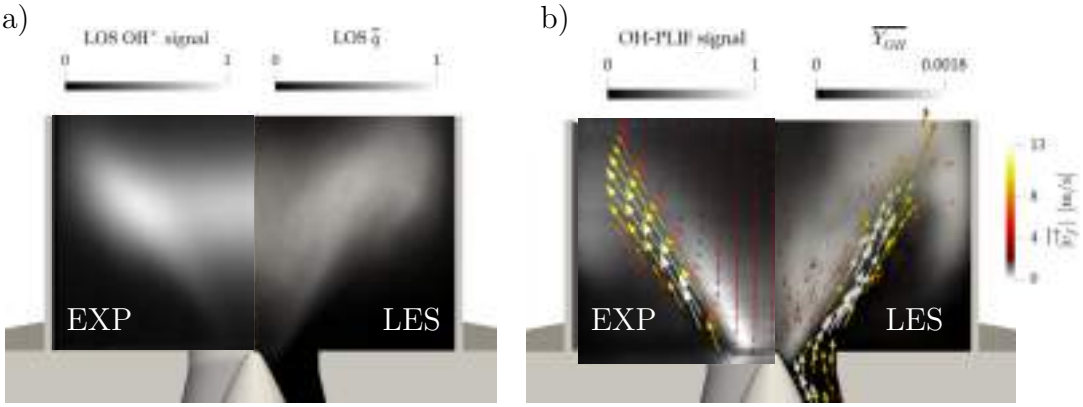

Figure 6.5: Validation of CHT simulations. (a) Comparison of experimental normalized time-averaged Line of Sight (LOS) OH* chemiluminescence image with LOS predicted heat release rate $\bar{\dot{q}}$. (b) Comparison of experimental normalized time-averaged OH-PLIF signal with predicted OH mass fraction $\overline{Y_{OH}}$. The arrows are tangential to the experimental and numerical time-averaged velocity field in the plane $\overrightarrow{\overline{v_{//}}}$. Their length and color indicate the velocity magnitude. Case *A*: 0% H_2 [59].

The flame tip reaches a height of 50 mm from the backplane and low OH intensity is predicted in the Outer Recirculation Zones (ORZs). Experimental and numerical time-averaged velocity field in the plane $\overrightarrow{\overline{v_{//}}}$ are indicated by arrows that are tangential to the velocity vector and whose length and color indicate the velocity magnitude. Both in experiments and LES, a high velocity region (i.e. white arrows) is present at the swirler exit. The CRZ is clearly indicated by the downward velocity vectors while in the ORZ the velocity component in the plane remains very weak (for a more quantitative comparison see Ref. [59]).

The instantaneous solid temperature is shown in Fig. 6.6 (a) with an instantaneous iso-contour of predicted heat-release rate $\dot{q}$ at 10% of $\dot{q}_{max}$. The temperature of the chamber walls on the internal side reaches a maximum value of around 1300 K at 70 mm from the backplane where the flame is close to the walls. The temperature goes down when proceeding toward the backplane where the flame is only sporadically present. The backplane has a temperature of around 570 K while the centerbody tip is close to 850 K. Figure 6.6 (b) shows the time-averaged temperature $\overline{T}$ and heat-release rate $\bar{\dot{q}}$ in a cut plane, the fluid domain being delimited by a white line. The flow reaches 1800 K in the CRZ and downstream of the flame tip where burnt gases are present while ORZs present lower temperature. The red iso-contour corresponds to a temperature of 450 K and shows the pre-heating of the fresh gases due to the heated solid.

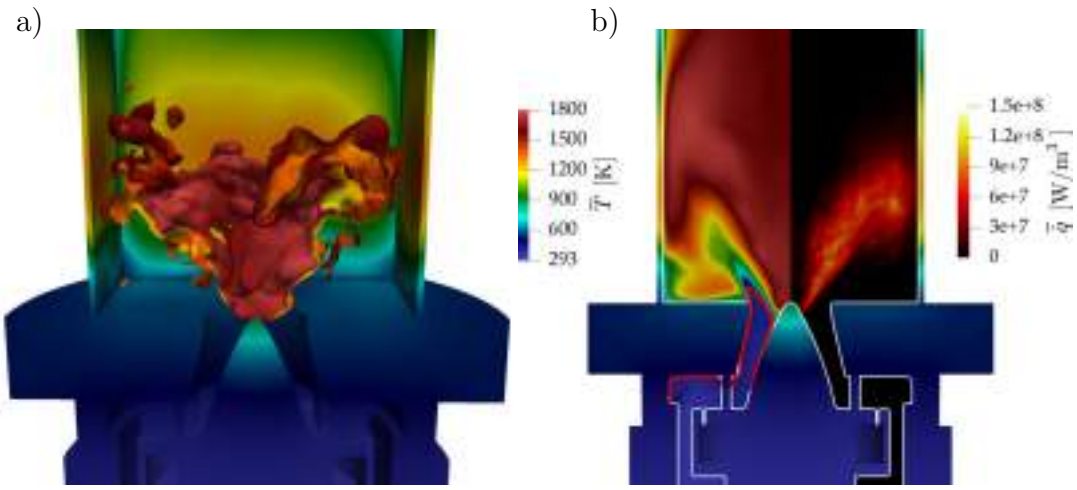

Figure 6.6: (a) Instantaneous field of solid temperature with iso-contour of heat-release rate $\dot{q}$ at 10% of maximum value. (b) Cut-plane showing the time-averaged temperature $\overline{T}$ and heat release rate $\overline{\dot{q}}$ predicted by CHT simulations. Red iso-contour corresponds to temperature of 450 K, showing the pre-heating of the fresh gases due to the warmed-up solid. The fluid domain is delimited by a white line to visualize the separation between solid and the fluid parts. Case *A*: 0%. H_2 [59].

6.3.2 Case *B*: 20% H_2 enrichment

Figure 6.7 (a) presents the experimental pressure fluctuations recorded in the plenum (blue) and at the combustion chamber backplane (black) as well as the volume-integrated OH* chemiluminescence signal (red) that is an indicator of the experimental volume-integrated heat release rate. The pressure signal presents the same fluctuations levels than case A, having an amplitude of 400 Pa in the plenum, while the amplitude in the combustion chamber is close to 200 Pa. The fluctuations of the volume-integrated OH* chemiluminescence signal (red) appears not to be correlated to the pressure fluctuations, suggesting that thermoacoustic oscillations are not present in this case. Three small peaks appear in the signal spectra, computed using a Fast Fourier Transform (FFT) algorithm and presented in Figure 6.7 (b). The weak amplitude of the peaks (smaller than 10 Pa in the chamber signal) confirms that no thermoacoustic activity takes place for this operating condition.

The corresponding numerically-predicted time evolution of the heat release rate (red) and pressure oscillations in the plenum (blue) and at the combustion chamber backplane (black) are presented in Fig. 6.8 (a). The pressure fluctuation amplitude in the chamber and in the plenum is of the order of 400 Pa and corresponds to the level observed experimentally (Fig. 6.7). Heat release rate fluctuations are not correlated with pressure fluctuations. The power spectra computed via Fast-Fourier Transform (FFT) are presented in Fig. 6.8 (b) and

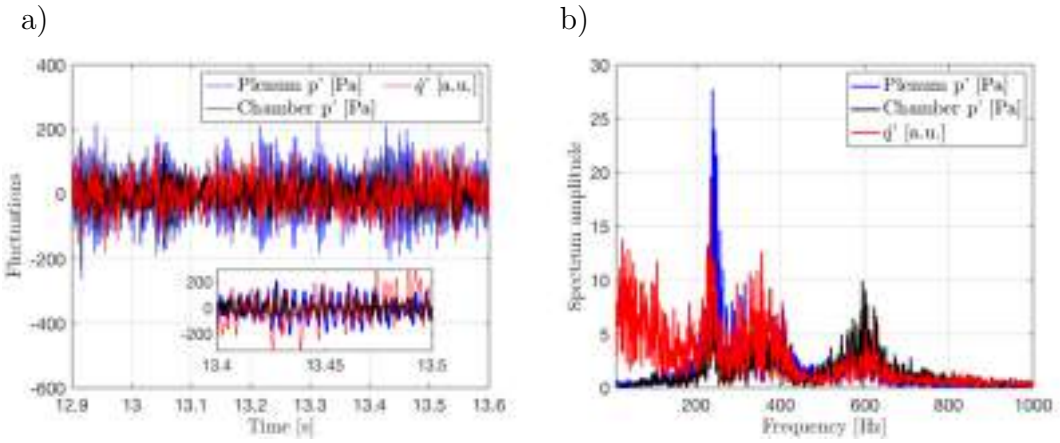

Figure 6.7: (a) Experimental fluctuations of recorded pressure in the plenum (blue) and at the combustion chamber backplane (black) and of the volume-integrated OH* chemiluminescence signal (red). (b) The signals spectra obtained via Fast Fourier Transform (FFT). Case *B*: 20% H_2.

confirm this observation. A stronger peak is predicted for the chamber pressure at 430 Hz but it is not correlated with heat release rate fluctuations, leading to the conclusion that the 20% H_2-enrichment does not lead to main differences in the flame dynamics if compared to the pure CH_4 case.

H_2-enrichment produces however some noticeable differences in the flame shape and stabilization. Figure 6.9 (a) presents the comparison of experimental normalized time-averaged Line of Sight (LOS) OH* chemiluminescence image with LOS predicted heat release rate $\overline{\dot{q}}$. The flame presents a clear V-shape and appears to be sensibly shorter if compared to the pure CH_4 case, Fig. 6.5(a). The flame is relatively more distant from the combustion chamber and presents a higher signal region in the central part while no flame is observed downstream the centerbody tip. For both cases, LES are able to correctly retrieve the right flame shape, providing a very good agreement in terms of flame angle and length. Figure 6.9 (b) presents a more quantitative comparison of experimental normalized time-averaged OH-PLIF signal with LES predicted OH mass fraction on a vertical plane. The flame has clearly a V-shape with the higher OH concentration close to the centerbody tip. Low OH concentration is present in the ORZs and in the CRZ just downstream the centerbody tip. Also, for this case, LES correctly predicts the flame shape and angle. If compared to the reference pure CH_4 flame, Fig. 6.5(b), OH field is more concentrated with weaker experimental signal and lower predicted mass fraction in the CRZ. However, the 20% H_2-enrichment does not modify the peak value of the predicted OH mass fraction that remains very similar to the reference flame. Also in this case, no OH signal is observed in the high velocity region at the injector exit, as indicated by the arrows that are

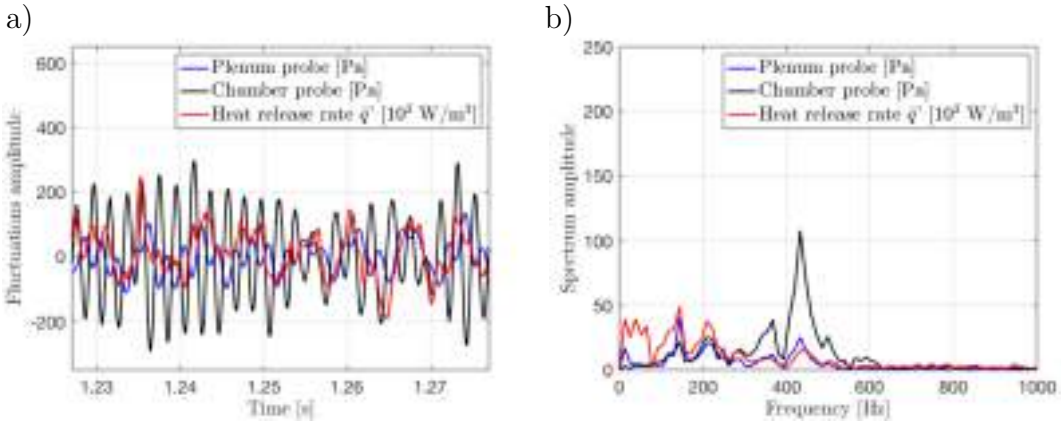

Figure 6.8: (a) Predicted fluctuations of pressure in the plenum (blue) and at the combustion chamber backplane (black) and heat release rate (red). (b) Signals spectra obtained via Fast Fourier Transform (FFT). Case *B*: 20% H_2.

tangential to the experimental and numerical time-averaged velocity field in the plane $\overrightarrow{\overline{v_{//}}}$ and whose length and color indicate the velocity magnitude.

A more quantitative comparison of the experimental and the LES velocity field is provided by Fig. 6.10 and Fig. 6.11. Figure 6.10 presents the profiles of mean (a) axial, (b) radial and (c) tangential velocity components at different measurement planes downstream of the combustion chamber backplane for LES in comparison to sPIV experimental data. LES is able to correctly predict the velocity field that corresponds to a classical swirled-flow with a vortex breakdown due to combustion. The axial velocity (a) indeed shows an extended CRZ, indicated by the negative velocity along the axis. The (b) radial and (c) tangential velocity components are also well predicted by LES and show a progressive reduction in the maximum amplitude as proceeding downstream. At the same time, Figure 6.11 presents the profiles of rms for the (a) axial, (b) radial and (c) tangential velocity components. Considering the low velocity magnitude (see the scale), LES turns out to be in satisfactory agreement with the experimental values. A slight overestimation of the peaks is visible on the three components and it is probably due on one side to the longer LES averaging-time[1] needed to reach statistical convergence of the rms small values and on the other side to the experimental uncertainties. The latter hypothesis is further confirmed by noticing that the most significant discrepancy between LES and experiments happens for the tangential component of velocity: this poorer match is not unexpected as in sPIV it is well established that measurement uncertainty in the out-of-plane

[1]Note that in the present work, a simulation time of 100 ms is considered for flow field statistics and post-processing.

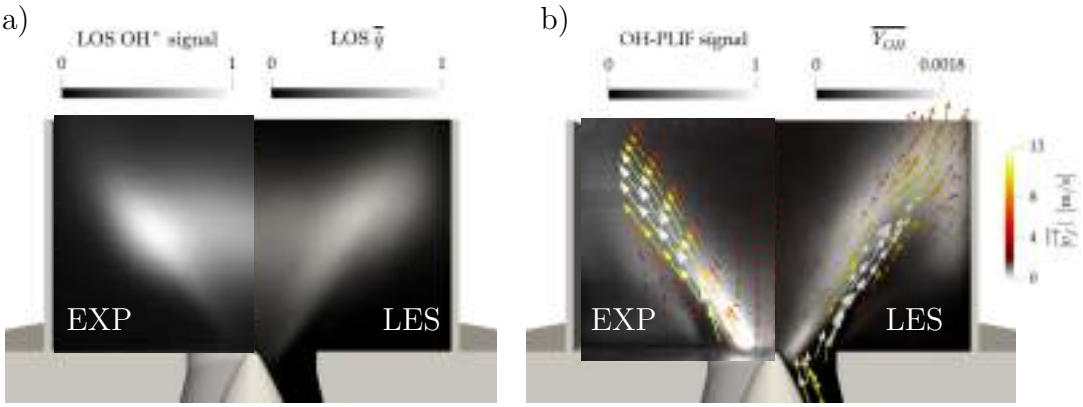

Figure 6.9: Validation of CHT simulations. (a) Comparison of experimental normalized time-averaged Line of Sight (LOS) OH* chemiluminescence image with LOS predicted heat release rate $\overline{\dot{q}}$. (b) Comparison of experimental normalized time-averaged OH-PLIF signal with predicted OH mass fraction. The arrows are tangential to the experimental and numerical time-averaged velocity field in the plane $\overline{\overrightarrow{v}_{//}}$. Their length and color indicate the velocity magnitude. Case *B*: 20% H_2.

direction (in this case, the tangential) is typically higher than for the in-plane components of velocity [184].

The differences between the 20% H_2-enrichment flame and the pure CH_4 flame can be further analyzed by looking at Fig. 6.12 that presents the CHT predictions of the instantaneous solid temperature with an iso-contour of heat-release rate $\dot{q}$ at 10% of maximum value. The temperature of the chamber walls on the internal side reaches a maximum value of around 1250K, which is slightly lower than the pure CH_4 flame, Fig. 6.6 (a), probably due to the larger distance between the flame tip and the chamber walls. The backplane instead presents a temperature close to 580 K, very similar to the reference flame. On the contrary, the centerbody tip presents a much larger temperature, close to 1000 K, probably due to the different flame stabilization. Indeed, the iso-contour of heat-release rate $\dot{q}$ shows that the flame is stabilized sensibly closer to the centerbody and slightly more upstream, probably due to the higher laminar flame speed and the larger resistance to strain of the 20% H_2-enriched flame if compared to the pure CH_4 case. At the same time, the flame is shorter with a reduced lift-off distance from the backplane in the ORZs. Figure 6.12 (b) shows the predicted time-averaged temperature $\overline{T}$ and heat-release rate $\overline{\dot{q}}$ in a vertical plane. The fluid domain is delimited by a white line. The flow reaches the maximum temperature in the CRZ and downstream of the flame tip where burnt gases are present while ORZs present lower temperature. Compared to the pure CH_4 flame, Fig. 6.6(b), the adiabatic flame temperature is only slightly higher, leading to a quite similar fluid temperature $\overline{T}$. The red iso-contour, which corresponds to a temperature

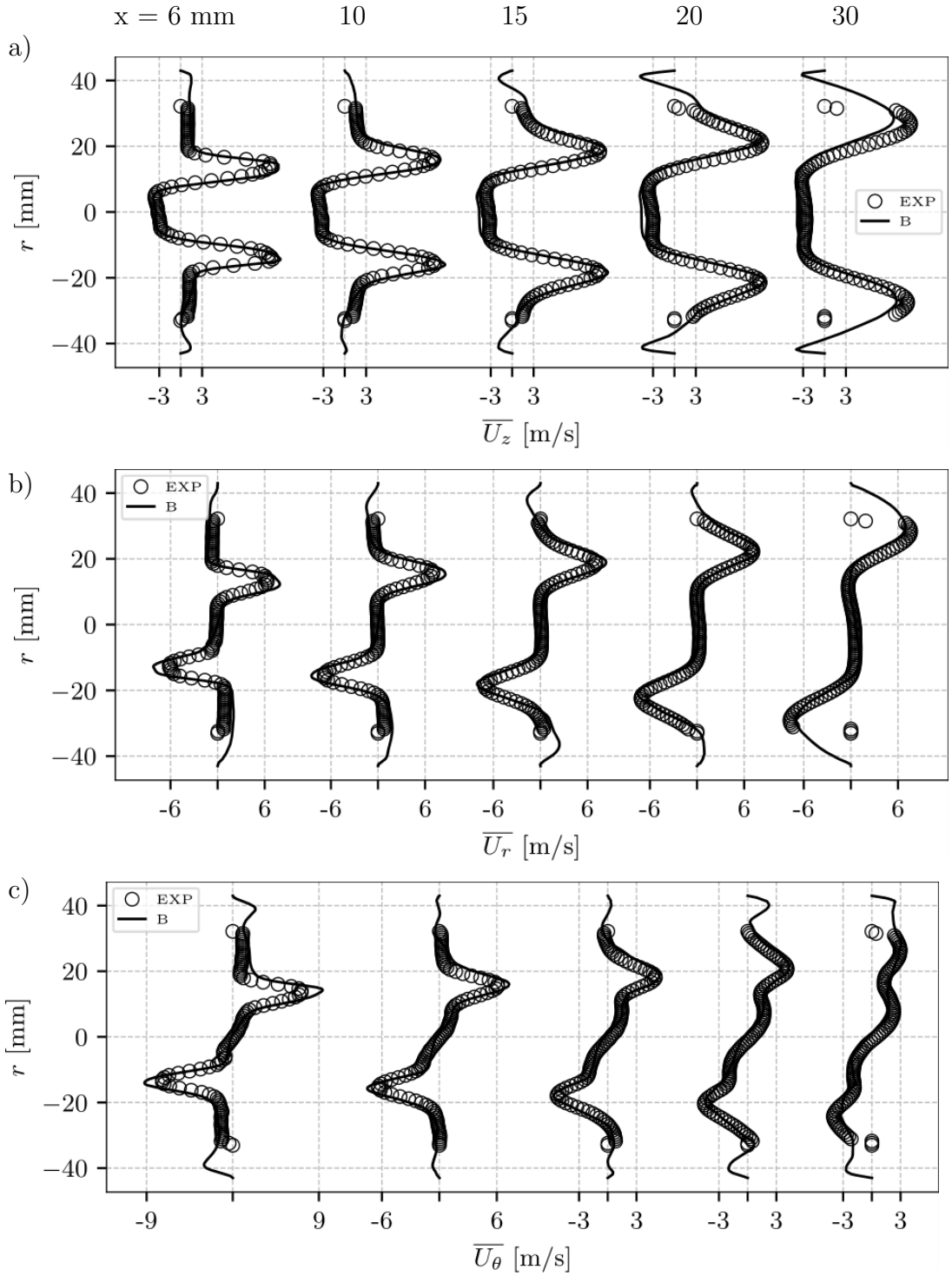

Figure 6.10: Profiles of mean (a) axial, (b) radial and (c) tangential velocity components at measurement planes at x = 6, 10, 15, 20 and 30 mm downstream of the combustion chamber backplane for LES in comparison to experiments. Case *B*: 20% H_2.

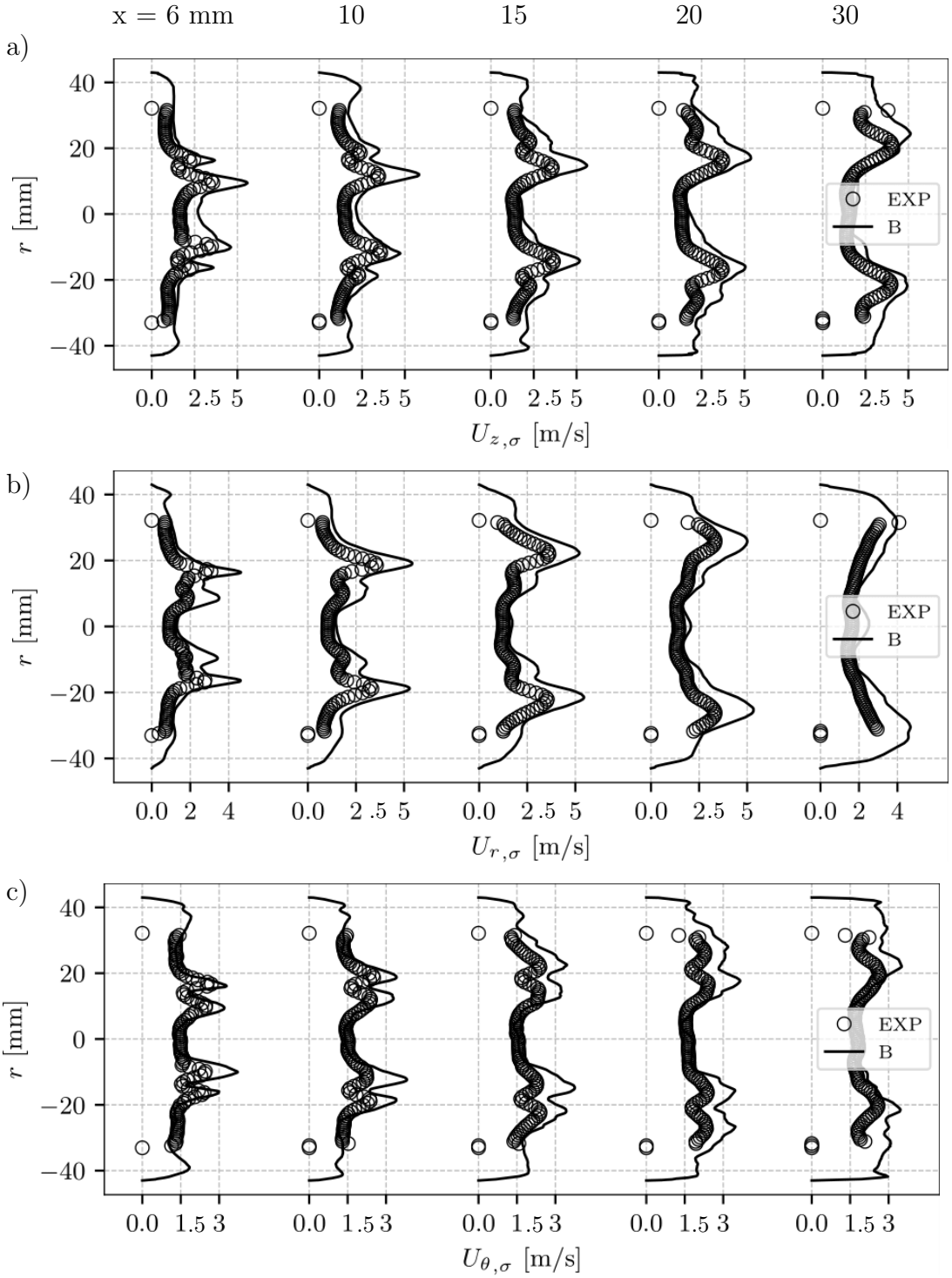

Figure 6.11: Profiles of RMS (a) axial, (b) radial and (c) tangential velocity components at measurement planes at x = 6, 10, 15, 20 and 30 mm downstream of the combustion chamber backplane for LES in comparison to experiments. Case *B*: 20% H_2.

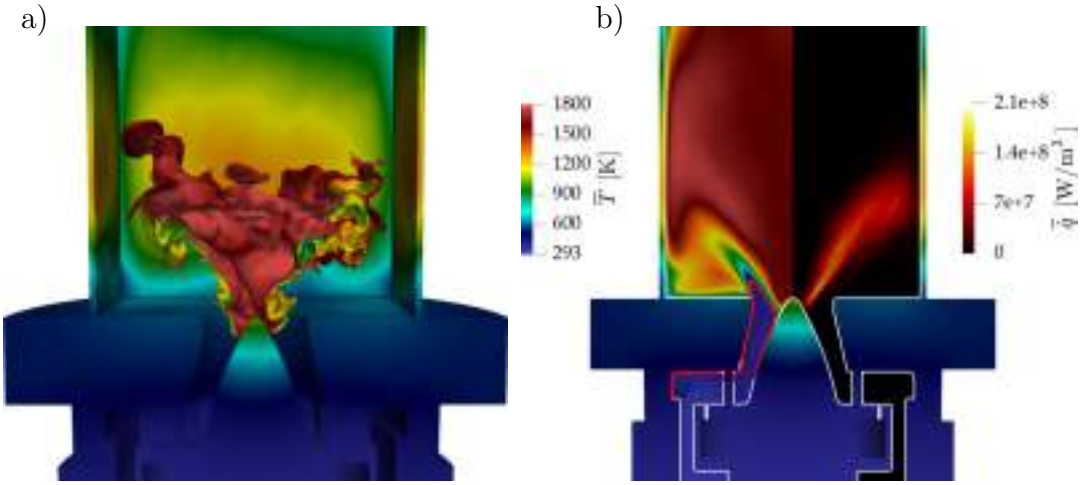

Figure 6.12: (a) Instantaneous field of solid temperature with iso-contour of heat-release rate $\dot{q}$ at 10% of maximum value. (b) Cut-plane showing the time-averaged temperature $\overline{T}$ and heat release rate $\overline{\dot{q}}$ predicted by CHT simulations. Red iso-contour corresponds to temperature of 450 K, showing the pre-heating of the fresh gases due to the warmed-up solid. The fluid domain is delimited by a white line to visualize the separation between solid and the fluid parts. Case *B*: 20% H_2.

of 450 K, shows that the pre-heating of the fresh gases due to the warmed-up solid is similar to the pure methane case but it is shifted upstream near the centerbody walls since the centerbody tip has larger temperature. Hence, the 20% H_2-enrichment leads to a globally similar temperature field with respect to the pure methane flame but to a remarkable larger temperature at the centerbody tip that then affects the flame stabilization and the pre-heating of the gases.

6.3.3 Case *C*: 50% H_2-enrichment

The flame dynamics significantly changes when 50% of H_2 enriches the fuel mixture. Figure 6.13 (a) presents the experimental pressure fluctuations recorded in the plenum (blue) and at the combustion chamber backplane (black) with the fluctuations of the volume-integrated OH* chemiluminescence signal (red) that is an indicator of the experimental volume-integrated heat release rate. The pressure oscillations are notably higher than for the low H_2-enriched and the pure CH_4 flames, reaching an amplitude of 1000 Pa and 600 Pa for the plenum and chamber probes respectively. A zoom of the signals shows that the heat release rate fluctuation seems correlated to the pressure fluctuations, with a phase difference within the $\pi/2$ limit, satisfying the well-known Rayleigh criterion [177] and hence indicating the presence of a thermoacoustic activity. This hypothesis is confirmed by looking at Fig. 6.13 (b) that presents the power spectra of the

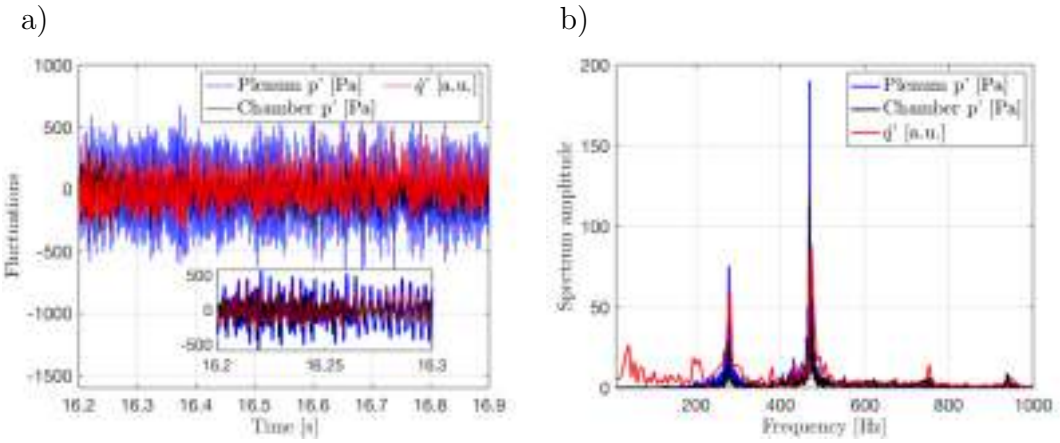

Figure 6.13: (a) Experimental fluctuations of recorded pressure in the plenum (blue) and at the combustion chamber backplane (black) and of the volume-integrated OH* chemiluminescence signal (red). A zoom on a part of the signals helps visualize the correlation between the OH* chemiluminescence signal fluctuations and the pressure oscillations. (b) Signals spectra obtained via Fast Fourier Transform (FFT). Case *C*: 50% H_2.

full signals computed using a Fast Fourier Transform (FFT) algorithm. Both the pressure spectra and the volume-integrated OH* chemiluminescence spectrum show two strong peaks at 280 Hz and 470 Hz. The second mode appears to be significantly larger with respect to the first one, reaching an amplitude of around 200 Pa and 130 Pa for the plenum and chamber probes respectively. The same peaks are present in the volume-integrated OH* chemiluminescence spectrum, showing that the flame responds to the two modes, hence suggesting the presence of bi-modal oscillation.

The presence of two modes both in the pressure signals and in the volume-integrated heat release rate underlines the complexity of the analyzed system. In a recent experimental work performed by Kushwaha *et. al.* [240], the PRECCINSTA test bench was operated at different thermal powers P_{th}, equivalence ratios ϕ and H_2-enrichment levels and a first classification of the experimentally observed flame dynamical states was proposed. The authors focused on the $P_{th} = 20$kW cases and classified four different flame dynamics: period-1 limit cycle oscillations (P1-LCO), period-2 LCO (P2-LCO), chaotic oscillations (CO) and intermittency (I). In both P1-LCO and P2-LCO unstable cases, the heat release rate fluctuations were responding to a single frequency f_1 oscillation. Although P1-LCO the chamber pressure was presenting a single peak, for the case P2-LCO state, the pressure spectrum was presenting two peaks for which $f_2/f_1 \approx 2$ and $f_1 = 283$ Hz. The state of intermittency [243], instead, was characterized by the occurrence of epochs of low amplitude aperiodic oscillations amidst bursts of large-amplitude

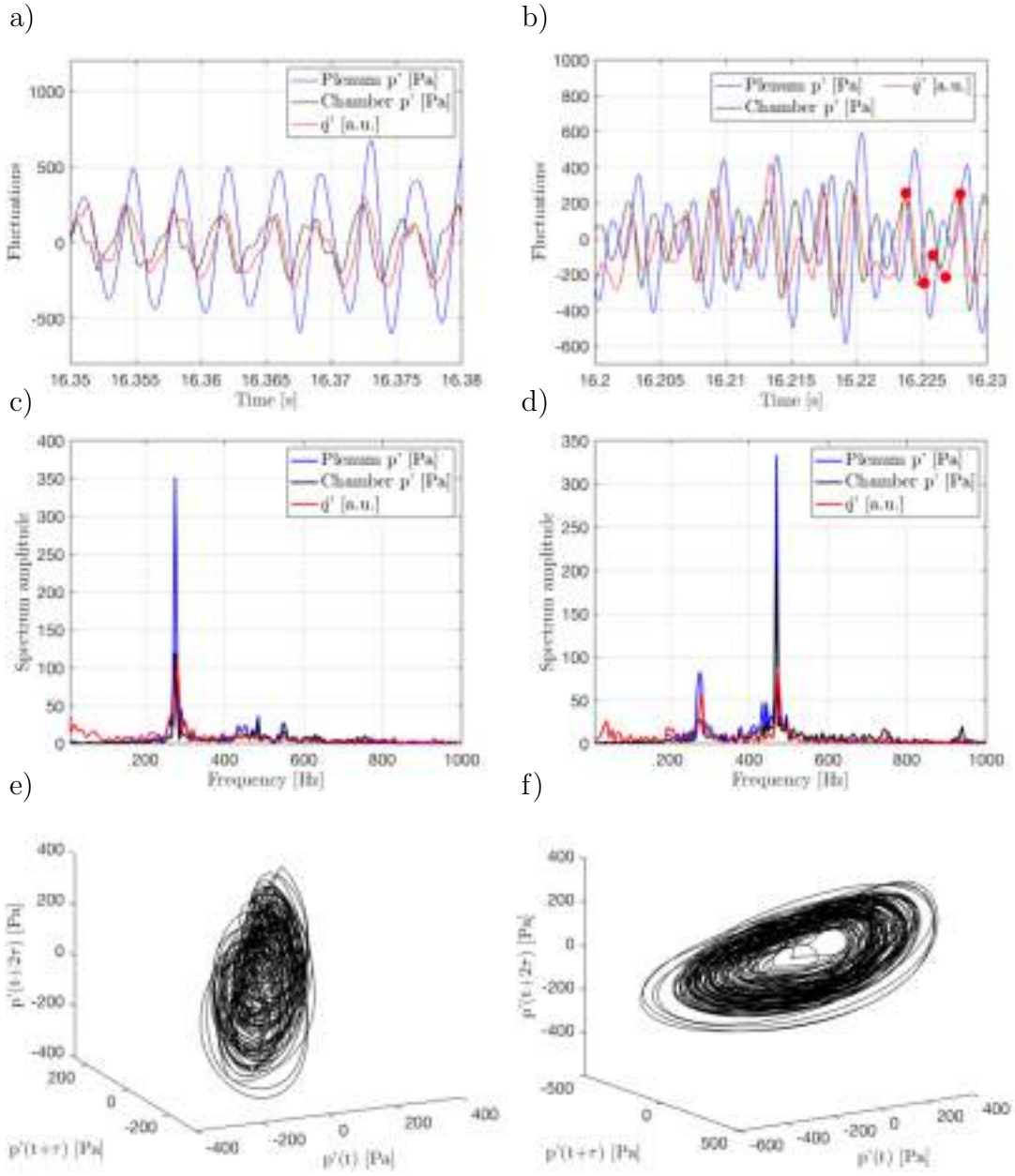

Figure 6.14: Experimental pressure fluctuations recorded in the plenum (blue) and at the combustion chamber backplane (black) with fluctuations of the volume-integrated OH* chemiluminescence signal (red) for (a) prevalent first mode (PM1) and (b) prevalent second mode (PM2) dynamics. Signals spectra obtained via Fast Fourier Transform (FFT) for (c) PM1 and (d) PM2. Three-dimensional phase space representation of the pressure fluctuations recorded at the combustion chamber for (e) PM1 and (f) PM2. Case *C*: 50% H_2.

periodic oscillations interspersed in an apparently random manner. This type of oscillations has been reported in many turbulent thermoacoustic systems previously studied [244]. Case C here analyzed would be classified (but not showed) by Kushwaha *et. al.* [240] as intermittent. Our analysis would suggest instead a more complex dynamics for this case if compared to the $P_{th} = 20$ kW cases effectively analyzed by Kushwaha *et. al.*.

Indeed, the flame of the present case is observed to respond to two modes at 280 Hz and 470 Hz as pointed out in the volume-integrated OH* chemiluminescence spectrum of Fig. 6.13 (b), a condition which was never observed by Kushwaha *et. al.* [240]. However, these two peaks are present also in the chamber pressure spectrum, making it similar to a P2-LCO dynamical state, despite the fact that f_2 is not an harmonic of f_1. Intermittency is nonetheless visible when looking at the relative importance of the two modes: while the flame couples mainly with the second mode for the major part of the experimental signal, there are epochs where the first mode becomes prevalent and the second mode is weaker both in the heat release rate and pressure oscillations. To better explain this mechanism and perform a more detailed analysis of the flame dynamics, the experimental signals have been divided into two parts and analyzed separately in Fig. 6.14. The temporal evolution of the pressure fluctuations recorded in the plenum (blue) and in the combustion chamber (black) together with the fluctuations of volume-integrated OH* chemiluminescence signal (red) are showed in Fig. 6.14 (a) and Fig. 6.14 (b) for the prevalent first mode (PM1) and the prevalent second mode (PM2) dynamics respectively. As visible in Fig. 6.14 (a), in some epochs the flame couples mainly with the first mode showing a PM1 dynamics: a strong peak is visible at 280 Hz in the signals spectra in Fig. 6.14 (c). The plenum pressure, the chamber pressure and the heat release rate oscillate almost in phase at 280 Hz, while a second weaker peak is visible for the chamber pressure at 470 Hz but the heat release rate does not respond to this mode, leading to a limit cycle oscillation that has been extensively observed and analyzed in the PRECCINSTA test bench for pure CH_4 flames (see for example Meier *et al.* [27] and Franzelli *et al.* [130]). However, the three-dimensional phase space representation of the pressure fluctuation recorded at the combustion chamber for the PM1 dynamics and presented in Fig. 6.14 (e) shows that the oscillations amplitude is not constant during the PM1 dynamics, indicating that this condition is not self-sustained for long time. A different situation can be observed during the PM2 dynamics, Fig. 6.14(b): the plenum pressure (blue), the chamber pressure (black) and the global heat release rate (red) clearly show bi-modal oscillations. The heat release rate oscillates with a phase difference less then $\pi/2$

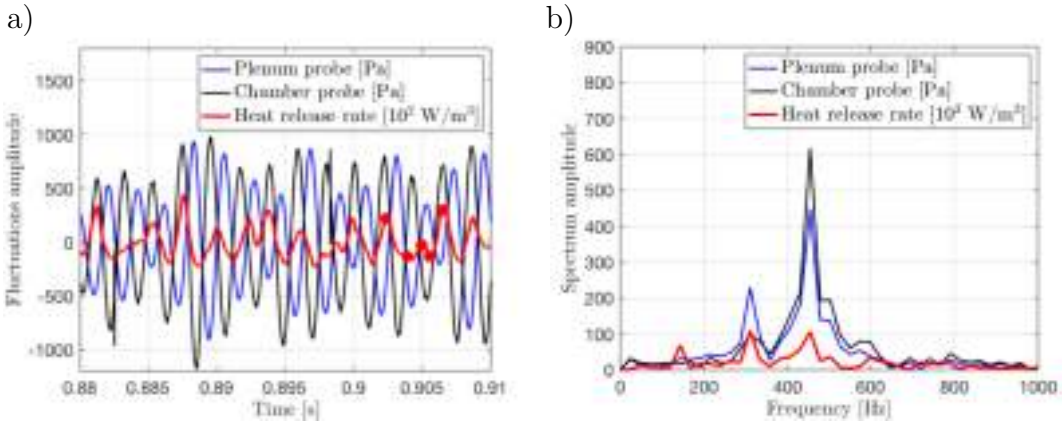

Figure 6.15: (a) LES predicted fluctuations of pressure in the plenum (blue) and at the combustion chamber backplane (black) and heat release rate (red). (b) Signals spectra obtained via Fast Fourier Transform (FFT). Case *C*: 50% H_2.

with respect to the chamber pressure, satisfying the Reyleigh criterion, but the chamber pressure fluctuates in opposition of phase with respect to the plenum pressure. The signal spectra presented in Fig. 6.14 (d) confirms these observations and show that the prevalent mode is the one at 470 Hz while a weaker peak is visible for the heat release rate and for the plenum pressure at 280 Hz. The fact that f_2 is not an harmonic of f_1 leads to a volume-integrated OH* chemiluminescence signal that oscillate with a non-repeatable pattern and exhibits strong peaks followed by lower peaks due to the combination of the two modes. Moreover, the three-dimensional phase space representation of the pressure fluctuation recorded at the combustion chamber for the PM2 dynamics presented in Fig. 6.14 (f) shows how the pressure amplitude is much more constant than for the PM1 dynamics, suggesting that this is the "natural" state of the system: indeed this is the dynamics that is prevalent for the major part of the experimental signals. Therefore, case C can be classified as a P2-BMO (two peaks in pressure signals and heat release rate) in which the relative importance of the two modes varies intermittently with the second mode being statistically prevalent (PM2) on the first one (PM1), as observed in Fig. 6.13.

The system dynamics being quite complex, it is legitimate to ask whether CHT LES simulations are able to correctly predict the flame dynamics. The numerically-predicted fluctuations of pressure in the plenum (blue) and at the combustion chamber backplane (black) and heat release rate (red) are presented in Fig. 6.15 (a). Pressure oscillations are notably higher than cases A and B and reach an amplitude of 1500 Pa, in line with the experimental trend. Note that the LES slight overestimation of the pressure levels is a typical outcome

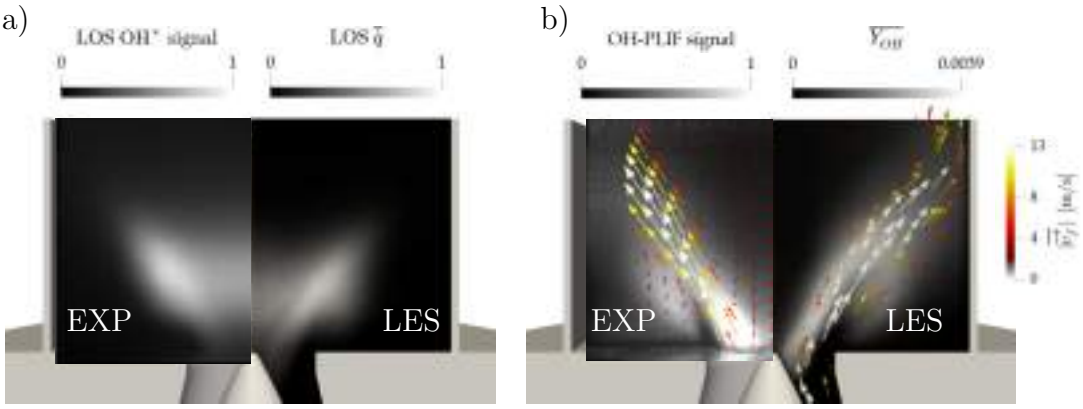

Figure 6.16: Validation of CHT simulations. (a) Comparison of experimental normalized time-averaged Line of Sight (LOS) OH* chemiluminescence image with LOS predicted heat release rate $\dot{\bar{q}}$. (b) Comparison of experimental normalized time-averaged OH-PLIF signal with predicted OH mass fraction $\overline{Y_{OH}}$. The arrows are tangential to the experimental and numerical time-averaged velocity field in the plane $\overline{\overrightarrow{v}}_{//}$. Their length and color indicate the velocity magnitude. Case *C*: 50% H_2.

when simulating thermoacoustic oscillations since experimentally there can be damping due to losses of acoustic energy at the boundaries of the system that cannot be fully reproduced by LES. For example, vibration of the combustion chamber walls may reduce the oscillation amplitudes [11, 179]. Plenum pressure (blue) fluctuates in opposition of phase with the chamber pressure (black), while the heat release rate (red) oscillates in phase with the chamber pressure, satisfying the Rayleigh criterion and indicating the presence of self-sustained thermoacoustic oscillations. The amplitude of the oscillations are not constant through time for both the pressure signal and the heat release rate, suggesting the presence of a multi modal oscillation. As it happens in experiments, also in LES the heat release rate shows peaks of different amplitude according to the combination of the different modes. The signal spectra obtained via Fast Fourier Transform (FFT) are presented in Fig. 6.15 (b) and confirm the presence of bi-modal self-sustained oscillations. In particular, two peaks are visible both in the pressure signals and in the heat release rate. The first weak peak is at 310 Hz and is satisfactory close to the experimental value (i.e. 280 Hz), while the second one, which is much stronger, matches the experimental frequency of 470 Hz. Therefore, LES is correctly able to retrieve the prevalent second mode (PM2) dynamics with the heat release rate that correctly responds to both the two modes, as evidenced by the signal spectrum.

Validation of the numerically-predicted flame shape can be performed by looking at Fig. 6.16 (a) presenting a comparison of the experimental normal-

ized time-averaged Line of Sight (LOS) OH* chemiluminescence image with the LOS integration of predicted heat release rate $\bar{\dot{q}}$. The flame appears to be drastically shorter and much more compact with respect to the pure CH_4 and the 20% H_2-enriched flames due to the increase in laminar flame speed due to larger hydrogen enrichment (see Appendix C on the chemical scheme reduction for a more detailed discussion). The flame therefore does not reach anymore the lateral chamber walls and stabilizes much upstream. LES is able to correctly predict the flame shape while the predicted flame length is slightly underestimated. A more detailed comparison is performed in Fig. 6.16 (b), showing the experimental normalized time-averaged OH-PLIF signal and the numerically-predicted OH mass fraction $\overline{Y_{OH}}$. In both experiments and LES, the OH field is less extended compared to cases *A* and *B* but its reduction in length is less evident if compared to the decrease in flame length visible from the heat release rate field. For example, the OH field almost reaches the lateral chamber walls while the heat release rate is much more compact. At the same time, the peak value of the OH mass fraction is more than double with respect to the other cases and the higher value is reached just downstream the centerbody tip. Some OH is visible also in the ORZs indicating that, as opposed to cases *A* and *B*, some reactions happen also in these regions leading to a reduced flame lift-off distance from the backplane. The corresponding acceleration of the flow due to combustion is visible from the arrows that are tangential to the experimental and numerical time-averaged velocity field in the plane $\overrightarrow{\overline{v}_{//}}$. Their length and color indicate the velocity magnitude and show that no OH signal is observed in the high velocity region just downstream the centerbody tip.

A more quantitative validation of the velocity field can be performed by comparing the LES profiles of mean (a) axial, (b) radial and (c) tangential velocity components with the experimental data at different measurement planes downstream of the combustion chamber backplane in Fig. 6.17. The axial velocity component, Fig. 6.17(a), shows an extended CRZ whose magnitude is well captured by LES. The latter is able to predict the correct opening of the jet (i.e. flame angle) as already observed from the flame shape validation. The radial velocity, Fig. 6.17 (b), and the tangential velocity, Fig. 6.17(c), components LES profiles present satisfactory agreement with the experimental data, in terms of jet opening and magnitude. RMS profiles of (a) axial, (b) radial and (c) tangential velocity components at different measurement planes are presented in Fig. 6.18. Also in this case, LES results are in satisfactory agreement with experimental data. The LES slight overestimation of the rms velocity components can be attributed to the uncertainty of the experimental data (see the small absolute

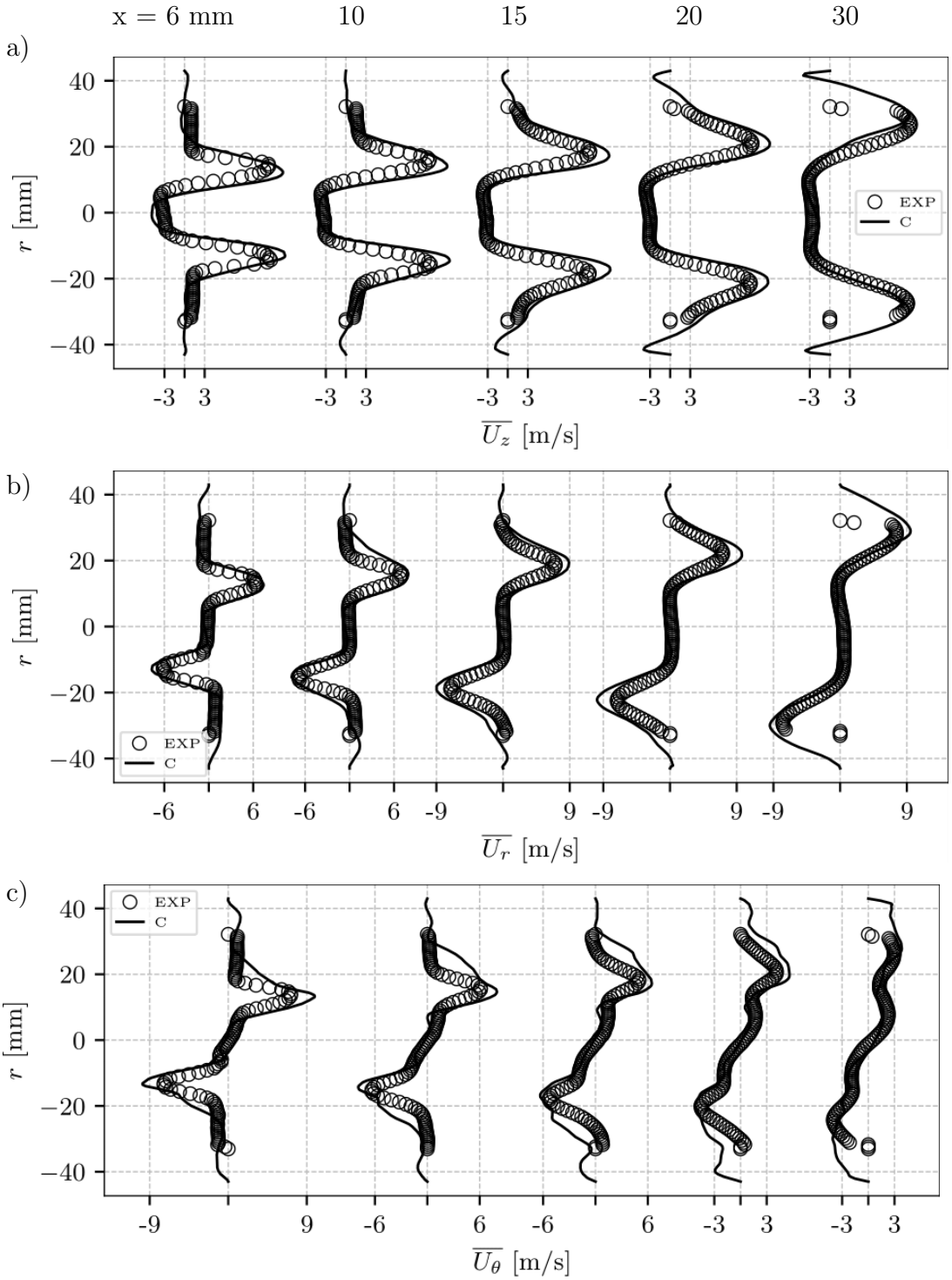

Figure 6.17: Profiles of mean (a) axial, (b) radial and (c) tangential velocity components at measurement planes at x = 6, 10, 15, 20 and 30 mm downstream of the combustion chamber backplane for LES in comparison to experiments. Case *C*: 50% H_2.

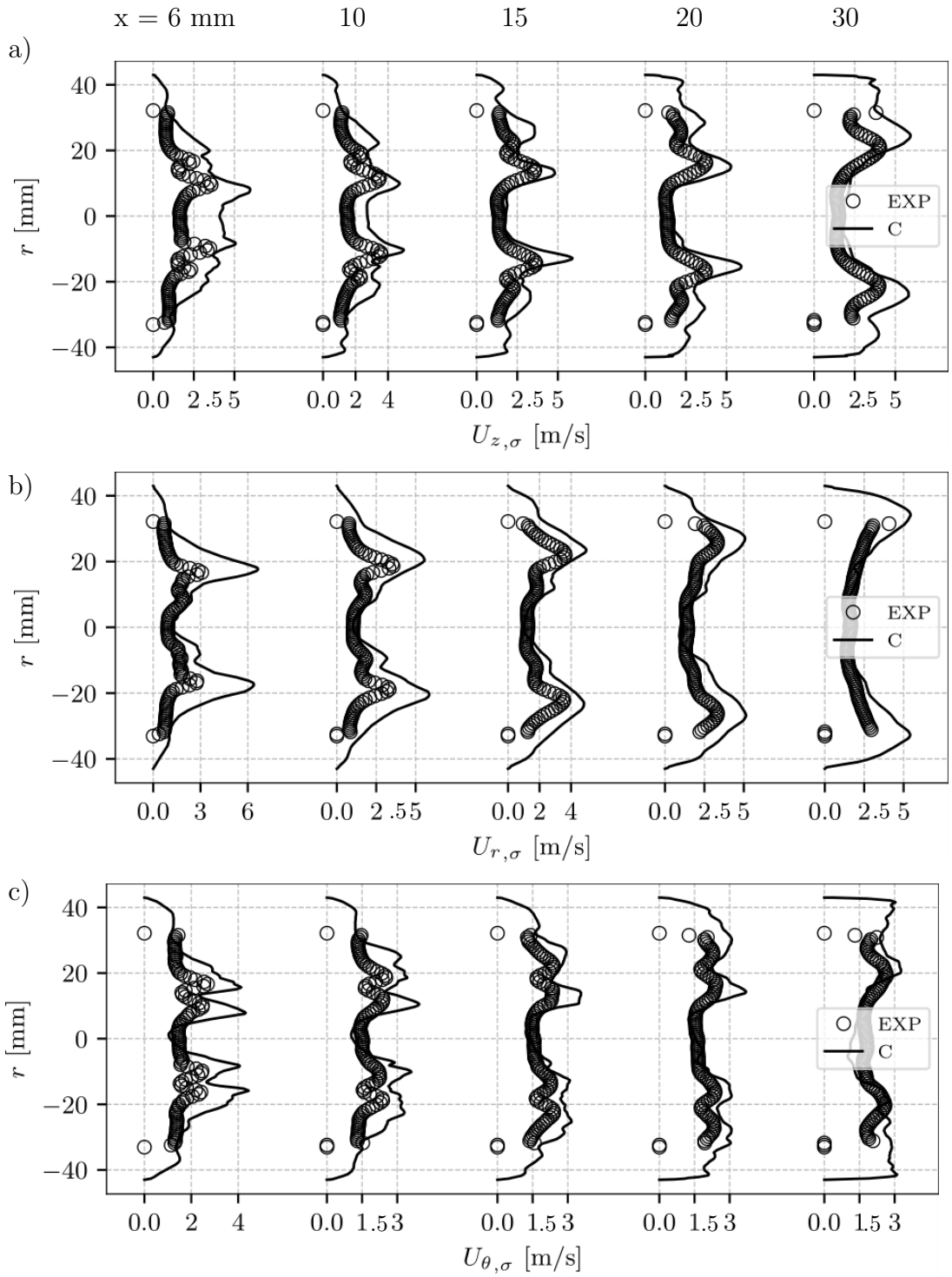

Figure 6.18: Profiles of RMS (a) axial, (b) radial and (c) tangential velocity components at measurement planes at x = 6, 10, 15, 20 and 30 mm downstream of the combustion chamber backplane for LES in comparison to experiments. Case *C*: 50% H_2.

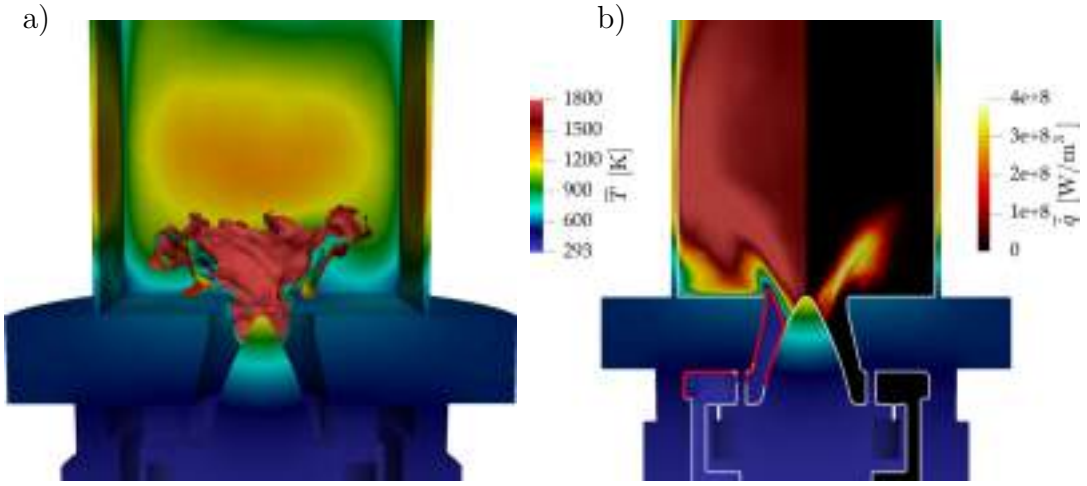

Figure 6.19: (a) Instantaneous field of solid temperature with iso-contour of heat-release rate $\dot{q}$ at 10% of maximum value. (b) Cut-plane showing the time-averaged temperature $\overline{T}$ and heat release rate $\overline{\dot{q}}$ predicted by CHT simulations. Red iso-contour corresponds to temperature of 450 K, showing the pre-heating of the fresh gases due to the warmed-up solid. The fluid domain is delimited by a white line to visualize the separation between solid and the fluid parts. Case *C*: 50% H_2.

magnitude of the rms), to the possibly larger averaging time needed to reach full statistical convergence and to the slightly larger pressure levels oscillations predicted by LES.

Results of the CHT simulations are presented in Fig. 6.19. The instantaneous field of solid temperature with iso-contour of heat-release rate $\dot{q}$ at 10% of maximum value is presented in Fig. 6.19 (a). The combustion chamber walls and the backplane have a temperature similar to the low hydrogen-enriched and to the pure methane flames. Major differences are visible at the centerbody tip that reaches a temperature of around 1200 K, much higher than the other two cases. The flame clearly gets shorter with a reduced lift-off distance from the backplane. In addition, the stabilization point of the flame gets more upstream during the thermoacoustic oscillations, explaining the warmer temperature of the centerbody tip. Figure 6.19 (b) presents the predicted time-averaged temperature $\overline{T}$ and heat release rate $\overline{\dot{q}}$ on a cut-plane. Being the flame length reduced, the combustion chamber results to be sooner filled by hot burnt gases while also the ORZs get warmer. The red iso-contour corresponds to temperature of 450 K and shows how the pre-heating of the fresh gases happens more upstream due to the higher warmed-up centerbody. The time-averaged heat release rate field $\overline{\dot{q}}$ presents a blurry flame root near the centerbody tip, indicating that the flame stabilization point moves in time during the thermoacoustic oscillations.

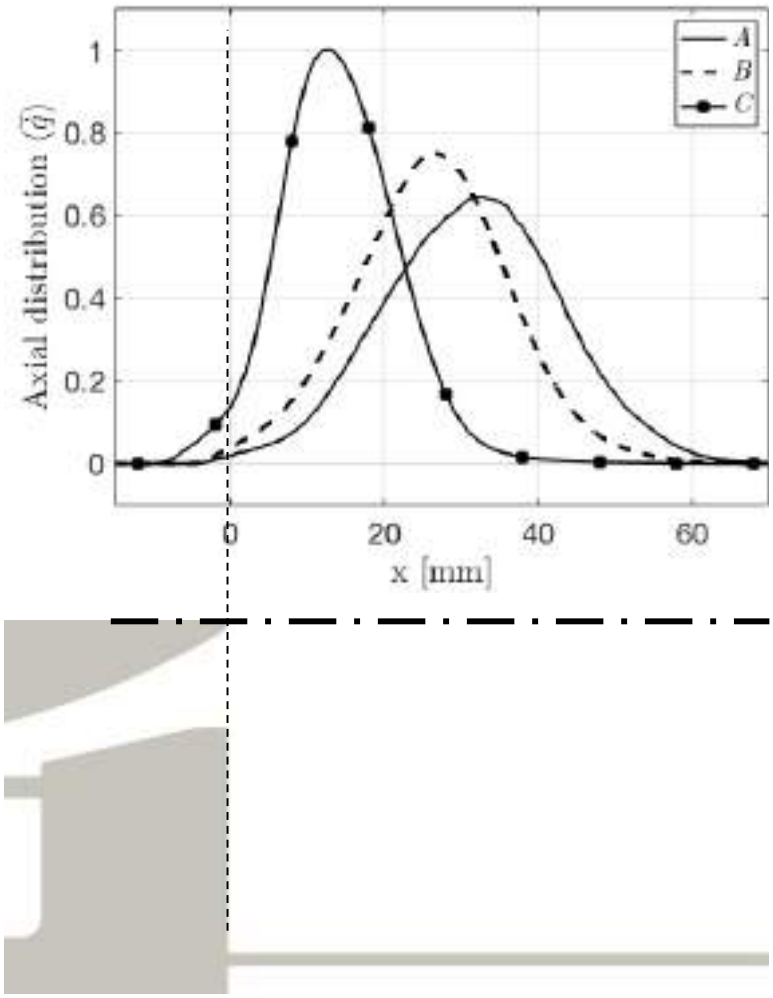

Figure 6.20: Comparison of normalized axial distributions of time-averaged heat release rate $\langle\bar{\dot{q}}\rangle$ for cases *A*, *B* and *C*.

6.3.4 H_2-enrichment impact on the instability driving mechanisms

Once the three flames have been presented via experimental data and CHT simulations, it is possible to further analyze the impact of H_2-enrichment on the flame stabilization and dynamics. First, to obtain a more quantitative comparison between the three flames in terms of shape and stabilization, the time-averaged heat release rate can be integrated over the combustor cross section S_c to obtain the one-dimensional mean axial distribution $\langle\bar{\dot{q}}\rangle$:

$$\langle\bar{\dot{q}}\rangle(x) = \frac{1}{S_c}\iint_{S_c}\bar{\dot{q}}(x,y,z)dydz. \tag{6.1}$$

The normalized axial distributions of time-averaged heat release rate $\langle\bar{\dot{q}}\rangle$ for cases A, B and C are presented in Fig. 6.20. The pure methane flame (case A)

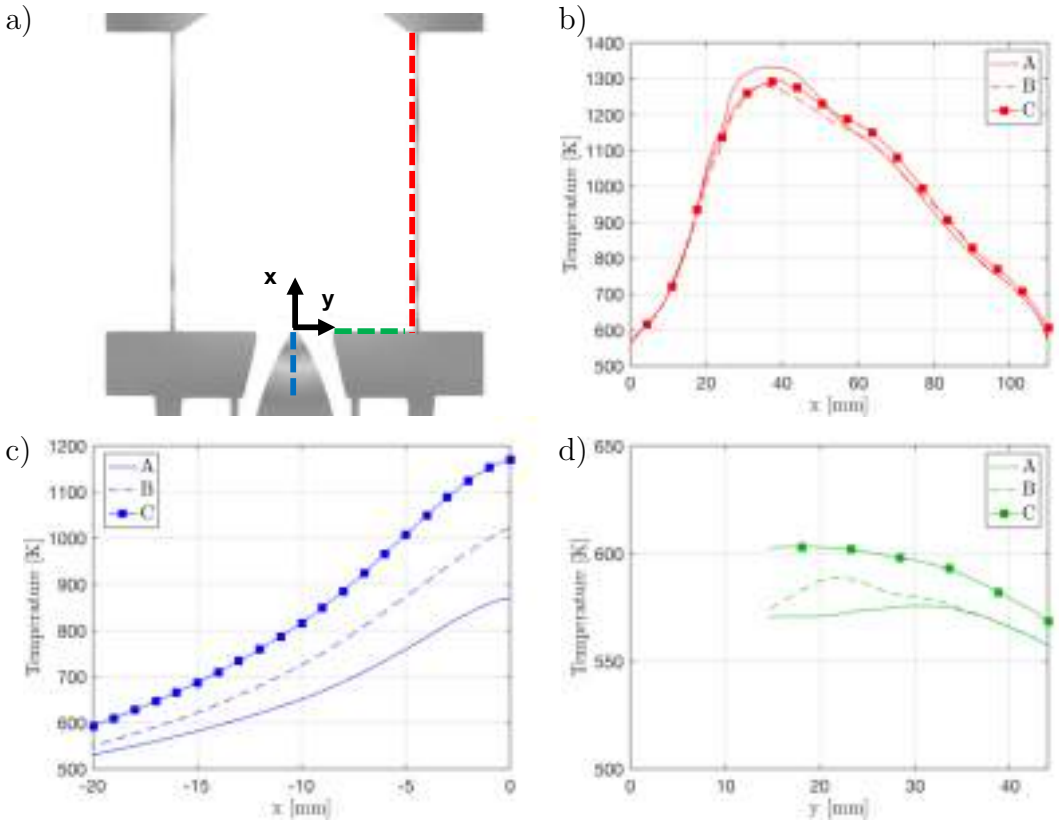

Figure 6.21: Comparison of CHT-predicted solid temperature for flames *A*, *B* and *C*. (a) Schematic of the test bench with location of the profiles. Temperature profiles (b) along the internal side of the combustion chamber walls, (c) through the centerbody and (d) at the backplane.

presents the most spread out axial distribution, with a maximum heat release rate at around 35 mm from the backplane and a weak heat release rate at the centerbody tip axial location (i.e. 0 mm). When 20% H_2-enrichment is considered (case *B*), the mean axial distribution changes: the flame becomes slightly shorter and it is shifted upstream, presenting a higher maximum of heat release rate around 25 mm downstream of the backplane. The flame root stabilization point does not largely differ from the pure methane case in terms of location but presents increased values of heat release rate more upstream. The 50% H_2-enriched case instead shows significant differences in the axial distribution of mean heat release rate. The latter has a notably higher maximum, located around 14 mm from the backplane, and the flame is more compact and shifted upstream. At the same time, the mean stabilization location of the flame root is shifted also up to 10 mm from the backplane in the upstream direction. Hence, the axial distribution of mean heat release rate is slightly different for flames *A* and *B* but drastically changes for flame *C* when hydrogen enrichment is sufficiently high to produce significant changes in the flame properties (e.g. laminar flame speed).

Clearly, the various mean heat release distributions lead to differences in the solid temperatures. To have a better quantification, a comparison of the CHT-predicted solid temperature for flames A, B and C is presented in Fig. 6.21. The schematic of the test bench, Fig. 6.21(a), helps visualize the location of the profiles. The temperature profiles along the internal side of the combustion chamber walls, Figure 6.21(b), are very similar for the three flames, except for the peak at 40 mm from the backplane where case A exhibits slightly larger values than the hydrogen cases, probably due to the longer flame that reaches the chamber walls. On the contrary, the temperature field at the centerbody, Figure 6.21(c), differs significantly for the three cases. Being the heat release rate distribution more compact and stabilized upstream at higher levels of hydrogen enrichment, flame C exhibits larger centerbody tip temperature than cases A and B. Note that in case B the centerbody tip temperature is notably higher than the pure methane flame even if the mean heat release rate axial distribution is not so different, suggesting that the solid temperature is more sensitive to low levels of hydrogen enrichment than the mean heat release rate distribution. Finally, the temperature profiles at the chamber backplane, Figure 6.21(d), show a similar trend due to the reduction of the flame lift-off distance when increasing the hydrogen content. However, the absolute temperature differences remain quite modest, leaving to the solid temperature at the centerbody tip the main difference between the three analyzed cases.

In the literature, as underlined in the introduction, hydrogen enrichment leads to higher flame temperature and more compact flames that in turns may cause not only larger localized thermal load, as observed in the CHT results, but also to differences in the mean sound speed field, affecting the thermoacoustic modes of the combustor [67, 68, 69]. The computed time-averaged sound speed $\overline{c}$ are therefore compared in Fig. 6.22 for flames (a) A, (b) B and (c) C. A globally lower sound speed value is achieved for cases A and B than flame C. As expected, the slight difference in temperature fields for cases A and B lead to marginal differences in the sound speed field. The 50%-enriched case instead presents more evident differences, especially near the centerbody and in the ORZs, due to the higher adiabatic flame temperature, to its shorter length and to the reduced lift-off distance from the backplane. However, except for this localized differences, the mean global sound speed in the combustion chamber is quite similar for all the three flames, indicating that for the thermal power P_{th} considered, the hydrogen enrichment levels used are not sufficiently high to bring large differences in the sound speed fields and hence in the system acoustic modes.

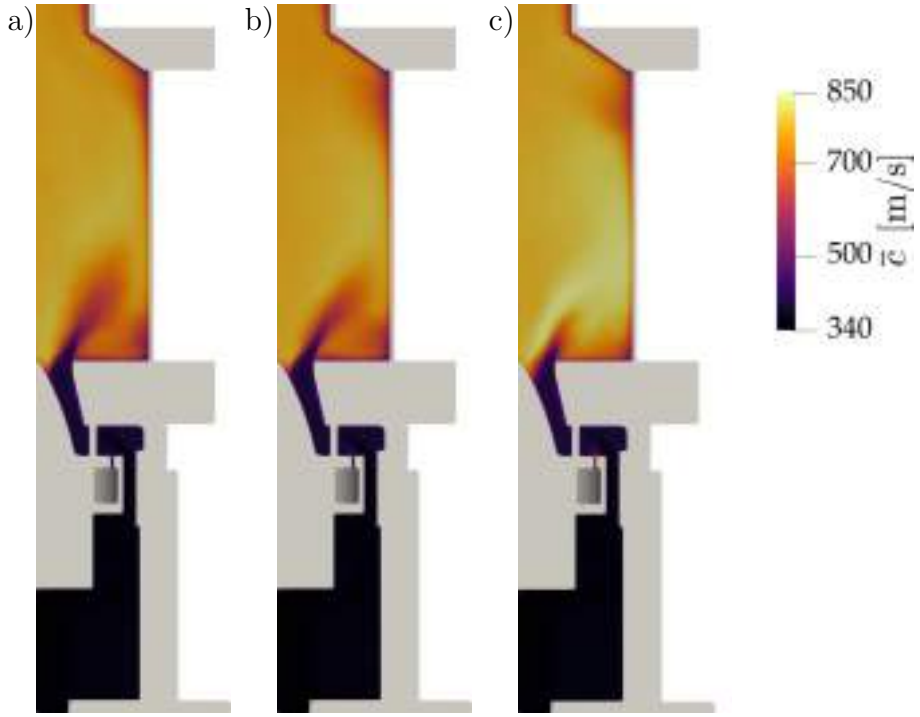

Figure 6.22: LES-predicted time-averaged sound speed field $\bar{c}$ for cases (a) *A*, (b) *B* and (c) *C*.

To confirm this hypothesis, the mean temperature fields have been used to compute the acoustic modes of the system using the AVSP Helmholtz solver [53], showing no significant differences in the frequencies of the first modes for the three cases[1]. While flames A and B have the first three acoustic modes at a frequency of 275, 482 and 581 Hz, flame C shows slightly higher frequencies at 280 Hz, 486 HZ and 583 Hz, confirming the marginal impact of the 50% hydrogen enrichment on the acoustic modes of the system.

The acoustic modes for flame C are presented in Fig. 6.23. The first mode is predicted at a frequency of 280 Hz. Modulus and phase data, Fig. 6.23(a-b), suggest that this 280 Hz mode is the 1/4 wave (or bulk) mode of the system: the amplitude of the pressure oscillation $|p'|$ is larger in the plenum, Fig. 6.23(a), and both the chamber and the plenum oscillate in phase, Fig. 6.23(b). The thermoacoustic oscillations experimentally observed for flame C for the prevalent first mode (PM1) dynamics, Fig. 6.14(a), at a frequency of 280 Hz correspond to the frequency of the 1/4 wave mode, suggesting that the flame couples with this first mode during the PM1 dynamics: also experimentally the plenum and the chamber oscillate in phase, with the plenum oscillation amplitude being larger

[1]Note that, in the Helmholtz solver, a velocity node has been imposed for the air and fuel inlets, while a pressure node has been imposed at the combustion chamber outlet as acoustic boundary conditions.

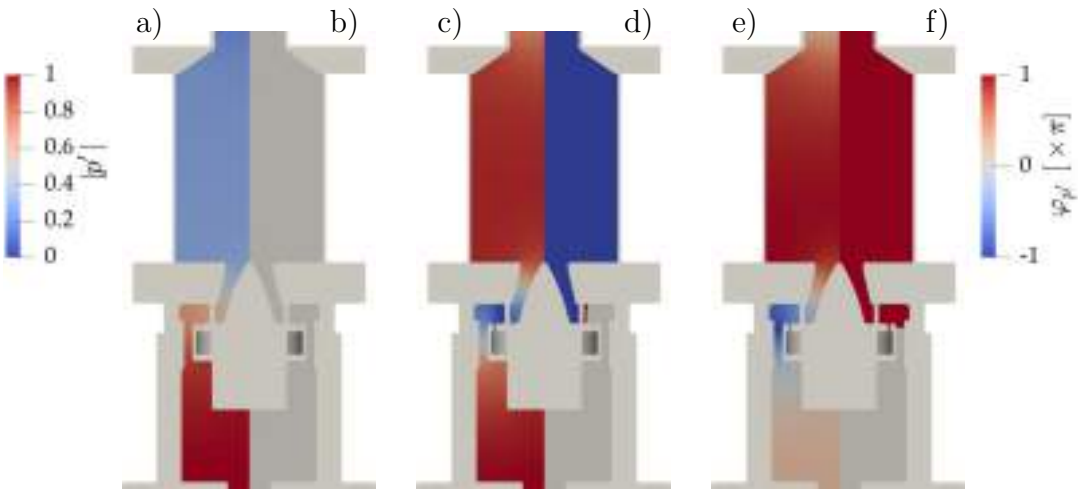

Figure 6.23: Acoustic modes computed with the Helmholtz solver for flame *C*. (a) Amplitude and (b) phase of the first acoustic (plenum) mode at 280 Hz. (c) Amplitude and (d) phase of the second acoustic (chamber) mode at 486 Hz. (e) Amplitude and (f) phase of the third acoustic mode at 583 Hz.

than the chamber one, as in the first acoustic mode. Note that this first acoustic mode is the one that is generally excited when dealing with unstable pure methane flames during limit cycle oscillations in the PRECCINSTA test bench, as for example in the work from Meier *et al.* [27] and Franzelli *et al.* [130].

The amplitude and phase of the second acoustic mode at 486 Hz are shown in Fig. 6.14 (c) and Fig. 6.14 (d), respectively. It corresponds to a 3/4 wave (chamber) mode: a pressure antinode is found in the combustion chamber and both the two volumes of the system (i.e. combustion chamber and plenum) oscillate in phase opposition. Flame *C* couples with this second mode during the prevalent second mode (PM2) dynamics, Fig. 6.14(b), at an experimental frequency of 470 Hz, slightly lower than the computed frequency of the second acoustic mode. Note that both experimentally and numerically the plenum pressure oscillates almost in opposition of phase with respect to the combustion chamber pressure: amplitude of the chamber oscillations are however not-constant and lower than the plenum ones due to the combination of the second mode with the first acoustic mode oscillations at 280 Hz, Fig. 6.14(b). To the author's knowledge, the coupling of the flame with this second mode has never been observed in this test bench when dealing with classical pure methane flames and it is therefore a unique characteristic of the hydrogen enriched flame.

The amplitude and phase of the third acoustic mode at 586 Hz are presented in Fig. 6.14 (e) and Fig. 6.14 (f), respectively. Plenum and chamber pressures oscillate in opposition of phase, while the higher oscillation amplitude happen in the combustion chamber. Traces of this mode are visible also in experiments and

LES during the PM1 dynamics, Fig. 6.14(a), but the flame does not couple with this mode.

Having understood that the PM2 dynamics, characteristic of the hydrogen-enriched flame, is due to the coupling of the flame with the first two acoustic modes of the system, it is now interesting to further analyze the flame dynamics during the thermoacoustic oscillations. To do so, Fig. 6.24 presents the phase-locked instantaneous fields of experimental normalized time-averaged OH-PLIF signal (up) in comparison to LES-predicted OH mass Y_{OH} (down) during the thermoacoustic oscillations. The signals being a combination of two modes, the amplitude of oscillation is not constant and depends on the interference between the two modes in time, giving rise to a series of large and small peaks in the pressure and heat release rate signals. To analyze the PM2 dynamics, five equivalent instants for experiments and LES are considered as depicted in Fig. 6.14 (b) and Fig. 6.15 (a), respectively. Instants (a) and (e) correspond to two large consecutive peaks in the volume-integrated OH* chemiluminescence signal (up) and the predicted heat release rate. Instant (b) and (d) correspond to two minima while instant (c) corresponds to a small intermediate peak of the signals. At the beginning, when the heat release rate reaches a large maximum, Fig. 6.24(a), the flame is quite elongated and LES correctly captures the flame front wrinkling due to turbulence or the increase of the flame surface observed experimentally. LES shows that the flame roots are stabilized quite upstream at the centerbody walls while the flame branches are distant and almost vertical at the base (i.e. parallel to the axial direction) as in the experiments. After the large burst of heat release rate, the signal reaches a minimum, Fig. 6.24(b), when the flame surface clearly reduces both in experiment and LES: the flame is much shorter and the tips are closer to the backplane. The flame roots are stabilized downstream just at the centerbody tip and are much closer than instant (a), showing a concave curvature indicating that the flame is moving downstream. This movement of the flame root upstream and downstream has been analyzed in some unstable pure methane cases, such as Franzelli *et al.* [130], and it was showed to be linked to rich-fuel gas pockets periodically released in the combustion chamber at the frequency of the system first acoustic mode. At instant (c), a small peak of the heat release rate is now reached: the flame surface clearly increases and the flame gets longer but the flame wrinkling appears to be less significant than the large peak of heat release rate of instant (a). The flame roots are again stabilized upstream and almost vertical while being much closer if compared to instant (a). A new minimum is reached at instant (d). The flame length has not changed significantly but the flame roots are moving upstream, as showed by the convex

Figure 6.24: Phase-locked instantaneous fields of experimental normalized time-averaged OH-PLIF signal (up) and LES-predicted OH mass Y_{OH} (down) during the thermoacoustic oscillations. Five equivalent instants are considered during the PM2 dynamics for experiments and LES as depicted in Fig. 6.14 (b) and Fig. 6.15 (a), respectively. Instants (a) and (e) correspond to two large consecutive peaks in the volume-integrated OH* chemiluminescence signal (up) and the predicted heat release rate. Instant (b) and (d) correspond to two minima while instant (c) corresponds to a small intermediate peak of the signals. Case *C*.

curvature. Finally, instant (e) shows the flame at a large peak of heat release rate. Equivalently to instant (a), the flame length and surface are maximum with a significant wrinkling of the flame front due to turbulence. A strong OH signal is present both in experiments and in LES just above the right corner of the backplane. If one looks more carefully, the same strong signal pocket can be seen also at instants (a) and (c), suggesting the presence of vortical structures periodically detached from the backplane and causing the flame roll-up. With the limits of choosing equivalent instants in non-constant amplitude oscillations, LES is found to be able to correctly predict the flame dynamics in comparison with experiments, providing also insights on the flame roots stabilization that are not visible with experimental OH-PLIF diagnostics only.

Flame dynamics is further investigated in Fig. 6.25, presenting instantaneous LES-predicted fields of hydrogen mass fraction Y_{H_2} (left) and flow vorticity normal to the plane $\omega_\perp$ with superimposed the heat release rate $\dot{q}$ during the thermoacoustic oscillations. The same five instants depicted in Fig. 6.15 (a) and discussed in Fig. 6.24 are considered. At instant (a), the flame is clearly elongated and the flame roots are vertical and stabilized upstream at the centerbody walls. The flow vorticity shows a strong activity along the flame branch, explaining the flame front wrinkling, and also a strong structure (in purple) just above the backplane right corner. The vortices appear to detach from the centerbody tip and from the backplane corner, affecting the flame front. At the same time, the hydrogen mass fraction field presents a non uniform distribution with the flow near the centerbody more rich in hydrogen than the flame tips. The successive minimum of heat release rate at instant (b) is characterized by a much shorter flame, as already observed from the OH-PLIF signal. The hydrogen field is more homogeneous just upstream the flame front, suggesting that the homogeneous region visible upstream of the flame root at instant (a) was convected downstream. The flame tips being much closer to the backplane, the vortical structure at the backplane right corner is strongly interacting with the flame front. Also since the flame roots are stabilized further downstream they are subject to the region of large flow vorticity starting at the centerbody tip. Note also that after the swirler the fuel jet is not deviated, indicating low velocity at this instant of the thermoacoustic oscillations. When a successive small peak of heat release rate is reached at instant (c), the flame is again elongated and the flame roots are stabilized upstream. However, the vortex at the backplane right corner is less important while the flow vorticity is wrinkling the flame front near to the centerbody tip. The hydrogen pocket near the flame front has further moved downstream, leaving the flame roots facing a relatively poor hydrogen region (dark blue at the left

Figure 6.25: Phase-locked instantaneous LES-predicted fields of hydrogen mass fraction Y_{H_2} (left) and flow vorticity normal to the plane $\omega_\perp$ with superimposed the heat release rate $\dot{q}$ during the thermoacoustic oscillations. Five instants are considered during the PM2 dynamics for LES as depicted in Fig. 6.15 (a). Instants (a) and (e) correspond to two large consecutive peaks in the predicted heat release rate. Instant (b) and (d) correspond to two minima while instant (c) corresponds to a small intermediate peak of the signal. Case *C*.

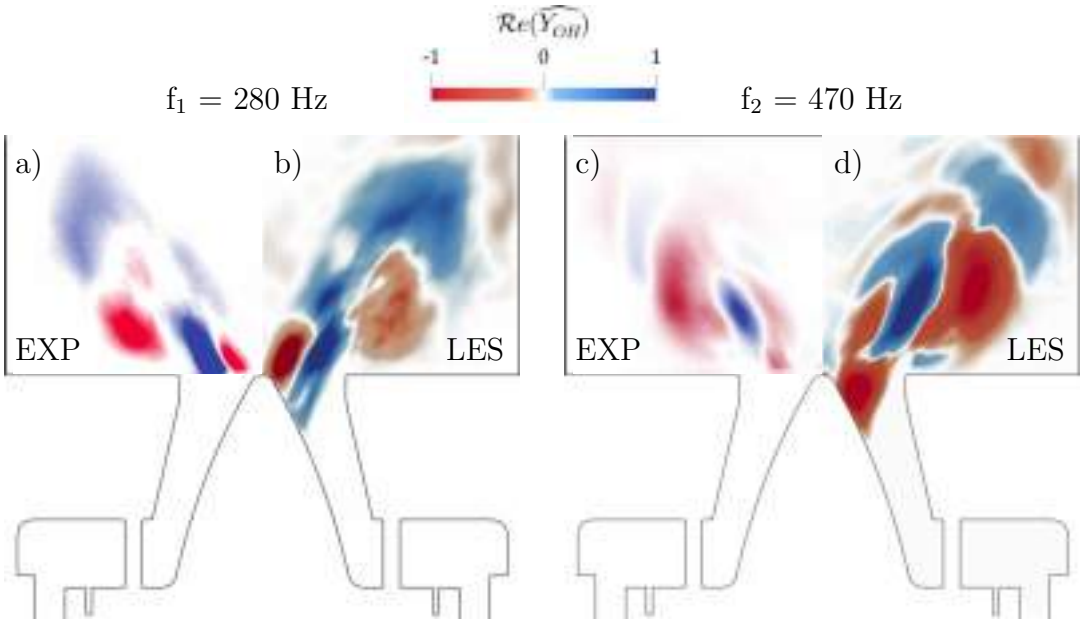

Figure 6.26: Cut-plane showing the Dynamic Mode Decomposition (DMD) at (a-b) the first (280 Hz) and (c-d) the second (470 Hz) acoustic modes frequencies during the PM2 flame dynamics. Comparison of normalized real part of the experimental OH-PLIF signal and the LES-predicted OH mass fraction in frequency domain $\mathcal{R}e(\widehat{Y_{OH}})$. Case *C*.

backplane corner). At the fuel injection tube, the deviation of the fuel jet is now evident due to the pressure oscillations in the swirler: rich fuel gas pockets are periodically released into the test chamber. The minimum of heat release rate at instant (d) presents a shorter flame if compared to instant (c) with the flame roots stabilized more downstream. Two vortical structures are clearly visible at the right backplane corner (in purple) and close to the centerbody tip (in green) but the large flame length avoids strong interactions with the vortex detaching from the backplane. On the left, the hydrogen-rich pocket is convected further downstream and reaches now the flame tip. A new maximum is reached at instant (e): flame wrinkling is more evident and the two vortical structures from the centerbody tip and the backplane have reached the flame front, increasing the flame surface and the heat release rate. To resume, the present analysis suggests that the flame dynamics is characterized by four periodic phenomena: the change in flame length and flame surface, the stabilization point of the flame roots that moves upstream/downstream along the centerbody walls, the flapping of the jet fuel causing rich gas pockets to be released in the combustion chamber and finally the vortical structures detaching from the centerbody tip and the backplane interacting with the flame front yielding wrinkling and flame roll-up.

To perform a more accurate flame dynamics analysis and have a more quan-

titative comparison between experiments and LES, the flame response is also investigated using Dynamic Mode Decomposition [185] (DMD). DMD allows to reconstruct the oscillating modes of the system and extract the response of the variables of interest at a certain frequency [186]. For the present study, since the 50% H_2-enriched case presents bi-modal thermoacoustic oscillations, the frequencies of interest are selected at the first (280 Hz)[1] and at the second (470 Hz) acoustic modes of the system. To compare the flame dynamics at the frequencies of interest both in experiments and LES, experimental OH-PLIF signal and LES-predicted OH mass fraction are selected as variables of interest for the DMD analysis[2]. DMD input for the experimental data is 1000 OH-PLIF images while, for the simulations, the input is 2300 instantaneous 3D LES fields. Once the DMD is obtained, it is possible to compare and investigate the coherent spatial features. Figure 6.26 presents a cut-plane showing the Dynamic Mode Decomposition (DMD) at (a-b) the first and (c-d) the second acoustic modes frequencies during the PM2 flame dynamics. In both cases, the normalized real part for the experimental OH-PLIF signal is compared to the predicted OH mass fraction in the frequency domain $\mathcal{R}e(\widehat{Y_{OH}})$. The spatial distributions of the OH signal at the system first and second acoustic modes for both LES and experiments show coherent regions, indicating the presence of a OH signal response to the thermoacoustic oscillation at these frequencies of interest, a result that was expected since the OH mass fraction is strictly linked to the flame front position. For the first mode, Fig. 6.26 (a-b), the two largest red coherent regions correspond both in experiments (a) and in LES (b) to the zones just downstream the backplane corner and at the centerbody tip where the OH variation is significant. On the contrary, the region at the swirler exit shows a marked blue color, indicating strong OH variation in opposition of phase with respect to the two red regions just mentioned. This blue region extends, both in LES and in experiments, for all the flame branches up to the flame tips. At the same time, the DMD at the second acoustic mode frequency (Fig. 6.26 (c-d) presents the same two relevant red coherent regions corresponding, both in experiments (c) and in LES (d), to the zones just downstream the backplane corner and to the centerbody tip but, for this mode, the amplitude OH variation appear to be of the same order of magnitude for these two regions. On the contrary, the two most significant blue coherent regions are visible just downstream the red zones, namely at the flame

[1]Note that, since numerically the oscillations at the first mode correspond to a frequency slightly higher (i.e. 310 Hz), clearly the latter is used for extracting the DMD from LES data.

[2]Note that, complementarily, DMD analysis could be performed on OH* chemiluminescence images compared to heat release rate. Here OH is preferred as it provides directly information on the plane.

tips and at the center of the flame branches. The extremely good match between DMD spatial distribution of experimental OH-PLIF signal and LES OH mass fraction gives further confidence to the correct reproduction of the flame dynamics by LES. Besides the simulations validation, DMD mode of the OH signals can provide useful information about the flame oscillation mode. Results indicate that the two red regions correspond to the zones of high flow vorticity periodically observed in LES (see Fig. 6.25 and to the corresponding high levels of OH signals observed both in experiments and LES (see Fig. 6.24).

It is important here to stress the modeling efforts put in LES in order to achieve the correct flame dynamics prediction. In particular, four factors have been determined to be essential for achieving a high-fidelity LES:

- CHT context: hydrogen enrichment can significantly modify the thermal boundary conditions and the flame dynamics in the PRECCINSTA test rig has been showed to strongly depend on the heat transfer at the walls [59]. Not correctly modeling the heat transfer would bring to a mismatch in the predicted flame dynamics.

- Dynamic efficiency model: a dynamic formulation is needed to take into account variations in flow vorticity and flame wrinkling during the thermoacoustic oscillation [136]. In particular, when the periodically detaching vortices interact with the flame front, the dynamic model predicts higher flame wrinkling and hence heat release rate. Not considering the effect of flow vorticity would lead to an unsatisfactory description of the flame-vortex interaction in the LES context.

- Mesh resolution: a proper discretization of the computational domain is needed when dealing with H_2-enriched flame due to the lower flame thickness[1]. Moreover, in this specific case, due to the strong importance of the flow vorticity during the thermoacoustic oscillation, a lower mesh resolution would result in a less accurate prediction of the flow turbulent activity [70].

- Chemical scheme: an ARC scheme has been seen to be of fundamental importance to correctly capture the flame dynamics, providing better results if compared to simplified two-step chemistry.

[1]Note that the SMR approach presented in Chapter 3 is able to account for mesh requirements driven by thermoacoustic oscillations. The refinement region is defined indeed from the probability to find the flame in a certain region and the latter takes into account cases in which the flame shape and stabilization change in time due for example to thermoacoustic oscillations.

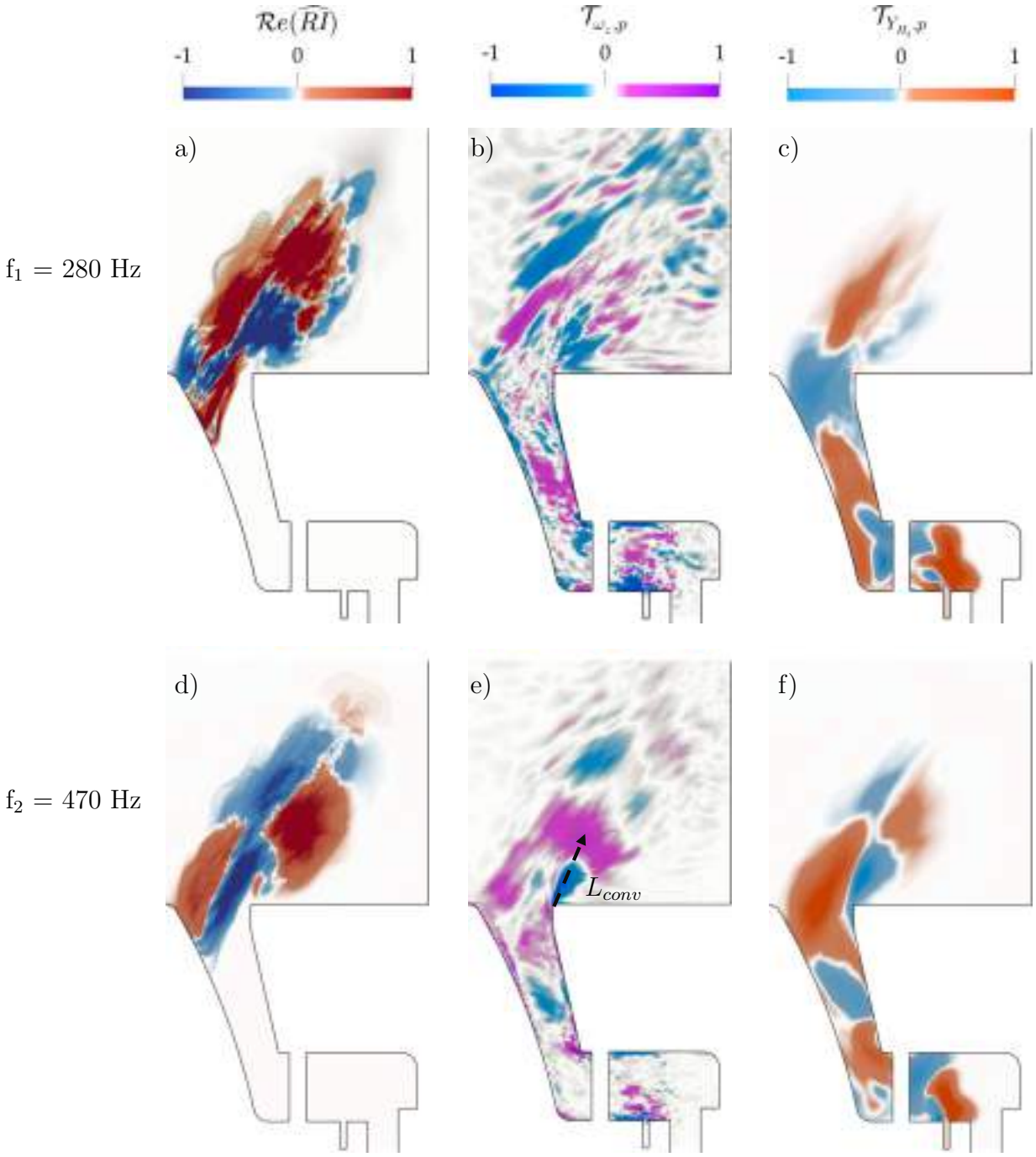

$f_1 = 280$ Hz

$f_2 = 470$ Hz

Figure 6.27: Cut-plane showing the Dynamic Mode Decomposition (DMD) at 280 Hz (top) and 470 Hz (bottom). (a-d) Normalized real part of the Rayleigh index formulation in frequency domain $\mathcal{R}e(\widehat{RI})$. (b-e) Normalized flow vorticity - pressure fluctuations correlation index $\mathcal{T}_{\omega_\perp,p}$. (c-f) Normalized H_2 mass fraction - pressure fluctuations correlation index $\mathcal{T}_{Y_{H_2},p}$. Case *C*.

Once the LES has been validated, to confirm the strong relation between the 50% H_2-enriched flame dynamics and the vortical structures detaching from the centerbody walls and backplane, DMD of the LES data for pressure (p), heat release rate ($\dot{q}$), flow vorticity normal to the plane ($\omega_\perp$), OH mass fraction (Y_{OH}) and H2 mass fraction (Y_{H_2}) are obtained. Thanks to these DMD modes, the coherent spatial features of each variable are accessible and can be compared in terms of phase relative to a reference variable (here pressure). If the heat release rate $\dot{q}$ is selected and the phase difference relative to the pressure DMD mode is computed, a three-dimensional Rayleigh index can be obtained using $\mathcal{R}e(\widehat{RI}) = \mathcal{T}_{q,p} = |\hat{p}||\hat{q}|\cos(\varphi_q - \varphi_p)$ [187, 188]. In the same manner, a vorticity - pressure fluctuations correlation index can be defined as $\mathcal{T}_{\omega_\perp,p} = |\hat{p}||\hat{\omega_\perp}|\cos(\varphi_{\omega_\perp} - \varphi_p)$ and a H_2 mass fraction - pressure fluctuation correlation index follows $\mathcal{T}_{Y_{H_2},p} = |\hat{p}||\hat{Y_{H_2}}|\cos\left(\varphi_{Y_{H_2}} - \varphi_p\right)$ indicating whether fluctuations of flow vorticity $\omega_\perp$ and of H_2 mass fraction Y_{H_2} respectively are contributing positively or negatively to pressure oscillations and hence to thermoacoustic instability. Figure 6.27 presents (a-d) the DMD modes of normalized real part of the Rayleigh index formulation in frequency domain $\mathcal{R}e(\widehat{RI})$, (b-e) the normalized flow vorticity - pressure fluctuations correlation index $\mathcal{T}_{\omega_\perp,p}$ and (c-f) the normalized H_2 mass fraction - pressure fluctuations correlation index $\mathcal{T}_{Y_{H_2},p}$ for the first (top) and the second (bottom) system acoustic modes frequencies. The spatial distribution of the Rayleigh index $\mathcal{R}e(\widehat{RI})$ presents coherent structures for both the first, Fig. 6.27(a), and the second modes, Fig. 6.27(d), as expected during self-sustained thermoacoustic oscillation. For the first mode, Fig. 6.27(a), the flame root at the centerbody walls, together with the flame tips and middle branch, are positively contributing to the oscillation (i.e. red zones) since heat release rate variation happen in phase with pressure oscillation (i.e. positive Rayleigh index). On the contrary, the parts of the flame at the centerbody tip and the region just downstream of the backplane corner are damping the oscillation at this first acoustic frequency. For the second mode instead, Fig. 6.27(d), these are exactly the two regions that are positively contributing to the oscillation (i.e. red zones), namely at the centerbody tip and just downstream the backplane corner (which is the strongest one) where a significant periodical fluctuation of OH signal has been observed both experimentally and in LES, Fig. 6.26. This means that the flame root and the external branches close to the backplane produce heat release rate oscillation in phase with pressure, hence sustaining the thermoacoustic oscillation at this second acoustic mode frequency. On the contrary, the parts of the flame that are negatively contributing to the instability are the flame tips and the flame root when it reaches an upstream position (i.e. blue regions). The

pressure oscillation is therefore enhanced when the the flame root is stabilized at the centerbody tip and the flame external branches burn close to the backplane corners. The different behaviour at the two frequencies modes therefore indicate that different flame parts respond to the two modes. When the flame root is stabilized upstream, heat relase rate oscillation enhances pressure oscillation at the first mode. On the contrary, when the flame root is stabilized just at the centerbody tip and the flame burns just downstream the backplane corner, i.e. red regions in Fig. 6.27(d), heat release rate oscillation enhances the second mode pressure fluctuations.

The analysis of the spatial distribution of the flow vorticity - pressure index $\mathcal{T}_{\omega_\perp,p}$ confirms the strong relation between the vortical structures and the thermoacoustic oscillations, Fig. 6.27(b-e), at the system second acoustic mode. Indeed, while at the first acoustic mode, the spatial distribution of $\mathcal{T}_{\omega_\perp,p}$ appears to be not consistent, for the second mode frequency, a coherent distribution can be noticed. In particular, the two purple regions at the centerbody walls and downstream the backplane show that flow vorticity is varying in phase with pressure, positively contributing to the pressure oscillations thanks to the increase of heat release rate (and OH signal) due to an increase in flame front wrinkling. Note that the small blue region just at the backplane corner indicates that flow vorticity increases (i.e. the vortex is detached from the backplane) when the pressure is decreasing: afterward the vortex is convected downstream and interacts in the purple region with the flame front, contributing positively to the instability. Indeed, the vortex characteristic convection time can be easily estimated from the mean velocity ($\approx$ 13 m/s) and from the distance between the backplane and the point of highest vorticity ($\approx$ 14 mm, see black arrow), giving a value of 1.07 ms, that is half the period of the second acoustic mode at 470 Hz. Note that the point of highest vorticity corresponds to the peak of mean heat release rate axial distribution (see Fig. 6.20): hydrogen is therefore responsible for reducing the length of the flame hence enhancing the interaction between the flame branches and the vortices periodically detaching form the backplane. On the contrary, the vortices at the centerbody walls detach when the pressure is already increasing (i.e. there are not blue regions near the walls) but suddenly interact with the flame roots that are stabilized at the centerbody.

Finally, Fig. 6.27 (c-f) present the H_2 mass fraction - pressure fluctuation correlation index $\mathcal{T}_{Y_{H_2},p}$. A coherent spatial distribution is observed for both the modes, indicating that the periodical fuel flapping of the jet produce H_2 mass fraction oscillation that enhance both the first and the second acoustic modes. Rich-fuel gas pockets are periodically released in the combustion chamber. For the

first mode, positive contribution (red) region is located at the centerbody walls, just upstream the position of the flame root when it is stabilized upstream. For the second mode, the main region of positive (red) contribution is at the flame root while, more downstream, the blue region indicates low levels of hydrogen mass fraction when pressure is increasing (see for example Fig. 6.25 (c) where the maximum of pressure corresponds to a rich fuel region near the flame roots and to a fuel leaner region at the flame tips). Moreover, the spatial structure of $\mathcal{T}_{Y_{H_2},p}$ at the backplane corner suggests that rich fuel gas pockets are convected downstream by the vortices detaching from the backplane corner when the pressure is decreasing (blue region just at the corner) and afterward positively contribute to the pressure oscillation (red region downstream). Therefore, results confirm that the PM2 flame dynamics is driven by both vortical structures periodically detaching at the system second acoustic mode from the centerbody walls and the backplane corner and, in addition, by fuel mass fraction variations that are linked to both the first and the second acoustic mode oscillations. To conclude, hydrogen addition is found to be able to promote the interaction between the flame front and the vortices thanks to reduction in the flame length if compared to the pure methane and the low H_2-enriched cases [222] (see Fig. 6.20, therefore explaining why the system second acoustic mode is excited only when a 50% hydrogen enrichment is considered.

6.4 Conclusions

The impact of H_2-enrichment on flame stabilization and combustion dynamics of a CH_4 lean partially-premixed turbulent swirling flame is studied both experimentally and by LES.

To do so, the well-known PRECCINSTA test bench is operated at different levels of hydrogen enrichement while acquiring synchronized OH-PLIF imaging, sPIV velocity fields data, LOS OH* chemiluminescence images and pressure signal recordings. Numerically, LES simulations in the Conjugate Heat Transfer (CHT) context are performed for three flames operating with different hydrogen enrichment levels: the pure methane flame A, the 20% H_2-enriched flame B and the 50% H_2-enriched flame C. LES results are first validated against experimental data in terms of predicted velocity fields, heat release rate distribution, OH mass fraction and pressure signals in the combustion chamber and in the plenum, all quantities providing satisfactory agreement.

Hydrogen addition results in modifications of both the flame stabilization and its dynamics. The 20% H_2-enriched flame B presents a more compact heat release

rate distribution with respect to the pure methane flame A: the flame is slightly shorter due to the increase in laminar flame speed while the higher adiabatic flame temperature together with the more upstream flame root stabilization lead to a notably higher centerbody tip temperature. However, both flames A and B present no relevant thermoacoustic oscillation and show relatively low pressure and heat release rate oscillations. On the contrary, when considering the 50% H_2-enriched case C, the flame has a notably more compact heat release rate distribution and a shorter length due to the significant increase in laminar flame speed. CHT results show that, while the chamber walls and the backplane surface temperatures are only marginally affected, the centerbody tip reaches a notably larger temperature if compared to flames A and B. At the same time, the flame dynamics drastically changes: significant thermoacoustic oscillation is observed both experimentally and numerically. The flame couples both with the system first and the second acoustic modes, showing bi-modal thermoacoustic oscillation. The relative importance of the pressure and heat release rate oscillations at the first or at the second acoustic mode frequencies changes in time but generally the oscillations at the second acoustic mode frequency are consistently higher compared to the ones at the first acoustic mode, defining a prevalent second mode (PM2) flame dynamics.

Differences in flow temperatures for the three flames do not lead to significant enough changes in the mean sound speed fields to justify relevant changes in the system acoustic modes, as confirmed by Helmholtz solver calculations. Therefore, the coupling of the flame with the acoustic modes is due to the change in the heat release rate distribution when a sufficiently large amount of hydrogen is injected.

Prediction of the flame dynamics of case C are further analyzed by comparing phase-locked equivalent instantaneous experimental OH-PLIF images to LES-predicted OH mass fraction. Four periodic phenomena are identified throughout the bi-modal oscillation: the change in flame length and flame surface, the stabilization point of the flame root that moves upstream/downstream along the centerbody walls, the flapping of the jet fuel causing rich gas pockets to be released in the combustion chamber and finally the vortical structures detaching from the centerbody tip and the backplane that then interact with the flame front leading to strong wrinkling and flame roll-up. Dynamic Mode Decomposition (DMD) analysis of both OH-PLIF images and LES 3D fields at the system first and second acoustic modes confirm the presence of these phenomena: vortical structures are periodically detached at the system second acoustic mode from the backplane corner and the centerbody walls causing the flame front wrinkling and hence an increase in heat release rate that in turns positively contribute to

the thermoacoustic oscillation, especially at the backplane corner. In addition, a non-homogenous fuel distribution caused by the periodic fuel jet flapping leads to in-phase oscillation of heat release rate at both the first and the second acoustic modes.

To conclude, near 50% H_2-enrichment of the PRECCINSTA partially-premixed methane swirling flame strongly affects the flame shape and length, its stabilization and the resulting combustion dynamics, producing bi-modal thermoacoustic oscillation. Reduction in flame length is found to be a key element in the excitation mechanism of the higher frequency chamber mode, since it enhances the flame interactions with the vortices periodically detaching from the backplane. For all considered H_2-enrichment cases, LES proved to be able to successfully predict the complex flame dynamics in the CHT context, providing interesting insights about the hydrogen addition impact on the test rig components temperature.

Chapter 7

Elevated pressure effect

Contents

This Chapter analyses the pressure and hydrogen enrichment effects on the stabilization and combustion dynamics of a partially-premixed swirled-stabilized flame operated at 1, 3 and 5 bar, with H_2 enriched mixtures up to 40% by volume. Large Eddy Simulation (LES) is performed to analyze flame stabilization and dynamics for all cases. Since both turbulence and chemical time scales are significantly affected by pressure, it is a challenge for LES to compute such changes. The thickened flame (TFLES) model is used here with a Static Mesh Refinement (SMR) strategy to describe flame turbulence interactions to ensure that all flames are resolved similarly at 1, 3 and 5 bar. This requires to significantly increase the mesh size. An Analytically Reduced Chemistry (ARC) scheme is employed to describe CH_4-H_2/Air chemistry. LES is validated against experimental multi-kHz repetition-rate OH* chemiluminescence, OH Planar Laser Induced Fluorescence (PLIF), stereoscopic Particle Image Velocimetry (sPIV) and pressure recordings, all predictions providing satisfactory agreement. The dynamics of the different flames it then addressed. First, the impact of hydrogen at atmospheric pressure is investigated. While the reference natural gas flame (1 bar, 0% H_2) presents a lifted M-shape with a strong Precessing Vortex Core (PVC), 40% H_2-enrichment modifies the flame which becomes an attached V-shape, with a weakened PVC and the

triggering of a thermoacoustic oscillation at the system first acoustic mode. Second, the impact of mean pressure is analyzed by fixing the H_2-enrichment while increasing the mean pressure to 3 and then 5 bar. As the pressure increases, the flame becomes more compact and the chemical as well as the turbulent time scales change, potentially affecting the flame/turbulence interaction. For these points, the thermoacoustic oscillation at the first system acoustic mode rapidly disappears and stable conditions are recovered. Note that these results are being considered for publication in *Combustion and Flame* [245].

7.1 Introduction

As society evolves towards a green economy to face the global climate change, the combustion community is expected to develop new technologies and design low emissions combustors for the aviation and energy sectors. Such design still remains a challenge because lean combustion systems which is the path for low pollutant emissions are more prone to different flame dynamics issues, such as thermoacoustic instabilities [23, 24], lean blow-off [14, 15] and extinctions [16]. In the past decades, both experiments and Large Eddy Simulation (LES) have been widely used to support this research process. As the experiments are of fundamental importance to characterize combustion systems and validate numerical simulations, LES has demonstrated its large potential in predicting reactive flows in complex industrial configurations [19, 23, 24, 77]. In particular, the understanding of combustion instabilities has clearly progressed through the analysis of flames in academic experiments that allow also for developing and validating theoretical models. However, when it comes to real engines, the situation is more complex and introduce new physics that is difficult to study in laboratories. Academic combustors are indeed usually scaled down in terms of power density and pressure with respect to real engines, this potentially affecting the appearance of combustion instabilities due to the impact of elevated pressure on the flame shape and stabilization process [147]. Pressure can indeed change the flame oscillation amplitude and phase [246] as well as the interaction between the flame and the vortices, potentially affecting the flame response to acoustic perturbation [247]. Being combustion instabilities in real engines already a complex topic in its own, considering the addition of hydrogen (or hydrogen-rich gases) in existing gas turbines as a solution to decarbonize aviation and energy sectors is way more challenging [210, 215, 216, 217]. If compared to classical hydrocarbon fuels, hydrogen presents indeed much higher reactivity and a wider flammability range [191] as well as higher flame speeds [190]. These peculiar

chemical properties yield different flame shapes and stabilization process while potentially inducing flame dynamics issues such as flashback [220, 221] as well as thermoacoustic instabilities [11, 25, 67, 68, 69]. Therefore, both elevated pressure and hydrogen enrichment, which is likely to be present in the future generation of lean combustors, can modify the flame and both must be taken into account when dealing with these new combustion technologies. In this context, different studies involving complex experimental measurements and numerical simulations are available in the literature for which a brief review is hereafter proposed.

Experimentally, to get closer to the power density and Reynolds number of real engines, combustors must be operated at elevated pressure with preheated fresh gases. These experiments are generally complex from a technical point of view and, therefore, there are not many facilities available worldwide in which one can study high pressure combustion in complex geometries. Slabaugh *et. al* [248] underlined the various challenges that must be overcome in the development of an optically accessible and high-power combustion test rig, the main challenge being the resolution of all the spatial and temporal scales that characterize the turbulent reacting flow. The latter depends indeed both on the chemical reactions (which in turns depend on temperature, density and mass fraction gradients) and on the turbulent scales of the flow (which are linked to the turbulent Reynolds number). In high power density facilities, since the turbulence Reynolds number increases, the range of scales is wider, hence demanding for much higher spatial and temporal resolutions in terms of diagnostics. On top of that, usually the signal to noise ratio is largely lower if compared to atmospheric burners due to laser sheet absorption effects, as observed by Boxx *et al.* [249] although they demonstrated the feasibility of performing high-speed Particle Image Velocimetry (PIV) and OH Planar Laser Induced Fluorescence (OH-PLIF) measurements at 5 bar. Soon after, Slabaugh *et al.* [250] applied laser diagnostics for PIV/OH-PLIF measurements on a liquid-fueled combustor at 14 bar, observing strong refractive index variation across the flame causing lower resolution of the resulting PIV images. In this wake, some experimental studies have been performed on spray combustion at elevated pressure. Dhanuka *et al.* [29] obtained an accurate visualization of the interaction between the flame and the aerodynamic flow field at 4.5 bar but they did not observe significant effect of pressure on the flame structure. On the contrary, in the work of Malbois *et al.* [251] who analyzed a lean-premixed aero-engine injection system up to 13.8 bar using liquid kerosene, the flame, studied with CH* chemiluminescence measurements, presented a V-shape or a tulip shape based on the operating condition. Overall, a more compact structure was obtained as pressure increased. Other works studied the flame

shape and fuel drop size, such as Hicks *et al.* [252] in a high pressure combustor up to 13 bar on 3x3 array of swirled liquid fuel injectors. Equivalently, Orain *et al.* [253] studied different innovative injection systems at pressure higher than 10 bar. More recently, Chterev *et al.* [28] analyzed the interaction between a liquid fuel, the aerodynamic field and the flame front in a combustor up to 5 bar.

When it comes to combustion instabilities in high power density combustors, only few studies have been performed. For example, Kheirkhah *et al.* [254] experimentally investigated the dynamics of thermoacoustics oscillation in an aeronautical gas turbine model combustor fueled with liquid Jet A fuel at a pressure of 10 bar. The HIPOT burner, an elevated pressure version of the well-known PRECCINSTA gas turbine model combustor [27], has recently been characterized by Slabaugh *et al.* [255] at elevated thermal power density using simultaneous OH* chemiluminescence, sPIV and OH-PLIF. In this specific work, they observed the occurrence of hydrodynamic instabilities such as Helical Vortices (HV) in the shear layers and a Precessing Vortex Core (PVC) in the Central Recirculation Zone (CRZ) [139, 256, 257]. These hydrodynamic structures are seen able to affect the velocity field evolution in the CRZ [141, 258, 259, 260], the flame stabilization by rolling up and distorting the flame front [261, 262] as well as the heat release by changing the flame surface area [141, 258, 259, 260]. The fact that this type of interaction between the PVC and the flame (usually present in the atmospheric PRECCINSTA rig [259, 260, 261]) was also observed at high density power when considering low equivalence ratio conditions opened new questions on the effect of pressure on the combustion dynamics. More recently, Zhang *et al.* [258] confirmed the key importance of the PVC in the support of thermoacoustic oscillations even at elevated pressure despite very different hydrodynamic time-scales if compared to the equivalent atmospheric configuration.

Numerically, LES has been widely applied to turbulent reacting flows in real gas-turbine combustors at elevated power density, focusing on flame stabilization, dynamics and even pollutant emissions [19]. Already more than one decade ago, Moin *et al.* [263] and Boudier *et al.* [82, 264] assessed the predictive capability of a low-Mach-number and a compressible LES code, respectively, on a complex reacting flow in a combustor operated at high pressure, achieving good agreement with experimental data. Soon after, Schmitt *et al.* [265] analyzed in detail the combustion instability in a realistic gas turbine combustion chamber while identifying also the mechanism at the base of the thermoacoustic oscillation performing a first prediction of the nitric oxide emissions levels. In the same wake, and decade later, Jaravel *et al.* [37] used high-fidelity LES coupled with an Analytically Reduced Chemistry (ARC) to predict pollutant formation in a real

engine configuration, showing that mixing and strain are playing a significant role. More recently, Legros *et al.* [266] conducted an experimental and numerical study of a lean premixed liquid injection system designed for helicopter engines with a pressure ranging from 4 to 18 bar, focusing on the impact of the fuel droplet distribution on the flame structure.

When it comes to hydrogen enrichment, many experimental and numerical works have been performed to analyze the effect of hydrogen addition on CH_4/air flames (see also Chapters 5 and 6). Starting with laminar flames, hydrogen is known to increase the mixture laminar flame speed [193, 194, 196], while extending the lean blow-off and extinction limits [197, 198] and potentially changing flame dynamics [199]. A direct consequence of these observations is that hydrogen also modifies the flame shape and the heat release rate distribution in more complex swirled-stabilized flames [224, 225, 226, 227]. When considering H_2-enrichment in such configurations, the flame becomes shorter and more robust [201, 202] with a clear increase of peak OH concentration and a change in the flame structure [25, 201] as well as flame stabilization process. For example, Guiberti *et al.* [142] and Shanbhogue *et al.* [204] showed that a high H_2 concentration can increase the probability of stabilizing confined swirled M-flames. On top of that, hydrodynamic instabilities, such as PVC and HV, have been reported as sensitive to hydrogen enrichment [67] since they are susceptible to the density field non-homogeneities [141, 267].

Recently, Beita *et al.* [268] presented a review of the hydrogen enrichment impact on combustion instabilities for gas turbine applications. Hydrogen can affect the gain and phase of the Flame Transfer Function (FTF) [269, 270, 271] as well as self-sustained thermoacoustic instabilities by causing for example a shift in the system acoustic modes [230, 232, 233, 235, 272] or a change in the flame shape [67, 204, 226, 234, 273, 274, 275, 276]. In some cases, a reduction of the thermoacoustic oscillation has been observed both experimentally [210, 237, 277] and numerically [237]. Contrarily, Kang and Kim [236] showed that compact pure hydrogen flames can excite high-frequency instabilities while keeping the system stable in the low frequency range. A similar behavior was observed numerically by Moëll *et al.* [208] who showed how hydrogen increased the oscillation amplitude of high-frequency modes while damping low frequency instabilities. Also Zhang and Ratner [235] demonstrated that H_2 addition on a lean premixed swirled flame can trigger instabilities and shift the primary acoustic oscillation from low to high-frequency oscillations. Experimentally and very recently, the PRECCINSTA combustor has been fueled with different H_2-enrichment levels to study the impact on the flame stabilization and dynamics at atmospheric pressure [239, 240]. LES

of this configuration has been also performed using Conjugate Heat Transfer context and showing that hydrogen enrichment produces more compact flames, increases the thermal load on the combustor walls and causes the onset of a bi-modal thermoacoustic oscillation [25] (Chapter 6).

While elevated power density and hydrogen enrichment configurations have been widely investigated in the literature as briefly presented previously, only few experimental works analyzed the effect of hydrogen addition in combustors operated at high pressure. Recently, Zhang *et al.* [226] operated a low swirl burner with different bulk velocities, hydrogen enrichment, equivalence ratios and pressure up to 3 bar. Experiments showed that hydrogen can trigger thermoacoustic instabilities and that pressure is linked to changes in the flame front curvature and local flame surface. In parallel, the HIPOT PRECCINSTA burner was operated by Chterev and Boxx [67] at elevated pressure (up to 5 bar) with different hydrogen enrichment levels, presenting the impact on the flame shape, PVC and thermoacoustic frequency as well as its amplitude. H_2 enrichment in that cases increases the phase delay between the oscillating pressure field and the heat release by decreasing the flame length while simultaneously increasing the sound speed in the combustor. Indlekofer *et al.* [273] then operated an annular combustion chamber at intermediate pressures (up to 3.3 bar) with CH_4-H_2 blends for which different azimuthal thermoacoustic instabilities appeared. Here again pressure is shown to mainly affect the flame height and intensity during the high-amplitude instabilities, while only marginally affecting the low-amplitude ones. The same rig was subsequently operated by Ahn *et al.* [278] to investigate the effect of equivalence ratio variation on the flame transient thermoacoustic response.

To the best of the author's knowledge, there is still no specific numerical work investigating the effects of both pressure and hydrogen enrichment on the flame stabilization and its dynamics. This Chapter aims at filling this gap by proposing LES of the PRECCINSTA HIPOT burner enriched with hydrogen (up to 40% by vol.) and operated at elevated pressure (up to 5 bar). Sections 7.2 and 7.3 describe the experimental and numerical setup, respectively, underlining the modeling challenges of predicting high power density flows. The impact of hydrogen enrichment at atmospheric pressure is discussed in section 7.4. Finally, the effect of elevated pressure while keeping the same H_2-enrichment level is investigated in section 7.5. As pressure increases, flames get more compact, the thermoacoustic oscillation disappears and the chemical as well as the turbulent time scales significantly change affecting the flame/turbulence interaction.

a) b)

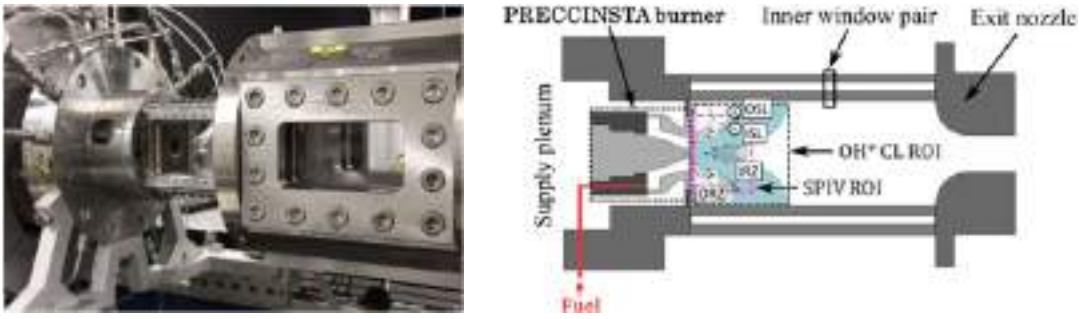

Figure 7.1: (a) Picture and (b) schematic of the experimental test bench showing the injector with the combustion chamber. Region of Interest for experimental diagnostics is also indicated [67].

Case	P [bar]	H_2 [% fuel vol.]	$\dot{m}_{air}$ [g/s]	$\dot{m}_{CH_4}$ [g/s]	$\dot{m}_{H_2}$ [g/s]	T_{inlet} [K]	ϕ	P_{th}
REF	1.05	0%	17.6	0.74	-	608	0.71	37KW
P1H40	1.05	40%	17.2	0.62	0.05	590	0.71	37KW
P3H40	3.05	40%	53.7	1.85	0.15	636	0.71	111KW
P5H40	5.02	40%	89.5	3.08	0.26	642	0.71	185kW

Table 7.1: Summary of the operating conditions considered in the present work.

7.2 Experimental setup

The High Pressure Optical test rig (HIPOT) burner, an elevated pressure version of the well-known PRECCINSTA gas turbine model combustor operated by DLR [27], is presented in Fig. 7.1 that illustrates (a) a picture and (b) the schematic of the combustion chamber [67, 255, 258]. In this setup, dry pre-heated air is fed through the plenum and 12 radial swirler vanes impose a swirling motion to the flow before entering the combustion chamber. Hydrogen-enriched natural gas[1] is injected into the air stream through 12 small holes of 1 mm in diameter located within the radial swirler in a "technically premixed" mode. The combustion chamber has a square section of 80 x 80 mm^2, a total length of 200 mm and quartz windows to allow optical access for diagnostics. Note that the inner test section quartz windows are back-face air-cooled like the combustion chamber backplane and centerbody. At the end of the combustion chamber, hot gases pass through a cone-shaped exhaust pipe of 18 mm in diameter to end in the "turning module" whose pressure is controlled by a water-cooled throttle valve. The rig is equipped with several synchronous experimental diagnostic techniques. The three velocity components in the axial-radial plane of the combustion chamber are measured through a Stereoscopic Particle Image Velocimetry (sPIV) tech-

[1]Natural gas composition was 93% CH_4, 4% C_2H_6, 1.5% N_2, 1% CO_2, and 0.5% heavy hydrocarbons. Note that in LES, CH_4 is considered as fuel.

nique. Planar Laser-Induced Fluorescence (PLIF) measurements of OH radicals are also performed to visualize the flame as well as Line-of-Sight (LOS) integration of OH* chemiluminescence that is then used as a qualitative indicator of the heat release rate for lean premixed flames [170]. Pressure is also recorded in the plenum, in the combustion chamber and in the turning module to characterize the flame thermoacoustic response. Measurements of the solid temperature at the centerbody and at the turning module are acquired through thermocouples embedded 5.5 and 2 mm below the surface, respectively. Heat transfer at the combustion chamber walls and at the backplane is estimated from the cooling mass flow rate and the corresponding increase in temperature of the cooling-air. Cooling-air is injected into the turning module after having cooled the combustion chamber quartz walls.

This configuration of the PRECCINSTA burner has been recently characterized by Slabaugh *et al.* [255] and further analyzed by Zhang *et al.* [258] at elevated thermal power density. Chterev and Boxx [67] were the first to operate the rig with different levels of hydrogen enrichment to investigate the effect of pressure and hydrogen on the flame dynamics. The operating conditions considered for a global equivalence ratio of $\phi = 0.71$ and a thermal power of $P_{th} = 37$,kW/bar are summarized in Tab. 7.1. Case *REF* refers to the condition without hydrogen admixture at atmospheric pressure. Cases *P1H40*, *P3H40* and *P5H40* refer to flames enriched by 40% of hydrogen (by volume) at 1, 3 and 5 bar, respectively.

7.3 LES setup and modeling challenges

Figure 7.2 presents the computational domain used for LES with an overview of the unstructured mesh used for Case *REF*. The full-length air plenum and the turning module are covered by the simulations. Pressure is directly imposed at the end of the small transverse tube in the turning module to mimic the throttle valve. The inlet fuel geometry is meshed using 12 small tubes (shown in red) without the fuel plenum: to help visualize the partially-premixed fuel injection in the swirler, an instantaneous isocontour of CH_4 is also shown in red. The AVBP LES code (cerfacs.fr/avbp7x/index.php) is used to solve the compressible Navier-Stokes multi-species equations (Chapter 2). The TTGC scheme (third order in time and space) is used to discretize the convective terms [48] while the SIGMA turbulent closure is employed for the LES sub-grid model [46]. In such industrial configurations, flames are usually too thin to be resolved on the numerical grid without asking for unfeasible High Performance Computing (HPC) resources. A solution is then to use the dynamic formulation of the thickening flame model

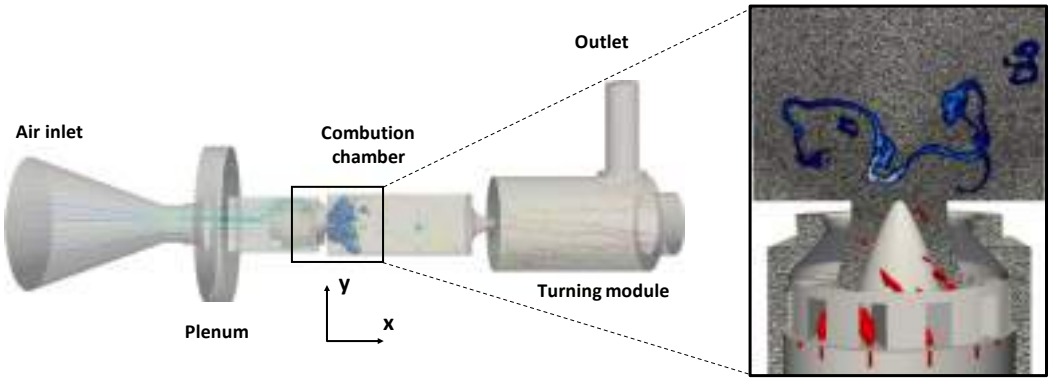

Figure 7.2: LES computational domain (23M cells) for Case *REF*. The full-length air plenum and the turning module are taken into account. Pressure is imposed at the outlet to mimic the throttle valve. The twelve fuel injectors are included in the mesh: an instantaneous isocontour of CH_4 (in red) helps visualize the "technical" injection of fuel. An instantaneous field of heat release rate for Case *REF* is also shown in blue in an horizontal plane.

(DTFLES) [64], for which the reactive layer is artificially thickened by reducing the diffusive terms. Since a thickened flame is less sensitive to turbulence, an efficiency function Ξ_Δ is introduced to account for the corresponding reduction of flame surface [61]. A dynamic formulation of the Charlette efficiency function [62] is used here to locally estimate the model parameter β_{Ch} during the simulation, following previous works on the atmospheric PRECCINSTA configuration [25, 136]. The CH_4-H_2/Air kinetic scheme relies on a novel Analytically Reduced Chemistry (ARC) mechanism consisting of 18 transported species, 144 reactions, and 12 quasi-steady state species, derived from the detailed PoliMi scheme [241] using ARCANE [65] and recently validated for the PRECCINSTA atmospheric flame with different H_2-enrichment [25]. This kinetic scheme has been further validated through Cantera (www.cantera.org) calculations of a 1D-premixed and 1D-counterflow premixed flames using detailed schemes at elevated pressures (see Appendix C). Transport properties are described by a constant mixture Prandtl number and a constant Schmidt number different for each species [71]. Inlet and outlet boundary conditions are modeled with the Navier-Stokes Characteristic Boundary Conditions (NSCBC) [30]. The flow is choked both at the air inlet (through a multi-perforated plate) and at the throttle valve (only at elevated pressure), while the acoustic impedance of the fuel line was reported to have marginal impact on the thermoacoustic oscillation [59]. Following these observations, relaxation coefficients of $K_{air} = 1 \times 10^5$ s^{-1}, $K_{fuel} = 5 \times 10^5$ s^{-1} and $K_{outlet} = 5 \times 10^3$ s^{-1} are imposed on the air inlet, the fuel inlet and the outlet, respectively for the NSCBC method. When it comes to walls,

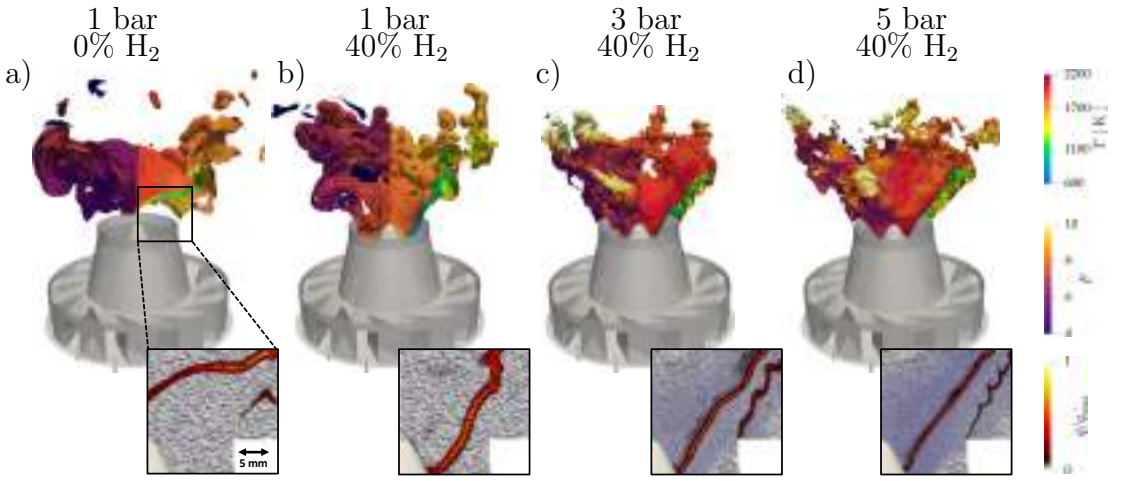

Figure 7.3: Iso-surfaces of $\dot{q} = 10\%\ \dot{q}_{max}$ colored by thickening field F (on the left) and temperature field T (on the right) for Cases (a) *REF* (23M mesh), (b) *P1H40* (23M), (c) *P3H40* (65M) and (d) *P5H40* (144M). A zoom on the flame root showing the grid and the normalized field of heat release rate is also presented. Note that, as a result of the Static Mesh Refinement procedure, a similar thickening field is used for all the flames.

a no-slip condition is used and heat transfer is taken into account by imposing a reference temperature T_{ref} and a suitable thermal resistance R so that, if T_f is the fluid temperature at the wall, the local heat flux Φ_q can be computed as $\Phi_q = (T_f - T_{ref})/R$ [59]. The experimentally measured temperature values for the centerbody and the turning module are used as T_{ref} together with R values that account for the corresponding heat conduction. Complementarily, for the backplane and the combustion chamber walls, T_{ref} is imposed as the average air-cooling temperature and R is tuned to match the experimentally measured heat losses for each operating point[1]. Finally, thermal radiation from the hot gases is accounted for through an Optically Thin Assumption (OTA) [172] for the most radiating species CH_4, CO, CO_2, and H_2O. In such a case, gases are assumed to be optically thin and re-absorption is neglected while the Planck mean-absorption coefficients are provided for each species as polynomial functions of temperature [173].

7.3.1 Modeling challenges at elevated pressure

The LES mesh used for cases *REF* and *P1H40* consists of $23M$ tetrahedral cells. This grid has a characteristic size in the flame zone just downstream of the cen-

[1]Note that, contrarily to Chapter 6, HRT approach is here used instead of the more complex CHT approach. Temperature values for the centerbody tip and heat transfer values are indeed experimentally measured for all the operating conditions considered. In addition, fresh gases are significantly pre-heated before entering the plenum, suggesting that pre-heating due to the warm centerbody walls is likely negligible compared to the atmospheric PRECCINSTA case.

Case	P [bar]	η [μm]	δ [μm]	δ_{th} [μm]	s_L [m/s]	Re [10^4]	Re_t [10^4]	Ka	Da
P1H40	1.05	25.0	57	338	1.2	2.7	1.2	3.7	29.3
P3H40	3.05	12.3	29	138	0.91	8.1	3.0	4.0	43.3
P5H40	5.02	8.4	23	96	0.73	13.4	5.0	5.1	44.0

Table 7.2: Effect of pressure on the turbulent reactive flow time scales. Flame properties are evaluated at the global equivalence ratio of ϕ = 0.71.

terbody tip of $\Delta_x = 300\ \mu m$. With this resolution, a y^+ value lower than unity is achieved at the centerbody tip and $y^+ \sim 3$ at the chamber and backplane walls at 1 bar. The reasonably low value of the non-dimensional wall distance hence allows the use of a wall resolved LES approach and a satisfactory estimation of the thermal boundary layer behavior.

For elevated pressure cases, more attention is to be paid on the LES numerical modeling as pressure (and high power density) modifies the different time scales that characterize these turbulent reactive flows (Table 7.2). First of all, the Reynolds number significantly increases with pressure [45]. If the exit injector diameter D (i.e. 28 mm) is chosen as characteristic length L and the characteristic velocity u is taken to be the bulk velocity $4\ \dot{m}\ /\ \rho\pi D^2$ for all cases to be considered, the Reynolds number reads 2.7×10^4, 8.1×10^4 and 1.34×10^5 for cases *P1H40*, *P3H40* and *P5H40*, respectively. Complementarily, the turbulent Reynolds number Re_t can be computed taking the characteristic length L as integral scale length and the bulk RMS velocity at the injector exit as characteristic velocity u' (i.e., ≈ 20 m/s for all conditions), presenting significant increase with pressure. Re_t reads 1.2×10^4, 3×10^4 and 5×10^4 for cases *P1H40*, *P3H40* and *P5H40*, respectively. As a consequence, the smallest turbulent scale, the Kolmogorov length scale η goes from 25.0 μm to 12.3 μm and 8.4 μm for cases *P1H40*, *P3H40* and *P5H40*, respectively. Note that an increase of pressure from 1 bar to 3 bar halves η while, a further increase to 5 bar only slightly decreases it.

Pressure does not only affect turbulence time scales, it also affects chemical reactions. For an equivalence ratio of 0.71, the laminar flame speed S_L decreases from 1.2 m/s at atmospheric pressure to 0.91 m/s and 0.73 m/s at 3 and 5 bar, respectively. The thermal flame thickness δ_{th} also reduces from 338 μm to 138 and then 96 μm. At the same time, the diffusive flame thickness δ, computed as the ratio between thermal diffusion to S_L, reduces from 57 μm to 29 and then 23 μm. As a consequence, the chemical time scale τ_c, computed as δ/S_L, passes from 48 μs for Case *P1H40* to 32 and 31 μs for cases *P3H40* and *P5H40*, respectively.

Therefore, both turbulence and chemical time scales are affected by pressure. The ratio between these two time scales controls the flame-turbulence/vortices interaction. The latter can be characterized by two non-dimensional numbers, depending on the turbulent length scale considered, namely the Karlovitz number Ka and the Damköhler number Da [38] that compare the chemical time scale τ_c to the Kolmogorov time τ_k and the integral time scales τ_t, respectively, and can be defined as[1]

$$Ka = \frac{1}{Da\left(\eta_k\right)} = \frac{\tau_c}{\tau_k} = \frac{u'\left(\eta_k\right)/\eta_k}{s_L/\delta} = \left(\frac{Pr\ l_t}{\delta}\right)^{-1/2}\left(\frac{u'\left(l_t\right)}{s_L}\right)^{3/2} = Pr\left(\frac{\delta}{\eta_k}\right)^2, \tag{7.1}$$

$$Da = Da\left(l_t\right) = \frac{\tau_t}{\tau_c} = \frac{l_t/u'\left(l_t\right)}{\delta/s_L}. \tag{7.2}$$

The Karlovitz number compares the the smallest turbulent time scales and the chemical time scale: it indicated whether the Kolmogorov scale is able or not to modify the inner flame structure. Computing Ka (Table 7.2) reveals that pressure only slightly affects the Karlovitz number and hence the interaction between the Kolmogorov scale and the flame front because both Kolmogorov scale η (τ_k) and flame thickness δ (τ_c) decrease with pressure. Therefore, pressure does not modify the interactions between the small turbulent scales and the flame. The Damköhler number, instead, describes the interaction between large vortical structures and the flame front by comparing the integral time scale to the chemical one. To compute the Damköhler number, the integral time scale τ_t can be taken as the ratio between the characteristic length L as integral scale length and the RMS velocity u'. In that case, the Damköhler number goes from a value of 29.3 at atmospheric pressure to 43.3 and 44.0 for 3 and 5 bar, respectively (Table 7.2). Indeed, since the integral characteristic time and the large vortical structure remain essentially the same, due to the reduction in the chemical time scale, the Damköhler number increases with pressure.

Therefore, since both turbulence and chemical time scales are decreased by pressure and the Damköhler number changes potentially affecting flame/vortices interactions, there is a clear challenge for LES to properly capture such changes and mesh requirements become rapidly critical. Here, a comparison of predictions with a model as TFLES requires in principle the same relative thickening of the various flame fronts and hence grid adaptation. To properly increase resolution, a Static Mesh Refinement (SMR) is introduced to refine the grid for cases *P3H40* and *P5H40* by prescribing a proper resolution goal in the flame region so that

[1]Note that equations from Ref. [38] have been modified to take into account the non-unity Prandtl number.

the same artificial thickening and hence the same combustion modeling for all flames is produced [70]. Prescribing a thickening goal of $F \sim 8$, the procedure leads to grids of 65M cells and 144M cells for Cases *P3H40* and *P5H40*, respectively. The increase in cells number is not linear with the reduction in δ_{th} but increases with its cube when pressure goes up. Hence, the observed increase in cells number underlines the need for HPC resources when dealing with elevated pressure combustors if requiring reasonable resolution of the flame front.

Figure 7.3 presents iso-surfaces of heat release rate $\dot{q} = 10\%\ \dot{q}_{max}$ colored by the thickening field F (on the left) and temperature T (on the right) for (a) Case *REF* (23M mesh), (b) Case *P1H40* (23M), (c) Case *P3H40* (65M) and (d) Case *P5H40* (144M). A zoom on the flame root showing the grid and the normalized field of heat release rate $\dot{q}/\dot{q}_{max}$ is also presented to visualize the resolution of the flame front. As expected, due to the use of SMR, a similar instantaneous thickening field is obtained while resolving all flames. The flame thickness significantly reduces when increasing both pressure and hydrogen enrichment levels.

7.4 Hydrogen effect at atmospheric pressure

Experimental measurements and LES predictions of the reference Case *REF* (1 bar, 0% H_2) and Case *P1H40* (1 bar, 40% H_2) are discussed now to highlight the impact of hydrogen enrichment at atmospheric pressure. First, H_2 addition effect on the flame shape and stabilization is discussed (section 7.4.1). Then, the thermoacoustic response and the flame dynamics are analyzed (section 7.4.2).

7.4.1 Flame shape and stabilization

Figure 7.4(a-b) presents the experimentally measured time-averaged LOS-integrated OH* chemiluminescence image compared to the LOS predicted heat release rate $\bar{\dot{q}}$ for (a) Case *REF* and (b) Case *P1H40*, respectively. For the reference case without hydrogen (Fig. 7.4(a)) the flame presents a lifted M-shape both in experiments and LES. In good agreement with the experimentally measured OH* chemiluminescence signal, the Outer Recirculation Zones (ORZ) do not present any heat release rate. In contrast, when 40% hydrogen enrichment is added to the fuel, the flame takes on a V-shape. It attaches to the centerbody tip and the flame length reduces, Fig. 7.4(b).

The shape change also appears in the experimentally measured time-averaged OH-PLIF signal compared to the computed OH mass fraction[1] $\overline{Y_{OH}}$ in Fig. 7.4(c-

[1]Note that the measured OH-PLIF signal is here considered to be proportional to OH mass fraction as a first approximation. However, more generally, OH-PLIF is not a direct measure of

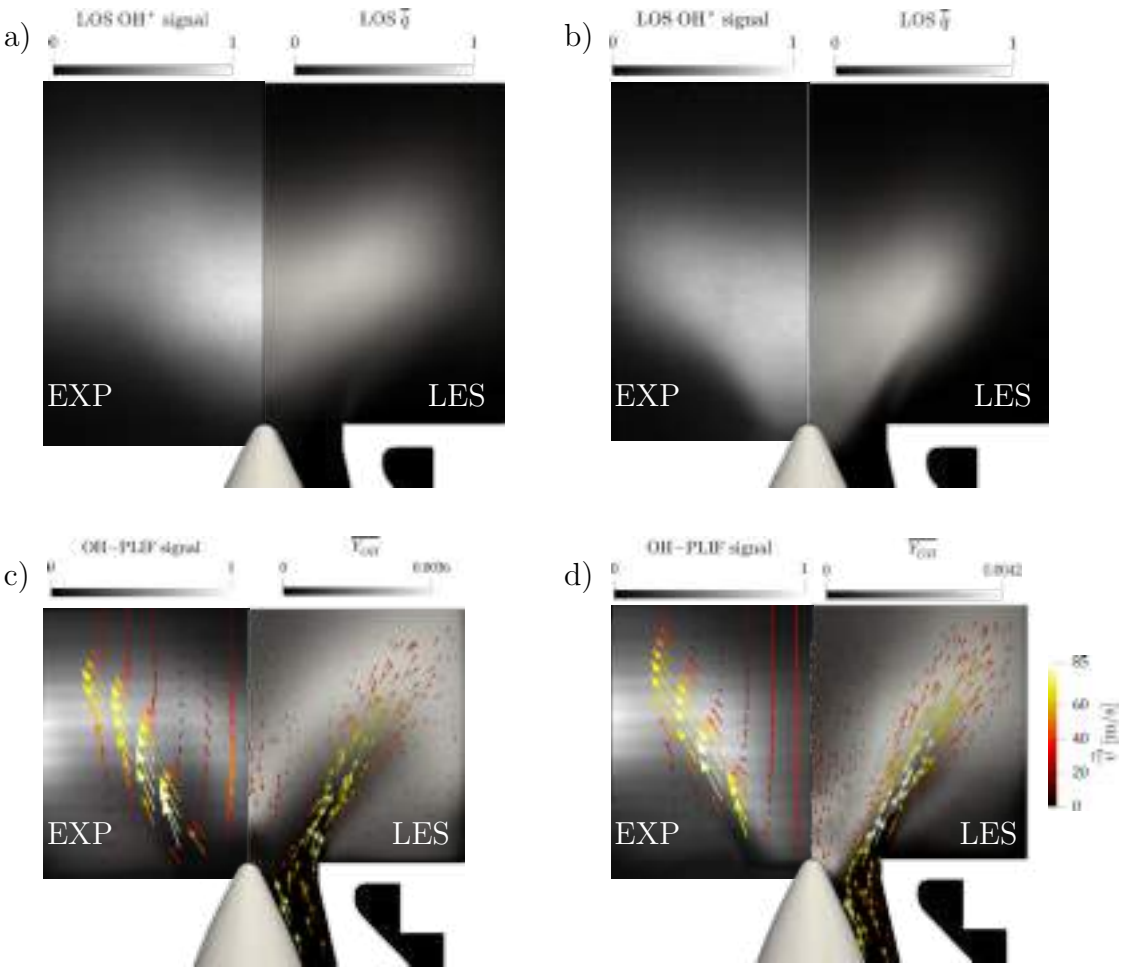

Figure 7.4: Experimentally measured time-averaged LOS-integrated OH* chemiluminescence image and time-averaged OH-PLIF signal compared to predicted LOS heat release rate $\overline{\dot{q}}$ and OH mass fraction $\overline{Y_{OH}}$ for Cases (a-c) *REF* and (b-d) *P1H40*, respectively. The arrows are tangential to the measured and computed time-averaged velocity field in the plane $\overline{v}$. Their length and color indicate the velocity magnitude.

d) for Case *REF* and Case *P1H40*, respectively. The arrows are tangential to the experimentally measured and numerically computed time-averaged velocity field in the plane $\overline{v}$, the length and color of the vector indicating the velocity magnitude. Both in experiments and LES, no OH signal is observed close to the centerbody tip in the reference case, confirming that the flame is not attached to the centerbody walls, Fig. 7.4(c). However, OH is present in the ORZs, pointing to high temperatures in these specific regions. No OH is detected in the high velocity region at the injector exit, as indicated by the velocity vectors. For this case, LES correctly captures both the flame shape and its stabilization process/location as well as the velocity field experimentally measured. Quantita-

OH number density since measurements can be affected, among others, by pressure, quenching, laser and signal absorption.

tive comparison of mean and RMS velocity components are presented in Fig. 7.5 Fig. 7.6, respectively. The axial velocity (a) shows an extended CRZ, indicated by the negative velocity values. The (b) radial and (c) tangential velocity components are also well predicted by LES.

When hydrogen is added to the fuel mixture, the flame assumes a V-shape, with flame roots well attached to the centerbody tip, as indicated by the high values of OH signal on Fig. 7.4(d). Contrarily to Case *REF*, the CRZ presents lower OH signal while the OH mass fraction peak value is notably higher [201]. Again, LES correctly predicts the experimental velocity field and the flow acceleration due to the increased combustion intensity while no OH is observed in the high velocity region just at the injector exit. The flame is now able to stabilize at the centerbody tip walls in the shear layer region. This change is due to the increased laminar flame speed and the higher resistance to strain of hydrogen enriched flames (see Appendix C).

Quantitative comparison of mean and RMS velocity components are presented in Fig. 7.7 Fig. 7.8, respectively. The V-shape of the flame induce stronger CRZ, as indicated by the negative values of mean axial velocity component. Also in this case, LES is in satisfactory agreement with experimental data.

A more direct comparison of flame shapes and stabilization is provided in Fig. 7.9. To do so, the normalized time-averaged heat release rate $\overline{\dot{q}}/\overline{\dot{q}}_{max}$ predicted via LES is shown for both (a) Case *REF* and (b) Case *P1H40*, the added white isocontours indicating 10% of $\overline{\dot{q}}_{max}$. The reference flame (Fig. 7.9(a)) presents a lifted M-shape, it is longer and the heat release rate reaches the side chamber walls. A strong heat release rate region appears along the axis, downstream of the centerbody tip. Low heat release rate regions are found near the centerbody walls and at the backplane corner, indicating that the flame is sporadically present in these regions while never being fully stabilized. Contrarily, (b) Case *P1H40* shows that the flame root is firmly stabilized at the centerbody walls, as confirmed by the large values of heat release rate. A blurry region of $\overline{\dot{q}}$ is noticeable downstream of the centerbody tip, suggesting that, from time to time, flame branches are present in this region. The flame tip is now positioned farther away from the side chamber walls, the flame being shorter.

To achieve a more quantitative comparison, the normalized time-averaged heat release rate fields are integrated over the combustor cross section S_c. In such a case, one-dimensional mean axial distributions $\langle\overline{\dot{q}}\rangle$ are obtained for both

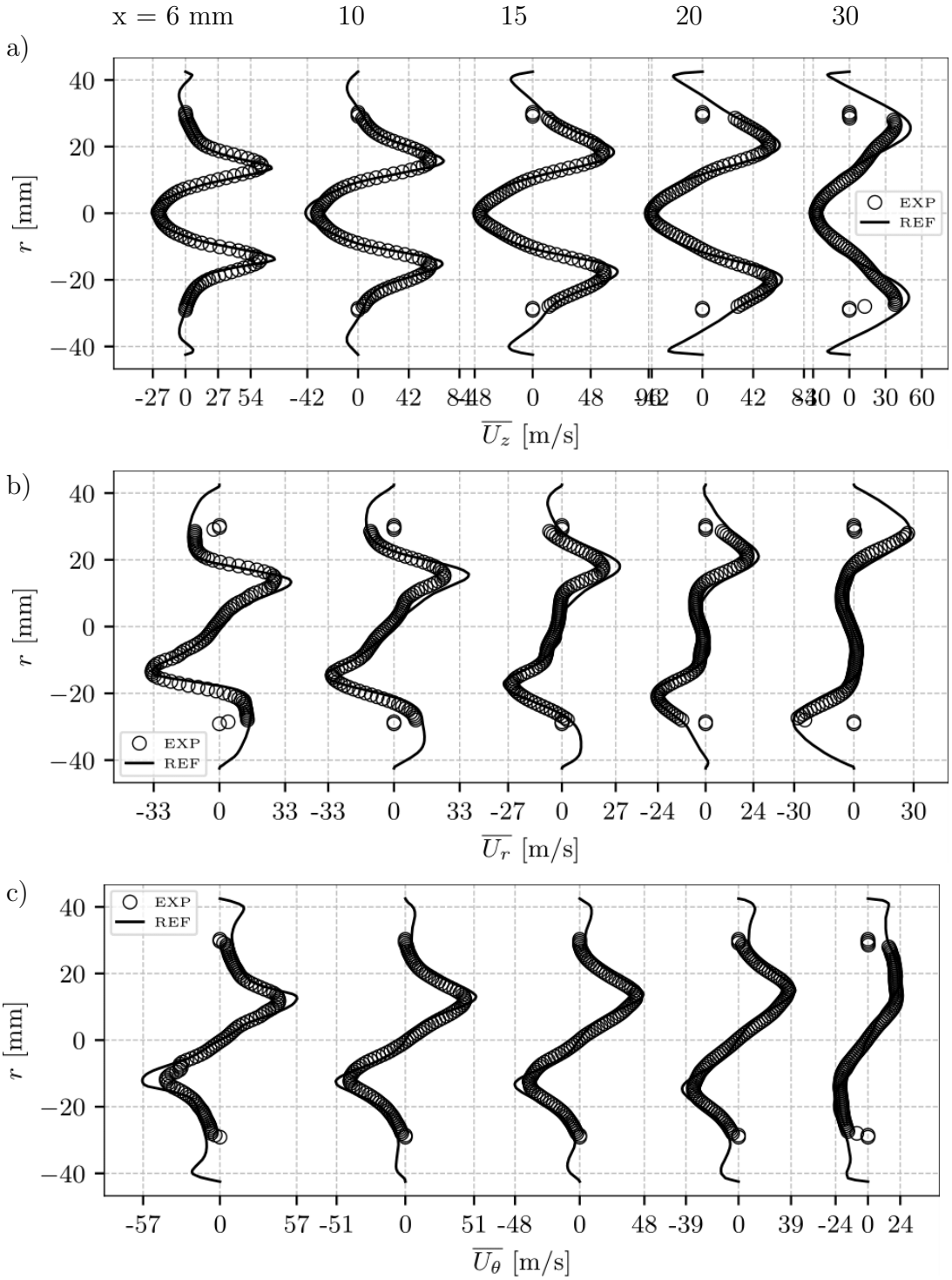

Figure 7.5: Profiles of mean (a) axial, (b) radial and (c) tangential velocity components at measurement planes at x = 6, 10, 15, 20 and 30 mm downstream of the combustion chamber backplane for LES in comparison to experiments. Case *REF*: 0% H_2, 1 bar.

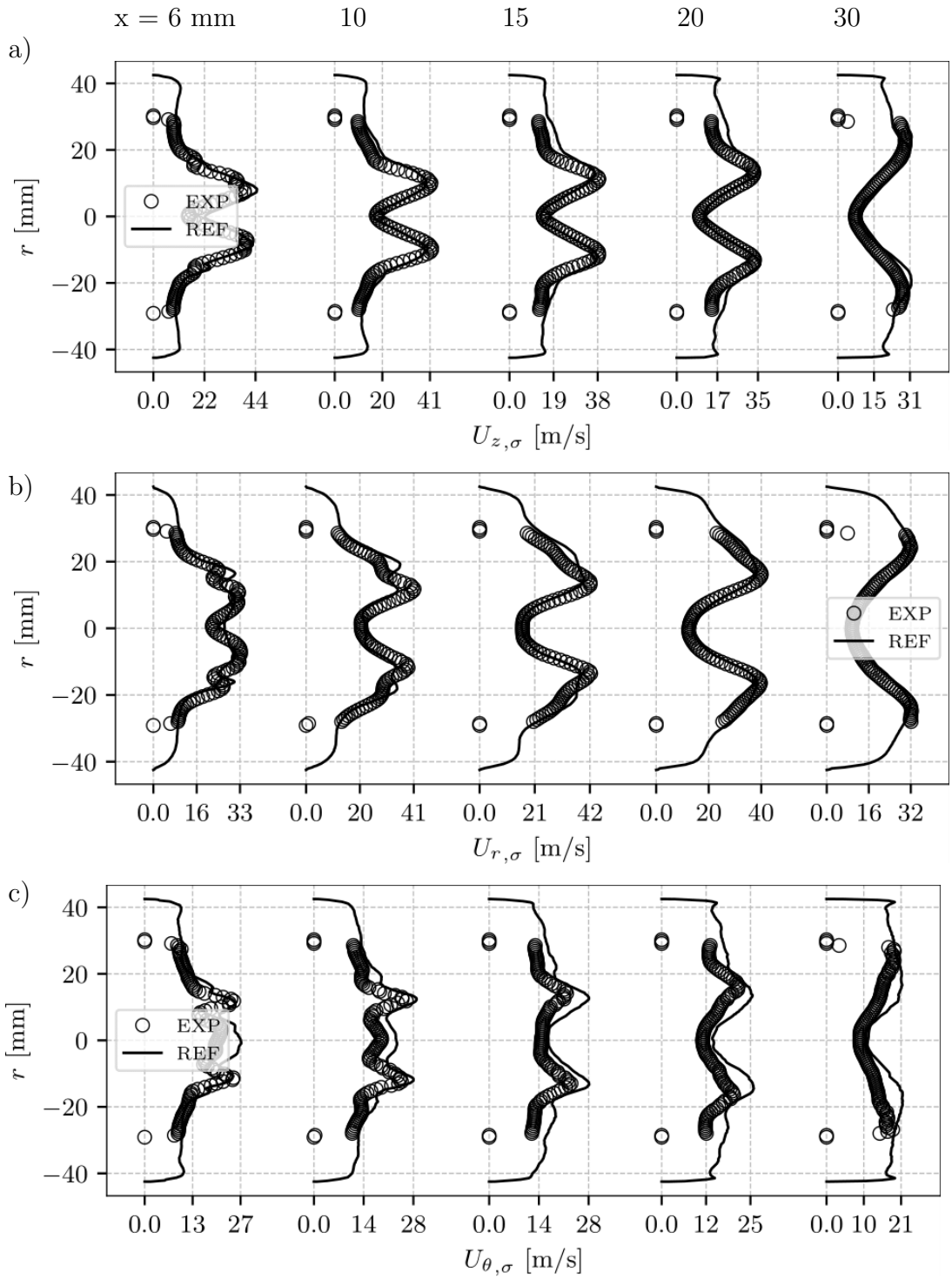

Figure 7.6: Profiles of RMS (a) axial, (b) radial and (c) tangential velocity components at measurement planes at x = 6, 10, 15, 20 and 30 mm downstream of the combustion chamber backplane for LES in comparison to experiments. Case *REF*: 0% H_2, 1 bar.

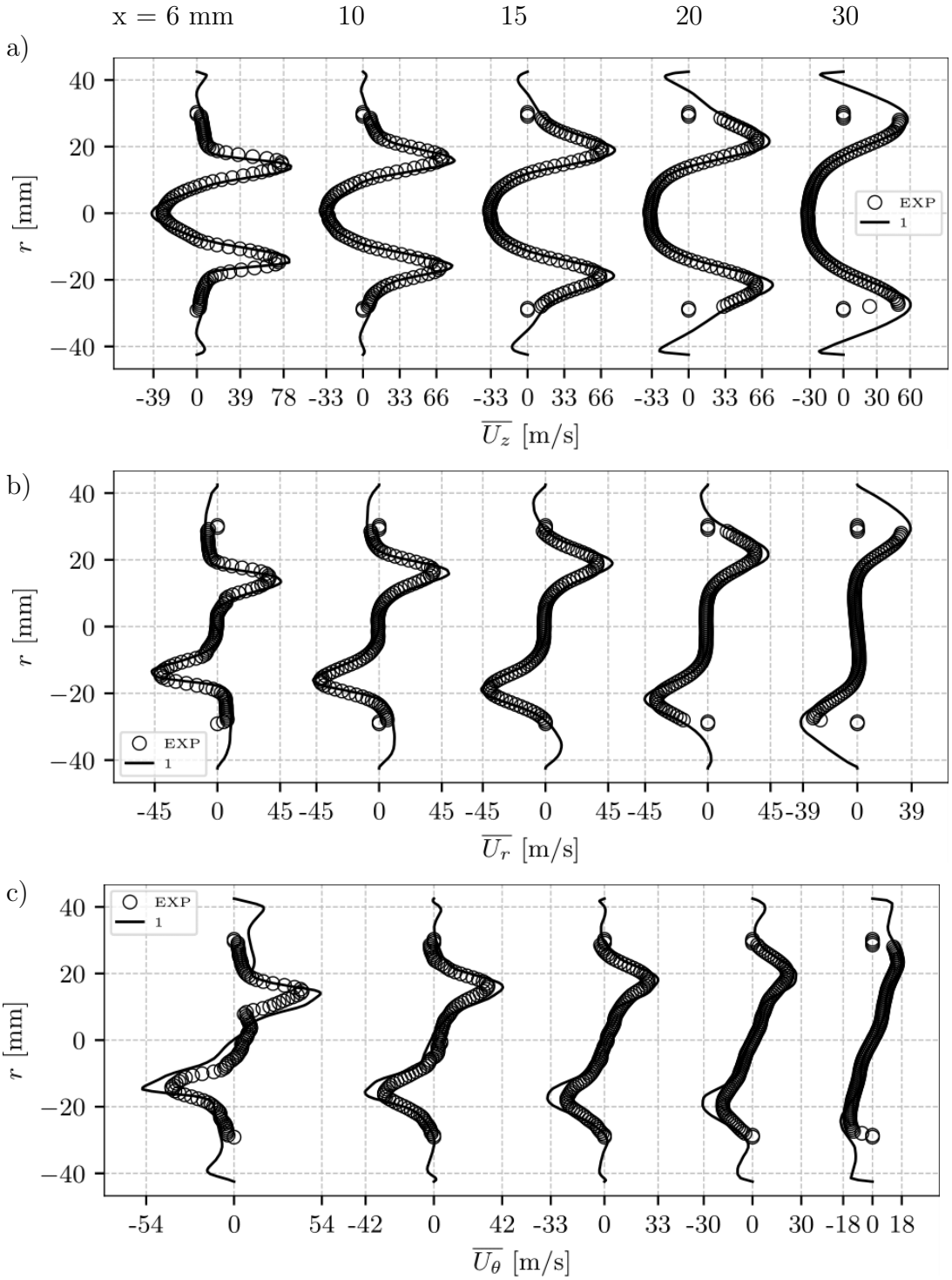

Figure 7.7: Profiles of mean (a) axial, (b) radial and (c) tangential velocity components at measurement planes at x = 6, 10, 15, 20 and 30 mm downstream of the combustion chamber backplane for LES in comparison to experiments. Case *P1H40*: 40% H_2, 1 bar.

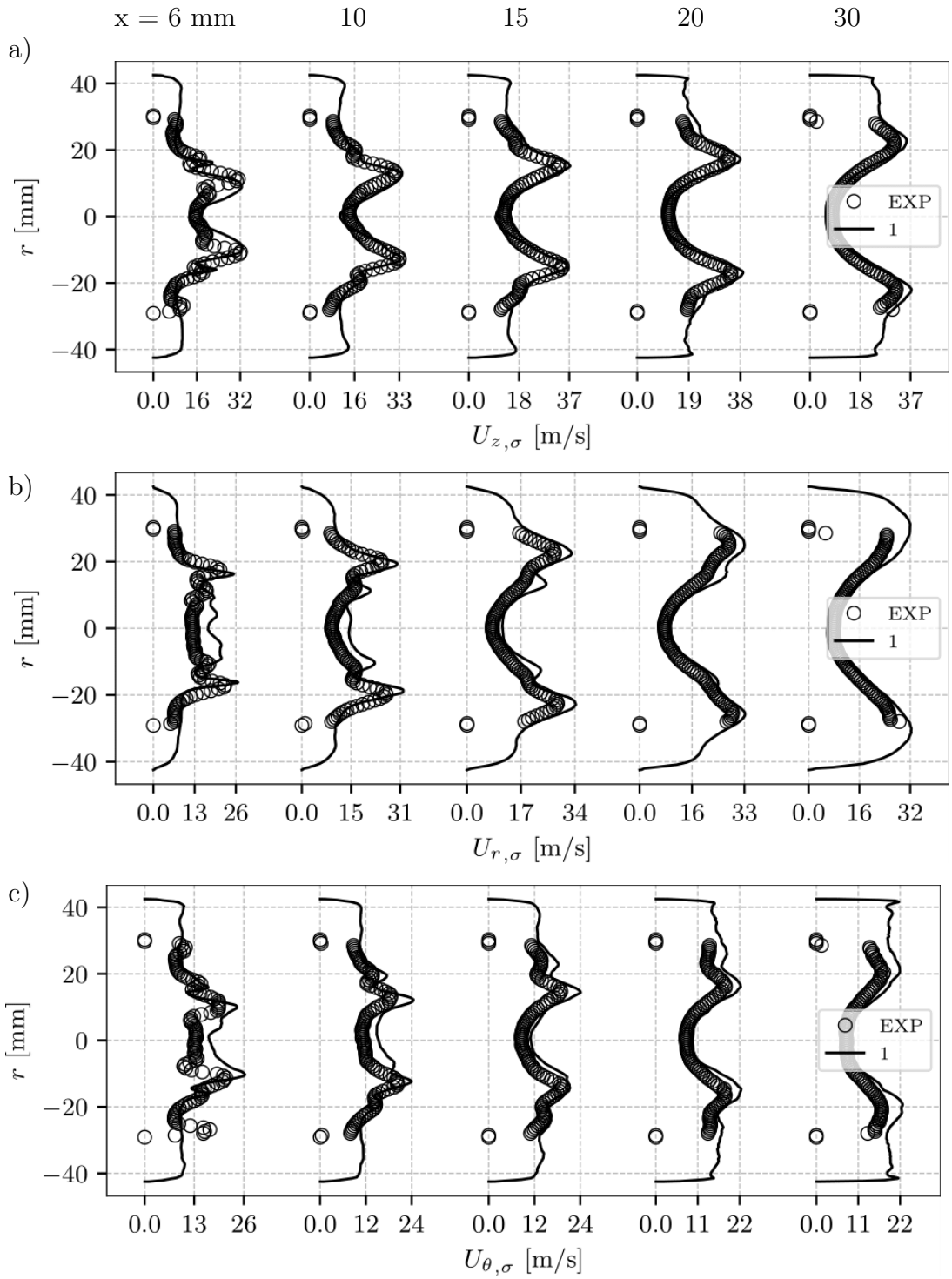

Figure 7.8: Profiles of RMS (a) axial, (b) radial and (c) tangential velocity components at measurement planes at x = 6, 10, 15, 20 and 30 mm downstream of the combustion chamber backplane for LES in comparison to experiments. Case *P1H40*: 40% H_2, 1 bar.

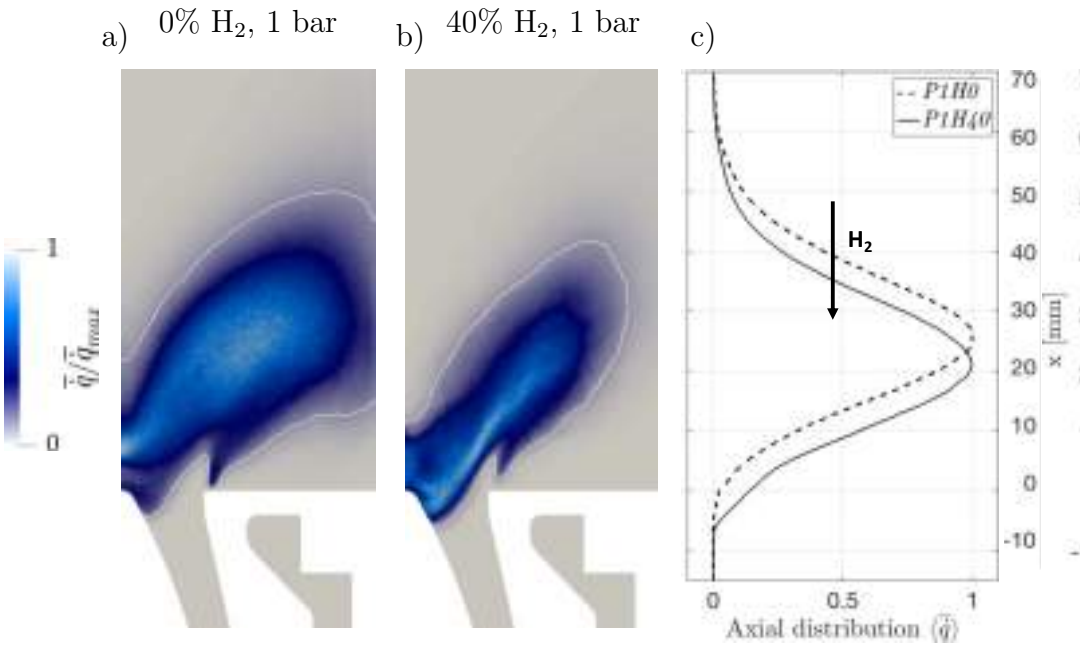

Figure 7.9: Normalized time-averaged heat release rate $\overline{\dot{q}}/\overline{\dot{q}}_{max}$ predicted via LES for Cases (a) *REF* and (b) *P1H40*. (c) Mean axial distribution $\langle\overline{\dot{q}}\rangle$. White isocontours indicate 10% of $\overline{\dot{q}}_{max}$.

cases in Fig. 7.9(c), as expressed by

$$\langle\overline{\dot{q}}\rangle(x) = \frac{1}{S_c}\iint_{S_c}\overline{\dot{q}}(x,y,z)dydz. \tag{7.3}$$

The effect of hydrogen enrichment on the flame stabilization and length is evident. When 40% hydrogen admixture is considered, both the peak of heat release rate and the flame stabilization point are shifted upstream with a shift of about 10 mm: the flame is more compact.

Visualization of the unsteadiness in a flow-field can be conveyed and illustrated through an instantaneous view of the Q-criterion identifying the presence of coherent vortical structures [279]. Figure 7.10 compares a Q-criterion isosurface at Q = 280 $\overline{U_x^2}/D_{inj}^2$ colored by pressure superimposed to a field of instantaneous normalized heat release rate $\dot{q}/\dot{q}_{max}$ for (a) Case *REF* and (b) Case *P1H40*. Both cases show the presence of a Precessing Vortex Core (PVC), identified through a low pressure value (colored in green). The lifted M-flame presents a strong PVC that impacts the flame downstream of the centerbody tip and can cause the blurry heat release rate region along the axis in Fig. 7.9(a). The PVC is still present when the flame assumes a V-shape, as opposed to what was generally observed in the atmospheric PRECCINSTA burner in which V flames are usually found to suppress the formation of the PVC. However, as experimentally observed [67], the PVC strength is significantly reduced, as indicated by the volume taken by the green Q-criterion isosurface. Despite this change, the PVC is still able to

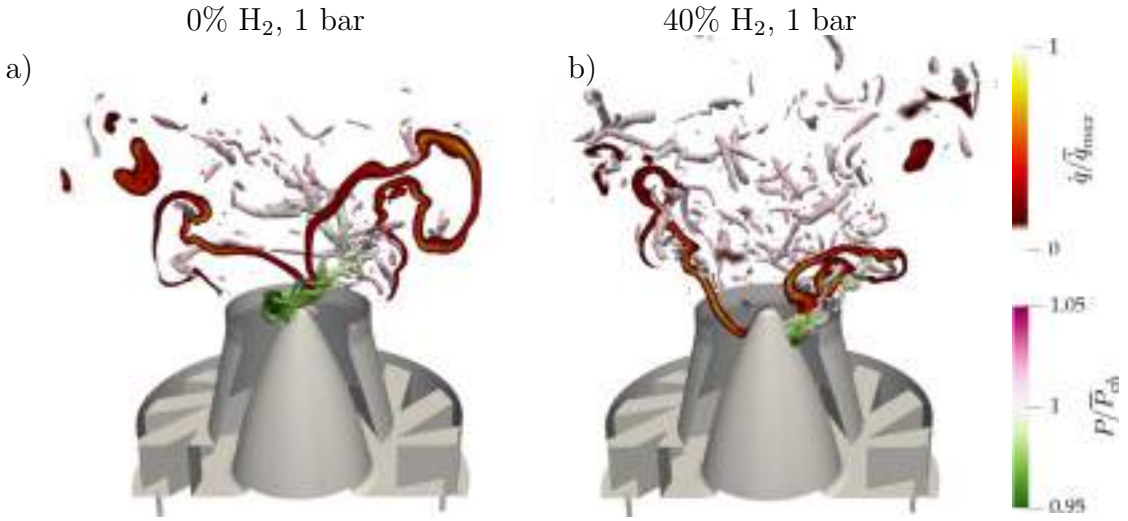

Figure 7.10: Comparison of instantaneous isosurface of Q-criterion at Q = 280 $\overline{U_x^2}/D_{inj}^2$ colored by pressure and field of instantaneous normalized heat release rate $\dot{q}/\dot{q}_{max}$ for Cases (a) *REF* and (b) *1*.

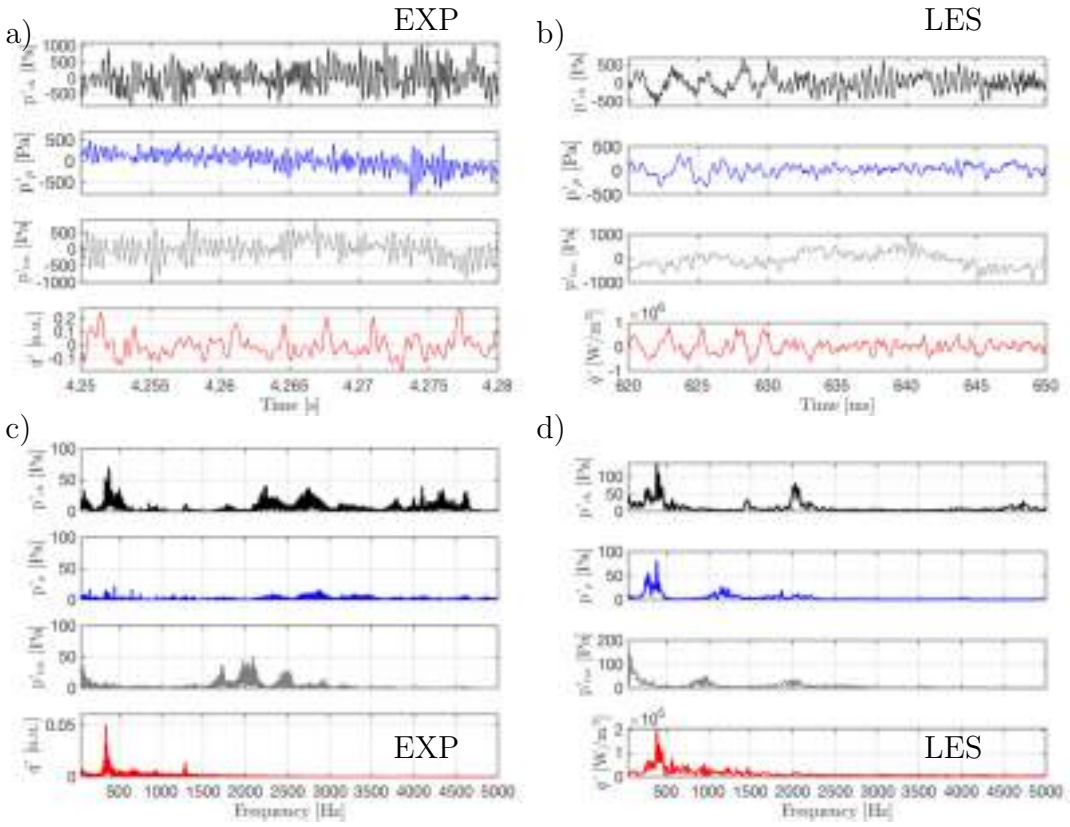

Figure 7.11: (a) Experimentally measured and (b) LES-predicted fluctuations of pressure in the combustion chamber (black), plenum (blue) and turning module (gray). The red line reports (a) volume-integrated OH* chemiluminescence signal and (b) heat release rate. (c-d) Signals spectra. Case *REF*: 0% H_2, 1 bar.

interact and distort the flame branches, causing the widen heat release rate region downstream of the centerbody in Fig. 7.9(b). No particular difference in terms of dimensions can be observed between these two cases when it comes to the vortical structures detaching from the backplane, indicating that the flame shape does not significantly impact the flow topology in the outer flow region.

7.4.2 Thermoacoustic response and flame dynamics

Figure 7.11 presents the (a) experimentally measured and (b) LES-predicted fluctuations of pressure in the combustion chamber (black), plenum (blue) and turning module (gray) for Case *REF*. The red line reports (a) the experimental volume-integrated OH* chemiluminescence signal and (b) the numerically predicted heat release rate. Both in experiments and LES, pressure oscillation levels in the combustion chamber, plenum and turning module reach approximately 1000 Pa. Fluctuation of OH* chemiluminescence signal and heat release rate are weak and do not correlate with pressure fluctuations in the combustion chamber. Corresponding spectra are presented in Fig. 7.11(c-d) for the experiments and LES, respectively. Pressure spectrum in the combustion chamber shows a weak peak at 380 Hz (80 Pa) and broad band noise in the high frequency range, above 2000 Hz. LES predicts a small peak at 390 Hz and also noise in the high frequency range. Note that some activity is present in the turning module at this high frequency range, suggesting that the noise registered is linked to acoustic modes of the turning module. OH* chemiluminescence and heat release rate spectra also exhibit the same peaks around 380 Hz both in experiments and LES, suggesting a weak coupling between heat release rate fluctuation and chamber pressure. However, the pressure fluctuation levels at this frequency in the combustion chamber (80 Pa) can be considered small compared to the global level of pressure fluctuation (i.e. 1000 Pa), indicating that no significant thermoacoustic activity is present. One can finally underline the presence in the experimental OH* chemiluminescence spectrum of a small peak at 1280 Hz which corresponds to the PVC frequency as reported by Chterev and Boxx [67].

When 40% hydrogen admixture is considered, the flame thermoacoustic response changes significantly. Figure 7.12 presents the (a) measured and (b) computed oscillations of pressure in the combustion chamber (black), plenum (blue) and turning module (gray) for Case *1*. The red line reports (a) the experimental volume-integrated OH* chemiluminescence signal and (b) the LES-predicted heat release rate. While pressure oscillations in the plenum and in the turning module

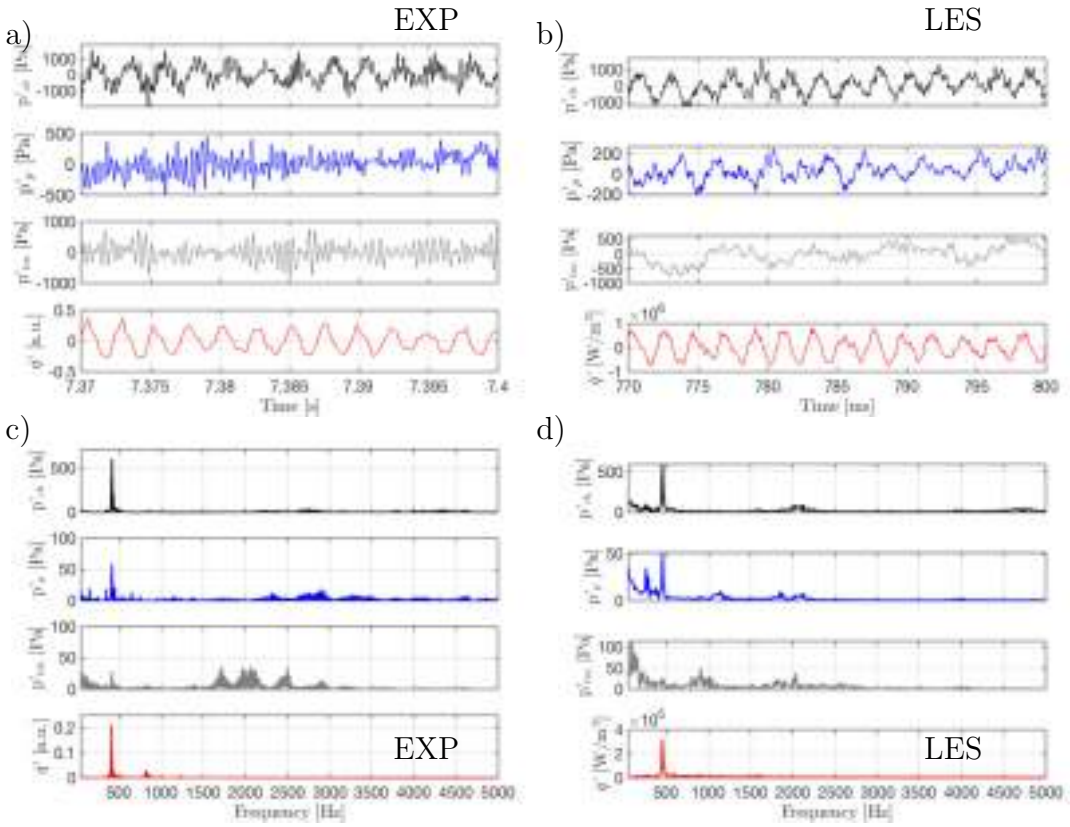

Figure 7.12: (a) Experimentally measured and (b) LES predicted fluctuations of pressure in the combustion chamber (black), plenum (blue) and turning module (gray). The red line reports (a) volume-integrated OH* chemiluminescence signal and (b) heat release rate. (c-d) Signals spectra. Case *1*: 40% H_2, 1 bar.

are of the same order of magnitude as for the reference case, pressure fluctuations in the combustion chamber are notably higher both in the experiments and LES (i.e. 2 kPa). The OH* chemiluminescence and the heat release rate signals furthermore oscillate in a coherent way and seem to be correlated to the pressure fluctuation in the combustion chamber. Corresponding measured and computed spectra are showed in Fig. 7.12(c-d), respectively: experimental measurements show strong peaks in the combustion chamber pressure (600 Pa) as well as in the OH* chemiluminesce spectra at 420 Hz, indicating that a thermoacoustic activity is present when 40% hydrogen enrichment is considered. LES correctly predicts the thermoacoustic limit-cycle at 440 Hz, as well as the proper pressure chamber oscillation level (600 Pa). Experimentally, high frequency noise is still observed in the turning module but is no longer recorded in the combustion chamber.

To investigate the nature of this thermoacoustic activity, the AVSP Helmholtz solver [53] is used to compute the acoustic modes of the system. To do so, the LES-predicted time-averaged sound speed fields $\bar{c}$, shown in Fig. 7.13 of (a) Case

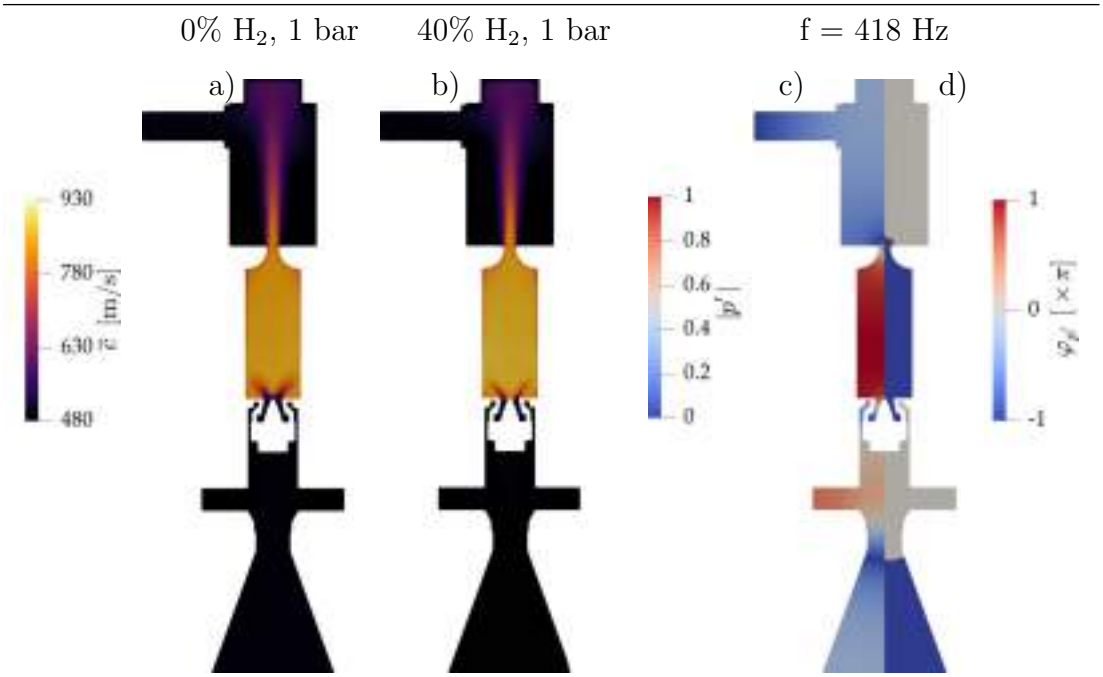

Figure 7.13: LES-predicted time-averaged sound speed field $\bar{c}$ for Cases (a) *REF* and (b) *1*. (c) Amplitude and (d) phase of the first acoustic (chamber) mode at 418 Hz computed with the Helmholtz solver for Case *1*.

REF and (b) Case *P1H40*, are used as an input to the Helmholtz solver. Adding H_2 only slightly impacts the mean temperature field, leading to weak differences in the corresponding time-averaged sound speed fields. As a consequence, the first acoustic mode of the system shows negligible differences in terms of mode shape and frequency. One acoustic mode is found at a frequency close to the peak recorded for Case *1*: i.e. 420 Hz. This mode, predicted at 418 Hz by LES, corresponds to a 3/4 wave (chamber) mode[1].

Dynamics of the H_2-enriched flame during the thermoacoustic oscillation is shown in Fig. 7.14 through instantaneous fields of the experimental OH-PLIF signal (top), LES-predicted OH mass Y_{OH} (middle) and hydrogen mass fraction Y_{H_2} (left, bottom) as well as the flow normal vorticity to the visualized plane $\omega_\perp$ (right, bottom). Red and white isocontours refer respectively to the heat release rate $\dot{q}$ at 10% of $\dot{q}_{max}$ and a low pressure value. Four equivalent phases are considered during the thermoacoustic oscillation for the experiments and LES. Instants (a) and (c) correspond respectively to the maximum and the minimum of OH* chemiluminescence and heat release rate signals while instants (b) and

[1]In the Helmholtz solver, a velocity node has been imposed for the air and fuel inlets as acoustic boundary conditions since flow is choked through small holes at the air inlet and acoustic BCs at the fuel inlet does not play a significant role [59]. A pressure node has been imposed at the turning module outlet, since at atmospheric condition the outlet valve is not choked. Note also that the Mach number at the combustion chamber nozzle exit is of the order of 0.5 but the AVSP Helmholtz solver is a zero Mach code so it does not take into account mean flow velocity and compressibility effects in the computation of the acoustic modes.

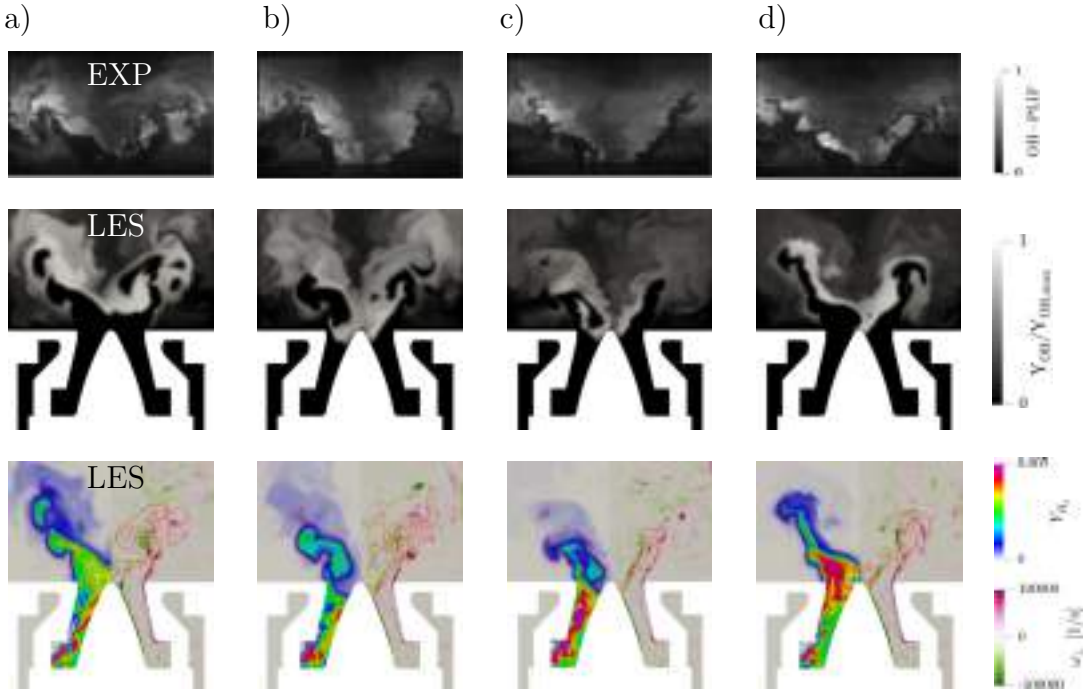

Figure 7.14: Instantaneous fields during the thermoacoustic oscillation of : experimentally measured OH-PLIF signal (top), LES-predicted OH mass Y_{OH} (middle) and hydrogen mass fraction Y_{H_2} (left, bottom) and flow vorticity normal to the plane $\omega_\perp$ (right, bottom). Red and white iso-contour refer to with heat release rate $\dot{q}$ at 10% of $\dot{q}_{max}$ and low pressure respectively. Four equivalent instants are considered during the thermoacoustic oscillation for experiments and LES. Instants (a) and (c) correspond to a maximum and a minimum respectively in the volume-integrated OH* chemiluminescence signal and the predicted heat release rate. Case *P1H40*: 1 bar, 40% H_2.

(d) correspond to a phase difference of $\pi/2$. Both experimentally, Fig. 7.14(top), and numerically, Fig. 7.14(middle), a classical flame response to a longitudinal mode is observed. The flame eventually detaches from the centerbody walls at instant (a), when the heat release rate is maximum, flame surface being notably smaller at instant (c), when the heat release rate is minimum. The stabilization point of the flame does move considerably during the thermoacoustic oscillation. As observed in Fig. 7.14(bottom), fuel-rich pockets are released in the combustion chamber and produce equivalence ratio fluctuations: a mechanism similar to the one observed in the atmospheric PRECCINSTA burner [27]. At the same time, (d) the interaction between the vortical structures detaching from the backplane corner and the flame is evidenced as well as the (d) flame front distortion due to the PVC (highlighted by the low-pressure white isocontour). The latter explains the wide heat release rate region visible along the axis of the domain shown in Fig. 7.9(b), the PVC being able to drag the flame front toward the region downstream of the centerbody tip.

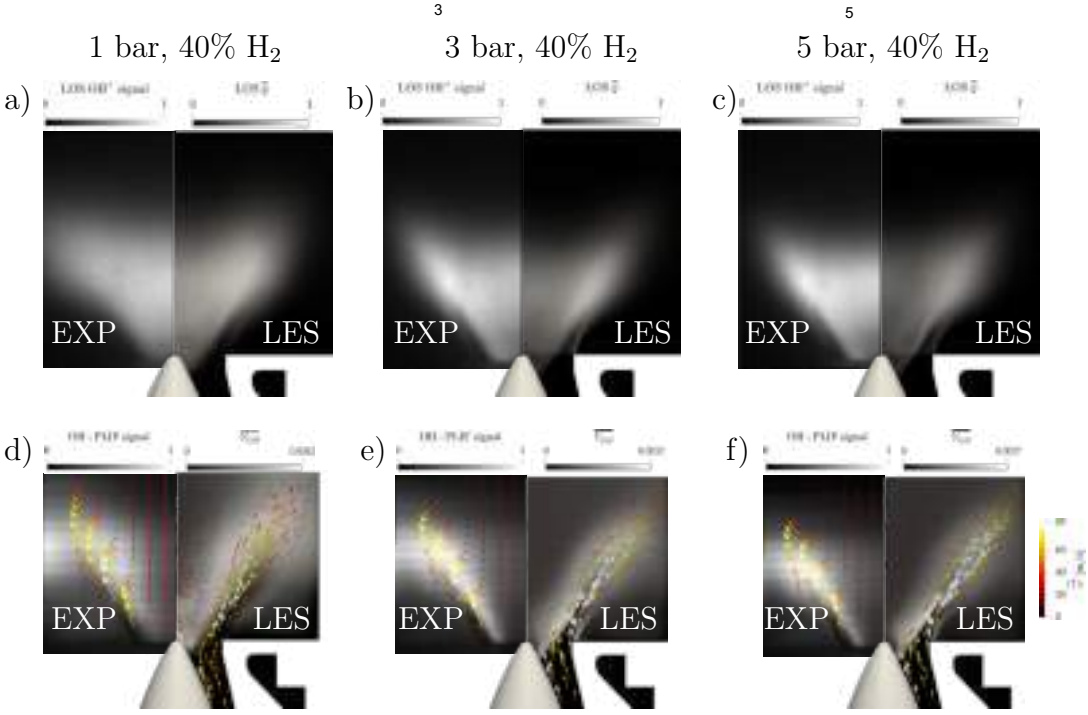

Figure 7.15: Experimentally measured time-averaged LOS-integrated OH* chemiluminescence image and time-averaged OH-PLIF signal compared to predicted LOS heat release rate $\overline{\dot{q}}$ and OH mass fraction $\overline{Y_{OH}}$ for cases (a-d) *P1H40*, (b-e) *P3H40* and (c-f) *P5H40*, respectively. The arrows are tangential to the measured and computed time-averaged velocity field in the plane $\overline{v}$. Their length and color indicate the velocity magnitude.

7.5 Elevated pressure effect

Measurements and computations of Case *P3H40* (3 bar, 40% H_2) and Case *P5H40* (5 bar, 40% H_2) are hereafter presented and compared to Case *P1H40* (1 bar, 40% H_2), showing the impact of elevated pressure on hydrogen enriched flames. The effect on the flame shape and its stabilization is discussed in section 7.5.1 while the change in the flame thermoacoustic response is analyzed in section 7.5.2. Finally, a discussion on the reactive flow time scales at different pressures is provided in section 7.5.3.

7.5.1 Flame shape and stabilization

Figure 7.15(a-c) compares the time-averaged LOS-integrated OH* chemiluminescence image to the LOS-integrated heat release rate $\overline{\dot{q}}$ computed via LES for (a) Case *P1H40*, (b) Case *P3H40* and (c) Case *P5H40*, respectively. While the 1 bar H_2-enriched flame (Fig. 7.15(a)) presents a V-shape attached to the centerbody tip as observed in section 7.4.1, the 3 bar and the 5 bar cases (Fig. 7.15(b-c),

respectively) present an attached M-shape for which the flame is anchored both at the centerbody tip and at the backplane. As pressure increases from 1 to 3 bar, the flame length and angle are significantly reduced while, a further increase in pressure to 5 bar only slightly modifies the flame shape. The experimental time-averaged OH-PLIF images are compared to the numerical OH mass fraction $\overline{Y_{OH}}$ in Fig. 7.4(c-e) for (a) Case *P1H40*, (b) Case *P3H40* and (c) Case *P5H40*, respectively. The arrows provide a qualitative comparison between the experimentally measured and the LES-predicted velocity field in the plane $\overline{v}$, their length and color indicating the velocity magnitude. Both in experiments and LES, increasing pressure leads to a reduction in the OH field extension: while at atmospheric pressure it reaches the view's limit, at 3 and 5 bar the height is decreased. At the same time, OH is increasingly present in the ORZs as the pressure increases, due to the secondary flame branches that appear to be closer to the backplane corner at 3 and 5 bar. Contrarily, for all cases, no OH is detected in the high velocity region at the injector exit. Note that the OH peak value predicted via LES is reducing when increasing pressure, indicating the corresponding reduction in OH specie lifetime. Note also that the OH signal just downstream of the centerbody tip decreases with pressure. Overall and for all cases, LES is found to be in satisfactory agreement with experimentally measured quantities and it correctly reproduces the shape change from a V-flame toward an attached M-flame with a corresponding reduction in length with elevated pressure. The latter is likely due to the decrease in chemical time scale (and hence increase in reactivity) for high pressure flames (see section 7.5.3).

Quantitative comparison of mean and RMS velocity profiles for Cases *P3H40* and *P5H40* are presented in Fig. 7.16, Fig. 7.17, and Fig. 7.18, Fig. 7.19, respectively. As the Reynolds increases with pressure, also the grid required resolution to correctly predict the velocity field raises. In the present work, the use of the SMR approach allows to have a satisfactory agreement with experimentally measured quantities also at elevated pressure, as observed from the plotted profiles.

Figure 7.20 presents the normalized time-averaged heat release rate $\overline{\dot{q}}/\overline{\dot{q}}_{max}$ predicted via LES for (a) Case *P1H40*, (b) Case *P3H40* and (c) Case *P5H40*, while the white isocontour indicates the 10% of $\overline{\dot{q}}_{max}$. The flame at atmospheric pressure (Fig. 7.20(a)) clearly presents a V-shape attached at the centerbody while (b) Case *P3H40* and (c) Case *P5H40* show a M-shape attached both at the centerbody tip and at the backplane. As the flame transits towards a M-shape, it gets more compact as clearly visible in Fig. 7.20(d) which presents the one-dimensional mean axial distribution of heat release rate $\langle\overline{\dot{q}}\rangle$, while the stabilization point at the centerbody wall does not change. The heat release

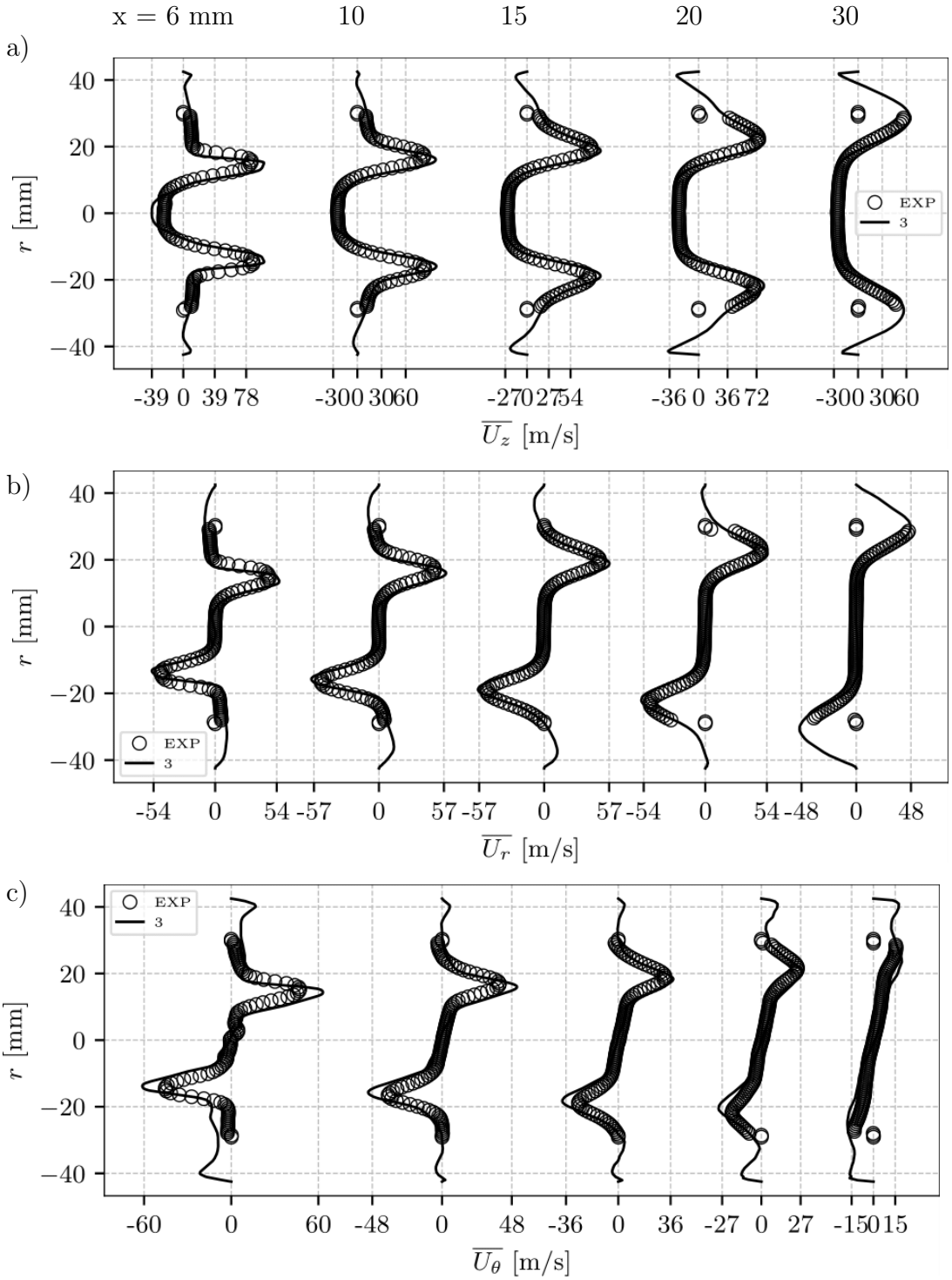

Figure 7.16: Profiles of mean (a) axial, (b) radial and (c) tangential velocity components at measurement planes at x = 6, 10, 15, 20 and 30 mm downstream of the combustion chamber backplane for LES in comparison to experiments. Case *P3H40*: 40% H_2, 3 bar.

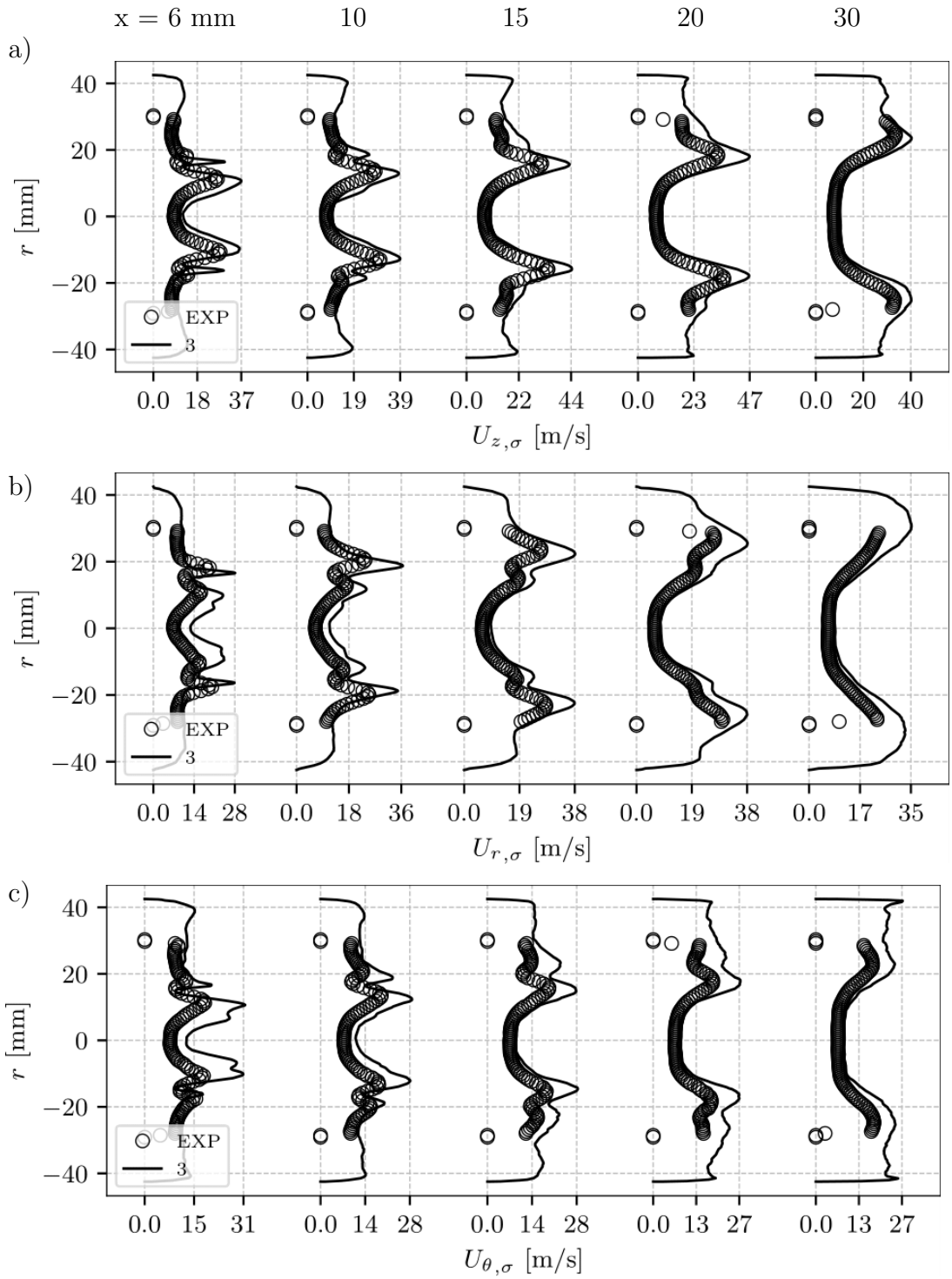

Figure 7.17: Profiles of RMS (a) axial, (b) radial and (c) tangential velocity components at measurement planes at x = 6, 10, 15, 20 and 30 mm downstream of the combustion chamber backplane for LES in comparison to experiments. Case *P3H40*: 40% H_2, 3 bar.

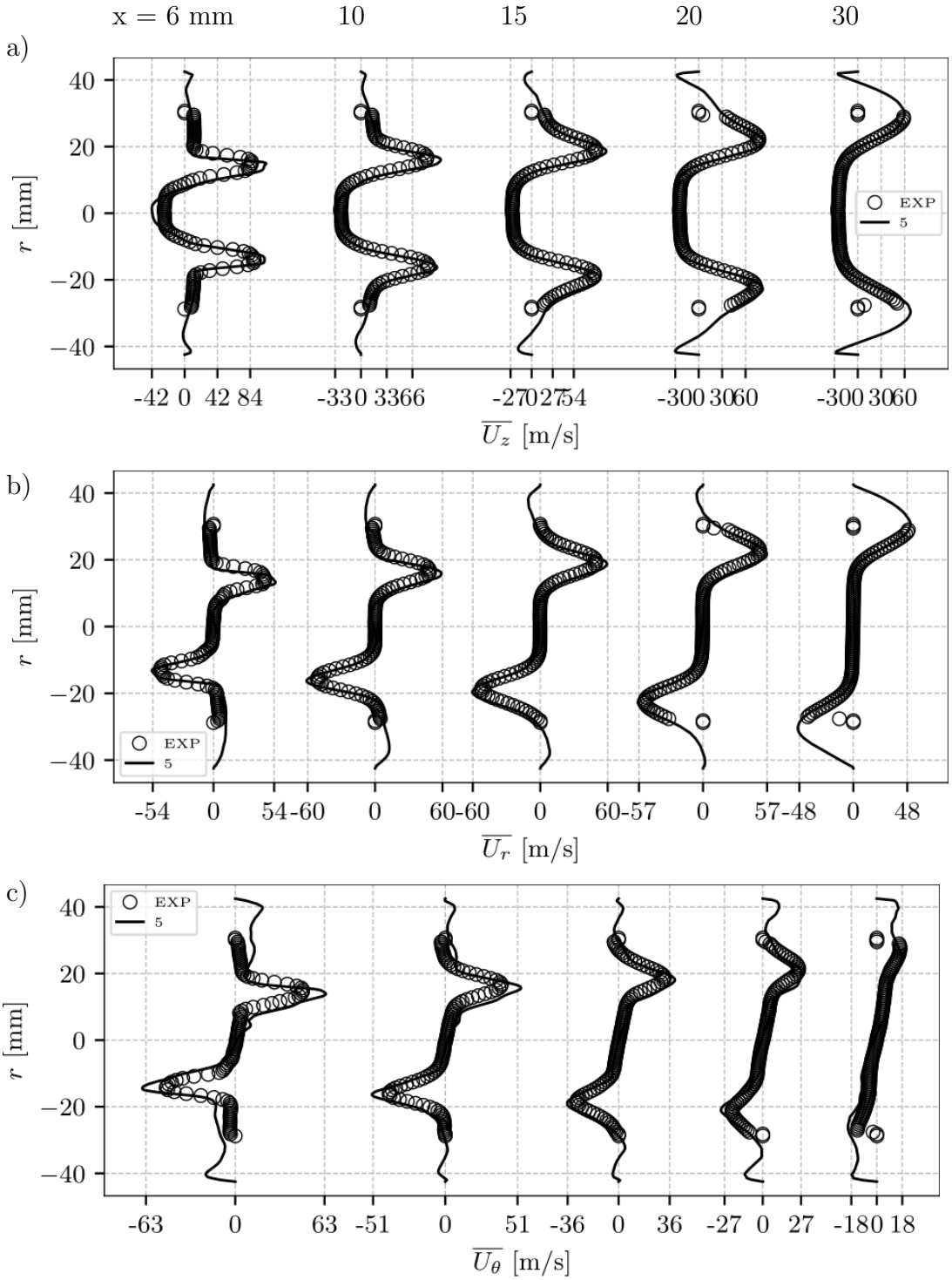

Figure 7.18: Profiles of mean (a) axial, (b) radial and (c) tangential velocity components at measurement planes at x = 6, 10, 15, 20 and 30 mm downstream of the combustion chamber backplane for LES in comparison to experiments. Case *P5H40*: 40% H_2, 5 bar.

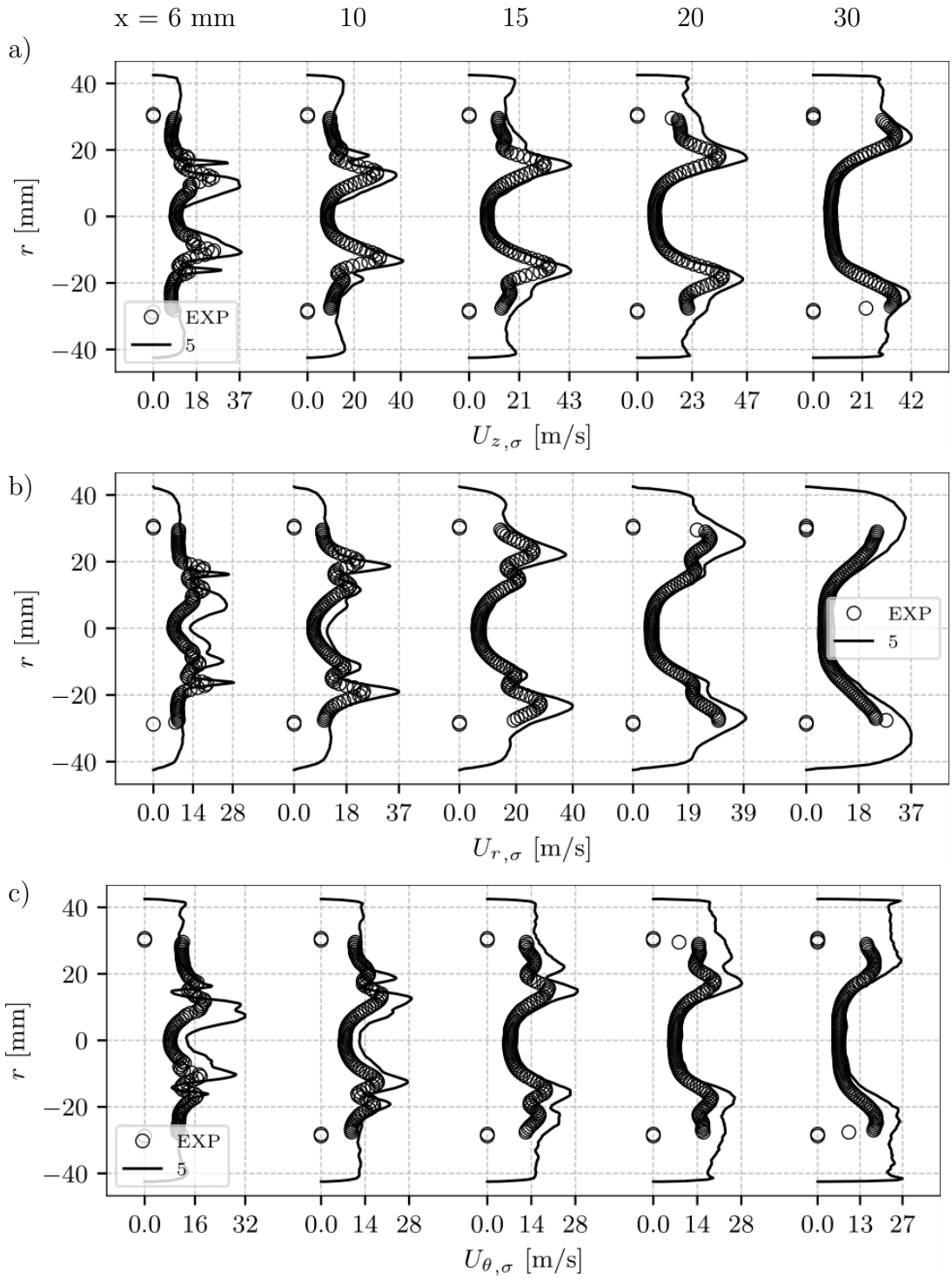

Figure 7.19: Profiles of RMS (a) axial, (b) radial and (c) tangential velocity components at measurement planes at x = 6, 10, 15, 20 and 30 mm downstream of the combustion chamber backplane for LES in comparison to experiments. Case *P5H40*: 40% H_2, 5 bar.

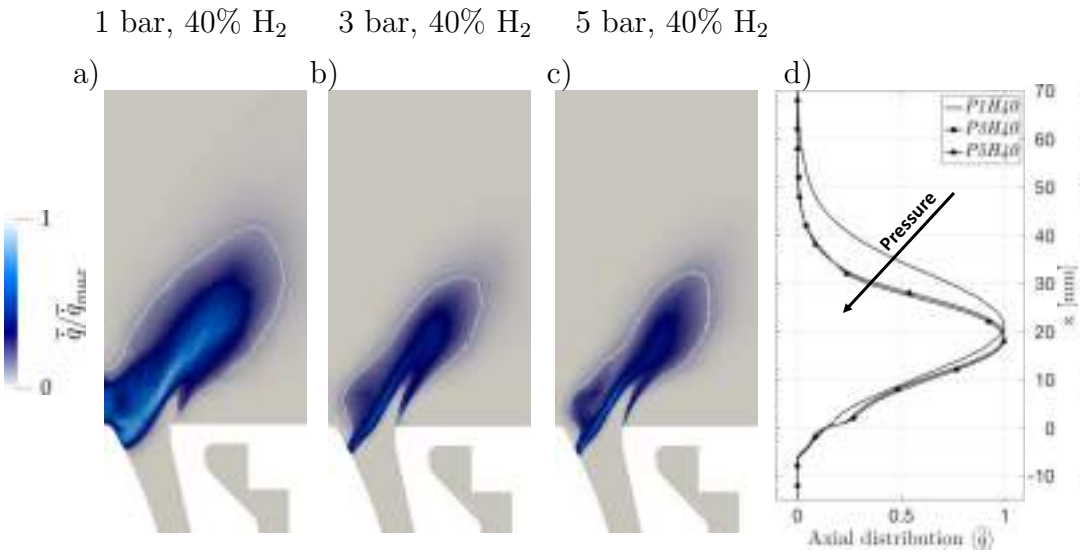

Figure 7.20: Normalized time-averaged heat release rate $\bar{\dot{q}}/\bar{\dot{q}}_{max}$ predicted via LES for Cases (a) *P1H40*, (b) *P3H40* and (c) *P5H40*. (d) Mean axial distribution $\langle\bar{\dot{q}}\rangle$. White isocontours indicate 10% of $\bar{\dot{q}}_{max}$.

rate distribution significantly changes when passing from 1 to 3 bar. However, it remains essentially the same when further increasing the pressure to 5 bar.

7.5.2 Thermoacoustic response

As pressure increases, the thermoacoustic response of the flame changes. Figure 7.21 presents (a) the measured and (b) the computed oscillations of pressure in the combustion chamber (black), plenum (blue) and turning module (gray) for Case *P3H40*. The red line reports (a) the volume-integrated OH* chemiluminescence signal and (b) the computed heat release rate. Both in experiments and LES, pressure oscillation levels in the combustion chamber and plenum are of the order of 2 kPa while experimentally the turning module exhibits epochs of large pressure fluctuations of approximately 10 kPa. Fluctuations of OH* chemiluminescence and heat release rate are however weak and not correlated to pressure fluctuations in the combustion chamber. To confirm this observation, corresponding spectra are presented in Fig. 7.21(c-d) for the experiments and LES, respectively. As the power density increases due to pressure increase, more modes are excited and different peaks appear in the spectra. Recorded pressure in the combustion chamber shows a weak peak at 483 Hz (150 Pa) that is predicted via LES near 510 Hz. The same peaks appear in both the OH* chemiluminescence and heat release rate spectra, suggesting a weak thermoacoustic coupling at these frequencies. The pressure fluctuation amplitude in the combustion chamber remains small and this Case *P3H40* can be considered as stable, i.e. with

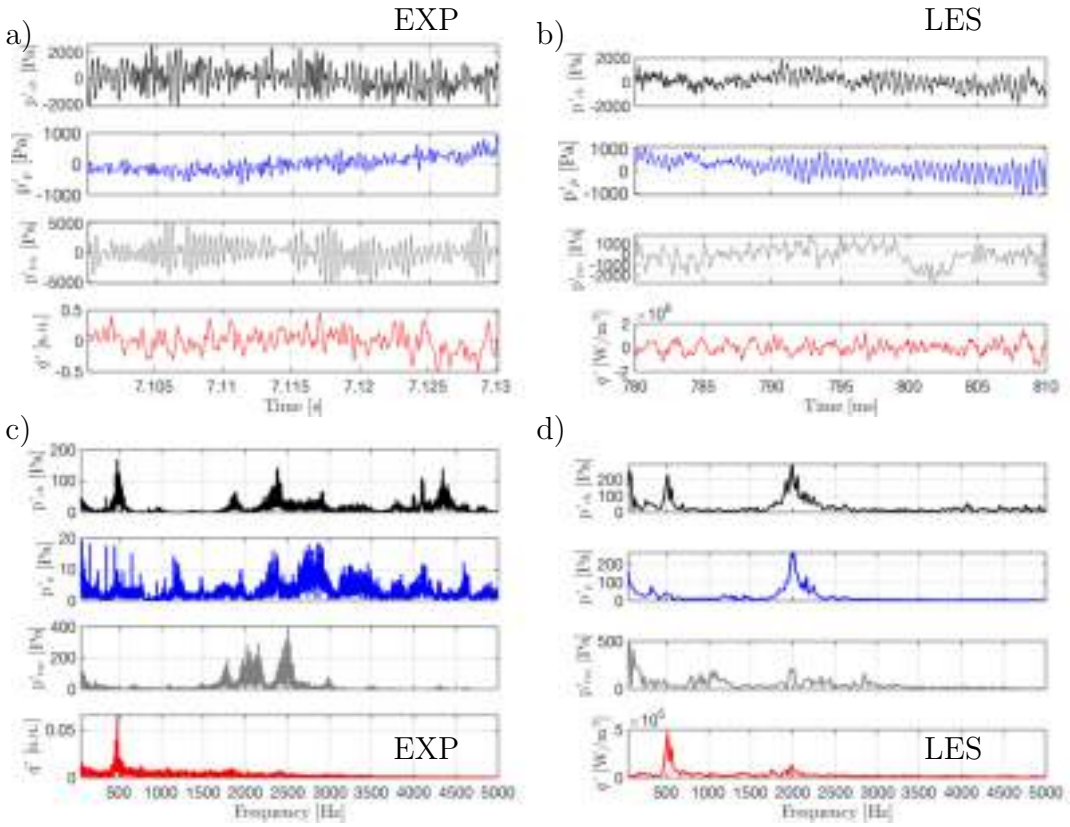

Figure 7.21: (a) Experimentally measured and (b) LES-predicted fluctuations of pressure in the combustion chamber (black), plenum (blue) and turning module (gray). The red line reports (a) volume-integrated OH* chemiluminescence signal and (b) heat release rate. (c-d) Signals spectra. Case *P3H40*: 40% H_2, 3 bar.

no strong thermoacoustic activity. Broad band noise with some potential peaks at higher frequencies are however visible in the chamber, turning module and plenum. This time, since the low frequency mode is weaker compared to Case *P1H40*, the high frequency range noise is more evident, similarly to Case *REF*.

A similar thermoacoustic response is observed at 5 bar. Figure 7.21 shows (a) the measured and (b) computed pressure fluctuations in the combustion chamber (black), plenum (blue) and turning module (gray) for Case *P5H40*. The OH* chemiluminescence and heat release rate signals are shown in red in Fig. 7.21(a-b), respectively. As pressure is further increased, the pressure oscillation amplitude in the chamber, plenum and turning module increase both in the experiments and LES while the heat release rate and the OH* chemiluminescence oscillations do not seem to be in phase with the pressure chamber fluctuation. Corresponding spectra in Fig. 7.21(c-d) confirm this observation and underline that, as pressure increases, the high frequency noise intensity gets larger while the low frequency range oscillations remain small. OH* chemiluminescence and heat release rate

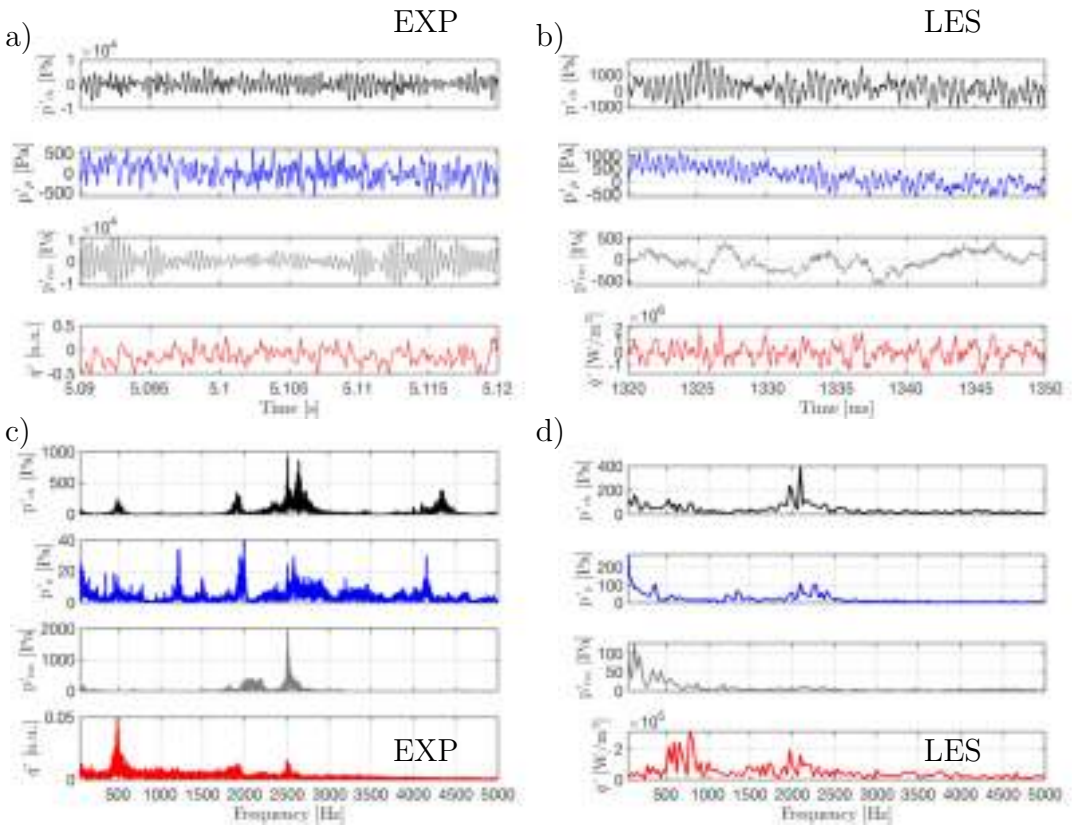

Figure 7.22: (a) Experimentally measured and (b) LES predicted fluctuations of pressure in the combustion chamber (black), plenum (blue) and turning module (gray). The red line reports (a) volume-integrated OH* chemiluminescence signal and (b) heat release rate. (c-d) Signals spectra. Case *P5H40*: 40% H_2, 5 bar.

spectra do show small peaks at 490 Hz and 530 Hz respectively, but the importance of the pressure oscillation in the combustion chamber at these frequencies remains negligible (200 Pa) compared to the global level of pressure fluctuations: this case can again be considered as thermoacoustically stable. Pressure is therefore found to consistently reduce the thermoacoustic oscillation in the low frequency range while increasing the high frequency activity although it does not couple with the heat release rate fluctuation.

This different thermoacoustic response can be due either to the flame shape change induced by the elevated pressure or to a change in the acoustic modes of the system. The latter mainly depends on the mean temperature field (that in turns affects the sound speed field) and on the acoustic boundary conditions. Figure 7.23 presents the computed time-averaged sound speed field $\overline{c}$ for (a) Case *P1H40*, (b) Case *P3H40* and (c) Case *P5H40* and clearly disqualifying such a process. In the elevated pressure cases, the turning module outlet valve is choked, meaning that it acoustically behaves like a wall (i.e. zero velocity fluctuation),

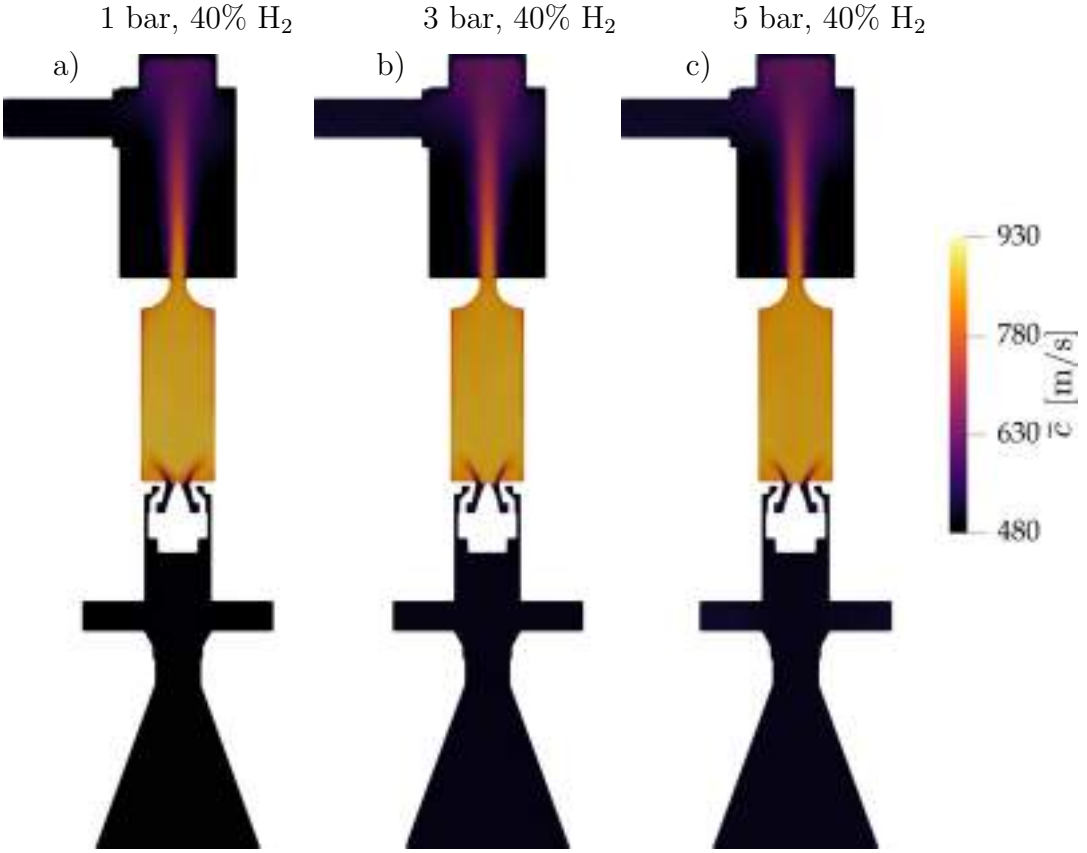

Figure 7.23: LES-predicted time-averaged sound speed field $\bar{c}$ for Cases (a) *1*, (b) *3* and (c) *5*.

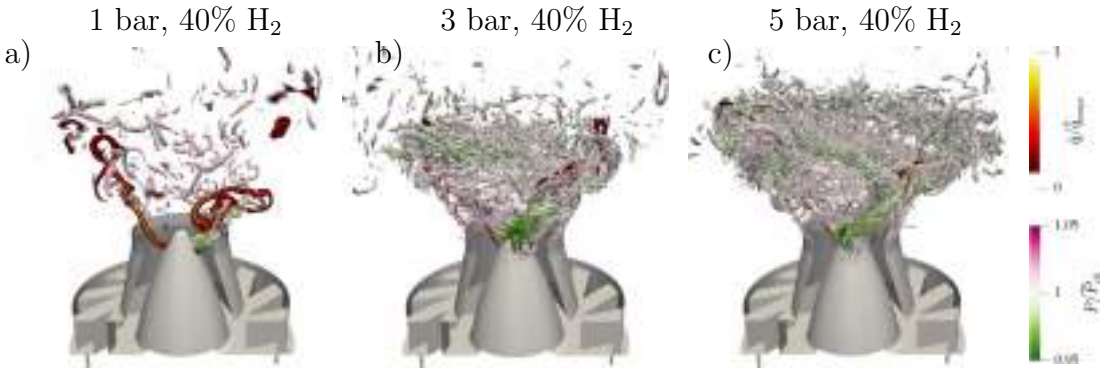

Figure 7.24: Comparison of instantaneous isocontour of Q-criterion at Q = 280 $\overline{U_x^2}/D_{inj}^2$ colored by pressure and field of normalized heat release rate $\dot{q}$ for Cases (a) *P1H40*, (b) *P3H40* and (c) *P5H40*.

which is not the case at atmospheric pressure. In such a case, the AVSP computation resulted in only a slight increase of the mode frequency, i.e. from 418 Hz at 1 bar to 432 Hz at 5 bar. Therefore, the effect of pressure on the system acoustic modes in the low frequency range is negligible and the change in the flame thermoacoustic response at elevated pressure is likely due to the changes in the flame shape and, hence, its response to acoustic oscillations [280].

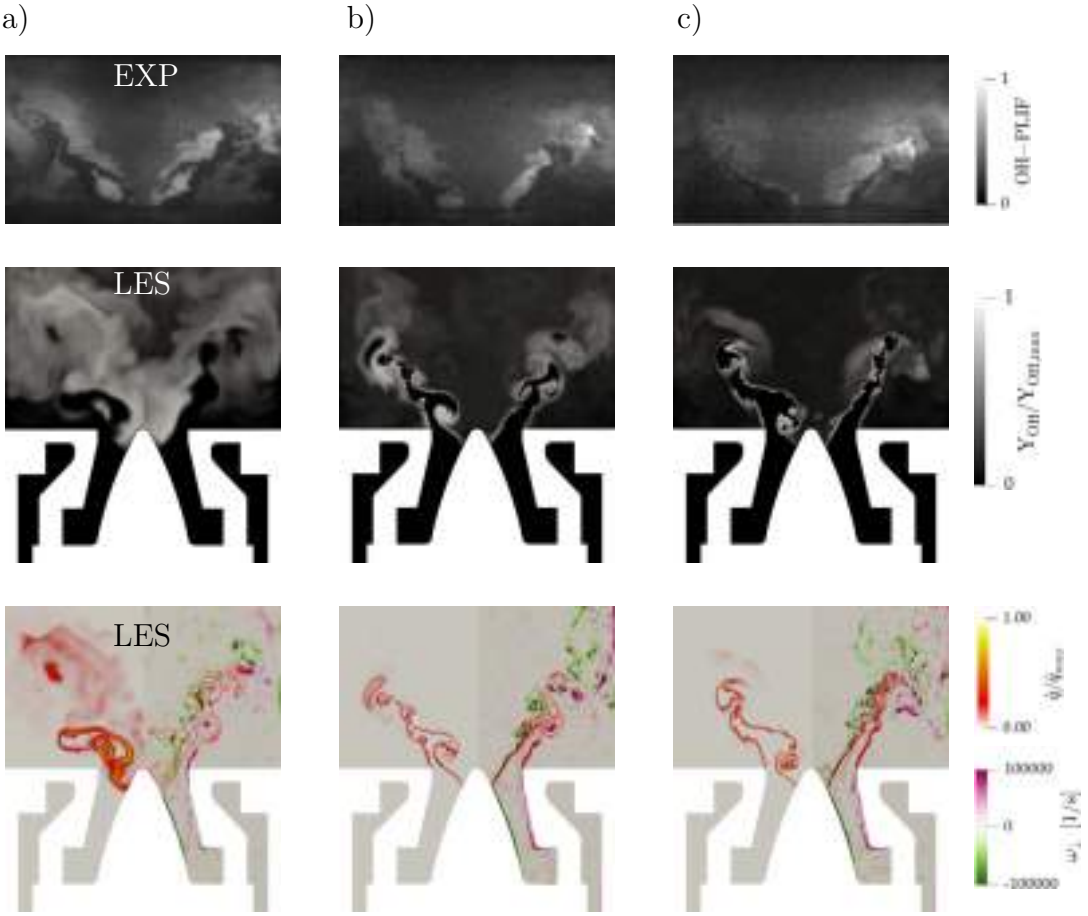

Figure 7.25: Instantaneous fields of the experimentally measured OH-PLIF signal (top), LES-predicted OH mass fraction Y_{OH} (middle), heat release rate $\dot{q}$ (left, bottom) and flow vorticity normal to the plane $\omega_\perp$ (right, bottom). Red and white isocontour refer to heat release rate $\dot{q}$ at 10% of $\dot{q}_{max}$ and low pressure respectively. Cases (a) *P1H40*, (b) *P3H40* and (c) *P5H40*.

7.5.3 Turbulent reactive flow time scales

Increasing pressure modifies the Reynolds number affecting the flow turbulence scales (Table 7.2). This effect is clearly visible in Fig. 7.24 that compares instantaneous isocontour of Q-criterion at Q = 280 $\overline{U_x^2}/D_{inj}^2$ colored by pressure and fields of normalized heat release rate $\dot{q}$ for (a) Case *P1H40*, (b) Case *P3H40* and (c) Case *P5H40*. While the PVC is clearly present in all cases as also observed experimentally by Chterev and Boxx [67], the dimensions and the structures of the vortical structures change. According to the increase in Reynolds number, when pressure increases, vortices become smaller and more numerous, potentially changing the interaction with the flame front due to the reduction in the turbulent time and length scales.

At the same time, pressure also affects chemical reactions. Figure 7.25 presents instantaneous fields of measured OH-PLIF signal (top), numerical OH mass frac-

tion Y_{OH} (middle), heat release rate $\dot{q}$ (left, bottom) and flow vorticity normal to the plane $\omega_{\perp}$ (right, bottom) for (a) Case *P1H40*, (b) Case *P3H40* and (c) Case *P5H40*. Red and white isocontours refer to heat release rate $\dot{q}$ at 10% of $\dot{q}_{max}$ and low pressure respectively. OH-PLIF images and computed OH fields clearly reveal the reduction in chemical time scale due to pressure. As pressure increases, the OH field gets thinner: since OH has a very long lifetime compared to that of the heat-release reactions persists in the burned gases long after the heat-release reactions are complete, further underlining the strong reduction in chemical time scale τ_c. At the same time, computed heat release rate fields show that flame thickness is drastically reduced at 3 and 5 bar: the flame front seems more corrugated by turbulence and vortical structures[1].

When it comes to vortex-heat release interaction, the Damköhler number is known to be a critical parameter since, for example, it can induce modifications in the heat release pattern due to periodic vortex shedding [281]. At the same time, Da has been reported to modify the interaction between the flame and the PVC. The latter has indeed two main effects on the flame: it leads to roll-up of the reaction zone at the flame base increasing heat release rate and it can introduce considerable aerodynamic stretch yielding local quenching or extinction of the flame front [282]. A similar behavior is noted in Fig. 7.25. At low Damköhler number (a) at atmospheric pressure, the PVC clearly causes the flame to roll-up at the flame base with an increase of heat release rate but the propagation of the flame is affected by local quenching and extinction. Due to the high vortex-induced aerodynamic stretch, part of the heat release is delayed and shifted downstream. Eventually, flame pockets detach from the main flame branches and form pockets of OH visible both in the experiments and LES. At higher Damköhler number (b-c) instead, when pressure is above 3 bar, the PVC causes the flame to roll-up and increases the local heat release rate. However the vortex-induced aerodynamic stretch appears to be lower and stretch does not seem to significantly affect reaction or the flame branches. Proper prediction of such phenomena due to time scales change at elevated pressure needs adequate grid resolution criteria and hence it is possible thanks to careful attention devoted to the LES modeling.

[1]Note that in LES the correctly prediction of flame thickness reduction is due to the mesh refinement procedure that allow to resolve the flame with the same thickening value, as illustrated in section 7.3

7.6 Conclusions

The impacts of mean pressure and hydrogen addition on the stabilization and combustion dynamics of a partially-premixed swirled-stabilized flame were studied experimentally and numerically. Experimentally, the PRECCINSTA burner was operated at elevated pressure, up to 5 bar, and the natural gas flame was enriched up to 40% of H_2 by volume. Numerically, LES results were validated against experimentally measured quantities such as OH* chemiluminescence and OH-PLIF images, stereoscopic particle image velocimetry (sPIV) and pressure recordings data, providing satisfactory agreement for all quantities. Particular attention is devoted to the choice of the numerical modeling. An Analytically Reduced Chemistry (ARC) kinetic scheme is able to correctly describe the CH_4-H_2/Air chemistry at elevated pressure. Since pressure significantly impacts the turbulent reactive flow scales, Static Mesh Refinement (SMR) approach is used for discretizing the fluid domain and allow for correctly resolving the different flames with the same combustion modeling at all pressured. Four flames were hence selected for LES simulations. Case *REF* corresponds to the reference natural gas flame (1 bar, 0% H_2), while cases *P1H40*, *P3H40* and *P5H40* refer to 40% H_2-enriched flames at 1, 3 and 5 bar, respectively.

Hydrogen enrichment at atmospheric pressure affects the flame stabilization, its shape and the corresponding thermoacoustic response. Flame *REF* (1 bar, 0% H_2) presents a lifted M-shape with a strong Precessing Vortex Core (PVC) and no significant thermoacoustic response. When hydrogen addition is considered (Case *P1H40*), the flame takes on an attached V-shape, the PVC is weaker and the flame couples with the combustion chamber first acoustic mode at 420 Hz in a limit-cycle thermoacoustic oscillation that is predicted by LES in satisfactory agreement with experimental data. Computation of the acoustic modes of the system through an Helmholtz solver show no significant differences, confirming that the different thermoacoustic response is due to the flame shape change. The latter is likely due to the notably higher flame speed and increased resistance to strain of the H−2-enriched flame.

Elevated pressure modifies in turn the flame shape, its thermoacoustic response and also the characteristic time scales of turbulent reactive flows. As pressure increases, Cases *P3H40* and *P5H40* present attached M-shape flames that get shorter and more compact. The combustor becomes more noisy but the coupling between the first acoustic mode and the heat release rate, which was present at atmospheric conditions, disappears. No significant change in the first acoustic chamber mode is captured by the Helmholtz solver, suggesting that the

flame shape changes is the critical parameter that explains the different thermoacoustic response at elevated pressure. Finally, pressure modifies the characteristic time scales of the turbulent reactive flow. As pressure raises, the Reynolds number increases reducing the Kolmogorov turbulent scale and the turbulent time scale τ_k, hence changing the dimensions and the relative strength of the vortical structures. At the same time, the laminar flame speed, the thermal flame thickness and the chemical time scale τ_c decrease. While the decrease in turbulent and chemical time scales are of the same order of magnitude (the Karlovitz number remains almost constant), the Damköhler number significantly increases with pressure, leading to a modification in the flame/vortical structures interaction.

Therefore, both hydrogen enrichment and elevated pressure are found to significantly affect the flame shape, its stabilization and the corresponding thermoacoustic response in the HIPOT PRECCINSTA burner. Change of flame shape is the key element of the different thermoacoutic response and it is likely due to the different flame properties linked to hydrogen enrichment and to the modification of the chemical and turbulent time scales linked to elevated pressure. For all cases, LES successfully predicts the complex turbulent reactive flow, hence confirming the potential of numerical simulations in investigating high-power density flames close to real engines operating conditions.

Part III

Spinning Combustion Technology

Chapter 8

The NTNU burner: stabilization of spinning flame

Contents

To reduce the carbon footprint of the aviation sector, aeronautical companies have been striving to lower engine emissions via the development of reliable lean combustors. In this context, effort has been devoted to the better understanding of various flame dynamics with emphasis on thermoacoustic instabilities, lean blow-off and extinctions. In line with this effort, Safran Helicopter Engines has recently developed and patented the revolutionary spinning combustion technology (SCT) for its next generation of combustors. This technology has indeed great flexibility when it comes to ignition and blow-off capabilities. To better understand the various physical mechanisms occurring in a SCT combustor, a joint numerical and experimental analysis of the flame stabilization in this spinning combustion technology framework has been devised. On the experimental side, the NTNU atmospheric annular combustor has been modified to introduce a relevant azimuthal component of velocity while operating under premixed fuel conditions, following the SCT concept. Note that to reduce temperature at the backplane of the chamber, film cooling is incorporated to avoid fuel injector damage. On the numerical side, high fidelity Large Eddy Simulations of the test bench have been carried out with the AVBP code developed at CERFACS, providing insights on the flame stabilization in this unique SCT geometry. In particular, it is noted that there is a strong interaction between the cooling film and the highly

swirled flames exiting from the fuel injector bend. In that respect, changing the injector or global equivalence ratios while operating the SCT is shown to affect the combustion of this design. Note that these results have been published in *Proceedings of ASME Turbo Expo* [77].

8.1 Introduction

Development of low-emission gas turbine combustors is a major design challenge for propulsion and land-based power generation applications. Indeed, multiple numerical and experimental studies have been carried out, showing that lean combustors typically present various and undesirable flame dynamics issues, such as thermoacoustic instabilities [9, 10, 11, 12, 13], lean blow-off [14, 15] and extinctions [16, 17]. To support this design challenge, together with experiments, Large Eddy Simulation (LES) approach has been mainly used because of its ability to accurately predict the interactions between turbulent flow, spray and flame for stabilized flames [19, 33] or even pollutant emissions [34, 35, 36, 37].

When it comes to existing designs, different strategies have been proposed to develop lean combustors that are capable of stable operation over an extended operative range. In certain cases, both passive and active control systems have been proposed for the control of thermoacoustic instabilities [178]. Acoustic dampers for example, such as Helmholtz resonators, have been successfully employed to suppress combustion instabilities in gas turbine combustors [283, 284]. Adjustment of fuel flow distribution has also been investigated, yielding the apparition of radial and axial fuel staging [285], asymmetric fuel distribution [286] and pilot fuel [287]. Changes in fuel injector geometry has equivalently been proven to be an effective strategy for reducing combustion instabilities [288]. More recently, hydrogen-enriched flames have become popular due to the effect of hydrogen on stability and pollutant formation [7, 8].

Other non-conventional combustion systems have also been proposed to enhance combustion efficiency and combustor operability. The Trapped Vortex Combustor, for example, has been proposed to offer improvements in lean blow out and high altitude relight due to enhanced flame stabilization in the vortex trapped inside the combustor cavity [289, 290].

In an effort to meet regulation objectives, Safran Helicopter Engines has recently developed and patented the innovative spinning combustion technology (SCT) for its next generation of combustors: i.e. the ARRANO engine used in the Airbus Helicopters H160 [18]. The main concept behind SCT is to introduce

a strong azimuthal flow in the annular chamber that enhances flame-flame interactions so as to improve ignition and blow-off capabilities, while also improving stability over a wide range of operating conditions. Note that although swirling flows are typical nowadays in the combustion community for single injectors and have been extensively studied in the literature [19, 20], "global" swirling flow is much less frequent when it comes to aeronautical applications (e.g. Short Helical Combustor [21], CHAIRLIFT combustor [22]) and much needs to be understood.

This work aims at presenting and analyzing SCT to fill the observed gap of knowledge about spinning flow in combustion. For this purpose, following the SCT concept, the NTNU atmospheric annular combustor has been modified to introduce a relevant azimuthal component of velocity and LES have been performed at CERFACS to get more insights in this spinning flame. In this Chapter, first the modified geometry is presented together with instrumentations and measurements used to carry out the experimental test campaign. The numerical approach is then discussed. Second, after a successful validation of the numerical results with experiments, global flame shape and spinning flame stabilization mechanisms are presented and analyzed for the reference case. Finally, two different operating conditions are considered to investigate the effect on flame stabilization of fuel injector local equivalence ratio and combustor global equivalence ratio. This last stage underlines the importance of these two parameters in spinning combustion systems.

8.2 Experimental setup

8.2.1 SCT atmospheric annular combustor

The experimental setup developed at NTNU to support SHE test benches observations at design phases, corresponds to a lab-scale SCT helicopter engine as seen in Fig. 8.1. This test bench geometry is based on the annular combustor first conceived in Cambridge [291, 292], and has been modified for the purpose of this study. Now it consists of six fuel injector-cooling duct pairs arranged in an annular configuration as seen in Fig. 8.2 and Fig. 8.3.

For operation, a premixed air-ethylene mixture is fed into the plenum chamber of diameter $D_p = 212\,\text{mm}$, and height $L_p = 200\,\text{mm}$, which features a hemispheric body of diameter $D_h = 140\,\text{mm}$ at the exit. The plenum and the combustion chamber are linked by six straight injector tubes of height $H_t = 145\,\text{mm}$, which deliver the mixture to the six fuel injector bends located at the backplane of the combustor chamber. When it comes to the combustion chamber itself, it has

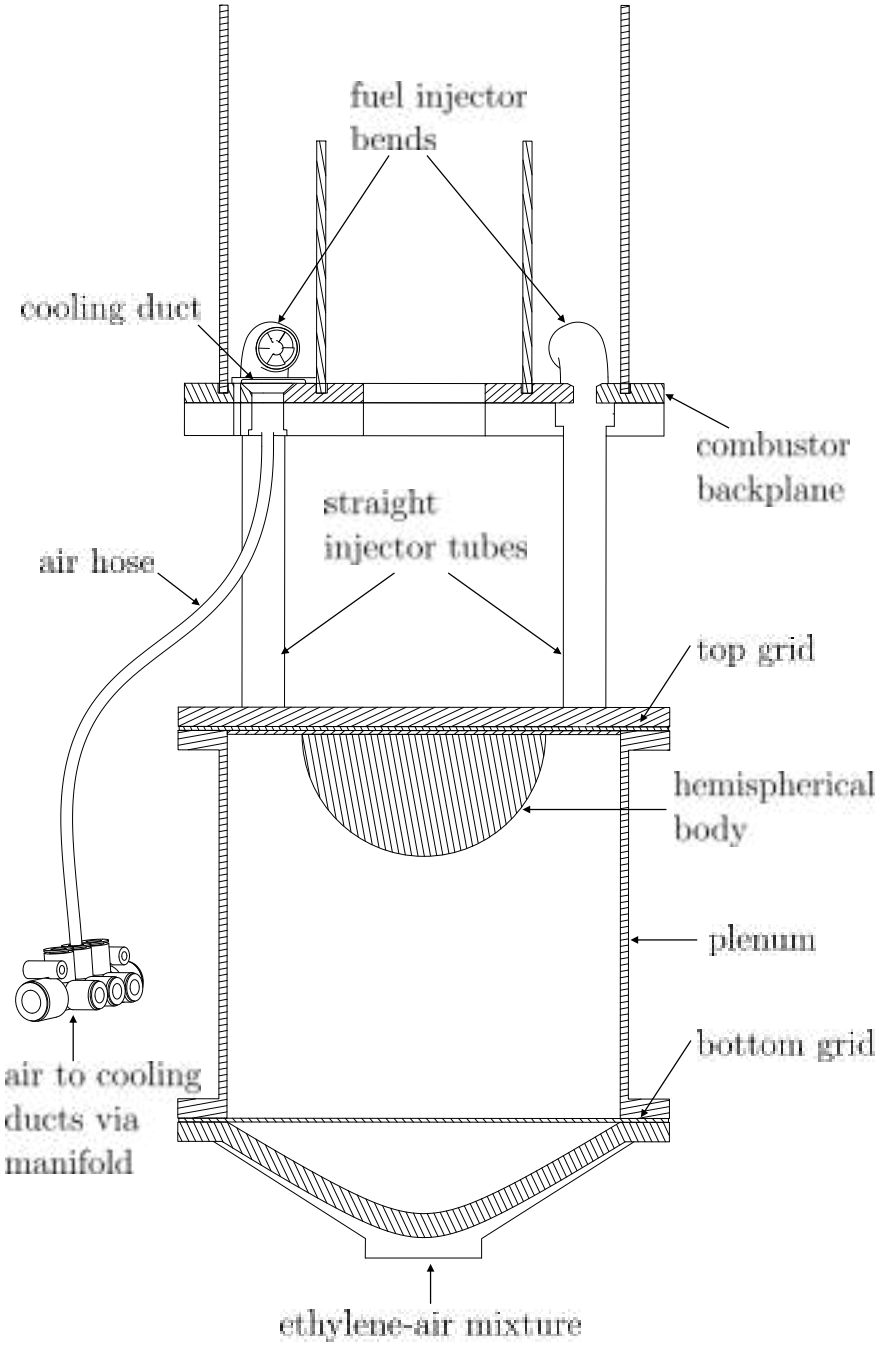

Figure 8.1: Schematic of the laboratory scale SCT engine.

Figure 8.2: Photo of the laboratory scale SCT engine.

an inner diameter of $D_{c,i} = 127\,\text{mm}$ and outer diameter of $D_{c,o} = 212\,\text{mm}$. The height of the inner and outer combustor walls are $H_i = 130\,\text{mm}$ and $H_o = 200\,\text{mm}$ respectively. They are made of quartz for optical access. Finally, a separate piping system supplies air to the cooling ducts via individual hose pipes connected to a manifold.

The geometry of the combustor backplane, the fuel injector bend and the cooling duct are shown in Fig. 8.3. The fuel injector is a 90° bend pitched by $\beta = 5°$ downwards and rotated by $\alpha_f = 23°$ towards the inner combustor wall. The cooling duct is rotated by $\alpha_c = 12°$ inwards. The proximity of the main injector outlet to the cooling duct (at 15 mm) results in flames that are directed towards the surface of the cooling film. When it comes to the main fuel injectors, a six-vane swirler, with a geometric swirl number of 1.22 [291], is placed at the exit of each bend. They are oriented in a counter-clockwise direction when looking at the bend outlet.

8.2.2 Instrumentation and measurements

The air and fuel flow rates are regulated by Alicat mass flow controllers (MFCs) which have an accuracy of ± 0.8% of the reading + 0.2% of the full scale. A 2000-slpm MFC supplies the necessary flow rate for the air in the premixed fuel mixture, while a 225-slpm MFC is used for the fuel. An additional 1000-slpm MFC adjusts the air flow rate through the cooling ducts.

Planar-induced laser fluorescence (PLIF) is performed by means of a diode-pumped, frequency-doubled Nd:YAG laser (Edgewave IS 400-2-L) operated at 10

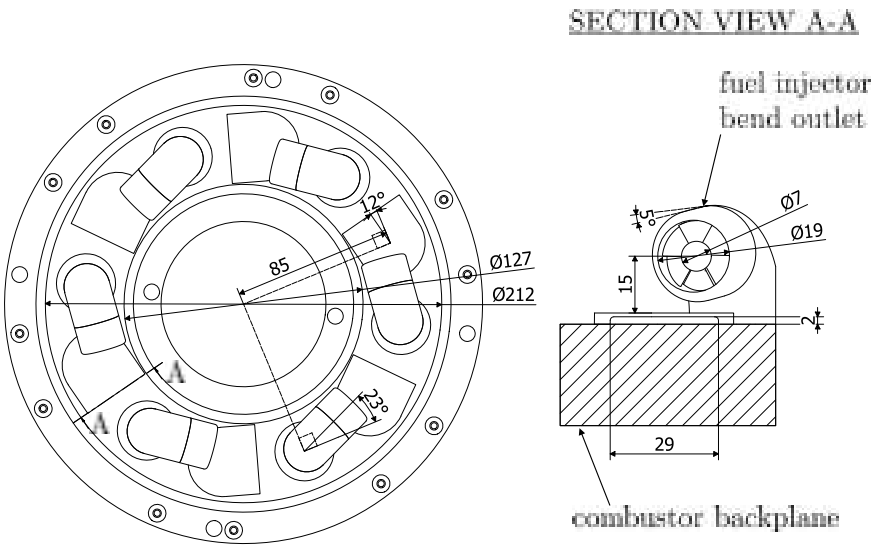

Figure 8.3: Geometric details of the laboratory scale SCT engine.

kHz to pump a Sirah Credo dye laser using ethanol-dissolved Rhodamine 6G. The output ultra-violet pulse from the dye laser has an energy of 0.3 mJ, with an approximate wavelength of 293.56 nm. A Phantom V2012 cameras is fitted with an intensifier (LaVision IRO), a macro-extension tube, and an UV filter (centre wavelength of 310 nm with a full width at half maximum of 10 nm) for PLIF imaging. A gate width of 100 ns is used. For OH luminescence imaging, a Photron SA1.1 camera is used instead, with a gate width of 80,000 ns. For each operating case, 5000 OH luminescence and PLIF images are acquired at 10 kHz. The PLIF images have an image resolution of 800 x 896 pixels, corresponding to a spatial resolution of 0.063 mm/pixel. The OH images have an image resolution of 768 x 768 pixels, corresponding to a spatial resolution of 0.083 mm/pixel.

Prior to this, the non-reactive velocity flow profile at the fuel injector outlet is characterised using hot-wire anemometry.

8.2.3 Operating conditions

The SCT combustor is operated with ethylene-air premixed at equivalence ratios between 0.8 to 1.0, and bulk velocities between 16 to 25 m/s. No combustion instabilities were observed within this operating range. For the purpose of investigating the flame stabilization of this combustor, it is decided that the bulk velocity v_b for each fuel injector will be fixed at 18 m/s in all cases presented in this Chapter. The equivalence ratios are then varied depending on the case. In the following, the local equivalence ratio, ϕ, refers to the equivalence ratio of the premixed ethylene-air mixture of the fuel injector. The global equivalence

ratio, Φ, refers to the effective air-fuel ratio within the combustion chamber considering the introduction of the additional air from the cooling ducts. Three cases, as indicated in Table 8.1, have been selected for numerical simulations and experiments.

Case	ϕ	Φ	Cooling rate ($\times 10^{-3}$m^3/s)
A	1.0	0.65	15.0
B	1.0	0.80	7.2
C	0.8	0.65	6.7

Table 8.1: Summary of the operating conditions.

Case A is considered here as the reference case, then cases B and C have been selected due to their similar cooling rates of approximately 7×10^{-3}m^3/s. Case B has the same local equivalence ratio as case A but with a different cooling rate. One can thus investigate the effect of cooling on the flame stabilization. Case C has instead the same global equivalence ratio as case A but with a different local equivalence ratio allowing to analyze the local equivalence ratio effect.

8.3 Numerical setup

High-fidelity LES are performed using AVBP (Chapter 2). The classical WALE turbulent closure for the subgrid Reynolds stresses [293] is used while to accurately solve for the convective terms, the third order accurate Taylor-Galerkin scheme [48] is adopted. The turbulent combustion model is the classical dynamic TFLES model that allows to correctly solve the flame regions[1]. The Charlette efficiency model with a standard coefficient $\beta_{Ch} = 0.5$ is also used to model flame-turbulence interaction effects [61].

The domain used for LES is shown in Fig. 8.4 and consists of one periodic sector, comprising the fuel injector and the cooling duct, since sector-to-sector variations have been experimentally found to be negligible. It has been discretized using an unstructured mesh which has been refined. The mesh refinement approach of Chapter 3 has been applied to refine the mesh in the flame regions. The final computational grid consists of approximately 33M tetrahedral elements, Fig. 8.4. Note that, using the above described approach, the refined grid yields satisfactory matching with experimental pressure loss (and hence velocity field) and reasonable y$^+$ values at the walls (e.g. maximum value is 6) keeping the cost of the simulations reasonable: i.e. without having the need to use very low time

[1]Note that, in this case, the flame sensor is based on the fuel oxidation reaction and flame is artificially thickened to have 5 points across the flame front.

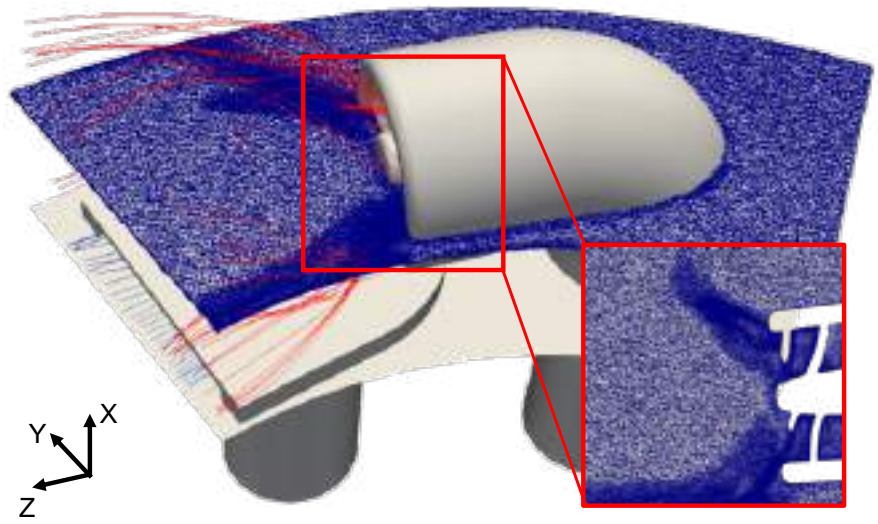

Figure 8.4: LES computational domain with zoom on mesh detail on a vertical plane cut. Chamber walls and periodic boundaries are not shown. Cooling flow and fuel injector flow streamlines are showed in blue and red respectively. In the CRS, X axis is vertical and Z axis is aligned with fuel injector axis while origin is positioned at the center of the fuel injector exit.

steps and too many cells while satisfying requirements for a wall resolved LES. The resulting characteristic mesh size is lower than 0.4 mm in the flame region, leading to low thickening values (i.e. maximum thickening applied is 10).

Inlets and outlets are treated using the Navier-Stokes Characteristic Boundary Conditions [30] imposing the velocity profile for a fully-developed turbulent flow at the injector inlets with a bulk velocity reported in Tab. 8.1. No-slip condition is imposed at the chamber backplane wall along with a thermal condition that is imposed for each operating condition through a measured temperature profile. When it comes to the lateral chamber walls, they are set as no-slip with a heat loss that is taken into account by imposing a suitable thermal resistance computed assuming a conduction coefficient of $\lambda = 2.17$ W/mK for the 4 mm thick quartz wall and a typical heat resistance for the external natural convection of $R = 5E-2$ m^{2}K/W. Note that, for all the computed operating conditions of Tab. 8.1, the resulting temperature profile is in good agreement with the one measured with movable thermocouples on the internal side of the flame tube, Fig. 8.5(b). Location of experimental data is shown in Fig. 8.5(a) by the dotted yellow line. Due to the good behavior of the simplified approach used for the combustion chamber walls, the same method has been also used for the cooling plate for a first analysis, even if more complex tools for conjugate simulations exist as illustrated in Chapter 4. Indeed, the used approach takes into account the heat conduction

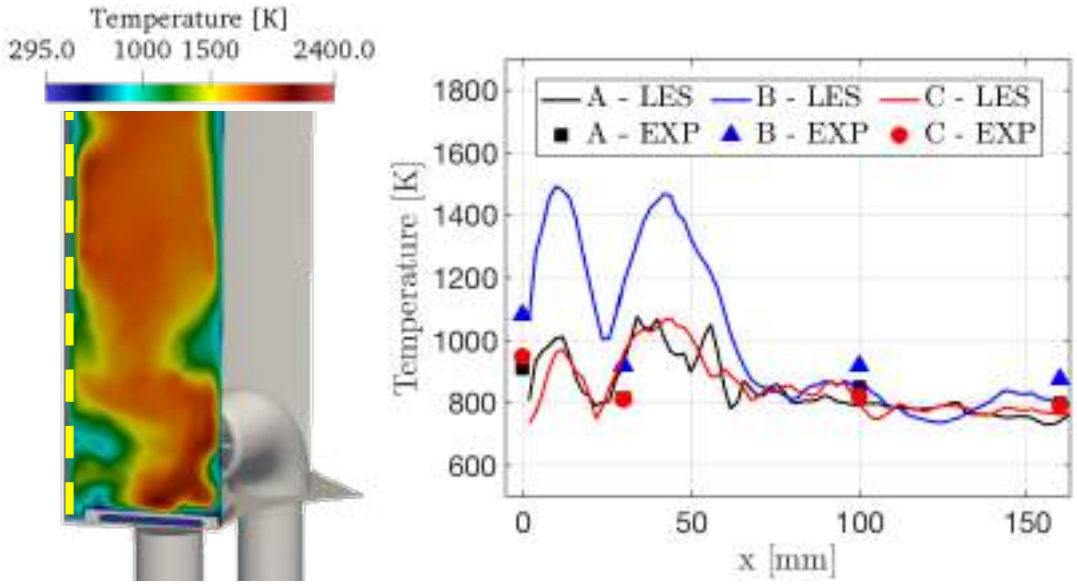

Figure 8.5: Computed field of time averaged temperature (a) (Tab. 8.1 - case B) on a planar cut aligned with cooling duct exit, showing experimental data location (dotted yellow line). Comparison between computed and experimental temperature axial profiles (b) on the combustion chamber wall in steady conditions (Tab. 8.1 - cases A, B, C.)

through the cooling plate and hence heat transfer to the cooling flow. First, average thermal resistance has been determined for both internal and external flow streams on the cooling plate, considering typical Nusselt number correlations to take into account forced convection [294], together with the thermal resistance of the metal plate. In this manner, the total thermal resistance seen by the external flow is imposed as the sum of internal flow thermal resistance and metal plate thermal resistance (and viceversa for the internal flow). A posteriori, it has been verified that the heat flux integrated over the external surface of the cooling plate is equal to the heat flux integrated over the internal surface, meaning that the heat lost by the flame is heating the cooling flow through the plate. The method therefore results to be fully consistent providing a computed heat to the cooling flow of 140 W (for case A in Tab. 8.1).

For combustion, the C_2H_4/Air reaction is described by the two-step mechanism[1] 2S BFER that includes 6 species and 2 reactions (C_2H_4 oxidation and CO-CO_2 equilibrium) and which has been validated against detailed schemes and experimental data, Fig. 8.6.

[1]Note that in this Chapter, a two-step mechanism is preferred over more detailed mechanisms to limit the cost of the simulation while achieving satisfactory prediction of the laminar flame speed for C_2H_4/Air mixture. In Chapter 9 instead, a more expensive ARC scheme is used for CH_4/Air mixture to better capture the flame response to strain, that is indeed critical in lean-blow out predictions.

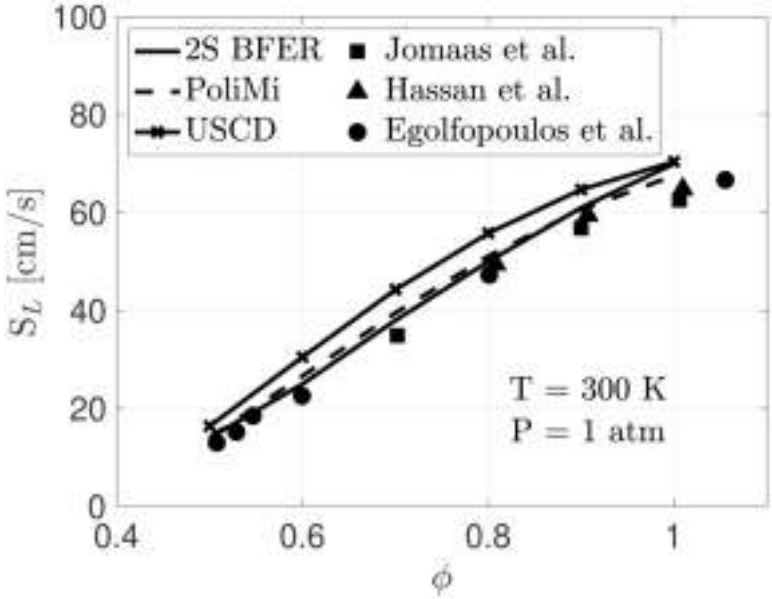

Figure 8.6: Laminar flame speed of C_2H_4/Air mixture as a function of equivalence ratio. Two step mechanism with simplified transport model is compared with PoliMi and UCSD detailed schemes [295] with complex transport model and with experimental data by Jomaas *et al.* [296], Hassan *et al.* [297] and Egolfopoulos *et al.* [298].

8.4 Results and discussion

Before discussing the reactive simulations, the LES time averaged cold flow velocity field is first presented. To visualize the different streams coming from the cooling duct and from the fuel injector, a mixing variable Z can be computed so as it is 0 when the two streams are separated and 1 when they are completely mixed. It is possible hence to visualize the two streams by using an isosurface of Z. In Fig. 8.7(a) an isosurface equal to 0.5 is colored by the velocity magnitude and shows how the air film coming from the cooling duct impinges and wraps around the following downstream fuel injector tube. One also notes that the swirled motion imposed by the six injector vanes creates six branches of high velocity at the exit of the injector: the most internal jet impinging the cooling plate and the inner chamber wall due to the fuel injector rotation angle α_f.

Complementarily to this flow organization, good match with the experimental results is obtained for global quantities such as the fuel injector pressure loss: $\Delta_{p,LES}$= 2325 Pa compared to the experimental value of $\Delta_{p,exp}$= 1952 Pa. This agreement is confirmed by a direct local comparison in Fig. 8.7(b) of the computed velocity profile against the experimental values for a horizontal line at the fuel injector exit. Although the LES predicts a slightly more opened jet compared to the experiments, it is to be noted that velocity has been experimentally measured

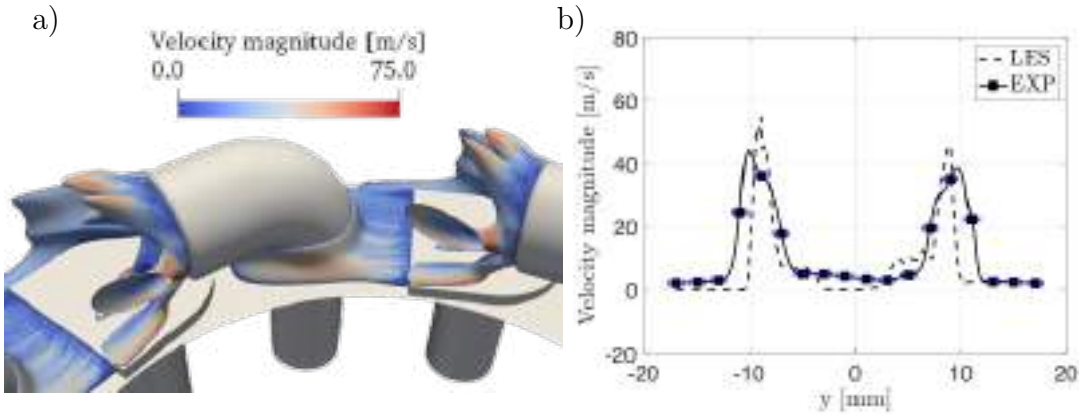

Figure 8.7: Computed isosurface of mixing variable Z (0.5) colored by velocity magnitude (a) and comparison between numerical and experimental velocity profiles along a horizontal line at the fuel injector exit (b). Experimental error bars are showed in blue. The cooling film investing the fuel injector and the central low velocity zone downstream the swirler are clearly visible.

without the chamber walls. If one considers also the measurement error (showed as error bars), the LES velocity profile is in fair agreement with the experimental data.

More details about this non-conventional velocity field are shown in Fig. 8.8(a-c), where LES time averaged contours of velocity components along the x, y and z axes are shown respectively on a cut plane parallel to the fuel injector axis (i.e. xz plane). One clearly notes here that the velocity field is not symmetric with respect to the injector axis due to the imposed swirl motion and because of the presence of the downstream fuel injector, Fig. 8.8(b). The imposed swirling motion is also clearly visible on the y component of velocity, Fig. 8.8(a). Furthermore and because of the injector imposed swirl, a vortex-breakdown occurs: the system features a central re-circulation zone (CRZ) that is highlighted by the zero z velocity component isoline (thick white line) in Fig. 8.8(c).

8.4.1 Spinning flame stabilization

The reference reactive case, case A of Tab. 8.1, is now detailed. The experimental flame shape obtained taking the external side view point and the associated line-of-sight (LOS) OH chemiluminescence signal, Fig. 8.9(a), is compared to the LOS of the predicted heat release rate, Fig. 8.9(b). As evidenced by this comparison, the computed global flame shape is in good agreement with the experiment in terms of stabilization distance from the fuel injector exit, flame length and angle. An upper branch of the flame clearly appears while no flame is present in the small triangular zone just downstream the fuel injector exit. At the bottom, two

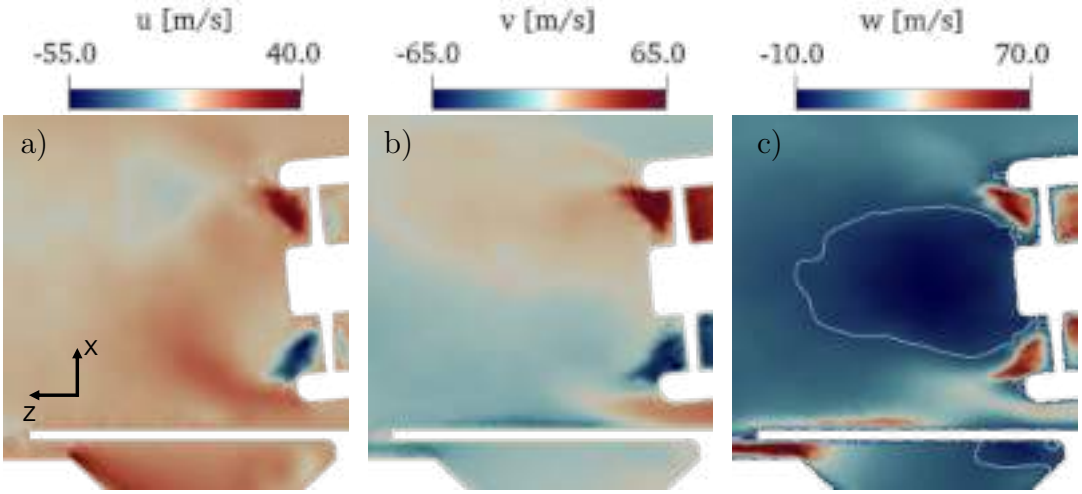

Figure 8.8: Computed fields of velocity components along x (a), y (b) and z (c) axis on xz plane (i.e. planar cut aligned with fuel injector axis). White isoline corresponds to zero velocity component along z axis. Time average solution.

flame branches that touch the cooling plate can be observed, a feature that LES correctly predicts just downstream of the cooling plate underlining the importance of the assumed thermal boundary conditions. At the Fig. 8.9(b) bottom left corner, a low intensity region corresponding to the internal flame branch coming from the previous upstream fuel injector is also captured by the simulation.

In order to have a more quantitative comparison, experimental Planar-Laser induced fluorescence (PLIF) images of the flame have been obtained, showing the flame surface density on the xz plane. In Fig. 8.10(a), the PLIF image is presented and compared to the heat release rate obtained with LES, Fig. 8.10(b). From this comparison, the global flame shape is seen to be correctly retrieved by LES, both in terms of flame length and angle. In particular, the lower part of the flame is very close to the cooling plate both in the experiment and the simulation (for which the flame is thicker due to the use of TFLES model) and the high intensity of this region comparatively to the region closer to the injector (i.e. x = -12 mm, z = 5 mm) suggests that the film cooling coming from the upstream cooling duct makes the flame move to this region ($\dot{q}$ is more blurry). The small flame region experimentally detected in the left corner (i.e. x = -15 mm, z = 5 mm) is not predicted by LES, probably due to thermal conditions imposed at the fuel injector lip. Note that the presence of the flame in this region can be worrying for the life time of the cooling plate which can be exposed to high thermal stresses for this specific operating condition. This is explained by the tip induced recirculation bubble of the top cooling plate visible on Fig. 8.8(c). The

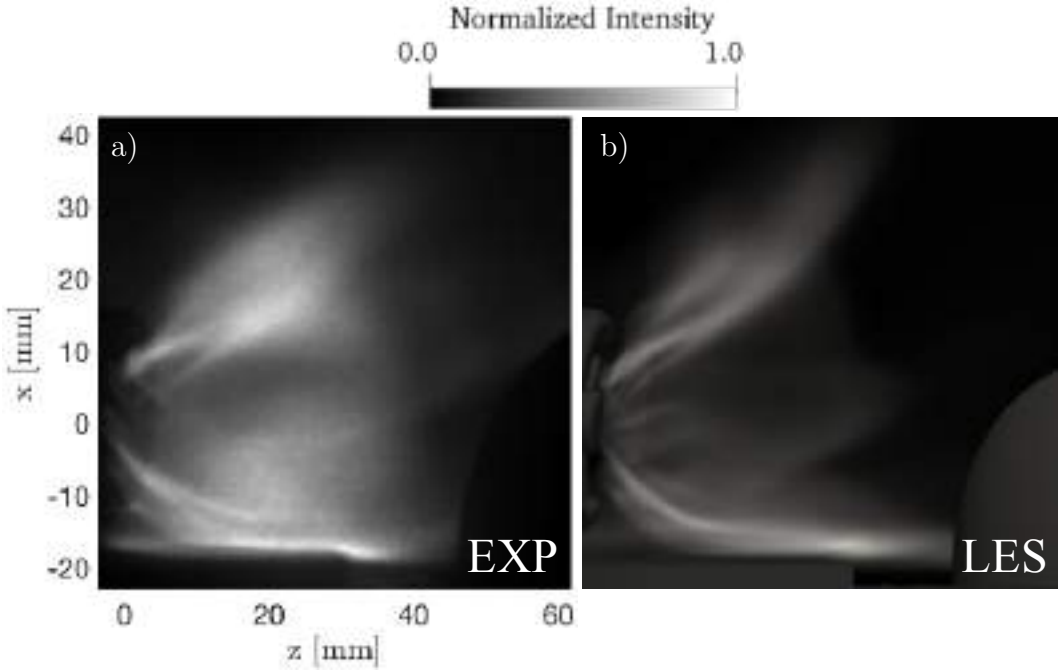

Figure 8.9: Comparison between experimental LOS integration of OH chemiluminescence (a) and computed LOS integration of heat release rate (b). ϕ (local) = 1 and Φ (global) = 0.65.

upper part of the flame is also correctly predicted by LES showing that the flow shear layer at the fuel injector exit determines the flame shape in that specific region (as already underlined by the triangular zone without $\dot{q}$ of Fig. 8.9).

To conclude a well-established six branch flame clearly arises in Fig. 8.11(a) where the computed heat release iso-surface at 10% of $\dot{q}_{max}$ is presented and colored by the local flow temperature. One can recognize the two inner branches (2) and (3) that interact with the internal chamber wall while the lower branch (1) reaches the following fuel injector, which in fact corresponds to the low intensity region visible in the bottom left corner of Fig. 8.9(a-b). The two outer branches, (4) and (5), appear to be shorter and do not reach the external chamber wall. Finally, the lower branch (6) stabilizes very close to the cooling plate, as can be seen also from the cut plane of Fig. 8.11(b) where we present, from the internal point of view, the predicted time-averaged temperature field with the isoline of heat release rate at 10% of its maximum value. Thanks from this view, the lower branch (6) is seen to reach the end of the cooling plate, the thermal boundary condition leading a wall temperature of around 1000 K. Note that higher temperature values are reached even if no flame is present, namely at the bottom right corner of Fig. 8.11(b). Here the heat transfer from the internal side of the cooling tube is less efficient due to the low velocity values (see re-circulation bubble in

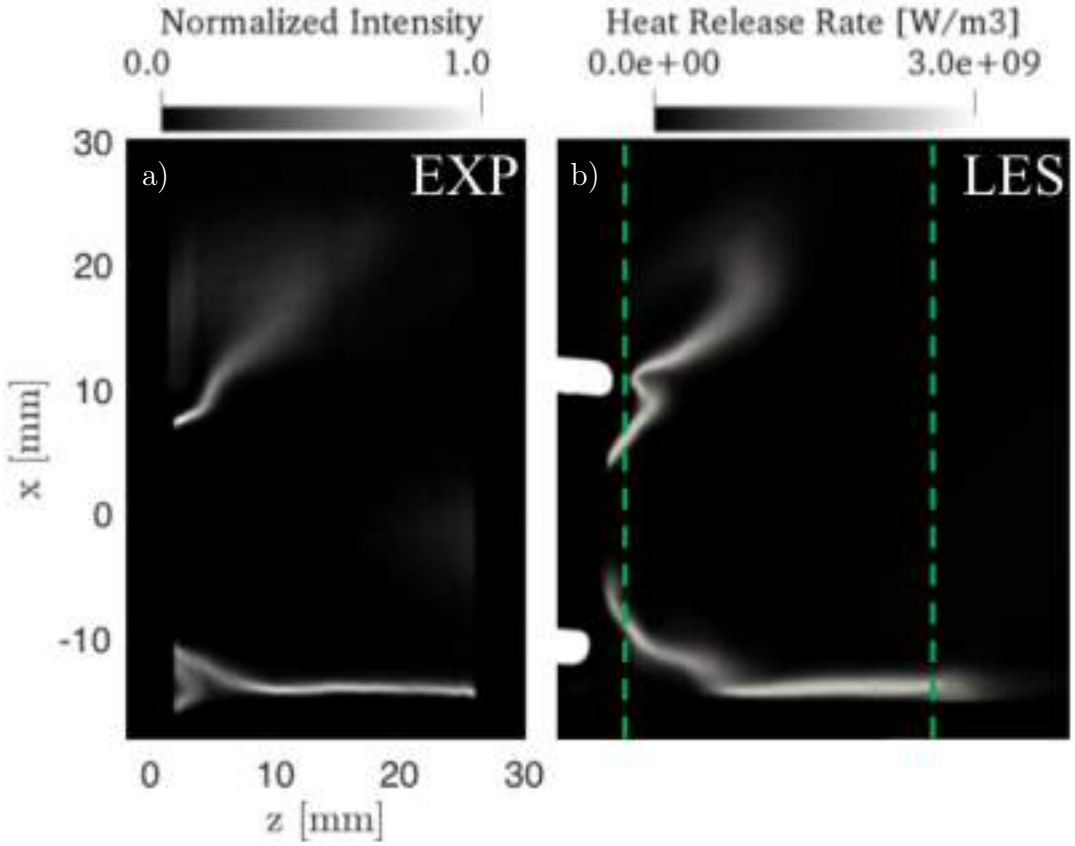

Figure 8.10: Comparison between experimental PLIF-detected flame surface density (a) and heat release rate (b) on the xz plane. Green dotted lines indicate laser path during experiments. ϕ (local) = 1 and Φ (global) = 0.65.

Fig. 8.8(b)) and is insufficient to shield this region from the hot flow coming from the neighboring flame.

A flame stabilization mechanism can be inferred by looking at Fig. 8.12(a) where we present the predicted time-averaged contour of the tangential velocity in a planar cut aligned with the fuel injector axis. In this case, the white isoline corresponds to a zero tangential velocity and the red isoline indicates 10% of maximum heat release. Comparing with the map for the cold flow of Fig. 8.8(b), Fig. 8.12(a) shows that a vortex-breakdown with the formation of a complete and extended central re-circulation zone is achieved even with combustion. The flame hence stabilizes in the low velocity regions just downstream the fuel injector, close to the zero tangential velocity isoline. The high velocity region above the cooling plate then prevents the flame to attach to the wall and the high intensity region just downstream the cooling plate is stabilized by the small re-circulation zone created by the cooling plate. To better understand the stabilization of the flame in this small re-circulation zone, the Takeno flame index is computed [213]. To

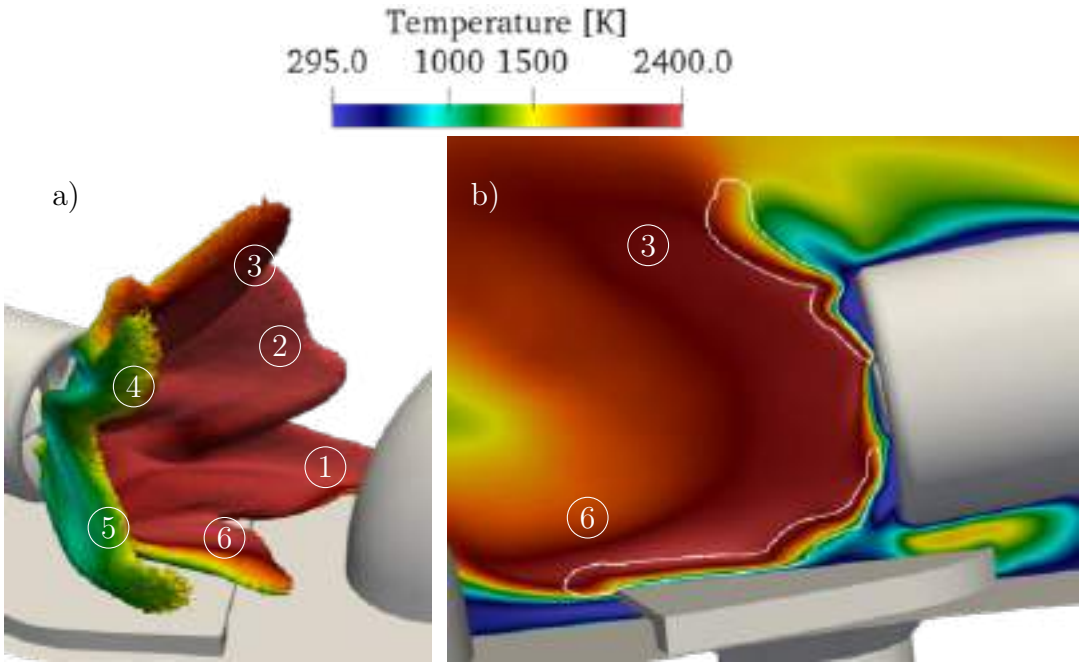

Figure 8.11: Computed heat release rate iso-surface at 10% of $\dot{q}_{max}$ colored by temperature (a) and planar cut showing temperature field with white isoline of $\dot{q}$ at 10% of $\dot{q}_{max}$. Time average solution. ϕ (local) = 1 and Φ (global) = 0.65.

do so, variables are conditioned by the heat release rate to underline the regions in which heat release is more relevant:

$$FI_{C_2H_4} = \left. \frac{\nabla_{O_2} \cdot \nabla_{C_2H_4}}{|\nabla_{O_2} \cdot \nabla_{C_2H_4}|} \right|_{\dot{q}>10\%\ \dot{q}_{max}} \tag{8.1}$$

It is then shown on Fig. 8.12(b) along with line integral convolution of the velocity vector [299] colored by the Takeno flame index together with the red isoline corresponding to a heat release rate value of 10% of $\dot{q}_{max}$. The big re-circulation zone downstream of the fuel injector and the wake immediately downstream the cooling plate are clearly visible. It is also interesting to note that, while most of the C_2H_4 burns in a premixed mode (i.e. positive flame index), in the wake region downstream the cooling plate, the injected cooling film makes the C_2H_4 burn in a diffusive mode (i.e. negative flame index), underlining the interaction between the flame and the cooling film. This local diffusion flame result to be a characteristic feature of this operating condition in which high cooling mass flow rate creates a large oxygen gradient in this small recirculation zone and makes the stochiometric fuel stream to burn in a diffusion mode. Note that this region of high heat release rate has been noticed also in the experiments, Fig. 8.9(a): its impact on the flame shape is the anchoring of the lower branch (6) in this recir-

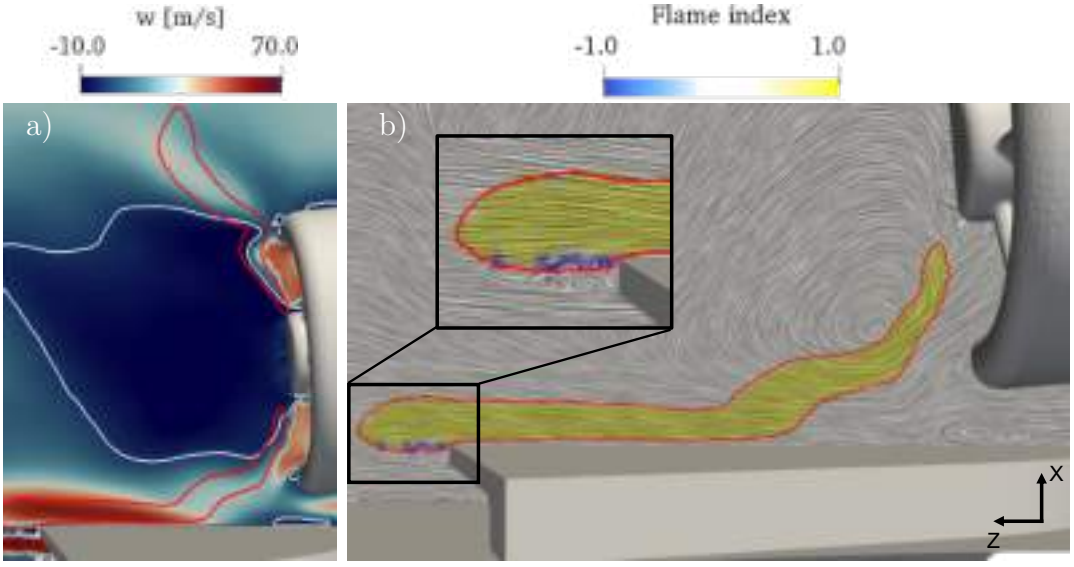

Figure 8.12: Computed field of tangential velocity on a planar cut aligned with fuel injector axis with white isoline of zero value (a). Line integral convolution velocity field (streamlines) colored by Takeno flame index (b). Red isoline corresponds to a heat release rate value 10% of $\dot{q}_{max}$. Time average solution. ϕ (local) = 1 and Φ (global) = 0.65. A zoom of the small re-circulation zone downstream the cooling plate is shown.

culation zone near the cooling plate, pushing toward the backplane the branch tip and avoiding it to reach the following injector, Fig. 8.11(a). This operating condition results to be safe for the combustor, since high cooling mass flow rate avoids the cooling plate tip to reach too high temperatures.

8.4.2 Global equivalence ratio effect

The strong interaction between the flame and the cooling film is more evident if changing the operating conditions of the burner. First, the reactive case B (Tab. 8.1) is discussed and compared with the reference case A. For this condition, the local equivalence ratio is kept constant, ϕ (local) = 1 like in the reference case while the global equivalence ratio is increased to Φ (global) = 0.8 instead of Φ (global) = 0.65. This is obtained by correspondingly decreasing the film cooling mass flow rate.

To validate the simulations, experimental flame shape obtained taking the LOS integration of the OH chemiluminescence signal, Fig. 8.13(a), is compared with the LOS of the predicted heat release rate, Fig. 8.13(b). Again, the computed global flame shape is seen to be in good agreement with the experiment in terms of stabilization position, flame length and angle. These can also be noticed to be

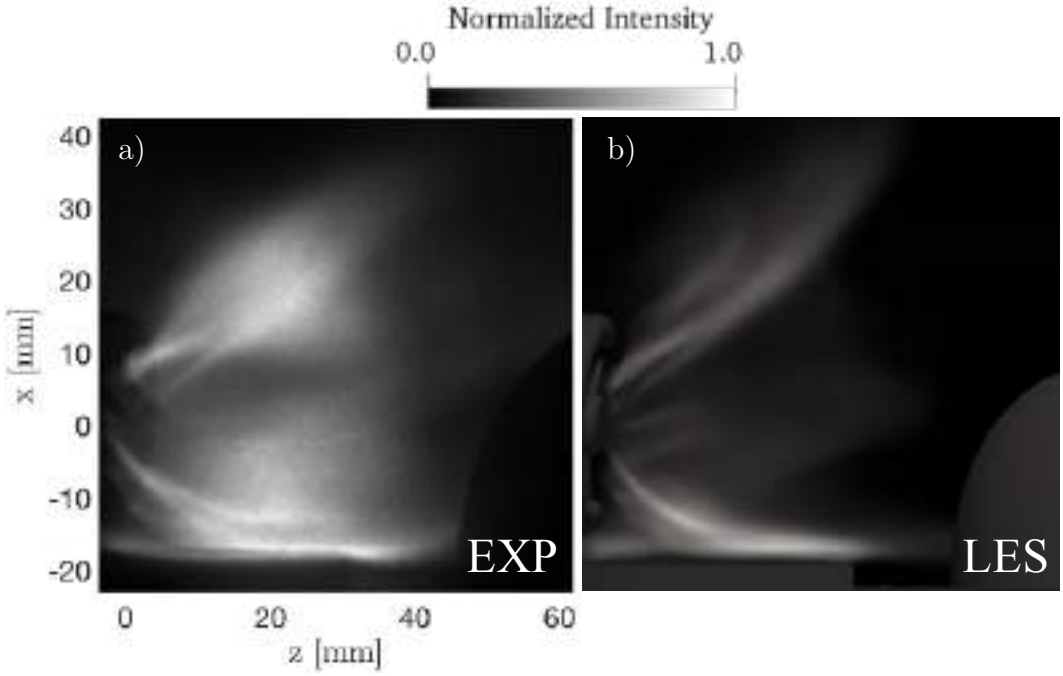

Figure 8.13: Comparison between experimental LOS integration of OH chemiluminescence (a) and computed LOS integration of heat release rate (b). ϕ (local) = 1 and Φ (global) = 0.8.

globally unchanged if compared to the reference case. Differences can nevertheless be identified from the computed LOS images of Fig. 8.9(b) and Fig. 8.13(b). First, the low intensity region at the bottom left corner of Fig. 8.9(b) is more evident in Fig. 8.13(b), indicating that the most inner branch (1) of the flame coming from the previous upstream fuel injector is stronger. Second, there is no more prediction of the heat release rate peak immediately downstream the cooling plate in Fig. 8.13(b). This is due to the lesser amount of air injected that causes a weaker wake region which inhibits the small diffusion flame visible in Fig. 8.12(b).

Quantitative comparison can be assessed by looking at Fig. 8.14 where an experimental PLIF image of the flame (a) is presented and compared to the heat release rate field predicted by LES (b) where it is possible to see how the flame global shape and angle are fairly retrieved by the simulations. Indeed, the lower part of the flame is correctly predicted by LES and this time there is also a weak region of predicted $\dot{q}$ in the lower left corner (i.e. z = 3 mm, x = - 15 mm). However, and more generally, the predicted temperature of the fuel injector lip appears to be slightly lower to the experimental one. In the upper part of the flame Fig. 8.14(b) presents a more wrinkled stabilization zone at the fuel injector exit and a slightly longer flame with respect to experiments.

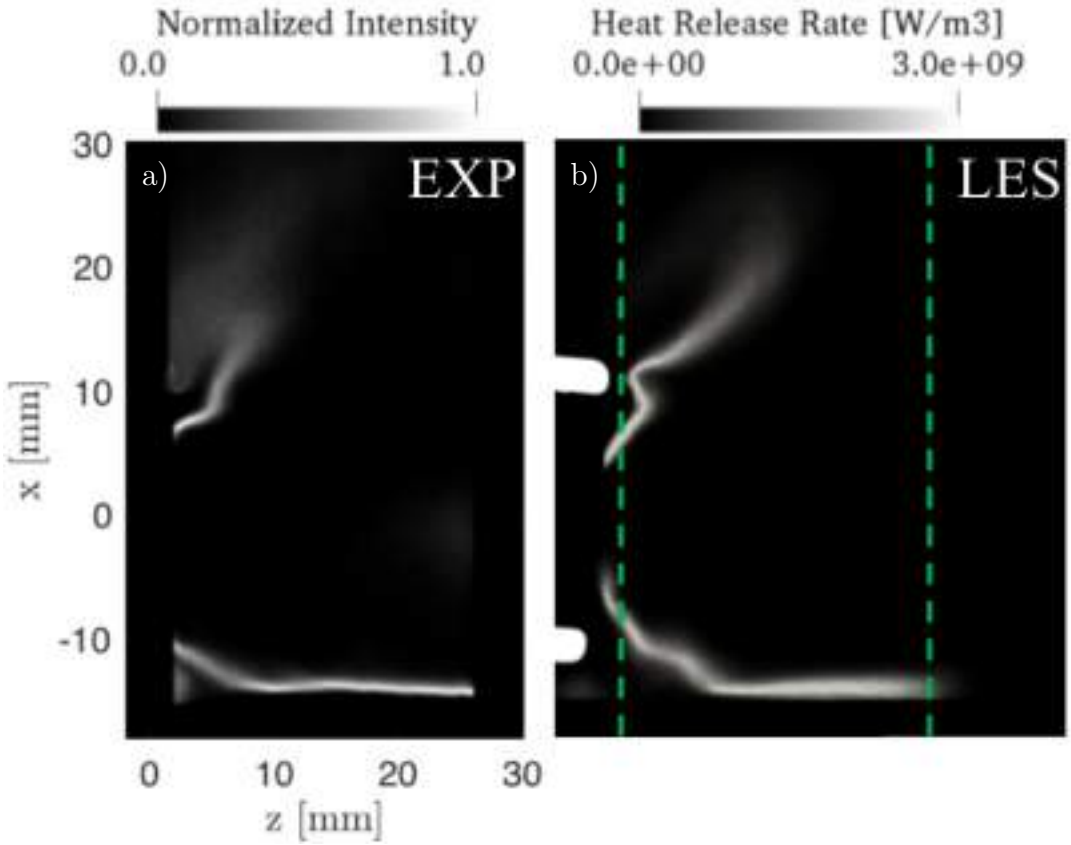

Figure 8.14: Comparison between experimental PLIF-detected flame surface density (a) and heat release rate (b) on the xz plane. Green dotted lines indicate laser path during experiments. ϕ (local) = 1 and Φ (global) = 0.8.

Comparisons between experimental results and simulations of case A, Fig. 8.10, reveal that by increasing the global equivalence ratio, the upper branch of the flame opens more and the $\dot{q}$ intensity is more uniform on the lower part since the upstream cooling flow is reduced and does not disturb flame stabilization on the cooling plate.

More precise differences in flame stabilization can be observed by comparing Fig. 8.11(a) to Fig. 8.15(a) where the computed iso-surface of heat release rate at 10% of $\dot{q}_{max}$ value colored by the local flow temperature are presented. While the inner part of the flame remains unchanged (branches (1) and (2)), the outer part (branches (4) and (5)) and the bottom part change due to the reduction in cooling film mass flow rate. In particular, the outer branches (4) and (5) are consistently longer and reach the outer chamber wall while in Fig. 8.11(a) they are rapidly quenched by the higher mass flow rate coming from the upstream cooling duct which is mainly directed toward the external side of the chamber. The bottom branch (6) is finally shorter and spreads over the cooling plate. The branch tip

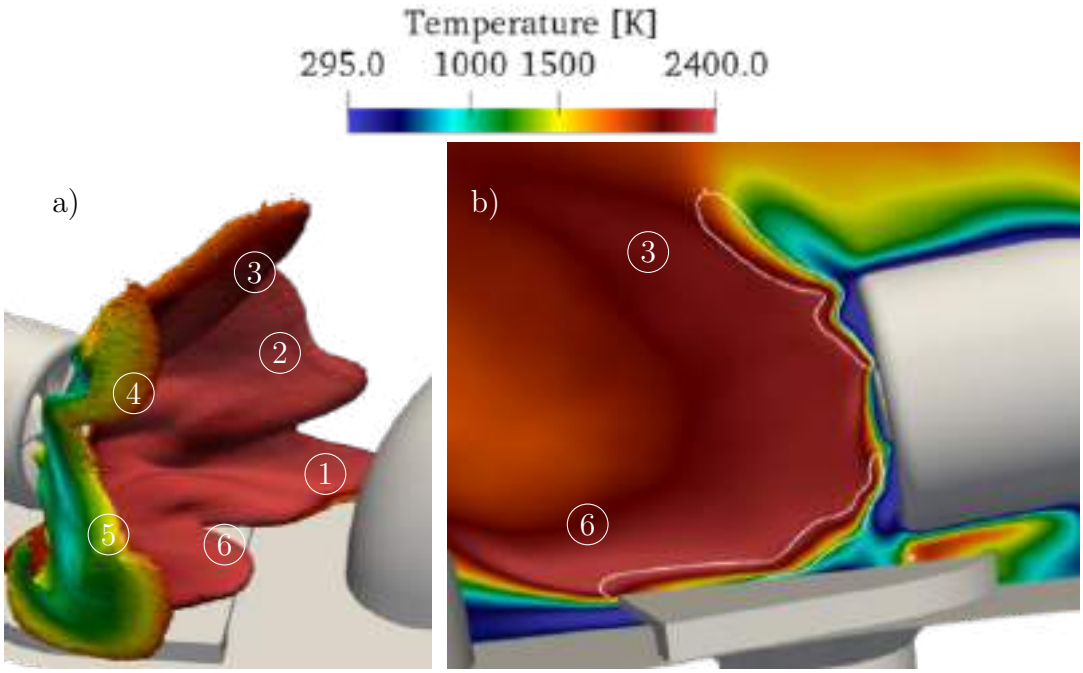

Figure 8.15: Computed heat release iso-surface at 10% of $\dot{q}_{max}$ colored by temperature (a) and planar cut showing temperature field with white isoline of $\dot{q}$ at 10% of $\dot{q}_{max}$. Time average solution. ϕ (local) = 1 and Φ (global) = 0.8.

just downstream the cooling plate visible in Fig. 8.11(a) is now no longer present, confirming the absence of diffusion flame in the small wake region.

The shorter lower part of the flame can be better observed in Fig. 8.15(b) where the computed temperature field is presented together with an isoline of heat release rate. Compared to Fig. 8.11(b), the thermal conditions at the cooling plate surface are hotter due, on one hand, to the smaller amount of fresh air coming from the upstream cooling duct and, on the other hand, to the reduced heat transfer coefficient in the internal side due to lower velocities. This local trend respects as expected the global trend which yields higher temperatures due to higher global equivalence ratios. Therefore, the global equivalence ratio influences the local thermal conditions of the cooling plate: a lower global equivalence ratio brings a more spread lower branch (6) of the flame. The different velocity field in the outer part of the chamber controls instead the length of the outer flame branches (4) and (5): these are expected to be longer if the global equivalence ratio is higher.

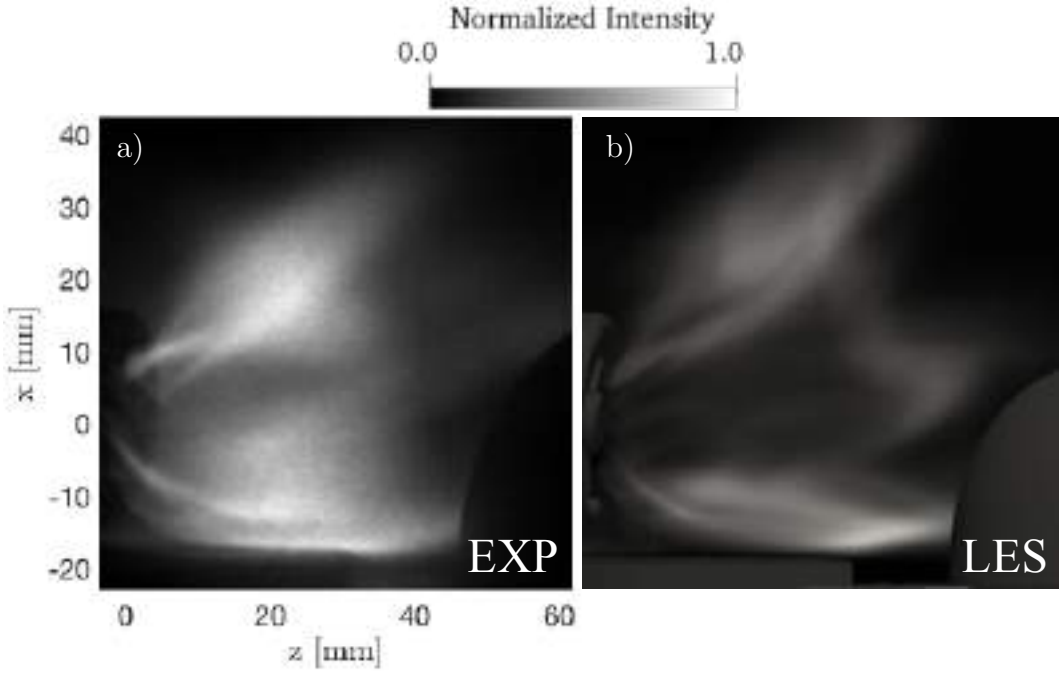

Figure 8.16: Comparison between experimental LOS integration of OH chemiluminescence (a) and computed LOS integration of heat release rate (b). ϕ (local) = 0.8 and Φ (global) = 0.65.

8.4.3 Local equivalence ratio effect

The effect of the local equivalence ratio on the flame can be assessed by analyzing the last reactive case C (Tab. 8.1). For this operating condition, the local equivalence ratio is reduced to ϕ (local) = 0.8 while the global equivalence ratio is kept constant at Φ (global) = 0.65 like in the reference case. Due to the decrease in local equivalence ratio, the needed film cooling mass flow rate to keep the same global equivalence ratio is reduced and roughly corresponds in this case to the mass flow rate used in case B. This allows the investigation of the film cooling injection velocity effect.

Comparison between experimental LOS integration of OH chemiluminescence and computed LOS integration of heat release rate is presented in Fig. 8.16(a-b). Predicted flame global shape, angle and length are again in good agreement with the experiment, confirming that for this operating condition our modeling approach is still adequate. Looking at LOS images, the new flame appears to be slightly longer if compared to both other two cases as generally expected when reducing the equivalence ratio (see laminar flame speed evolution with equivalence ratio shown in Fig. 8.6).

The flame is clearly longer if compared to cases A and B when looking at Fig. 8.17 where an experimental PLIF image of the flame (a) is compared to

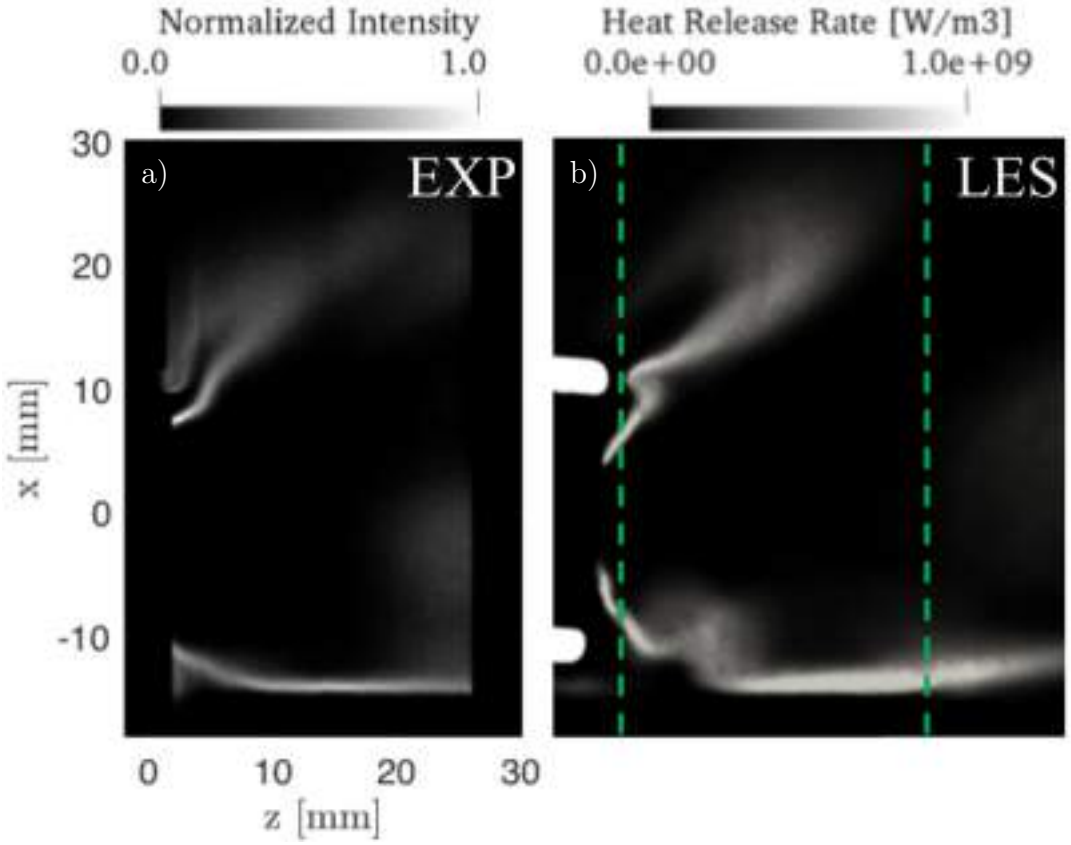

Figure 8.17: Comparison between experimental PLIF-detected flame surface density (a) and heat release rate (b) on the xz plane. Green dotted lines indicate laser path during experiments. ϕ (local) = 0.8 and Φ (global) = 0.65.

heat release rate field predicted by LES (b). Also in this case, the flame global shape and angle are corrected predicted by LES. The lower part of the flame presents a region in the left corner in which the flame is weaker due to the lower global equivalence ratio end hence higher film cooling which invests the flame, as it happens in case A, Fig. 8.10. The upper part of the flame presents the same angle as for case A, concluding that the flow field in that region is affected by the global equivalence ratio. This time, the predicted temperature of the fuel injector lip appears to be correct since LES fairly reproduce the weak region of $\dot{q}$ nearby the upper lip (i.e. z = 5 mm, x = 20 mm).

Figure 8.18(a) then shows the computed heat release iso-surface at 10% of $\dot{q}_{max}$ colored by the local flow temperature. While the global equivalence ratio mainly affects the flame outer branches, the local equivalence ratio clearly makes all six branches longer than the reference case. At the same time the cooling film mass flow rate is still enough to avoid the flame to reach the downstream fuel injector tube. On the outer side, flame branch (4) touches the outer chamber wall,

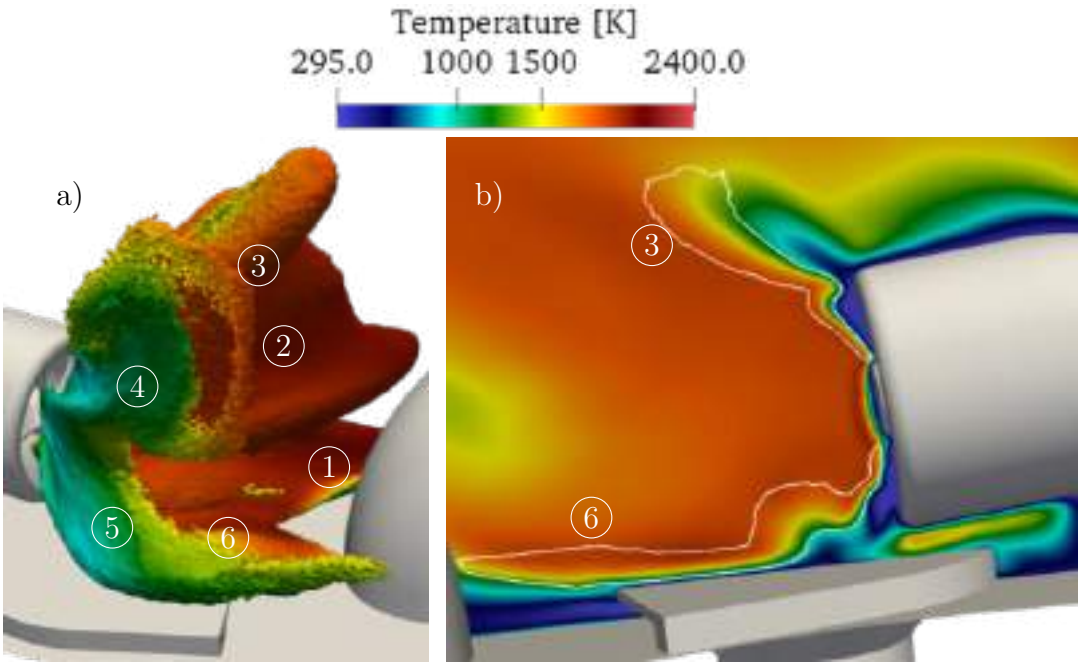

Figure 8.18: Computed heat release iso-surface at 10% of $\dot{q}_{max}$ colored by temperature (a) and planar cut showing temperature field with white isoline of $\dot{q}$ at 10% of $\dot{q}_{max}$. Time average solution. ϕ (local) = 0.8 and Φ (global) = 0.65.

indicating that its length is influenced only by the local equivalence ratio and not by the value of the film cooling injection velocity or the global equivalence ratio parameter itself, since in cases A and B no influence has been found from these two parameters. A different mechanism regulates the outer branch (5) which turns out to be influenced by both the global and local equivalence ratios since a lower local equivalence ratio makes it longer while its angle seems regulated by the global equivalence ratio: by decreasing the latter, the branch opens and touches the wall. In fact, even if in case C, Fig. 8.18(a), this branch is longer compared to case B, Fig. 8.15(a), it does not reach the outer wall because the global equivalence ratio is lower and the flame angle remains the same as in case A, Fig. 8.11(a).

The computed temperature field shown in Fig. 8.18(b) confirms that the thermal conditions at the cooling plate surface is regulated by the global equivalence ratio (and not by the value of the cooling film injection velocity) since the predicted thermal boundary layer is very close to the one of Fig. 8.11(b) and obtained for the reference case A.

While in conditions A and B, the flame is far from the following injector, in condition C the flame appears to be closer to the following injector but it never touches it since flame branches (1) and (6) are deviated toward the chamber walls

by the velocity field. This condition is not critical for the combustor since, as said, the thermal conditions at the walls are controlled by the global equivalence ratio, which is the same as in case A. Therefore, the cooling plate walls, as well as the following injector walls, are not exposed to higher thermal stresses compared to the other cases. The reason for this behavior is that even if the flame is longer and the isosurface at 10% of $\dot{q}_{max}$ is closer to the following injector, adiabatic flame temperature is lower (i.e. lower local equivalence ratio) and the two effects result in thermal conditions at the walls which are not critical, Fig. 8.11(b).

To conclude, the local equivalence ratio has been showed to globally influence the length of all six flame branches, while the flame angle in the horizontal direction and the thermal conditions at the chamber backplane are mainly controlled by the global equivalence ratio. In parallel, the value of the cooling film injection velocity (which is roughly the same for case B and C) is found not to influence the flame shape and its stabilization, leaving the two equivalence ratios the control of the spinning combustion burner.

8.5 Conclusions

In this Chapter a joint numerical and experimental analysis of the flame in the new spinning combustion technology framework developed and patented by Safran Helicopter Engines is presented. First, the geometry of the modified NTNU annular combustor is described, pointing out interesting points about the design process and the generation of the velocity azimuthal component in the annular chamber. Second, the LES modeling framework is detailed and the main results of the predictions are analyzed. In agreement with the experiments, the unconventional geometry produces high-swirled flames, each of them being made up of six well distinct branches. The resulting flame stabilizes in the low velocity region immediately downstream the injector and strongly interacts with the chamber walls, backplane and cooling film. The burner is probed for three different operating conditions, giving the possibility to analyze the effect of the fuel injector local equivalence ratio, the combustor global equivalence ratio and the film cooling injection velocity while keeping the fuel injector mass flow rate constant. The global equivalence ratio is showed to influence the flame angle in the horizontal direction as well as the thermal conditions of the chamber backplane. In particular, higher global equivalence ratio increases the flame angle and exposes the chamber backplane and outer wall to higher thermal stress. Reduction of the local equivalence ratio instead is showed to globally increase the length of all six flame branches, without modifying the flame opening. On the contrary, only a

marginal role is found to be played by the film cooling injection velocity, leaving the control of the flame positioning in such a spinning combustion system mainly to be a function of the local and global equivalence ratios. These two parameters turn out to be the most important design parameters to be taken into account for future studies.

Chapter 9

Lean Blow-Out dynamics

Contents

This Chapter analyses the lean blow-out (LBO) behavior for the Spinning Combustion Technology (SCT) recently developed by Safran Helicopter Engines (SHE) for its next generation of combustors. This technology relies on the introduction of a strong azimuthal component of velocity to increase flame/flame interaction and gain in engine operability as well as blow-off capabilities. Experimentally, a modified annular combustor, reproducing the main physics behind SCT real engines, is operated at NTNU close to LBO conditions. Two different burner configurations are analyzed to observe the impact of the fuel injector orientation on the LBO limits. Numerically, Large Eddy Simulations (LES) of these two configurations are performed to get more insights into LBO. In terms of modeling, an Analytically Reduced Chemistry (ARC) kinetic scheme is employed to describe the CH_4/Air chemical reactions. Note that ARC is here preferred over the cheaper two step mechanism used in Chapter 8 to more accurately predict the flame response to strain, which is indeed a critical mechanism in lean-blow out dynamics. Heat transfer at the walls is modeled with Conjugate Heat Transfer (CHT) and results are compared to adiabatic simulations. LES is successfully validated against experimentally measured multi-kHz repetition-rate OH* chemiluminescence images and photomultiplier signals (PMT), providing

satisfactory agreement for all the measured quantities. In terms of method and to address LBO, starting from stable flame conditions, the air mass flow rate is gradually increased while keeping the fuel mass flow rate constant, thereby significantly affecting the flame stabilization. In both experiments and simulations, as the equivalence ratio decreases, the flame gets at first more elongated, then it detaches from the swirler bluff-body and finally it stabilizes on the top of the injectors in a continuous lifted annular shape flame before the occurrence of the LBO event. Decrease in consumption speed and in flame resistance to stretch are found to be the key parameters behind the change in flame shape and its stabilization. Among the two configurations, the one with stronger flame/flame interaction presents higher LBO limits, explaining the SCT increased blow-off capabilities and giving insights for improving real engine operability. Note that these results are being considered for publication in *Combustion and Flame* [300].

9.1 Introduction

Nowadays, the aviation and energy sectors are currently facing the need to decarbonize combustion technologies and design low emission combustors to deal with global climate change as outlined in Chapter 1. In this context, even though there is no supernational regulation currently controlling the helicopter engine emissions, Safran Helicopter Engines has recently developed the Spinning Combustion Technology (SCT) for its next generation of combustors, i.e. the ARRANO engine employed in the Airbus Helicopters H160 [18, 77]. The main interest of SCT, aside from the industrial point of view that calls for a reduction in engine weight and cost, is the great operability of the engine when it comes to faster light around and lower LBO limits. SCT relies on the introduction of a relevant azimuthal component of velocity in the annular chamber to enhance flame/flame interactions (Chapter 8). The improvement in LBO capabilities offered by this technology is very appealing but it is clearly not understood and more insights in the LBO mechanisms of such swirling flows are needed. Indeed, to the best of author's knowledge, this type of global swirling flow has not been extensively investigated in the literature, the only work being the one proposed in Chapter 8 to investigate the flame stabilization in stable operating conditions [77].

Focusing on LBO, different experimental studies have been carried out [17, 301, 302, 303] but much needs to be done to fully understand the driving mechanisms of blow-out initiation as well as propagation [304]. As suggested by Kumar *et al.* [301], these triggering events could be associated to local extinction events, alteration in temperature, fuel composition or hydrodynamic stability. However,

no study has yet been able to determine specific critical events which result in the final blow out. These studies also suggest that events leading to an eventual blow-off in an annular combustor are different from the one observed in single sector configurations [305]. Williams *et al.* [306] and Kundu *et al.* [307, 308] identified the LBO event through the balance between the heat provided by the burnt gases to the fresh gases and the one produced by reactions. Similarly, Longwell *et al.* [309] considered the recirculation zone as a well stirred reactor and looked at the balance between the reaction rate and the rate of entrainment of fresh mixture in the recirculation zone. Plee *et al.* [310] in parallel suggested to look at the competition between the fluid mechanic and the chemical times in the shear-layer while Zukoski [311] proposed to look at the contact time of the fresh gases with the burnt gases compared to the ignition time. Local extinction of the flame by aerodynamic stretch has also been individuated as a driving mechanism by different authors [312]. Recently, a review on LBO for bluff-body flames has been carried out by Shanbhogue *et al.* [313]. The authors were prone to confirm the need for a flamelet-based description of the flame front since different experiments and numerical findings showed no evidence of well stirred reactor behaviors or chemical ignition time as key parameters [314]. If right, two mechanisms can therefore extinguish such flames, namely stretch and heat loss both modifying the diffusion process around the flame front [38, 315] and determining the LBO event when a certain level of stretch is reached. However, the identification of a well-defined critical stretch is a complex challenge when it comes to real turbulent flames. What is usually observed is that local flame extinction causes in turn a significant modification of the flame shape that then causes LBO and the whole flame front extinction [313]. At the same time, fewer works focused on the LBO mechanisms in swirl-stabilized flames. Muruganandam and Seitzman [316] as well as Zhang *et al.* [317] detected local extinctions and modifications of the recirculation zone as key events in the LBO process as it happens for bluff-body stabilized flames. Kariuki [304] observed the same LBO process as reported by Chaudhuri *et al.* [318] for unconfined and confined flames with and without swirl. The LBO event was observed in these cases to be anticipated by the local extinction and fragmentation of the flame front: the following introduction of fresh gases in the central recirculation zone making ineffective the re-ignition in the shear layer finally yielding the detachment of the flame root. More recently, An *et al.* [319] observed that the lift-off of a premixed swirl stabilized flame was characterized by different phenomena, such as the local extinction of the flame and the presence of a Precessing Vortex Core (PVC) that increased the strain applied to the flame root, finally leading to the flame blowout.

In parallel, Large Eddy Simulation (LES) was carried out to predict LBO both in gaseous [320, 321] and liquid fuelled [322, 323] laboratory scale combustors. For example, the swirl-stabilized methane-air flame operated by Cavaliere *et al.* [302] has been widely simulated both in premixed [324] and non-premixed [320, 323, 325] configurations. Zhang and Mastorakos [320] employed a LES-CMC approach and observed different local flame extinction and strong heat release rate fluctuations, overpredicting the experimental LBO mass flow rate by 25%. The same configuration was then simulated by Ma *et al.* [321] both with the Flamelet Progress Variable (FPV) and the Thickened Flame (TF) models. The experimental air mass flow rate at LBO was again overpredicted but a better prediction was achieved with the TF model that resulted in a longer lift-off height and in an earlier LBO event which ended up being closer to experimental findings. Note that the recorded heat release rate variance was identified as a good sensor to detect the LBO event before its occurrence. Palies *et al.* [324] recently carried out simulations of the premixed configuration and obtained satisfactory agreement with experimental data, except for the latest times of the LBO sequence, identifying the motion of cooler combustion products into the recirculation zone as a key phenomenon leading to LBO. A turbulent premixed flame was also investigated by Farrace *et al.* [326] who confirmed the reliability of the LES-CMC approach in the prediction of LBO. Flame front fragmentation and different pockets of OH peaks were observed in agreement with experimental data. More recently, Nassini *et al.* [327] first demonstrated the LBO prediction capabilites of LES with an extended version of the Turbulent Flame Closure (TFC) [328] by simulating the Cambridge swirl flame of Cavaliere *et al.* [302]. Then, they applied the proposed approach to a real scale swirl lean combustor, reaching good agreement with the experimentally measured data obtained on the full-annular test bench [26]. In the same line, few recent studies have carried out numerical simulations in realistic gas turbine burners operated at high pressure [329, 330]. For example, Esclapez *et al.* [15] investigated the LBO event with different fuels: in contrast to empirical correlations available in the literature, a limited role of the fuel composition was found on LBO limits, the spray characteristics being instead one of the key parameters.

While most of the recalled studies have focused on the effect of strain-rate on the local flame extinction, the effect of heat transfer has not been so widely investigated even though it is known to potentially affect the flame shape [142], its stabilization [143] and its dynamics [59, 147, 148, 149]. Typically, Sigfrid *et al.* [331] experimentally showed that the fresh gas temperature has an impact on

the LBO limit of a premixed flame in an industrial gas turbine combustor. Numerically, Massey *et. al* [157] showed the impact of wall heat transfer modeling on the lift-off height of a lean swirl-stabilized flame close to LBO conditions. Despite such observations, the major part of LES studies available in the literature was performed either with adiabatic [324] or simplified thermal boundary conditions [327]. In this context, a more accurate prediction of the wall heat transfer would be provided by a Conjugate Heat Transfer (CHT) approach, for which the LES solver is coupled with a heat conduction code that solves for the temperature field in the solid parts of the combustor. Different recent studies are available in literature and show the higher accuracy of CHT compared to adiabatic and simplified thermal boundary conditions when it comes to the prediction of flame stabilization and its dynamics [59, 66, 112, 166, 169] (see Chapter 4) but, to the best of the author's knowledge, it has never been assessed in conditions close to LBO.

This Chapter aims at filling this gap of knowledge by using high-fidelity LES in the Conjugate Heat Transfer (CHT) context to point out the LBO dynamics in the recently developed (and never investigated) Spinning Combustion Technology. To this scope, the NTNU annular burner has been recently adapted to introduce a relevant azimuthal component of velocity to mimic the SCT physics (Chapter 8) [77]. In this work, two burner configurations (that differ in the fuel injector orientation) are operated close to LBO conditions by gradually increasing the air mass flow rate, the experimental setup being presented in section 9.2.

In terms of numerical modeling, section 9.3, CH_4/Air reactions are described through an Analytically Reduced Chemistry (ARC) mechanism and a dynamic formulation of the TFLES combustion model is used [64] with the relaxation sensor to detect and artificially thicken the flame front [242]. CHT simulations are performed by coupling the AVBP LES solver with the AVTP heat-conduction solver [54, 55] using the methodology illustrated in Chapter 4. Experimental findings such as LBO limits and flame shape evolution are analyzed in section 9.4 while corresponding adiabatic and CHT numerical predictions are presented in section 9.5.1 and section 9.5.2 for the two investigated configurations, respectively. Finally, the observed flame dynamics and LBO mechanisms are discussed in section 9.6.

9.2 Experimental setup

The initial annular laboratory scale combustor setup is illustrated in Fig. 9.1 [291, 292]. Thanks to a modular design of the test bench, it is possible to equally

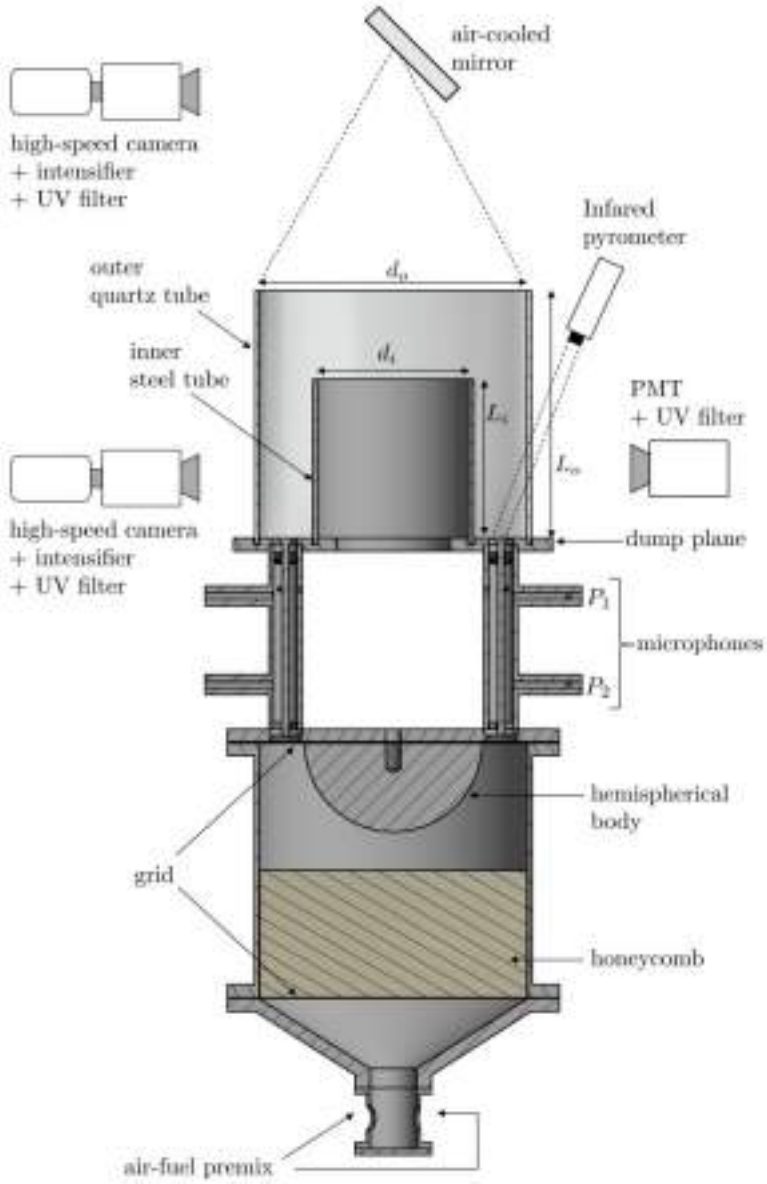

Figure 9.1: Schematic of the atmospheric annular combustor.

distribute from 6 or up to 18 burners around a chamber whose diameter is 170 mm. Likewise, different shapes of injector exits can be used. The combustion chamber has been described in Chapter 8. In the present case, a premixed air-methane mixture is fed to the plenum chamber instead of the air-ethylene mixture previously used (Chapter 8). This change in fuel mixture is due to the influence of the configuration on the LBO limits which is experimentally observed to be greater with methane due to its smaller consumption speed and thus it is easier to study.

For the purpose of the present study, SHE commissioned a major modification to the original atmospheric annular combustor so as to introduce the capacity of

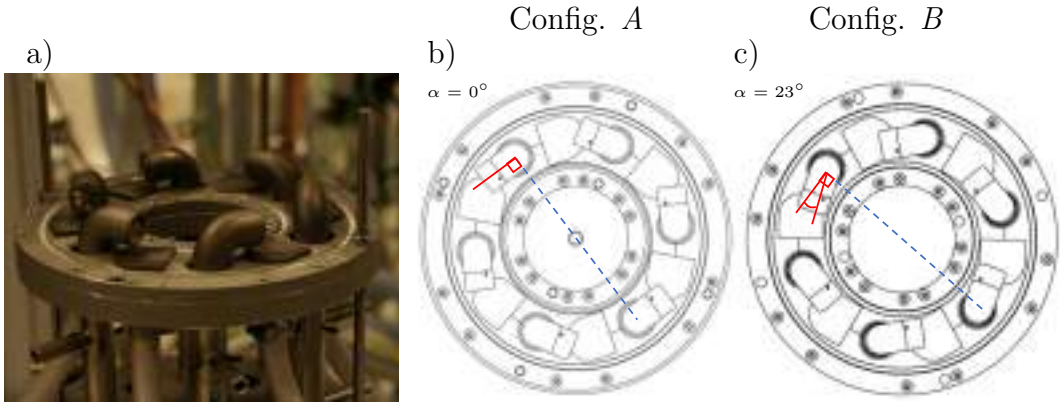

Figure 9.2: (a) Picture of the laboratory scale SCT burner. Schemes of the two configurations considered in the present work: (b) Configuration *A* with "not-oriented" injectors and (c) Configuration *B* with "oriented" injectors.

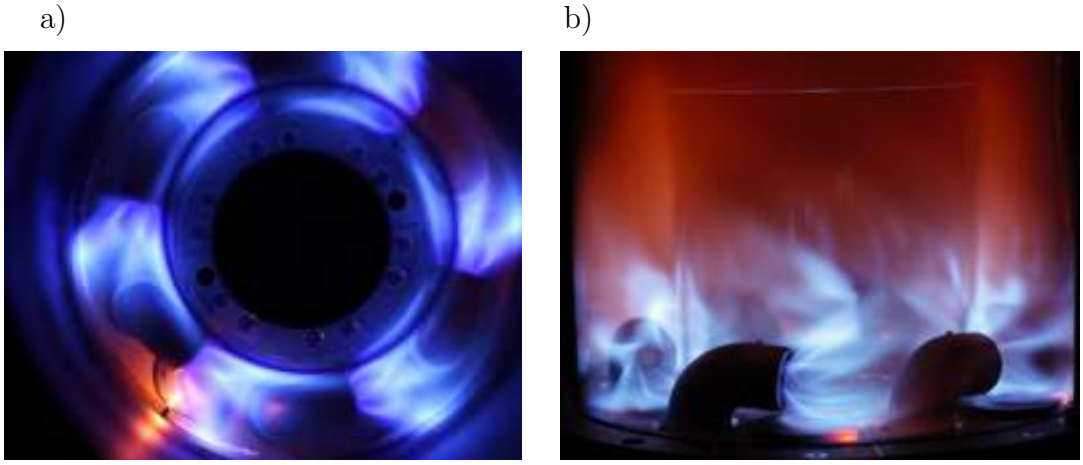

Figure 9.3: (a) Top and (b) side photographs of the spinning flames in the SCT combustor. Configuration *B*.

producing a strong mean azimuthal component of velocity while operating under premixed fuel conditions, Fig. 9.2(a), as illustrated in Chapter 8. In this new set-up, a six-vane swirler, with a geometric swirl number of 1.22 [291], is placed at the exit of each bent fuel injector.

The relative position of one injector to the next is now characterized by the angle α as shown in Fig. 9.2(b-c). Two configurations are considered for the present work. In the case of $\alpha = 0°$, the burner axis is positioned 90° to the chord (in blue) passing by two injectors situated 180° apart in the "not-oriented" Configuration A, Fig. 9.2(b). For $\alpha = 23°$, the injector outlet is tilted inwards, directing flames along the inner combustor wall, and towards the subsequent injector located downstream in the so-called "oriented" Configuration B, Fig. 9.2(c), hence producing a pseudocontinuous arc of flames, as shown in Fig. 9.3. Note that injectors can also be tilted towards the backplane by an angle β. In this work,

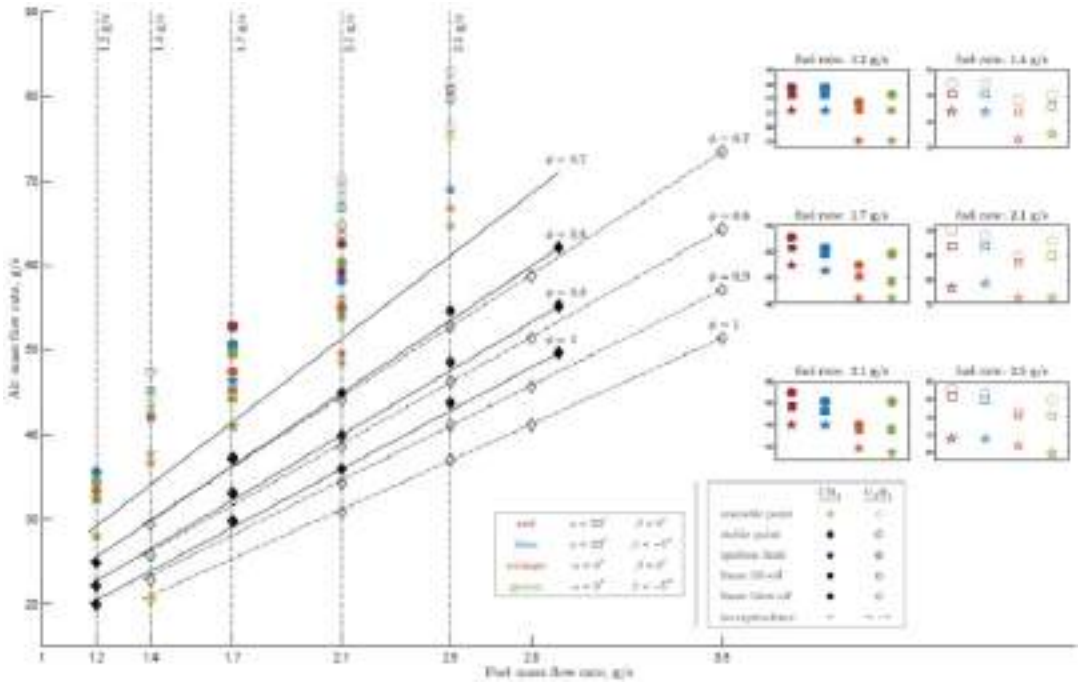

Figure 9.4: Map of experimentally observed stability points, ignition limits, and lean blow-off for different fuels and configurations.

β is kept at 0 and injector exits are parallel to the chamber backplane since this angle has been experimentally observed to have a limited influence on the LBO limit.

For the experiments, the air and fuel flow rates are regulated by Alicat mass flow controllers (MFCs) which have an accuracy of $\pm$ 0.8% of the reading + 0.2% of the full scale. A 2000-slpm MFC supplies the necessary flow rate for the air in the premixed fuel mixture, while a 225-slpm MFC is used for the fuel. Blow-out experimental curves were obtained by fixing the fuel rate, and then increasing the air flow rate in steps of 1 to 2% every 20 s until blow-out occurres, similarly to the method adopted by Wiseman *et al.* [332]. Measurements were repeated multiple times over a wide range of mass flow conditions to ensure the repeatability of these experimental results and to map the LBO limits of each configuration, Fig. 9.4. For the present work, a fixed CH_4 mass flow rate of 1.7 g/s is considered and the air mass flow rate is gradually increased starting from stable conditions far from LBO conditions. Note that a separate piping system can supply air to the cooling ducts positioned in between each injector [77]. However, when investigating LBO limits, it is observed that when the cooling ducts are turned on, the experiments are much less reproducible. Hence, air cooling is turned off for all the following experimental data (and for the corresponding numerical simulations).

The burner is also equipped with different diagnostics, Fig. 9.1. Pressure

recordings are available at the injector tubes. An Optris infared 3MH-CF4 thermometer is used for non-intrusive temperature measurement at the cooling plate center. It has a spectral range of 2:3 μm, response time of 1 ms, temperature range of 373 to 873 K, with an accuracy of $\pm$(2 K + 0.3 % of reading). Imaging the sequence of LBO is made possible by placing an air cooled mirror downstream of the combustion chamber, in the wake of the exhaust gases as shown in Fig. 9.1. The mirror is angled at 45° to reflect the flame images onto a Phantom V2012 camera operating at 5 kHz. In parallel, a Phantom V2012 camera attached to a LaVision High-Speed Intensified Relay Optics unit and a UV filter, allowing a band-pass center wavelength of 310 nm, and 10 nm width, is used for OH* chemiluminsecence side imaging. Six Hamamatsu H11902-113 photosensor modules are deployed for flame detection at individual burner positions, at a height of 30 mm and 125 mm from the backplane. The PMTs have a spectral response of 185 nm to 700 nm, and are fitted with UV filters which have a center wavelength of 310 nm, and 10 nm width. In addition, extension tubes and slits of varying apertures are fitted over the PMTs to allow the adjustment of the field of view (FOV). In all cases, the FOV at the burner exit mid-plane is kept constant at 22 mm for the minor axis, and 33 mm for the major axis.

9.3 Numerical modeling

The computational domain used in this study is presented in Fig. 9.5(a). Note that, to reduce the cost of computations to reasonable values and hence descent use of the available High Power Computing (HPC) resources, only a 60° periodic sector is considered[1]. In LES, the plenum is not considered and the premixed mixture is injected at the tube inlet. The atmosphere is however taken into account at the end of the combustion chamber (not shown). An instantaneous field of heat release rate predicted via LES-CHT for Configuration B is also shown in blue, Fig. 9.5(a). LES is performed using the AVBP code (cerfacs.fr/avbp7x/index.php) that solves for the compressible Navier-Stokes multi-species equations (Chapter 2). The SIGMA turbulent closure is employed for the sub-grid stresses [46] and the TTGC scheme (third order in time and space) is used for the discretization of the convective terms [48]. The LES computational grids for both Configurations B and A consist of 38M tetrahedral cells and are

[1]During the experiments and in real engine tests as well, intermittent blow out and re-ignition for some of the injectors have been observed (see Chapter 10). Of course, periodicity assumption does not allow for the prediction of this particular mechanism. Nevertheless, overall LBO limits and flame shape evolution are well retrieved. Full annular simulation of the LBO process can be considered as future next steps.

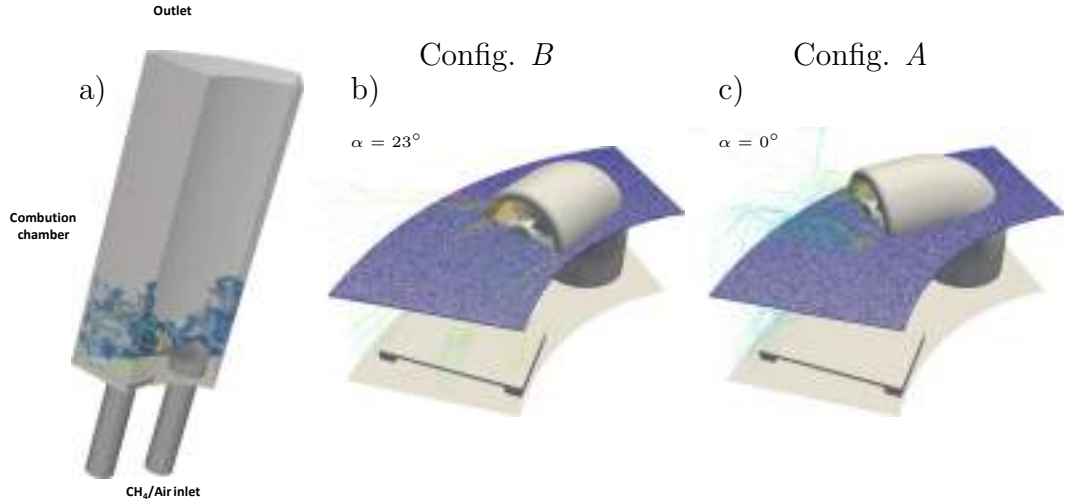

Figure 9.5: (a) Periodical computational domain used in LES with overview of the 38M cells mesh for configurations (b) *B* and (c) *A*. Note that in LES the atmosphere is taken into account at the end of the combustion chamber (not shown). An instantaneous field of heat release rate predicted via LES-CHT for configuration *B* is also shown in blue.

shown in Fig. 9.5(b-c), respectively. Since the flame was experimentally observed to significantly change close to LBO, the computational grid is not only refined in the region of the stable flame following the SMR approach of Chapter 3 [70, 77] but a homogeneous refinement is applied to the entire primary zone[1]. The final mesh has a characteristic size in the combustion region of $\Delta_x = 350\ \mu m$ assuring a $y^+ \sim 5$ at the chamber walls, hence allowing the use of a wall resolved LES approach (no slip condition on all walls) and a reasonable estimation of the thermal boundary layer. Note that the region near the cooling plate has been further refined with $\Delta_x = 100\ \mu m$ (leading to a y^+ lower than unity) to well reproduce the flame/wall interaction observed in the author's previous study [77]. Finally, Navier-Stokes Characteristic Boundary Conditions (NSCBC) [30] are used with a relaxation factor of $K_{inlet} = 1 \times 10^2\ \mathrm{s}^{-1}$ and $K_{outlet} = 1 \times 10^5\ \mathrm{s}^{-1}$ at the inlet and outlet, respectively.

When it comes to the combustion model, the dynamic formulation of the thickened flame model (DTFLES) [64] is employed. An efficiency function Ξ_Δ is introduced to compensate for the reduction of flame surface and flame/turbulence interaction [61]. In particular, a dynamic formulation of the Charlette efficiency function [62] is used to have a local on-the-fly estimation of the model parameter

[1]LBO is indeed a dynamic process, likewise ignition, and a DMR approach would be of greater interest compared to a SMR approach.

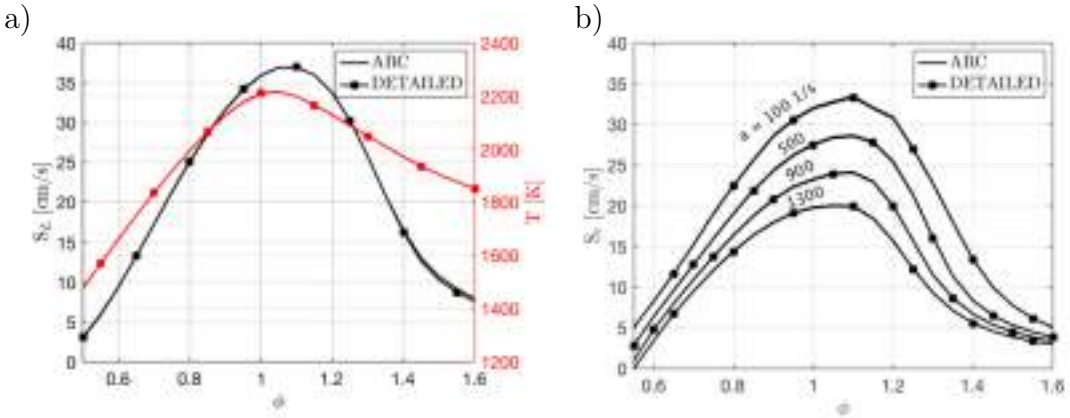

Figure 9.6: Validation of the ARC scheme against the detailed PoliMi CRECK mechanism with a mixture transport model using Cantera for atmospheric CH_4-air flames. (a) Comparison of adiabatic flame temperature (red) and laminar flame speed (black) as a function of the equivalence ratio ϕ for unstrained premixed 1D flame. (b) Evolution of the consumption speed as a function of the equivalence ratio ϕ and the strain rate a in the counterflow premixed 1D configuration, i.e. fresh premixed gases opposed to burnt equilibrium products.

β_{Ch} since it has showed to have significant impact on flame transient simulations [333]. CH_4/Air chemistry is modeled through an Analytically Reduced Chemistry (ARC) kinetic scheme consisting of 18 transported species, 144 reactions, and 12 quasi-steady state species, derived from the detailed PoliMi CRECK scheme [241] using ARCANE [65]. This kinetic scheme has been recently validated through Cantera (www.cantera.org) calculations of 1D-premixed flames against experimental data and detailed schemes [25] (see Chapter 6). This approach is here preferred over the more conventional and computationally less expensive 2 step scheme used in Chapter 8 because of the higher accuracy of ARC schemes in predicting flame stabilization [47] and flame response to strain, which is critical when considering near LBO conditions[1]. When it comes to transport properties, a simplified model is used that accounts for constant non-unity laminar Lewis numbers and different species laminar diffusivities [71]. Further validation of the ARC scheme with the simplified transport model against the detailed mechanism with a mixture transport model for atmospheric CH_4-air flames at $T_{inlet} = 293$ K is provided in Fig. 9.6. The comparison of the adiabatic flame temperature (red) and the laminar flame speed (black) as a function of the equivalence ratio ϕ in 1D unstrained premixed flame configurations shows perfect agreement between

[1]Note that, in this regards, the TFLES model employed modifies the flame response to stretch, as recently showed by Popp *et al.* [334]. To limit this effect, the grid used is refined so as to require the use of low thickening values.

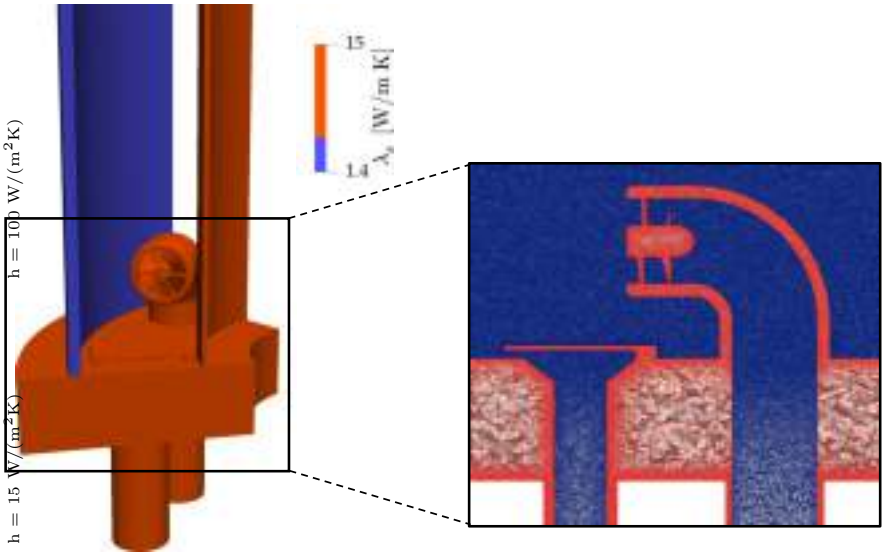

Figure 9.7: Computational domain used in CHT simulations with overview of the solid (red) and fluid (blue) meshes with thermal boundary conditions for the AVTP heat-conduction solver. Assumed thermal conductivities λ_s for quartz (blue) and stainless steel (orange) are also indicated [59].

the ARC scheme and the detailed one, Fig. 9.6(a). Likewise, Fig. 9.6(b) presents the evolution of the consumption speed S_c as a function of the flame strain rate, a, and equivalence ratio ϕ in the strained premixed 1D configuration, i.e. fresh premixed gases are opposed to burnt equilibrium products. The consumption speed is here evaluated from the integral of the heat release rate $\dot{q}$, that is:

$$S_c = \frac{1}{\rho_f \left(T_b - T_f\right)} \int_{-\infty}^{+\infty} \frac{\dot{q}}{c_p} \, dx, \tag{9.1}$$

where c_p is the specific heat at constant pressure, T_b is the burnt gas temperature, T_f and ρ_f refer to the fresh gas temperature and density, respectively [38]. The strain rate a corresponds to the global value evaluated for each flame as the sum of the jet velocities divided by the domain width, i.e. $(u_{fresh} + u_{burnt})/L$. Note also that flame strain can be considered as representative of the total flame stretch since curvature is zero in 1D flames [328]. Once again, the ARC mechanism is observed to correctly recover the flame response to strain rate. In particular, as strain increases, the consumption speed reduces (as expected for methane/air mixtures) and the flame eventually extinguishes, a feature that can potentially play a relevant role on the onset of LBO [312].

As said, a CHT approach is used to account for heat-transfer at the combustor walls by coupling the AVBP LES solver with the AVTP code that solves for heat conduction in the solid [54, 55]. In terms of process, the two solvers run in parallel

and exchange the solid surface temperature T_s as well as the heat flux Φ_q at the boundaries at each coupling iteration [25, 59, 66] (see Chapter 4). Note that the different nature of the heat transfer and fluid dynamics problems ask for careful attention when it comes to coupling the two solvers, in particular:

- the characteristic flow time τ_f is much smaller than the solid heat transfer characteristic time τ_s. The first is typically in the order of milliseconds and can be computed as the flow-through time $\tau_f = \rho V/\dot{m}$ where ρ is the flow density, V is the combustion chamber volume and $\dot{m}$ is the mass flow rate. The second is in the order of seconds and can be computed as $\tau_s = V_s \rho_s C_s / hS$ where S is the surface area, V_s and ρ_s are the solid volume and density while h is the heat transfer coefficient [176].

- the time step at which the two solvers advance are different. In compressible LES, the time step δt follows the Courant-Friedrichs-Lewy (CFL) condition that yields a time step δt_f of the order of 10^{-8} s for typical academic combustion applications. In AVTP, the time step follows the Fourier number and leads to a time step δt_s of the order of 10^{-5} s.

According to the different time steps, it is possible to synchronize the two solvers by letting them perform a different number of iterations in between two consecutive exchange points. In such a case, the large heat transfer characteristic time would require very long LES simulations (and hence unfeasible HPC resources) to have a converged solid steady state temperature. In addition, since experimentally the equivalence ratio is decreased slowly compared to the solid heat transfer characteristic time τ_s, a sound assumption is that the solid is always in equilibrium with the fluid temperature. Therefore, to speed up the convergence toward a solid steady state temperature and to let the solid be in equilibrium with the fluid temperature even though the reduced LES simulations duration, the two solvers can be de-syncronized in time by increasing the number of iterations performed by AVTP compared to AVBP between two consecutive coupling iterations. Note that this approach is equivalent to decreasing the heat capacity of the solid and, hence, the characteristic time of the heat transfer in the solid ${\tau_s}^1$.

The computational domain used for AVTP simulations is presented in Fig. 9.7 (shown only for Config. *B*). The solid mesh is shown in red and the fluid one

[1] In the present work, assuming $\tau_s = 10$ s and $\tau_f = 10$ ms, to have the solid always in equilibrium with the fluid temperature (i.e. $\tau_f \simeq 10\ \tau_s$) requires to speed up the physical time in the solid by a factor of 10^4. Considering $\delta t_s = 10^{-5}$ s and $\delta t_f = 10^{-8}$, this means to perform 10 iterations with AVTP for each iteration performed by AVBP.

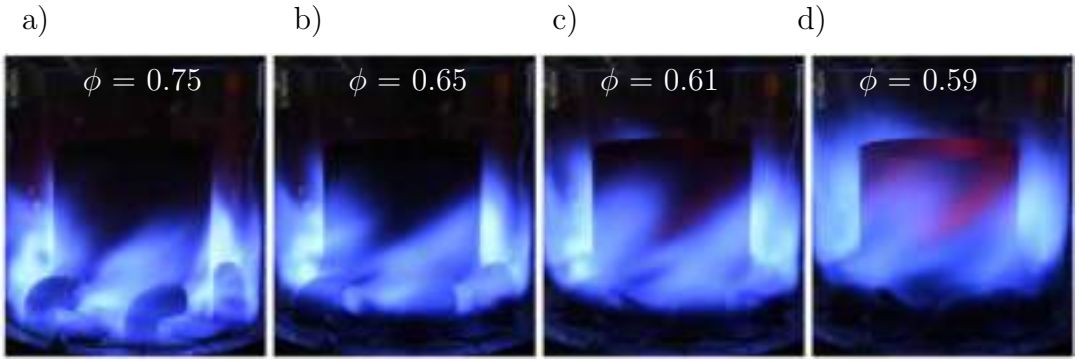

Figure 9.8: Sequence of DSLR images showing the flame shape evolution leading to lean blow-out. Configuration *B*.

is in blue. The solid is discretized using 14M tetrahedral elements with at least 5 points across the thin chamber walls. An implicit first-order Euler scheme and a second-order Galerkin diffusion scheme are used for time integration and spatial discretization, respectively. Figure 9.7 indicates also the assumed thermal conductivities λ_s for quartz and stainless steel. Note that the thermal boundary conditions for the solid surfaces that are not in contact with the fluid domain (e.g. external chamber walls and tubes) are set through heat exchange coefficients (Fig. 9.7) [59].

9.4 Experimental findings

Experimental findings for configurations A and B are hereafter presented showing the LBO limits, the flame shape and stabilization evolution.

To first provide an overview of the possible stages leading to blow-out, sequential flame images are taken with a DSLR camera and are presented in Fig. 9.8 for configuration B. In both configurations, it is observed that with decreasing ϕ, well-attached flames start to elongate (a). The flames then detach and become lifted flames (b) to finally merge and form a single flame front around the entire circumference of the annulus (c-d) at lower equivalence ratios.

Such a flame shape evolution can be identified precisely via recorded PMT signals or temperature evolution of the cooling plate. Figure 9.9 presents the temporal evolution of (a) the injected equivalence ratio ϕ, the PMT signals at (b) 30 mm, (c) 125 mm from the backplane and (d) the temperature of the cooling plate. As ϕ is gradually reduced from 0.65 to 0.6, the PMT signal at 30 mm (i.e. pointing at the injector exit) slightly decreases while the PMT_{125} stays close to zero. At $\phi = 0.6$, the decrease registered by PMT_{30} and the increase registered by PMT_{125} are accentuated while the temperature of the cooling plate starts decreasing indicating a rapid lift-off of the flame. Note in particular that, at ϕ

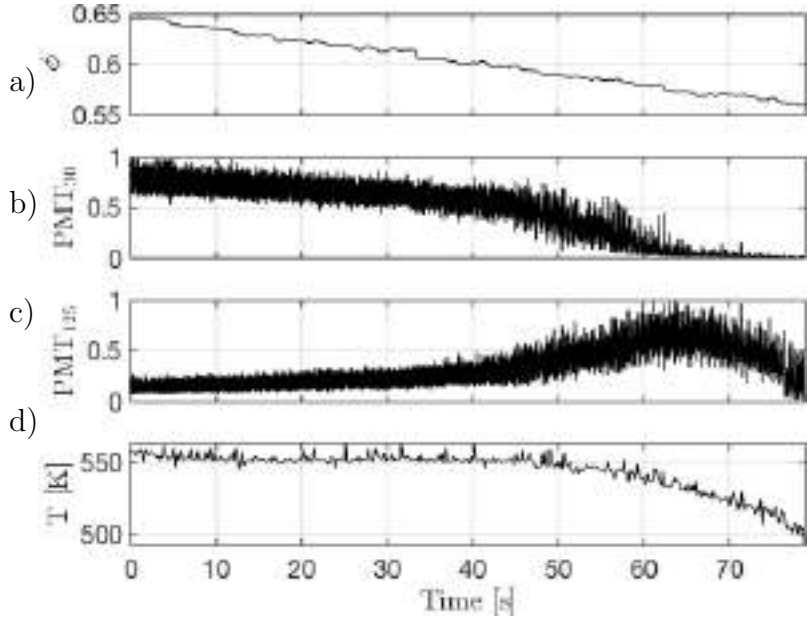

Figure 9.9: Experimentally measured (a) equivalence ratio ϕ, (b) PMT signal at 30 mm height, (c) PMT signal at 125 mm and (d) temperature evolution recorded at the cooling plate. Configuration *B*.

= 0.58 the flame shape transition is completed: PMT_{30} reaches zero meaning that the flame is no longer present at the injector exit while PMT_{125} reaches its maximum. Soon after, at $\phi = 0.57$ the flame finally extinguishes.

To obtain a more quantitative visualization of the flame lift-off process, the instantaneous LOS OH* side images are integrated over the horizontal direction to yield the one-dimensional OH* axial distribution $\langle OH^* \rangle$ as expressed by,

$$\langle OH^* \rangle(x,t) = \frac{1}{L_y} \iint_{L_y} OH^*(x,y,t)\ dy. \tag{9.2}$$

Figure 9.10 presents the experimentally measured integrated intensity of (a) the OH* signal from the side, noted I_{side}, and (b) the visible light from the top, noted I_{top}. Figure 9.10(c) shows the axial one-dimensional distribution of OH* signal from the side $\langle OH^* \rangle$ as a function of the distance from the backplane x and of the equivalence ratio ϕ for Configuration *B*. The evolution of I_{side}, Fig. 9.10(a), follows the slight decrease of PMT_{30} until $\phi = 0.6$ to then suddenly drop indicating that the flame is stabilizing downstream until $\phi = 0.58$ when no flame is anymore detected from the side camera. At the same time, I_{top}, Fig. 9.10(b), shows the constant intensity level, indicating that all the fuel is always burnt until $\phi = 0.57$ when the signal starts decreasing and LBO occurs. The axial one-dimensional distribution $\langle OH^* \rangle$, Fig. 9.10(c), provides more detailed information about the flame position transition. First of all, no flame is generally detected below 20

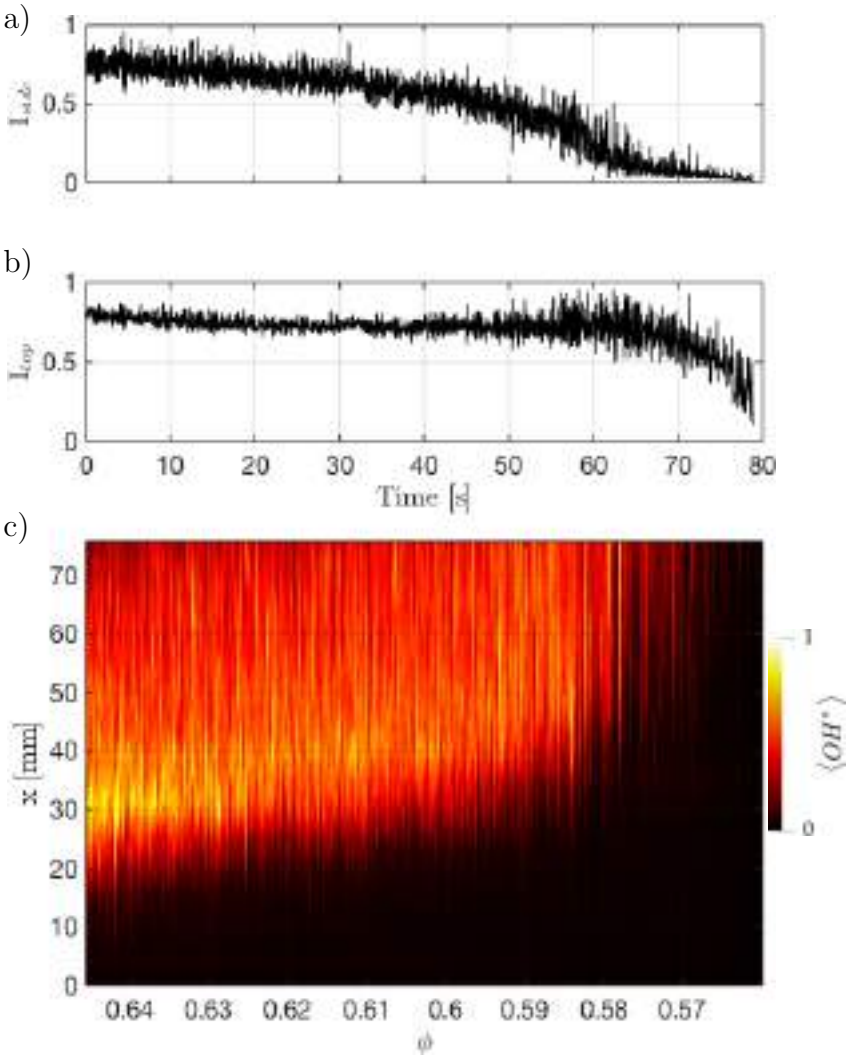

Figure 9.10: Experimentally measured integrated intensity of (a) visible light from the top and (b) OH* signal from the side. (c) Axial one-dimensional distribution of OH* signal from the side $\langle OH^* \rangle$ as a function of the equivalence ratio ϕ. Configuration *B*.

mm from the backplane and until $\phi = 0.63$, the maximum signal intensity happening at 30 mm. From this point, the maximum signal location starts moving downstream and stabilizes around 40 mm, i.e. the flame lift-off starts (point P1, see Table 9.1). From $\phi = 0.6$ on (P2), the flame rapidly moves downstream and is no more firmly stabilized close to the injector. At $\phi = 0.58$ (P3), the flame is stabilized further downstream and appears to move upstream sporadically until LBO finally occurs at $\phi = 0.57$ (P4).

The same trend is observed also for Configuration *A*. Figure 9.11 presents the experimentally measured (a) equivalence ratio ϕ, the PMT signals at (b) 30 mm and (c) 125 mm height as well as (d) the temperature evolution recorded at the cooling plate. As the equivalence ratio decreases, the PMT_{30} OH* signal,

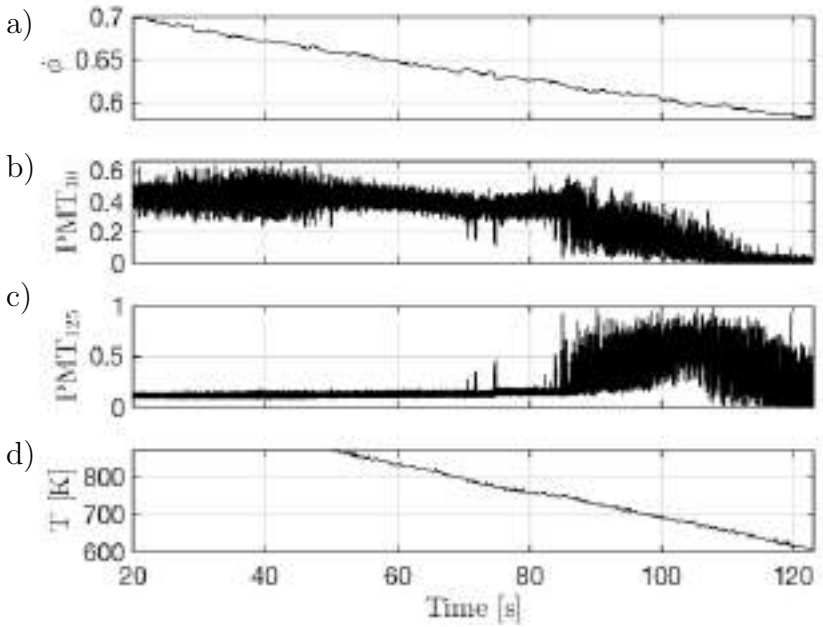

Figure 9.11: Experimentally measured (a) equivalence ratio ϕ, PMT signals at (b) 30 mm and (c) 125 mm height as well as (d) the temperature evolution recorded at the cooling plate. Configuration *A*.

Fig. 9.11(b), exhibits large fluctuations, corresponding to local extinctions and re-ignition in a manner similar to what has been previously reported on single sector flames [17]. The OH* signal starts to slightly decrease at $\phi = 0.66$ (P1), then it presents much larger fluctuations with a rapid decrease at $\phi = 0.63$ (P2) and finally reaches zero values at $\phi = 0.61$ (P3). At the same time, the PMT_{125} signal, Fig. 9.11(c), shows almost zero values until P2, when the abrupt change in flame stabilization causes an increase of OH* signal. Note how this change in flame stabilization is notably faster if compared to Configuration *B* that presented lower signal gradients. Again, the maximum registered by PMT_{125} corresponds to P3, when PMT_{30} is zero, and it denotes the complete flame extinction for $\phi = 0.6$ (P4). Note that the temperature evolution measured at the cooling plate, Fig. 9.11(d), shows a linear decrease after P1, when the flame starts its lift-off process, as already evidenced for Configuration *B*.

The experimentally measured integrated intensity of the OH* signal from the side I_{side} and of the visible light from the top I_{top} for Configuration *A* are shown in Fig. 9.12(a-b), respectively. Figure 9.12(c) presents the corresponding axial one-dimensional distribution of OH* signal from the side, i.e. $\langle OH^* \rangle$, as a function of the distance from the backplane x and the equivalence ratio ϕ. The main flame transition events occurring until LBO occurs can be easily spotted from the I_{side} signal. The latter is almost constant until $\phi = 0.66$ when it starts

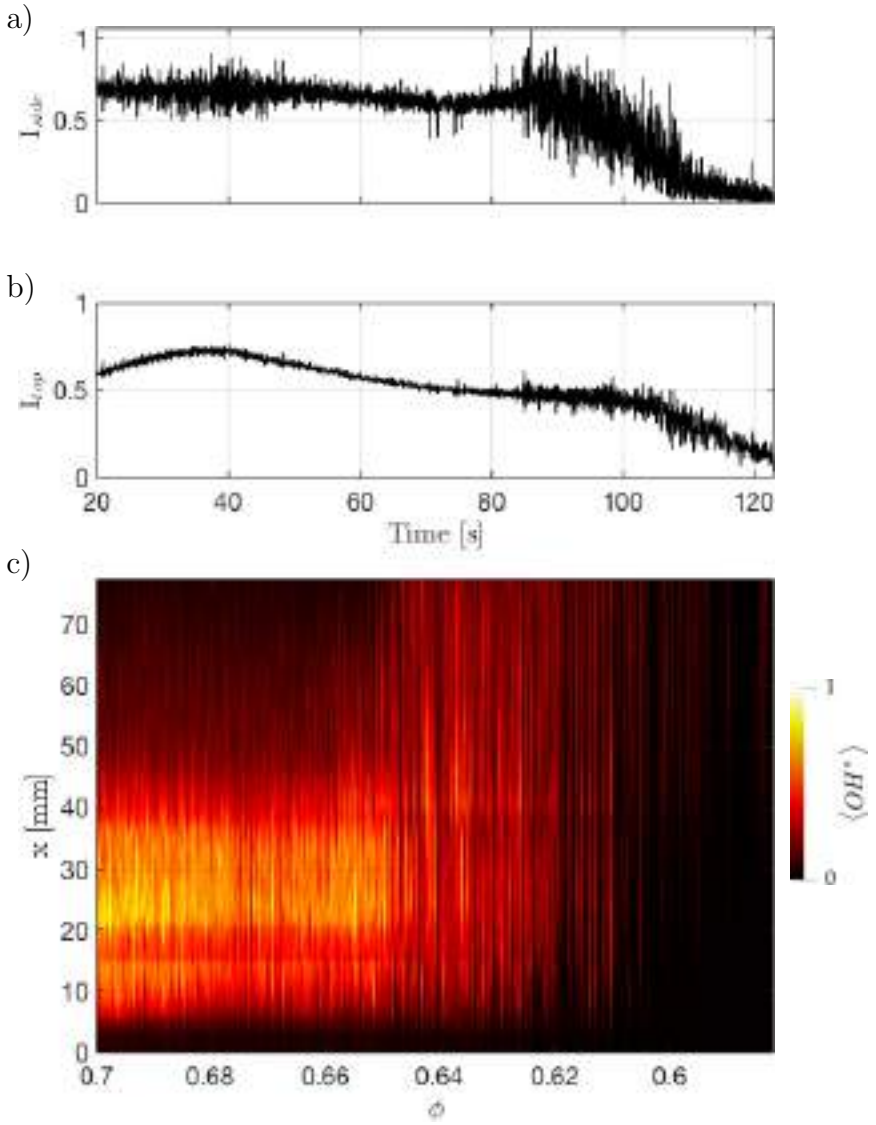

Figure 9.12: Experimentally measured integrated intensity of (a) visible light from the top and (b) OH* signal from the side. (c) Axial one-dimensional distribution of OH* signal from the side $\langle OH^* \rangle$ as a function of the equivalence ratio ϕ. Configuration *A*.

slightly decreasing (P1), then a sudden change in signal gradient happens at $\phi =$ 0.63 (P2) and finally no flame is detected from the side camera starting from ϕ = 0.61 (P3). At this instant, the I_{top} signal also starts decreasing reaching near zero values soon after and indicating the complete extinction of the flame (P4).

Table 9.1 summarizes the equivalence ratios ϕ at which the observed main flame transition events occur until complete flame extinction for both configurations. Although the same trend and flame shape transition events can be noticed in both cases, Configuration *A* presents the same events consistently at higher equivalence ratios (i.e. $\sim +0.03$), indicating lower capabilities in terms of LBO and suggesting that a strong role is played by the injector orientation angle and

Configuration	P1 Lift-off starts	P2 Rapid decrease of PMT_{30}	P3 $PMT_{30} = 0$	P4 LBO
A	$\phi = 0.66$	0.63	0.61	0.6
B	$\phi = 0.63$	0.6	0.58	0.57

Table 9.1: Summary of the experimentally observed equivalence ratios ϕ at which main flame transition events occur until LBO for Configuration *B* and *A*. Experimental uncertainty is ± 0.01.

hence by the flame-flame interaction[1].

9.5 LES predictions and method

When it comes to predicting the LBO dynamics with LES, to keep the simulated physical time reasonable and hence the computational cost acceptable, an accelerated procedure is employed to analyze the flame shape evolution until complete flame extinction. To this scope, starting from an equivalence ratio of $\phi = 0.82$ where the flame is in a stable condition, the air mass flow rate is suddenly increased by 2 g/s (for the annular rig), while keeping the fuel mass flow rate constant at 1.7 g/s, hence leading to a step reduction of the equivalence ratio of approximately 5%, as generally proposed in the literature for such studies [26]. Note that subsequent reductions in equivalence ratio before P1 (i.e. when the lift-off process starts) are performed after at least 3 characteristic flow-through times τ_f ($\sim$10 ms considering the flow and the distance of 100 mm from the backplane). Since P1 is reached, the equivalence ratio reduction procedure by steps is notably slowed down, i.e. waiting for at least 10 τ_f since the flame is expected to more slowly adapt to these leaner conditions and for which it is not anymore firmly stabilized at the injector exit. Note that, even with this adopted procedure, the total physical time simulated for each LES is considerable ($\sim$1.2 s). Note also that all simulations performed represent only one single flow realization, and therefore cannot be statistically significant if compared to the 20 tests performed experimentally. Bearing in mind these limits, numerical predictions with adiabatic boundary conditions and CHT approaches are illustrated in sections 9.5.1 and 9.5.2 for Configuration A and Configuration B, respectively with the objective of investigating the issue of the thermal response in light of the numerical modeling choices.

[1]Note that experimentally more than 20 tests have been performed for each configuration in order to have a statistically relevant LBO limit. Being all the runs results widely consistent, only one set of typical LBO data is here shown for each configuration.

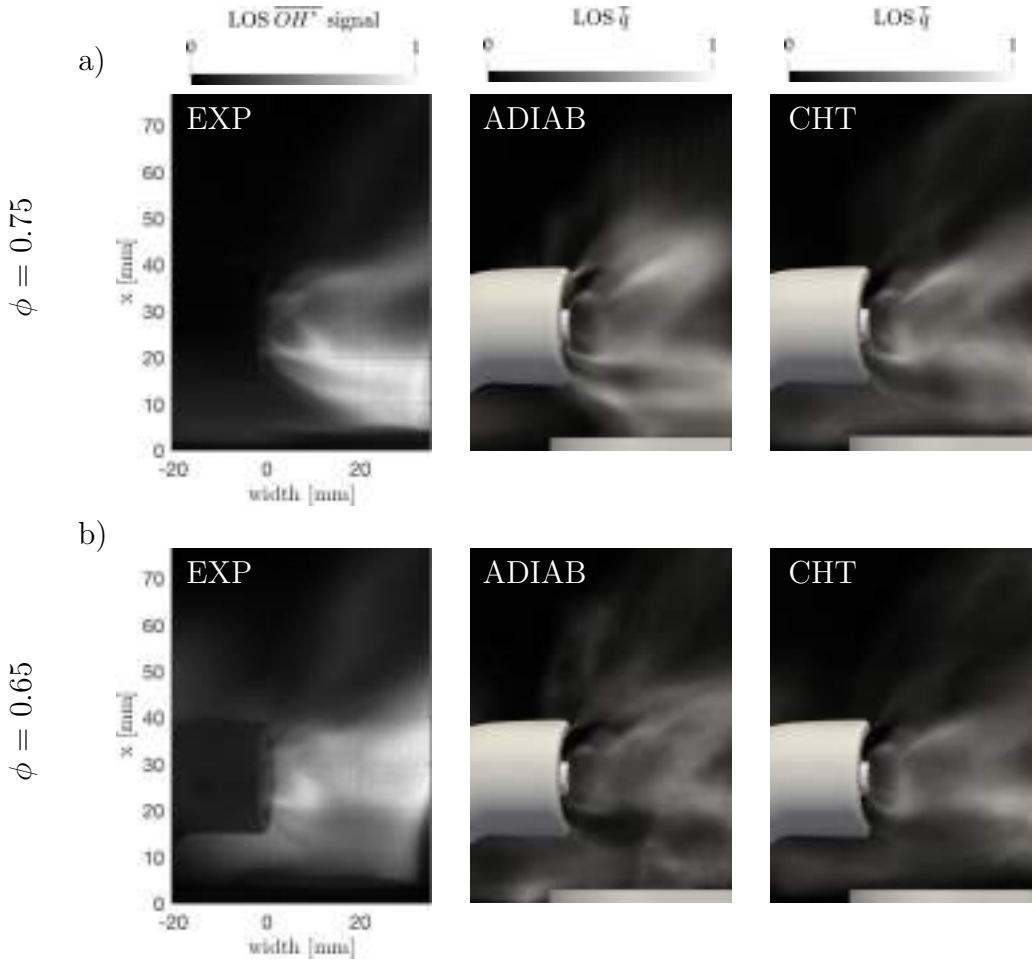

Figure 9.13: Experimentally measured time-averaged LOS-integrated OH* chemiluminescence image compared to predicted time-averaged LOS heat release rate $\overline{\dot{q}}$ by the adiabatic and the CHT simulations for an equivalence ratio of (a) $\phi = 0.75$ and (b) $\phi = 0.65$. Configuration *A*.

9.5.1 Configuration *A*

The experimentally observed flame shape and stabilization are first compared to the one issued by the numerical prediction in Fig. 9.13 for a starting equivalence ratio of (a) $\phi = 0.75$, for which the flame is stable, and (b) $\phi = 0.65$, i.e. just after the flame starts its lift-off process (P1, $\phi = 0.66$). Experimentally measured line-of-Sight (LOS) integration of the OH* chemiluminescence is a qualitative indicator of the heat release rate for lean premixed flames [170] and, therefore, it is here compared to the LOS of the time-averaged heat release rate $\overline{\dot{q}}$ predicted by the adiabatic and CHT simulations[1]. Starting with the point for which ϕ = 0.75, Fig. 9.13(a), the flame is experimentally stabilized close to the injector exit, with most of the significant signal positioned at a height of approximately 20 mm from the backplane. At that point, both adiabatic and CHT simulations

[1]Note that predicted fields considered here are time-averaged for 10 τ_f.

globally recover the flame shape although the adiabatic case overestimates the flame aperture angle compared to experiments and the CHT results. This difference is mainly due to the stabilization of the flame near the injector outer walls and in the outer shear layer for the adiabatic case, i.e. a M-shape flame is predicted. Contrarily, in the experiment and the CHT simulation, the flame stabilizes near the inner body of the injector exit and only in the inner shear layer of the swirled flow. No flame is predicted near the outer shear layer due to the difference in temperature of the injector walls, i.e. a V-shape flame is observed. As a consequence, above 40 mm, while experiments and CHT show weak signals, the adiabatic simulations predict more intense heat release rate fields. Shifting to a later time and recalling that, when the equivalence ratio is reduced to ϕ = 0.65 (below P1), Fig. 9.13(b), the flame starts its lift-off process, the largest signal is experimentally observed further downstream, at 30 mm from the backplane. The measured OH* chemiluminescence signal appears at this stage more blurry, indicating that the flame is less firmly stabilized at the injector exit and is elongated [77]. Both adiabatic and CHT simulations recover this change in flame shape and also predict more elongated flames. However, the adiabatic simulation still presents some heat release rate in the outer shear layer of the swirled-flow at the injector exit, i.e. V-shape flame is still present.

As discussed before, at later instants, flame lift off and LBO proceed. To follow this dynamics including LBO, a reduction of the equivalence ratio by steps is performed in LES and, as the simulation proceeds, volume-averaged and maximum quantities are recorded to monitor the dynamics. Obtained temporal evolutions are provided on Fig. 9.14 with (a)-(e) the equivalence ratio ϕ, (b)-(f) the volume-averaged heat release rate $\dot{q}$, (c)-(g) the maximum temperature T_{max} and (d)-(h) the maximum OH mass fraction in the domain $Y_{OH,max}$ issued by the adiabatic and the CHT simulations, respectively. Note that the equivalence ratio, Fig. 9.14(a)-(e), is decreased from ϕ = 0.65 to 0.62 and finally 0.6 for both simulations. In the adiabatic case, the heat release rate $\dot{q}$ only slightly decrease during the simulation, suggesting that the fuel is not fully burnt in the control volume. Note that, at t = 1140 ms, a minimum of $\dot{q}$ is visible, soon after the last decrease of equivalence ratio to 0.6 has happened but then $\dot{q}$ recovers and seems to remain stable even though fluctuations are present. Maximum values of (c) temperature and (d) OH mass fractions on the other hand decrease very rapidly after each equivalence ratio step. Since the maximum temperature corresponds to the adiabatic flame temperature, a decrease when leaner mixtures are considered is expected, Fig. 9.6. Equivalently, since OH mass fraction is linked to the flame reactivity, it is also expected to reduce. Switching from the adiabatic

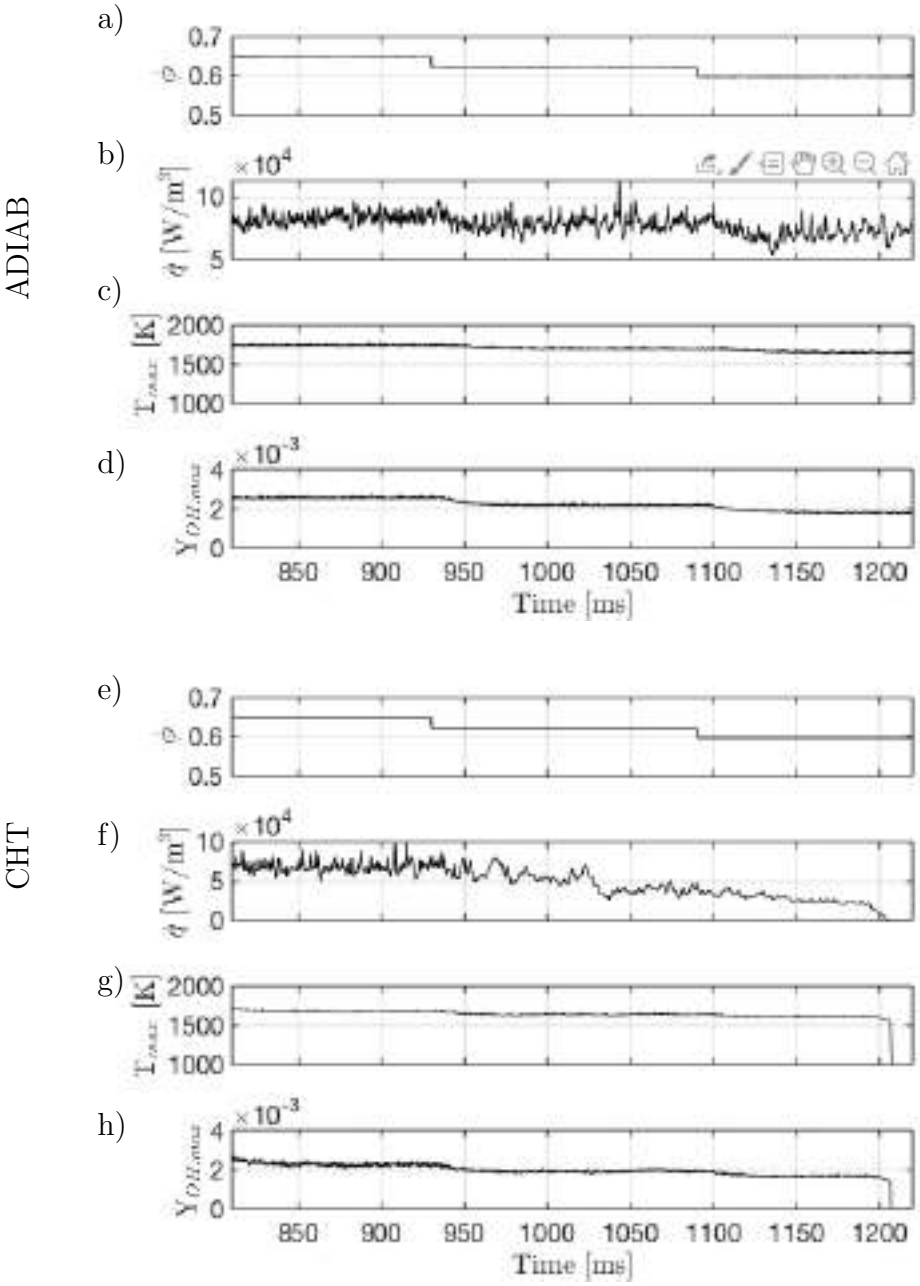

Figure 9.14: Temporal evolution from the adiabatic and the CHT LES simulations of (a)-(e) equivalence ratio ϕ, (b)-(f) volume-averaged heat release rate $\dot{q}$, (c)-(g) maximum temperature $\mathbf{T}_{max}$ and (d)-(h) maximum OH mass fraction in the domain $\mathbf{Y}_{OH,max}$. Configuration *A*.

to the CHT LES prediction however changes slightly the evolutions. The CHT simulation predicts a stable volume-averaged $\dot{q}$ at $\phi = 0.65$. At t = 950 ms, soon after the change of the inlet condition, the evolution clearly changes: fluctuation levels are like the ones of the adiabatic case but appear for lower values of ϕ, i.e. 0.6. The signal seems also to stabilize around a lower value of heat release

rate and a further decrease in equivalence ratio produces flame extinction at t = 1210 ms. This is not the case for the adiabatic simulation. Overall the CHT simulation predicts a flame extinction at an equivalence ratio of $0.62 < \phi_{LBO} < 0.6$ which is in good agreement with the observed experimental value considering the experimental uncertainty of ± 0.01 (see Table 9.1).

The dynamics leading to LBO is presented in more details in Fig. 9.15, comparing the experimentally measured LOS-integrated OH* chemiluminescence images with the instantaneous LOS heat release rate $\bar{\dot{q}}$ fields predicted by the adiabatic as well as the CHT simulations. Note that, in the following, information is recast based on the equivalence ratio values. Starting with $\phi = 0.74$ (a) the flames are well attached to the injector exit and get elongated taking a smaller flame angle as the mixture become leaner (b). The adiabatic simulation generally predicts more compact flames with heat release rate happening in the outer shear layer, as already observed in Fig. 9.13. At lower ϕ (c-d), the flames look more blurry and the lift-off process starts, the flame stabilizing further downstream of the injector exit in the CHT simulation. Note that the adiabatic LES starts showing a region of fresh gases in the Central Recirculation Zone (CRZ) of the injector but the flame remains stabilized in the outer shear layer contrarily to the CHT case, Fig. 9.15(d). At the last instants (e-f), the flame clearly stabilizes further downstream with most of the signal observed above the injector in both the CHT prediction as well as the experiment before flame extinction. The adiabatic solution instead shows a flame that is still burning close to the injector even for a value of $\phi = 0.6$ (f) and in a manner similar to what is happening in the CHT simulation but at $\phi = 0.65$ (d). This indicates that there is a delay in flame shape transition induced by the initial flame stabilization and shape that is in part governed by the thermal boundary condition.

A more quantitative comparison of the flame shape transition process is presented in Fig. 9.16 which shows the normalized axial one-dimensional evolution of the heat release rate $\langle \dot{q} \rangle$ as a function of ϕ predicted by (a) the adiabatic and (b) the CHT simulations[1], in a manner similar to Fig. 9.12. Clearly, with this representation, the adiabatic simulation predicts large values of $\dot{q}$ in the bottom region of the combustor, i.e. around 10 mm from the backplane, until an equivalence ratio of 0.71. When ϕ is further reduced, i.e. to 0.68, the peak moves downstream around 25 mm from the backplane to finally stabilize around 40 mm at $\phi = 0.65$. Note that for this case, part of the flame is always present in the bottom region until $\phi = 0.6$, although most of it is stabilized above the injector.

[1]Note that 64 3D LES fields were used for the axial integration of the heat release rate, leading to a time resolution of 10 ms.

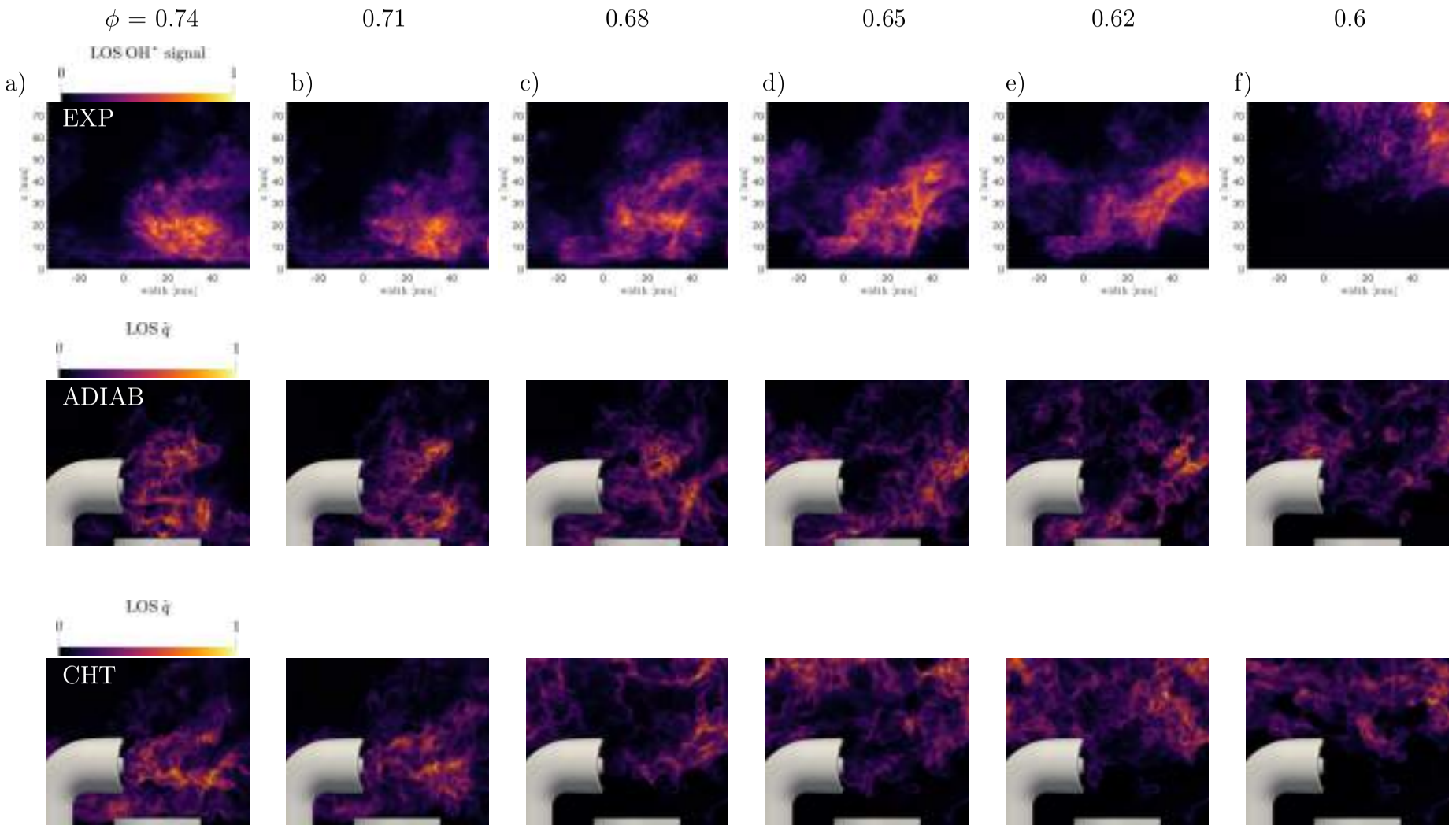

Figure 9.15: Experimentally measured LOS-integrated OH* chemiluminescence image compared to instantaneous LOS heat release rate $\overline{\dot{q}}$ field predicted by the adiabatic and the CHT simulations for different equivalence ratio ϕ. Configuration *A*.

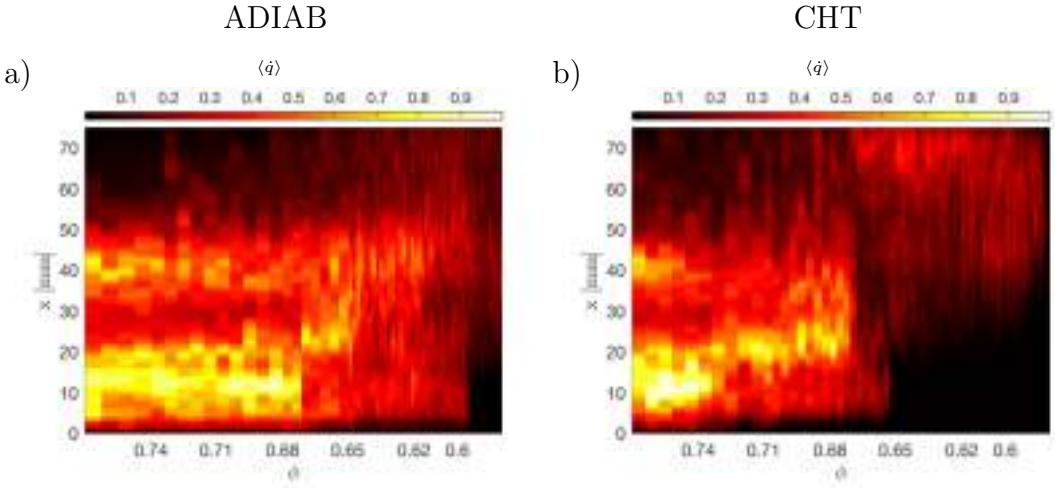

Figure 9.16: Axial one-dimensional evolution of the heat release rate $\langle \dot{q} \rangle$ as a function of the equivalence ratio ϕ predicted by (a) the adiabatic and (b) the CHT simulations. Configuration *A*.

For the CHT simulation, the flame shape transition appears sooner. At $\phi = 0.71$ the flame is indeed already stabilized near 25 mm while lift-off started at $\phi = 0.68$ (P1), slightly before the experimental observations (i.e. $\phi = 0.66$), Fig. 9.12. For lower equivalence ratio values, the flame is fully lifted and stabilized above the injector until a final flame extinction occurs.

More insights into the flame shape evolution at different values of injected equivalence ratios can be obtained from Fig. 9.17 and Fig. 9.18 for the adiabatic and the CHT simulations, respectively. Flame visualization is provided by (a-b) isosurfaces of heat release rate $\dot{q}$ at 10% of its maximum value colored by temperature. A cut plane through the center of the injector exit further shows the (c) temperature, T, (d) heat release rate, $\dot{q}$, and (e) OH mass fraction fields at the provided instants[1]. For the adiabatic simulation and $\phi = 0.68$, Fig. 9.17, the flame is attached at the injector exit and it is pushed along the external chamber wall due to the outward orientation of the injector in Configuration *A*. The combustion chamber is also seen to be rapidly filled with burnt gases at the equilibrium temperature and the cut plane clearly shows a M-shape flame. At $\phi = 0.62$, the flame is no longer present in the CRZ at the injector exit but it is still present in the bottom region, near the backplane, and it stabilizes on the outer injector wall, as visible from the $\dot{q}$ field. The OH peak value reduces and the flame is barely present at the cut-plane height of interest. Finally, at $\phi = 0.6$, the flame is completed lifted, i.e. it takes a full torus like shape around the full chamber and no heat release rate is present close to the chamber backplane. The outer

[1]Note that 1-sector periodic LES solutions are duplicated to better visualize the LBO dynamics and the flame-flame interaction.

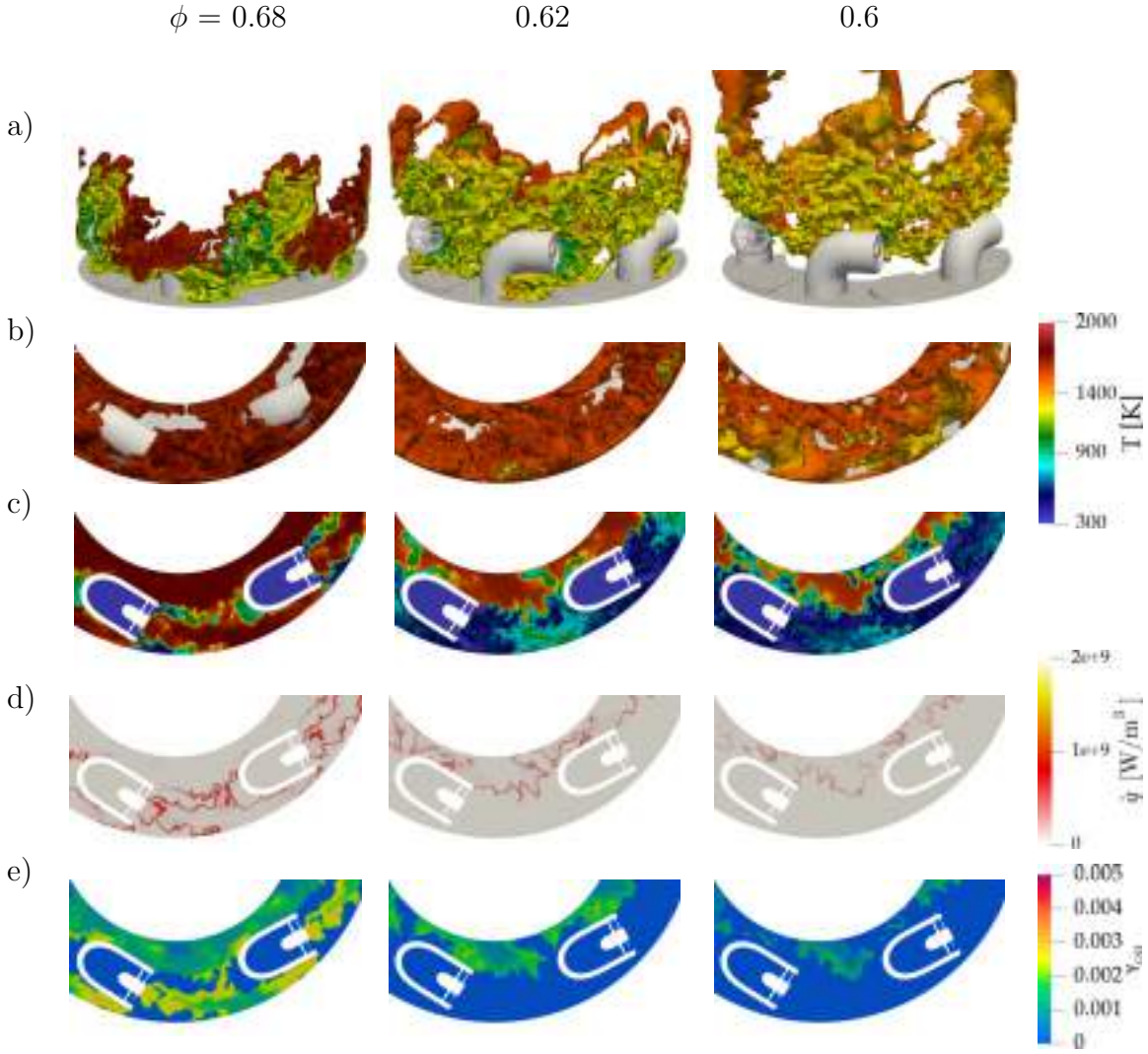

Figure 9.17: Adiabatic LES prediction of flame shape evolution and blow out at different equivalence ratios for Configuration *A*. (a-b) Iso-surface of heat release rate $\dot{q}$ at 10% of its maximum value colored by temperature T. Cut plane showing (c) the temperature T, (d) the heat release rate $\dot{q}$ and (e) the OH mass fraction fields. Images correspond to instants (c), (e) and (f) of Fig. 9.15.

part of the combustion chamber close to the quartz wall is furthermore filled with fresh gases, as indicated by the low temperature values, while burnt gases remain close to the inner chamber wall. Fields of $\dot{q}$ and of OH mass fraction show also that combustion intensity is significantly reduced on the cut plane as the flame is stabilized in a continuous lifted annular shape as experimentally observed.

The CHT simulation, Fig. 9.18, shows the same flame shape evolution but shifted toward richer mixture values. Note that the instantaneous temperature of the solid wall issued by such a simulation is also shown together with the isosurface of heat release rate (a). At $\phi = 0.82$, the flame is well anchored at the

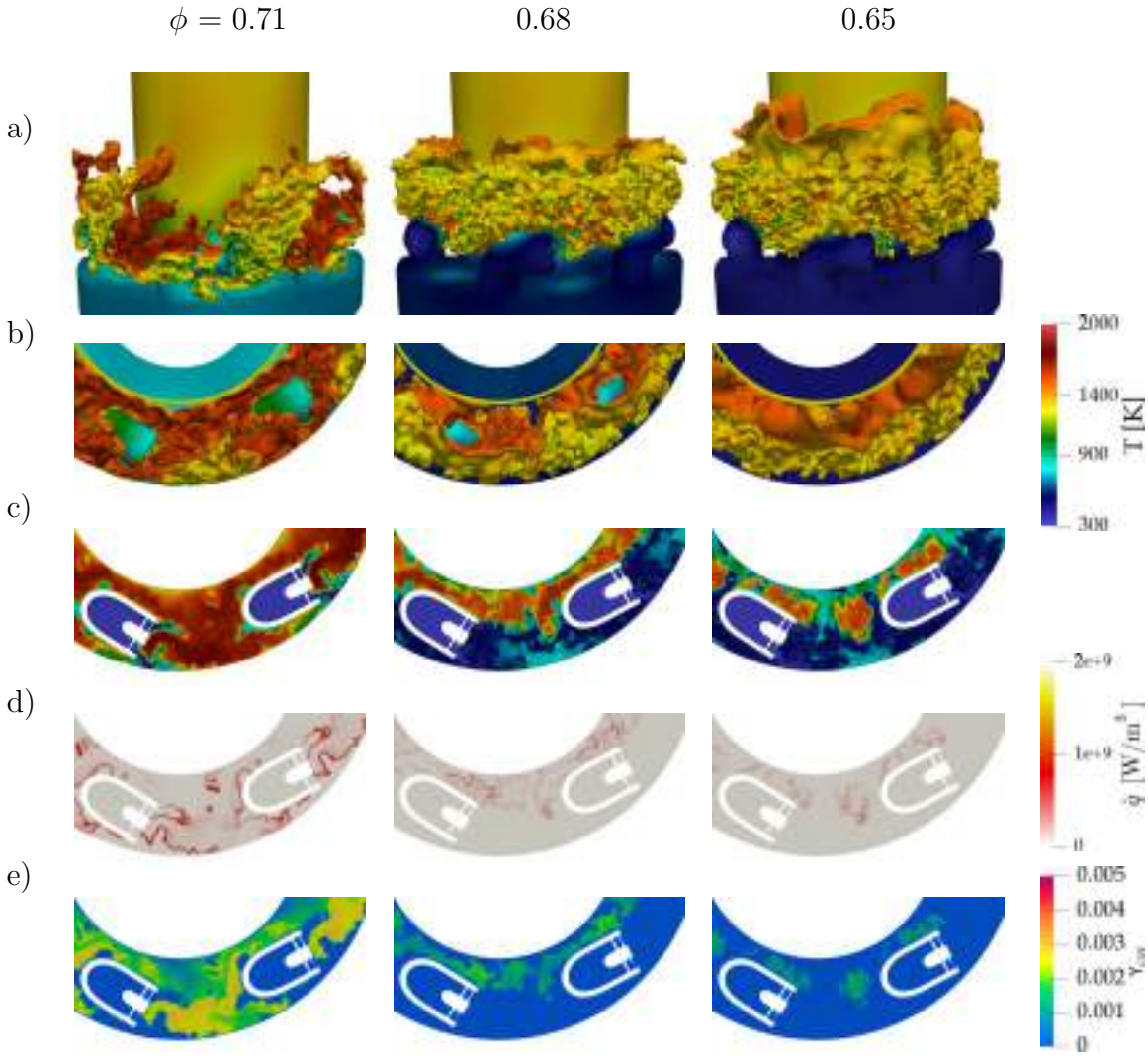

Figure 9.18: CHT-LES prediction of flame shape evolution and blow out at different equivalence ratios for Configuration *A*. (a-b) Isosurface of heat release rate $\dot{q}$ at 10% of its maximum value colored by temperature T. Cut plane showing (c) the temperature T, (d) the heat release rate $\dot{q}$ and (e) the OH mass fraction fields. Images correspond to instants (b), (c) and (d) of Fig. 9.15.

injector exit, but contrarily to the adiabatic prediction, it takes a V-shape (d) and it is hence more elongated going further downstream the injector axis. The OH field (e) presents the same level of peak value at the injector exit but lower values close to the inner chamber wall due to the lower predicted temperature caused by heat transfer at the wall (c). When ϕ is reduced to 0.71, the flame is more elongated (a) and already forms a continuous annular shape: i.e. collapsed with the downstream flames (b) while the OH peak signal further reduces, in a manner similar to what the adiabatic simulation predicts but at $\phi = 0.68$. Proper lift-off starts at $\phi = 0.68$ (P1). The flame stabilizes on the top of the injector

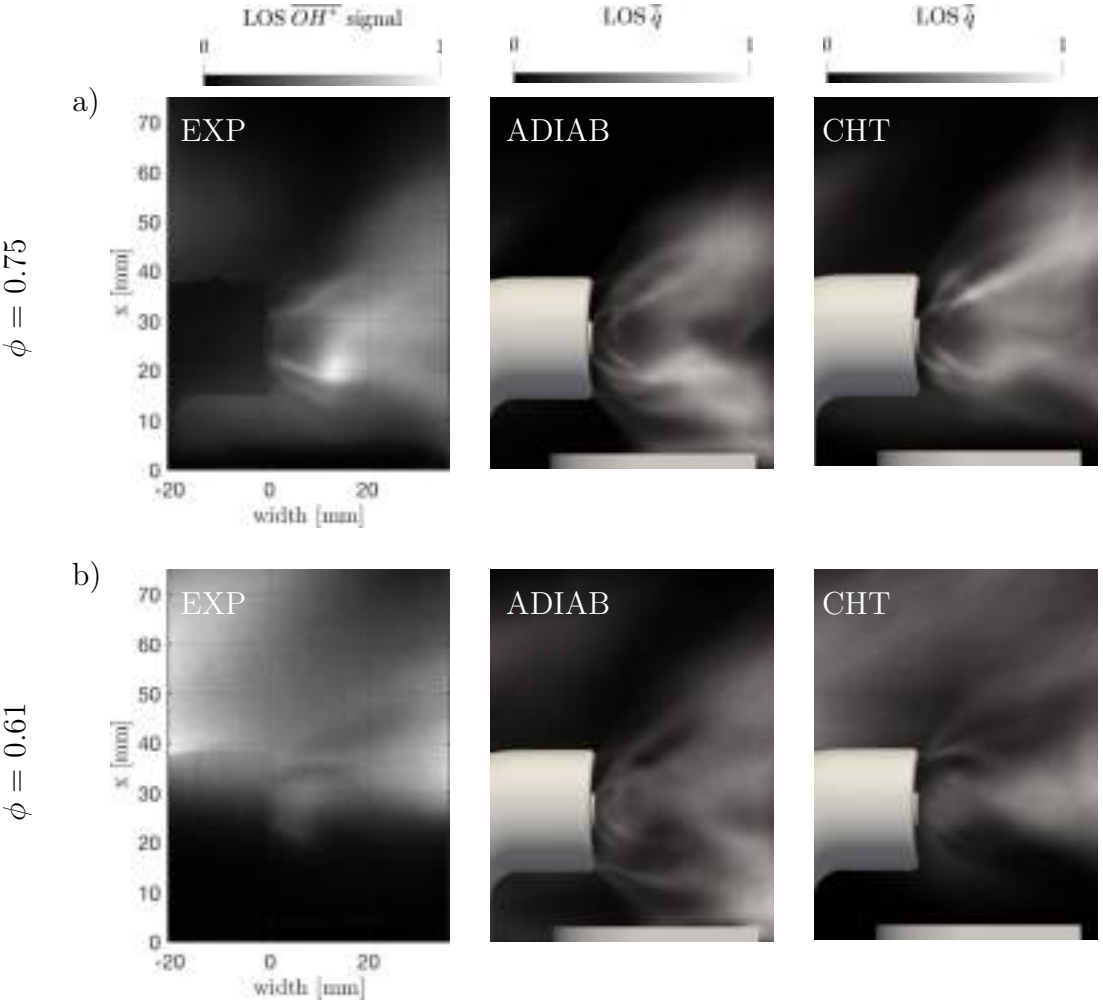

Figure 9.19: Experimentally measured time-averaged LOS-integrated OH* chemiluminescence image compared to predicted time-averaged LOS heat release rate $\overline{\dot{q}}$ by the adiabatic and the CHT simulations for an equivalence ratio of (a) $\phi = 0.75$ and (b) $\phi = 0.61$. Configuration *B*.

while some heat release rate still happens close to the injector exit. Note how the predicted solid temperature changes according to the flame position, i.e. the backplane presents much lower temperature values compared to richer mixture conditions. Finally, at $\phi = 0.65$, flame lift-off is completed with heat release rate and OH signal only sporadically present at the injector height, a condition similar to what adiabatic simulation predicts only at $\phi = 0.6$, confirming that heat transfer at the wall plays an important role in determining the flame shape evolution during the LBO event.

9.5.2 Configuration *B*

The injector orientation (i.e. α angle, see section 9.2) has been observed to play an important role in determining the flame stabilization and dynamics during the

LBO process (see Fig. 9.4). Therefore it is interesting to analyze the flame dynamics also for Configuration *B*. Figure 9.19 compares the experimentally measured LOS OH* chemiluminescence to the LOS-integrated time-averaged heat release rate $\bar{\dot{q}}$ predicted by the adiabatic and the CHT simulations for an equivalence ratio of (a) $\phi = 0.75$, corresponding to stable conditions, and (b) $\phi = 0.61$, soon after the start of the flame lift-off process (P1, $\phi = 0.63$). With richer mixture values, Fig. 9.19(a), the flame is stabilized at the injector exit, in the CRZ of the swirled flow, with the largest OH* signal being located 20 mm from the backplane, similarly to Configuration *A*. A good match is here again observed in terms of flame shape and angle for the CHT results while the adiabatic simulation tends to underestimate the flame length and predict a more compact flame with a larger opening angle due to the presence of heat release rate in the outer shear layer, Fig 9.13(a). In this case and due to the imposed adiabatic condition, the flame spreads over the cooling plate close to the backplane, a situation not observed in the experimental data or in the CHT results. Reducing the equivalence ratio at $\phi = 0.61$, Fig. 9.19(b), a clear difference in flame shape and stabilization can be observed. The experimental OH* chemiluminescence signal is shifted downstream and the flame seems to be only partially stabilized in the CRZ of the swirled flow at the injector exit while most of the heat release rate happens further downstream on the top of the injector wall. CHT results show good agreement in terms of flame shape, stabilization and lift-off height. Even though, the adiabatic simulation recovers the increase in flame length due to the reduction in equivalence ratio, lift-off is marginal and the flame is still well stabilized in the CRZ of the injector, indicating also in this configuration that a delay in flame shape transition is present due to the imposed adiabatic conditions.

When it comes to LBO, Configuration *B* has been simulated with the same accelerated procedure as for Configuration *A*, showing similar trends in the flame shape evolutions. Figure 9.20 presents the temporal evolution during the last steps of (a)-(e) equivalence ratio ϕ, (b)-(f) volume-averaged heat release rate $\dot{q}$, (c)-(g) maximum temperature T_{max} and (d)-(h) maximum OH mass fraction in the domain $Y_{OH,max}$ predicted by the adiabatic and the CHT simulations, respectively. The equivalence ratio ϕ is decreased by step from $\phi = 0.61$ to 0.59 for (e) the CHT simulation and it is then further reduced to 0.57 for (a) the adiabatic simulation. Indeed, in the CHT simulation, the heat release rate $\dot{q}$ (f) shows larger fluctuations around t = 510 ms, soon after the reduction of ϕ to 0.59, leading to the flame extinction. The adiabatic simulation instead predicts stable $\dot{q}$ (b) for the same equivalence ratio and a further reduction of ϕ to 0.57 is needed to finally extinguish the flame, confirming the delay in flame shape evolution already

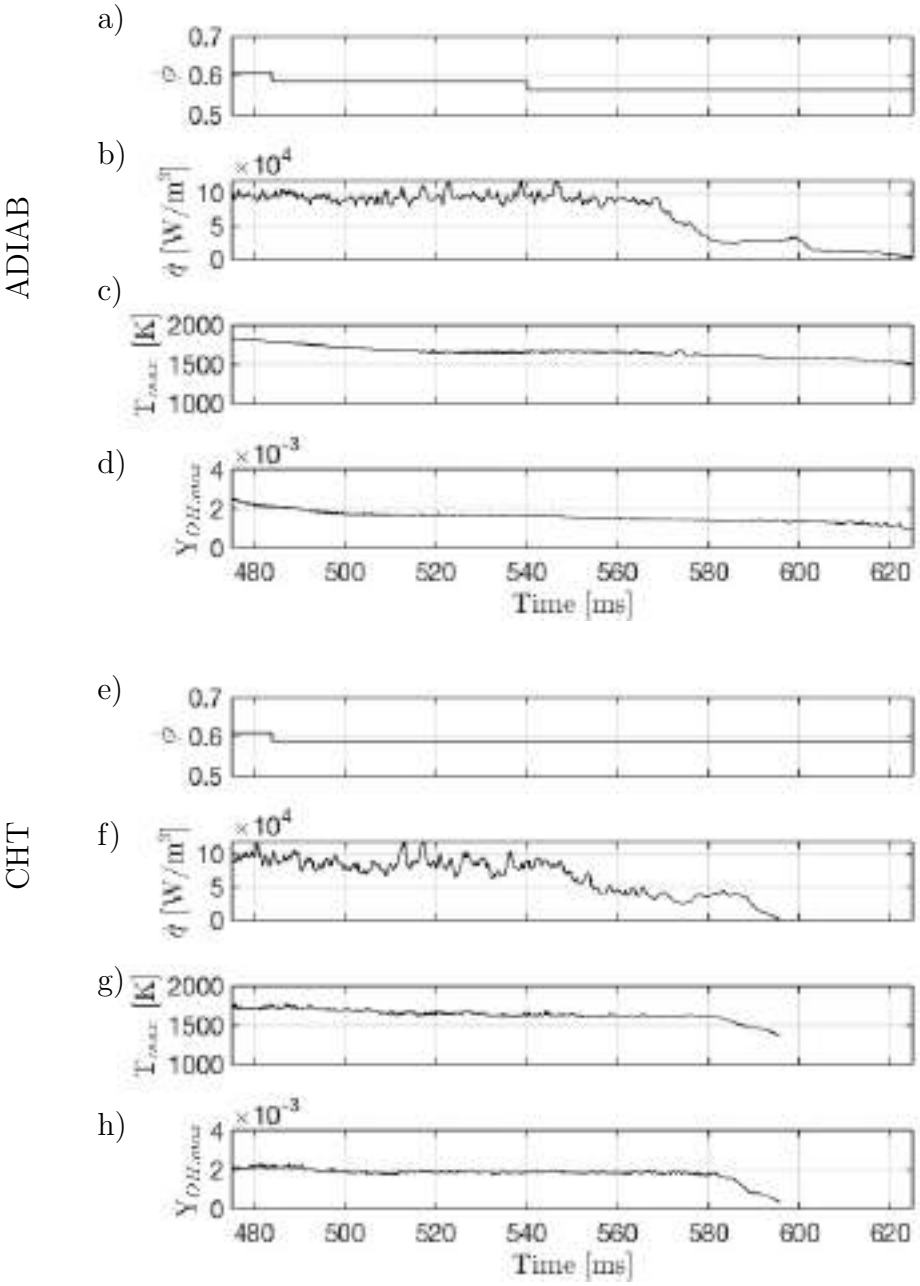

Figure 9.20: Temporal evolution from the adiabatic and the CHT LES simulations of (a)-(e) equivalence ratio ϕ, (b)-(f) heat release rate $\dot{q}$, (c)-(g) maximum temperature $\mathbf{T}_{max}$ and (d)-(h) maximum OH mass fraction in the domain $\mathbf{Y}_{OH,max}$ for configuration *B*.

observed. Temporal evolution of maximum OH mass fraction and maximum temperature show similar decreasing trends for both simulations directly linked to the decrease in ϕ. Therefore, in these particular flow realizations, the adiabatic simulation predicts the final flame extinction for an equivalence ratio $0.57 < \phi_{LBO} < 0.59$ in agreement with the observed experimental value of $\phi = 0.57$

± 0.01 (Table 9.1), while the CHT simulation results in a slightly higher limit at $0.59 < \phi_{LBO} < 0.61$.

Figure 9.21 compares LOS-integrated OH* chemiluminescence images to the instantaneous LOS of $\bar{\dot{q}}$ field predicted by the adiabatic and the CHT simulations for different equivalence ratios close to the LBO event. Two instants are showed at $\phi = 0.61$: the flame is observed to sporadically climb upstream and burn in the CRZ at the injector swirler exit (a) or to be pushed downstream and burn further from the injector exit (b). This phenomenon is visible both in the experimental data and in the numerical simulations, no matter the thermal boundary condition imposed. However, only the CHT results in a lifted flame in good agreement with the experiments, as observed also in Fig. 9.19(b), when the adiabatic simulation predicts a large heat release rate close to the combustion chamber backplane. Further reduction in ϕ up to 0.59 leads to a flame that, in all cases, is no more capable of climbing upstream to burn in the CRZ. This step leads to a complete lift-off of the flame in the experiments (d) that is well stabilized on the top of the injector wall. The same happens for the CHT simulation (d-f) but after a small peak of heat release rate is achieved (g), i.e. t = 547 ms in Fig. 9.20(f), the flame is finally blown out (h). Note that, LBO happens in the experiments only for $\phi = 0.57$ (e-h) just like in the adiabatic simulation. The latter however fails in capturing the flame shape evolution and the flame lift-off also for the leanest mixture (e-g). Flame extinction hence seems to happen in this case in a more sudden way comparatively to the more gradual flame shape evolution observed both in the experiments and the CHT results.

Figure 9.22 presents the axial one-dimensional evolution of the integrated heat release rate $\langle \dot{q} \rangle$ as a function of time (and ϕ) close to the LBO event as predicted by (a) the adiabatic and (b) the CHT simulations [1]. The adiabatic simulation predicts $\langle \dot{q} \rangle$ mainly close to the backplane soon after the reduction of ϕ to 0.57 and just before the flame extinction. Note that before the switch to ϕ = 0.59, larger signal is predicted at the bottom around x = 10 mm, indicating that the flame is strongly stabilized in this region. Note also how the lift-off of the flame happens in a sudden manner soon after the reduction of ϕ to 0.57, as opposed to the gradual increase in flame lift-off observed experimentally, Fig. 9.10. The CHT simulation instead, Fig. 9.22(b), is able to recover the gradual flame shape evolution. At $\phi = 0.61$, the high time resolution allows to pick up the reattachment and detachment of the flame from the injector exit with the heat release rate sporadically present in the CRZ, i.e. the phenomenon observed in

[1] Note that, for each simulation, 150 3D LES fields have been used for the axial integration of the heat release rate, leading to a time resolution of 1 ms.

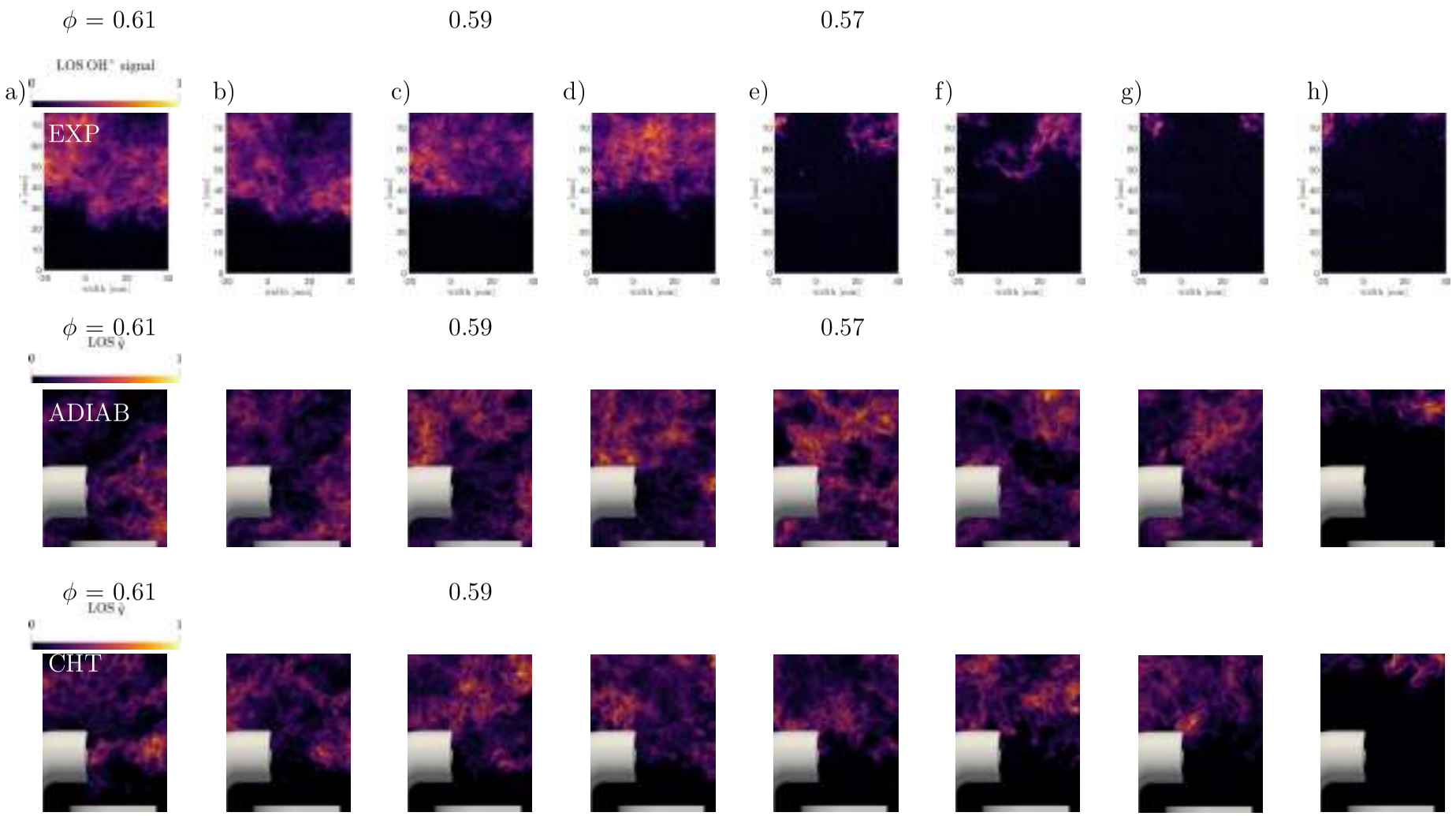

Figure 9.21: Experimentally measured LOS-integrated OH* chemiluminescence image compared to instantaneous LOS heat release rate $\overline{\dot{q}}$ field predicted by the adiabatic and the CHT simulations for different equivalence ratio ϕ. Configuration *B*.

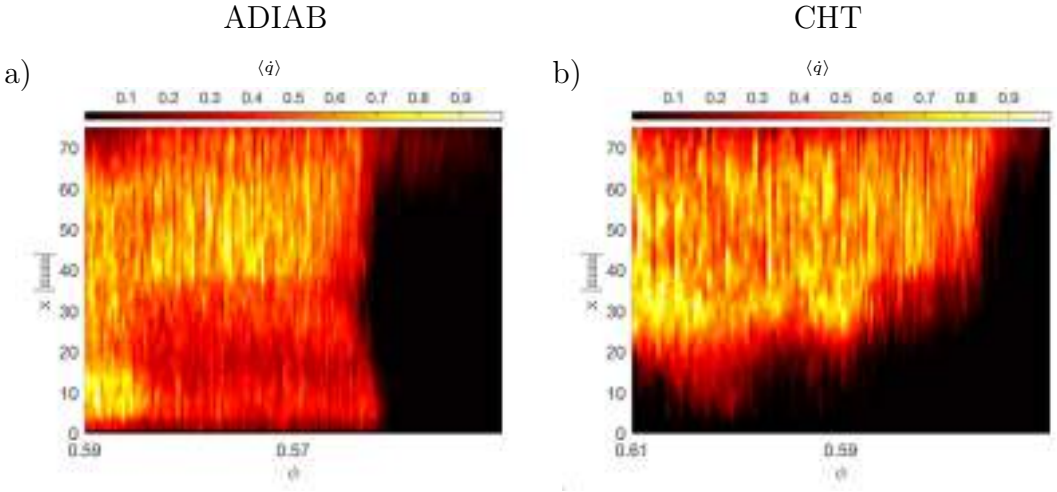

Figure 9.22: Axial one-dimensional evolution of the heat release rate $\langle \dot{q} \rangle$ as a function of the equivalence ratio ϕ predicted by (a) the adiabatic and (b) the CHT simulations. Configuration *B*.

Fig. 9.21(a-b). At lower equivalence ratio values, the flame lift-off is completed and it stabilizes on the top of the injector until the full extinction occurs.

Visualization of the flame shape evolution and blow out as predicted by the adiabatic and the CHT simulations is presented in Fig. 9.23 and Fig. 9.24, respectively. Fields shown correspond to instants (a), (b), (d) and (g) of Fig. 9.21. For each of them, visualization of the flame dynamics is provided by (a-b) 3D isosurfaces of heat release rate $\dot{q}$ at 10% of its maximum value and is colored by temperature T as well as by a cut plane showing (c) the temperature, T, (d) the heat release rate, $\dot{q}$, and (e) the OH mass fraction fields. Both simulations show the phenomenon of successive ignition and extinction of the flame in the CRZ at the injector exit at $\phi = 0.61$ (c-d). However, while CHT predicts well lifted-off flames with a continuous annular flame front, Fig. 9.24(b), the adiabatic simulation presents flame fronts that are merged only along the inner chamber wall, Fig. 9.23(b). As expected, the OH field (e) presents a more diffused distribution in the adiabatic case, as a consequence of the higher temperature in the combustion chamber due to the neglected wall heat transfer. At lower ϕ, the third instant shows more elongated flames and then a continuous annular flame front for the adiabatic simulation when a complete flame lift-off is predicted by the CHT LES. In both cases, the flame is no longer capable of stabilizing in the CRZ created by the injector swirled flow. Finally, last instants correspond to the maximum of heat release rate $\dot{q}$ before flame extinction for a ϕ of 0.57 and 0.59 for the adiabatic and the CHT results, respectively. In the adiabatic case, the flame is still present close to the combustion chamber backplane even tough its surface is further extended downstream. CHT reveals instead a dynamics much closer

Figure 9.23: Adiabatic LES prediction of flame shape evolution and blow out at different equivalence ratios for Configuration *B*. (a-b) Isosurface of heat release rate $\dot{q}$ at 10% of its maximum value colored by temperature T. Cut plane showing (c) the temperature T, (d) the heat release rate $\dot{q}$ and (e) the OH mass fraction fields. Images correspond to instants (a), (b), (d) and (g) of Fig. 9.21.

Configuration	ϕ_{P1}			ϕ_{LBO}		
	EXP	ADIAB	CHT	EXP	ADIAB	CHT
A	0.66	0.61	0.67	0.6	not detected	0.61
B	0.63	0.58	0.61	0.57	0.58	0.6

Table 9.2: Summary of experimentally observed and numerically predicted LBO limits. Uncertainty is ± 0.01 both in experiments and LES.

to the experimental data, with a flame that is stabilized on the top of the injectors before the final LBO event. The experimentally observed and numerically predicted LBO limits for both configurations are summarized in Table 9.2.

9.6 Lean Blow-Out mechanisms

Overall, the observed LBO dynamics is found to be characterized by a gradual flame lift-off and shape evolution until a global flame extinction occurs. While

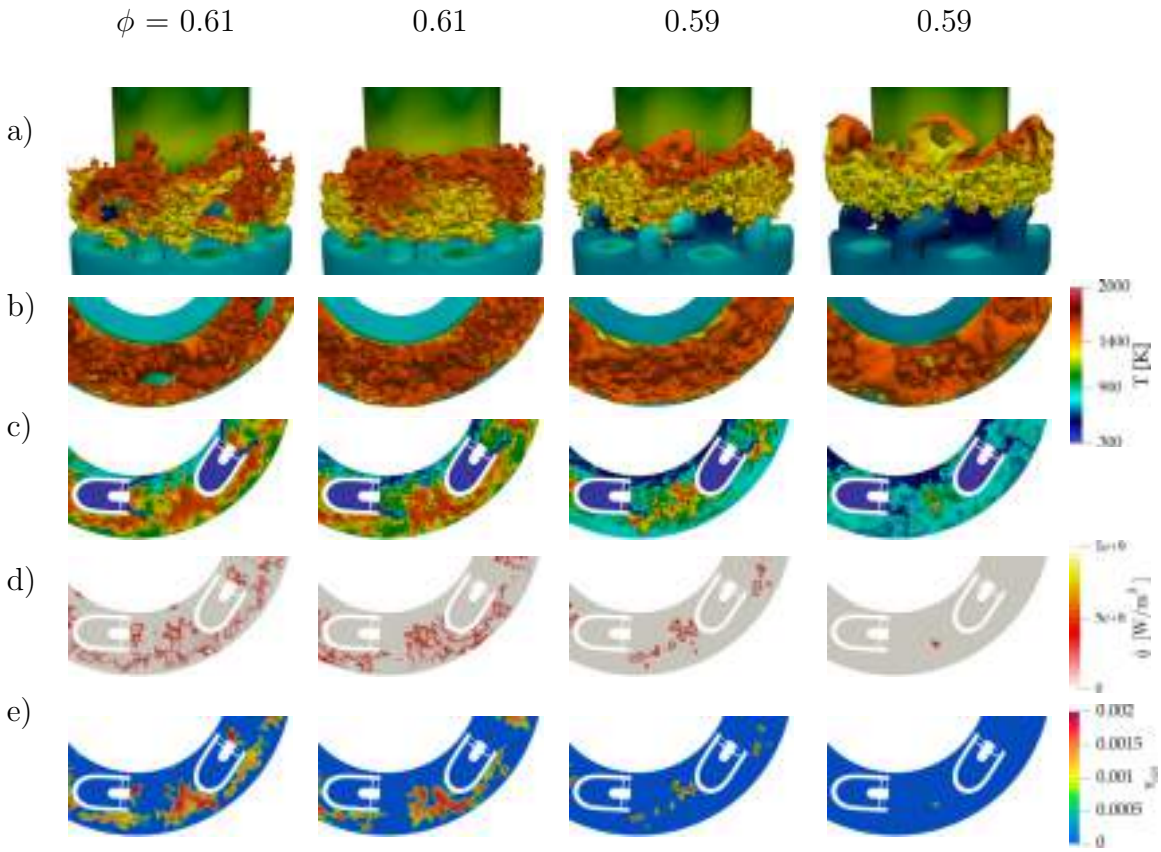

Figure 9.24: CHT LES prediction of flame shape evolution and blow out at different equivalence ratios for Configuration *B*. (a-b) Isosurface of heat release rate $\dot{q}$ at 10% of its maximum value colored by temperature T. Cut plane showing (c) the temperature T, (d) the heat release rate $\dot{q}$ and (e) the OH mass fraction fields. Images correspond to instants (a), (b), (d) and (g) of Fig. 9.21.

two mechanisms can be responsible for the local flame extinction, i.e. stretch and heat loss [38, 315], the flame shape evolution can be linked to the reduction of flame consumption speed due to leaner mixtures, Fig. 9.6(a). In the present work, the flame surface is defined through the isosurface of heat release rate $\dot{q}$ at 10% of its maximum value since the fuel mass flow rate and hence the total $\dot{q}$ are constant. The flame surface is evaluated with a time resolution of 10 ms as the integral of the efficiency function Ξ_Δ over the isosurface of $\dot{q} = 10\%\ \dot{q}_{max}$

$$S_{flame} = \iint_{\dot{q}\ =\ 0.1\ \dot{q}_{max}} \Xi_\Delta\ dA. \tag{9.3}$$

Note that the introduction of the efficiency function Ξ_Δ in the integral is needed to compensate for the reduction of flame surface due to the reduced flame/turbulence interaction when considering the artificially thickened flame model [49, 61].

Due to the reduction in consumption speed, flame surface is expected to increase to burn the same amount of fuel mass flow rate $\dot{m}_{fuel}$ and provide the same

total heat release rate so that,

$$\dot{m}_{fuel} = \rho_f < s_c >_s S_{flame}, \tag{9.4}$$

where $< s_c >_s$ is the average flame consumption speed along the surface [38]. Clearly, if $\dot{m}_{fuel}$ stays constant and ρ_f presents small variations, S_{flame} has to increase to balance the decrease in $< s_c >_s$, explaining the flame shape evolution when considering leaner mixtures. Note that $< s_c >_s$ depends not only on ϕ but also on the fresh gas temperature T_f[1] as well as on the stretch rate κ applied to the flame. The latter is generally defined as the rate of the flame surface variation per unit area and represents the deformation of the flame front caused by the flow field. It can be expressed as,

$$\kappa = \frac{1}{S_{flame}} \frac{dS_{flame}}{dt} = (\delta_{ij} - n_i n_j) \frac{\partial u_i}{\partial x_j} + S_l \frac{\partial n_i}{\partial x_i} = a + \sigma_c \tag{9.5}$$

where δ_{ij} is the Kronecker delta, n is the vector normal to the flame front and S_l is the laminar flame speed. Stretch rate can be hence divided into two contributions, namely the strain rate tangential to the flame front a and the flame curvature σ_c. The last contribution is usually much lower than the strain rate for practical applications involving highly turbulent flows, i.e. Karlovitz number > 0.1, and therefore it can be neglected so that $\kappa \sim a$ [26, 335]. Therefore, it is possible to evaluate the flame strain rate in LES by computing the flow strain rate tensor and by subtracting the component normal to the flame surface. The vector normal to the flame surface is easily identified through the temperature gradient,

$$n = -\frac{\nabla T}{\|\nabla T\|}. \tag{9.6}$$

Note that the so computed flame strain rate corresponds to the resolved part only while the sub-grid contribution is here neglected as a first approximation, the resolved flame strain being assumed as a good indicator of flame stretch rate.

Figure 9.25(a-b) presents the flame surface S_{flame} evolution predicted by (a) the adiabatic and (b) the CHT simulations as a function of ϕ. Both simulations present a progressive increase of the flame surface as the mixture gets leaner. Figure 9.25(c-d) presents the temporal evolution of the mean absolute volume-averaged flame strain rate, $\widetilde{a}$, (blue) and its standard deviation, $\widetilde{a_\sigma}$, (red) as predicted by the adiabatic and the CHT simulations. Note that the flame volume is here arbitrarily identified with the threshold $\dot{q} > 0.01\dot{q}_{max}$. As opposed to the flame surface evolution, both simulations predict a decreasing trend for $\widetilde{a}$ and $\widetilde{a_\sigma}$

[1]Note that CHT-LES is able to capture the pre-heating of the fresh gases due to the warm-up solid [59].

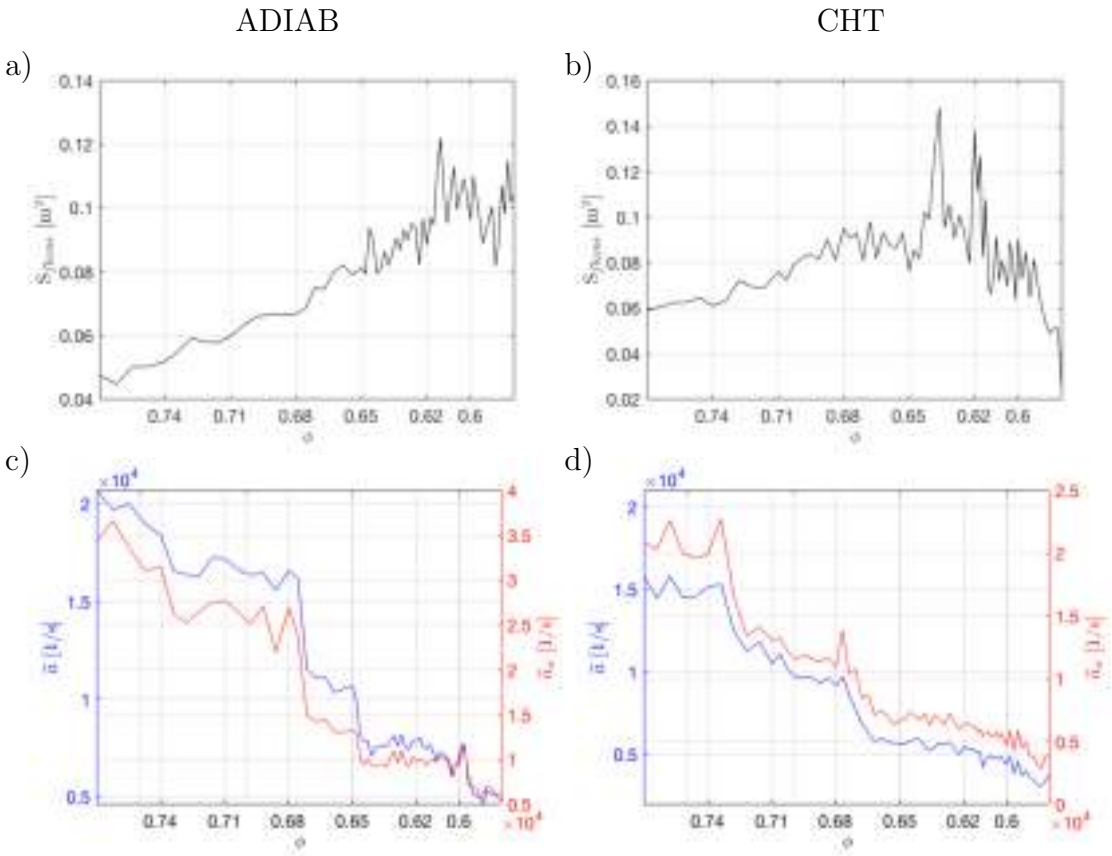

Figure 9.25: Flame surface S_{flame} evolution predicted by (a) the adiabatic and (b) the CHT simulations as a function of the equivalence ratio ϕ. Flame-averaged strain mean $\widetilde{a}$ (blue) and standard deviation $\widetilde{a_\sigma}$ (red) evolutions as predicted by (c) the adiabatic and (d) the CHT simulations. Configuration *A*.

with a large drop at $\phi = 0.68$ and $\phi = 0.71$ followed by a more gradual drop at $\phi = 0.65$ and $\phi = 0.68$ for the adiabatic and the CHT simulations, respectively. This drops in $\widetilde{a}$ suggest that a sudden change in flame stabilization happens at these instants and that, as already observed, this modification is consistently delayed with adiabatic boundary conditions. The evolution of the flame surface and of the mean strain rate explains the flame shape evolution observed both experimentally and numerically. As the lean mixtures get leaner, the flame surface increases to compensate for the reduction in consumption speed. At the same time, the leaner flame cannot withstand anymore the high strain rate and moves in regions where the strain rate is lower, i.e. $\widetilde{a}$ decreases.

Figure 9.26 helps visualizing the temporal evolution of the flame strain distribution presenting (a-b) the normalized points number m/m_{max} as a function of the strain a and the equivalence ratio ϕ, (c)-(e) the isosurface of heat release rate $\dot{q}$ at 10% of its maximum value colored by a at different ϕ and (d)-(f) the

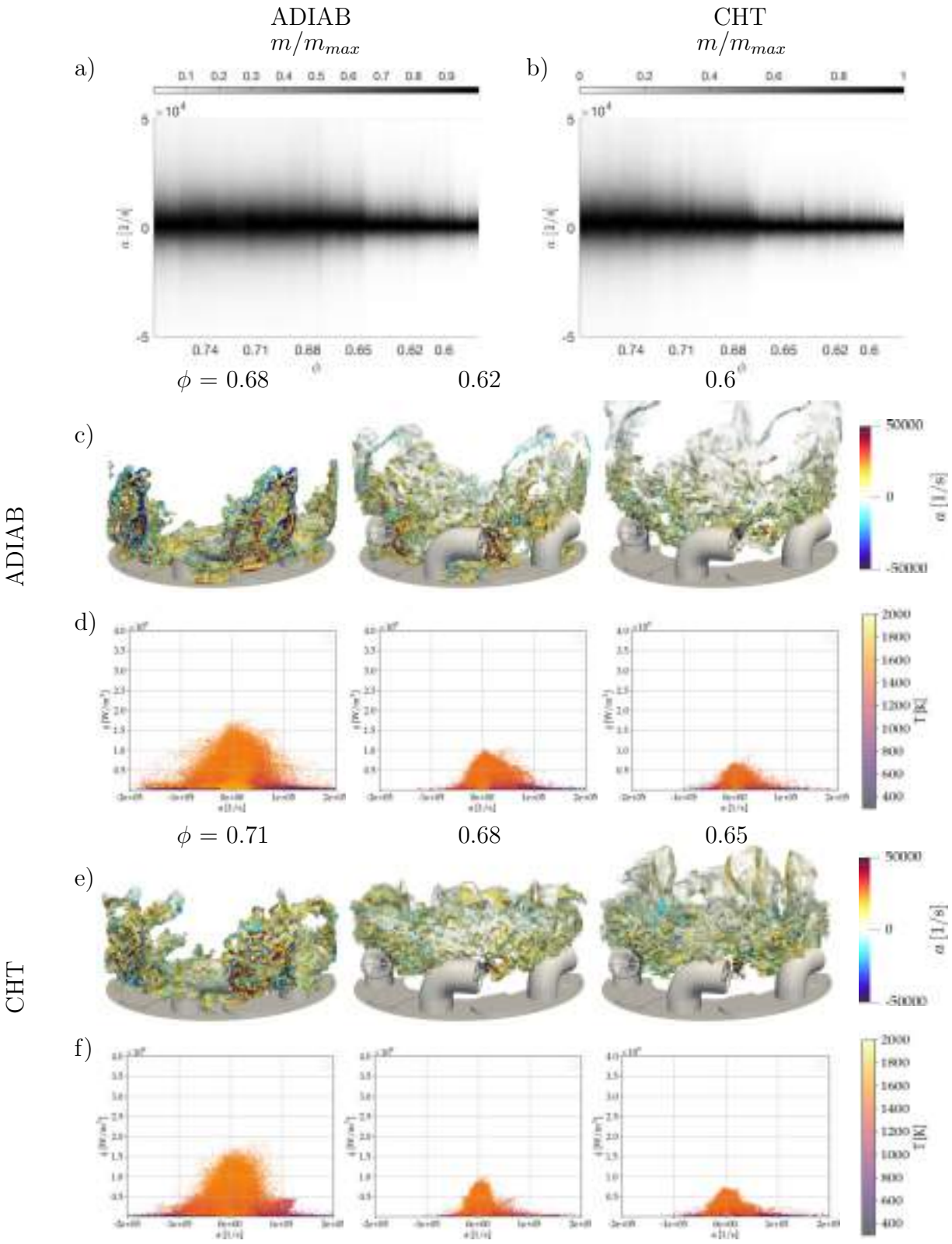

Figure 9.26: Evolution of the flame strain distribution for Configuration *A* predicted by the adiabatic and the CHT simulations. (a-b) Normalized points number m/m_{max} as a function of the strain a and the equivalence ratio ϕ. (c)-(e) Isosurface of heat release rate $\dot{q}$ at 10% of its maximum value colored by a at different ϕ. (d)-(f) Scatter plots for the flame showing $\dot{q}$ as a function of a and colored by T. Solutions correspond to instants in Fig. 9.17 and Fig. 9.18.

corresponding scatter plots for the flame volume showing $\dot{q}$ as a function of a and colored by T. As indicated by $\widetilde{a}$ and $\widetilde{a_\sigma}$ in Fig. 9.25(c-d), the distribution of the strain rate abruptly changes at $\phi = 0.68$ and $\phi = 0.71$ for (a) the adiabatic and (b) the CHT simulations, presenting a distribution of points closer to low strain values. Looking at the isosurface of $\dot{q}$ colored by a (c)-(e) one can notice that the region of large strain rate corresponds to the bottom region of the burner close to the backplane and to the CRZ at the injector exit. Note that the adiabatic simulation (d) predicts larger strain compared to the CHT one (f), these points corresponding to the swirled flow outer shear layer where the M-shape flame is stabilized only when adiabatic conditions are considered, Fig. 9.13. As the flame gets leaner, the flame surface needs to increase elongating the flame, but the latter cannot sustain anymore the large strain rate values at the chamber backplane, i.e. the lift-off process starts at $\phi = 0.68$ and 0.71 in (c-e), respectively. Soon after, the flame cannot withstand the strain rate in the CRZ and tends to stabilize further downstream, causing the small drop in $\widetilde{a}$, Fig. 9.25(c-d), at $\phi = 0.62$ and 0.68 for adiabatic and CHT results, respectively. Note also that, the adiabatic simulation predicts higher strain values which clearly correspond to the outer shear layer region at the swirler exit (c) at $\phi = 0.62$. Finally, as a leaner mixture is considered, the flame surface reaches the maximum value and it stabilizes on the top of the injectors, where it is subject to a minimum strain rate value. The major role played by flame strain suggests also an explanation for the observed delay in flame shape evolution when considering the adiabatic boundary condition. When adiabaticity is imposed and heat losses are not taken into account, flames tend indeed to be more resistant to large values of strain rate and can persist in the same region of large strain values even at lower ϕ compared to the CHT prediction, inducing a delay in the flame shape evolution and in the final LBO event.

To confirm these observations, a closer look to the final LBO event is provided for Configuration B in Fig. 9.27, presenting (a-b) the flame surface S_{flame} evolution and (c-d) the mean flame-averaged strain $\widetilde{a}$ (blue) as well as its standard deviation $\widetilde{a_\sigma}$ (red) evolutions as predicted by the adiabatic and the CHT simulations, respectively[1]. Globally, the same trend is recovered for the flame surface, i.e. it increases until the final drop and the flame extinction. At the same time, $\widetilde{a}$ and $\widetilde{a_\sigma}$ show a progressive reduction but with a particular difference between adiabatic and CHT predictions. The latter shows a gradual reduction of strain rate indicating that the flame is gradually moving toward regions of low

[1]Note that, in this case, a temporal resolution of 1 ms is used.

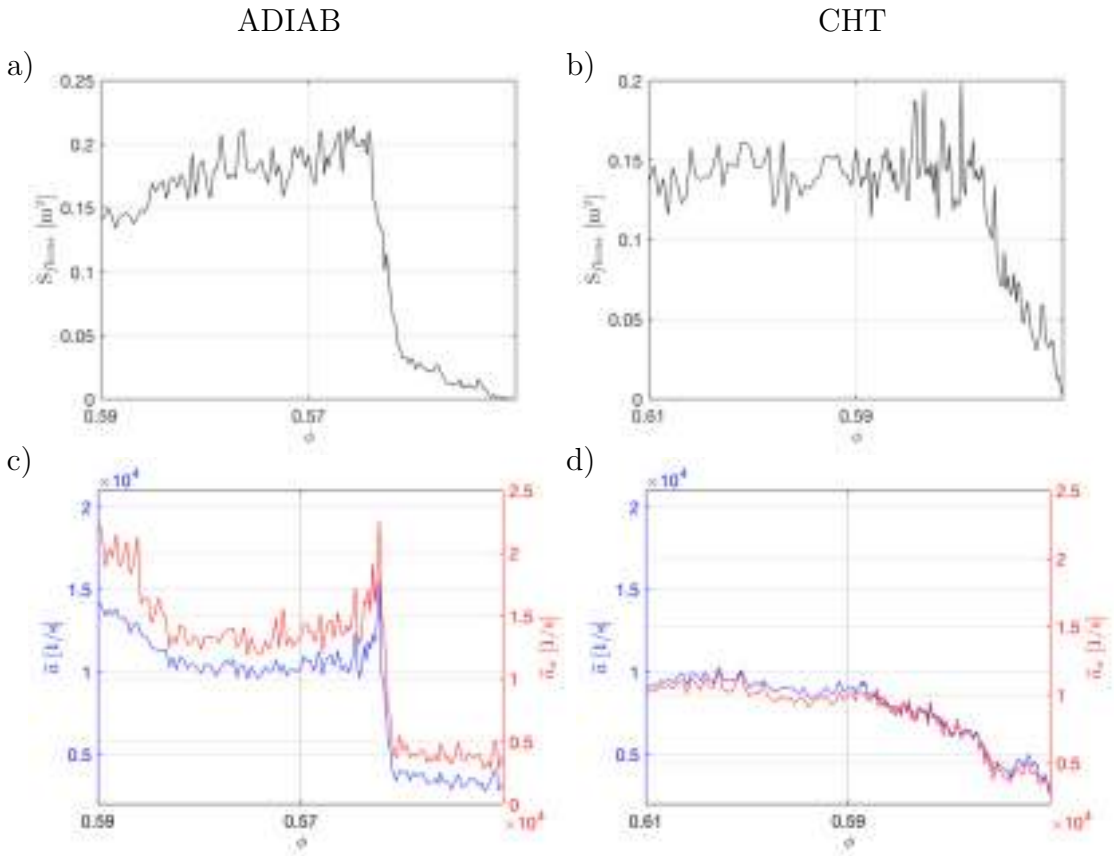

Figure 9.27: Flame surface S_{flame} evolution predicted by (a) the adiabatic and (b) the CHT simulations as a function of the equivalence ratio ϕ. Flame-averaged strain mean $\widetilde{a}$ (blue) and standard deviation $\widetilde{a_\sigma}$ (red) evolutions as predicted by (c) the adiabatic and (d) the CHT simulations. Configuration *B*.

strain rate but it eventually does not succeed in stabilizing itself and finally extinguishes. The adiabatic result instead predicts a peak of strain rate soon after the reduction in ϕ (and increase in air mass flow rate), suggesting that the flame is suddenly subject to large strain values that it cannot withstand and blows out since it is still stabilized close to the injector exit. Note that adiabatic and CHT-LES predict $\widetilde{a}$ in the order of 10^4 for ϕ of 0.59 and 0.61 before flame extinction, respectively. These values are present in Configuration 00 at notably higher ϕ: 0.68 and 0.65, Fig. 9.25, suggesting that the injector orientation plays a major role in the strain rate that the flame has to withstand. In particular, an injector pointed outward as in Configuration *A* causes the flame to be pushed toward the external chamber wall, increasing the average strain rate and eventually leading to early flame shape evolution and anticipated flame extinction, explaining the lower LBO capabilities of this configuration.

Finally, Fig. 9.28 presents the evolution of the flame strain distribution for

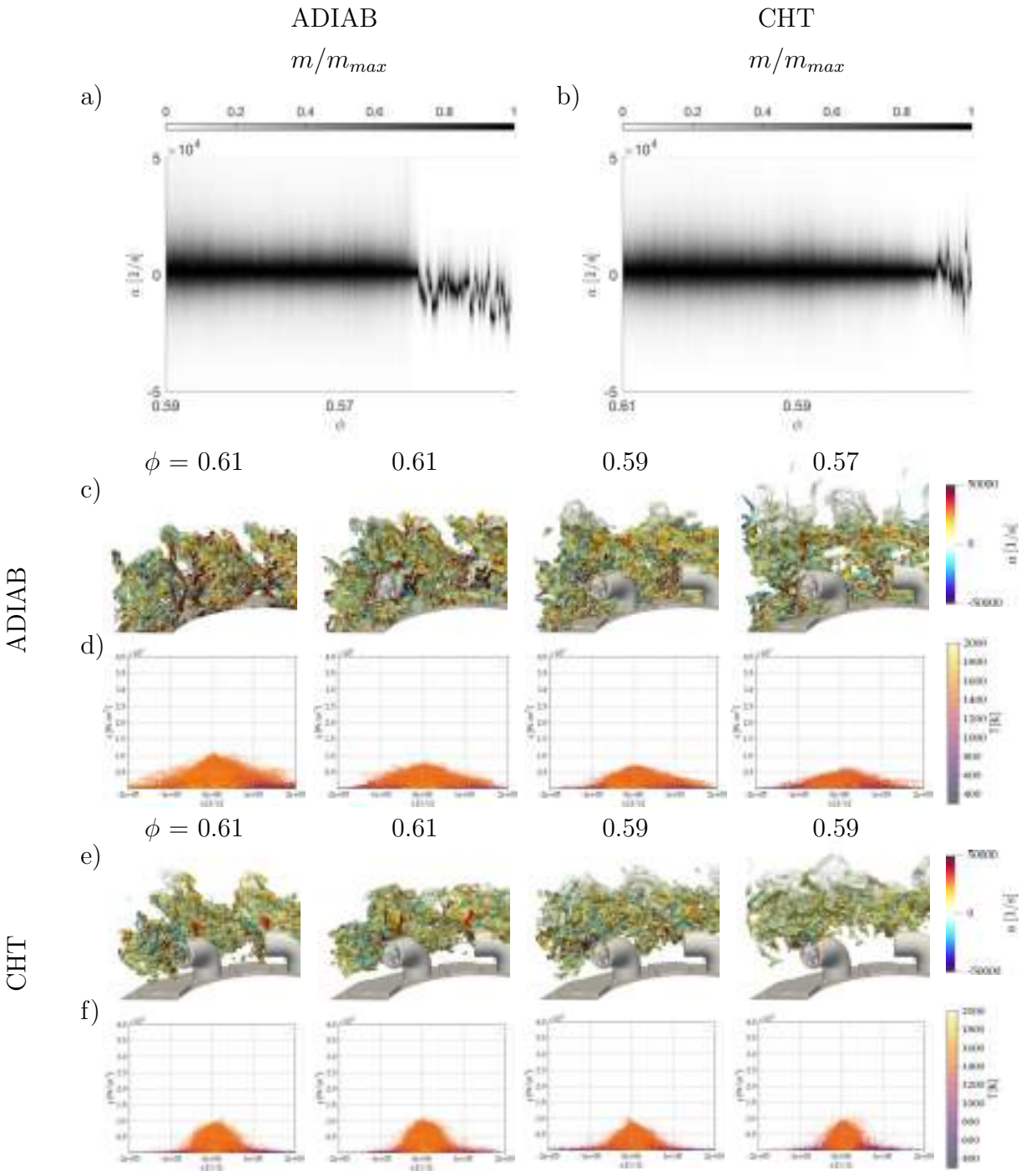

Figure 9.28: Evolution of the flame strain distribution for Configuration *B* predicted by the adiabatic and the CHT simulations. (a-b) Normalized points number m/m_{max} as a function of the strain a and the equivalence ratio ϕ. (c)-(e) Isosurface of heat release rate $\dot{q}$ at 10% of its maximum value colored by a at different ϕ. (d)-(f) Scatter plots for the flame showing $\dot{q}$ as a function of a and colored by T. Solutions correspond to instants in Fig. 9.23 and Fig. 9.24.

Configuration B. In particular, (a-b) show the normalized points number m/m_{max} as a function of the strain a and the equivalence ratio ϕ, (c-e) the isosurface of heat release rate $\dot{q}$ at 10% of its maximum value colored by a at different ϕ and (d-f) the scatter plots for the flame showing $\dot{q}$ as a function of a and colored by T. After the last reduction in ϕ, (a-b) both simulations show a reduction in points subject to high strain, i.e. the leaner flame cannot withstand anymore high levels of strain rate and local extinction occurs until global flame extinction occurs. The isosurfaces of $\dot{q}$ (c-e) confirm this observation, showing increasing regions of local flame extinction as the mixture gets leaner. The reduction of points subject to high strain is also visible from the scatter plots (d-f). Likewise Configuration A, adiabatic results show higher strain rate levels compared to CHT ones, indicating that the flame is capable of withstanding larger stretch, hence delaying the flame shape evolution and the final LBO event.

9.7 Conclusions

The lean blow-out (LBO) dynamics in the Spinning Combustion Technology (SCT) recently developed by Safran Helicopter Engines (SHE) is analyzed. Experimentally, a modified annular combustor that reproduces the main physics behind SCT real engines is operated at NTNU close to LBO conditions. Two configurations are analyzed to get more insights into the impact of the fuel injector orientation on the LBO limits. Starting from stable flame conditions, the air mass flow rate is gradually increased while keeping the fuel mass flow rate constant, significantly affecting the flame stabilization. Numerically, Large Eddy Simulation (LES) of these two configurations is performed. In terms of modeling, an Analytically Reduced Chemistry (ARC) kinetic scheme is employed for describing the CH_4/Air chemical reactions and for proper capturing the effect of strain rate on flame consumption speed. The AVBP LES code is coupled with the AVTP code that solves for heat conduction in the solid in the Conjugate Heat Transfer (CHT) context to provide realistic thermal boundary conditions. Note that, to require feasible HPC resources, an accelerated procedure is used in LES to trigger LBO, i.e. the equivalence ratio is steeply decreased.

In terms of dynamics, as leaner mixtures are considered, the flame gets at first more elongated, then it start to lift-off from the backplane and finally it detaches from the swirler bluff-body and it stabilizes on the top of the injectors in a continuous lifted annular shape before global extinction occurs. Both CHT-LES and adiabatic simulations results are found to globally recover this dynamics, as compared to experimental measured quantities, such as OH* chemiluminescence

images and photomultiplier signals (PMT). However, while CHT LES precisely predicts the LBO limits and the flame shape evolution, adiabatic simulations tend to slightly but consistently underestimate the equivalence ratio at which the flame shape transition and the final extinction occur due to the stronger stabilization of the flame close to the injector walls.

Analysis of the flame surface evolution reveals that, in all cases, the flame surface increases as the mixture gets leaner in order to compensate for the reduction in flame consumption speed. At the same time, the flame resistance to stretch reduces and flame is found to move toward regions where strain rate is lower, i.e. at first the flame lifts off from the backplane and then it goes out from the Central Recirculation Zone (CRZ) at the injector exit. Finally, the flame is completely lifted off and it takes a continuous lifted annular shape, stabilizing in the region of minimum strain rate. A further reduction in ϕ causes at first local flame extinction with the presence of holes in the flame surface and then it leads to complete extinction.

Among the two configurations, the one with the fuel injector oriented outward presents a constantly higher flame strain rate and subsequently lower LBO limits while the other configuration with stronger flame/flame interaction offers higher LBO limits, explaining the SCT increased blow-off capabilities with respect to classical engine designs. In both configurations, CHT-based simulations are found to correctly retrieve the flame dynamics and generally provide better results if compared to adiabatic simulations, suggesting that heat transfer at the wall should be carefully taken into account to achieve high-fidelity prediction of LBO in such complex industrial configurations.

Chapter 10

Design of a SCT industrial burner

Contents

This application Chapter presents the design and the experimental as well as the numerical preliminary characterization of a new SCT industrial burner. For this part of the work LES was used as an industrial design tool at SHE (October 2020) to propose a modification of the NTNU test bench to have a closer correspondence to real helicopter engines. After design and manufacturing, this new combustor was then experimentally and numerically characterized during the secondment performed at NTNU (September 2021) in the framework of the MAGISTER European Project. The burner is showed to be fully operational and to comply with various industrial criteria used to design real combustors at SHE, confirming the maturity of the LES modeling approach to analyze and design novel aeronautical engines. Note that this Chapter presents a qualitative overview of the results that have been accepted for publication in the *Journal of Engineering for Gas Turbines and Power* and presented at *ASME Turbo Expo 2022* [336].

10.1 Industrial requirements and design criteria

The first modification proposed on the NTNU annular bench (i.e. *V1*) and analyzed in Chapter 8 and Chapter 9 already allowed to retrieve some of the physics of SCT real engines and to understand the flame stabilization and dynamics

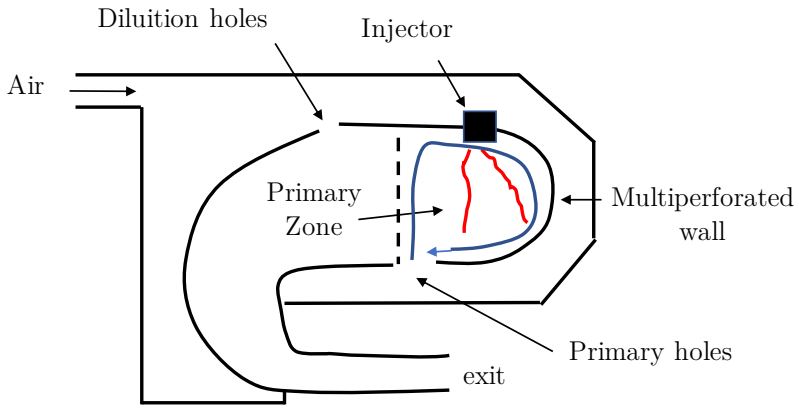

Figure 10.1: Scheme of the flow topology in SHE real helicopter engines.

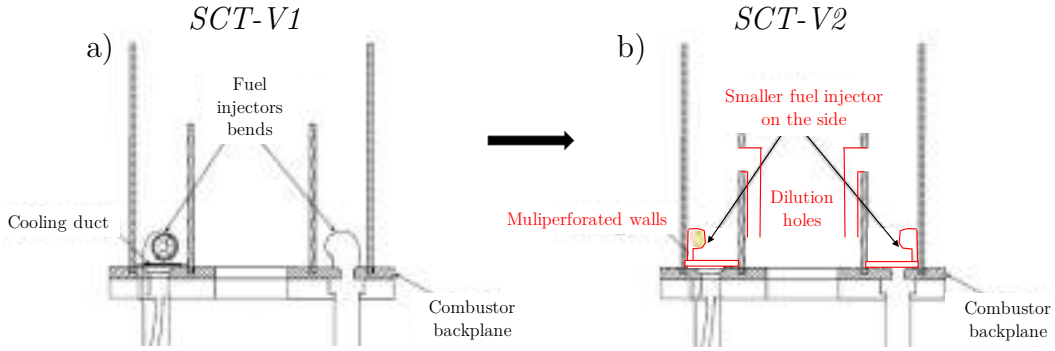

Figure 10.2: Scheme of (a) the NTNU *SCT-V1* and of (b) the proposed modification *SCT-V2* to retrieve flow topology of SHE real engines.

when considering operating conditions close to LBO. This design lies also within most of SHE combustor design rules when it comes to combustor dimensions, inter-injector distance and swirl level. However, when it comes to the exact flow topology of real engines, Fig. 10.1, few criteria are not satisfied and should be fulfilled in the next version, such as the presence of a primary combustion zone, the use of multiperforated wall for cooling and the aerodynamic load as well as the mean combustor velocity. In particular:

- the relative pressure loss of the combustor *SCT-V1* is too low, equal to 2% P_0 while in real engines it is of the order of 3-4%;
- the aerodynamic blockage between the injectors (i.e. injector's exit diameter compared to combustor section) is too large with respect to to real engines;
- the cooling airflow velocity at the combustor backplane is provided by cooling film in *SCT-V1*, while in real engines it is provided by multi-perforation.

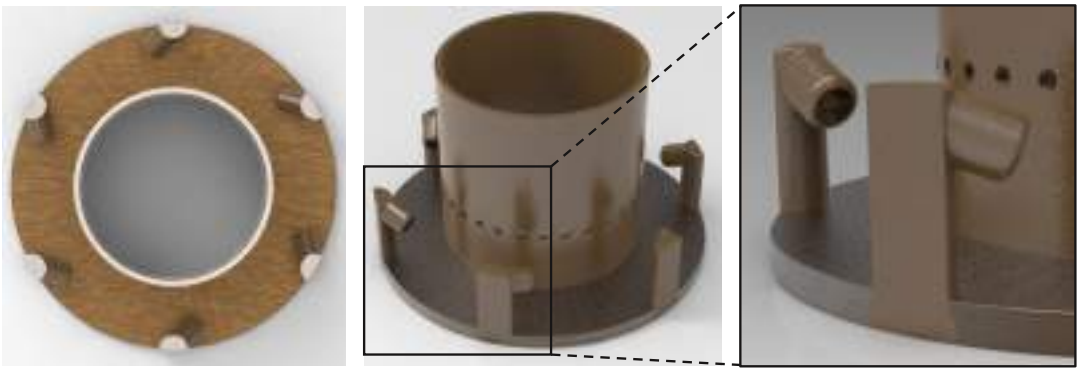

Figure 10.3: Geometric CAD model of the *SCT-V2* proposed modification.

Design point	$\dot{m}_{CH_4}$ [g/s]	ϕ_{inj}	ϕ_{PZ}	$\dot{m}_{air,inj}$ [g/s]	$\dot{m}_{air,PH}$ [g/s]	$\dot{m}_{air,MP}$ [g/s]	P_{th} [kW]
I	1.5	1.2	0.6	21.55	18	9.63	83
II	1.125	1.2	0.6	16.16	13.5	7.22	62
III	0.75	1.2	0.6	10.77	9	4.81	41.5

Table 10.1: Design points for *SCT-V2*.

As depicted in Fig. 10.2 , to retrieve the same flow topology as in SHE engines, the proposed modifications are:

- To reduce the injector diameter and effective area to reduce the aerodynamic blockage and increase the pressure loss;
- To push the injector close to the outer wall to reduce the aerodynamic blockage;
- To introduce effusion cooling through multi-perforation at the combustor backplane;
- To add primary holes downstream the injector to introduce a recirculation zone and close the flame primary zone.

The design point has been chosen to fulfill the SHE design rules for SCT engines in terms of aerodynamic load, mean combustor velocity, pressure loss, multiperforation and primary holes number. Note that, the additional constraints from the annular test rig geometry (e.g. inner and outer diameters) and due to the maximum mass flow rates available at the NTNU laboratory were taken into account during the process. Table 10.1 reports the design point I considered for *SCT-V2*. ϕ_{inj} ϕ_{PZ} refer respectively to the injector and to the primary zone equivalence ratio. The latter is computed considering 2/3 of air coming from the

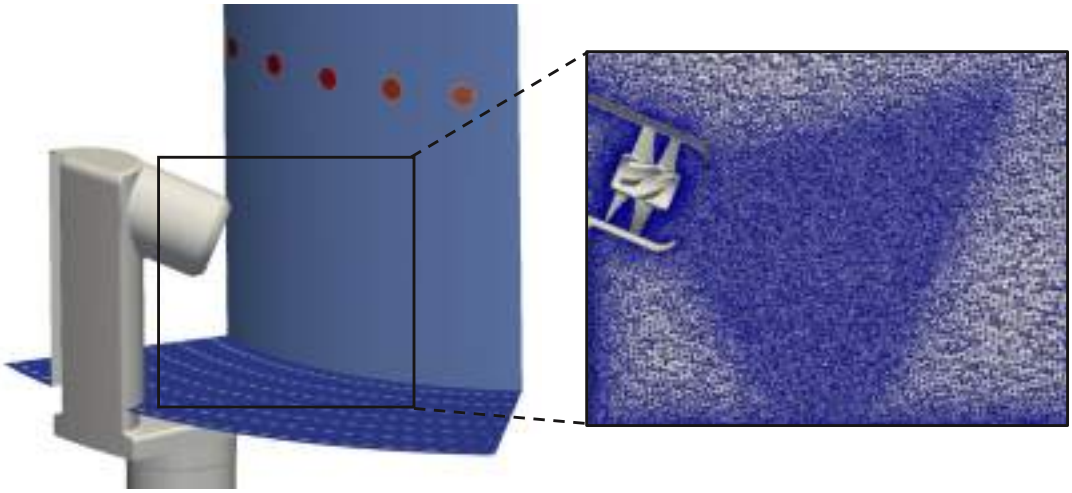

Figure 10.4: Periodical computational domain used in LES with overview of the 15M cells mesh. Note that the atmosphere is taken into account at the end of the combustion chamber (not shown).

primary holes $\dot{m}_{air,PH}$ is participating to the primary zone combustion plus the air from the injector $\dot{m}_{air,inj}$ and from the multiperforated wall $\dot{m}_{air,MP}$. Lower thermal power points II and III were not originally considered for design but have been investigated during the test bench characterization of section 10.3.

The proposed design is presented in Fig. 10.3, showing the geometric CAD model. The injector swirler diameter has been reduced to 13.2 mm and the injector has been pushed to the outer wall to increase the pressure loss and to reduce the aerodynamic blockage, respectively. Injectors are inclined 45 ° toward the backplane and 22.5 ° toward the inner wall while the distance of the injector exit center from the backplane is 30 mm. Note that the injector exit diameter is further reduced at the exit to reproduce real engine injector geometries. At the same time, multiperforated walls are added to the backplane with holes having 0.5 mm diameter and a 60 ° inclination in the direction of the spinning azimuthal flow. Finally primary holes are introduced on the inner wall to form the primary combustion zone and create a recirculation zone as in Fig. 10.1.

10.2 Preliminary simulations and design optimization

Before manufacturing, LES is used to study the flame stabilization and to confirm as well as optimize the design. Indeed, some geometrical parameters have still to be determined and cannot be simply chosen on the base of 1D industrial tools or design criteria. In particular, the injector exit geometry (i.e. exit diameter) and the position as well as the diameter of the primary holes need to be optimized.

The computational domain used in this study is presented in Fig. 10.4. A 60° periodic sector is considered for simulations and the premixed mixture is injected at the tube inlet without considering the plenum. The grid consist of 15M cells and has been refined in the expected flame region. LES is performed using the AVBP code with the modeling used in Chapter 9 when it comes to the LES SIGMA turbulent closure [46], the TTGC numerical scheme [48], the NSCBC boundary conditions [30] and the thickened flame model (DTFLES) [48, 61, 64]. To speed up the computations, CH_4/Air chemistry is modeled through a 2-step kinetic scheme and adiabatic thermal boundary conditions are imposed at the walls. Note that multiperforated wall and primary holes are not meshed but air mass flow rate is directly imposed at these walls by locally modifying the boundary condition. This strategy allows for easily changing the number, position and dimensions of these geometrical features without the need of modifying the CAD and creating a new mesh.

At first, the position (x = 50 mm from the backplane) and the diameter (D_{PH} = 4.1 mm) of the primary holes are fixed while the impact of the exit injector geometry on the flame shape and stabilization is analyzed. Three injector exit geometries diameters are considered, namely the 13.2 mm (without restriction) and the 11.5 mm as well as the 10 mm that present a restriction to mimic real engines geometry. Figure 10.5 presents (a) the injector geometries, (b) the cut-planes showing the normalized time-averaged heat release rate field $\overline{\dot{q}}/\overline{\dot{q}}_{max}$ and (c-d) the isosurfaces of $\overline{\dot{q}}$ at 10% of $\overline{\dot{q}}_{max}$ colored by time-averaged temperature $\overline{T}$. In all cases, Fig. 10.5(b), the flame stabilizes in the Central Recirculation Zone (CRZ) of the injector with heat release rate happening in the outer shear layer, probably due to the adiabatic boundary conditions imposed, as seen in Chapter 9. Note that some heat release rate is visible at the primary holes in all cases as a result of the rich injector conditions. A major difference is seen instead when it comes to heat release rate in the inner shear layer, close to the injector exit center. As the exit diameter is reduced, the flame hardly stabilizes at the injector exit center and assumes a M-shape in the 10 mm case when the pressure loss and the bulk velocities increase. The isosurfaces of $\overline{\dot{q}}$, Fig. 10.5(c-d) show that the flame angle and shape also change. In the case without restriction, the flame angle is larger and the flame reaches the outer wall, potentially inducing high thermal load. The flame assumes a "flower" shape and the six branches can be clearly identified, as seen for *SCT-V1* in Chapter 8. However, as the exit diameter is further reduced to 11.5 and 10 mm, the flames are more compact, their opening angle reduce and the isosurface of $\overline{\dot{q}}$ stabilizes further from the outer wall, potentially reducing the thermal load.

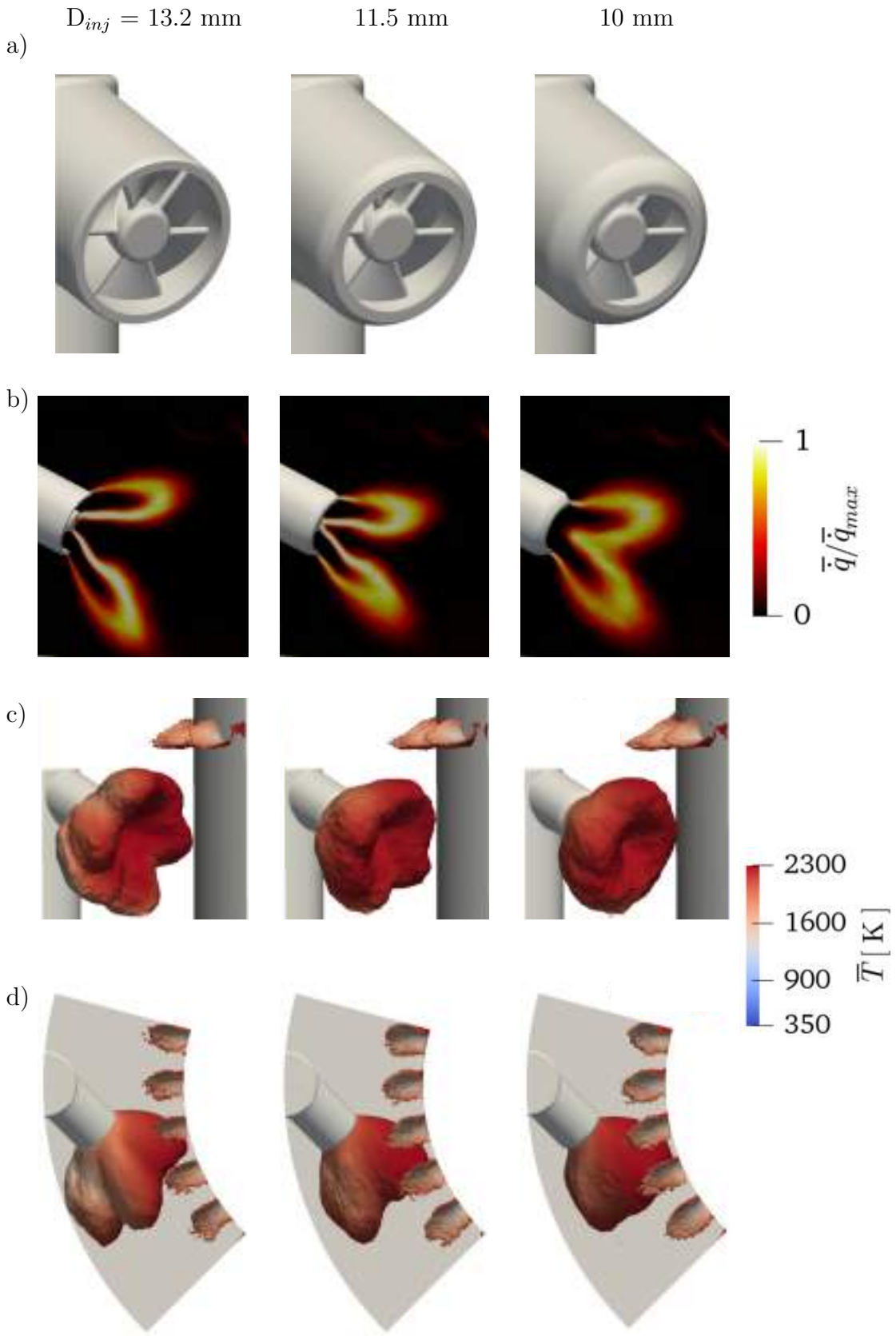

Figure 10.5: Comparison of flame shape stabilization for different injector exit diameters. (a) Injector geometries. (b) Cut-planes showing the normalized time-averaged heat release rate field $\overline{\dot{q}}/\overline{\dot{q}}_{max}$. (c-d) Isosurfaces of $\overline{\dot{q}}$ at 10% of $\overline{\dot{q}}_{max}$ colored by time-averaged temperature $\overline{T}$.

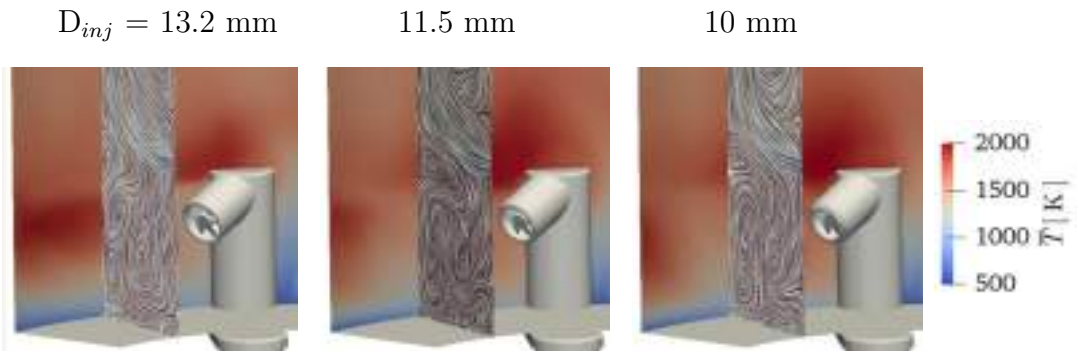

Figure 10.6: Comparison of time-averaged temperature $\overline{T}$ at the outer wall for the different injector exit geometries. Radial cut-planes show the flow topology by means of streamlines computed as line integral convolution of the velocity vector [299].

This observation is confirmed in Fig. 10.6, showing the time-averaged temperature $\overline{T}$ at the outer wall for the different injector exit geometries. As expected, outer wall temperature is lower as the injector exit diameter reduces and the flame stabilizes further from the wall. Radial cut-planes show also the flow topology by means of streamlines computed as line integral convolution of the velocity vector [299]. The injector recirculation zone is more important in the case without restriction and in the 11.5 mm case compared to the 10 mm one, explaining the difference in flame stabilization at the injector exit center. Therefore, the 11.5 mm case seems to be the better tradeoff since the flame is sufficiently compact to stabilize further from the outer wall and, at the same time, the injector CRZ is sufficiently strong to let the flame stabilize close to the injector exit center. Note however that, no matters the injector diameter, a high temperature region is visible over the injector, potentially inducing high thermal load on the outer wall.

To check if primary holes play a role in the observed spot of high temperature, Fig. 10.7 compares the flame shape and stabilization for different height from the backplane of the primary holes, namely x_{PH} = 50 mm and 40 mm. In particular, it presents (a) the isosurfaces of $\overline{\dot{q}}$ at 10% of $\overline{\dot{q}}_{max}$ colored by time-averaged temperature $\overline{T}$ and the cut-planes showing (b) the normalized time-averaged temperature $\overline{T}$ as well as (c) the flow topology by means of line integral convolution of the velocity vector. Flame shape and stabilization is very similar for both cases, Fig. 10.7(a), but, in the x_{PH} = 40 mm case, the heat release rate at the primary holes is interacting with the flame stabilized in the CRZ. A hole is also visible in the isosurface of $\overline{\dot{q}}$ close to the injector exit, likely due to the flow coming from the primary hole just on the top of the injector. This observation

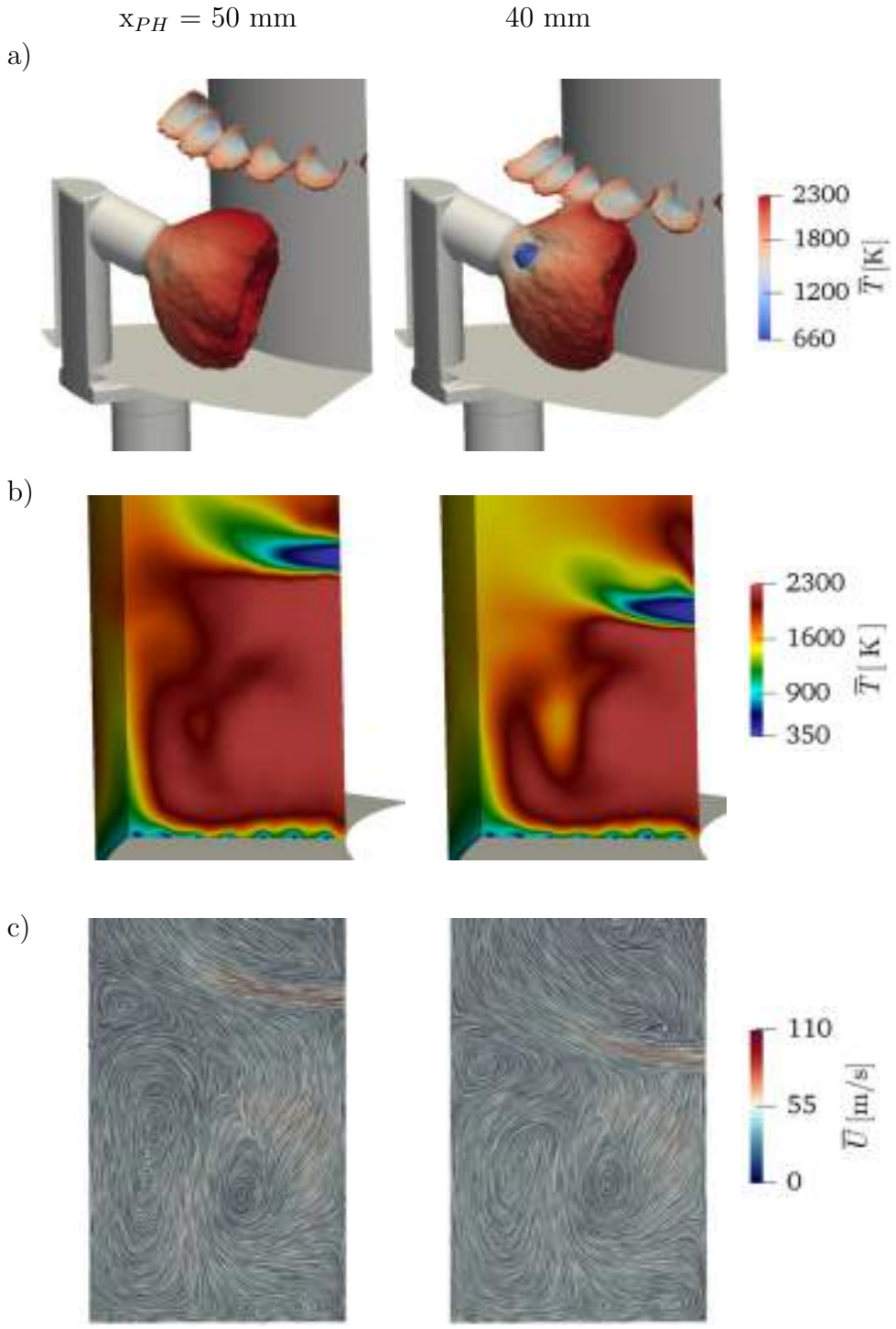

Figure 10.7: Comparison of flame shape and stabilization for different height from the backplane of the primary holes. (a) Isosurfaces of $\overline{\dot{q}}$ at 10% of $\overline{\dot{q}}_{max}$ colored by time-averaged temperature $\overline{T}$. Cut-planes showing (b) the normalized time-averaged temperature $\overline{T}$ and (c) the flow topology by means of line integral convolution of the velocity vector.

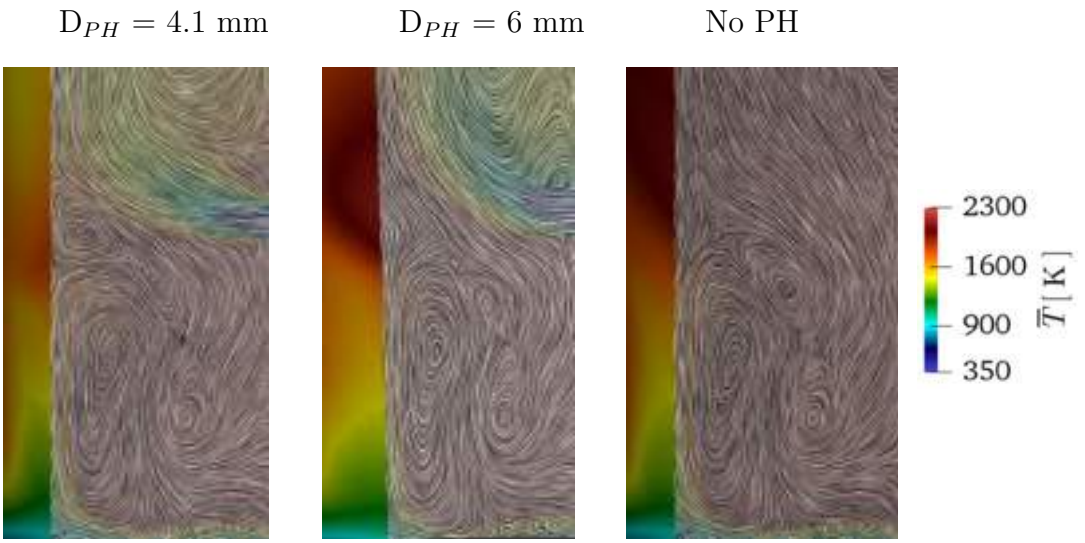

Figure 10.8: Effect of jet penetration on the time-averaged temperature $\overline{T}$ at the outer wall and on the flow topology on radial cut-planes.

is confirmed by looking at the time-averaged temperature $\overline{T}$ field, Fig. 10.7(b). The recirculation zone created by the primary holes in the 40 mm case is able to better cool down the outer wall with respect to the 50 mm case case. Moreover, the 40 mm case results in a more uniform temperature field both on the outer wall and toward the exit of the combustor (not shown)[1]. However, part of the flow is pushed down by the external recirculation zone, causing the hole in the time-averaged flame surface. More details on the flow topology are recovered from Fig. 10.7(c). In both cases, the primary holes create external recirculation zone on the top of the CRZ created by the injector and the injected flow close the primary zone of the combustor. In the 40 mm case however, the primary zone is smaller and the velocity field is pushed toward the backplane as observed. Therefore, the perfect tradeoff would be to have an intermediate distance from the backplane, x_{PH} = 45 mm, to reduce the temperature at the outer wall and to limit the interaction between the primary holes flow and the flame surface stabilized at the injector CRZ.

The effect of jet penetration on the time-averaged temperature $\overline{T}$ at the outer wall and on the flow topology on radial cut-planes is illustrated in Fig. 10.8 for D_{PH} of 4.1 mm and 6 mm and for the case without primary holes. Flame shape is essential the same in all cases, confirming that in the x_{PH} = 50 mm case there is no large interaction of the primary holes with the flame as confirmed by the

[1]Note that the temperature field at the exit of the combustion chamber is a critical parameter for the design of real engines since it affects the thermal load on the downstream turbine. For that reason, a more uniform temperature field represents an improved design.

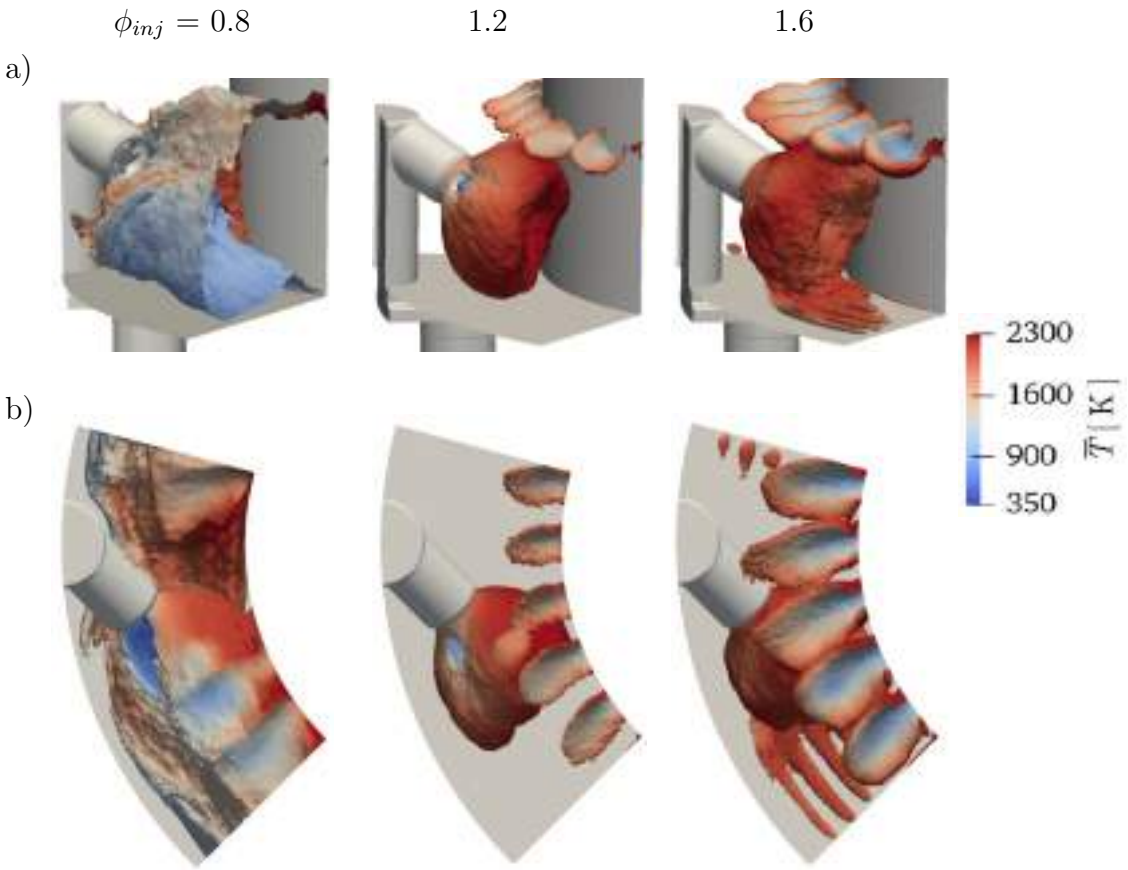

Figure 10.9: Effect of injector equivalence ratio on flame shape. Isosurfaces of $\overline{\dot{q}}$ at 10% of $\overline{\dot{q}}_{max}$ colored by time-averaged temperature $\overline{T}$

lenght of the different recirculation zones. Note that the recirculation zone at the top is no longer visible if the primary holes are not present. In the 6 mm case, the primary holes jet penetration is much less (at constant mass flow rate to respect design point I, Tab.10.1) and, as a consequence, the outer wall temperature is higher. Therefore, a diameter of 4.1 mm seems to be a good tradeoff for the considered design point.

Finally, the effect of the operating conditions on the flame shape and stabilization is presented in Fig. 10.9, showing the isosurfaces of $\overline{\dot{q}}$ at 10% of $\overline{\dot{q}}_{max}$ colored by time-averaged temperature $\overline{T}$ for an injector equivalence ratio of 0.8, 1.2 and 1.6. As it happens in real engines combustor, when increasing the equivalence ratio of the injector (having constant the air mass flow rate), the flame starts to stabilize at the primary holes and along the multiperforated wall. At the same time, when reducing the equivalence ratio of the injector, the flame moves out from the injector CRZ and stabilizes in the region between the injector, the primary holes and the multiperforated wall. Note that, as opposed to what happens in *SCT-V1* close to LBO conditions (Chapter 9), the flame does not leave the

primary zone that results to be strongly closed by the primary holes that create a recirculation zone as in real combustors, Fig. 10.1.

As a results of these preliminary simulations, the design of the *SCT-V2* has been optimized and all the geometrical parameters have been determined. In particular, for the injector exit geometry, a diameter of 11.5 mm results to be a good tradeoff to have good flame stabilization and low temperature on the outer wall due to the more compact flame. When it comes to the primary holes, a diameter of 4.1 mm has showed a good jet penetration if compared to 6 mm case whose penetration is insufficient to close the primary zone and cool down the outer wall. The optimal height of the primary holes is in between the two cases analyzed here (i.e. 45 mm) since, the lower the distance from the backplane, the more the primary holes interact with the flame and cool down the outer wall. The following discussion with NTNU research group and with the manufacturing company confirmed the feasibility of the proposed modification, the only difference being the diameter of the holes for the multiperforated walls. The latter was increased from 0.5 to 1 mm to avoid issues in the manufacturing process. While in real engines this would cause an increase in the air mass flow rate through the multiperforation since the pressure loss is fixed for all the combustion chamber, in the NTNU case, the mass flow rate can be regulated separately for the injector, the primary holes and the multiperforated walls. As a consequence, the design point air mass flow rate can still be injected through the multiperforation with however lower pressure drop and resulting velocity, marginally impacting the flow topology.

10.3 Test bench characterization

After design and manufacturing, the *SCT-V2* burner has been experimentally and numerically characterized during the secondment performed at NTNU (September 2021) in the framework of the MAGISTER European Project. Note that, during this secondment, experiments are lead by the PhD candidate Yi Hao Kwah (NTNU) with the support of the author and viceversa for LES. Objective of this characterization are as follows:

- Stability map: to determine of the stability map of the burner in terms of ignition and LBO limits;
- Operability: to study the LBO dynamics and the light-around as well as the ignition processes;

a)

b)

Figure 10.10: (a) Picture of the *SCT-V2* combustor and (b) instantaneous flame image [336].

- Staged combustion: to investigate the possibility to improve the LBO and ignition limits by changing the distribution of fuel among the injectors. Having richer injectors and leaner ones can improve the operability? [1].

To determine the stability map of the burner, the ratio among the different air mass flow rates is kept constants as in real engines the air distribution is controlled by the pressure loss only and cannot be change during operation. To change the operating point, the total air mass flow rate can be modified as for design points II and III in Table 10.1. For each point, the thermal power can be changed by modifying the fuel mass flow rate.

In the following, the experimental and numerical setup are presented in section 10.3.1. The effect of the injector equivalence ratio on the flame shape and

[1]Note that in real engines some injectors are operated at richer conditions with respect to other to improve operability. The idea here is to investigate this process and get more insights into this phenomenon.

a) b)

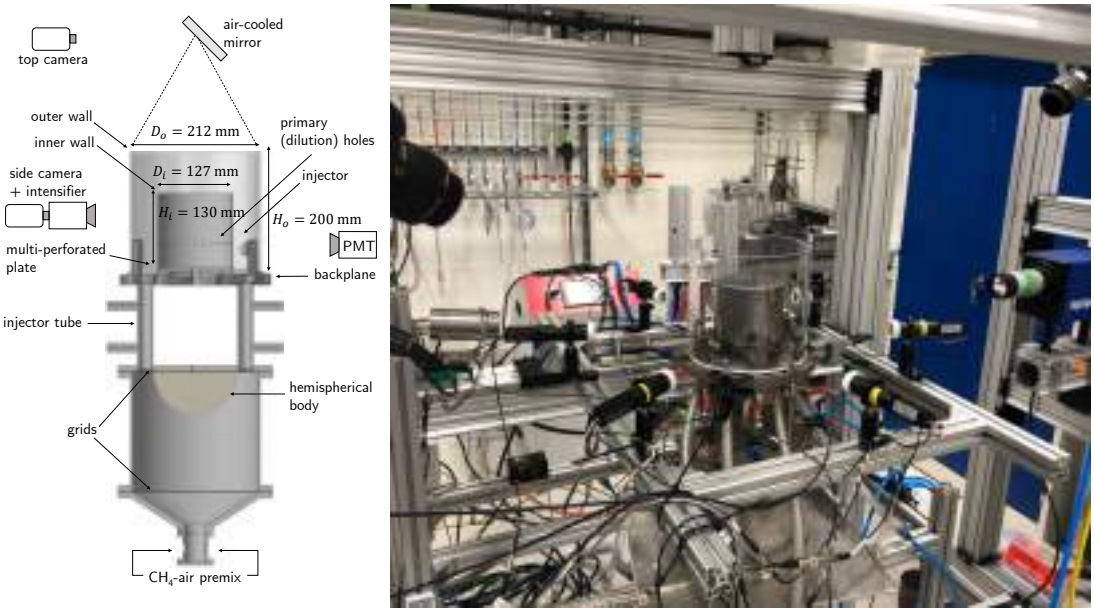

Figure 10.11: ((a) Scheme of the burner with the relevant diagnostics [336] and (b) picture of the experimental setup.

stabilization is discussed in section 10.3.2. Finally, the ignition process and the LBO dynamics are qualitatively presented in section 10.3.3.

10.3.1 Experimental and numerical setup

Figure 10.10 presents (a) the picture of the manufactured *SCT-V2* combustor and (b) an instantaneous flame image [336]. Note that the outer wall is made by a large quartz window to allow for using optical diagnostics.

A schematic of the burner with the relevant diagnostics is provided in Fig. 10.11 together with a picture of the experimental setup. The diagnostics used in Chapters 8 and 9. In particular, one photomultiplier (PMT) for each flame is used for recording OH* chemiluminescence 1D signals. A high-speed Phantom V2012 camera provides visualization of the flames from the top via an air-cooled mirror. OH* chemiluminscence side images are recorded by a second high-speed camera equipped with a LaVision High-Speed Intensified Relay Optics unit and a UV filter (centred at 310±10 nm). In addition, measurements of the temperature on the internal wall are provided by a pyrometer while temperature on the external part of the backplane and at the outer wall are measured through two thermocouples. Ignition procedure is similar to what is performed in the MICCA combustor [337] and it is performed via an electrode connected to a Danfoss EB14 transformer located 10 mm downstream of the injector. Sparks are produced continuously

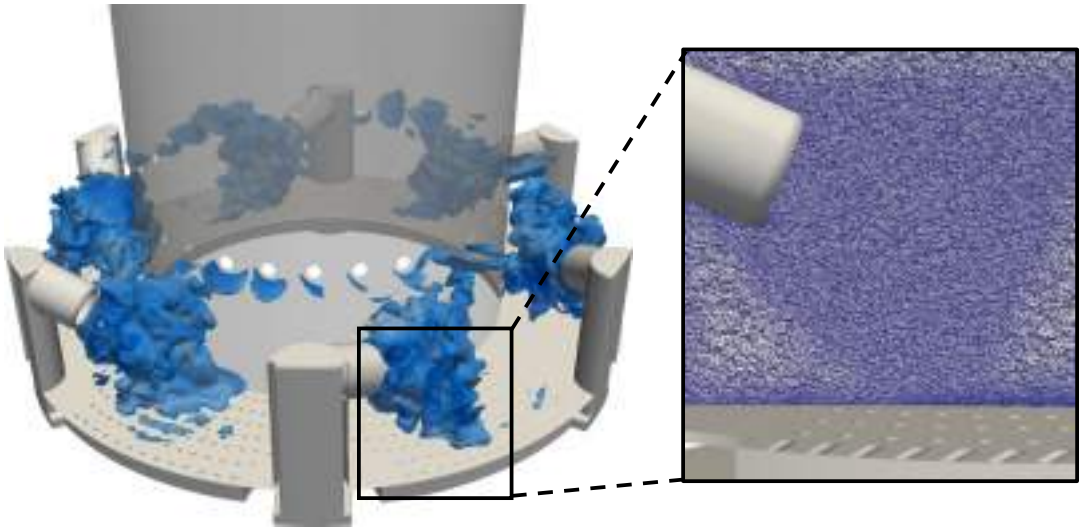

Figure 10.12: LES computational domain with zoom on the mesh at the multiperforated wall. Isosurfaces of instantaneous heat release rate $\dot{q}$ is also shown.

every 20 ms with an energy of 50mJ that is is two order of magnitude larger than the minimum ignition energy (i.e. 0.6mJ) for CH_4 at $\phi = 0.7$ [336, 338].

LES is performed with the modeling presented in section 10.2. Experimentally measured temperature at the internal and outer walls as well as the backplane are imposed in LES with a suitable thermal resistance, as depicted in Chapter 4. The LES computational domain is presented in Fig. 10.12. The grid comprises the full annular combustor and is composed by 96M cells, i.e. 16M cells for each sector. Note that, this time, the primary holes and the multiperforated plate are discretized since the geometry is already optimized. At least 6 cells are placed in the multiperforation holes to allow for a reasonable resolution of the injection velocity profiles.

10.3.2 Flame shape and stabilization

The effect of the injector equivalence ratio on the flame shape and stabilization is at first discussed. Figure 10.13 presents (a-c) the experimentally measured time-averaged LOS-integrated OH* chemiluminescence images compared to (b-d) the predicted time-averaged LOS heat release rate $\overline{\dot{q}}$ for design points I and III (Table 10.1) and injector equivalence ratio of $\phi = 1.6$ and $\phi = 1.25$. For low equivalence ratio, the visual from the top of the flames both in (a) experiments and (b) LES reveal that flames stabilize close to the injector exits and do not strongly interact. At higher equivalence ratio instead, flames stabilize further

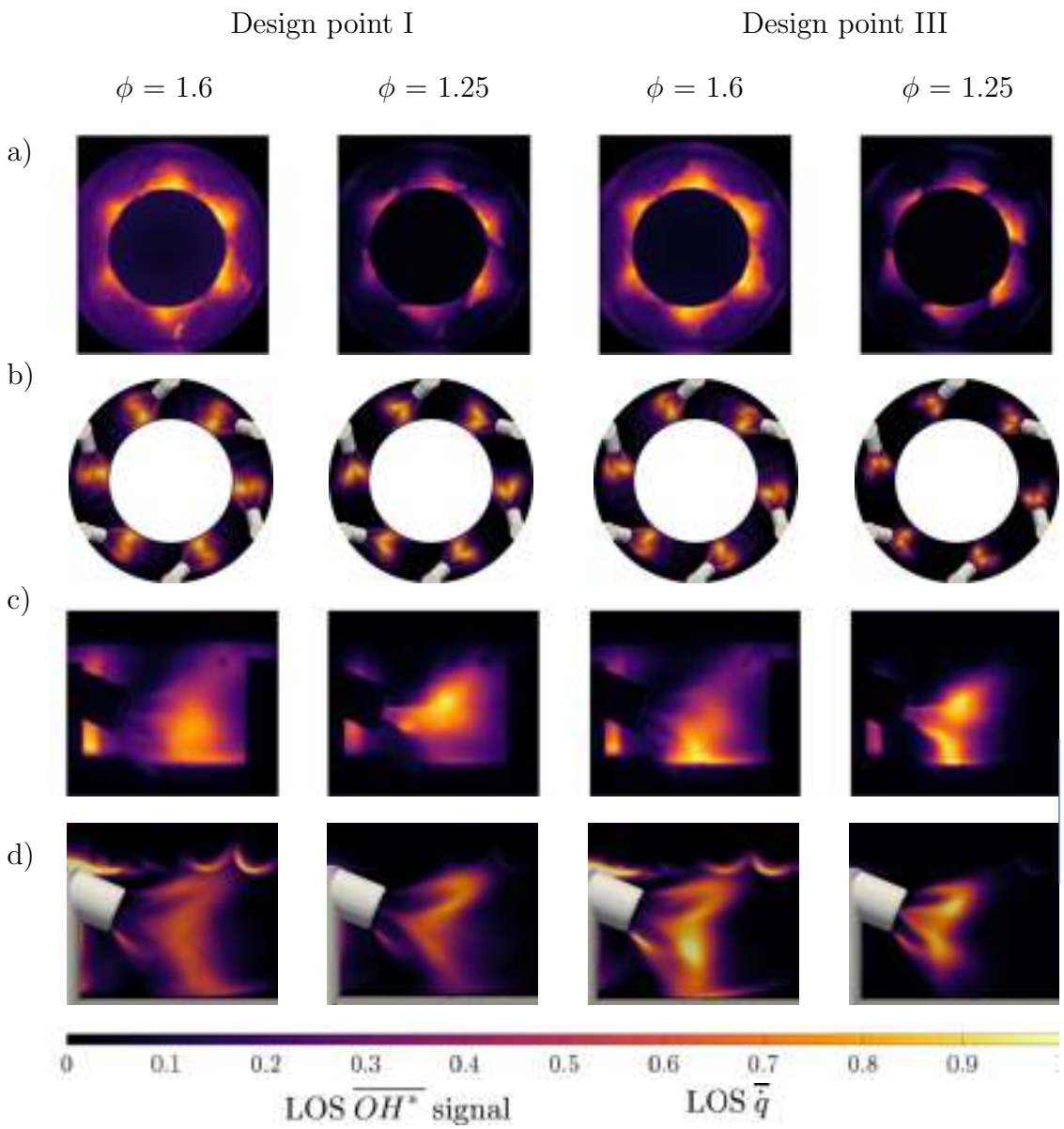

Figure 10.13: (a-c) Experimentally measured time-averaged LOS-integrated OH* chemiluminescence images compared to (b-d) predicted time-averaged LOS heat release rate $\overline{\dot{q}}$ for design points I and III and injector equivalence ratio of $\phi = 1.6$ and $\phi = 1.25$.

from the injectors and one can hardly detect the separation between the different flames that hence take on a continuous annular shape. This observations are confirmed by looking at (c) the side OH* images. For both design points, as the equivalence ratio gets richer, the flame stabilizes downstream of the injector and heat release rate is present also at the primary holes and at the backplane, i.e. the flame is looking for air and stabilizes in leaner regions. Note that, for design point III, the interaction with the backplane is stronger and it is likely due to the reduced air mass flow rate and hence velocity injection through the multiperforated plate. As the equivalence ratio becomes leaner instead, flames

stabilize close to the injector exit in the CRZ and the interaction with air coming from the backplane and the primary holes is less important. Note that, also for these leaner condition, the flame is more compact and tends to stabilize closer to the backplane for design point III compared to design point I, where the heat release rate is more widened. (d) LES correctly captures the flame shape evolution and the different stabilization according to the change in equivalence ratio, predicting the interaction with the multiperforated plate as well as the primary holes for the richest conditions while showing also the stabilization of the flame in the injector CRZ for $\phi = 1.25$. Note that this peculiar behavior is typical of real helicopter engines. The latter usually operate at local rich conditions close to the injector for increasing operability capabilities and then dilution air is introduced to reduce the hot gases temperature and the pollutant emissions, such as NOx.

The different flame shape and stabilization is better shown in Fig. 10.14, presenting isosurfaces of computed time-averaged heat release rate $\overline{\dot{q}}$ at 10% of its maximum value colored by temperature $\overline{T}$ for the same conditions as Fig. 10.13. At $\phi = 1.6$, as the total air mass flow rate reduces (i.e. passing from design point I to design point III) flames become more compact and interact more with the air coming from the multiperforated plate, due to the reduced pressure loss. When reducing the equivalence ratio to 1.25, flames are well stabilized in the CRZ of the injector and weak heat release rate is present at the primary holes and at the backplane. Note that, the flames being more compact, the flame isosurfaces are well distinct, as observed also in Fig. 10.13. Note also that a hole in the $\overline{\dot{q}}$ isosurfaces is visible close to the injector exit in all conditions, especially for the low thermal power ones. This is likely due to the air injection coming from the primary hole on the top of the injector, as noticed also in Fig. 10.7.

10.3.3 Operability: LBO and ignition dynamics

When it comes to the combustor operability, three configurations have been tested. Figure 10.15 presents the schemes of the (a) unstaged and (b-c) staged configurations. While in the unstaged "classical" configuration, all the injectors are fed with the same fuel mass flow rate, in the staged configurations three injectors are fed differently with respect to the others in an attempt to increase the global LBO and ignition limits. In particular, injectors with the same color have the same fuel mass flow rate.

To obtain the ignition limits, for each design point, the injector equivalence ratio is gradually increased until the combustor successfully ignites. For the LBO

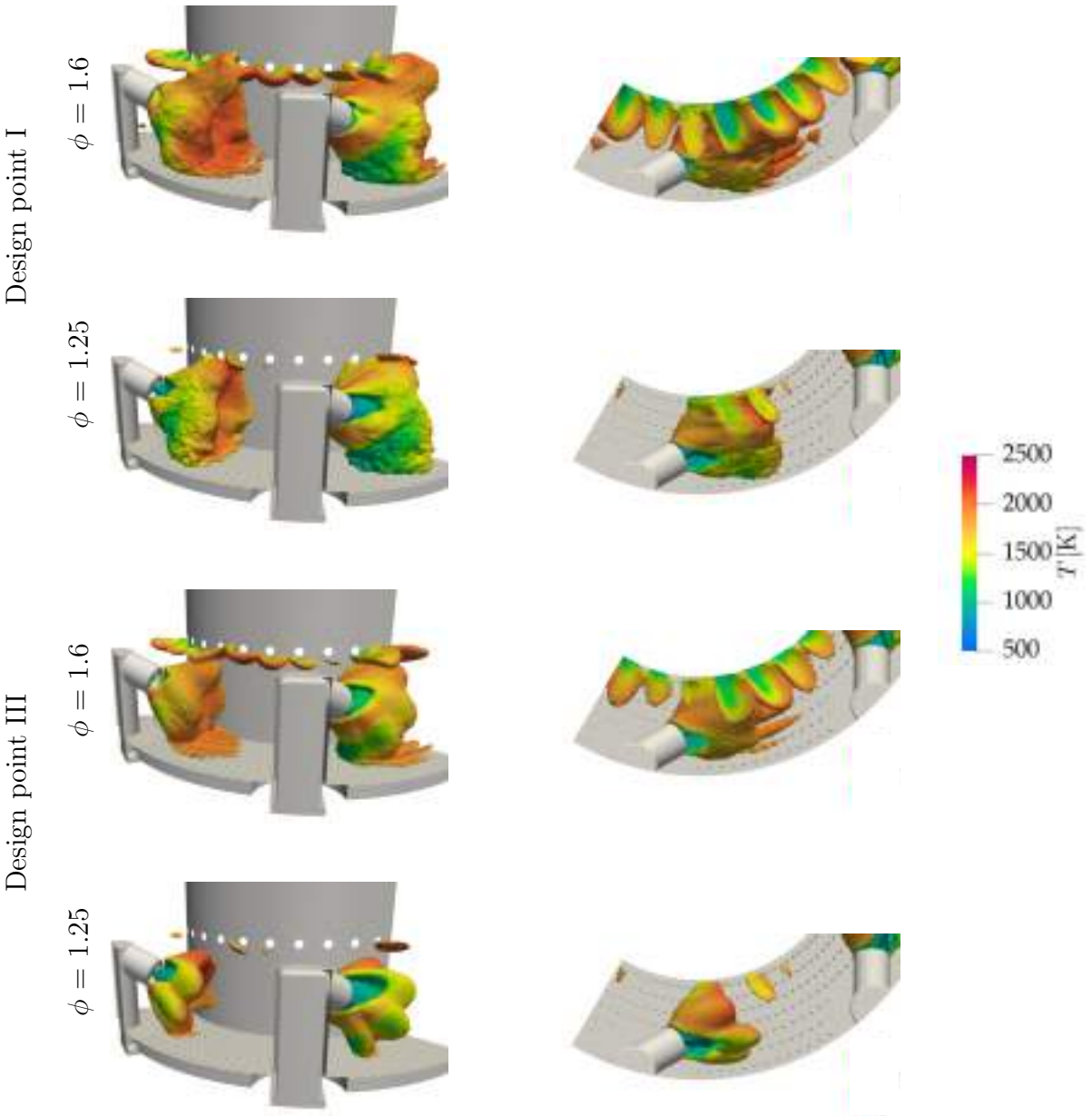

Figure 10.14: Isosurfaces of time-averaged heat release rate $\overline{\dot{q}}$ at 10% of its maximum value colored by temperature $\overline{T}$ for design points I and III and injector equivalence ratio of $\phi = 1.6$ and $\phi = 1.25$.

limits instead, starting from stable conditions, the injector equivalence ratio is gradually decreased until LBO[1]. Figure 10.16 presents the stability map showing the LBO and ignition limits for the three design points of Table 10.1. Air flow rate takes into account the total mass flow rate through the multiperforated wall and the injectors as well as 2/3 of the air coming from the primary holes, which are assumed to participate to combustion in the primary zone. As expected, when the total air mass flow rate (and hence the bulk velocity) reduces, both

[1]Experimentally, more than 10 tests are performed for each ϕ to verify the operability limits.

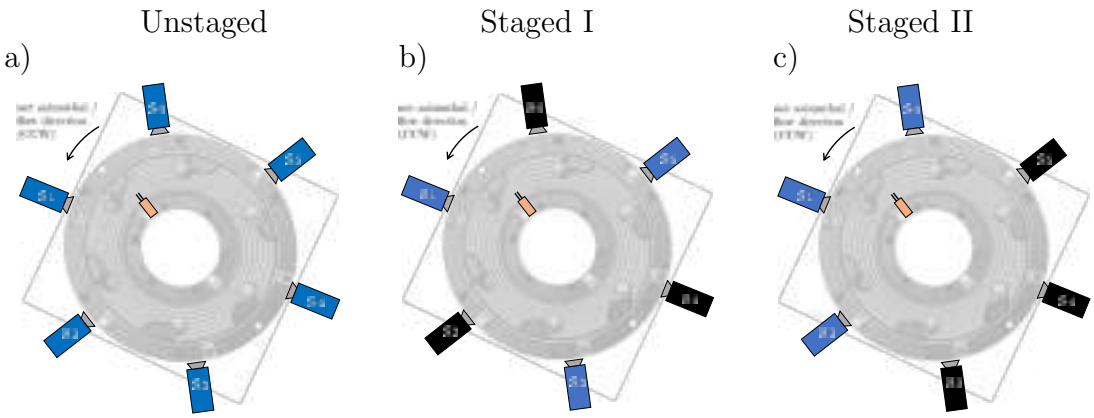

Figure 10.15: Schemes of the (a) unstaged and (b-c) staged configurations. In the staged configurations, injectors with the same color have the same fuel mass flow rate.

the ignition and the LBO limits improve. For design point III, the ignition and LBO limits of staged configurations are also indicated, showing that a relevant improvement in engine operability can be achieved by feeding some injectors with richer mixtures. The combustor can indeed be successfully ignited and operated at lower global equivalence ratios and hence lower thermal power if compared to unstaged classical configurations. Note however that the best configurations for LBO and ignition are not the same. While for LBO, the best staged configuration is the alternated one, i.e. staged I in Fig. 10.15(b), the best configuration for ignition is the staged II, Fig. 10.15(c). Note also that for ignition, the position of the spark with respect to the rich/lean injectors is a relevant information, i.e. the best ignition limit is achieved in the configuration as Fig. 10.15(c), namely with the spark just downstream the first (blue) rich injector.

A possible explanation of the increased operability limits in the staged configurations can be linked to the flame/flame interaction. In LBO, the injectors running with richer mixtures act as pilot injectors, sustaining the lean downstream flames. It is therefore not surprising that the best staged configuration is the one alternating rich and lean injectors. For ignition instead, rich conditions upstream the injector helps in the formation of the kernel that travels downstream and can easily ignite the rich injector downstream. Sometimes, the injector just downstream is observed to miss the ignition and the following injector ignites if it is also a rich one. This observation can be confirmed by looking at Fig. 10.17, presenting the experimental ignition sequence for design points I and III at an equivalence ratio $\phi = 1.6$ and at the leanest ignition limit in the unstaged configuration. Each circle corresponds to one run, the 10 concentric circles being 10 independent runs and allowing for statistical analysis. The color on one run corresponds to the ignition sequence, i.e. the first injector to ignite

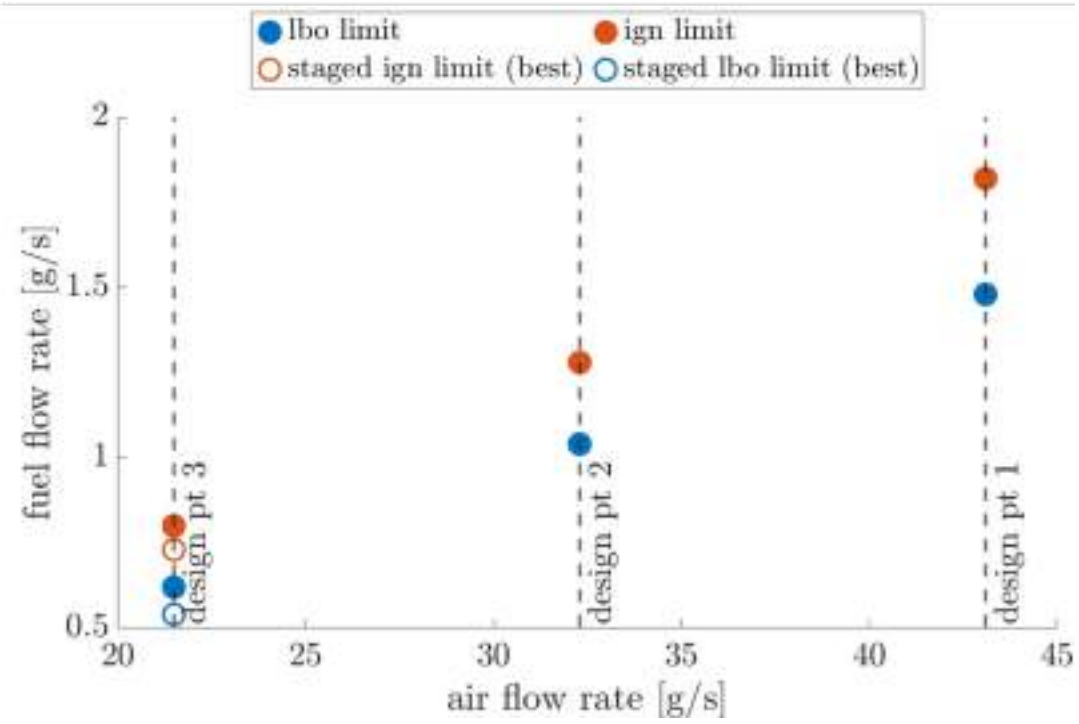

Figure 10.16: Stability map showing the LBO and ignition limits for the three design points of Table 10.1. Air flow rate takes into account the mass flow rate through the multiperforated wall, the injectors and 2/3 of the air coming from the primary holes. Ignition and LBO limits for staged configurations for design point III are also indicated [336].

is the dark blue one and the last injector is the red one. For each run there is a small circle symbol comparing on the light around time to the average value on the 10 realizations. For design point I and $\phi = 1.6$, the first injector to ignite is the one just donwstream the spark and the ignition sequence is very coherent, following the azimuthal flow direction. For the same equivalence ratio, but lower thermal power at design point III, the first injector to ignite is always the one just downstream the spark but sometimes the kernel is able to move upstream due to the reduced bulk velocity and it ignites the injector upstream the spark before igniting all the other injectors. The same phenomenon happens also at lower equivalence ratios, especially when one is close to the ignition limit, indicating a less coherent ignition sequence.

Figure 10.18 presents the ignition dynamics for design point I at $\phi = 1.6$. Experimental top visual images are compared to computed isosurfaces of $\dot{q}$ at different instants after the ignition. Due to the large bulk velocity, the flame front is not able to move upstream and the ignition sequence follows the azimuthal mean flow. LES is found to retrieve the right ignition dynamics and predicts a light around time in the order of 25 ms, in satisfactory agreement with the

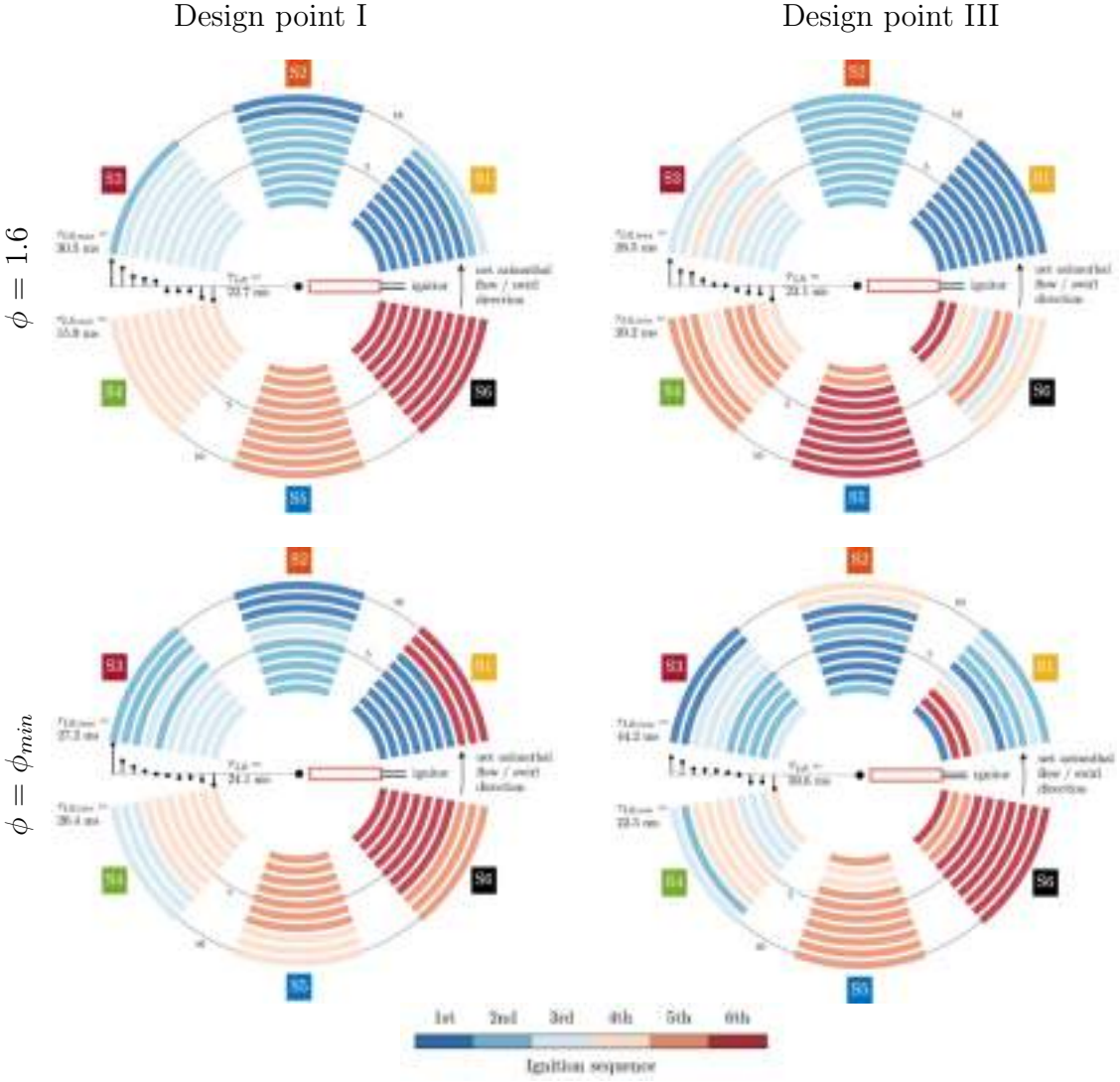

Figure 10.17: Experimental ignition sequence for design points I and III at an equivalence ratio $\phi = 1.6$ and at the leanest ignition limit [336]. Unstaged Configuration. Each circle represents an experimental run.

experiments, presenting however a faster evolution of the kernel in the during the first instants[1].

For lower thermal conditions, LES is able to predict an ignition sequence that does not follow anymore the mean azimuthal flow. Figure 10.19 presents the ignition dynamics for design point III at $\phi_{rich} = 1.3$ and $\phi_{lean} = 1.05$ in the Staged configuration II. Computed isosurfaces of heat release rate $\dot{q}$ at different instants after the ignition. In this case, the reduced bulk velocity allows the flame

[1]The Soft Ignition with Relaxed Temperature (SIRT) model is used in LES. The latter imposes a target temperature in a sphere using a temporal and a spatial Gaussian masking to avoid creating large gradients. In this LES, the location of the sphere (D = 20 mm) corresponds to the spark location in experiments. A temperature target of 2000K is used. Note that the energy deposited with this model is larger compared to the one deposited experimentally with the spark and can explain the faster development of the kernel in the first instants of the simulations with respect to experiments.

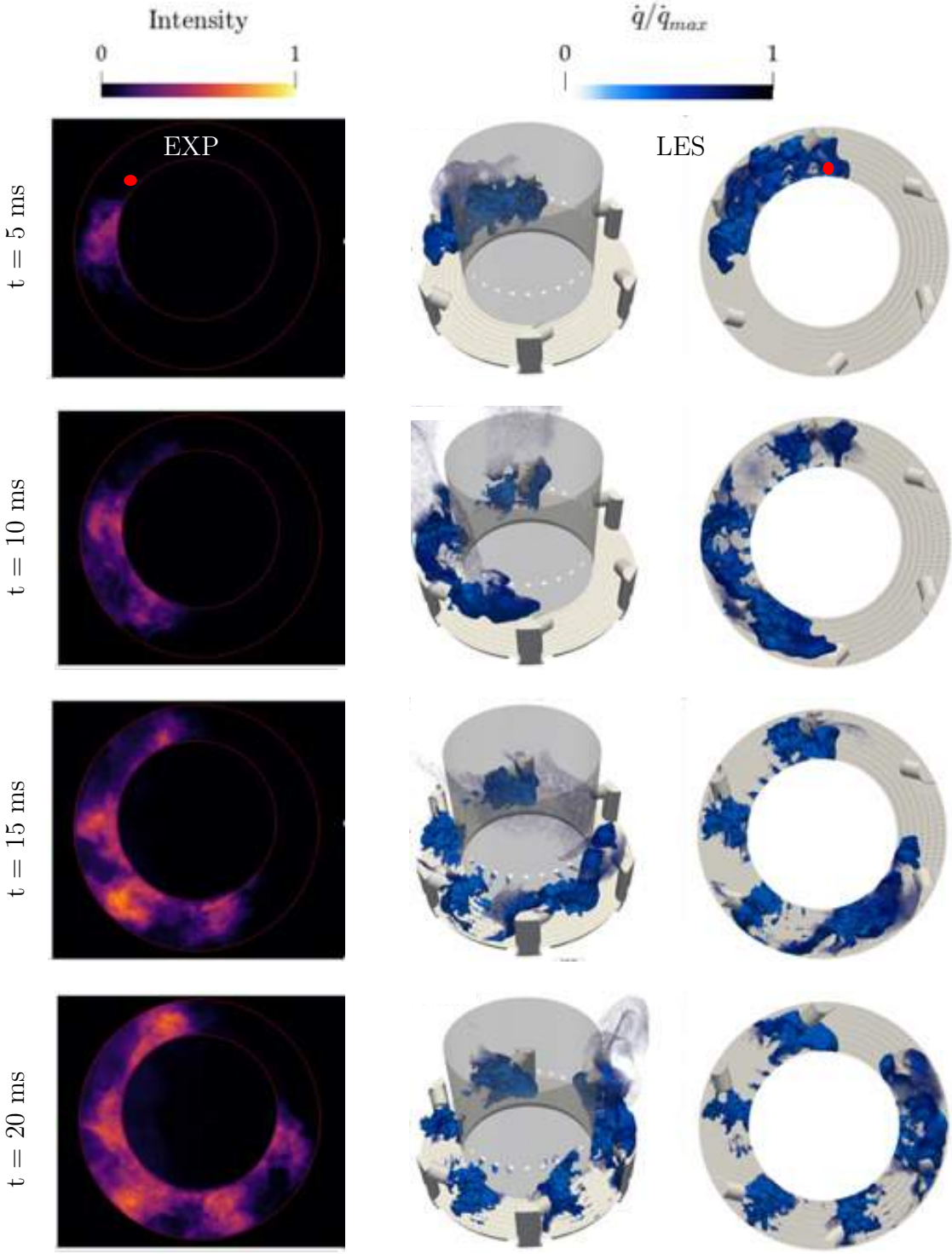

Figure 10.18: Ignition dynamics for design point I at $\phi = 1.6$. Experimental top visual images compared to computed isosurfaces of heat release rate $\dot{q}$ at different instants after the ignition.

front to move upstream toward the first rich injector. According to the reduced mean azimuthal velocity, also the light-around time seems larger and the ignition process is slowed down.

When it comes to LBO dynamics, the *SCT-V2* combustor is also found to reproduce the same phenomena observable in real helicopter engines. Figure 10.20 shows the LBO dynamics in the real Arrano helicopter engine compared to experiments and LES performed on the *SCT-V2* NTNU burner at design point III. Images refer to successive instants and show (b-c) the blow-out and (d) the successful re-ignition of the downstream injector due to the increased flame-flame interaction. Therefore, the upstream injector acts as a pilot flame as it is able to sustain and re-ignite the downstream flame. This explains also the higher LBO limits of the staged configurations and in general the improved operability of the SCT engines.

10.4 Final remarks

The new *SCT-V2* industrial burner is presented with the performed design process and its experimental as well as numerical introductory characterization. A preliminary design is proposed to increase the relative pressure loss of the combustor, reduce the aerodynamic blockage between the injectors, introduce cooling through multiperforated wall and primary holes in order to produce a combustion primary zone following the SHE design criteria. LES is then used as an industrial tool to optimize this design in terms of injector exit geometry and primary holes geometric parameters to improve the flame stabilization and to reduce the thermal load on the combustor parts. After manufacturing, the burner is characterized through experiments and LES to obtain its stability map. The flame shape evolution and its stabilization according to the different operating conditions follows the same behavior as in real helicopter engines. As the injector equivalence ratio increases, the flame moves out from the injector CRZ and stabilizes downstream, interacting with the air coming from the multiperforated wall and the primary holes. When it comes to the combustion dynamics, very peculiar phenomena are also observed. Ignition sequence is strongly dependent on the selected operating conditions and LBO dynamics shows blow-out and re-ignition of single injectors, as in real engines. Moreover, ignition and LBO limits can be improved by changing the feeding pattern of the injectors in a staged configuration, confirming the relevance of the flame/flame interaction when it comes to engine operability and explaining the improved capabilities of SCT engines. Therefore, the *SCT-V2* burner is showed to be fully operational and to comply

with various industrial criteria used to design real combustors, confirming the maturity of the LES approach to analyze and design novel aeronautical engines.

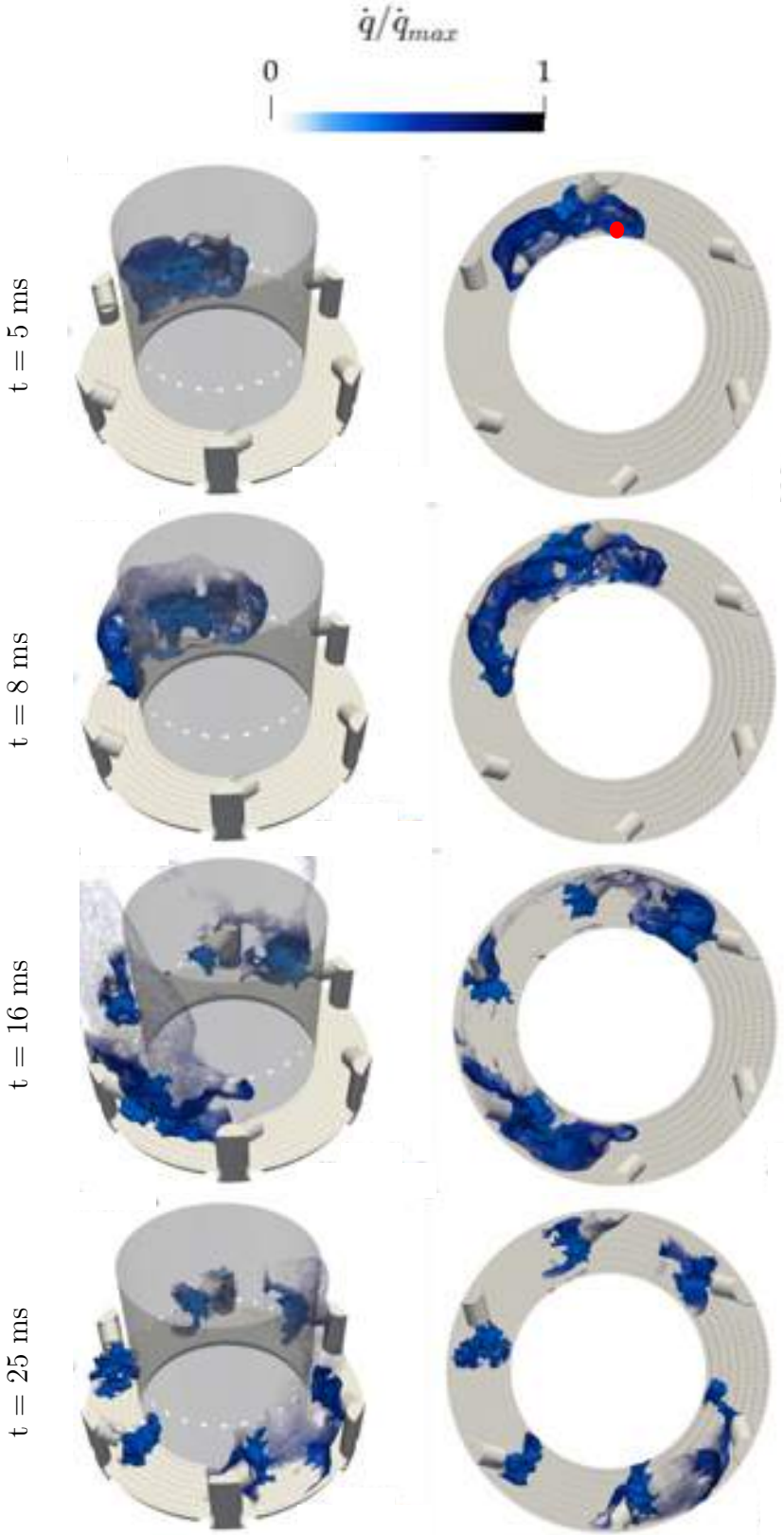

Figure 10.19: Ignition dynamics for design point III at $\phi_{rich} = 1.3$ and $\phi_{lean} = 1.05$. Staged configuration II. Computed isosurfaces of heat release rate $\dot{q}$ at different instants after the ignition.

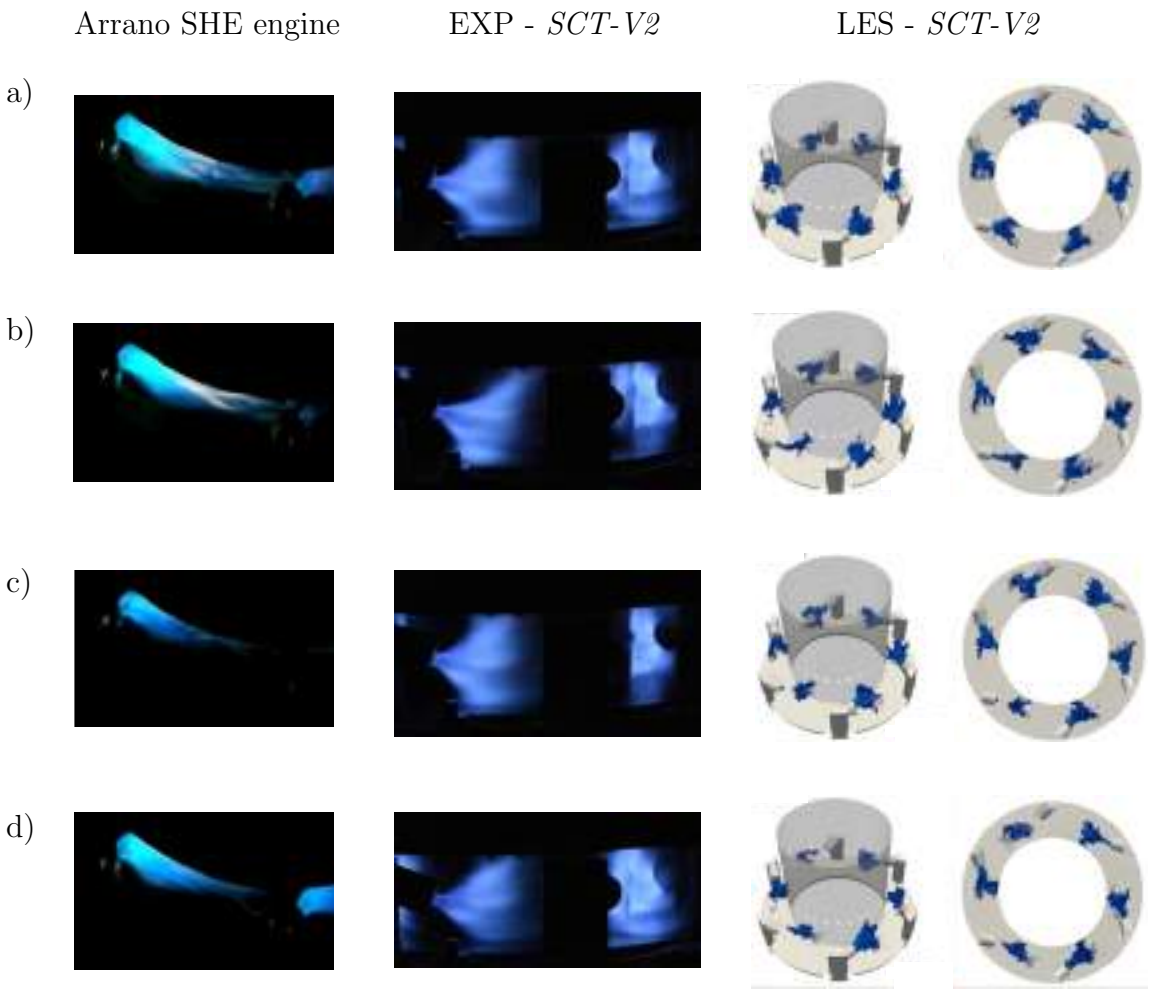

Figure 10.20: Lean Blow-Out dynamics in the real Arrano helicopter engine compared to experiments and LES performed on the *SCT-V2* NTNU burner. Images refer to successive instants and show (b-c) the blow-out and (d) the successful re-ignition of the downstream injector due to the increased flame-flame interaction.

Chapter 11

Conclusions and perspectives

Contents

11.1 PhD work summary

This PhD thesis focused on the assessment of Large Eddy Simulation (LES), in a Conjugate Heat Transfer (CHT) context, for predicting engine operability when dealing with innovative technologies, covering the cases of different fuel compositions like hydrogen, as well as a new combustor geometry: the Spinning Combustion Technology (SCT). To this scope, the present work coped with three research questions:

- Which developments and methods are needed for LES to support the design challenge of new (low-carbon) combustion technologies?
- Is it possible to analyze the effect of hydrogen enrichment on classical hydrocarbon flame dynamics?
- Can we study the Spinning Combustion Technology to get more insights on the improved operability capabilities?

The first objective was therefore to individuate the main modeling difficulties that high-fidelity LES would encounter when simulating new combustion technologies. Among the different challenges, three developments were found to be the keystone for achieving good LES prediction, namely the required tradeoff between discretization accuracy and simulations cost, the modeling of heat transfer at the walls, and the development of accurate chemical mechanism as well as variable transport properties. Indeed, both H_2-enrichment and real engine conditions

yield reduced flame thickness, leading to more stringent requirements in terms of domain discretization. On top of that, flame stabilization location cannot be predicted in new combustor technologies a priori, generally leading to not-optimized hand-made meshes. To overcome this issue, a new Static Mesh Refinement (SMR) strategy based on physical Quantities of Interest (QOI) was proposed in LES of turbulent reactive flows. The method was successfully validated on different configurations and it was found able to identify the relevant physics of turbulent reacting flows that are essential for the overall LES accuracy. LES accuracy was also found to be strongly affected by the imposed thermal boundary conditions. The correct prediction of wall heat transfer was showed to be of fundamental importance to capture the experimental thermoacoustic behaviour of a partially premixed swirled stabilize flame. More generally, this confirmed that high fidelity can be achieved for combustion LES solvers only when precise boundary conditions are used not only for the inflow and outflow acoustic impedances but also for the wall thermal boundary conditions. When dealing with non-conventional fuels, such as hydrogen, careful attention has to be paid on the chemistry description and transport model. In particular, LES predictions were found to be influenced by the adopted transport models highlighting the importance of using complex transport properties in any LES involving hydrogen combustion.

The second research question was addressed by studying the impact of H_2 enrichment of a CH_4 partially-premixed turbulent swirling flame both at atmospheric conditions and at elevated pressure (up to 5 bar). Both hydrogen enrichment and elevated pressure were found to significantly affect the flame shape, its stabilization and the corresponding thermoacoustic response. In addition, modifications of the flame shape varied the thermal load on combustor elements changing their maximum operative temperature. Change of flame shape was found to be the key element of the different thermoacoutic response and it is likely due to the different flame properties linked to hydrogen enrichment and to the modification of the chemical and turbulent time scales linked to elevated pressure. As pressure significantly impacts the turbulent reactive flow scales, SMR approach was required to discretize the fluid domain and allow for correctly resolving the different flames with the same combustion modeling at all pressures. With this approach, LES successfully predicted the complex turbulent reactive flow, hence confirming the potential of numerical simulations in investigating high-power density flames close to real engine operating conditions.

To address the third research question, the flame stabilization and the flame dynamics in the SCT was analyzed by performing LES of the NTNU modified annular combustor that reproduces the main physics behind SCT real engines.

Global and local equivalence ratios were found to play a major role in controlling the flame positioning in such a spinning combustion system and they turned out to be the most important design parameters. When it comes to the dynamics, among the two configurations analyzed, the one with the fuel injector oriented outward presented a constantly higher flame strain rate and subsequently lower LBO limits while the other configuration with stronger flame/flame interaction offered higher LBO limits, explaining the SCT increased blow-off capabilities with respect to classical engine designs. CHT-based simulations were found to correctly retrieve the flame dynamics and generally provide better results if compared to adiabatic simulations, suggesting that heat transfer at the wall should be carefully taken into account to achieve high-fidelity prediction of LBO in such a complex industrial configuration. As a conclusive demonstration, LES was used as an industrial design tool to propose a new modification of the NTNU test bench to have a closer correspondence with the real helicopter engine. This new test bench was then showed to be fully operational and to comply to various industrial criteria used to design real combustors at SHE, confirming the maturity of this modeling strategy to analyze novel aeronautical engines.

By addressing these challenges, the author demonstrated the assessment of LES, in a CHT context, for predicting engine operability when dealing with innovative technologies and therefore highlighted the central role of High Power Computing (HPC) and high-fidelity LES in the transition towards a decarbonized future.

11.2 Future works

Although this PhD thesis has contributed to the analysis of H_2-enriched flames and the Spinning Combustion Technology, it opens also a wide range of questions that still need to be addressed.

First of all, since this work focused on H_2-enriched flames up to 50% by volume, a fundamental future step will be to study pure hydrogen flame configurations in which the technological and modeling limits are more heavily present. To this regard, the developed methodologies for H_2/CH_4 blends need to be extended to full-H2 swirl-stabilized flames to analyze the complex turbulent flame structure and its stabilization mechanisms. On top of that, it's true that H_2 does no directly produces CO_2 but attention should be paid on other pollutant emitted, such as NOx that increases with the higher adiabatic flame temperature of hydrogen. From an operational point of view, when moving towards pure hydrogen, flashback becomes also a central problem. Hence focus should be devoted

in evaluating the propensity and the mechanisms leading to unsafe flashback in a wide range of operating conditions.

Second, the SCT has been analyzed in terms of lean-blow out capabilities but much still needs to be understood when it comes to different operating conditions or configurations. SCT needs also to be further investigated for different operability capabilities, such as ignition limits and light-around time. On top of that, although the preliminary characterization of the new NTNU SCT burner has been already performed, future studies are needed to get more insight into the physics behind LBO and ignition increased capabilities of this burner.

Finally, one can think of joining the two investigated strategies by introducing hydrogen in the SCT to gain in engine operability with respect to classical lean combustors while reducing CO_2 emissions compared to classical carbon-based fuels. Of course, beside hydrogen, Sustainable Aviation Fuel (SAF), which are produced from biomasses, can also be used for reducing the carbon footprint of helicopter engines and a study in this direction would surely be of great interest to test and analyze the versatility of the SCT to different types of fuels.

In conclusions, this PhD thesis results push a little step towards a low-carbon future but there are still many potential technological limits for existing and novel combustor designs that the combustion community needs to break to finally complete the path toward decarbonization. It might seem daunting but the biggest challenges get overcome one step at a time. I'm sure we can do it.

Appendices

Appendix A

Operating procedure and correlations for implementing the HRT method

This appendix illustrates the operating procedure and some useful correlations for implementing the HRT method. Indeed, whether or not temperature experimental data are available, a good guess for the thermal resistances can be set for each surface as an equivalent resistance R_{eq}, similarly to an electric circuit, assuming that radiation and convection act in parallel.

$$R_{eq} = R_{cond} + \frac{1}{1/R_{conv} + 1/R_{rad}}. \tag{A.1}$$

To compute the different resistances, the following equations can be used:

$$R_{cond} = L_s/\lambda_s, \tag{A.2}$$

$$\frac{1}{R_{conv}} = h_{conv} = \frac{\lambda_{air}}{L_{conv}} \left(0.68 + \frac{0.67 \mathrm{Ra}_L^{1/4}}{(1 + (0.492/\,\mathrm{Pr})^{9/16})^{4/9}} \right), \tag{A.3}$$

$$R_{rad} = \frac{1}{\epsilon\sigma} \frac{T_{wall} - T_{ambient}}{T_{wall}^4 - T_{ambient}^4}. \tag{A.4}$$

where L_s is the characteristic length of the conduction problem (e.g. thickness of the wall), λ_s the solid thermal conductivity, L_{cv} the characteristic length of the convection problem (e.g. length of the wall), Ra_L the Rayleigh number based on the characteristic length L, Pr the Prandtl number, ϵ the emissivity and σ the Stefan–Boltzmann constant. Note that Eq. A.3 is valid for natural convection from a vertical plate and for $10^{-1} < \mathrm{Ra}_L < 10^9$ but standard correlations are available in literature for other flow conditions [174, 175]. It is also worth underlining that in Eq. A.3 the flow properties have to be determined for an average

temperature $T_{flow} = (T_{ambient} + T_{wall})/2$ and hence requires the estimation of T_{wall}. The same applies for Eq. A.4.

When temperature experimental data are not available, the depicted methodology can give reasonable values for the thermal resistances and avoid the use of adiabatic conditions. However, if experimental data are available, a tuning procedure can be performed starting from these initial values.

In the present study, the initial values for the centerbody and backplane have been calculated neglecting convection and radiation (i.e. the temperature of the solid was expected to be low) and considering a characterictic length $L_s = 36$ mm (i.e. the height of the bluff-body) and a thermal conductivity $\lambda_s = 15$ W/m K. This results in a $R_{initial} = 2.4\times10^{-3}$ m^{2}K/W. For the chamber walls instead, T_{wall} is assumed to be close to 1200 K: radiation cannot be neglected. A value of $\epsilon_{quartz} = 0.8$ is assumed to compute the R_{rad}. R_{conv} is determined assuming a characteristic length $L_{cv} = 114$ mm (i.e. height of the chamber walls), a $Ra_L = 5.8\times10^6$ and a Pr = 0.7. $R_{conduction}$ is computed taking into account the 1.7 mm thickness of the walls and the $\lambda_s = 1.4$ W/m K. The resulting equivalent $R_{eq,\ initial} = 1\times10^{-2}$ m^{2}K/W. Note that these values have the same order of magnitude of the values found after the tuning procedure (section 4.3.1), verifying the assumptions.

To perform the iterative tuning procedure, a linearization of the thermal problem was used. The heat flux Φ_q at the wall can be determined as follows:

$$\Phi_{q,\ initial} = \frac{T_{wall} - T_{ref}}{R_{eq,\ initial}} = \frac{T_{flow} - T_{wall}}{R_{flow}} \tag{A.5}$$

where T_{flow} is the temperature of the flow inside the combustion chamber near the wall (out of the thermal boundary layer) and R_{flow} is the corresponding convection resistance. Performing the first LES with $R_{eq,\ initial}$ one finds the unknown variables T_{wall}, T_{flow} and R_{flow}. At this point, we can assume, as a first approximation, that the variation of R_{flow} (and hence the thermal boundary layer) with T_{wall} is negligible. Therefore, if we impose the $T_{wall,\ exp}$ in Eq. we can compute $R_{eq,\ step1}$:

$$\Phi_{q,\ step1} = \frac{T_{wall,\ exp} - T_{ref}}{R_{eq,\ step1}} = \frac{T_{flow} - T_{wall,\ exp}}{R_{flow}}, \tag{A.6}$$

$$R_{eq,\ step1} = \frac{T_{wall,\ exp} - T_{ref}}{T_{flow} - T_{wall,\ exp}} R_{flow}. \tag{A.7}$$

LES is then performed with the new value of $R_{eq,\ step1}$ and a new estimation of T_{wall} is produced. If the latter is sufficiently close to $T_{wall,\ exp}$ the tuning procedure is completed, otherwise a new iteration is performed. In the present

study, starting from reasonable values for the resistances, a single iteration was needed to reach satisfactory agreement with $T_{wall,exp}$.

Appendix B

Transport property modeling

The simplified transport properties adopted in AVBP consist in a constant mixture Prandtl (Pr) number and a constant Schmidt (Sc) number for each species of the chemical scheme. These values are optimized during the mechanism reduction procedure. Pr and Sc numbers for the ARC scheme used in the simulations of Chapter 5 are summarized in Tab. B.1.

Property	Specie	Value
Schmidt	H_2	0.207
	H	0.124
	O	0.484
	O_2	0.751
	OH	0.493
	H_2O	0.558
	HO_2	0.749
	H_2O_2	0.754
	CH_3	0.679
	CH_4	0.682
	CO	0.755
	CO_2	0.944
	CH_2O	0.868
	CH_3O	0.888
	CH_3OH	0.889
	C_2H_2	0.891
	C_2H_4	0.900
	C_2H_6	0.988
	CH_2CO	1.025
	N_2	0.717
Prandlt	Mixture	0.712

Table B.1: Constant Schmidt number for each species and mixture Prandtl number used in the simplified transport model.

To take into account the variability of the transport properties when considering a mixture with light molar weight components (e.g. H_2), a database of Prandtl number and N_2 Schmidt number as a function of the ternary mixture composition (i.e. CH_4, H_2, N_2) has been computed with the complex-transport module of Cantera. The results of this analysis are showed in Fig. 2(d) of the manuscript. It is then straightforward to compute a polynomial fitting of these two variables and express them as a function of the molar fraction X of CH_4 and H_2 (i.e. the two independent variables), as follows:

$$\text{Prandtl} = f(\mathrm{X}_{\mathrm{CH_4}}, \mathrm{X}_{\mathrm{H_2}}) = f_{00} + f_{10}\mathrm{X}_{\mathrm{CH_4}} + f_{01}\mathrm{X}_{\mathrm{H_2}} + ... + f_{ab}{\mathrm{X}_{\mathrm{CH_4}}}^{a}{\mathrm{X}_{\mathrm{H_2}}}^{b} \quad \text{(B.1)}$$

$$\text{N}_2\text{ Schmidt} = g(\mathrm{X}_{\mathrm{CH_4}}, \mathrm{X}_{\mathrm{H_2}}) = g_{00} + g_{10}\mathrm{X}_{\mathrm{CH_4}} + g_{01}\mathrm{X}_{\mathrm{H_2}} + ... + g_{cd}{\mathrm{X}_{\mathrm{CH_4}}}^{c}{\mathrm{X}_{\mathrm{H_2}}}^{d} \quad \text{(B.2)}$$

In particular, the function f in Eq. (B.1) and the function g in Eq. (B.2) have been chosen to be a piecewise-defined polynomials with respect to $\mathrm{X}_{\mathrm{CH_4}}$ and $\mathrm{X}_{\mathrm{H_2}}$ with the coefficients being determined in order to reduce the root mean square errors with respect to the database from Cantera. The resulting polynomial fitting is able to correctly provide the exact Prandtl number and N_2 Schmidt number, with a coefficient of determination R_2 of 0.9996, while not worsening the code performance. Table B.2 and Tab. B.3 report the coefficients used in the piecewise-defined fitting functions and their intervals of validity for the Pr number and the N_2 Sc number functions, respectively.

Coefficient (f_{ab})	Value	Interval
f_{00}	0.7076	
f_{10}	0.02157	
f_{01}	-1.608	
f_{20}	-0.013	
f_{11}	0.3687	
f_{02}	3.643	
f_{30}	-0.003734	
f_{21}	0.04177	
f_{12}	-0.5402	
f_{03}	-3.758	
f_{40}	-0.0001393	for X_{CH_4} in [0,1] and X_{H_2} in [0,1-X_{CH_4}]
f_{31}	-0.03073	
f_{22}	-0.3168	
f_{13}	-0.2286	
f_{04}	1.302	
f_{50}	-0.001286	
f_{41}	0.001784	
f_{32}	0.09282	
f_{23}	0.4952	
f_{14}	0.7872	
f_{05}	0.3903	

Table B.2: Coefficient of the piecewise-defined polynomial in Eq. B.1 expressing the mixture Prandtl number as a function of X_{CH_4} and X_{H_2}.

Coefficient (g_{cd})	Value	Interval
g_{00}	1.295	
g_{10}	-1.574	
g_{01}	4.886	
g_{20}	7.229	
g_{11}	-35.28	
g_{02}	-7.989	
g_{30}	-18.36	
g_{21}	94.96	
g_{12}	56.5	
g_{03}	5.543	
g_{40}	20.05	for X_{CH_4} in [0.05,1] and X_{H_2} in [0.05,1-X_{CH_4}]
g_{31}	-109.1	
g_{22}	-115.2	
g_{13}	-39.54	
g_{04}	-0.1024	
g_{50}	-7.872	
g_{41}	44.01	
g_{32}	71.57	
g_{23}	39.7	
g_{14}	10.76	
g_{05}	-2.227	
g_{00}	2.833	
g_{10}	-32.13	
g_{01}	-0.04449	
g_{11}	69.78	
g_{02}	0.3827	
g_{12}	-108.3	for X_{CH_4} in [0,0.05] and X_{H_2} in [0.05,1-X_{CH_4}]
g_{03}	-3.604	
g_{13}	90.81	
g_{04}	6.146	
g_{14}	-28.94	
g_{05}	-4.295	
g_{00}	0.717	
g_{10}	10.05	for X_{CH_4} in [0,0.05] and X_{H_2} in [0,0.05-X_{CH_4}]
g_{01}	42.32	
g_{d00}	2.66	
g_{d10}	-28.82	for X_{CH_4} in [0,0.05] and X_{H_2} in [0.05-X_{CH_4},0.05]
g_{d01}	3.457	

Table B.3: Coefficient of the piecewise-defined polynomial in Eq. B.2 expressing the N_2 Schmidt number as a function of X_{CH_4} and X_{H_2}.

Appendix C

Chemistry reduction and validation

This appendix presents the chemical scheme used in the LES of PRECCINSTA (Chapter 6), HIPOT (Chapter 7) and NTNU (Chapter 9) burners. First the derivation of the scheme and the validation at atmospheric pressure for different hydrogen enrichment levels is discussed in section C.1. Then validation at elevated pressure is provided in section C.2.

C.1 H_2-enrichment

The Analytically Reduced Chemistry (ARC) developed for this study was derived to achieve an accurate description of the combustion process of air/CH_4/H_2 flames for several mixing conditions. The reduction was carried out with the ARCANE code co-developed by CERFACS and Cornell University [65]. It is a fully automatic multi-step reduction tool relying on DRGEP [339], chemical lumping [340] and Quasi-Steady State Assumption [341].

CRECK detailed mechanism [241] was chosen as a reference for this work because of its extensive use in the community.
To guaranty the accuracy of the mechanism, several canonical cases were included in the sampled data needed by the reduction. The cases and the error thresholds associated on interest quantities are detailed in Tab. C.1.

For each target case, the entire reduction procedure is performed considering pure methane having the following targets: Heat release rate, H_2. The reduced ARC mechanism generated by ARCANE comprises 18 transported species, 245 reactions and 12 species in Quasi-Steady State:

- Transported species: N_2, H_2, H, O_2, O, H_2O, OH, H_2O_2, HO_2, CO, CO_2, CH_4, CH_3, CH_3OH, CH_2O, C_2H_6, C_2H_4, C_2H_2

Reactor type	Isochoric 0D reactor	Freely propagating premixed flame
Temperature [K]	1000-2000	300
Pressure [bar]	1	1
Equivalence ratio	1	0.7, 1, 1.4
Error threshold on auto-ignition delay time	4%	/
Error threshold on laminar flame speed	/	5%
Error threshold on maximum heat release rate	/	5%
Error threshold on maximum temperature	1%	1%

Table C.1: Table summarizing the cases used for the reduction and the associated threshold errors.

- QSS species: CH_2, $CH_2(S)$, C, CH, CH_3O_2, CH_3O, CH_2OH, HCO, C_2H_5, C_2H_3, CH_2CO, $HCCO$

Detailed description of the reactions is given in Tab. C.2. The mechanism was validated on a broader operability spectrum compared to reduction cases. This is performed assuming one-dimensional CH_4/H_2/air premixed flames up to 50 % (by volume) hydrogen enrichment as in the PRECCINSTA cases studied in in Chapter 6. Results for pure methane/air and 50% H2 enriched flames are displayed in Fig. C.1 and Fig. C.2, respectively, showing good agreement between the ARC and the detailed mechanism.

C.2 Elevated pressure

The kinetic scheme has been further validated through Cantera (www.cantera.org) calculations of a 1D-premixed flames using detailed schemes at elevated pressures and up to 40% (by volume) hydrogen enrichment as in the HIPOT PRECCINSTA cases studied in Chapter 7. Results for pure 40% H_2-enriched flames are displayed in Figures C.3, C.4, C.5 and C.6 for the laminar flame speed, the flame thickness, the adiabatic flame temperature and the maximum OH mass fraction, respectively. All quantities show good agreement between the ARC and the detailed mechanism.

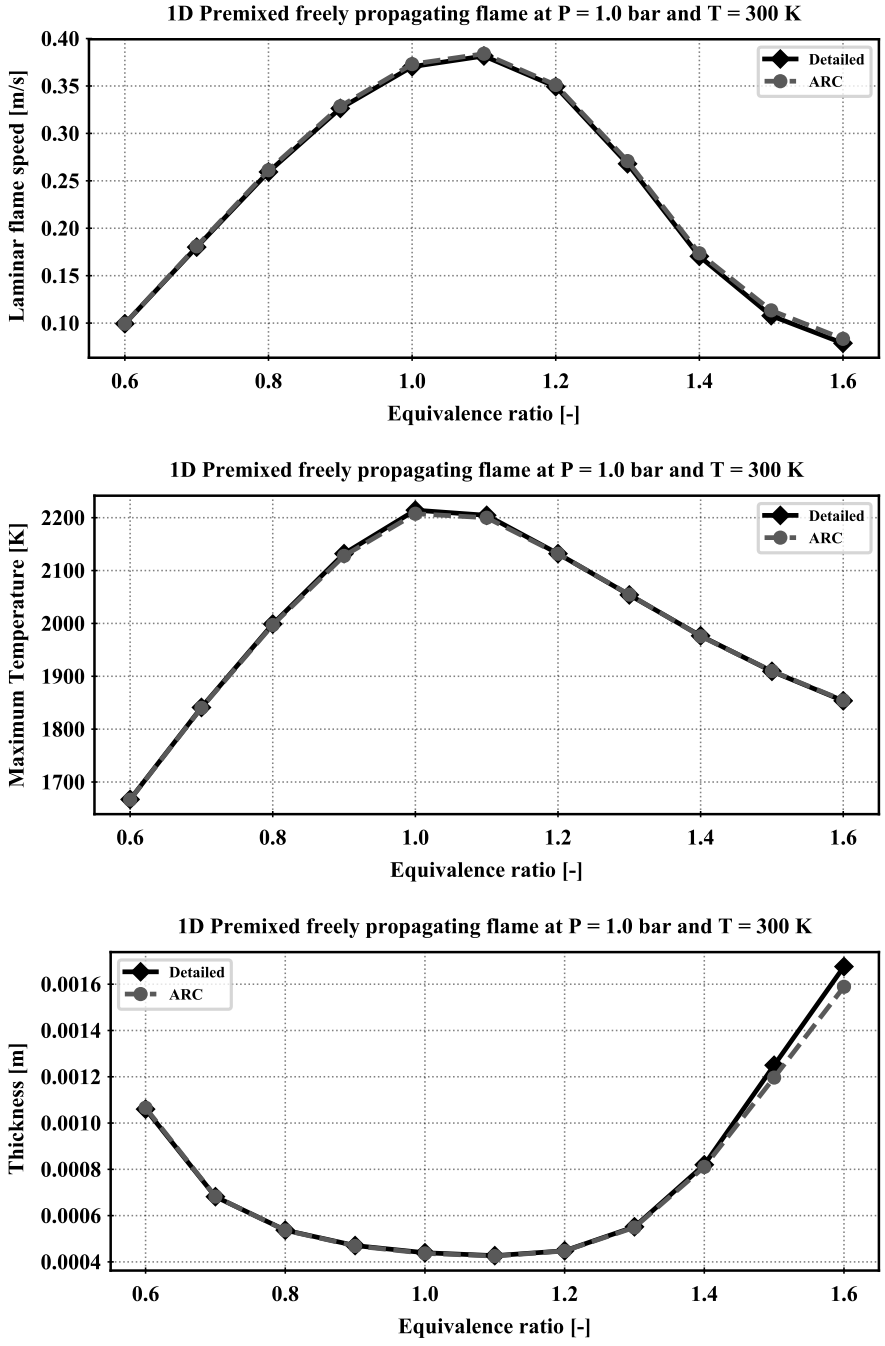

Figure C.1: Validation of the ARC mechanism for pure CH_4/air case.

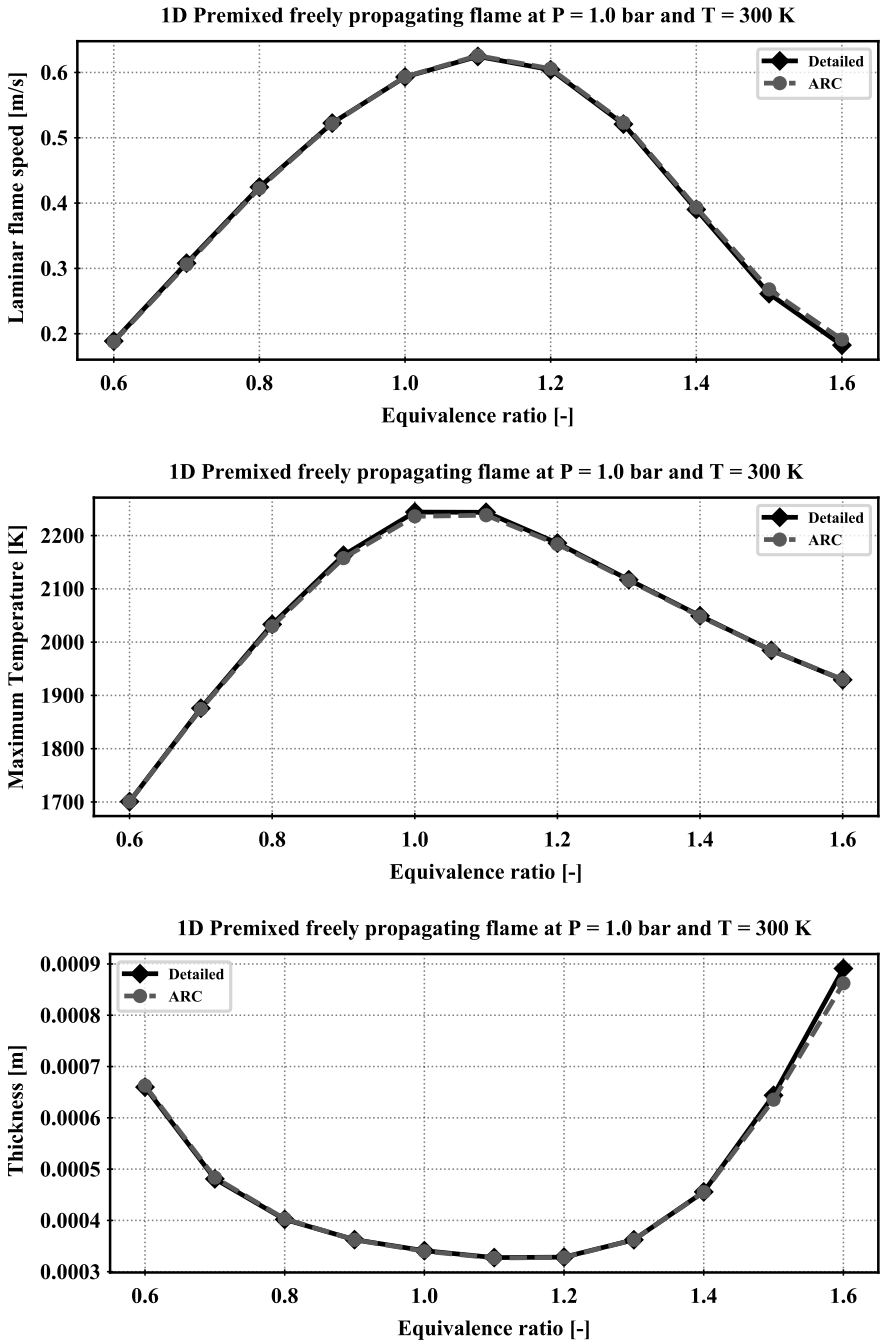

Figure C.2: Validation of the ARC mechanism for 50% (by volume) H_2 enriched case.

a)

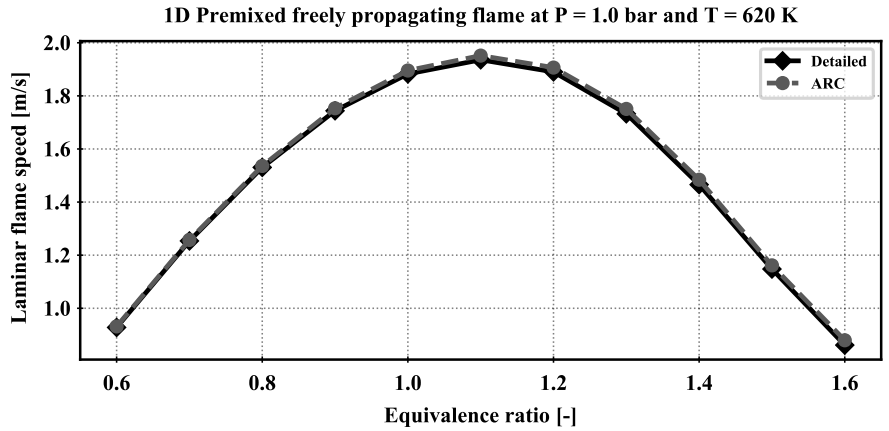

b)

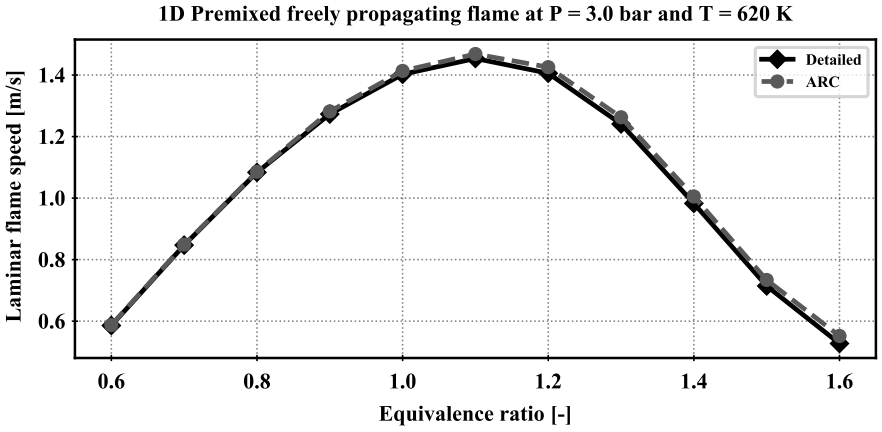

c)

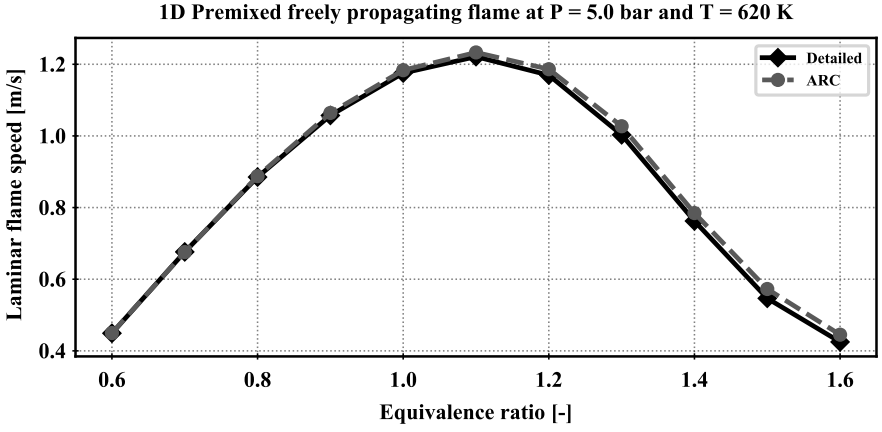

Figure C.3: Laminar flame speed as a function of the equivalence ratio. ARC mechanism compared to the detailed scheme for Cases (a) *P1H40*, (b) *P3H40* and (c) *P5H40*.

a)

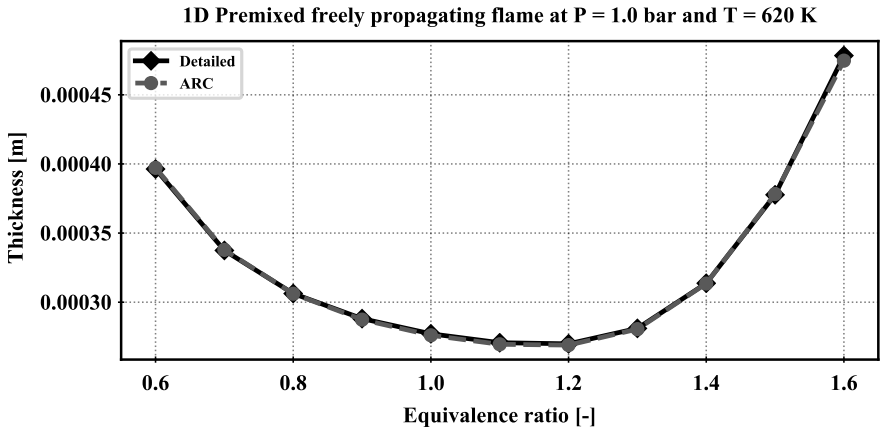

b)

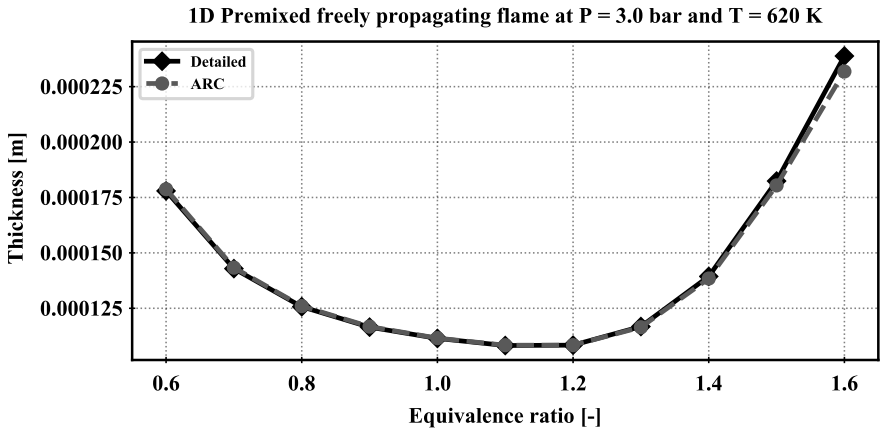

c)

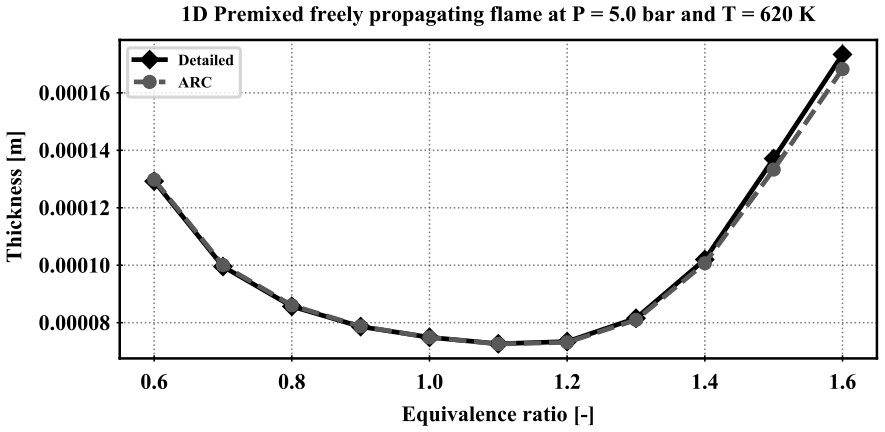

Figure C.4: Flame thickness as a function of the equivalence ratio. ARC mechanism compared to the detailed scheme for Cases (a) *P1H40*, (b) *P3H40* and (c) *P5H40*.

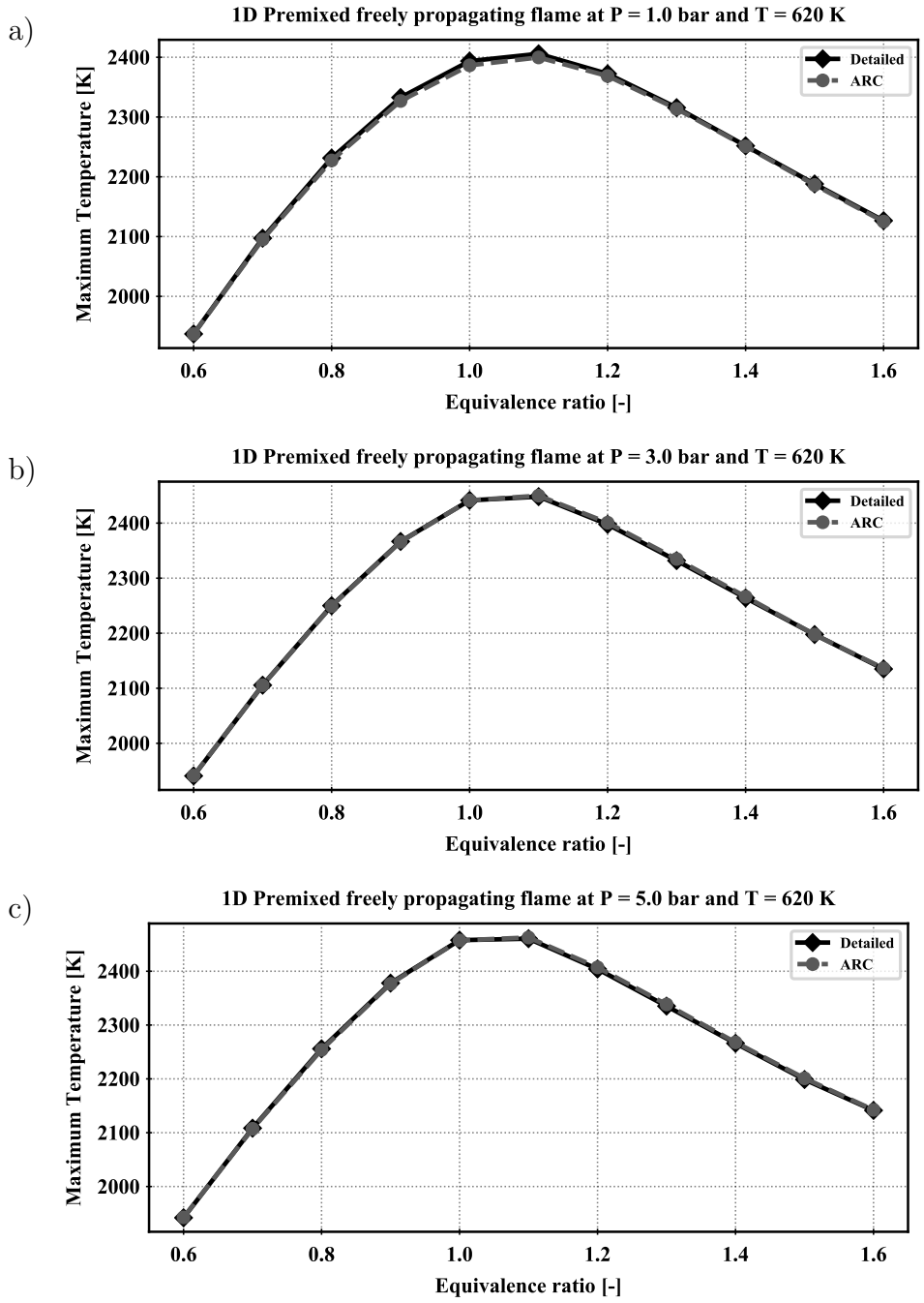

Figure C.5: Adiabatic flame temperature as a function of the equivalence ratio. ARC mechanism compared to the detailed scheme for Cases (a) *P1H40*, (b) *P3H40* and (c) *P5H40*.

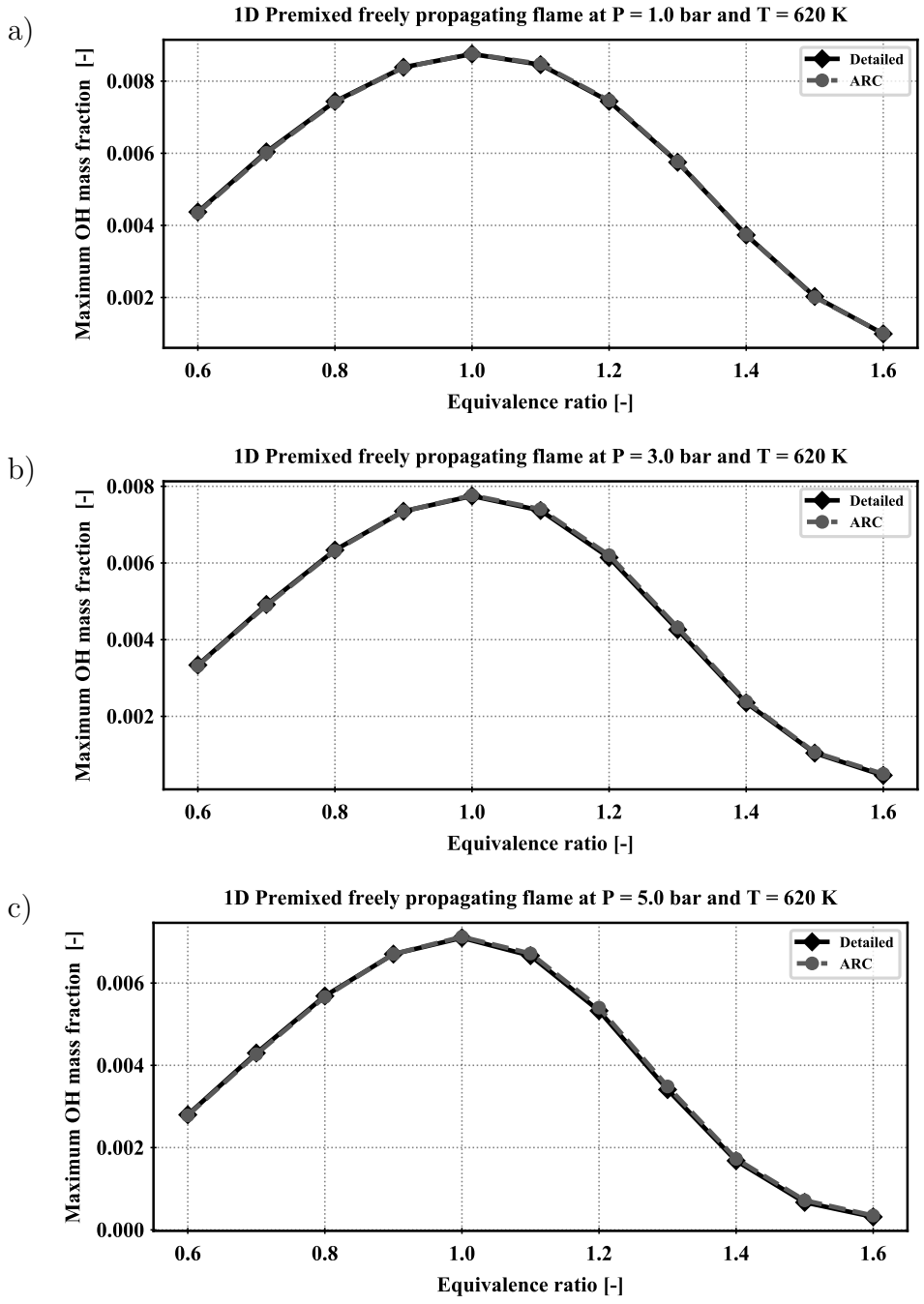

Figure C.6: Maximum OH mass fraction as a function of the equivalence ratio. ARC mechanism compared to the detailed scheme for Cases (a) *P1H40*, (b) *P3H40* and (c) *P5H40*.

Table C.2: List of reactions with A the pre-exponential factor in $m^{3(n-1)})/kmol^{n-1})/s$ with n the order of the reaction, b the temperature exponent and Ea the activation energy in $J/kmol$. In the case of fall-off reactions, two sets of Arrhenius coefficients are specified, the first one being the low temperature set and the second one the high temperature set.

No.	Reaction	A	b	E_a
1	H2 + M ⟷ 2 H + M	4.577000E+16	-1.400000E+00	4.368096E+08
	CH4:2.00E+00 CO:1.90E+00 CO2:3.80E+00 H2:2.50E+00 H2O:1.20E+01			
2	H2 + O ⟷ H + OH	5.080000E+01	2.670000E+00	2.632573E+07
3	H2 + OH ⟷ H + H2O	4.380000E+10	0.000000E+00	2.924616E+07
4	2 O + M ⟷ O2 + M	6.165000E+09	-5.000000E-01	0.000000E+00
	CH4:2.00E+00 CO:1.90E+00 CO2:3.80E+00 H2:2.50E+00 H2O:1.20E+01			
5	H + O2 ⟷ O + OH	1.140000E+11	0.000000E+00	6.395662E+07
6	H + OH + M ⟷ H2O + M	3.500000E+16	-2.000000E+00	0.000000E+00
	CH4:2.00E+00 H2:7.30E-01 H2O:3.65E+00			
7	H2O + O ⟷ 2 OH	6.700000E+04	1.704000E+00	6.270477E+07
8	H + O + M ⟷ OH + M	4.714000E+12	-1.000000E+00	0.000000E+00
	CH4:2.00E+00 CO:1.50E+00 CO2:2.00E+00 H2:2.50E+00 H2O:1.20E+01			
9	H2O2 (+M) ⟷ 2 OH (+M)	2.490000E+21	-2.300000E+00	2.039658E+08
	4.30E-01 1.00E-30 1.00E+30 0.00E+00	2.000000E+12	9.000000E-01	2.039658E+08
	CO:2.8E+00 CO2:1.6E+00 H2:3.7E+00 H2O:7.7E+00 H2O2:7.7E+00 N2:1.5E+00 O2:1.2E+00			
10	H + H2O2 ⟷ H2O + OH	2.410000E+10	0.000000E+00	1.661048E+07
11	H + H2O2 ⟷ H2 + HO2	2.150000E+07	1.000000E+00	2.510400E+07
12	H2O2 + O ⟷ HO2 + OH	9.550000E+03	2.000000E+00	1.661048E+07
13	H2O2 + OH ⟷ H2O + HO2	1.740000E+09	0.000000E+00	1.330512E+06
14	H2O2 + OH ⟷ H2O + HO2	7.590000E+10	0.000000E+00	3.041350E+07
15	H + HO2 ⟷ 2 OH	7.079000E+10	0.000000E+00	1.234280E+06
16	H + HO2 ⟷ H2 + O2	1.140200E+07	1.082700E+00	2.317016E+06
17	HO2 + O ⟷ O2 + OH	3.250000E+10	0.000000E+00	0.000000E+00
18	HO2 + OH ⟷ H2O + O2	7.000000E+09	0.000000E+00	-4.572945E+06
19	HO2 + OH ⟷ H2O + O2	4.500000E+11	0.000000E+00	4.572945E+07
20	2 HO2 ⟷ H2O2 + O2	1.000000E+11	0.000000E+00	4.619504E+07
21	2 HO2 ⟷ H2O2 + O2	1.900000E+08	0.000000E+00	-5.894942E+06
22	H + O2 (+M) ⟷ HO2 (+M)	1.737000E+13	-1.230000E+00	0.000000E+00
	6.70E-01 1.00E-30 1.00E+30 1.00E+30	4.650000E+09	4.400000E-01	0.000000E+00
	CH4:2.0E+00 CO:1.9E+00 CO2:3.8E+00 H2:1.3E+00 H2O:1.0E+01			
23	CO + O (+M) ⟷ CO2 (+M)	1.173000E+18	-2.790000E+00	1.753514E+07
		1.362000E+07	0.000000E+00	9.974656E+06
	CO:1.8E+00 CO2:3.6E+00 H2:2.0E+00 H2O:1.2E+01			
24	CO + OH ⟷ CO2 + H	7.015000E+01	2.053000E+00	-1.488249E+06
25	CO + OH ⟷ CO2 + H	5.757000E+09	-6.640000E-01	1.388251E+06
26	CO + HO2 ⟷ CO2 + OH	1.570000E+02	2.180000E+00	7.506096E+07
27	CO + O2 ⟷ CO2 + O	1.119000E+09	0.000000E+00	1.995768E+08

No.	Reaction	A	b	E_a
28	CH3 + H (+M) ⟷ CH4 (+M)	2.477000E+27	-4.760000E+00	1.020896E+07
	7.83E-01 7.40E+01 2.94E+03 6.96E+03	1.270000E+13	-6.300000E-01	1.602472E+06
	CH4:2.0E+00 CO:1.5E+00 CO2:2.0E+00 H2:2.0E+00 H2O:6.0E+00			
29	CH4 + H ⟷ CH3 + H2	6.140000E+02	2.500000E+00	4.011201E+07
30	CH4 + O ⟷ CH3 + OH	1.020000E+06	1.500000E+00	3.598240E+07
31	CH4 + OH ⟷ CH3 + H2O	5.830000E+01	2.600000E+00	9.162960E+06
32	CH4 + HO2 ⟷ CH3 + H2O2	1.130000E-02	3.740000E+00	8.790584E+07
33	CH3 + HO2 ⟷ CH4 + O2	1.160000E+02	2.230000E+00	-1.264405E+07
34	CH2 + CH4 ⟷ 2 CH3	2.460000E+03	2.000000E+00	3.460168E+07
35	CH2(S) + N2 ⟷ CH2 + N2	1.500000E+10	0.000000E+00	2.510400E+06
36	CH2(S) + H2O ⟷ CH2 + H2O	3.000000E+10	0.000000E+00	0.000000E+00
37	CH2(S) + CO ⟷ CH2 + CO	9.000000E+09	0.000000E+00	0.000000E+00
38	CH2(S) + CO2 ⟷ CH2 + CO2	7.000000E+09	0.000000E+00	0.000000E+00
39	CH2(S) + O2 ⟶ CO + H + OH	2.800000E+10	0.000000E+00	0.000000E+00
40	CH2(S) + O2 ⟷ CO + H2O	1.200000E+10	0.000000E+00	0.000000E+00
41	CH2(S) + O ⟷ CO + H2	1.500000E+10	0.000000E+00	0.000000E+00
42	CH2(S) + O ⟷ H + HCO	1.500000E+10	0.000000E+00	0.000000E+00
43	CH2(S) + H2 ⟷ CH3 + H	7.000000E+10	0.000000E+00	0.000000E+00
44	CH2(S) + H ⟷ CH + H2	3.000000E+10	0.000000E+00	0.000000E+00
45	CH2(S) + OH ⟷ CH2O + H	3.000000E+10	0.000000E+00	0.000000E+00
46	CH2(S) + CO2 ⟷ CH2O + CO	1.400000E+10	0.000000E+00	0.000000E+00
47	CH2 + H (+M) ⟷ CH3 (+M)	3.200000E+21	-3.140000E+00	5.146320E+06
	6.80E-01 7.80E+01 2.00E+03 5.59E+03	2.500000E+13	-8.000000E-01	0.000000E+00
	CH4:2.0E+00 CO:1.5E+00 CO2:2.0E+00 H2:2.0E+00 H2O:6.0E+00			
48	CH2 + O2 ⟷ HCO + OH	1.060000E+10	0.000000E+00	6.276000E+06
49	CH2 + O2 ⟶ CO2 + 2 H	2.640000E+09	0.000000E+00	6.276000E+06
50	CH2 + O ⟶ CO + 2 H	5.000000E+10	0.000000E+00	0.000000E+00
51	CH2 + H ⟷ CH + H2	3.000000E+10	0.000000E+00	0.000000E+00
52	CH2 + OH ⟷ CH + H2O	1.130000E+04	2.000000E+00	1.255200E+07
53	CH + O2 ⟷ HCO + O	3.300000E+10	0.000000E+00	0.000000E+00
54	CH + O ⟷ CO + H	5.700000E+10	0.000000E+00	0.000000E+00
55	CH + H ⟷ C + H2	1.100000E+11	0.000000E+00	0.000000E+00
56	CH + OH ⟷ H + HCO	3.000000E+10	0.000000E+00	0.000000E+00
57	CH + H2O ⟷ CH2O + H	1.774000E+13	-1.220000E+00	9.957920E+04
58	CH + CO2 ⟷ CO + HCO	1.700000E+09	0.000000E+00	2.866040E+06
59	C + OH ⟷ CO + H	5.000000E+10	0.000000E+00	0.000000E+00
60	C + O2 ⟷ CO + O	5.000000E+10	0.000000E+00	0.000000E+00
61	CH3 + O2 (+M) ⟷ CH3O2 (+M)	6.850000E+18	-3.000000E+00	0.000000E+00
	6.00E-01 1.00E+03 7.00E+01 1.70E+03	7.812000E+06	9.000000E-01	0.000000E+00
62	CH3 + O2 ⟷ CH3O + O	7.546000E+09	0.000000E+00	1.184909E+08
63	CH3 + O2 ⟷ CH2O + OH	2.641000E-03	3.283000E+00	3.391132E+07
64	CH3 + O ⟷ CH2O + H	5.540000E+10	5.000000E-02	-5.690240E+05

No.	Reaction	A	b	E_a
65	CH3 + OH ⟷ CH2(S) + H2O	5.282000E+14	-1.518000E+00	7.414048E+06
66	CH3 + OH ⟷ CH2O + H2	1.650000E+04	9.730000E-01	-8.409840E+06
67	CH3 + OH ⟷ CH2OH + H	4.686000E+07	8.330000E-01	1.492014E+07
68	CH3 + OH ⟷ CH3O + H	1.230000E+06	1.011000E+00	4.999880E+07
69	CH3 + OH ⟷ CH2 + H2O	4.293000E+01	2.568000E+00	1.672680E+07
70	CH3 + HO2 ⟷ CH3O + OH	1.000000E+09	2.690000E-01	-2.876500E+06
71	CH3O2 + O ⟷ CH3O + O2	3.600000E+10	0.000000E+00	0.000000E+00
72	CH3O2 + H ⟷ CH3O + OH	9.600000E+10	0.000000E+00	0.000000E+00
73	CH3O2 + OH ⟷ CH3OH + O2	6.000000E+10	0.000000E+00	0.000000E+00
74	CH3OH (+M) ⟷ CH3 + OH (+M) -4.75E-01 3.56E+04 1.12E+03 9.02E+03	1.500000E+40	-6.995000E+00	4.099994E+08
75	CH3OH (+M) ⟷ CH2(S) + H2O (+M) 2.54E+00 3.29E+03 4.73E+04 4.71E+04	2.084000E+18	-6.150000E-01	3.871899E+08
76	CH3OH (+M) ⟷ CH2OH + H (+M) -7.39E+01 3.70E+04 4.15E+04 5.22E+03	1.430000E+44	-8.227000E+00	4.159611E+08
77	CH3OH + H ⟷ CH3O + H2	3.121000E+18	-1.017000E+00	3.837230E+08
78	CH3OH + H ⟷ CH2OH + H2	3.390000E+39	-7.244000E+00	4.402836E+08
79	CH3OH + O ⟷ CH3O + OH	7.896000E-03	5.038000E+00	3.534116E+08
80	CH3OH + O ⟷ CH2OH + OH	1.990000E+02	2.560000E+00	4.309520E+07
81	CH3OH + OH ⟷ CH3O + H2O	3.070000E+02	2.550000E+00	2.276096E+07
82	CH3OH + OH ⟷ CH2OH + H2O	3.880000E+01	2.500000E+00	1.288672E+07
83	CH3OH + O2 ⟷ CH3O + HO2	3.880000E+02	2.500000E+00	1.288672E+07
84	CH3OH + O2 ⟷ CH2OH + HO2	1.500000E-01	3.030000E+00	-3.192392E+06
85	CH3OH + HO2 ⟷ CH3O + H2O2	3.080000E+01	2.650000E+00	-3.375233E+06
86	CH3OH + HO2 ⟷ CH2OH + H2O2	3.580000E+01	2.270000E+00	1.789267E+08
87	CH3 + CH3OH ⟷ CH2OH + CH4	3.580000E+02	2.270000E+00	1.789267E+08
88	CH3 + CH3OH ⟷ CH3O + CH4	1.220000E+09	0.000000E+00	8.397581E+07
89	CH3OH + HCO ⟷ CH2O + CH2OH	3.260000E+10	0.000000E+00	7.858472E+07
90	CH3O + CH3OH ⟷ CH2OH + CH3OH	2.130000E-04	3.953000E+00	2.951854E+07
91	CH2OH + O2 ⟷ CH2O + HO2	3.220000E+00	2.425000E+00	3.589663E+07
92	CH2OH + O2 ⟷ CH2O + HO2	9.630000E+00	2.900000E+00	5.485224E+07
93	CH2OH + H ⟷ CH2O + H2	3.000000E+08	0.000000E+00	1.704562E+07
94	CH2OH + HO2 ⟷ CH2O + H2O2	1.510000E+12	-1.000000E+00	0.000000E+00
95	CH2OH + OH ⟷ CH2O + H2O	2.410000E+11	0.000000E+00	2.099113E+07
96	CH2OH + O ⟷ CH2O + OH	6.000000E+09	0.000000E+00	0.000000E+00
97	CH3O + O2 ⟷ CH2O + HO2	1.200000E+10	0.000000E+00	0.000000E+00
98	CH3O + H ⟷ CH2O + H2	2.400000E+10	0.000000E+00	0.000000E+00
99	CH3O + HO2 ⟷ CH2O + H2O2	4.200000E+10	0.000000E+00	0.000000E+00
100	CH3 + CH3O ⟷ CH2O + CH4	4.380000E-22	9.500000E+00	-2.301618E+07
101	H + HCO (+M) ⟷ CH2O (+M) 7.82E-01 2.71E+02 2.76E+03 6.57E+03 CH4:2.0E+00 CO:1.5E+00 CO2:2.0E+00 H2:2.0E+00 H2O:6.0E+00	2.000000E+10	0.000000E+00	0.000000E+00
		3.010000E+08	0.000000E+00	0.000000E+00
		1.200000E+10	0.000000E+00	0.000000E+00
		1.350000E+18	-2.570000E+00	5.962200E+06
		1.090000E+09	4.800000E-01	-1.087840E+06

No.	Reaction	A	b	E_a
102	CO + H2 (+M) ⟷ CH2O (+M)	5.070000E+21	-3.420000E+00	3.529120E+08
	9.32E-01 1.97E+02 1.54E+03 1.03E+04	4.300000E+04	1.500000E+00	3.330464E+08
	CH4:2.0E+00 CO:1.5E+00 CO2:2.0E+00 H2:2.0E+00 H2O:6.0E+00			
103	CH2O + O2 ⟷ HCO + HO2	8.070000E+12	0.000000E+00	2.235093E+08
104	CH2O + O ⟷ HCO + OH	6.260000E+06	1.150000E+00	9.455840E+06
105	CH2O + H ⟷ H2 + HCO	5.740000E+04	1.900000E+00	1.146416E+07
106	CH2O + OH ⟷ H2O + HCO	7.820000E+04	1.630000E+00	-4.414120E+06
107	CH2O + HO2 ⟷ H2O2 + HCO	1.880000E+01	2.700000E+00	4.819968E+07
108	CH2O + CH3 ⟷ CH4 + HCO	3.830000E-02	3.360000E+00	1.804141E+07
109	CH2O + CH3O ⟷ CH3OH + HCO	6.620000E+08	0.000000E+00	9.598096E+06
110	HCO + M ⟷ CO + H + M	5.700000E+08	6.600000E-01	6.221608E+07
	CH4:2.00E+00 CO:1.50E+00 CO2:2.00E+00 H2:2.00E+00 H2O:6.00E+00			
111	HCO + O2 ⟷ CO + HO2	7.580000E+09	0.000000E+00	1.715440E+06
112	HCO + O ⟷ CO + OH	3.020000E+10	0.000000E+00	0.000000E+00
113	H + HCO ⟷ CO + H2	7.340000E+10	0.000000E+00	0.000000E+00
114	HCO + OH ⟷ CO + H2O	3.011000E+10	0.000000E+00	0.000000E+00
115	CH3 + HCO ⟷ CH4 + CO	2.650000E+10	0.000000E+00	0.000000E+00
116	HCO + O ⟷ CO2 + H	3.000000E+10	0.000000E+00	0.000000E+00
117	HCO + HO2 ⟶ CO2 + H + OH	3.000000E+10	0.000000E+00	0.000000E+00
118	CH2O + H (+M) ⟷ CH2OH (+M)	1.270000E+26	-4.820000E+00	2.732152E+07
	7.19E-01 1.03E+02 1.29E+03 4.16E+03	5.400000E+08	4.540000E-01	1.506240E+07
	CH4:2.0E+00 CO:1.5E+00 CO2:2.0E+00 H2:2.0E+00 H2O:6.0E+00			
119	CH3O (+M) ⟷ CH2O + H (+M)	1.867000E+22	-3.000000E+00	1.017005E+08
	9.00E-01 2.50E+03 1.30E+03 1.00E+99	6.800000E+13	0.000000E+00	1.094953E+08
	CH4:2.0E+00 CO:1.5E+00 CO2:2.0E+00 H2:2.0E+00 H2O:6.0E+00			
120	2 CH3 (+M) ⟷ C2H6 (+M)	8.054000E+25	-3.750000E+00	4.107014E+06
	0.00E+00 5.70E+02 1.00E+30 1.00E+30	2.277000E+12	-6.900000E-01	7.317816E+05
	CO:2.0E+00 CO2:3.0E+00 H2O:5.0E+00			
121	C2H5 + H (+M) ⟷ C2H6 (+M)	1.990000E+35	-7.080000E+00	2.797004E+07
	8.42E-01 1.25E+02 2.22E+03 6.88E+03	5.210000E+14	-9.900000E-01	6.610720E+06
	C2H6:3.0E+00 CH4:2.0E+00 CO:1.5E+00 CO2:2.0E+00 H2:2.0E+00 H2O:6.0E+00			
122	C2H6 + O2 ⟷ C2H5 + HO2	6.030000E+10	0.000000E+00	2.170241E+08
123	C2H6 + O ⟷ C2H5 + OH	3.550000E+03	2.400000E+00	2.439272E+07
124	C2H6 + H ⟷ C2H5 + H2	1.150000E+05	1.900000E+00	3.150552E+07
125	C2H6 + OH ⟷ C2H5 + H2O	1.480000E+04	1.900000E+00	3.974800E+06
126	C2H6 + HO2 ⟷ C2H5 + H2O2	3.460000E-02	3.610000E+00	7.079328E+07
127	C2H6 + CH2(S) ⟷ C2H5 + CH3	1.200000E+11	0.000000E+00	0.000000E+00
128	C2H6 + CH3 ⟷ C2H5 + CH4	5.550000E-07	4.720000E+00	1.351850E+07
129	C2H6 + CH3O ⟷ C2H5 + CH3OH	2.410000E+08	0.000000E+00	2.966456E+07
130	C2H4 + H (+M) ⟷ C2H5 (+M)	1.419000E+33	-6.642000E+00	2.413750E+07
	-5.69E-01 2.99E+02 -9.15E+03 1.52E+02	9.569000E+05	1.463000E+00	5.669320E+06
	CH4:2.0E+00 CO:1.5E+00 CO2:2.0E+00 H2:2.0E+00 H2O:6.0E+00			

No.	Reaction	A	b	E_a
131	C2H5 + H ⟷ C2H4 + H2	2.000000E+09	0.000000E+00	0.000000E+00
132	C2H5 + CH3 ⟷ C2H4 + CH4	1.180000E+01	2.450000E+00	-1.222146E+07
133	2 CH3 ⟷ C2H5 + H	3.100000E+11	-3.620000E-01	5.595054E+07
134	C2H5 + O2 ⟷ C2H4 + HO2	1.843000E+04	1.130000E+00	-3.014990E+06
135	C2H3 + H (+M) ⟷ C2H4 (+M)	1.400000E+24	-3.860000E+00	1.389088E+07
	7.82E-01 2.07E+02 2.66E+03 6.10E+03	6.080000E+09	2.700000E-01	1.171520E+06
	CH4:2.0E+00 CO:1.5E+00 CO2:2.0E+00 H2:2.0E+00 H2O:6.0E+00			
136	C2H4 + M ⟷ C2H2 + H2 + M	2.610000E+13	0.000000E+00	2.837714E+08
	CH4:2.00E+00 CO:1.50E+00 CO2:2.00E+00 H2:2.00E+00 H2O:6.00E+00			
137	C2H4 + O2 ⟷ C2H3 + HO2	4.220000E+10	0.000000E+00	2.410951E+08
138	C2H4 + H ⟷ C2H3 + H2	5.070000E+04	1.930000E+00	5.418280E+07
139	C2H4 + OH ⟷ C2H3 + H2O	2.230000E+01	2.745000E+00	9.269652E+06
140	C2H4 + CH3O ⟷ C2H3 + CH3OH	1.200000E+08	0.000000E+00	2.824200E+07
141	C2H4 + CH3 ⟷ C2H3 + CH4	9.760000E-01	2.947000E+00	6.337923E+07
142	C2H4 + CH3 ⟷ C2H3 + CH4	8.130000E-08	4.417000E+00	3.696899E+07
143	C2H4 + O ⟷ CH3 + HCO	7.453000E+03	1.880000E+00	7.656720E+05
144	CH + CH4 ⟷ C2H4 + H	6.000000E+10	0.000000E+00	0.000000E+00
145	CH2(S) + CH3 ⟷ C2H4 + H	2.000000E+10	0.000000E+00	0.000000E+00
146	C2H4 + OH ⟷ CH2O + CH3	1.780000E+02	1.680000E+00	8.621132E+06
147	C2H2 + H (+M) ⟷ C2H3 (+M)	6.346000E+25	-4.664000E+00	1.581552E+07
	7.88E-01 -1.02E+04 1.00E-30 0.00E+00	1.710000E+07	1.266000E+00	1.133446E+07
	CH4:2.0E+00 CO:1.5E+00 CO2:2.0E+00 H2:2.0E+00 H2O:6.0E+00			
148	C2H3 + O2 ⟷ C2H2 + HO2	2.150000E+04	1.190000E+00	1.408753E+07
149	C2H3 + O2 ⟷ C2H2 + HO2	4.600000E-02	2.760000E+00	-2.061875E+06
150	C2H3 + O2 ⟷ CH2CO + OH	1.060000E+00	2.390000E+00	2.585712E+07
151	C2H3 + O2 ⟷ CH2CO + OH	5.260000E-04	3.010000E+00	7.434968E+06
152	C2H3 + O2 ⟷ CH2O + HCO	2.730000E+32	-7.320000E+00	4.945488E+07
153	C2H3 + O2 ⟷ CH2O + HCO	6.080000E+12	-1.310000E+00	2.701609E+06
154	C2H3 + O2 ⟶ CH2O + CO + H	6.360000E+32	-7.320000E+00	4.945488E+07
155	C2H3 + O2 ⟶ CH2O + CO + H	1.420000E+13	-1.310000E+00	2.701609E+06
156	C2H3 + O2 ⟷ CH3O + CO	1.030000E+08	-3.300000E-01	-3.128795E+06
157	C2H3 + O2 ⟷ CH3O + CO	5.770000E+18	-3.540000E+00	1.996605E+07
158	C2H3 + O2 ⟷ CH3 + CO2	7.250000E+28	-6.700000E+00	4.368096E+07
159	C2H3 + O2 ⟷ CH3 + CO2	5.320000E+10	-1.140000E+00	1.868993E+06
160	C2H3 + H ⟷ C2H2 + H2	9.635250E+10	0.000000E+00	0.000000E+00
161	C2H3 + OH ⟷ C2H2 + H2O	3.011000E+10	0.000000E+00	0.000000E+00
162	C2H3 + CH3 ⟷ C2H2 + CH4	3.920000E+08	0.000000E+00	0.000000E+00
163	C2H2 + O ⟷ CH2 + CO	7.395000E+05	1.280000E+00	1.034285E+07
164	C2H2 + O ⟷ H + HCCO	2.958000E+06	1.280000E+00	1.034285E+07
165	C2H2 + HO2 ⟷ CH2CO + OH	6.030000E+06	0.000000E+00	3.325862E+07
166	C2H2 + HCO ⟷ C2H3 + CO	1.000000E+04	2.000000E+00	2.510400E+07
167	C2H2 + OH ⟷ CH2CO + H	7.528000E+03	1.550000E+00	8.811504E+06

No.	Reaction	A	b	E_a
168	C2H2 + OH ⟷ CH3 + CO	1.277000E+06	7.300000E-01	1.079054E+07
169	CH2CO (+M) ⟷ CH2 + CO (+M)	3.000000E+12	0.000000E+00	2.384880E+08
		3.000000E+13	0.000000E+00	2.970640E+08
	CH4:2.0E+00 CO:1.5E+00 CO2:2.0E+00 H2:2.0E+00 H2O:6.0E+00			
170	C2H3 + O ⟷ CH2CO + H	3.000000E+10	0.000000E+00	0.000000E+00
171	CH2CO + H ⟷ CH3 + CO	7.770000E+05	1.450000E+00	1.163152E+07
172	CH3 + HCO ⟷ CH2CO + H2	4.900000E+05	7.500000E-01	3.522928E+06
173	CH + CH2O ⟷ CH2CO + H	9.460000E+10	0.000000E+00	-2.154760E+06
174	CH2CO + O ⟷ CH2 + CO2	1.750000E+09	0.000000E+00	5.648400E+06
175	CH2CO + OH ⟷ CH2OH + CO	2.000000E+09	0.000000E+00	-4.225840E+06
176	CH2CO + CH3 ⟷ C2H5 + CO	4.769000E+01	2.312000E+00	3.961411E+07
177	HCCO + OH ⟶ 2 CO + H2	1.000000E+11	0.000000E+00	0.000000E+00
178	HCCO + O ⟶ 2 CO + H	8.000000E+10	0.000000E+00	0.000000E+00
179	CH + CO + M ⟷ HCCO + M	7.570000E+16	-1.900000E+00	0.000000E+00
180	H + HCCO ⟷ CH2(S) + CO	1.000000E+11	0.000000E+00	0.000000E+00
181	HCCO + O2 ⟶ 2 CO + OH	1.910000E+08	-2.000000E-02	4.267680E+06
182	HCCO + O2 ⟶ CO + CO2 + H	4.780000E+09	-1.420000E-01	4.811600E+06
183	C2H4 + CH2(S) ⟷ C2H3 + CH3	4.160000E+21	-3.190000E+00	4.083584E+07
184	C2H4 + CH2(S) ⟷ C2H3 + CH3	4.920000E+06	1.020000E+00	2.509438E+06
185	C2H3 + CH2O ⟷ C2H4 + HCO	1.420000E+07	2.090000E-01	1.646069E+07
186	C2H2 + O ⟶ CH2CO	1.000000E+10	0.000000E+00	6.276000E+07
187	CH2CO + O ⟶ 2 HCO	2.000000E+10	0.000000E+00	9.623200E+06
188	CH2CO + O ⟶ CH2O + CO	1.000000E+09	0.000000E+00	2.092000E+07
189	CH2CO + OH ⟶ CH3 + CO2	1.000000E+10	0.000000E+00	0.000000E+00
190	CH2CO + O2 ⟶ CH2O + CO2	1.000000E+11	0.000000E+00	1.548080E+08
191	CH2CO + O2 ⟶ CO + HCO + OH	3.000000E+11	0.000000E+00	1.673600E+08
192	CH2CO + HO2 ⟶ CH2O + CO + OH	1.000000E+07	0.000000E+00	2.092000E+07
193	CH2CO ⟶ H + HCCO	1.500000E+14	0.000000E+00	4.284416E+08
194	HCCO + OH ⟷ CO + H + HCO	1.000000E+10	0.000000E+00	0.000000E+00
195	HCCO + O2 ⟷ CO2 + HCO	2.400000E+08	0.000000E+00	-3.573136E+06
196	C2H2 + O2 ⟷ HCCO + OH	2.000000E+04	1.500000E+00	1.255200E+08
197	C2H5 + CH2O ⟷ C2H6 + HCO	1.839000E+02	2.000000E+00	2.475710E+07
198	C2H3 + CH3OH ⟷ C2H4 + CH2OH	2.035000E+02	2.000000E+00	3.311259E+07
199	C2H5 + CH3OH ⟷ C2H6 + CH2OH	6.895000E+01	2.000000E+00	4.403898E+07
200	CH2CO + H ⟶ H2 + HCCO	1.500000E+11	0.000000E+00	5.910565E+07
201	CH2CO + CH3 ⟶ CH4 + HCCO	2.500000E+09	0.000000E+00	6.333664E+07
202	CH2CO + O2 ⟶ HCCO + HO2	7.454000E+03	2.000000E+00	2.141071E+08
203	CH2CO + OH ⟶ H2O + HCCO	1.747000E+03	2.000000E+00	7.107947E+06
204	CH2CO + O ⟶ HCCO + OH	5.921000E+03	2.000000E+00	3.564722E+07
205	CH2CO + HO2 ⟶ H2O2 + HCCO	2.357000E+02	2.000000E+00	8.285462E+07
206	O + OH + M ⟷ HO2 + M	1.000000E+10	0.000000E+00	0.000000E+00
207	CO + H2O ⟷ CO2 + H2	2.000000E+08	0.000000E+00	1.589920E+08

No.	Reaction	A	b	E_a
208	CH + OH ⟷ C + H2O	4.000000E+04	2.000000E+00	1.255200E+07
209	C2H5 + O2 ⟶ CH2O + CH3O	1.000000E+11	0.000000E+00	1.004160E+08
210	C2H5 + O2 ⟶ CH2O + CH3 + O	1.000000E+10	0.000000E+00	1.129680E+08
211	C2H5 + HO2 ⟶ CH2O + CH3 + OH	5.000000E+09	0.000000E+00	0.000000E+00
212	CH3O2 ⟷ CH2O + OH	1.500000E+13	0.000000E+00	1.966480E+08
213	CH3O2 + OH ⟶ CH3O + HO2	3.000000E+09	0.000000E+00	0.000000E+00
214	CH3O2 + HO2 ⟶ CH2O + H2O + O2	5.000000E+07	0.000000E+00	0.000000E+00
215	CH2O + CH3O2 ⟶ CH2O + CO + H2 + OH	2.000000E+08	0.000000E+00	4.602400E+07
216	CH3O2 + CO ⟶ CH3O + CO2	1.000000E+11	0.000000E+00	1.004160E+08
217	CH2 + O ⟷ CO + H2	5.000000E+10	0.000000E+00	0.000000E+00
218	CH2 + OH ⟷ CH2O + H	3.000000E+10	0.000000E+00	0.000000E+00
219	CH2 + CO2 ⟷ CH2O + CO	1.100000E+08	0.000000E+00	4.184000E+06
220	CH2(S) + O ⟷ CO + 2 H	3.000000E+10	0.000000E+00	0.000000E+00
221	CH + CH3 ⟷ C2H3 + H	3.000000E+10	0.000000E+00	0.000000E+00
222	C + CH3 ⟷ C2H2 + H	5.000000E+10	0.000000E+00	0.000000E+00
223	CH2(S) + CH4 ⟷ 2 CH3	4.300000E+10	0.000000E+00	0.000000E+00
224	2 CH3 ⟶ C2H4 + H2	5.000000E+11	0.000000E+00	1.338880E+08
225	C2H6 ⟷ C2H4 + H2	3.000000E+13	0.000000E+00	3.284440E+08
226	CH3OH + H ⟶ CH3 + H2O	6.500000E+08	0.000000E+00	2.217520E+07
227	CH2O + O ⟶ CO2 + 2 H	2.000000E+10	0.000000E+00	2.092000E+07
228	CH2O + OH ⟶ CO2 + H + H2	1.000000E+08	0.000000E+00	0.000000E+00
229	C2H2 + HO2 ⟶ CH2O + HCO	5.000000E+09	0.000000E+00	6.276000E+07
230	CH2O + HCO ⟷ CH3 + CO2	5.000000E+08	0.000000E+00	2.510400E+07
231	C2H3 + CH2O ⟶ C2H2 + 0.5 CH2OH + 0.5 CH3O	5.000000E+08	0.000000E+00	2.510400E+07
232	CH3O + CO ⟷ CH3 + CO2	5.000000E+08	0.000000E+00	2.719600E+07
233	C2H2 + O2 ⟶ CH2O + CO	3.000000E+08	0.000000E+00	1.087840E+08
234	C2H4 + O2 ⟶ 2 CH2O	1.000000E+11	0.000000E+00	2.008320E+08
235	C2H2 + O2 ⟶ 2 HCO	3.000000E+08	0.000000E+00	1.129680E+08
236	C2H4 + O2 ⟶ CH3O + HCO	1.000000E+11	0.000000E+00	1.799120E+08
237	CH3 + O + M ⟶ CH3O + M	5.000000E+10	0.000000E+00	0.000000E+00
238	HCO + HO2 ⟷ CO + H2O2	4.000000E+08	0.000000E+00	0.000000E+00
239	CH3O + OH ⟶ CH2O + H2O	1.500000E+10	0.000000E+00	0.000000E+00
240	CH2OH + CH3 ⟶ CH2O + CH4	1.500000E+10	0.000000E+00	0.000000E+00
241	C2H3 + C2H6 ⟷ C2H4 + C2H5	6.105000E+02	2.000000E+00	3.192066E+07
242	C2H6 + HCCO ⟶ C2H5 + CH2CO	3.852000E+02	2.000000E+00	3.357898E+07
243	C2H4 + O ⟷ C2H3 + OH	1.083000E+04	2.000000E+00	3.674372E+07
244	C2H4 + HO2 ⟷ C2H3 + H2O2	4.310000E+02	2.000000E+00	8.302897E+07
245	C2H4 + HCCO ⟶ C2H3 + CH2CO	3.424000E+02	2.000000E+00	5.087752E+07

Bibliography

[1] BP, Statistical Review of World Energy globally consistent data on world energy markets, 2020. 2, 3

[2] V. Smil, Energy transitions: global and national perspectives, ABC-CLIO, 2016. 2, 3

[3] U.S. Energy Information Administration, April 2021 Monthly Energy Review, Vol. 26, 2021. 3

[4] International Energy Agency, Global Energy Review: The impacts of the Covid-19 crisis on global energy demand and CO2 emissions, 2021. 4, 5

[5] International Energy Agency, Net Zero by 2050 - A Roadmap for the Global Energy, 2021. 4

[6] McKinsey & Company, Hydrogen-powered aviation: a fact-based study of hydrogen technology, economics, and climate impact by 2050, 2020. 7, 8, 9, 10, 11

[7] E. R. Hawkes, J. H. Chen, Direct numerical simulation of hydrogen-enriched lean premixed methane-air flames, Combust. Flame 138 (3) (2004) 242–258. 11, 220

[8] P. Strakey, T. Sidwell, J. Ontko, Investigation of the effects of hydrogen addition on lean extinction in a swirl stabilized combustor, Proceedings of the Combustion Institute 31 (2) (2007) 3173–3180. 11, 220

[9] T. Lieuwen, H. Torres, C. Johnson, B. T. Zinn, A mechanism of combustion instability in lean premixed gas turbine combustors, J. Eng. Gas Turbines Power 123 (1) (2000) 182–189. 12, 220

[10] J. Lee, D. Santavicca, Experimental diagnostics for the study of combustion instabilities in lean premixed combustors, Journal of propulsion and power 19 (5) (2003) 735–750. 12, 220

[11] T. Lieuwen, V. Yang (Eds.), Combustion instabilities in gas turbine engines: operational experience, fundamental mechanisms and modeling, Progress in astronautics and aeronautics, American Institute of Aeronautics and Astronautics, Reston, VA, USA, 2005. 12, 15, 100, 134, 156, 181, 220

[12] A. Dowling, S. Hubbard, Instability in lean premixed combustors, Proceedings of the Institution of Mechanical Engineers, Part A: Journal of Power and Energy 214 (4) (2000) 317–332. 12, 220

[13] W.-P. Shih, J. G. Lee, D. A. Santavicca, Stability and emissions characteristics of a lean premixed gas turbine combustor, in: Symposium (International) on Combustion, Vol. 26, Elsevier, 1996, pp. 2771–2778. 12, 220

[14] Y. Sommerer, D. Galley, T. Poinsot, S. Ducruix, F. Lacas, D. Veynante, Large eddy simulation and experimental study of flashback and blow-off in a lean partially premixed swirled burner, J. Turbul. 5 (37) (2004) 1–3. 12, 15, 41, 180, 220

[15] L. Esclapez, P. C. Ma, E. Mayhew, R. Xu, S. Stouffer, T. Lee, H. Wang, M. Ihme, Fuel effects on lean blow-out in a realistic gas turbine combustor, Combust. Flame 181 (2017) 82–99. 12, 15, 41, 180, 220, 246

[16] F. Rebosio, A. Widenhorn, B. Noll, M. Aigner, Numerical simulation of a gas turbine model combustor operated near the lean extinction limit, in: ASME Turbo Expo, American Society of Mechanical Engineers Digital Collection, 2010, pp. 603–612. 12, 41, 180, 220

[17] M. Stöhr, I. Boxx, C. Carter, W. Meier, Dynamics of lean blowout of a swirl-stabilized flame in a gas turbine model combustor, Proc. Combust. Inst. 33 (2011) 2953–2960. 12, 220, 244, 259

[18] N. Savary, G. Taliercio, The safran helicopter engine spinning flame combustor concept to meet customer needs, 42nd European Rotorcraft Forum September 5-8, 2016, Lille, France. 14, 220, 244

[19] L. Y. Gicquel, G. Staffelbach, T. Poinsot, Large eddy simulations of gaseous flames in gas turbine combustion chambers, Prog. Energ. Combust. 38 (2012) 782–817. 14, 18, 41, 81, 136, 180, 182, 220, 221

[20] Y. Huang, V. Yang, Effect of swirl on combustion dynamics in a lean-premixed swirl-stabilized combustor, Proceedings of the Combustion Institute 30 (2) (2005) 1775–1782. 14, 221

[21] B. Ariatabar, R. Koch, H.-J. Bauer, D.-A. Negulescu, Short Helical Combustor: Concept Study of an Innovative Gas Turbine Combustor With Angular Air Supply, Journal of Engineering for Gas Turbines and Power 138. 14, 221

[22] Investigation of Adjacent Lifted Flames Interaction in an Inline and Inclined Multi-Burner Arrangement, Vol. Volume 3B: Combustion, Fuels, and Emissions of Turbo Expo: Power for Land, Sea, and Air. 14, 221

[23] P. Wolf, G. Staffelbach, A. Roux, L. Gicquel, T. Poinsot, V. Moureau, Massively parallel les of azimuthal thermo-acoustic instabilities in annular gas turbines, Comptes Rendus Mécanique 337 (2009) 385–394. 15, 41, 136, 180

[24] E. Lo Schiavo, D. Laera, E. Riber, L. Gicquel, T. Poinsot, Effects of liquid fuel/wall interaction on thermoacoustic instabilities in swirling spray flames, Combust. Flame 219 (2020) 86–101. 15, 41, 87, 92, 136, 180

[25] P. W. Agostinelli, D. Laera, I. Chterev, I. Boxx, L. Gicquel, T. Poinsot, On the impact of h2-enrichment on flame structure and combustion dynamics of a lean partially-premixed turbulent swirling flame, Combust. Flame 241 (2022) 112120. 15, 134, 181, 183, 184, 187, 253, 255

[26] P. C. Nassini, D. Pampaloni, R. Meloni, A. Andreini, Lean blow-out prediction in an industrial gas turbine combustor through a LES-based CFD analysis, Combust. Flame 229 (2021) 111391. 15, 246, 261, 278

[27] W. Meier, P. Weigand, X. R. Duan, R. Giezendanner-Thoben, Detailed characterization of the dynamics of thermoacoustic pulsations in a lean premixed swirl flame, Combust. Flame 150 (2007) 2–26. 15, 43, 68, 69, 70, 71, 87, 88, 93, 96, 97, 100, 102, 137, 138, 141, 154, 165, 182, 185, 203

[28] I. Chterev, N. Rock, H. Ek, B. Emerson, J. Seitzman, N. Jiang, S. Roy, T. Lee, J. Gord, T. Lieuwen, Simultaneous imaging of fuel, OH, and three component velocity fields in high pressure, liquid fueled, swirl stabilized flames at 5kHz, Combust. Flame 186 (2017) 150–165. 15, 182

[29] S. Dhanuka, J. Driscoll, H. Mongia, Instantaneous flow structures in a reacting gas turbine combustor, in: 44th AIAA/ASME/SAE/ASEE Joint Propulsion Conference & Exhibit, 2008, p. 4683. 15, 181

[30] T. Poinsot, S. Lele, Boundary conditions for direct simulations of compressible viscous flows, J. Comput. Phys. 101 (1992) 104–129. 17, 34, 35, 46, 54, 90, 100, 122, 141, 187, 226, 252, 290

[31] P. Sagaut, Large eddy simulation for incompressible flows: an introduction, Springer Science & Business Media, 2006. 17, 28, 46

[32] U. Piomelli, Large-eddy simulation: achievements and challenges, Prog. Aerosp. Sci. 35 (4) (1999) 335–362. 17, 28, 41

[33] P. Wolf, R. Balakrishnan, G. Staffelbach, L. Y. Gicquel, T. Poinsot, Using les to study reacting flows and instabilities in annular combustion chambers, Flow Turbul. Combust. 88 (1-2) (2012) 191–206. 18, 41, 220

[34] J. Lamouroux, S. Richard, Q. Malé, G. Staffelbach, A. Dauptain, A. Misdariis, On the combination of large eddy simulation and phenomenological soot modelling to calculate the smoke index from aero-engines over a large range of operating conditions, in: ASME Turbo Expo 2017: Turbomachinery Technical Conference and Exposition, American Society of Mechanical Engineers Digital Collection, 2017. 18, 220

[35] H. Pitsch, Improved pollutant predictions in large-eddy simulations of turbulent non-premixed combustion by considering scalar dissipation rate fluctuations, Proc. Combust. Inst. 29 (2) (2002) 1971–1978. 18, 41, 220

[36] A. Felden, L. Esclapez, E. Riber, B. Cuenot, H. Wang, Including real fuel chemistry in LES of turbulent spray combustion, Combust. Flame 193 (2018) 397–416. 18, 41, 220

[37] T. Jaravel, E. Riber, B. Cuenot, G. Bulat, Large Eddy Simulation of an industrial gas turbine combustor using reduced chemistry with accurate pollutant prediction, Proc. Combust. Inst. 36 (3) (2017) 3817–3825. 18, 122, 182, 220

[38] T. Poinsot, D. Veynante, Theoretical and numerical combustion, RT Edwards, Inc., 2005. 23, 27, 28, 190, 245, 254, 277, 278

[39] K. K. Kuo, R. Acharya, Fundamentals of turbulent and multiphase combustion, John Wiley & Sons, 2012. 24

[40] K. K. Kuo, Principles of combustion, Wiley, 2005. 25, 26

[41] W. Sutherland, LII. The viscosity of gases and molecular force , London, Edinburgh, Dublin Philos. Mag. J. Sci. 36 (223) (1893) 507–531. 25

[42] A. Ern, V. Giovangigli, Multicomponent transport algorithms, Vol. 24, Springer Science & Business Media, 1994. 27

[43] A. Ern, V. Giovangigli, Impact of detailed multicomponent transport on planar and counterflow hydrogen/air and methane/air flames, Combust. Sci. Technol. 149 (1) (1999) 157–181. 27

[44] J. O. Hirschfelder, C. F. Curtiss, R. B. Bird, Molecular theory of gases and liquids, 1964. 27

[45] S. B. Pope, Turbulent flows (2001). 28, 42, 189

[46] F. Nicoud, H. B. Toda, O. Cabrit, S. Bose, J. Lee, Using singular values to build a subgrid-scale model for large eddy simulations, Phys. Fluids 23 (2011) 085106. 30, 31, 90, 186, 251, 290

[47] B. Rochette, F. Collin-Bastiani, L. Gicquel, O. Vermorel, D. Veynante, T. Poinsot, Influence of chemical schemes, numerical method and dynamic turbulent combustion modeling on LES of premixed turbulent flames, Combust. Flame 191 (2018) 417–430. 31, 36, 37, 43, 49, 55, 60, 64, 253

[48] O. Colin, M. Rudgyard, Development of High-Order Taylor-Galerkin Schemes for LES, J. Comput. Phys. 162 (2000) 338–371. 31, 90, 186, 225, 251, 290

[49] O. Colin, F. Ducros, D. Veynante, T. Poinsot, A thickened flame model for large eddy simulations of turbulent premixed combustion, Phys. Fluids 12 (7) (2000) 1843–1863. 31, 35, 49, 277

[50] V. Moureau, P. Domingo, L. Vervisch, Design of a massively parallel cfd code for complex geometries, Comptes Rendus Mécanique 339 (2-3) (2011) 141–148. 32

[51] G. Chen, Q. Xiong, P. J. Morris, E. G. Paterson, A. Sergeev, Y. Wang, Openfoam for computational fluid dynamics, Not. AMS 61 (4) (2014) 354–363. 32

[52] COMSOL Multiphysics, Introduction to comsol multiphysics®, COMSOL Multiphysics, Burlington, MA, accessed Feb 9 (1998) 2018. 32

[53] F. Nicoud, L. Benoit, C. Sensiau, T. Poinsot, Acoustic modes in combustors with complex impedances and multidimensional active flames, AIAA J. 45 (2007) 426–441. 32, 111, 164, 201

[54] F. Duchaine, A. Corpron, L. Pons, V. Moureau, F. Nicoud, T. Poinsot, International Journal of Heat and Fluid Flow Development and assessment of a coupled strategy for conjugate heat transfer with Large Eddy Simulation : Application to a cooled turbine blade, Int. J. Heat Fluid Flow 30 (2009) 1129–1141. 32, 35, 38, 102, 247, 254

[55] F. Duchaine, S. Mendez, F. Nicoud, A. Corpron, Conjugate heat transfer with Large Eddy Simulation for gas turbine components, Comptes Rendus Mécanique 337 (2009) 550–561. 32, 35, 38, 102, 247, 254

[56] G. I. Taylor, A. E. Green, Mechanism of the production of small eddies from large ones, Proc. R. Soc. London. Ser. A - Math. Phys. Sci. 158 (895) (1937) 499–521. 32

[57] S. Laizet, E. Lamballais, High-order compact schemes for incompressible flows: A simple and efficient method with quasi-spectral accuracy, J. Comput. Phys. 228 (16) (2009) 5989–6015. 33

[58] A. Abdelsamie, G. Fru, T. Oster, F. Dietzsch, G. Janiga, D. Thévenin, Towards direct numerical simulations of low-Mach number turbulent reacting and two-phase flows using immersed boundaries, Comput. Fluids 131 (2016) 123–141. 33

[59] P. W. Agostinelli, D. Laera, I. Boxx, L. Gicquel, T. Poinsot, Impact of wall heat transfer in Large Eddy Simulation of flame dynamics in a swirled combustion chamber, Combust. Flame 234 (2021) 111728. 35, 39, 84, 137, 139, 141, 142, 143, 144, 145, 172, 187, 188, 202, 246, 247, 254, 255, 256, 278

[60] T. Butler, P. O'rourke, A numerical method for two dimensional unsteady reacting flows 16 (1) (1977) 1503–1515. 35, 49

[61] F. Charlette, D. Veynante, C. Meneveau, A power-law wrinkling model for LES of premixed turbulent combustion: Part I - non-dynamic formulation and initial tests, Combust. Flame 131 (2002) 159–180. 35, 49, 54, 91, 140, 187, 225, 252, 277, 290

[62] F. Charlette, C. Meneveau, D. Veynante, A Power-Law Flame Wrinkling Model for LES of Premixed Turbulent Combustion Part II: Dynamic Formulation, Combust. Flame 197 (2002) 181–197. 35, 49, 140, 187, 252

[63] G. Kuenne, A. Ketelheun, J. Janicka, LES modeling of premixed combustion using a thickened flame approach coupled with FGM tabulated chemistry, Combust. Flame 158 (9) (2011) 1750 – 1767. 35, 49

[64] J. P. Legier, T. Poinsot, D. Veynante, Dynamically thickened flame LES model for premixed and non-premixed turbulent combustion, Proc. Summer Program, Cent. Turbul. Res. (2000) 157–168. 35, 49, 91, 140, 187, 247, 252, 290

[65] Q. Cazères, P. Pepiot, E. Riber, B. Cuenot, A fully automatic procedure for the analytical reduction of chemical kinetics mechanisms for computational fluid dynamics applications, Fuel 303 (2021) 121247. 37, 140, 187, 253, 324

[66] C. Kraus, L. Selle, T. Poinsot, Coupling heat transfer and large eddy simulation for combustion instability prediction in a swirl burner, Combust. Flame 191 (2018) 239–251. 38, 84, 86, 95, 104, 137, 247, 255

[67] I. Chterev, I. Boxx, Effect of hydrogen enrichment on the dynamics of a lean technically premixed elevated pressure flame, Combust. Flame 225 (2021) 149–159. 38, 39, 134, 136, 163, 181, 183, 184, 185, 186, 198, 200, 214

[68] T. Hussain, M. Talibi, R. Balachandran, Investigating the effect of local addition of hydrogen to acoustically excited ethylene and methane flames, Int. J. Hydrogen Energy 44 (2019) 11168–11184. 38, 134, 163, 181

[69] S. Barbosa, M. C. De La Garcia, S. Ducruix, B. Labegorre, F. Lacas, Control of combustion instabilities by local injection of hydrogen, Proc. Combust. Inst. 31 (2007) 3207–3214. 38, 134, 163, 181

[70] P. W. Agostinelli, B. Rochette, D. Laera, J. Dombard, B. Cuenot, L. Gicquel, Static mesh adaptation for reliable large eddy simulation of turbulent reacting flows, Phys. Fluids 33 (2021) 035141. 39, 41, 90, 91, 140, 172, 191, 252

[71] D. Laera, P. W. Agostinelli, L. Selle, Q. Cazères, G. Oztarlik, T. Schuller, L. Gicquel, T. Poinsot, Stabilization mechanisms of CH4 premixed swirled flame enriched with a non-premixed hydrogen injection, Proc. Combust. Inst. 38 (2021) 6355–6363. 39, 71, 87, 91, 92, 119, 122, 136, 187, 253

[72] C. Yu, Z. Xiao, X. Li, Scale-adaptive subgrid-scale modelling for large-eddy simulation of turbulent flows, Phys. Fluids 29 (3) (2017) 035101. 41

[73] M. H. Silvis, R. A. Remmerswaal, R. Verstappen, Physical consistency of subgrid-scale models for large-eddy simulation of incompressible turbulent flows, Phys. Fluids 29 (1) (2017) 015105. 41

[74] S. Roux, G. Lartigue, T. Poinsot, U. Meier, C. Bérat, Studies of mean and unsteady flow in a swirled combustor using experiments, acoustic analysis, and large eddy simulations, Combust. Flame 141 (2005) 40–54. 41, 69, 84, 87

[75] V. Moureau, P. Domingo, L. Vervisch, From large-eddy simulation to direct numerical simulation of a lean premixed swirl flame: Filtered laminar flame-pdf modeling, Combust. Flame 158 (2011) 1340–1357. 41, 69, 84, 87

[76] Y. Huang, H. G. Sung, S. Y. Hsieh, V. Yang, Large-Eddy Simulation of Combustion Dynamics of Lean-Premixed Swirl-Stabilized Combustor, J. Propuls. Power 19 (5) (2003) 782–794. 41, 84, 86, 137

[77] P. W. Agostinelli, Y. H. Kwah, S. Richard, G. Exilard, J. R. Dawson, L. Gicquel, T. Poinsot, Numerical and experimental flame stabilization analysis in the new spinning combustion technology framework, ASME Turbo Expo 2020, Paper No. GT2020-15035, p. V04AT04A058 (13 pages). 41, 43, 84, 87, 136, 180, 220, 244, 247, 250, 252, 263

[78] H. Lu, W. Chen, C. Zou, H. Yao, Large-eddy simulation of Sandia Flame F using structural subgrid-scale models and partially-stirred-reactor approach, Phys. Fluids 31 (4) (2019) 045109. 41

[79] H. Choi, P. Moin, Grid-point requirements for large eddy simulation: Chapman's estimates revisited, Phys. Fluids 24 (1) (2012) 011702. 41

[80] S. Rezaeiravesh, M. Liefvendahl, Effect of grid resolution on large eddy simulation of wall-bounded turbulence, Phys. Fluids 30 (5) (2018) 055106. 41

[81] X. I. A. Yang, K. P. Griffin, Grid-point and time-step requirements for direct numerical simulation and large-eddy simulation, Phys. Fluids 33 (1) (2021) 015108. 41

[82] G. Boudier, L. Gicquel, T. Poinsot, Effects of mesh resolution on large eddy simulation of reacting flows in complex geometry combustors, Combust. Flame 155 (1-2) (2008) 196–214. 41, 182

[83] K. M. Almohammadi, D. B. Ingham, L. Ma, M. Pourkashan, Computational fluid dynamics (CFD) mesh independency techniques for a straight blade vertical axis wind turbine, Energy 58 (2013) 483–493. 41

[84] P.-J. Frey, F. Alauzet, Anisotropic mesh adaptation for cfd computations, Comput. Methods in Appl. Mech. Eng. 194 (48-49) (2005) 5068–5082. 41, 42

[85] A. Loseille, A. Dervieux, F. Alauzet, Fully anisotropic goal-oriented mesh adaptation for 3d steady euler equations, J. Comput. Phys. 229 (8) (2010) 2866–2897. 41

[86] C. Hertel, J. Fröhlich, Error reduction in les via adaptive moving grids, in: Quality and Reliability of Large-Eddy Simulations II, Springer, 2011, pp. 309–318. 42

[87] M. Rai, D. Anderson, The use of adaptive grids in conjunction with shock capturing methods, in: 5th Computational Fluid Dynamics Conference, 1981, p. 1012. 42

[88] M. J. Berger, J. Oliger, Adaptive mesh refinement for hyperbolic partial differential equations, J. Comput. Phys. 53 (3) (1984) 484–512. 42

[89] E. Pomraning, K. Richards, P. Senecal, Modeling turbulent combustion using a rans model, detailed chemistry, and adaptive mesh refinement, Tech. rep., SAE Technical Paper (2014). 42

[90] N. A. Pierce, M. B. Giles, Adjoint and defect error bounding and correction for functional estimates, J. Comput. Phys. 200 (2) (2004) 769–794. 42

[91] J.-D. Müller, M. Giles, Solution adaptive mesh refinement using adjoint error analysis, in: 15th AIAA Computational Fluid Dynamics Conference, 2001, p. 2550. 42

[92] D. A. Venditti, D. L. Darmofal, Grid adaptation for functional outputs: application to two-dimensional inviscid flows, J. Comput. Phys. 176 (1) (2002) 40–69. 42

[93] K. J. Fidkowski, D. L. Darmofal, Review of output-based error estimation and mesh adaptation in computational fluid dynamics, AIAA J. 49 (4) (2011) 673–694. 42

[94] W. N. Dawes, The Simulation of Three-Dimensional Viscous Flow in Turbomachinery Geometries Using a Solution-Adaptive Unstructured Mesh Methodology, J. Turbomach. 114 (3) (1992) 528–537. 42

[95] Z. Ali, P. G. Tucker, Multiblock structured mesh generation for turbomachinery flows, in: Proceedings of the 22nd International Meshing Roundtable, Springer, 2014, pp. 165–182. 42

[96] Z. Ali, P. C. Dhanasekaran, P. G. Tucker, R. Watson, S. Shahpar, Optimal multi-block mesh generation for cfd, Int J Comut Fluid Dyn 31 (4-5) (2017) 195–213. 42

[97] L. Frazza, A. Loseille, F. Alauzet, Anisotropic mesh adaptation for turbomachinery applications, in: 23rd AIAA Computational Fluid Dynamics Conference, 2017, p. 3299. 42

[98] G. Vivarelli, N. Qin, S. Shahpar, Combined hessian and adjoint error-based anisotropic mesh adaptation for turbomachinery flows, in: 55th AIAA Aerospace Sciences Meeting, 2017, p. 1946. 42

[99] G. Vivarelli, N. Qin, S. Shahpar, D. Radford, Efficient adjoint-based mesh adaptation applied to turbo-machinery flows, in: Turbo Expo: Power for Land, Sea, and Air, Vol. 51012, American Society of Mechanical Engineers, 2018, p. V02CT42A049. 42

[100] J. Gou, X. Yuan, X. Su, Adaptive mesh refinement method based investigation of the interaction between shock wave, boundary layer, and tip vortex in a transonic compressor, Proc. Inst. Mech., Part G: Journal of Aerospace Engineering 232 (4) (2018) 694–715. 42

[101] J. Larsson, Q. Wang, The prospect of using large eddy and detached eddy simulations in engineering design, and the research required to get there, Philos. T. R. Soc. A. 372 (2022) (2014) 20130329. 42, 43

[102] O. Antepara, O. Lehmkuhl, R. Borrell, J. Chiva, A. Oliva, Parallel adaptive mesh refinement for large-eddy simulations of turbulent flows, Comput. Fluids 110 (2015) 48–61. 42

[103] S. Toosi, J. Larsson, Towards systematic grid selection in les: Identifying the optimal spatial resolution by minimizing the solution sensitivity, Comput. Fluids (2020) 104488. 42

[104] R. Payri, R. Novella, M. Carreres, M. Belmar-Gil, Modeling gaseous non-reactive flow in a lean direct injection gas turbine combustor through an advanced mesh control strategy, Proc. Inst. Mech., Part G: Journal of Aerospace Engineering (2020) 0954410020919619. 42

[105] P. Benard, G. Balarac, V. Moureau, C. Dobrzynski, G. Lartigue, Y. d'Angelo, Mesh adaptation for large-eddy simulations in complex geometries, Int. J. Numer. Methods Fluids 81 (12) (2016) 719–740. 42

[106] G. Daviller, M. Brebion, P. Xavier, G. Staffelbach, J.-D. Müller, T. Poinsot, A mesh adaptation strategy to predict pressure losses in les of swirled flows, Flow Turbul. Combust. 99 (1) (2017) 93–118. 42, 43, 44, 45, 47

[107] M. Emmett, E. Motheau, W. Zhang, M. Minion, J. B. Bell, A fourth-order adaptive mesh refinement algorithm for the multicomponent, reacting compressible navier–stokes equations, Combust. Theory Model 23 (4) (2019) 592–625. 43

[108] A. Sjunnesson, C. Nelsson, E. Max, LDA Measurements of velocities and turbulence in a bluff body stabilized flame, 4th International Conference on Laser Anemometry - Advances and Application, ASME 3 (1991) 83–90. 43, 53, 54

[109] A. Sjunnesson, P. Henrikson, CARS measurements and visualization of reacting flows in a bluff body stabilized flame, 28th Joint Propulsion Conference and Exhibit, AIAA 92-3650. 43, 53

[110] A. Sjunnesson, S. Olovsson, B. Sjöblom, Validation Rig-A tool for flame studies, 10th International Symposium on Air Breathing Engines (1991) 385–393. 43, 53

[111] P. A. T. Cocks, M. C. Soteriou, V. Sankaran, Impact of numerics on the predictive capabilities of reacting flow LES, Combust. Flame 162 (9) (2015) 3394–3411. 43, 53

[112] C. Fureby, Large Eddy Simulation of turbulent reacting flows with conjugate heat transfer and radiative heat transfer, Proc. Combust. Inst. 38 (2021) 3021–3029. 43, 85, 87, 137, 247

[113] V. Sankaran, T. Gallagher, Grid convergence in les of bluff body stabilized flames, in: 55th AIAA Aerospace Sciences Meeting, 2017, p. 1791. 43

[114] S. A. Drennan, G. Kumar, S. Liu, Developing grid-convergent LES simulations of augmentor combustion with automatic meshing and adaptive mesh refinement, AIAA SciTech Forum - 55th AIAA Aerosp. Sci. Meet. 2017 (January). 43

[115] P. Bénard, G. Lartigue, V. Moureau, R. Mercier, Large-eddy simulation of the lean-premixed preccinsta burner with wall heat loss, Proc. Combust. Inst. 37 (4) (2019) 5233–5243. 43, 69, 70, 71, 72, 74, 75, 81, 86, 87, 95, 96, 137

[116] C. Dapogny, C. Dobrzynski, P. Frey, Three-dimensional adaptive domain remeshing, implicit domain meshing, and applications to free and moving boundary problems, J. Comput. Phys. 262 (2014) 358–378. 44

[117] S. M. Mitran, A comparison of adaptive mesh refinement approaches for large eddy simulation, Tech. rep., Washington Univ Seattle Dept of Applied Mathematics (2001). 44

[118] P. Chassaing, R. Antonia, F. Anselmet, L. Joly, S. Sarkar, Variable density fluid turbulence, Vol. 69, Springer Science & Business Media, 2002. 45

[119] F. Kock, H. Herwig, Entropy production calculation for turbulent shear flows and their implementation in cfd codes, Int. J. Heat Fluid Fl. 26 (4) (2005) 672–680. 46

[120] O. Zeman, Dilatation dissipation: the concept and application in modeling compressible mixing layers, Phys. Fluids A: Fluid Dynamics 2 (2) (1990) 178–188. 46

[121] H. Pitsch, Large-Eddy Simulation of Turbulent Combustion, Annu. Rev. Fluid Mech. 38 (1) (2005) 453–482. 49

[122] A. Ghani, T. Poinsot, L. Gicquel, G. Staffelbach, LES of longitudinal and transverse self-excited combustion instabilities in a bluff-body stabilized turbulent premixed flame, Combust. Flame 162 (11) (2015) 4075–4083. 53

[123] N. Zettervall, K. Nordin-Bates, E. J. K. Nilsson, C. Fureby, Large Eddy Simulation of a premixed bluff body stabilized flame using global and skeletal reaction mechanisms, Combust. Flame (2017) 1–22. 53

[124] T. Schønfeld, M. Rudgyard, Steady and unsteady flows simulations using the hybrid flow solver AVBP, AIAA J. 37 (11) (1999) 1378–1385. 53

[125] P. D. Lax, B. Wendroff, Difference schemes for hyperbolic equations with high order of accuracy, Commun. Pure Appl. Math. 17 (1964) 381–398. 53

[126] N. Guezennec, T. Poinsot, Acoustically nonreflecting and reflecting boundary conditions for vorticity injection in compressible solvers, AIAA J. 47 (2009) 1709–1722. 54

[127] P. Weigand, X. Duan, W. Meier, U. Meier, M. Aigner, C. Bérat, Experimental investigations of an oscillating lean premixed ch4/air swirl flame in a gas turbine model combustor, in: European Combustion Meeting, 2005. 69

[128] P. Weigand, W. Meier, X. Duan, M. Aigner, Laser based investigations of thermo-acoustic instabilities in a lean premixed gas turbine model combustor, in: ASME Turbo Expo: Power for Land, Sea, and Air, Vol. 42363, 2006, pp. 237–245. 69

[129] Z. Yin, P. Nau, W. Meier, Responses of combustor surface temperature to flame shape transitions in a turbulent bi-stable swirl flame, Exp. Therm. Fluid Sci. 82 (2017) 50–57. 69, 70, 87, 88, 92, 93, 94, 97, 105, 137

[130] B. Franzelli, E. Riber, L. Y. Gicquel, T. Poinsot, Large Eddy Simulation of combustion instabilities in a lean partially premixed swirled flame, Combust. Flame 159 (2012) 621–637. 69, 87, 94, 100, 102, 154, 165, 166

[131] B. Franzelli, E. Riber, B. Cuenot, Impact of the chemical description on a Large Eddy Simulation of a lean partially premixed swirled flame, Comptes Rendus Mécanique 341 (2013) 247–256. 69, 87

[132] D. Fredrich, W. P. Jones, A. J. Marquis, The stochastic fields method applied to a partially premixed swirl flame with wall heat transfer, Combust. Flame 205 (2019) 446–456. 69, 70, 87, 97, 104

[133] J. Galpin, A. Naudin, L. Vervisch, C. Angelberger, O. Colin, P. Domingo, Large-eddy simulation of a fuel-lean premixed turbulent swirl-burner, Combust. Flame 155 (2008) 247–266. 69

[134] B. Fiorina, R. Vicquelin, P. Auzillon, N. Darabiha, O. Gicquel, D. Veynante, A filtered tabulated chemistry model for les of premixed combustion, Combust. Flame 157 (2010) 465–475. 69

[135] G. Albouze, T. Poinsot, L. Gicquel, Chemical kinetics modeling and les combustion model effects on a perfectly premixed burner, Comptes Rendus Mécanique 337 (2009) 318–328. 69

[136] P. S. Volpiani, T. Schmitt, D. Veynante, Large eddy simulation of a turbulent swirling premixed flame coupling the TFLES model with a dynamic wrinkling formulation, Combust. Flame 180 (2017) 124–135. 69, 87, 141, 172, 187

[137] D. Fredrich, W. P. Jones, A. J. Marquis, Thermo-acoustic instabilities in the preccinsta combustor investigated using a compressible les-pdf approach, Flow Turbul. Combust. 106 (2021) 1399–1415. 69, 70, 87, 97

[138] F. Gao, E. E. O'Brien, A large-eddy simulation scheme for turbulent reacting flows, Phys. Fluids A Fluid Dyn. 5 (6) (1993) 1282–1284. 70

[139] N. Syred, A review of oscillation mechanisms and the role of the precessing vortex core (PVC) in swirl combustion systems, Prog. Energy Combust. Sci. 32 (2006) 93–161. 81, 182

[140] M. Stöhr, K. Oberleithner, M. Sieber, Z. Yin, W. Meier, Experimental Study of Transient Mechanisms of Bistable Flame Shape Transitions in a Swirl Combustor, J. Eng. Gas Turbines Power 140 (1) (2018) 011503. 81

[141] K. Oberleithner, M. Stöhr, S. H. Im, C. M. Arndt, A. M. Steinberg, Formation and flame-induced suppression of the precessing vortex core in a swirl combustor: Experiments and linear stability analysis, Combust. Flame 162 (8) (2015) 3100–3114. 81, 182, 183

[142] T. Guiberti, D. Durox, P. Scouflaire, T. Schuller, Impact of heat loss and hydrogen enrichment on the shape of confined swirling flames, Proc. Combust. Inst. 35 (2015) 1385–1392. 84, 119, 135, 183, 246

[143] L. Tay Wo Chong, T. Komarek, M. Zellhuber, J. Lenz, C. Hirsch, W. Polifke, Influence of Strain and Heat loss on Flame Stabilization in a Non-Adiabatic Combustor, Proceedings of European Combustion Meeting (2009) 1–6. 84, 246

[144] P. Zhao, L. Wang, N. Chakraborty, Analysis of the flame-wall interaction in premixed turbulent combustion, J. Fluid Mech. 848 (2018) 193–218. 84

[145] F. N. Egolfopoulos, H. Zhang, Z. Zhang, Wall effects on the propagation and extinction of steady, strained, laminar premixed flames, Combust. Flame 109 (1997) 237–252. 84

[146] F. Duchaine, F. Boudy, D. Durox, T. Poinsot, Sensitivity analysis of transfer functions of laminar flames, Combust. Flame 158 (12) (2011) 2384–2394. 84, 85

[147] T. Poinsot, Prediction and control of combustion instabilities in real engines, Proc. Combust. Inst. 36 (1) (2017) 1–28. 84, 180, 246

[148] W. Polifke, Modeling and analysis of premixed flame dynamics by means of distributed time delays, Prog. Energy Combust. Sci. 79 (2020) 100845. 84, 246

[149] T. Schuller, T. Poinsot, S. Candel, Dynamics and control of premixed combustion systems based on flame transfer and describing functions, J. Fluid Mech. 894 (2020) P1. 84, 246

[150] D. Mejia, L. Selle, R. Bazile, T. Poinsot, Wall-temperature effects on flame response to acoustic oscillations, Proc. Combust. Inst. 35 (3) (2015) 3201–3208. 84

[151] K. S. Kedia, H. M. Altay, A. F. Ghoniem, Impact of flame-wall interaction on premixed flame dynamics and transfer function characteristics, Proc. Combust. Inst. 33 (1) (2011) 1113–1120. 84

[152] S. Hong, S. J. Shanbhogue, K. S. Kedia, A. F. Ghoniem, Impact of the flame-holder heat-transfer characteristics on the onset of combustion instability, Combust. Sci. Technol. 185 (10) (2013) 1541–1567. 84

[153] A. Cuquel, D. Durox, T. Schuller, Impact of flame base dynamics on the non-linear frequency response of conical flames, Comptes Rendus - Mec. 341 (1-2) (2013) 171–180. 85

[154] M. Lohrmann, H. Büchner, Prediction of stability limits for lp and lpp gas turbine combustors, Combustion science and technology 177 (12) (2005) 2243–2273. 85

[155] R. Heydarlaki, W. Aitchison, P. Kostka, S. Kheirkhah, Influences of initial and transient combustor wall-temperature on thermoacoustic oscillations of a small-scale power generator, Exp. Therm. Fluid Sci. 109 (2019) 109856. 85

[156] S. Berger, F. Duchaine, L. Y. Gicquel, Bluff-body Thermal Property and Initial State Effects on a Laminar Premixed Flame Anchoring Pattern, Flow, Turbul. Combust. 100 (2) (2018) 561–591. 85

[157] J. C. Massey, Z. X. Chen, N. Swaminathan, Modelling Heat Loss Effects in the Large Eddy Simulation of a Lean Swirl-Stabilised Flame, Flow, Turbul. Combust. 106 (2020) 1355–1378. 85, 247

[158] R. Kaess, W. Polifke, T. Poinsot, N. Noiray, D. Durox, T. Schuller, S. Candel, Cfd-based mapping of the thermo-acoustic stability of a laminar premix burner, in: Proceedings of the 2008 summer program, Citeseer, 2008, p. 289. 85

[159] A. Chatelier, T. Guiberti, R. Mercier, N. Bertier, B. Fiorina, T. Schuller, Experimental and Numerical Investigation of the Response of a Swirled Flame to Flow Modulations in a Non-Adiabatic Combustor, Flow, Turbul. Combust. 102 (2019) 995–1023. 85

[160] X. Han, D. Laera, A. S. Morgans, C. J. Sung, X. Hui, Y. Z. Lin, Flame macrostructures and thermoacoustic instabilities in stratified swirling flames, Proc. Combust. Inst. 37 (2019) 5377–5384. 86

[161] X. Han, D. Laera, D. Yang, C. Zhang, J. Wang, X. Hui, Y. Lin, A. Morgans, C.-J. Sung, Flame interactions in a stratified swirl burner: Flame stabilization, combustion instabilities and beating oscillations, Combust. Flame 212 (2020) 500 – 509. 86, 137

[162] H. G. Li, P. Khare, H. G. Sung, V. Yang, A Large-Eddy-Simulation Study of Combustion Dynamics of Bluff-Body Stabilized Flames, Combust. Sci. Technol. 188 (2016) 924–952. 86, 137

[163] A. Ghani, T. Poinsot, L. Gicquel, G. Staffelbach, LES of longitudinal and transverse self-excited combustion instabilities in a bluff-body stabilized turbulent premixed flame, Combust. Flame 162 (2015) 4075–4083. 86, 137

[164] P. Wolf, G. Staffelbach, L. Y. Gicquel, J. D. Müller, T. Poinsot, Acoustic and Large Eddy Simulation studies of azimuthal modes in annular combustion chambers, Combust. Flame 159 (2012) 3398–3413. 86, 137

[165] A. Urbano, L. Selle, G. Staffelbach, B. Cuenot, T. Schmitt, S. Ducruix, S. Candel, Exploration of combustion instability triggering using Large Eddy Simulation of a multiple injector liquid rocket engine, Combust. Flame 169 (2016) 129–140. 86, 137

[166] M. Shahi, J. B. Kok, J. C. Roman Casado, A. K. Pozarlik, Transient heat transfer between a turbulent lean partially premixed flame in limit cycle oscillation and the walls of a can type combustor, Appl. Therm. Eng. 81 (2015) 128–139. 86, 87, 137, 247

[167] S. R. Gubba, S. S. Ibrahim, W. Malalasekera, A. R. Masri, Measurements and LES calculations of turbulent premixed flame propagation past repeated obstacles, Combust. Flame 158 (12) (2011) 2465–2481. 86

[168] S. Gövert, D. Mira, J. B. Kok, M. Vázquez, G. Houzeaux, Turbulent combustion modelling of a confined premixed jet flame including heat loss effects using tabulated chemistry, Appl. Energy 156 (2015) 804–815. 86

[169] S. Berger, S. Richard, F. Duchaine, G. Staffelbach, L. Y. Gicquel, On the sensitivity of a helicopter combustor wall temperature to convective and radiative thermal loads, Appl. Therm. Eng. 103 (2016) 1450–1459. 87, 247

[170] B. Higgins, M. Q. McQuay, F. Lacas, J. C. Rolon, N. Darabiha, S. Candel, Systematic measurements of OH chemiluminescence for fuel-lean, high-pressure, premixed, laminar flames, Fuel 80 (2001) 67–74. 89, 139, 186, 262

[171] G. P. Smith, D. M. Golden, M. Frenklach, N. W. Moriarty, B. Eiteneer, M. Goldenberg, T. Bowman, R. K. Hanson, S. Song, W. C. Gardiner, V. V. Lissianski, Z. Qin, Gri-mech 3.0, http://www.me.berkeley.edu/gri_mech/, 1999. 91

[172] M. F. Modest, Radiative heat transfer, Academic press, 2013. 91, 142, 188

[173] W. L. Grosshandler, RADCAL: A Narrow Band Model for Radiation, NIST Tech. note 1402, 1993. 92, 142, 188

[174] S. Whitaker, Forced convection heat transfer correlations for flow in pipes, past flat plates, single cylinders, single spheres, and for flow in packed beds and tube bundles, AIChE J. 18 (2) (1972) 361–371. 92, 317

[175] S. W. Churchill, H. H. Chu, Correlating equations for laminar and turbulent free convection from a vertical plate, Int. J. Heat Mass Transf. 18 (1975) 1323–1329. 92, 317

[176] F. P. Incropera, A. S. Lavine, T. L. Bergman, D. P. DeWitt, Fundamentals of heat and mass transfer, Wiley, 2007. 95, 103, 255

[177] L. Rayleigh, The explanation of certain acoustical phenomena, Roy. Inst. Proc. 8 (1878) 536–542. 98, 151

[178] Y. Huang, V. Yang, Dynamics and stability of lean-premixed swirl-stabilized combustion, Prog Energ Combust 35 (4) (2009) 293–364. 100, 220

[179] J. M. Lourier, M. Stöhr, B. Noll, S. Werner, A. Fiolitakis, Scale Adaptive Simulation of a thermoacoustic instability in a partially premixed lean swirl combustor, Combust. Flame 183 (2017) 343–357. 100, 156

[180] L. Selle, F. Nicoud, T. Poinsot, Actual Impedance of Nonreflecting Boundary Conditions: Implications for Computation of Resonators, AIAA J. 42 (5) (2004) 958–964. 100

[181] G. Daviller, G. Oztarlik, T. Poinsot, A generalized non-reflecting inlet boundary condition for steady and forced compressible flows with injection of vortical and acoustic waves, Comput. Fluids 190 (2019) 503–513. 101

[182] J. Miles, The reflection of sound due to a change in cross section of a circular tube, The Journal of the Acoustical Society of America 16 (1) (1944) 14–19. 102

[183] F. Duchaine, S. Jauré, D. Poitou, E. Quémerais, G. Staffelbach, T. Morel, L. Gicquel, Analysis of high performance conjugate heat transfer with the OpenPALM coupler, Comput. Sci. Discov. 8 (2015) 15003. 103

[184] C. Willert, Stereoscopic digital particle image velocimetry for application in wind tunnel flows, Meas. Sci. Technol. 8 (1997) 1465–1479. 110, 148

[185] P. J. Schmid, Dynamic mode decomposition of numerical and experimental data, J. Fluid Mech. 656 (2010) 5–28. 112, 171

[186] F. Richecoeur, L. Hakim, A. Renaud, L. Zimmer, Dmd algorithms for experimental data processing in combustion, Proc. Summer Program, Cent. Turbul. Res. (2012) 459–468. 112, 171

[187] L. Magri, M. P. Juniper, J. P. Moeck, Sensitivity of the rayleigh criterion in thermoacoustics, J. Fluid Mech. 882 (2020) 1–11. 113, 174

[188] E. Lo Schiavo, D. Laera, E. Riber, L. Gicquel, T. Poinsot, On the impact of fuel injection angle in Euler–Lagrange large eddy simulations of swirling spray flames exhibiting thermoacoustic instabilities, Combust. Flame 227 (2021) 359–370. 113, 174

[189] S. Taamallah, K. Vogiatzaki, F. Alzahrani, E. Mokheimer, M. Habib, A. Ghoniem, Fuel flexibility, stability and emissions in premixed hydrogen-rich gas turbine combustion: Technology, fundamentals, and numerical simulations, Appl. Energy 154 (2015) 1020–1047. 119, 120, 134, 136

[190] F. Halter, C. Chauveau, N. Djebaïli-Chaumeix, I. Gökalp, Characterization of the effects of pressure and hydrogen concentration on laminar burning velocities of methane-hydrogen-air mixtures, Proc. Combust. Inst. 30 (2005) 201–208. 119, 134, 180

[191] Y. Zhang, J. Wu, S. Ishizuka, Hydrogen addition effect on laminar burning velocity, flame temperature and flame stability of a planar and a curved CH4-H2-air premixed flame, Int. J. Hydrogen Energy 34 (2009) 519–527. 119, 134, 180

[192] H. Guo, G. J. Smallwood, F. Liu, Y. Ju, Ö. L. Gülder, The effect of hydrogen addition on flammability limit and NOx emission in ultra-lean counterflow CH4/air premixed flames, Proc. Combust. Inst. 30 (1) (2005) 303–311. 119

[193] V. Di Sarli, A. D. Benedetto, Laminar burning velocity of hydrogen–methane/air premixed flames, Int. J. Hydrogen Energy 32 (2007) 637–646. 119, 135, 183

[194] Z. Chen, Effects of hydrogen addition on the propagation of spherical methane/air flames: A computational study, Int. J. Hydrogen Energy 34 (2009) 6558–6567. 119, 135, 183

[195] S. Bougrine, S. Richard, A. Nicolle, D. Veynante, Numerical study of laminar flame properties of diluted methane-hydrogen-air flames at high pressure and temperature using detailed chemistry, Int. J. Hydrogen Energy 36 (18) (2011) 12035–12047. 119

[196] T. Boushaki, Y. Dhué, L. Selle, B. Ferret, T. Poinsot, Effects of hydrogen and steam addition on laminar burning velocity of methane-air premixed flame: Experimental and numerical analysis, Int. J. Hydrogen Energy 37 (2012) 9412–9422. 119, 135, 183

[197] C. Jiménez, D. Michaels, A. F. Ghoniem, Stabilization of ultra-lean hydrogen enriched inverted flames behind a bluff–body and the phenomenon of anomalous blow–off, Combust. Flame 191 (2018) 86–98. 119, 135, 183

[198] Y. J. Kim, B. J. Lee, H. G. Im, Hydrodynamic and chemical scaling for blow-off dynamics of lean premixed flames stabilized on a meso-scale bluff-body, Proc. Combust. Inst. 37 (2019) 1831–1841. 119, 135, 183

[199] X. Kang, R. J. Gollan, P. A. Jacobs, A. Veeraragavan, Suppression of instabilities in a premixed methane–air flame in a narrow channel via hydrogen/carbon monoxide addition, Combust. Flame 173 (2016) 266–275. 119, 135, 183

[200] S. Bougrine, S. Richard, O. Colin, D. Veynante, Fuel composition effects on flame stretch in turbulent premixed combustion: Numerical analysis of flame-vortex interaction and formulation of a new efficiency function, Flow Turbul. Combust. 93 (2) (2014) 259–281. 119

[201] R. Schefer, D. Wicksall, A. Agrawal, Combustion of hydrogen-enriched methane in a lean premixed swirl-stabilized burner, Proc. Combust. Inst. 29 (2002) 843–851. 119, 135, 183, 193

[202] F. Cozzi, A. Coghe, Behavior of hydrogen-enriched non-premixed swirled natural gas flames, Int. J. Hydrogen Energy 31 (2006) 669–677. 119, 135, 183

[203] H. S. Kim, V. K. Arghode, M. B. Linck, A. K. Gupta, Hydrogen addition effects in a confined swirl-stabilized methane-air flame, Int. J. Hydrogen Energy 34 (2009) 1054–1062. 119, 135

[204] S. Shanbhogue, Y. Sanusi, S. Taamallah, M. Habib, E. Mokheimer, A. Ghoniem, Flame macrostructures, combustion instability and extinction strain scaling in swirl-stabilized premixed CH4/H2 combustion, Combust. Flame 163 (2016) 494–507. 119, 135, 136, 183

[205] P. Benard, V. Moureau, G. Lartigue, Y. D'Angelo, Large-Eddy Simulation of a hydrogen enriched methane/air meso-scale combustor, Int. J. Hydrogen Energy 42 (4) (2017) 2397–2410. 120

[206] D. Cicoria, C. Chan, Large eddy simulation of lean turbulent hydrogen-enriched methane-air premixed flames at high Karlovitz numbers, Int. J. Hydrogen Energy 41 (2016) 22479–22496. 120, 136

[207] R. Mercier, T. Guiberti, A. Chatelier, D. Durox, O. Gicquel, N. Darabiha, T. Schuller, B. Fiorina, Experimental and numerical investigation of the influence of thermal boundary conditions on premixed swirling flame stabilization, Combust. Flame 171 (2016) 42–58. 120, 136

[208] D. Moëll, D. Lörstad, X.-S. Bai, LES of Hydrogen Enriched Methane/Air Combustion in the SGT-800 Burner at Real Engine Conditions, in: Asme Turbo Expo, Paper No: GT2018-76434, 2018, p. V04BT04A023. 120, 136, 183

[209] R. Hilbert, F. Tap, H. El-Rabii, D. Thévenin, Impact of detailed chemistry and transport models on turbulent combustion simulations, Prog. Energy Combust. Sci. 30 (2004) 61–117. 120, 136

[210] G. Oztarlik, L. Selle, T. Poinsot, T. Schuller, Suppression of instabilities of swirled premixed flames with minimal secondary hydrogen injection 214 (2020) 266–276. 121, 134, 180, 183

[211] ARCANE, a new python-based chemistry reduction code, `www.chemistry.cerfacs.fr/en/arcane` (2019). 122

[212] J. F. Grcar, J. B. Bell, M. S. Day, The Soret effect in naturally propagating, premixed, lean, hydrogen–air flames, Proc. Combust. Inst. 32 (1) (2009) 1173–1180. 122

[213] H. Yamashita, M. Shimada, T. Takeno, A numerical study on flame stability at the transition point of jet diffusion flames, Symp. Int. Combust. Proc. 26 (1) (1996) 27–34. 128, 232

[214] A. L. Sánchez, F. A. Williams, Recent advances in understanding of flammability characteristics of hydrogen, Prog. Energy Combust. Sci. 41 (2014) 1–55. 129

[215] H. Yilmaz, O. Cam, I. Yilmaz, Experimental investigation of flame instability in a premixed combustor, Fuel 262 (2020) 116594. 134, 180

[216] G. Zang, J. Zhang, J. Jia, E. S. Lora, A. Ratner, Life cycle assessment of power-generation systems based on biomass integrated gasification combined cycles, Renew. Energy 149 (2020) 336–346. 134, 180

[217] P. S. P. Corrêa, J. Zhang, E. E. S. Lora, R. V. Andrade, L. R. de Mello e Pinto, A. Ratner, Experimental study on applying biomass-derived syngas in a microturbine, Appl. Therm. Eng. 146 (2019) 328–337. 134, 180

[218] R. K. Cheng, D. Littlejohn, W. A. Nazeer, K. O. Smith, Laboratory studies of the flow field characteristics of low-swirl injectors for adaptation to fuel-flexible turbines, J. Eng. Gas Turbines Power 130 (2008) 021501. 134

[219] M. C. Lee, J. Yoon, S. Joo, Y. Yoon, Gas turbine combustion characteristics of H2/CO synthetic gas for coal integrated gasification combined cycle applications, Int. J. Hydrogen Energy 40 (2015) 11032–11045. 134

[220] D. Ebi, R. Bombach, P. Jansohn, Swirl flame boundary layer flashback at elevated pressure: Modes of propagation and effect of hydrogen addition, Proc. Combust. Inst. 38 (2020) 6345–6353. 134, 181

[221] R. Ranjan, N. T. Clemens, Insights into flashback-to-flameholding transition of hydrogen-rich stratified swirl flames, Proc. Combust. Inst. 38 (2020) 6289–6297. 134, 181

[222] D. W. Davis, P. L. Therkelsen, D. Littlejohn, R. K. Cheng, Effects of hydrogen on the thermo-acoustics coupling mechanisms of low-swirl injector flames in a model gas turbine combustor, Proc. Combust. Inst. 34 (2013) 3135–3143. 134, 135, 176

[223] A. F. Ghoniem, A. Annaswamy, S. Park, Z. C. Sobhani, Stability and emissions control using air injection and H2 addition in premixed combustion, Proc. Combust. Inst. 30 (2005) 1765–1773. 135

[224] R. K. Cheng, D. Littlejohn, P. A. Strakey, T. Sidwell, Laboratory investigations of a low-swirl injector with H2 and CH4 at gas turbine conditions, Proc. Combust. Inst. 32 (2009) 3001–3009. 135, 183

[225] B. Ge, Y. Ji, Z. Zhang, S. Zang, Y. Tian, H. Yu, M. Chen, G. Jiao, D. Zhang, Experiment study on the combustion performance of hydrogen-enriched natural gas in a DLE burner, Int. J. Hydrogen Energy 44 (2019) 14023–14031. 135, 183

[226] J. Zhang, A. Ratner, Experimental study on the excitation of thermoacoustic instability of hydrogen-methane/air premixed flames under atmospheric and elevated pressure conditions, Int. J. Hydrogen Energy 44 (2019) 21324–21335. 135, 136, 183, 184

[227] P. Palies, M. Ilak, R. Cheng, Transient and limit cycle combustion dynamics analysis of turbulent premixed swirling flames, J. Fluid Mech 830 (2017) 681–707. 135, 183

[228] S. Schimek, S. Göke, C. Schrödinger, C. O. Paschereit, Flame Transfer Function Measurements With CH4 and H2 Fuel Mixtures at Ultra Wet Conditions in a Swirl Stabilized Premixed Combustor Volume 2: Combustion, Fuels and Emissions, Parts A and B (2012) 1335–1344. 135

[229] M. Emadi, D. Karkow, T. Salameh, A. Gohil, A. Ratner, Flame structure changes resulting from hydrogen-enrichment and pressurization for low-swirl premixed methane-air flames, Int. J. Hydrogen Energy 37 (2012) 10397–10404. 135

[230] J. Yoon, S. Joo, J. Kim, M. C. Lee, J. G. Lee, Y. Yoon, Effects of convection time on the high harmonic combustion instability in a partially premixed combustor, Proc. Combust. Inst. 36 (2017) 3753–3761. 135, 183

[231] P. M. Allison, J. F. Driscoll, M. Ihme, Acoustic characterization of a partially-premixed gas turbine model combustor: Syngas and hydrocarbon fuel comparisons, Proc. Combust. Inst. 34 (2013) 3145–3153. 135, 136

[232] J. Peng, Z. Cao, X. Yu, S. Yang, Y. Yu, H. Ren, Y. Ma, S. Zhang, S. Chen, Y. Zhao, Analysis of combustion instability of hydrogen fueled scramjet combustor on high-speed OH-PLIF measurements and dynamic mode decomposition, Int. J. Hydrogen Energy 45 (2020) 13108–13118. 135, 183

[233] N. A. Baraiya, S. R. Chakravarthy, Effect of syngas composition on high frequency combustion instability in a non-premixed turbulent combustor, Int. J. Hydrogen Energy 44 (2019) 6299–6312. 135, 183

[234] D. Kim, S. Joo, Y. Yoon, Effects of fuel line acoustics on the self-excited combustion instability mode transition with hydrogen-enriched laboratory-scale partially premixed combustor, Int. J. Hydrogen Energy 45 (2020) 19956–19964. 135, 183

[235] J. Zhang, A. Ratner, Experimental study of the effects of hydrogen addition on the thermoacoustic instability in a variable-length combustor, Int. J. Hydrogen Energy 46 (2021) 16086–16100. 136, 183

[236] H. Kang, K. T. Kim, High-frequency combustion dynamics of multi-element lean-premixed hydrogen-air flame ensemble, Combust. Flame 233 (2021) 111585. 136, 183

[237] J. Nam, J. J. Yoh, A numerical investigation of the effects of hydrogen addition on combustion instability inside a partially-premixed swirl combustor, Appl. Therm. Eng. 176 (2020) 115478. 136, 183

[238] A. Gruber, M. R. Bothien, A. Ciani, K. Aditya, J. H. Chen, F. A. Williams, Direct numerical simulation of hydrogen combustion at auto-ignitive conditions: Ignition, stability and turbulent reaction-front velocity, Combust. Flame 229 (2021) 111385. 136

[239] A. Datta, S. Gupta, S. Hemchandra, I. Chterev, I. Boxx, Impact of Hydrogen Addition on the Thermoacoustic Instability and, ASME Turbo Expo, Paper No. GT2021-58794, 2021, pp. 1–16. 137, 183

[240] A. Kushwaha, P. Kasthuri, S. A. Pawar, R. I. Sujith, Dynamical Characterization of Thermoacoustic Oscillations in a Hydrogen-Enriched Partially Premixed Swirl-Stabilized Methane/Air Combustor, ASME Turbo Expo 2021, Paper No. GT2021-60011, 2021, pp. 1–12. 137, 152, 154, 183

[241] E. Ranzi, A. Frassoldati, A. Stagni, M. Pelucchi, A. Cuoci, T. Faravelli, Reduced kinetic schemes of complex reaction systems: Fossil and biomass-derived transportation fuels, Int. J. Chem. Kinet. 46 (2014) 512–542. 140, 187, 253, 324

[242] T. Jaravel, Prediction of pollutants in gas turbines using large eddy simulation, Ph.D. thesis (2016). 140, 247

[243] V. Nair, G. Thampi, R. Sujith, Intermittency route to thermoacoustic instability in turbulent combustors, J. Fluid Mech. 756 (2014) 470–487. 152

[244] A. Samadhan, I. Raman, Transition to Thermoacoustic Instability in a Turbulent Combustor, J. Combust. Soc. Japan 60 (2018) 99–111. 154

[245] P. W. Agostinelli, D. Laera, I. Chterev, I. Boxx, L. Gicquel, T. Poinsot, Large Eddy Simulations of mean pressure and H_2 addition effects on the stabilization and dynamics of a partially-premixed swirled-stabilized flame, Combust. Flame - Submitted (2021) –. 180

[246] J. Zhang, A. Ratner, Effect of pressure variation on acoustically perturbed swirling flames, Proc. Combust. Inst. 36 (2017) 3881–3888. 180

[247] F. Di Sabatino, T. F. Guiberti, W. R. Boyette, W. L. Roberts, J. P. Moeck, D. A. Lacoste, Effect of pressure on the transfer functions of premixed methane and propane swirl flames, Combust. Flame 193 (2018) 272–282. 180

[248] C. D. Slabaugh, A. C. Pratt, R. P. Lucht, S. E. Meyer, M. Benjamin, K. Lyle, M. Kelsey, The development of an optically accessible, high-power combustion test rig, Rev. Sci. Instrum. 85 (3) (2014) 035105. 181

[249] I. Boxx, C. Slabaugh, P. Kutne, R. P. Lucht, W. Meier, 3 kHz PIV/OH-PLIF measurements in a gas turbine combustor at elevated pressure, Proc. Combust. Inst. 35 (2015) 3793–3802. 181

[250] C. D. Slabaugh, A. C. Pratt, R. P. Lucht, Simultaneous 5 kHz OH-PLIF/PIV for the study of turbulent combustion at engine conditions, Appl. Phys. B 118 (2015) 109–130. 181

[251] P. Malbois, E. Salaun, F. Frindt, G. Cabot, B. Renou, F. Grisch, L. Bouheraoua, H. Verdier, S. Richard, Experimental investigation with optical diagnostics of a lean-premixed aero-engine injection system under relevant operating conditions, in: Turbo Expo: Power for Land, Sea, and Air, Vol. 50855, American Society of Mechanical Engineers, 2017, p. V04BT04A022. 181

[252] Y. R. Hicks, C. M. Heath, R. C. Anderson, K. M. Tacina, Investigations of a combustor using a 9-point swirl-venturi fuel injector: recent experimental results, in: 20th International Symposium on Air Breathing Engines (ISABE 2011), 2012. 182

[253] M. Orain, F. Grisch, E. Jourdanneau, B. Rossow, C. Guin, B. Trétout, Simultaneous measurements of equivalence ratio and flame structure in multipoint injectors using PLIF, Comptes Rendus - Mec. 337 (2009) 373–384. 182

[254] S. Kheirkhah, J. D. Cirtwill, P. Saini, K. Venkatesan, A. M. Steinberg, Dynamics and mechanisms of pressure, heat release rate, and fuel spray coupling during intermittent thermoacoustic oscillations in a model aeronautical combustor at elevated pressure, Combust. Flame 185 (2017) 319–334. 182

[255] C. D. Slabaugh, I. Boxx, S. Werner, R. P. Lucht, W. Meier, Structure and dynamics of premixed swirl flames at elevated power density, AIAA J. 54 (3) (2016) 946–961. 182, 185, 186

[256] C. E. Cala, E. C. Fernandes, M. V. Heitor, S. I. Shtork, Coherent structures in unsteady swirling jet flow, Exp. Fluids 40 (2006) 267–276. 182

[257] H. Liang, T. Maxworthy, An experimental investigation of swirling jets, J. Fluid Mech. 525 (2005) 115–159. 182

[258] R. Zhang, I. Boxx, W. Meier, C. D. Slabaugh, Coupled interactions of a helical precessing vortex core and the central recirculation bubble in a swirl flame at elevated power density, Combust. Flame 202 (2019) 119–131. 182, 185, 186

[259] A. M. Steinberg, I. Boxx, M. Stöhr, C. D. Carter, W. Meier, Flow-flame interactions causing acoustically coupled heat release fluctuations in a thermo-acoustically unstable gas turbine model combustor, Combust. Flame 157 (12) (2010) 2250–2266. 182

[260] A. M. Steinberg, C. M. Arndt, W. Meier, Parametric study of vortex structures and their dynamics in swirl-stabilized combustion, Proc. Combust. Inst. 34 (2013) 3117–3125. 182

[261] I. Chterev, B. Emerson, T. Lieuwen, Velocity and stretch characteristics at the leading edge of an aerodynamically stabilized flame, Combust. Flame 193 (2018) 92–111. 182

[262] I. Chterev, C. W. Foley, D. Foti, S. Kostka, A. W. Caswell, N. Jiang, A. Lynch, D. R. Noble, S. Menon, J. M. Seitzman, T. C. Lieuwen, Flame and flow topologies in an annular swirling flow, Combust. Sci. Technol. 186 (8) (2014) 1041–1074. 182

[263] P. Moin, S. V. Apte, Large-eddy simulation of realistic gas turbine combustors, AIAA J. 44 (2006) 698–708. 182

[264] G. Boudier, L. Gicquel, T. Poinsot, D. Bissières, C. Bérat, Comparison of les, rans and experiments in an aeronautical gas turbine combustion chamber, Proc. Combust. Inst. 31 (2007) 3075–3082. 182

[265] P. Schmitt, T. Poinsot, B. Schuermans, K. P. Geigle, Large-eddy simulation and experimental study of heat transfer, nitric oxide emissions and combustion instability in a swirled turbulent high-pressure burner, J. Fluid Mech. 570 (2007) 17–46. 182

[266] S. Legros, C. Brunet, P. Domingo-Alvarez, P. Malbois, E. Salaun, G. Godard, M. Caceres, B. Barviau, G. Cabot, B. Renou, G. Lartigue, V. Moureau, S. Puggelli, S. Richard, M. A. Boukhalfa, F. Grisch, Combustion for aircraft propulsion: Progress in advanced laser-based diagnostics

on high-pressure kerosene/air flames produced with low-NOx fuel injection systems, Combust. Flame 224 (2021) 273–294. 183

[267] K. Oberleithner, S. Terhaar, L. Rukes, C. O. Paschereit, Why nonuniform density suppresses the precessing vortex core, J. Eng. Gas Turbines Power 135 (2013) 121506. 183

[268] J. Beita, M. Talibi, S. Sadasivuni, R. Balachandran, Thermoacoustic instability considerations for high hydrogen combustion in lean premixed gas turbine combustors: A review, Hydrogen 2 (1) (2021) 33–57. 183

[269] E. Æsøy, J. G. Aguilar, S. Wiseman, M. R. Bothien, N. A. Worth, J. R. Dawson, Scaling and prediction of transfer functions in lean premixed h2/ch4-flames, Combust. Flame 215 (2020) 269–282. 183

[270] Z. Lim, J. Li, A. S. Morgans, The effect of hydrogen enrichment on the forced response of ch4/h2/air laminar flames, Int. J. Hydrog. Energy 46 (2021) 23943–23953. 183

[271] S. Marragou, I. Boxx, L. Selle, T. Poinsot, T. Schuller, Measurements of the transfer function of partially premixed swirling flames in the PRECCINSTA gas turbine model combustor, in: Symposium on Thermoacoustics in Combustion: Industry meets Academia (SoTiC 2021). 183

[272] S. Nakaya, K. Omi, T. Okamoto, Y. Ikeda, C. Zhao, M. Tsue, H. Taguchi, Instability and mode transition analysis of a hydrogen-rich combustion in a model afterburner, Proc. Combust. Inst. 38 (4) (2021) 5933–5942. 183

[273] T. Indlekofer, B. Ahn, Y. H. Kwah, S. Wiseman, M. Mazur, J. R. Dawson, N. A. Worth, The effect of hydrogen addition on the amplitude and harmonic response of azimuthal instabilities in a pressurized annular combustor, Combust. Flame 228 (2021) 375–387. 183, 184

[274] T. Indlekofer, A. Faure-Beaulieu, N. Noiray, J. Dawson, The effect of dynamic operating conditions on the thermoacoustic response of hydrogen rich flames in an annular combustor, Combust. Flame 223 (2021) 284–294. 183

[275] J. Strollo, S. Peluso, J. O'Connor, Effect of hydrogen on steady-state and transient combustion instability characteristics, J. Eng. Gas Turbines Power 143 (7) (2021) 071023. 183

[276] T. Shoji, S. Tachibana, T. Suzuki, Y. Nakazumi, T. Yokomori, A new pattern of flame/flow dynamics for lean-premixed, low-swirl hydrogen turbulent jet flames under thermoacoustic instability, Proc. Combust. Inst. 38 (2) (2021) 2835–2843. 183

[277] A. Ghani, W. Polifke, Control of intrinsic thermoacoustic instabilities using hydrogen fuel, Proc. Combust. Inst. 38 (4) (2021) 6077–6084. 183

[278] B. Ahn, T. Indlekofer, J. Dawson, N. Worth, Transient thermoacoustic responses of methane/hydrogen flames in a pressurized annular combustor, in: Turbo Expo: Power for Land, Sea, and Air, Vol. 84942, American Society of Mechanical Engineers, 2021, p. V03AT04A017. 184

[279] J. Hunt, A. Wray, P. Moin, Eddies, stream, and convergence zones in turbulent ows., in: Annual Research Briefs, Center for Turbulence Research, Center for Turbulence Research, NASA Ames/Stanford Univ., 1988, pp. 193–208. 198

[280] D. Durox, T. Schuller, N. Noiray, S. Candel, Experimental analysis of nonlinear flame transfer functions for different flame geometries, Proc. Combust. Inst. 32 I (1) (2009) 1391–1398. 213

[281] K. Ahn, K. H. Yu, Effects of Damköhler number on vortex-flame interaction, Combust. Flame 159 (2012) 686–696. 215

[282] M. Stöhr, C. M. Arndt, W. Meier, Effects of Damköhler number on vortex-flame interaction in a gas turbine model combustor, Proc. Combust. Inst. 34 (2013) 3107–3115. 215

[283] W. Krebs, S. Bethke, J. Lepers, P. Flohr, B. Prade, C. Johnson, S. Sattinger, Thermoacoustic design tools and passive control: Siemens power generation approaches, Combustion Instabilities in Gas Turbine Engines Operational Experience, Fundamental Mechanisms and Modeling, 2005. 220

[284] J. Lepers, W. Krebs, B. Prade, P. Flohr, G. Pollarolo, A. Ferrante, Investigation of thermoacoustic stability limits of an annular gas turbine combustor test-rig with and without helmholtz-resonators, in: ASME Turbo Expo 2005: Power for Land, Sea, and Air, American Society of Mechanical Engineers Digital Collection, 2005, pp. 177–189. 220

[285] H. C. Mongia, T. Held, G. Hsiao, R. Pandalai, Challenges and progress in controlling dynamics in gas turbine combustors, Journal of Propulsion and Power 19 (5) (2003) 822–829. 220

[286] D. James, A solution for noise associated with a series staged dle combustion system, in: 2002 4th International Pipeline Conference, American Society of Mechanical Engineers Digital Collection, 2002, pp. 1231–1234. 220

[287] R. C. Steele, L. H. Cowell, S. M. Cannon, C. E. Smith, Passive control of combustion instability in lean premixed combustors, Journal of Engineering for Gas Turbines and Power 122 (3) (2000) 412–419. 220

[288] K. O. Smith, J. Blust, Combustion instabilities in industrial gas turbines: Solar turbines' experience, Combustion Instabilities in Gas Turbine Engines: Operational Experience, Fundamental Mechanisms, and Modeling (2005) 29–42. 220

[289] K. Hsu, L. Gross, D. Trump, W. Roquemore, Performance of a trapped-vortex combustor, in: 33rd Aerospace sciences meeting and exhibit, 1995, p. 810. 220

[290] K.-Y. Hsu, L. Goss, W. Roquemore, Characteristics of a trapped-vortex combustor, Journal of Propulsion and Power 14 (1) (1998) 57–65. 220

[291] N. A. Worth, J. R. Dawson, Modal dynamics of self-excited azimuthal instabilities in an annular combustion chamber, Combustion and Flame 160 (11) (2013) 2476–2489. 221, 223, 247, 249

[292] N. A. Worth, J. R. Dawson, Self-excited circumferential instabilities in a model annular gas turbine combustor: Global flame dynamics, Proceedings of the Combustion Institute 34 (2) (2013) 3127–3134. 221, 247

[293] F. Nicoud, F. Ducros, Subgrid-scale stress modelling based on the square of the velocity gradient tensor, Flow, turbulence and Combustion 62 (3) (1999) 183–200. 225

[294] F. Incropera, D. DeWitt, Introduction to heat transfer. 1985. 227

[295] C. Xu, A. A. Konnov, Validation and analysis of detailed kinetic models for ethylene combustion, Energy 43 (1) (2012) 19–29. 228

[296] G. Jomaas, X. Zheng, D. Zhu, C. K. Law, Experimental determination of counterflow ignition temperatures and laminar flame speeds of c2–c3 hydrocarbons at atmospheric and elevated pressures, Proceedings of the Combustion Institute 30 (1) (2005) 193–200. 228

[297] M. Hassan, K. Aung, O. Kwon, G. Faeth, Properties of laminar premixed hydrocarbon/air flames at various pressures, Journal of Propulsion and Power 14 (4) (1998) 479–488. 228

[298] F. Egolfopoulos, D. Zhu, C. K. Law, Experimental and numerical determination of laminar flame speeds: Mixtures of c2-hydrocarbons with oxygen and nitrogen, in: Symposium (International) on Combustion, Vol. 23, Elsevier, 1991, pp. 471–478. 228

[299] B. Cabral, L. C. Leedom, Imaging vector fields using line integral convolution, Tech. rep., Lawrence Livermore National Lab., CA (United States) (1993). 233, 292

[300] P. W. Agostinelli, Y. H. Kwah, S. Richard, G. Exilard, J. R. Dawson, L. Gicquel, T. Poinsot, On the lean blow-out dynamics in the Spinning Combustion Technology, Combust. Flame - Submitted (2021) –. 244

[301] R. M. Kumar, I. Chterev, D. Stepien, M. Sirignano, B. L. Emerson, C. A. Fugger, N. Jiang, S. Roy, T. C. Lieuwen, Near blowout dynamics of a premixed, swirl stabilized flame, Proc. Combust. Inst. 38 (2021) 6067–6075. 244

[302] D. E. Cavaliere, J. Kariuki, E. Mastorakos, A comparison of the blow-off behaviour of swirl-stabilized premixed, non-premixed and spray flames, Flow, Turbul. Combust. 91 (2013) 347–372. 244, 246

[303] R. Pathania, A. Skiba, R. Ciardiello, E. Mastorakos, Blow-off mechanisms of turbulent premixed bluff-body stabilised flames operated with vapourised kerosene fuels, Proc. Combust. Inst. 38 (2021) 2957–2965. 244

[304] J. Kariuki, J. R. Dawson, E. Mastorakos, Measurements in turbulent premixed bluff body flames close to blow-off, Combust. Flame 159 (2012) 2589–2607. 244, 245

[305] A. Bhattacharya, B. Gupta, S. Hansda, Z. Haque, A. Kumar, M. K. Mishra, S. De, A. Mukhopadhyay, S. Sen, Lean Blowout Phenomena and Prior Detection of Lean Blowout in a Premixed Model Annular Combustor, in: Gas

Turbine India Conference, Vol. Combustion, Fuels, and Emissions, Paper No. GTINDIA2019-2491, 2019, p. V002T04A009. 245

[306] G. C. Williams, H. C. Hottel, A. C. Scurlock, Flame stabilization and propagation in high velocity gas streams, Symp. Combust. Flame Explos. Phenom. 3 (1948) 21–40. 245

[307] K. M. Kundu, D. Banerjee, Theoretical analysis on flame stabilization by a bluff-body, Combust. Sci. Technol. 17 (1977) 153–162. 245

[308] K. M. Kundu, D. Banerjee, D. Bhaduri, On flame stabilization by bluff-bodies, J. Eng. Gas Turbines Power 102 (1980) 209–214. 245

[309] J. P. Longwell, E. E. Frost, M. A. Weiss, Flame Stability in Bluff Body Recirculation Zones, Ind. Eng. Chem. 45 (1953) 1629–1633. 245

[310] S. L. Plee, A. M. Mellor, Characteristic time correlation for lean blowoff of bluff-body-stabilized flames, Combust. Flame 35 (1979) 61–80. 245

[311] E. E. Zukoski, Flame stabilization on bluff bodies at low and intermediate reynolds numbers, Ph.D. thesis, California Institute of Technology (1954). 245

[312] S. Yamaguchi, N. Ohiwa, T. Hasegawa, Structure and blow-off mechanism of rod-stabilized premixed flame, Combust. Flame 62 (1985) 31–41. 245, 254

[313] S. J. Shanbhogue, S. Husain, T. Lieuwen, Lean blowoff of bluff body stabilized flames: Scaling and dynamics, Prog. Energy Combust. Sci. 35 (2009) 98–120. 245

[314] J. F. Driscoll, Turbulent premixed combustion: Flamelet structure and its effect on turbulent burning velocities, Prog. Energy Combust. Sci. 34 (2008) 91–134. 245

[315] C. K. Law, Combustion physics, Cambridge university press, 2010. 245, 277

[316] T. M. Muruganandam, J. M. Seitzman, Origin of lean blowout precursors in swirled gas turbine combustors, 43rd AIAA Aerosp. Sci. Meet. Exhib. - Meet. Pap. (2005) 10405–10416. 245

[317] Q. Zhang, D. R. Noble, S. J. Shanbhogue, T. Lieuwen, Piv measurements in h2/ch4 swirling flames under near blowoff conditions, in: 5th US Combustion Meeting, Organized by the Western States Section of the Combustion Institute and Hosted by the University of California at San Diego, 2007. 245

[318] S. Chaudhuri, S. Kostka, M. W. Renfro, B. M. Cetegen, Blowoff dynamics of bluff body stabilized turbulent premixed flames, Combust. Flame 157 (2010) 790–802. 245

[319] Q. An, W. Y. Kwong, B. D. Geraedts, A. M. Steinberg, Coupled dynamics of lift-off and precessing vortex core formation in swirl flames, Combust. Flame 168 (2016) 228–239. 245

[320] H. Zhang, E. Mastorakos, Prediction of Global Extinction Conditions and Dynamics in Swirling Non-premixed Flames Using LES/CMC Modelling, Flow, Turbul. Combust. 96 (2016) 863–889. 246

[321] P. C. Ma, H. Wu, J. W. Labahn, T. Jaravel, M. Ihme, Analysis of transient blow-out dynamics in a swirl-stabilized combustor using large-eddy simulations, Proc. Combust. Inst. 37 (2019) 5073–5082. 246

[322] D. L. Black, C. E. Smith, Transient lean blowout modeling of an aero low emission fuel injector, 39th AIAA/ASME/SAE/ASEE Jt. Propuls. Conf. Exhib. (2003) 1–9. 246

[323] A. Tyliszczak, D. E. Cavaliere, E. Mastorakos, LES/CMC of blow-off in a liquid fueled swirl burner, Vol. 92, 2014. 246

[324] P. Palies, R. Acharya, Flame-resolved transient simulation with swirler-induced turbulence applied to lean blowoff premixed flame experiment, Combust. Flame 226 (2021) 14–30. 246, 247

[325] A. Giusti, E. Mastorakos, Detailed chemistry LES/CMC simulation of a swirling ethanol spray flame approaching blow-off, Proc. Combust. Inst. 36 (2) (2017) 2625–2632. 246

[326] D. Farrace, K. Chung, S. S. Pandurangi, Y. M. Wright, K. Boulouchos, N. Swaminathan, Unstructured LES-CMC modelling of turbulent premixed bluff body flames close to blow-off, Proc. Combust. Inst. 36 (2) (2017) 1977–1985. 246

[327] P. C. Nassini, D. Pampaloni, A. Andreini, R. Meloni, Large eddy simulation of lean blow-off in a premixed swirl stabilized flame, in: Turbo Expo: Power for Land, Sea, and Air, Vol. 58615, American Society of Mechanical Engineers, 2019, p. V04AT04A053. 246, 247

[328] L. Tay-Wo-Chong, M. Zellhuber, T. Komarek, H. G. Im, W. Polifke, Combined Influence of Strain and Heat Loss on Turbulent Premixed Flame Stabilization, Flow, Turbul. Combust. 97 (2016) 263–294. 246, 254

[329] J. Piehl, L. Bravo, W. Acosta, G. Kumar, S. Drennan, O. Samimi-Abianeh, On predictions of fuel effects on lean blow off limits in a realistic gas turbine combustor using finite rate chemistry, Proc. ASME Turbo Expo 4B-2018 (2018) 1–10. 246

[330] V. R. Hasti, P. Kundu, G. Kumar, S. A. Drennan, S. Som, S. H. Won, F. L. Dryer, J. P. Gore, Lean blow-out (LBO) computations in a gas turbine combustor, 2018 Jt. Propuls. Conf. (2018) 1–24. 246

[331] I. R. Sigfrid, R. Whiddon, R. Collin, J. Klingmann, Influence of reactive species on the lean blowout limit of an industrial DLE gas turbine burner, Combust. Flame 161 (2014) 1365–1373. 246

[332] S. Wiseman, M. Rieth, A. Gruber, J. R. Dawson, J. H. Chen, A comparison of the blow-out behavior of turbulent premixed ammonia/hydrogen/nitrogen-air and methane–air flames, Proc. Combust. Inst. 38 (2021) 2869–2876. 250

[333] S. Puggelli, D. Veynante, R. Vicquelin, Impact of dynamic modelling of the flame subgrid scale wrinkling in large-Eddy simulation of light-round in an annular combustor, Combust. Flame 230 (2021) 111416. 253

[334] S. Popp, G. Kuenne, J. Janicka, C. Hasse, An extended artificial thickening approach for strained premixed flames, Combustion and Flame 206 (2019) 252–265. 253

[335] N. Klarmann, T. Sattelmayer, W. Geng, F. Magni, Flamelet generated manifolds for partially premixed, highly stretched and non-adiabatic combustion in gas turbines, 54th AIAA Aerosp. Sci. Meet. 0 (2016) 1–14. 278

[336] Y. H. Kwah, P. W. Agostinelli, S. Richard, G. Exilard, S. Pascaud, L. Gicquel, J. R. Dawson, Ignition dynamics of a laboratory-scale spinning combustor, J. Eng. Gas Turbines Power - Accepted. (2022) Presented at ASME Turbo Expo 2022. 286, 297, 298, 299, 304, 305

[337] J.-F. Bourgouin, D. Durox, T. Schuller, J. Beaunier, S. Candel, Ignition dynamics of an annular combustor equipped with multiple swirling injectors, Combustion and Flame 160 (8) (2013) 1398–1413. 298

[338] M. Blanc, P. Guest, G. von Elbe, B. Lewis, Ignition of explosive gas mixtures by electric sparks: III. Minimum ignition energies and quenching distances ofmixtures of hydrocarbons and ether with oxygen and inert gases, Third Symposium on Combustion and Flame and Explosion Phenomena 3 (1) (1948) 363–367. 299

[339] P. Pepiot-Desjardins, H. Pitsch, An efficient error-propagation-based reduction method for large chemical kinetic mechanisms, Combust. Flame 154 (1-2) (2008) 67–81. 324

[340] P. Pepiot-Desjardins, H. Pitsch, An automatic chemical lumping method for the reduction of large chemical kinetic mechanisms, Combust. Theory Model. 12 (6) (2008) 1089–1108. 324

[341] T. Løvås, F. Mauss, C. Hasse, N. Peters, Development of adaptive kinetics for application in combustion systems, Proc. Combust. Inst. 29 (1) (2002) 1403–1410. 324